Geophysical Monograph Series

Including

IUGG Volumes
Maurice Ewing Volumes
Mineral Physics Volumes

Geophysical Monograph Series

119 **Radio Astronomy at Long Wavelengths** *Robert G. Stone, Kurt W. Weiler, Melvyn L. Goldstein, and Jean-Louis Bougeret (Eds.)*

120 **GeoComplexity and the Physics of Earthquakes** *John B. Rundle, Donald L. Turcotte, and William Klein (Eds.)*

121 **The History and Dynamics of Global Plate Motions** *Mark A. Richards, Richard G. Gordon, and Rob D. van der Hilst (Eds.)*

122 **Dynamics of Fluids in Fractured Rock** *Boris Faybishenko, Paul A. Witherspoon, and Sally M. Benson (Eds.)*

123 **Atmospheric Science Across the Stratopause** *David E. Siskind, Stephen D. Eckerman, and Michael E. Summers (Eds.)*

124 **Natural Gas Hydrates: Occurrence, Distribution, and Detection** *Charles K. Paull and Willam P. Dillon (Eds.)*

125 **Space Weather** *Paul Song, Howard J. Singer, and George L. Siscoe (Eds.)*

126 **The Oceans and Rapid Climate Change: Past, Present, and Future** *Dan Seidov, Bernd J. Haupt, and Mark Maslin (Eds.)*

127 **Gas Transfer at Water Surfaces** *M. A. Donelan, W. M. Drennan, E. S. Saltzman, and R. Wanninkhof (Eds.)*

128 **Hawaiian Volcanoes: Deep Underwater Perspectives** *Eiichi Takahashi, Peter W. Lipman, Michael O. Garcia, Jiro Naka, and Shigeo Aramaki (Eds.)*

129 **Environmental Mechanics: Water, Mass and Energy Transfer in the Biosphere** *Peter A. C. Raats, David Smiles, and Arthur W. Warrick (Eds.)*

130 **Atmospheres in the Solar System: Comparative Aeronomy** *Michael Mendillo, Andrew Nagy, and J. H. Waite (Eds.)*

131 **The Ostracoda: Applications in Quaternary Research** *Jonathan A. Holmes and Allan R. Chivas (Eds.)*

132 **Mountain Building in the Uralides Pangea to the Present** *Dennis Brown, Christopher Juhlin, and Victor Puchkov (Eds.)*

133 **Earth's Low-Latitude Boundary Layer** *Patrick T. Newell and Terry Onsage (Eds.)*

134 **The North Atlantic Oscillation: Climatic Significance and Environmental Impact** *James W. Hurrell, Yochanan Kushnir, Geir Ottersen, and Martin Visbeck (Eds.)*

135 **Prediction in Geomorphology** *Peter R. Wilcock and Richard M. Iverson (Eds.)*

136 **The Central Atlantic Magmatic Province: Insights from Fragments of Pangea** *W. Hames, J. G. McHone, P. Renne, and C. Ruppel (Eds.)*

137 **Earth's Climate and Orbital Eccentricity: The Marine Isotope Stage 11 Question** *André W. Droxler, Richard Z. Poore, and Lloyd H. Burckle (Eds.)*

138 **Inside the Subduction Factory** *John Eiler (Ed.)*

139 **Volcanism and the Earth's Atmosphere** *Alan Robock and Clive Oppenheimer (Eds.)*

140 **Explosive Subaqueous Volcanism** *James D. L. White, John L. Smellie, and David A. Clague (Eds.)*

141 **Solar Variability and Its Effects on Climate** *Judit M. Pap and Peter Fox (Eds.)*

142 **Disturbances in Geospace: The Storm-Substorm Relationship** *A. Surjalal Sharma, Yohsuke Kamide, and Gurbax S. Lakhima (Eds.)*

143 **Mt. Etna: Volcano Laboratory** *Alessandro Bonaccorso, Sonia Calvari, Mauro Coltelli, Ciro Del Negro, and Susanna Falsaperla (Eds.)*

144 **The Subseafloor Biosphere at Mid-Ocean Ridges** *William S. D. Wilcock, Edward F. DeLong, Deborah S. Kelley, John A. Baross, and S. Craig Cary (Eds.)*

145 **Timescales of the Paleomagnetic Field** *James E. T. Channell, Dennis V. Kent, William Lowrie, and Joseph G. Meert (Eds.)*

146 **The Extreme Proterozoic: Geology, Geochemistry, and Climate** *Gregory S. Jenkins, Mark A. S. McMenamin, Christopher P. McKay, and Linda Sohl (Eds.)*

147 **Earth's Climate: The Ocean–Atmosphere Interaction** *Chunzai Wang, Shang-Ping Xie, and James A. Carton (Eds.)*

148 **Mid-Ocean Ridges: Hydrothermal Interactions Between the Lithosphere and Oceans** *Christopher R. German, Jian Lin, and Lindsay M. Parson (Eds.)*

149 **Continent-Ocean Interactions Within East Asian Marginal Seas** *Peter Clift, Wolfgang Kuhnt, Pinxian Wang, and Dennis Hayes (Eds.)*

150 **The State of the Planet: Frontiers and Challenges in Geophysics** *Robert Stephen John Sparks and Christopher John Hawkesworth (Eds.)*

151 **The Cenozoic Southern Ocean: Tectonics, Sedimentation, and Climate Change Between Australia and Antarctica** *Neville Exon, James P. Kennett, and Mitchell Malone (Eds.)*

152 **Sea Salt Aerosol Production: Mechanisms Measurements, Methods and Models** *Ernie R. Lewis and Stephen E. Schwartz (Eds.)*

153 **Ecosystems and Land Use Change** *Ruth S. DeFries, Gregory P. Anser, and Richard A. Houghton (Eds.)*

154 **The Rocky Mountain Region: An Evolving Lithosphere** *Karl E. Karlstrom and G. Randy Keller (Eds.)*

Geophysical Monograph 155

The Inner Magnetosphere: Physics and Modeling

Tuija I. Pulkkinen
Nikolai A. Tsyganenko
Reiner H.W. Friedel
Editors

American Geophysical Union
Washington, DC 2005

Published under the aegis of the AGU Books Board

Jean-Louis Bougeret, Chair, Gray E. Bebout, Cari T. Friedrichs, James L. Horwitz, Lisa A. Levin, W. Berry Lyons, Kenneth R. Minschwaner, Andy Nyblade, Darrell Strobel, and William R. Young, members.

Library of Congress Cataloging-in-Publication Data

The inner magnetosphere: physics and modeling / Tuija I. Pulkkinen, Nikolai A. Tsyganenko, Reiner H.W. Friedel, editors.
p. cm. — (Geophysical monograph, ISSN 0065-8448; 155)
Includes bibliographical references and index.
ISBN 0-87590-420-3
1. Magnetospheric physics—Simulation methods. I. Pulkkinen, T. (Tuija), 1962- II. ëTiSyganenko, N.A. III. Friedel, Reiner H.W. IV. American Geophysical Union. V. Series.

QC809.M35I476 2005
538'.766—dc22
2005015772

ISBN 0-87590-420-3
ISSN 0065-8448

CONTENTS

III. External Driving of the Inner Magnetosphere

IV. Observational Specification of the Inner Magnetosphere

V. Large-Scale Models of the Inner Magnetosphere

PREFACE

As we become a space-faring culture, there is an increasing need for reliable methods to forecast the dynamics of electromagnetic fields, thermal plasma, and energetic particles in the geospace environment, as all these factors affect satellite-borne systems. From the electrodynamics viewpoint, on the other hand, the inner magnetosphere is a key element in the Sun-Earth connection chain of processes. Most notably, it is a region where a significant part of the storm-time energy input from the solar wind is deposited and dissipated.

Because the most interesting and crucially important phenomena, as noted, develop relatively close to Earth (in the transition region separating the innermost quasi-dipolar geomagnetic field from the magnetotail), understanding them is a complex task. Moreover, the stronger the disturbance, the deeper its impact penetrates into the inner magnetosphere. In this region plasma no longer behaves like a fluid, and the motion of energetic charged particles becomes important for the dynamics of the system. This fact leaves "particle simulations" as a primary tool for studying and understanding the dynamics of the inner magnetosphere during storms. An integral element of such simulations is an electromagnetic field model. Recent studies of the inner magnetosphere have substantially improved our understanding of its dynamics while creating new paradigms and reviving old controversies.

In this book we focus on clarifying issues related to the physics and structure of the inner magnetosphere. Toward this end, David Stern introduces the main part of the monograph with a brief historical review of early ring current studies. Five sections follow. Section I, which deals with the sources and losses of plasma and energetic particles in the inner magnetosphere, opens with two invited reviews (by Jordanova and Koskinen) and includes five contributed papers. Section II concentrates on the acceleration mechanisms, as addressed in an invited review by Baker and in six contributed papers. Section III analyzes external driving mechanisms of the inner magnetosphere, a subject of a long-standing debate that recently gained renewed interest by way of latest particle simulation results. It opens with an invited review (Ganushkina), followed by five contributed papers. Section IV focuses on some observational aspects of inner magnetosphere dyamics. Its lead, review paper (by Green and Fung) on electromagnetic wave studies in the inner magnetosphere would equally well fit in sections I or II, as such waves are an essential factor in particle loss and acceleration processes. The last section V contains five papers on large-scale modeling efforts of the inner magnetosphere, including latest results from using the RCM approach in modeling electric fields as well as MHD simulations.

In our effort to organize a forum on current understanding of processes in inner geospace, a Chapman Conference on the Physics and Modeling of the Inner Magnetosphere was held August 25-29, 2003, in Helsinki, Finland. This monograph largely derives from papers presented at that meeting. The monograph became possible owing to the help of many people. We are grateful to the members of the Program Committee: Joe Borovsky, Ioannis Daglis, Toshihiko Iyemori, Janet Kozyra, Rumi Nakamura, Joe Lemaire, Xinlin Li, and Victor Sergeev. We acknowledge the many scientists who served as referees for the papers in this monograph, and who provided numerous helpful, candid, and insightful critical comments. Their names are given below in a separate list. We also thank AGU book staff for their expert help in developing and producing this book.

Financial assistance from the National Science Foundation, NASA's Living With The Star Program, Academy of Finland, and the Vilho, Kalle and Yrjö Väisalä Foundation made it possible to support the participation of several students and young scientists in the Conference. The local organizing committee and the staff at the Finnish Meteorological Institute are gratefully acknowledged for smooth running of the Conference.

Tuija I. Pulkkinen
Nikolai A. Tsyganenko
Reiner H.W. Friedel

The Inner Magnetosphere: Physics and Modeling
Geophysical Monograph Series 155

10.1029/155GM00

List of reviewers

J. Albert, B. Anderson, R. Anderson, J. Berchem, P. Bespalov, J. Birn, J. Borovsky, D. Boscher, C. Cattell, I. Daglis, D. Delcourt, A. Dessler, M. Duldig, Y. Ebihara, S. Elkington, J. Foster, E. Flueckiger, N. Ganushkina, D. Hamilton, D. Heynderickx, T. Hill, F. Honary, R. Horne, J. Horwitz, M. Hudson, P. Janhunen, J. Jussila, S. Kanekal, T. Kikuchi, A. Klimas, W. Lennartsson, M. Liemohn, X. Li, G. Lu, R. Lysak, Y. Maltsev, R. Millan, M. Moldwin, T. Moore, D. Murr, R. Nakamura, P. Newell, T. O'Brien, S. Ohtani, T. Obara, Y. Omura, N. Ostgaard, C. Owen, J. Raeder, R. Rankin, G. Reeves, P. Reiff, B. Reinisch, A. Ridley, M. Schulz, R. Selesnick, K. Shiokawa, D. Sibeck, G. Siscoe, M. Sitnov, D. Smart, P. Song, H. Spence, R. Spiro, D. Stern, L. Svalgaard, M. Taylor, M. Thomsen, R. Thorne, B. Tsurutani, D. Vassiliadis, V. Vasyliunas, D. Weimer, R. Wolf.

A Historical Introduction to the Ring Current

David P. Stern

Laboratory for Extraterrestrial Physics (Emeritus), Goddard Space Flight Center, Greenbelt, Maryland

"One ring to rule them all" *(Vayliunas [1972], citing Tolkien)*

The first global observations of magnetic storms in the mid-1800s suggested that at such times a huge electric current circled the Earth, later named the ring current. Only in the satellite era was its nature established: carried mainly by ions around 20-200 *keV* which are trapped on field lines with L = 2-7, it is present at all times but is greatly reinforced during magnetic storms. Initially all ions were assumed to come from the solar wind, but after 1972 when trapped O^+ ions were also detected, it was gradually realized that ions drawn from the ionosphere and accelerated were major contributors. Attention has now returned to the magnetic storm, source of practically all the ring current, and to the electric fields which energize its ions. This short review traces the history of ring current research, and cites reviews and research articles where further details can be found.

DISCOVERY OF THE RING CURRENT

Magnetic storms were first observed in the 1700s, but it was Alexander von Humboldt who proposed the name. Humboldt, together with Gauss, Sabine and others, set up the first world-wide network of magnetic observatories (see *Stern* [1989, 1996, 2002]), which quickly showed such storms were world-wide, displaying essentially the same signature all around the equator. Typically, the north-south component of the field would decrease within a few hours by about 50-100 *nT*, then gradually recover over a day or longer. It was as if a huge electric current was temporarily turned on, circling the Earth's equator, and *Adolf Schmidt* [1916] named it the Ring Current.

Around 1850 the sunspot cycle was recognized, and shortly afterwards Sabine and others (see *Cliver* [1994a, b, 1995]) found a correlation between sunspot activity and large magnetic storms. In 1859, by a rare chance, Richard Carrington observed a large white-light flare erupt near a sunspot region, followed within a day by an extreme magnetic storm [*Tsurutani et al.*, 2003]. Although this observation stood alone for many years, it ultimately turned out that storms were indeed closely correlated with flares, and more recently, with coronal mass ejections. Big storms also tended to be accompanied by displays of the polar aurora ("northern lights") far equatorward from their usual locations–as far as Cuba, in 1859.

Around 1905 Maunder pointed out that moderate storms, recurring one solar rotation apart, tended to cluster near sunspot minimum; such storms are now seen [*Dessler and Fejer*, 1963] as triggered by the fast solar wind streams which define the interplanetary magnetic sector structure during low sunspot activity.

The location of the ring current, and the way the Sun promoted magnetic storms and auroral displays, remained a deep mystery for a long time. As recently as 1956, *Parker* [1956] proposed that the storm-time ring current might flow in the upper ionosphere, at an altitude of the order of 400 *km*. In that view, it was caused by the heating of the upper neutral atmosphere, causing it to lift the highly conducting outer layers. Those layers, assumed (as an approximation) to be perfectly conducting, carried with them, outwards, embedded magnetic field lines, causing the main field to weaken. A similar idea was later applied by Parker as "magnetospheric inflation" to more realistic models.

The Inner Magnetosphere: Physics and Modeling
Geophysical Monograph Series 155

10.1029/155GM01

He was challenged by *Hines* [*Hines*, 1957; *Parker*, 1958; *Hines and Parker*, 1958] who pointed out, among other things, that the ambient magnetic field inhibited electric currents driven by electric fields perpendicular to field lines. Those studies were largely based on the known MHD of isotropic plasma, while what was needed at this point was a better appreciation of the role of particle motion in a magnetic field.

Particle motion was first addressed around the turn of the 20th century in the work of Kristian Birkeland. Trying to model the polar aurora, Kristian Birkeland during the decade 1895-1905 aimed beams of electrons at a magnet (or away from it) in a vacuum chamber and noted they were steered towards the poles. His associate Carl Störmer tried to calculate their motion in a dipole field and soon showed (see *Stoermer* [1956]) that trapped orbits existed, which in principle could carry a ring current, though the energies he studied were unexpectedly high. Only in 1957 did *Singer* [1957] point out that low-energy ions and electrons could also be responsible, if present in sufficient numbers. He also showed that their motion could be calculated using the guiding center approximation, introduced by *Alfvén* [1950], yielding a motion similar to the one derived by Störmer using laborious integration. Then in 1957 artificial satellites entered the scene, making it possible to study the ring current *in-situ*.

Sorting out the observations took time. Van Allen's inner belt (1958) carried too little current to explain magnetic storms, and was also rather steady. Its protons (around 50 *MeV*) turned out to accumulate gradually from cosmic ray albedo; auroral particles, identified from stopping range and rocket data as electrons in the 10 *keV* range, were quite different. Clues to the actual situation came from Pioneer 3 (1958) and Pioneer 4 (1959) which observed an "outer belt" typically extending to 6-8 R_E (Earth radii) [*Van Allen and Frank*, 1959].

Sonnett et al. [1960], using Explorer 6 observations, were the first to note a decrease in the magnetic field due to the ring current, at distances of 6-7 R_E, a decrease now regularly monitored by synchronous satellites [*Rufenach et al.*, 1992]. Using a scattering experiment, aboard Explorer 12, *Davis and Williamson* [1963] showed that the outer belt had fluxes of positive particles above 200 *kev*, steeply dropping with growing energy; the maximum flux seemed to be in the unobserved region below 200 *keV*. That might have been the first clear observation of what is now recognized as the ring current ion population. At the same time, the idea of the storm-time ring current became better defined [*Parker and Dessler*, 1959].

Gradually satellites added information. *Lou Frank* [1967] using OGO 3 observed a large population of ions (presumed to be protons) of up to 50 *keV*, and later [*Frank*, 1971] showed it to be contiguous with that of the near-Earth plasma sheet. *Sugiura* [1972], using OGO3 and OGO 5, mapped the magnetic disturbance due to the quiet ring current and showed a field depression peaking at 35 *nT* at a radial distance of 3 R_E, extending further at midnight than at noon and concentrated within 2 R_E of the equatorial plane. Further from the equator the Earth field was strengthened.

The effects at Earth of the quiet-time ring current and cross tail current (hard to separate) amount to about 40 *nT*, southwards. When spherical harmonics of the main field were extracted from the data of the near-Earth magnetic survey satellite Magsat [*Langel and Estes*, 1985], it was found necessary to include a southward field of about 20 *nT*. Models give a northward magnetopause field of about 20 *nT*, so the ring and tail currents contribute −40 *nT*.

Even before trapped O^+ ions were observed by *Shelley et al*, [1972] (see further below), it had become clear that existing information about the ring current contained a huge gap [*Williams*, 1983]. Trapped ions had been observed below about 20 *keV* and above 200 *keV*, but not in the range in between, which seemed to contain most of the current and energy. The gap was finally closed (e.g. *Hamilton et al.*, 1988, also see *Daglis et al.* [1999]) by spacecraft with mass spectrometers, especially by CCE (Charge Composition Explorer, apogee 8.8 R_E) of the AMPTE mission, and by CRRES (Combined Release and Radiation Effects Satellite, initial apogee 6.3 R_E), a joint NASA-USAF mission. Both suggested a population peaking around 65 *keV*, although that peak, the energy distribution and the heavy ion content varied greatly with time.

AMPTE covered a time of low solar activity (just one large storm) and thus established a baseline inner ring current (3.5-7 R_E) for the quiet magnetosphere, with current density j averaging 1-4 nA/m^2 and peaking at 4-8 nA/m^2 [*Lui and Hamilton*, 1992]. CRRES operated during high solar activity and observed a number of large storms, including one on 3.24.1991, when a large interplanetary shock caused an abrupt acceleration of ions and electrons to 15-20 *MeV* [*Blake et al.*, 1992].

HOW DO THEY ENTER?

Early views of how ring current particles might enter the Earth's magnetic trap were speculative and uncertain [*Alfvén* 1939; *Smith*, 1963]. Ultimately the electric field $\boldsymbol{E}$ was recognized as the essential ingredient, an idea due to Alfvén. It is often advantageous to represent such $\boldsymbol{E}$ by the bulk flow velocity $\boldsymbol{u} = \boldsymbol{E} \times \boldsymbol{B}/B^2$ which it produces, also known as "the velocity of magnetic field lines" since it preserves the sharing of field lines by particles. A static electric field can be conveniently represented by a scalar potential Φ which, given $\boldsymbol{E}.\boldsymbol{B} = 0$, is also constant along magnetic field lines, but if $\partial \boldsymbol{B}/\partial t \neq 0$, one cannot easily use Φ, while using the bulk

velocity $\boldsymbol{v}$ to describe the electric field (especially with $\boldsymbol{E}.\boldsymbol{B} = 0$) remains appropriate and intuitively meaningful.

That was the approach used by *Dungey* [1961], who suggested that "magnetic reconnection" of the Earth's magnetic field lines with the interplanetary magnetic field (IMF) greatly strengthened the linkage to the solar wind and produced inside the magnetosphere a "global convection," a pattern of bulk flow. *Axford and Hines* [1961] pointed out that similar convection might accompany viscous-like momentum transfer at the magnetopause. Dungey's reconnection idea seemed confirmed when *Fairfield* [1966] noted that magnetic activity was enhanced during periods when the B_z component in the interplanetary magnetic field (IMF) pointed southward, and was suppressed when it pointed northward. Southward B_z (henceforth denoted B_s) allowed Earth-IMF interconnection with a minimum of bending of field lines.

These theories and others [*Axford, Petschek and Siscoe*, 1965] suggested that the source region for trapped particles might be an extended tail on the Earth's night side, and indeed IMP-1, launched in 1963, observed an equatorial plasma sheet there. Observations by *Frank* [1971] and *Vasyliunas* [1968] demonstrated that populations of ring current ions and electrons were contiguous with those of the plasma sheet (see also *Lui and Hamilton* [1992]). This led to a consensus that magnetic substorms and storms produced an intense temporary $\boldsymbol{E}$, convecting plasma sheet particles into the ring current region, where they were stranded when the surge subsided. In substorms such injections were observed by ATS1, 5 and 6 in synchronous orbit [*De Forest and McIlwain*, 1971], but there they did not seem to contribute a significant global ring current field.

THE ELECTRIC FIELD *E*

Where did $\boldsymbol{E}$ come from? In Dungey's crude model, moving "open" field lines connect to the "polar cap," a circular patch around the magnetic pole. They cause there a dawn-to-dusk electric field $\boldsymbol{E}$, consistent with their tailward motion (a subtle point to which we return later). Such $\boldsymbol{E}$ was indeed observed in low Earth orbit by Injun 5 and OGO 6 [*Cauffman and Gurnett,* 1971; *Heppner*, 1972]. In the simplest model–vacuum dipole plus constant southward field–the polar cap is a circle with a dawn-to-dusk polar field and with lines of constant potential Φ in the noon-midnight direction (the slightest asymmetry messes up this neat picture [*Stern*, 1973], but we ignore that now). Outside that circle, a fringing $\boldsymbol{E}$ is spread out by the ionosphere, which may be modeled as a sheet conductor with some (anisotropic) 2-D conductivity Σ [*e.g. Vasyliunas*, 1970, 1972; *Siscoe*, 1982; *del Pozo and Blanc*, 1994].

Where this situation is static, $\boldsymbol{E}$ in the ionosphere can be represented by a scalar potential Φ which, being constant along field lines, brings $\boldsymbol{E}$ along such lines to other parts of the magnetosphere. At every point this $\boldsymbol{E}$ causes a bulk flow $\boldsymbol{u} = \boldsymbol{E} \times \boldsymbol{B}/B^2$ (the bulk flow along $\boldsymbol{B}$ needs to be derived from other considerations), which provides the return flow of Dungey's model. One might expect $\boldsymbol{E}$ (and $\boldsymbol{u}$) to be kept out of the Earth's immediate vicinity by $\boldsymbol{E}_{cor}$, the electric field due to co-rotation of the ionosphere; $\boldsymbol{E}_{cor}$ diverts the flow around Earth, and it ultimately exits on the dayside magnetopause. If however the driving $\boldsymbol{E}$ fades before this motion is complete, convected particles are left magnetically trapped, and add to the ring current.

Vasyliunas [1970, 1972] showed that the presence of plasma in the inner magnetosphere greatly modifies this $\boldsymbol{E}$, in a way which can be represented, in this simple dipole model, by adding an extra Hall term Σ^* to the ionospheric conductivity in regions threading that plasma. The value of Σ^* is an integral over the plasma density–the more plasma, the larger Σ^*–and its effect is to rotate the external field and also weaken it, limiting its penetration close to the Earth. Such shielding-out of $\boldsymbol{E}$ has been observed, and was modeled by *Volland* [1973] and *Stern* [1975] using empirical approximate models, containing parameters which need be derived from data in each case. It is derived numerically, more accurately but still approximately, by the "Rice Convection Model" described further below.

To account for the inflow of plasma from the tail, one must include a cross-tail $\boldsymbol{E}$, originating from the fringing $\boldsymbol{E}$ in the polar ionosphere or from other sources. It is also directed dawn-to-dusk and is a feature of the models of Dungey and of Axford and Hines. Actually observed flows are highly variable, suggesting $\boldsymbol{E}$ is strongly time-dependent, with return flow occurring mainly during substorms; details are still being debated. *Schield et al.* [1969] realized that as such plasma was convected earthward, not only were its particles energized adiabatically, but they also ultimately reached a region where magnetic drifts became appreciable; they named it the "Alfvén layer" since Alfvén in 1939 predicted a somewhat similar process (assuming however plasma originating on the day side). Those drifts (unlike $\boldsymbol{u}$) do separate ions and electrons–ions drift towards dusk, electrons towards dawn–and to maintain charge neutrality, electric currents must flow in and out of the ionosphere, named Birkeland currents. In the notation of *Zmuda and Armstrong* [1973] who traced the global pattern of such currents, these are "region 2" (R2) Birkeland currents. If $\boldsymbol{E}$ in the polar cap ionosphere (a conductor) comes from the sheath along open lines, we may visualize the currents which convey it there as "region 1" (R1).

The local equations governing this process were derived and studied by *Vasyliunas* [1970]. The R2 currents close through the ionosphere and create there potential drops, which are propagated back along closed field lines and further affect the convection of plasma from the tail.

All these processes make the physics of convection into the inner magnetosphere too complicated to handle analytically. The first numerical solution, by *Jaggi and Wolf* [1973] at Rice University, was followed by a series of increasingly sophisticated versions of the "Rice Convection Model" (RCM). Later the RCM included details of the particle distribution function and ionospheric properties, but it did not model changes in the magnetic field $\boldsymbol{B}$. Some of the most recent results, combining MHD modeling of the global magnetosphere with the RCM approach, are reported in this monograph by [*Sazykin et al.*].

ACCELERATION PROCESSES

One would expect ions and electrons to be accelerated adiabatically as they convect from the weak field and long field lines of the plasma sheet to the strong field and short lines of the inner magnetosphere. This does happen, but the process is complicated by the time dependence of the electric field. It may take more observations, simulation and theory to clarify, for instance, the "injection boundary" phenomenon [*McIlwain*, 1974], which claimed particles were energized almost simultaneously along a line roughly following the earthward edge of the equatorial plasma sheet.

Another type of "instantaneous" acceleration was observed by CRRES [*Blake et al.*, 1992] at $L \sim 2.6$ on the sunward side, following the arrival of a strong interplanetary shock on 3.24.1991, and was explained by *Li et al.* [1993]. Ions and electrons inside the magnetosphere were accelerated by the shock almost instantaneously to 15 *MeV* and more. Other abrupt accelerations were reported at this meeting by *Baker et al.* and *Elkington et al.*, associated with the storm of 3.31.2001. Such events may be particularly important in accelerating *MeV* electrons of the outer radiation belt, as reported here by *Fennel et al.* Those electrons cause spurious signals in electronic circuits aboard spacecraft and are therefore a source of concern to mission planners; their source is still uncertain [*Li and Temerin*, 2001].

O^+ IONS

During the 1960s conventional wisdom held that all ring current ions originally entered from the solar wind, a-la Dungey, then convected into the inner magnetosphere from the tail, becoming adiabatically energized in the process. Then *Shelley et al.* [1972] reported observing energetic O^+ ions in the inner magnetosphere, probably coming from the ionosphere since oxygen in the solar wind is typically in the O^{6+} state.

Two processes responsible for accelerating such ions were first inferred using the S3-3 satellite [*Mozer*, 1977]. Both are by-products of near-Earth acceleration of auroral electrons by $E_{//}$ associated with Birkeland currents, mainly currents directed away from the ionosphere carried largely by precipitating electrons. To flow through the resistive ionosphere, such a current must be driven by (or generate) some voltage. Apparently, some of that available voltage is redirected to create $E_{//}$, which helps precipitating electrons overcome the mirror force; such $E_{//}$ expands the loss cone and makes possible a greater current density. As shown by *Persson* [1963; *see also Boström*, 2003, 2004] and confirmed observationally by *Evans* [1974], $E_{//}$ is concentrated near Earth, agreeing with simple theory which predicts a voltage proportional to $/B/$.

The same electric field also extracts O^+ ions from the ionosphere, accelerating them as upward beams, though because of their low mobility, they do not carry much current. Such ions were observed by S3-3, and more recently in greater detail by the FAST mission.

In addition, the non-maxwellian distribution function of accelerated electrons leads to local plasma instability, causing waves which heat O^+ ions, primarily in their velocity component perpendicular to $\boldsymbol{B}$. Such accelerated ions were observed higher up as "conics," velocity distributions peaked at some intermediate pitch angle, which by adiabatic conservation translated to 90° pitch at the (lower) altitude where perpendicular heating occurred.

If the motion of accelerated O^+ ions were strictly adiabatic, they would continue bouncing back and forth along their guiding field lines, gradually drifting to neighboring ones. Ion beams accelerated south of the equator would come down north of it, gradually getting reflected by a combination of the mirror force and $E_{//}$. This is not usually seen, suggesting active scattering by plasma waves far from Earth, helping such ions join the regular ring current.

It was estimated by *Daglis et al.* ([1999], Table 1) that at quiet times O^+ accounts for about 5% of the ring current population, rising to about 30% in small and medium storms, and 60% or more in intense ones; *Hamilton et al.* [1988] found that at the peak of one storm oxygen and nitrogen ions accounted for 59% of the energy density at $L = 3$-5. Ionospheric H+ in the three ranges is credited with about (30+, ~20, 10) percent. Typically 2-4% of the ring current consists of He++ (alpha particles) presumed to come from the solar wind, and of He+ (about 1%), which may come either from the ionosphere or from charge exchange collisions of He++ and neutral hydrogen.

THE QUIET-TIME RING CURRENT AND LIFETIMES OF PARTICLES

The ring current density $\boldsymbol{j}$ is contributed almost entirely by positive ions, which carry most of the energy. Even so, electron fluxes are much larger than ion fluxes, since both species

have the same density, but the lighter electrons move much faster; therefore spacecraft charging in the inner magnetosphere (distorting observations and sometimes causing damage) is due to fast electrons. Two components of $\boldsymbol{j}$ may be distinguished–the current due to actual transport by drifting charges, always flowing westward, and the magnetization current $\nabla\times\boldsymbol{M}$ ($\boldsymbol{M}$ is the density of magnetic moment) through which the plasma distribution modifies the profile of $\boldsymbol{j}$. In a relatively narrow band at the inner edge of the ring current, where the plasma pressure p drops sharply, $\nabla\times\boldsymbol{M}$ actually reverses the direction of $\boldsymbol{j}$, causing it to flow eastwards. In an isotropic plasma the sum-total current depends just on ∇p. Data-based models of $\boldsymbol{B}$ and $\boldsymbol{j}$ of the ring current were developed by *Tsyganenko* [2002].

Assuming that ring current ions are stably trapped, their lifetime is determined by loss processes, of which the most significant is charge exchange collisions with neutral hydrogen, a process first proposed by *Parker and Dessler* [1959] and analyzed in greater detail by *Liemohn* [1961]. Hydrogen forms the geocorona, the outermost layer of the atmosphere, a large cloud of hydrogen surrounding Earth up to 3-5 R_E, with a steep density gradient. It is the source of energetic neutral atoms (ENA) used by the IMAGE mission and by Polar for remotely sensing the ring current [*Williams, Roelof and Mitchell*, 1992]. For more about charge exchange lifetimes, see *Smith and Bewtra*, [1978]. At $L = 5$, lifetimes of near-equatorial 10 *keV* ions of (O^+, H+) are about (56, 17) hours, dropping to (28, 5.5) hours at $L = 3.5$; the charge-exchange cross section of H+ ions drops steeply above 50 *keV*, giving lifetimes of (11, 110) hours for 100 *keV* ions at $L = 3.5$ [*Daglis et al*, 1999]. Ions with smaller pitch angles dip deeper into the geocorona and have therefore much shorter lifetimes, leading to a pancake-shaped ring current.

The stormtime ring current, gauged by the *Dst** index (next section), usually decays slowly during the recovery phase of a storm, a process ascribed to charge exchange. Big storms near their peak, however, have a much faster decay, around 1-2 hours. A widely held explanation [*Liemohn et al.*, 2001] is that a majority of *Dst** at such times (up to 80%) comes from the partial ring current (PRC) of injected ions which are not trapped but enter from the night side and exit again on the day side, after an hour or two.

GAUGING THE RING CURRENT

A magnetic storm adds to the energy W of the ring current, by bringing in tail plasma and also by compressing the existing ring current; in both cases particles are convected into stronger $\boldsymbol{B}$ and shorter field lines, and adiabatically gain energy. The main magnetic signature of this process is an added southward contribution ΔB near Earth, weakening the field at the Earth's equator. *Dessler and Parker* [1959] used a simple model of the ring current to show that W was approximately proportional to ΔB (see also *Vasyliunas* [2001b]). Their formula was later shown by Sckopke [1966] to have a wider applicability, although *Carovillano and Siscoe* ([1973]; see also Liemohn, [2003]) showed it was not exact, just a fair approximation. The "DPS formula" is

$$\Delta B/B_0 = 2W/3W_m$$

where $B_0 \sim 30{,}000\ nT$ is the field at the dipole equator and $W_m \sim 8.10^{17}$ joule is the energy of the dipole field above the surface of the Earth.

The most common measure of ΔB is the *Dst* index, introduced by *Sugiura* [1964]. It averages the magnetic disturbance at 4 near-equator stations, corrected for latitude and for the *Sq* variation, and usually has a negative sign, signifying a weakening of the field. The actual ΔB due to the storm's ring current is often greater than what is observed, because observations also include an opposing ΔB due to compression of the magnetosphere, caused by increased pressure p of the solar wind. A corrected *Dst* index, due to injected ions alone, is usually derived afterwards (also denoted *Dst**), with an added term proportional to $p^{1/2}$.

Gonzalez et al. [1994] in their review of magnetic storms classified storms by the range to which their peak *Dst* (in *nT*) belonged, as small (−30,−50), moderate (−50,−100) and intense (<−100). In the intense storm of 4 November 2003 the initial estimate of *Dst* was −430 *nT*

THE NATURE OF MAGNETIC STORMS

Both storms and substorms involve intense plasma convection from the tail. Substorm convection can be observed at 6.6 R_E [*e.g. DeForest and Mozer*, 1971] but it does not seem to produce a significant ΔB, the way convection in a magnetic storm does. Both require a southward component B_s of the IMF [*Fairfield*, 1966]. The consensus is that while most substorms reflect "unloading" of energy stored in the tail, magnetic storms are "directly driven" by a strong coupling to the sheath and solar wind, along open field lines. The greater strength of that coupling seems to make the difference.

Analyzing magnetic observations in space from 37 storms, *Tsyganenko* [2003] found that in intense storms (*Dst* < −250 *nT*), even field lines near Earth, e.g. around $L = 3$, are severely stretched tailwards by the magnetic effects of the enhanced ring current. He concluded that this tail-like behavior at low L could explain why at the peak of large storms the electrojet and auroras descend to middle latitudes; so does the cusp [*Meng*, 1983]. The anomalous growth of the ring current may be similar to the blowing up of a rubber balloon: past a certain point, as the rubber thins out, resistance seems to drop and expansion becomes easier.

Several factors contribute to this strong coupling. The southward field B_s must be large and have a long duration ΔT. *Gonzalez et al.* [1994] in their detailed review of magnetic storm studies give minimum values of B_s for (small, moderate, large) storms as (3,5,10) nT and of ΔT as (1,2,3) hours. A study of 64 cases when the magnetopause was pushed back inside synchronous orbit [*Rufenach et al.*, 1989] contained only 8 cases with northward B_z, always small.

Large storms are often associated with magnetic clouds [*Burlaga and Behannon,* 1982; *Gonzalez et al.*, 1994, 1999], flux ropes associated with coronal mass ejections (CMEs); large B_s is often observed when Earth either enters or leaves them, and also in the "sheath" they pile up as they plow through the regular solar wind. Storms are also helped by fast streams in the solar wind, low in density but high in velocity; *Gonzalez et al.* [1994] implicate them in (23%, 45%, 90%) of (small, moderate, large) storms (see above). The correlation between such streams and moderate recurring storms around sunspot minimum was already noted by Maunder and was recently studied by *Tsurutani et al* [1995].

This effect of streams may be related to the role of the Earth's bow shock in Earth-solar wind coupling along "open" field lines. Such lines are often portrayed as conducting wires rooted on Earth but extending into the solar wind ([*Stern*, 1973], mea culpa), mapping the $\boldsymbol{v} \times \boldsymbol{B}$ field of the solar wind into the ionosphere. However, as *Vasyliunas* [2001a] has pointed out, open lines may not spread electric field the way wires do. With an open field line, part of it inside the magnetopause and part outside, the outer part may be bent by plasma flow, but this alone need not drag its interior portion along.

What changes this picture is the finite temperature of the plasma. Freshly reconnected "open" lines contain sheath plasma recently heated in the bow shock. Such plasma, because of its temperature, will spill over into the terrestrial part of the field line, imparting there momentum acquired with the solar wind. This momentum transfer causes near-Earth parts of open lines to keep pace with the outer parts (perhaps initially lagging somewhat). Along with this bulk flow comes the appropriate $\boldsymbol{E}$, passed to the ionosphere at the roots of the field lines. Ions in fast streams of the solar wind have more kinetic energy, get hotter after passing the bow shock, and hence create a stronger coupling to closed field lines. Interplanetary shocks may also provide heating.

To trace the origin of storms it is therefore necessary to study the region where open lines (and presumably, Region 1 Birkeland currents) enter the magnetosphere. Although "Polar" may have covered that region, better satellite coverage by constellations of satellites may be essential, especially since at times of magnetic storms, such locations probably shift rapidly.

CONCLUSION

Fashions in science come and go, but the long term well-being of a scientific area depends on the number and quality of its unsolved puzzles. In that respect, prospects for the study of the ring current and inner magnetosphere are good. To switch metaphors, it is now past the foothills, to where the high peaks are in sight–the nature of magnetic storms, the way the sheath is coupled to the polar cap and the tail to the near-Earth plasma, and above all, the way in which convection $\boldsymbol{E}$ arrives and develops. There may yet be exciting times ahead.

Acknowledgments. The author thanks Bill Burke, David Sibeck, Gang Lu, Mei Fok and especially Kolya Tsyganenko for their sage advice, as well as the two referees.

REFERENCES

Alfvén, Hannes, A theory of magnetic storms and of the aurorae, *K. Sven. Vetenskapakad., Handl.*, Ser. 3, 18(3), 1939. (Reprinted in part with comments by Alex Dessler and John Wilcox in *Eos*, 51, 180-194, 1970).

Alfvén, Hannes, *Cosmical Electrodynamics*, Oxford University Press, 1950.

Axford, W. Ian and Colin O Hines, A unifying theory of high-latitude geophysical phenomena and geomagnetic storms, Canad. *J. Phys.*, 39, 1433-1464, 1961.

Axford, W. Ian, Harry E. Petschek and George L. Siscoe, Tail of the magnetosphere, *J. Geophys. Res.*, 70, 1231-1236, 1965.

Blake, J.B, W.A. Kolasinski, R.W. Fillius and E.G. Mullen, Injection of electrons and protons with energies of tens of *MeV* into $L < 0$ on 24 March 1991, *Geophys. Res. Lett.*, 19. 821-4, 1992.

Boström, Rolf, Kinetic and space charge control of current flow and voltage drops along magnetic flux tubes. Kinetic effects, *J. Geophys Res.*, 108, (A4), Article COA5, citation 8004, 2003.

Boström, Rolf, Kinetic and space charge control of current flow and voltage drops along magnetic flux tubes, 2., Space charge effects, *J. Geophys Res.*, 109 (A1), Article A01208, 2004.

Burlaga, L.F. and K.W. Behannon, Magnetic clouds: Voyager observations between 2 and 4 AU, *Solar Physics.*, 81, 181-192, 1982.

Carovillano, R.L and G.L. Siscoe Energy and momentum theorems in magnetospheric processes, *Rev. Geophys.*, 11, 289-353, 1973.

Carringtron, Richard C., Description of a Singular Appearance seen in the Sun on September 1, 1859, M.N.R.A.S. vol. 20, 13-15, 1860 (see also http://adsbit.harvard.edu/cgi-bin/nph-iarticle_query?bibcode=1859MNRAS..20...13C).

Cauffman, P. David and Donald A. Gurnett Double-probe measurement of convection electric fields with the Injun 5 satellite, *J. Geophys. Res.*, 76, 6014-6027, 1971.

Cliver, E.W. Solar Activity and Geomagnetic Storms: The First 40 Years, *Eos*, 75, p. 569, 574, 575, 6 December 1994.

Cliver, E.W. Solar Activity and Geomagnetic Storms: The Corpuscular Hypothesis, *Eos 75*, 609, 612, 613, 27 December 1994.

Cliver, E.W. Solar Activity and Geomagnetic Storms, *Eos* 76, p. 55, 83, 21 Feb 1995.

Daglis, Ioannis, Richard M. Thorne, Wolfgang Baumjohann and Stefano Orsini, The Terrestrial Ring Current: Origin, Formation, and Decay, *Rev. Geophys.*, 37, 407-38, 1999.

Davis, Leo R. and J.M. Williamson, Low energy trapped protons, *Space Research*, 3, 365-375, North Holland Publ. Co., 1963.

DeForest, Sherman E. and Carl E. McIlwain, Plasma clouds in the magnetosphere, *J. Geophys. Res.*, 76, 3587-3611, 1971.

Del Pozo, C., and M. Blanc, Analytical self consistent model of the large-scale convection field, *J. Geophys. Res.*, 99, 4053-68, 1994.

Dessler, A.J. and E.N. Parker, Hydromagnetic theory of Geomagnetic Storms, *J. Geophys. Res.*, 64, p. 2239-52, 1959.

Dessler, A.J. and J.A. Fejer, Interpretation of the *Kp* index and M-region Geomagnetic Storms, *Planetary and Space Science*, vol. 11, 505-11, 1963.

Dungey, James W. Interplanetary magnetic field and the auroral zones, *Phys. Rev. Letters*, 6, 47-48,

Evans, D.S., Precipitating electron fluxes formed by a magnetic field aligned potential difference, *J. Geophys. Res.*, 79, 2853-8, 1974.

Fairfield, Donald H. and Lawrence G. Cahill, Jr. Transition region magnetic field and polar magnetic disturbances, *J. Geophys. Res.*, 71, 155-169, 1966.

Fok, M.-C, R.A. Wolf, R.W. Spiro and T.E. Moore, Comprehensive computational model of the Earth's ring current, *J. Geophys. Res.*, 106, 8417-24, 2001.

Frank, Louis A. On the extraterrestrial ring current during geomagnetic storms, *J. Geophys. Res.*, 72, 3753-67, 1967.

Frank, Louis A.. Relationship of the plasma sheet, ring current trapping boundary and plasmapause near the magnetic equator and local midnight, *J. Geophys. Res.*, 76, 6971-9, 1971.

Garner, T.W., Numerical experiments on the inner magnetospheric electric field, *J. Geophys. Res.*, 108, No. 10, SMP-8, 2003.

Gonzalez, W.D., B.T. Tsurutani and A.L. Clua de Gonzalez, Interplanetary Origin of Geomagnetic Storms, *Space Sci. Rev*, 88, 529-562, 1999.

Gonzalez, W.D., Jo-Ann Joselyn, Y. Kamide, Herb W. Kroehl, G. Rostoker, B.T. Tsurutani and V.M. Vasyliunas: What is a geomagnetic storm? *J. Geophys. Res.*, 99, 5771-92, 1994.

Hamilton, Douglas C., G. Gloeckler, F.M. Ipavich, W Stüdemann, B. Wilken and G. Kremser, Ring current development during the great geomagnetic storm of February 1986, *J. Geophys. Res.*, 93, 14,343-55, 1988.

Heppner, James P. Electric field variations during substorms: Ogo-6 measurements, *Planet. Space Sci.*, 20, 1475-1498, 1972.

Hines, Colin, O. On the geomagnetic storm effect, *J. Geophys. Res.*, 62, 491-3, 1957.

Hines, Colin O., and L.R. Owen Storey, Time constants in the geomagnetic storm effect, *J. Geophys. Res.*, 63, 671-682, 1958.

Hines, Colin O., and Eugene N. Parker, Statement of differences regarding the ring current effect, *J. Geophys. Res.*, 63, 691-2, 1958.

Jaggi, Radhe K. and Richard A. Wolf Self-consistent calculation of the motion of a sheet of ions in the magnetosphere, *J. Geophys. Res.*, 78, 2852-2866, 1973.

Langel, R.A.. and R.H. Estes, Large-scale, near-field magnetic field from external sources and the corresponding induced internal field, *J. Geophys. Res.*, 90, 2487-494 (1985).

Li, Xinlin and M.A. Temerin, The Electron Radiation Belt, *Space Science Reviews*, 95, 569-580, 2001.

Li, Xinlin., I Roth, M. Temerin, J. Wygant, M.K.Hudson and J.B. Blake, Simulation of the prompt energization and transport of radiation belt particles during the March 23, 1991 SSC, *Geophys. Res. Lett.*, 20, 2423, 1993.

Liemohn, Harold B. The lifetimes of radiation belt protons with energies between 1 *keV* and 1 *Mev*, *J. Geophys. Res.*, 66, 3593-3595, 1961.

Liemohn, Michael.W., J.U. Kozyra, M.F. Thomsen, J.L. Roeder, G. Lu, J.E. Borowsky and T.E. Cayton, Dominant role of the asymmetric ring current in producing the stormtime *Dst**, *J. Geophys. Res.*, 106, 10883-904, 2001.

Liemohn, Michael W., Yet another caveat to using the Dessler-Parker-Sckopke relation, *J. Geophys. Res.*, 108, A6, article SMP-18, 2003.

Lui, Anthony T.Y. and Douglas C. Hamilton, Radial Profiles of Quiet Time Magnetospheric Parameters, *J. Geophys. Res.*, 97, 19325-332, 1992.

McIlwain, C.E., Substorm Injection Boundaries, p. 143-154 in *Magnetospheric Physics*, B.M. McCormac (ed.), D. Reidel, Dordrecht, 1974.

Meng, C.-I., Case studies of the storm-time variation of the polar cusp, *J. Geophys. Res.*, 88, 137-149, 1983.

Mozer, Forrest *et al.* Observation of paired electrostatic shocks in the polar magnetosphere, *Phys. Rev. Lett.*, 38, 292-295, 1977.

Parker, E.N., On the Geomagnetic Storm Effect, *J. Geophys. Res.*, 61, 625-37, 1956.

Parker, E.N., Electrical conductivity in the geomagnetic storm effect, *J. Geophys. Res.*, 63, 437-8, 1958.

Parker, E.N. and C. Hines, Indadequacy of ring-current theory for the main phase of geomagnetic storms. *J. Geophys. Res.*, 63, 691-2, 1958.

Persson, H., Electric field along a magnetic line of force in a low density plasma, *Phys. Fluids*, 6, 1756-9, 1963.

Rufenach, Clifford L., R.F. Martin, Jr., and H.H. Sauer, A Study of Geosynchronous Magnetopause Crossings, *J. Geophys. Res.*, 94, 15125-134, 1989.

Rufenach, Clifford L., R.L. McPherron and J. Schaper, The quiet geomagnetic field at geosynchronous orbit and its dependence on solar wind dynamic pressure, *J. Geophys. Res.*, 97, 25-42, 1992.

Schield, Milo A., J. W. Freeman and A.J. Dessler, A source for field-aligned currents at auroral latitudes, *J. Geophys. Res.*, 74, 247-256, 1969.

Schmidt, A, *Abhandl. Kgl. Pr. Met. Inst*, 5, 37, 1916.

Sckopke, Norbert A general relation between the energy of trapped particles and the disturbance field near Earth, *J. Geophys. Res.*, 71, 3125-3130, 1966.

Singer, S. Fred, A new model of magnetic storms and aurorae, *Eos (Transact. Amer. Geophys. Union)*, 38, 175-190, 1957.

Siscoe, G.L., Energy coupling between regions 1 and 2 Birkeland current systems, *J. Geophys. Res.*, 87, 5124-30, 1982.

Shelley, E.G., R.G. Johnson and R.D. Sharp, Satellite Observations of Energetic Heavy Ions during a Geomagnetic Storm, *J. Geophys. Res.*, 77, 6104-110, 1972.

Smith, Edward J., Theoretical and Experimental Aspects of Ring Currents, pp. 316-373 in *Space Science* edited by Donald LeGalley, John Wiley, New York, 1963.

Smith, Paul H. and N.K. Bewtra, Charge exchange lifetimes for ring current ions, *Space Sci. Rev.*, 22, 301-318, 1978

Sonnett, Charles P., E.J. Smith, D.L. Judge and P.J. Coleman, Jr., Current systems in the vestigial geomagnetic field: Explorer VI, *Phys. Rev. lett.*, 4, 161-3, 1960.

Stern, D.P., A study of the electric field in an open magnetospheric model, *J. Geophys. Res.*, 78, 7292-7305 1973

Stern, D.P., The motion of a proton in the equatorial magnetosphere, *J. Geophys. Res.*, 80, 595-9, 1975.

Stern, D.P., A brief history of magnetospheric physics before the spaceflight era, *Rev. Geophys.*, 27, p. 103-114, 1989.

Stern, D.P., A brief history of magnetospheric physics during the space age, *Rev. Geophys.*, 34, 1-31, 1996.

Stern, D.P., A millennium of Geomagnetism, *Rev. Geophys.*, 40 (3), p. 1-1 to 1-30, Sept. 2002.

Störmer, Carl, *The Polar Aurora*, xvii+403 pp, Oxford University Press, New York, 1956.

Sugiura, Masahisa, Equatorial Current Sheet in the Magnetosphere, *J. Geophys. Res.*, 77, 6093-103, 1972.

Sugiura, M., Hourly values of the equatorial *Dst* for the IGY, *Annales of the International Geophysical Year*, 35, p. 9, Pergamon, NY 1964.

Tsurutani, Bruce T., W.D. Gonzalez, A.L.C. Gonzalez, F. Tang, J.K. Arballo and M. Okada, Interplanetary origin of geomagnetic activity in the declining phase of the solar cycle, *J. Geophys. Res.*, 100, 21717-33, 1995.

Tsurutani, Bruce.T., W.D. Gonzalez, G.S. Lakhina and S.Alex, The extreme magnetic storm of 1-2 September 1859, *J. Geophys. Res.*, 109, no. A7, article SSH-1, 2003.

Tsyganenko, N.A., A model of the near magnetosphere with a dawn-dusk asymmetry 1. Mathematical structure, SMP-10. 2. Parametrization and fitting to observations SMP-12, *J. Geophys. Res.*, 107, A8, 2002.

Tsyganenko, N.A., H.J. Singer and J.C. Kasper, Storm-time distortion of the inner magnetosphere: How severe can it get? *J. Geophys. Res.*, 109, no. A5, article SMP-18, 2003.

Van Allen, James A. and L.A. Frank, Radiation measurement to 658,300 *km* with Pioneer IV, *Nature*, 184, 219-224, 1959.

Vasyliunas, Vytenis M. A survey of low-energy electrons in the evening sector of the magnetosphere with OGO 1 and OGO 3, *J. Geophys. Res.*, 73, 2839-2884, 1968.

Vasyliunas, Vytenis M. Mathematical models of magnetospheric convection and its coupling to the ionosphere, p. 60-71 in *Particles and Fields in the Magnetosphere*, B.M. McCormac, ed., D. Reidel 1970.

Vasyliunas, Vytenis M. The interrelationship of magnetospheric processes, p. 29-38 in *Earth's Magnetospheric Processes*, B.M. McCormac, ed., D. Reidel, 1972.

Vasyliunas, Vytenis M, Electric Field and Plasma Flow: What Drives What? *Geophys. Res. Lett.*, 28, 2177-80, 1 June 2001a.

Vasyliunas, Vytenis M., Comment on "Simulation Study on fundamental properties of the storm-time ring current" by Y. Ebihara and M. Ejiri, *J. Geophys. Res.*, 106, 6321-2, 2001b.

Volland, H., A semiempirical model of the large-scale magnetospheric electric fields, *J. Geophys. Res.*, 78, 171-180, 1973.

Williams, Donald J., The Earth's Ring Current: Causes, Generation and Decay (Tutorial Lecturer) *Space Science Reviews*, 34, 223-234, 1983.

Williams, Donald J., E.C. Roelof and D.G. Mitchell Global magnetospheric imaging, *Rev. Geophys.*, 30, 183-208, 1992.

Zmuda, Alfred J. and James C. Armstrong The diurnal flow pattern of field-aligned currents, *J. Geophys. Res.*, 79, 4611-4619, 1974.

Mailing address: David P. Stern, 31 Lakeside Drive, Greenbelt, MD 20770, USA.

Sources, Transport, and Losses of Energetic Particles During Geomagnetic Storms

Vania K. Jordanova

Space Science Center, University of New Hampshire, Durham, New Hampshire

We discuss the main source, transport, and loss mechanisms for energetic (~1-300 keV) particles during geomagnetic storms. The importance of both solar wind and ionospheric sources is shown. Examples for ring current formation and decay from physics-based models using multi-point satellite measurements are given. Both numerical simulations and global imaging satellite data confirm the asymmetric ring current morphology during the main and early recovery storm phases; the ring current becomes symmetric during the late recovery phase. Ring current evolution depends on the interplay of time-dependent inflow of plasma from the magnetotail, earthward transport and acceleration, and outflow of plasma from the dayside magnetopause. The enhancement and drop of plasma sheet density at geosynchronous thus propagate inward and contribute to ring current buildup and decay, respectively. Recent global simulations suggest that magnetospheric convection plays a dominant role for ring current formation, although radial diffusion and substorm-induced electric fields contribute as well. In particular, radial diffusion injects particles at energies $E \geq 100$ keV deep into the magnetosphere ($L < 4$). Charge exchange, Coulomb collisions, and wave-particle interactions dominate the loss of medium, low, and high energy ring current ions, respectively. Intense EMIC waves are generated near the plasmapause during storm time. These waves scatter protons at $E \geq 10$ keV into the loss cone and reduce the total energy of the ring current H^+ component by more than 10%.

1. INTRODUCTION

Our planet Earth is immersed into the continuous flow of plasma from the Sun, called solar wind. The strong intrinsic magnetic field of the Earth deflects the bulk of this flow around the planet and forms a tear-drop shaped magnetic cavity known as the magnetosphere. This region, where the Earth's magnetic field dominates is populated by thermal and energetic charged particles whose motion is governed by the surrounding electric and magnetic fields. At near-Earth distances the particles at relativistic energies get trapped on closed geomagnetic field lines, thereby forming the radiation belts. Low-energy (thermal plasma) corotates with the Earth and forms the plasmasphere. The azimuthal drift of intermediate-energy (~10-200 keV) particles around the Earth, in opposite direction for the electrons and ions results in a ring current. The magnetic field disturbance caused by the ring current is registered in the magnetograms of near-equatorial ground-based stations as a decrease of the horizontal component of the Earth's magnetic field and is referred to as *Dst* index. The *Dst* index is used as a main measure of geomagnetic storm intensity. Besides the ring current which is of major interest to this study, other magnetospheric current systems are the tail, field-aligned, and magnetopause currents. The relative contribution of each of these currents to *Dst* is not yet well established, being

The Inner Magnetosphere: Physics and Modeling
Geophysical Monograph Series 155

10.1029/155GM02

estimated by different authors from minor [*Burton et al.*, 1975; *O'Brien and McPherron*, 2000; *Turner et al.*, 2000] to major [*Alexeev et al.*, 1996].

Satellite observations have shown that solar wind conditions are not steady but change with time reflecting the variety of phenomena occurring on the Sun, the most dynamical ones being flares and coronal mass ejecta (CME); so does the energy input to the magnetosphere. When solar wind plasma carrying a strong, persistent interplanetary magnetic field (IMF) oriented southward passes Earth, the large-scale electric field across the magnetotail intensifies and the earthward flow of ions and electrons inside the magnetosphere greatly increases. As a result the ring current population grows considerably, the magnetic field measured on the Earth's surface decreases rapidly, and a geomagnetic storm occurs. The intense IMF are associated with either CME and intrinsic fields, or the interaction of the high speed stream with the slower solar wind preceding it, and the shocked and compressed fields and plasma. The dominant mechanism coupling solar wind momentum and energy to the magnetosphere and driving disturbed magnetospheric conditions is thought to be reconnection of the interplanetary and terrestrial magnetic fields at the low-latitude, dayside magnetopause. Wave motions produced by viscous interaction between solar wind plasma and magnetosphere plasma seem to have only a minor contribution. Intense geomagnetic storms may have severe impacts on technological systems, causing damages to telecommunication satellites and power transmission lines and may pose serious health hazards. The response at Earth of the Sun's varying energy output and the forecast of geomagnetic activity is therefore of central interest to space science. To develop a predictive ring current and radiation belt model, a thorough understanding of the processes that operate in the inner magnetosphere is needed. An overview of our knowledge at present of these mechanisms is given in this paper.

2. SOURCES FOR RING CURRENT PLASMA

Detailed compositional ring current measurements at energies from few keV to few hundred keV were provided by the AMPTE/CHEM spectrometer [e.g., *Hamilton et al.*, 1988] and CRRES/MICS instrument [e.g., *Daglis*, 1997]. The distributions of the ion energy density for the four main ion species (H^+, O^+, He^+, and He^{++}), as well as for the total energy density in the outer ring current are shown in Figure 1 [*Daglis et al.*, 1993]. They are obtained averaging the 2.5 years measurements of the CHEM instrument for geomagnetically quiet (left) and active (right) conditions. It is clear that ions in the energy range ~10-200 keV contribute most to the total measured ion energy density. In addition, H^+ is the dominant ring current ion species, with O^+ contributing mostly during active times. Being averaged over all local times and all events with $AE < 30$ nT (quiet) and $AE > 700$ nT (active), these numbers are not representative for intense storms. The distribution can change drastically during large storms, when O^+ may become the dominant ring current ion near minimum *Dst*, as was the case for the February 1986 storm when O^+ contributed 47% of the total energy density compared with 36% for H^+ [*Hamilton et al.*, 1988]. The dominance of O^+ during the storm main phase was observed as well by the CRRES/MICS instrument [*Daglis*, 1997], however this satellite operated during solar maximum and this dominance may reflect the solar cycle dependence. The enhancement of heavy ion densities due to increased solar EUV fluxes during solar maximum was demonstrated by *Young et al.* [1982] using the Ion Composition Experiments on the ESA/GEOS spacecraft. A rise in O^+ density at geosynchronous altitude by a factor of ~8 with increasing geomagnetic activity was reported as well. In agreement, recent numerical simulations [*Jordanova et al.*, 2001c; *Kozyra et al.*, 2002] have shown that O^+ becomes the dominant ring current ion during the main phase of solar maximum great storms.

The discovery of O^+ in the plasma sheet in the 1970s indicated that besides the solar wind, another important source for the plasma sheet population is the terrestrial ionosphere. Before it was assumed that solar wind ions are the main source of magnetospheric plasma since they have higher initial energies (few keV) than ionospheric ions (eV to 10's of eV). The mechanisms by which thermal oxygen is extracted from the ionosphere, transported to the magnetosphere, and energized are still not well understood. It is more probable that these ions are injected at energies less than ~20 keV into the outer magnetosphere rather then being directly injected into the ring current [*Kamide et al.*, 1997], although observations of field-aligned ion beams at low $L < 7$ shells have been reported by *Sheldon et al.* [1998] during the storm of April 1996. The relative contribution of the solar wind and the ionosphere source is highly variable and depends on geomagnetic and solar activity [e.g., *Young et al.*, 1982].

The direct particle source for the ring current is the plasma sheet where ions of both solar wind and ionospheric origin are injected. During storm time plasma sheet particles are transported earthward, energized, and drift azimuthally around the Earth to form the ring current. The preexisting quiet time plasma sheet density, however, is not large enough to account for the storm time ring current intensifications, fresh plasma injections are needed [e.g., *Chen et al.*, 1994; *Jordanova et al.*, 1998a; *Thomsen et al.*, 1998]. Enhancements of plasma sheet density of various magnitudes have been indeed observed during storm times at geosynchronous and beyond [*Hamilton et al.*, 1988; *Borovsky et al.*, 1997]. On the other hand, *Ebihara and Ejiri* [2000] have demonstrated that plasma sheet

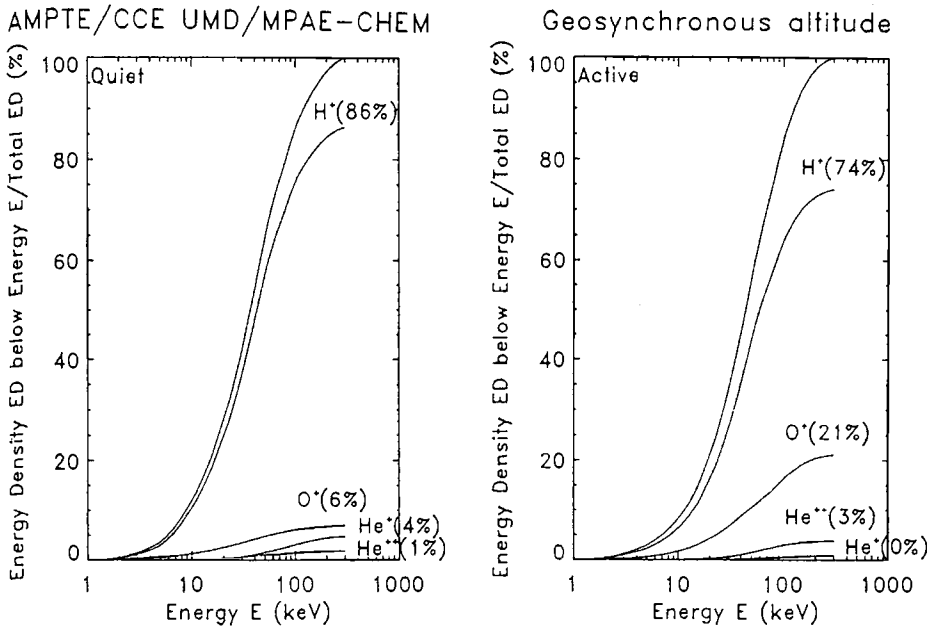

Figure 1. Accumulated percentage of the ion energy density at geosynchronous altitude as a function of energy, (left) at quiet times and (right) at active times [from *Daglis et al.*, 1993].

temperature changes may produce ring current recovery. Figure 2 shows how the convection electric field interplays with the plasma sheet density variations during the March 2001 geomagnetic storm [*Jordanova et al.*, 2003a]. The solar origin of this storm which was one of the biggest of this solar cycle ($Dst \approx -360$ nT) was a CME. A strong interplanetary shock hit the Earth's magnetosphere at ~01 UT on March 31. Two minima in the IMF $B_z \approx -40$ nT were observed at ~06 UT and ~14 UT on March 31. Correspondingly, two enhancements in the cross polar cap potential drop of ~200 kV magnitude and ~6 hours duration, separated by several hours of reduced convection occurred (Figure 2, top). The LANL instruments measured ion flux enhancement at geosynchronous for ~10 hours after the interplanetary shock. The magnitude of the fluxes gradually decreased after that. The plasma sheet density showed similar variation.

Energetic particle dynamics during the March 2001 storm were simulated with the ring current—atmosphere interactions model (RAM) developed by *Jordanova et al.* [1996a]. Data from the instruments on CLUSTER and LANL spacecraft were used for initial and boundary conditions of the model. The magnetic field disturbance on ground was calculated from three simulation runs (Figure 2, bottom). In the first model simulation (dotted line), the prestorm plasma sheet measurements at the start of the simulation (0130 UT March 30) were used as boundary conditions throughout the modeled period. In the second (solid line) the boundary

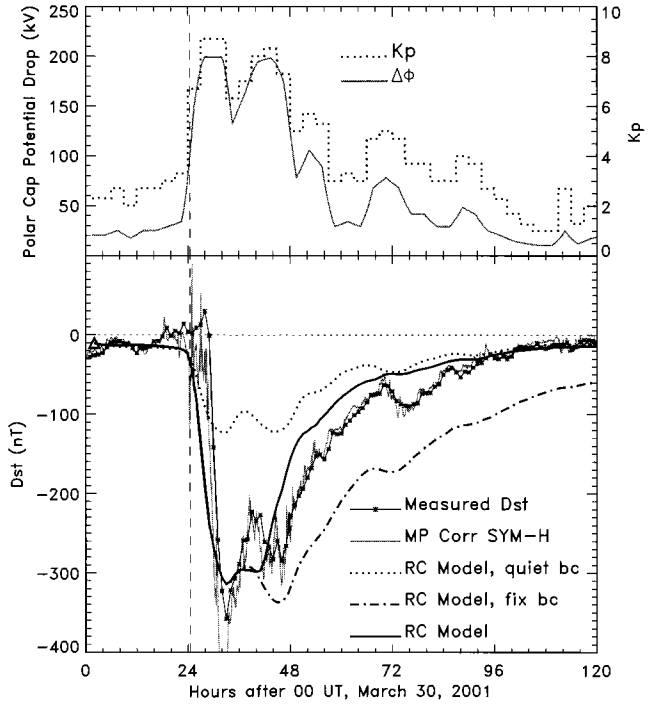

Figure 2. (top) Polar cap potential drop and *Kp* index. (bottom) Comparison of three model simulations with *Dst* and SYM-H measurements. The vertical guideline indicates the interplanetary shock. [from *Jordanova et al.*, 2003a].

conditions were updated as the storm evolved according to LANL geosynchronous measurements. In the third (dashed-dotted line), the boundary conditions were updated until hour 32 of the simulation and were kept at this enhanced level after that. The convection potential was kept the same in all three numerical simulations (Figure 2, top). It is clear that the simulation using prestorm plasma sheet density underestimates the measured $|Dst|$ index by more than 50%. In this case ring current energy enhancements are due solely to the convection electric field intensifications and we see that the two periods of enhanced convection are equally geoeffective, there is no preconditioning of the ring current. On the other hand, the simulation using the measured storm time plasma sheet LANL data (solid) shows good agreement with *Dst* and SYM-H observations (except near hour 36, which may be due to uncertainties in the electric or magnetic field models during the main phase of the storm, or to the contribution of other current systems). Finally, the third simulation using enhanced boundary conditions (dashed-dotted) indicates that the observed decrease of plasma sheet density during the recovery phase of this storm plays a significant role in the fast initial ring current decay. In fact, an additional ~50 nT increase in $|Dst|$ index occurs if this drop is not taken into account. In conclusion, knowledge of plasma sheet source population is necessary to accurately reproduce ring current storm time dynamics.

3. PARTICLE TRANSPORT AND ACCELERATION

There are three main mechanisms that contribute to the transport and acceleration of energetic (1-300 keV) particles in the inner magnetosphere: magnetospheric convection, radial diffusion, and substorm-induced electric fields. We present recent results suggesting that the variations in the strength of the ring current as the storm develops are mainly controlled by magnetospheric convection. Radial diffusion and substorm-induced electric fields play more likely a secondary role, however, their effects need further investigation.

3.1. Role of Magnetospheric Convection

Ring current fluxes intensify during the main phase of the storm owing to an enhancement in the convection electric field and subsequent earthward transport and adiabatic acceleration of plasma sheet particles; the fluxes decrease during the recovery phase of the storm, owing to a reduction in the convection electric field and dominance of various loss processes. The time-dependent variations in the convection electric field cause particles to move from open to closed drift paths and to become trapped. Particles that are not trapped and remain on open trajectories are lost through the dayside magnetopause. The convection electric field is thus an essential quantity in modeling ring current evolution, however, it is more time-variable and difficult to measure than the magnetic field and not many global electric field models have been developed. One of the most widely used inner magnetospheric convection and corotation model is the Volland-Stern [*Volland*, 1973; *Stern*, 1975] semiempirical model which has a simple analytical form; *Maynard and Chen* [1975] introduced a time dependence in the model using the 3 hour averaged planetary *Kp* index. This model gives a realistic description of the overall potential drop across the magnetosphere, and implementing it in RAM, a reasonable prediction of ring current contribution to *Dst* index was obtained [*Jordanova et al.*, 1998a; *Kozyra et al.*, 1998; *Liemohn et al.*, 1999]; this indicated the dominant role of magnetospheric convection in ring current energization and trapping. Nevertheless, detailed comparison of modeled ring current distributions with measured spectra [e.g., *Kistler et al.*, 1999; *Jordanova et al.*, 1999a] showed discrepancies at low L shells. During magnetically active periods strong electric fields were measured by the electric field instruments on CRRES [*Wygant et al.*, 1998; *Rowland and Wygant*, 1998] and on Cluster [*Matsui et al.*, 2003] spacecraft which differ from the Volland-Stern model. The enhanced electric fields appeared about an hour or more before a strong ring current forms on the duskside below $L = 5$. Much smaller electric fields were measured at larger L shells ($L = 5$ to 8) and on the dawnside.

Boonsiriseth et al. [2001] performed a comparative study of inner magnetospheric convection during the January 1997 magnetic storm. They improved the specification of the electric field using potentials generated by the assimilative mapping of ionospheric electrodynamics (AMIE) [*Richmond and Kamide,* 1988] to which they have added a penetration electric field (driven by partial ring current closure in the ionosphere) [*Ridley and Liemohn*, 2002]. Figure 3 shows the instantaneous measurements from the electric field instrument (EFI) on Polar on 10 January compared with electric fields from Volland-Stern and AMIE models with (MACEP) and without (MACEP-) the addition of the penetration field. The left panel corresponds to the dawnside inbound Polar pass from ~10 to $2R_E$ during the prestorm and early main phase. The effect of the asymmetric ring current is small at this time and MACEP and MACEP(-) are almost identical. EFI measured small electric fields in reasonable agreement with the models. The right panel corresponds to the duskside outbound pass during the storm main phase. Volland-Stern and MACEP(-) models significantly underestimate the electric field measured at low $L < 5$ shells, while the MACEP results are in good agreement with EFI data. This suggests that the electric field associated with the asymmetric ring current plays an important role in the duskside magnetosphere during magnetically active periods. Previous observational studies

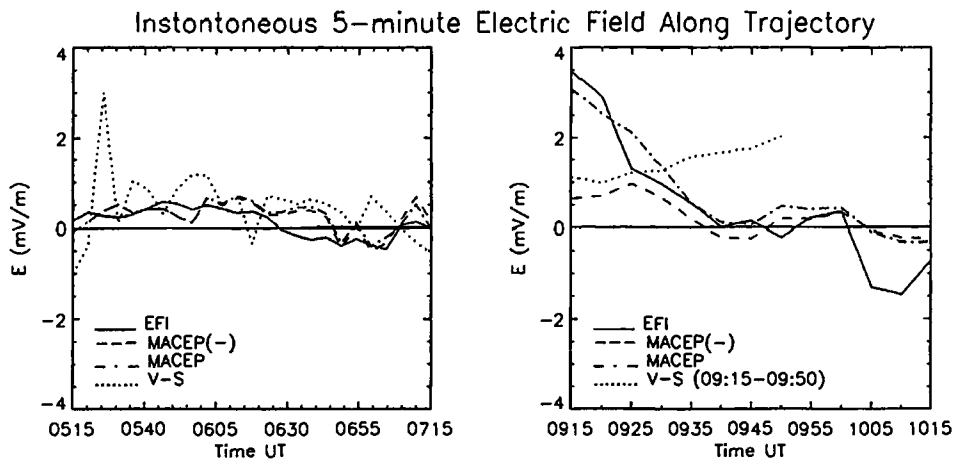

Figure 3. The electric fields measured from EFI and calculated from MACEP and Volland-Stern models along Polar trajectory on 10 January 1997 in the corotation frame of reference, (left) MLT ≅ 6 and (right) MLT ≅ 18. The Volland-Stern electric field is not calculated beyond 10 R_E. [from *Boonsiriseth et al.*, 2001].

[*Maynard et al.*, 1982] also indicated a penetration of the convection electric field to low L shells in the late evening and early morning local time sectors during disturbed times. Intensifications of the storm time electric field on the nightside, in the dusk-midnight quadrant, are predicted as well by self-consistent electric field calculations using the Rice Convection Model [*Wolf*, 1983; *Fok et al.*, 2001].

The effect of inner magnetospheric convection on ring current dynamics was recently investigated by *Jordanova et al.* [2001b; 2003b]. Figure 4 (top) shows ring current simulations during the main phase of the 10 January 1997 storm from our RAM model coupled with the high resolution MACEP model of *Boonsiriseth et al.* [2001]. Simulations using the *Kp*-dependent Volland-Stern model are shown for comparison in the bottom panel. Similar morphology is observed with both models during the prestorm quiet conditions (not shown). As the main phase of the storm proceeds, a very asymmetric ring current energy distributions develop and significant differences between the two models occur. The MACEP model electric field penetrates earthward and has larger magnitude than the Volland-Stern model, resulting in larger ring current injection and stronger asymmetry. The freshly injected 30-80 keV ring current ions on open drift paths during the main phase penetrate to L~3 and the ring current energy density intensifies from premidnight to postmidnight. Note that there is a factor of ~10 variation in the H^+ intensity with magnetic local time (MLT). The peak is rotated ~90° westward in Volland-Stern compared to MACEP, reflecting the rotation of the convection patterns. Larger energy gain is observed as well in the higher and lower ring current energy components in MACEP compared to Volland-Stern model. The total energy density has maximum near local midnight in MACEP, while it maximizes near dusk in Volland-Stern model. This morphology, however, lasts only for few hours, near minimum *Dst* the ring current energy density peak is located in the premidnight quadrant in both models. During the recovery phase of the storm the convection electric field decreases in both models and the trapped population evolves into a symmetric ring current [*Jordanova et al.*, 2003b].

The asymmetry of the ring current distribution during geomagnetic storms emerges not only from recent global numerical simulations [e.g., *Jordanova et al.*, 1999b; 2001c; *Liemohn et al.*, 2001] but it has been also confirmed by both in situ data [e.g., *Turner et al.*, 2001; *Ebihara et al.*, 2002] and global images [e.g., *Henderson et al.*, 1997; *C:son Brandt et al.*, 2002; *Baker et al.*, 2002]. This asymmetry emphasizes that magnetospheric convection governs ring current formation since a strong convection electric field accelerates and brings particles inward in L on the nightside where the energy density peak is located. The lower-energy particles subsequently follow eastward drift paths dominated by corotation, while the higher-energy particles surround the Earth westward dominated by gradient-curvature drifts. As shown in Figure 4 the location of the energy density peak in MLT and L shell depends on the convection electric field and particle energy. The deeper penetration of 30-80 keV ions and the location of the peak near midnight predicted with MACEP are in better agreement with recent ENA observations during storm time from the IMAGE satellite [e.g., *Mitchell et al.*, 2001; *C:son Brandt et al.*, 2002] than Volland-Stern predictions. This suggests that simulations using realistic electric and magnetic field models and self-consistent magnetosphere-ionosphere coupling studies combined with in situ and global measurements will help determine how the ring current morphology varies with storm phase. This problem has not been investigated in detail and will be a topic for further studies.

[redacted]

[redacted]

[redacted]

[redacted]

[redacted]

[redacted]

[redacted]

[redacted]

$$= \frac{\partial}{\partial \mu_{ij}} \left(\left[\left\langle \left[\left\langle F \right\rangle \right] \right\rangle \right] \right) + \frac{\partial}{\partial \mu_{ij}} \left(\left[\left\langle \left[\left\langle F \right\rangle \right] \right\rangle \right] \right) + \frac{\partial}{h(\mu_{ij})\, \mu_{ij}}$$

$$\propto \frac{\partial}{\partial \mu_{ij}} \left(\left[\left\langle \left[\left\langle F \right\rangle \right] \right\rangle \right] \right)$$

$$= \left\langle \left(\frac{\partial F}{\partial t} \right)_{rd} \right\rangle + \left\langle \left(\frac{\partial F}{\partial t} \right)_{oe} \right\rangle + \left\langle \left(\frac{\partial F}{\partial t} \right)_{oe} \right\rangle + \left\langle \left(\frac{\partial F}{\partial t} \right)_{wp} \right\rangle + \left\langle \left(\frac{\partial F}{\partial t} \right)_{wm} \right\rangle$$

[redacted]

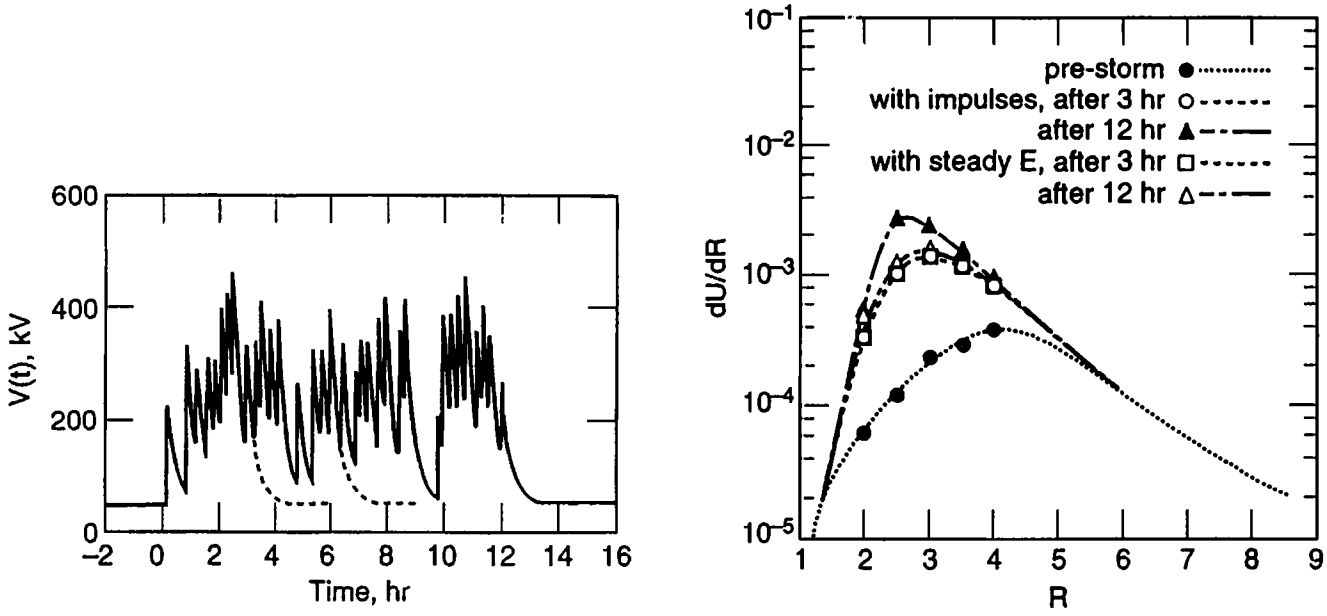

Figure 5. (left) Cross-tail potential used by *Chen et al.* [1994]. (right) Profiles of normalized ring current energy density during various storm conditions [from *Chen et al.*, 1997].

The left-hand side of the bounce-averaged kinetic equation (1) describes the convective drift of charged particles in a time-dependent magnetospheric electric field and is valid for both electrons and ions. Relativistic corrections are included in this equation using the relativistic factor $\gamma = 1 + E/m_o c^2$, where E is the kinetic energy and m_o is the rest mass; p is the relativistic momentum of the particle. The model considers a region in the equatorial plane spanning radial distances R_o from 2 R_E to 6.5 R_E and all magnetic local times, and equatorial pitch angle α_o from 0° to 90°, where $\mu_o = \cos(\alpha_o)$. The function $h(\mu_o) = S_B/2R_o$, where S_B is the half-bounce path length. We included the transport of relativistic particles as a result of electric and magnetic field fluctuations, using a radial diffusion term [e.g., *Schulz and Lanzerotti*, 1974; *Sheldon and Hamilton*, 1993] added to the right-hand side of the equation:

$$\left\langle \left(\frac{\partial F}{\partial t} \right)_{rd} \right\rangle = R_o^2 \frac{\partial}{\partial R_o} \left[\frac{1}{R_o^2} \langle D_{R_o R_o} \rangle \frac{\partial F}{\partial R_o} \right] \qquad (2)$$

where $D_{RoRo} = R_E^2 D_{LL}$. In an initial study, we used the radial diffusion coefficients D_{LL} from *Brautigam and Albert* [2000] which are time-dependent and parameterized by the storm time *Kp* index. The outer boundary conditions were modeled after geosynchronous data from the MPA and SOPA instruments on LANL satellites to reflect the time-dependent variation of the plasma inflow on the nightside. The loss terms included on the right-hand side of equation (1) are described in section 4.

The dynamics of the ring current (~10-200 keV) electron population have not been investigated in detail. Some preliminary studies indicate that the electron component provides between 10% and 25% of the total ring current energy [*Frank*, 1967]. The injection of plasma sheet electrons into the ring current during substorm activity leads to distributions that are unstable to the generation of whistler mode "chorus" waves. How effective are resonant interactions of radiation belt electrons with these waves in local acceleration and hardening of the high-energy tail population [e.g., *Horne and Thorne*, 1998] is yet to be determined. Figure 6 shows a test simulation obtained with our model for the development of energetic electrons during the October 2001 storm considering only convection (left) or convection and radial diffusion from magnetic field fluctuations (right). Losses due to scattering by plasma waves inside the plasmasphere were included in this initial study using a simplified loss term (F/τ_{wp}) with an appropriate timescale τ_{wp} [*Abel and Thorne*, 1998; *Albert*, 1999]. In contrast to ring current ions, charge exchange losses are not important for the electrons and were neglected in equation (1). To illustrate the effects of convective and diffusive transport the initial conditions were set to zero. It is evident from Figure 6 that radial diffusion is important for the transport of electrons with energy larger than ~100 keV; the transport of low-energy electrons is dominated by convection and eastward gradient-curvature drifts. As a result the ~30 keV electron flux exhibits a pronounced asymmetry during the main phase of the storm, intensifying primarily near dawn and penetrating below $L = 3$. The enhancement appears ~10 hours later on the duskside

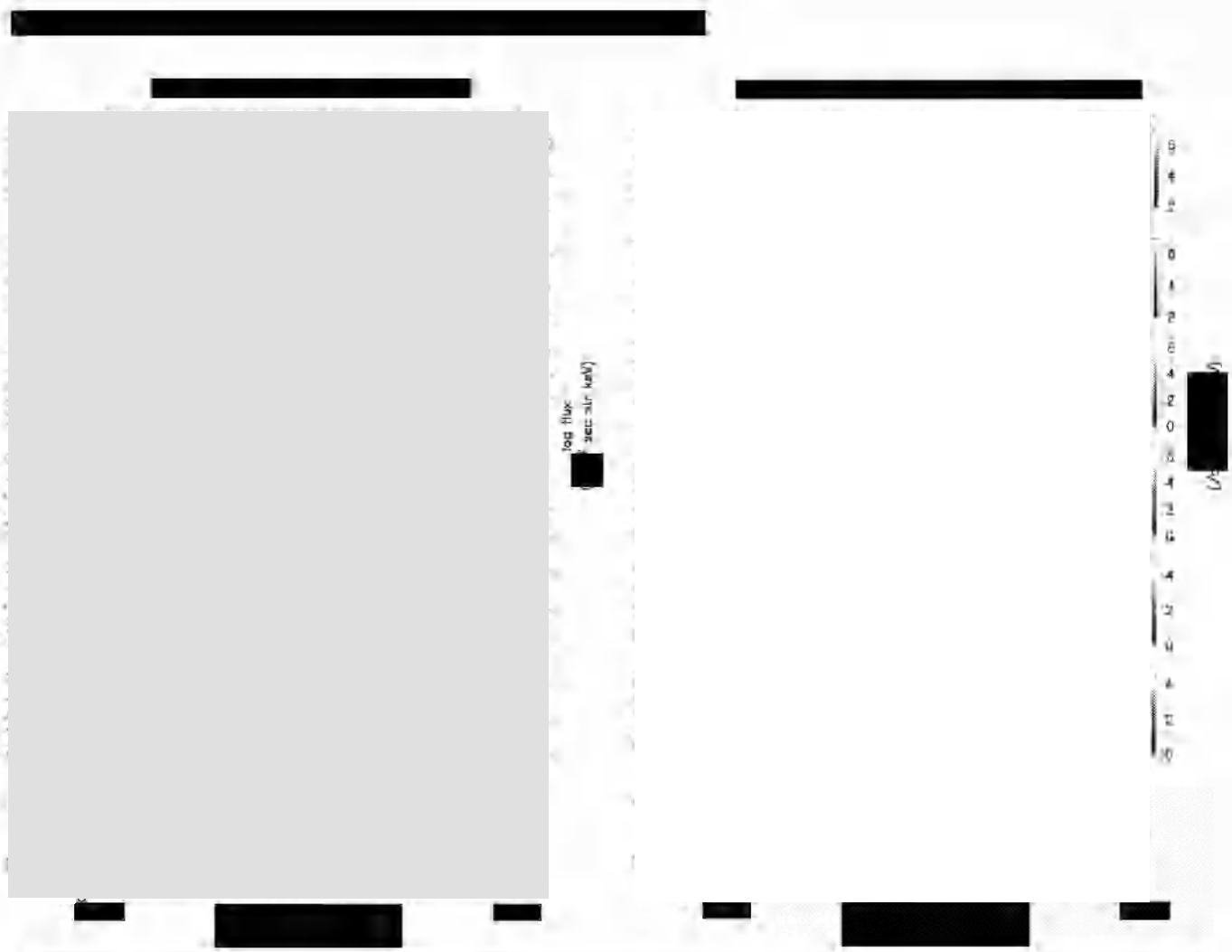

Tsyganenko [1989] model magnetic field; the time dependence was introduced through the observed variations of the *AE* index. In response to the induced electric field, the calculated energy content of the ring current fluctuated about a mean value determined by the quiescent electric field. *Wolf et al.* [1997] presented a series of computer experiments carried out with the Magnetospheric Specification and Forecast Model (MSFM), which solves the particle-conservation equation assuming isotropic pitch angle distributions. They demonstrated that convection electric fields play a far more important role in ring current injection than do substorm-associated induction fields. The authors also showed that periods of very strong convection, separated by periods of weak flow, are more effective in injecting particles deeper into the magnetosphere than a long period of moderately strong convection. On the other hand, *Fok et al.* [1999] studied the evolution of inner plasma sheet and ring current ions during two ideal substorm dipolarizations (with and without convection enhancement) and found that substorms enable the convection enhancement to create a robust ring current. *Ganushkina et al.* [2000] presented statistical results from Polar/CAMMICE measurements of "intense nose events" during which the plasma sheet ions have rapidly penetrated deep into the inner magnetosphere, well inside $L = 4$. They suggested that these structures are caused by short-lived intense electric fields that are formed in connection with substorm onset. Detailed measurements and simulations are needed in the future to clarify the extent to which substorms contribute to ring current buildup.

4. LOSSES OF ENERGETIC PARTICLES

The loss mechanisms identified as important for ring current decay are briefly discussed in this section [see also review by H. Koskinen in these proceedings]. (1) The most important among the collisional loss processes is charge exchange, where ring current ions are neutralized on collision with thermal exospheric hydrogen atoms [e.g., *Kistler et al.*, 1989] and produce energetic neutral atoms (ENA) which are no longer trapped by the Earth's magnetic field and are either lost in space or precipitate down to the atmosphere. (2) Coulomb collisions between energetic ring current ions and coexisting low-energy plasmaspheric populations result in energy transfer from the fast moving to the thermal particles and in angular deflection of the particles. The magnetospheric energy is transported down the magnetic field lines and creates ionospheric electron and ion temperature enhancements and optical emissions known as stable auroral red (SAR) arcs. The Coulomb decay proton lifetimes are comparable to or smaller than charge exchange lifetimes at low (< 5 keV) energies [*Fok et al.*, 1991]. (3) Scattering of ring current particles into the loss cone due to resonant interactions with electromagnetic ion cyclotron (EMIC) waves occurs on short timescales and was suggested to be important for ion loss [*Cornwall et al.*, 1970], especially during the main phase of the storm when ring current energy loss timescales may be as short as few hours. The plasma waves can also transfer energy from ring current H^+ to O^+ during magnetic storms [*Thorne and Horne*, 1994] and play an important role in heating the thermal electrons and ions [*Cornwall et al.*, 1971; *Gendrin and Roux*, 1980; *Thorne and Horne*, 1992]. The lifetimes of ring current protons resonating with EMIC waves are shorter than charge exchange lifetimes at high (>40 keV) energies [*Jordanova et al.*, 1996b]. (4) It was recently demonstrated that losses due to convective transport of ring current particles through the dayside magnetopause affect significantly the fast initial ring current decay [e.g., *Takahashi et al.*, 1990; *Jordanova et al.*, 1998a; *Liemohn et al.*, 1999]. The relative effect of all these loss mechanisms during various storm phases is still under investigation.

The effect of charge exchange and both energy degradation and pitch angle scattering due to Coulomb collisions on ring current H^+, He^+, and O^+ off-equatorially mirroring ions was addressed by *Jordanova et al.* [1996a; 1999a]. It was shown that the decrease of the distribution function by charge exchange losses and the buildup of a low-energy population due to Coulomb collisions proceed faster for particles with smaller pitch angles, since such particles encounter denser populations along their longer bounce paths. Comparisons of model results with ion spectra measured by the instruments on Polar spacecraft thus demonstrated that these losses have larger effect on the dayside spectra, at low L shells, and at higher magnetic latitudes; they reached maximum values for slowly drifting (~2-10 keV) particles within the stagnation dip. *Jordanova et al.* [1998b] investigated the effect of wave-particle interactions on ring current protons including for the first time in a global model not only pitch angle scattering, but energy diffusion by EMIC waves as well (mixed diffusion requires careful investigation since it may cause numerical instabilities and hasn't been incorporated yet). It was shown that pitch angle scattering reduces the magnitude of the distribution function at $E \geq 10$ keV by scattering particles into the loss cone, while energy diffusion smoothes the spectrum, causing the distribution to decrease at energies from ~10 keV to ~50 keV and to increase at higher energies, within the regions of EMIC waves excitation at dusk. Ring current ions followed westward drift paths around the Earth and reached dawn after several hours. The combined effects of scattering in the wave field and transport reduced the distribution at mid-energies (thus enhancing the dip) and increased it at higher energies at dawn. The effect of pitch angle scattering on the distribution function was larger than that of energy diffusion due to the larger diffusion coefficients.

We simulated the spatial and temporal evolution of H^+, O^+, and He^+ ring current ion distributions during the October 2001 storm using our relativistic RAM model (see section 3.2). All major loss processes were included on the right-hand side of equation (1), namely charge exchange, Coulomb collisions, wave-particle interactions, and loss due to collisions with the dense atmosphere (see *Jordanova et al.* [1996a; 2003b] for details). Charge exchange losses were calculated using the hydrogen geocoronal model of *Rairden et al.* [1986]. Coulomb collisions losses were calculated with the Fokker-Planck equation and the coupled plasmasphere model of *Rasmussen et al.* [1993]. The removal of particles at low altitudes due to collisions with the dense atmosphere was included using a loss term with a time scale of half a bounce period. Free ion outflow from the dayside boundary simulated the convective loss of particles through the dayside magnetopause. The growth rate of He^+ band EMIC waves due to the unstable ring current ion distributions was self-consistently calculated using the hot plasma dispersion relation; pitch angle diffusion of ring current protons by these waves was included in the model according to quasi-linear theory.

Figure 7 shows the temporal evolution of the total energy (dashed-dotted) of ring current H^+ as the storm progresses, calculated with our model considering (a) only convection, and subsequently adding (b) radial diffusion, and (c) EMIC waves scattering. The ring current energization from convection reaches maximum near hour~28, while minimum *Dst* is observed at hour~20 (see Figure 6). Radial diffusion enhances significantly the total energy of the ring current protons during the main phase and especially near hour 48. It does not shift, however, the energy maximum to earlier times. This is in agreement with previous studies [*Chen et al.*, 1997] indicating that radial diffusion is important for storms with longer main phase. Note that in this initial study we have used the *Kp*-dependent Volland-Stern convection model and radial diffusion coefficients of *Brautigam and Albert* [2000]. We expect a faster ring current buildup with more realistic electric field models [*Jordanova et al.*, 2003b] and this will be investigated in future extensions of

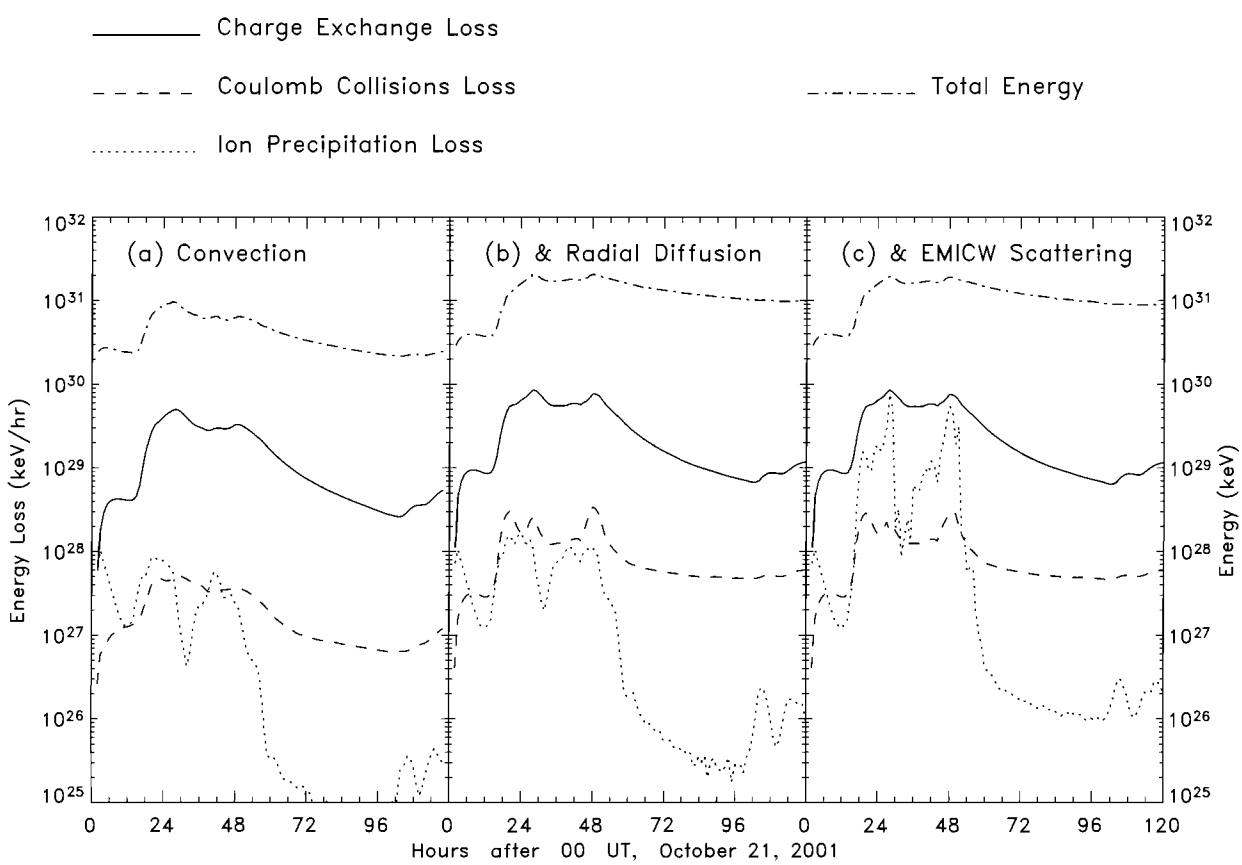

Figure 7. Ring current H^+ total energy (keV) and energy losses (keV/hr) during 21-25 October 2001, considering (a) only convection, and adding (b) radial diffusion, and (c) plasma waves scattering.

this work, as well as the dependence of our results on the choice of radial diffusion coefficients. Figure 7 displays as well the ring current H^+ energy losses due to charge exchange (solid), Coulomb collisions (dashed), and ion precipitation (dotted). Charge exchange losses are clearly the largest. Intense EMIC waves are excited primarily along the plasmapause near dusk during the main phase of the storm, and extend over all local times during the recovery phase [see also *Jordanova et al.*, 2001a]. Resonant interactions with these plasma waves scatter high-energy particles into the loss cone, which results in significant proton precipitation (Figure 7c) and more than 10% reduction of the total ring current energy. Ion precipitation losses become comparable to charge exchange losses near *Dst* minima, while Coulomb collisions losses remain about two orders of magnitude smaller. We thus find that the ring current energy loss by wave-particle interactions is larger than obtained in previous studies [*Kozyra et al.*, 1997; *Jordanova et al.*, 1998b] when radial diffusion was not considered and the high-energy ring current component remained undisturbed at the initial prestorm level. We have not yet calculated the effects of plasma wave scattering on the heavy ion components, nor energy or mixed diffusion. In addition, *Jordanova et al.* [2001c] showed that O^+ band EMIC waves may be excited during major storms; scattering by these and other plasma waves should be considered. All these topics will be addressed in future studies.

5. CONCLUSIONS

In this paper we discussed our current understanding on the dynamical evolution of energetic particles in the inner magnetosphere during storm time. In recent years progress has been made in identifying the origin of ring current ions, their energization and transport into $L < 7$, as well as their subsequent loss. It has been established that O^+ ions of ionospheric origin are an important constituent of the ring current and their contribution increases during major storms and solar maximum. Magnetic storms are associated with injections of new plasma into the ring current, not just a simple inward displacement of preexisting plasma population. Magnetospheric convection plays an important and probably dominant role in ring current buildup during the main phase of a storm; the relative contributions of the substorm-induced electric fields and radial diffusion are yet to be quantified. Ring current decay is controlled by the interplay of several factors: a reduced radial transport allowing internal loss processes to dominate, convective outflow of plasma through the dayside magnetopause, and reduced inflow of plasma from the magnetotail. Their contribution may vary with storm conditions and is being investigated at present. The modeling of magnetic storms is improving as our knowledge of the inner magnetospheric electric and magnetic fields and particle populations advances. The development of magnetosphere-ionosphere coupling models using self-consistent calculations of the fields, waves, and plasmas is necessary in the future to meet the requirements for accurate space weather predictions.

Acknowledgments. This work was supported in part by NSF under grant ATM-0309585 and NASA under grant NAG5-13512. Special thanks are due to Y. Miyoshi for his collaboration and useful discussions, and M. Thomsen and G. Reeves for help with LANL data processing.

REFERENCES

Abel, B. and R.M. Thorne, Electron scattering loss in Earth's inner magnetosphere 1. Dominant physical processes, *J. Geophys. Res.*, 103, 2385, 1998.

Albert, J.M., Analysis of quasi-linear diffusion coefficients, *J. Geophys. Res.*, 104, 2429, 1999.

Alexeev, I.I., E.S. Belenkaya, V.V. Kalegaev, Y.I. Feldstein, and A. Grafe, Magnetic storms and magnetotail currents, *J. Geophys. Res.*, 101, 7737, 1996.

Baker, D.N., R.E. Ergun, J.L. Burch, J.-M. Jahn, P.W. Daly, R. Friedel, G.D. Reeves, T.A. Fritz, and D.G. Mitchell, A telescopic and macroscopic view of magnetospheric substorm on 31 March 2001, *Geophys. Res. Lett.*, 29, 1862, doi:10.1029/2001GL014491, 2002.

Boonsiriseth, A., R.M. Thorne, G.Lu, V.K. Jordanova, M.F. Thomsen, D.M. Ober, and A.J. Ridley, A semiempirical equatorial mapping of AMIE convection electric potentials (MACEP) for the January 10, 1997, magnetic storm, *J. Geophys. Res.*, 106, 12903, 2001.

Bourdarie, S., D. Boscher, T. Beutier, J.-A. Sauvaud, and M. Blanc, Electron and proton radiation belt dynamic simulations during storm periods: A new asymmetric convection-diffusion model, *J. Geophys. Res.*, 102, 17541, 1997.

Borovsky, J.E., M.F. Thomsen, and D.J. McComas, The superdense plasma sheet: Plasmaspheric origin, solar-wind origin, or ionospheric origin?, *J. Geophys. Res.*, 10, 22089, 1997.

Brautigam, D.H., and J.M. Albert, Radial diffusion analysis of outer radiation belt electrons during the October 9, 1990, magnetic storm, *J. Geophys. Res.*, 105, 291, 2000.

Burton, R.K., R.L. McPherron, and C.T. Russell, An empirical relationship between interplanetary conditions and *Dst*, *J. Geophys. Res.*, 80, 4204, 1975.

C:son Brandt, P., S. Ohtani, D.G. Mitchell, M.-C. Fok, E.C. Roelof, and R. Demajistre, Global ENA observations of the storm main phase ring current: Implications for skewed electric fields in the inner magnetosphere, *Geophys. Res. Lett.*, 29(20), 10.1029/2002GL015160, 2002.

Chen, M.W., L.R. Lyons, and M. Schulz, Simulations of phase space distributions of storm time proton ring current, *J. Geophys. Res.*, 99, 5745, 1994.

Chen, M.W., M. Schulz, and L.R. Lyons, Modeling of ring current formation and decay: A review, in *Magnetic Storms*, *Geophys. Monogr. Ser.*, vol. 98, edited by B.T. Tsurutani, W.D. Gonzalez, Y. Kamide, and J.K. Arballo, p. 173, AGU, Washington, D. C., 1997.

Cornwall, J.M., F.V. Coroniti, and R.M. Thorne, Turbulent loss of ring current protons, *J. Geophys. Res.*, 75, 4699, 1970.

Cornwall, J.M., F.V. Coroniti, and R.M. Thorne, Unified theory of SAR arc formation at the plasmapause, *J. Geophys. Res.*, 76, 4428, 1971.

Daglis, I.A., The role of magnetosphere-ionosphere coupling in magnetic storm dynamics, in *Magnetic Storms*, *Geophys. Monogr. Ser.*, vol. 98, edited by B.T. Tsurutani, W.D. Gonzalez, Y. Kamide, and J.K. Arballo, p. 107, AGU, Washington, D.C., 1997.

Daglis, I.A., E.T. Sarris, and B. Wilken, AMPTE/CCE CHEM observations of the energetic ion population at geosynchronous altitudes, *Ann. Geophys.*, 11, 685, 1993.

Ebihara, Y., and M. Ejiri, Simulation study on fundamental properties of the storm-time ring current, *J. Geophys. Res.*, 105, 15843, 2000.

Ebihara, Y., M. Ejiri, H. Nilsson, I. Sandahl, A. Milillo, M. Grande, J.F. Fennell, and J.L. Roeder, Statistical distribution of the storm-time proton ring current: Polar measurements, *Geophys. Res. Lett.*, 29, 1969, doi:10.1029/2002GL015430, 2002.

Fok, M.C., J.U. Kozyra, A.F. Nagy, and T.E. Cravens, Lifetime of ring current particles due to Coulomb collisions in the plasmasphere, *J. Geophys. Res.*, 96, 7861, 1991.

Fok, M.C., T.E. Moore, and M.E. Greenspan, Ring current development during storm main phase, *J. Geophys. Res.*, 101, 15, 311, 1996.

Fok, M.C., T.E. More, and D.C. Delcourt, Modeling of inner plasma sheet and ring current during substorms, *J.Geophys. Res.*, 104, 14557, 1999.

Fok, M.-C., R.A. Wolf, R.W. Spiro, and T.E. Moore, Comprehensive computational model of the Earth's ring current, *J. Geophys. Res.*, 106, 8417, 2001.

Frank, L.A., Ring current during storms, *J. Geophys. Res.*, 72, 3753, 1967.

Ganushkina, N. Yu., *et al.*, Entry of plasma sheet particles into the inner magnetosphere as observed by Polar/CAMMICE, *J. Geophys. Res.*, 105, 25205, 2000.

Gendrin, R., and A. Roux, Energization of helium ions by proton-induced hydromagnetic waves, *J. Geophys. Res.*, 85, 4577, 1980.

Hamilton, D.C., G. Gloeckler, F.M. Ipavich, W. Studemann, B. Wilken, and G. Kremser, Ring current development during the great geomagnetic storm of February 1986, *J. Geophys. Res.*, 93, 14343, 1988.

Henderson, M.G., G.D. Reeves, H.E. Spence, R.B. Sheldon, A.M. Jorgensen, J.B. Blake, and J.F. Fennell, First energetic neutral atom images from Polar, *Geophys. Res. Lett.*, 24, 1167, 1997.

Horne, R.B., and R.M. Thorne, Potential waves for relativistic electron scattering and stochastic acceleration during magnetic storms, *Geophys. Res. Lett*, 25, 3011, 1998.

Jordanova, V.K., L.M. Kistler, J.U. Kozyra, G.V. Khazanov, and A.F. Nagy, Collisional losses of ring current ions, *J. Geophys. Res.*, 101, 111, 1996a.

Jordanova, V.K., J.U. Kozyra, and A.F. Nagy, Effects of heavy ions on the quasi-linear diffusion coefficients from resonant interactions with electromagnetic ion cyclotron waves, *J. Geophys. Res.*, 101, 19771, 1996b.

Jordanova, V.K., C.J. Farrugia, L. Janoo, J.M. Quinn, R.B. Torbert, K.W. Ogilvie, R. P. Lepping, J.T. Steinberg, D.J. McComas, and R.D. Belian, October 1995 magnetic cloud and accompanying storm activity: Ring current evolution, *J. Geophys. Res.*, 103, 79, 1998a.

Jordanova, V.K., *et al.*, Effect of wave-particle interactions on ring current evolution for January 10-11, 1997: Initial results, *Geophys. Res. Lett.*, 25, 2971, 1998b.

Jordanova, V.K., C.J. Farrugia, J.M. Quinn, R.B. Torbert, J.E. Borovsky, R.B. Sheldon, and W.K. Peterson, Simulation of off-equatorial ring current ion spectra measured by POLAR for a moderate storm at solar minimum, *J. Geophys. Res.*, 104, 429, 1999a.

Jordanova, V.K., R.B. Torbert, R.M. Thorne, H.L. Collin, J.L. Roeder, and J.C. Foster, Ring current activity during the early $B_z < 0$ phase of the January 1997 magnetic cloud, *J. Geophys. Res.*, 104, 24895, 1999b.

Jordanova, V.K., C.J. Farrugia, R.M. Thorne, G.V. Khazanov, G.D. Reeves, and M. F. Thomsen, Modeling ring current proton precipitation by electromagnetic ion cyclotron waves during the May 14-16, 1997, storm *J. Geophys. Res.*, 106, 7, 2001a.

Jordanova, V.K., L.M. Kistler, C.J. Farrugia, and R.B. Torbert, Effects of inner magnetospheric convection on ring current dynamics: March 10-12, 1998, *J. Geophys. Res.*, 106, 29705, 2001b.

Jordanova, V.K., R.M. Thorne, C.J. Farrugia, Y. Dotan, J.F. Fennell, M.F. Thomsen, G.D. Reeves, and D.J. McComas, Ring current dynamics during the July 13-18, 2000, storm period, *Solar Phys.*, 204, 361, 2001c.

Jordanova, V.K., L.M. Kistler, M.F. Thomsen, and C.G. Mouikis, Effects of plasma sheet variability on the fast initial ring current decay, *Geophys. Res. Lett.*, 30, 1311, doi:10.1029/2002GL016576, 2003a.

Jordanova, V.K., A. Boonsiriseth, R.M. Thorne, and Y. Dotan, Ring current asymmetry from global simulations using a high-resolution electric field model, *J. Geophys. Res.*, 108, 1443, doi:10.1029/2003JA009993, 2003b.

Kamide, Y., *et al.*, Magnetic storms: Current understanding and outstanding questions, in *Magnetic Storms*, *Geophys. Monogr. Ser.*, vol. 98, edited by B.T. Tsurutani, W.D. Gonzalez, Y. Kamide, and J.K. Arballo, p. 1, AGU, Washington, D. C., 1997.

Kistler, L.M., F.M. Ipavich, D.C. Hamilton, G. Gloeckler, B. Wilken, G. Kremser, and W. Stuedemann, Energy spectra of the major ion species in the ring current during geomagnetic storms, *J. Geophys. Res.*, 94, 3579, 1989.

Kistler, L.M., *et al.*, Testing electric field models using ring current ion energy spectra from the Equator-S Ion Composition (ESIC) instrument, *Ann. Geophys.*, 17, 1611, 1999.

Kozyra, J.U., V.K. Jordanova, R.B. Horne, and R.M. Thorne, Modeling of the contribution of electromagnetic ion cyclotron (EMIC) waves to stormtime ring current erosion, in *Magnetic Storms*, *Geophys. Monogr. Ser.*, vol. 98, edited by B.T. Tsurutani, W.D. Gonzalez, Y. Kamide, and J.K. Arballo, p. 187, AGU, Washington, D. C., 1997.

Kozyra, J.U., V.K. Jordanova, J.E. Borovsky, M.F. Thomsen, D.J. Knipp, D.S. Evans, D.J. McComas, and T.E. Cayton, Effects of a high density plasma sheet on ring current development during the November 2-6, 1993 magnetic storm, *J. Geophys. Res.*, 103, 26285, 1998.

Kozyra, J.U., M.W. Liemohn, C.R. Clauer, A.J. Ridley, M.F. Thomsen, J.E. Borovsky, J.L. Roeder, V.K. Jordanova, and W.D. Gonzalez, Multistep Dst development and ring current composition changes during the 4-6 June 1991 magnetic storm, *J. Geophys. Res.*, 107, doi:10.1029/2001JA000023, 2002.

Li, X., D.N. Baker, M. Temerin, G.D. Reeves, and R.D. Belian, Simulation of dispersionless injections and drift echoes of energetic electrons associated with substorms, *Geophys. Res. Lett.*, 25, 3763, 1998.

Liemohn, M.W., J.U. Kozyra, V.K. Jordanova, G.V. Khazanov, M.F. Thomsen, and T.E. Cayton, Analysis of early phase ring current recovery mechanisms during geomagnetic storms, *Geophys. Res. Lett.*, 26, 2845, 1999.

Liemohn, M.W., J.U. Kozyra, M.F. Thomsen, J.L. Roeder, G. Lu, J.E. Borovsky, and T.E. Cayton, Dominant role of the asymmetric ring current in producing the stormtime *Dst**, *J. Geophys. Res.*, 106, 10883, 2001.

Lyons, L.R., and M. Schulz, Access of energetic particles to stormtime ring current through enhanced radial "diffusion", *J. Geophys. Res.*, 94, 5491, 1989.

Matsui, H., J.M. Quinn, R.B. Torbert, V.K. Jordanova, W. Baumjohann, P.A. Puhl-Quinn, and G. Paschmann, Electric field measurements in the inner magnetosphere by Cluster EDI, *J. Geophys. Res.*, 108, 1352, doi:10.1029/2003JA009913, 2003.

Maynard, N.C., and A.J. Chen, Isolated cold plasma regions: Observations and their relation to possible production mechanisms, *J. Geophys. Res.*, 80, 1009, 1975.

Maynard, N.C., J.P. Heppner, and T.L. Aggson, Turbulent electric fields in the nightside magnetosphere, *J. Geophys. Res.*, 87, 1445, 1982.

Mitchell, D.G., K.C. Hsieh, C.C. Curtis, D.C. Hamilton, H.D. Voss, E.C. Roelof, and P.C. Brandt, Imaging two geomagnetic storms in energetic neutral atoms, *Geophys. Res. Lett.*, 28, 1151, 2001.

O'Brien, T.P., and R.L. McPherron, An empirical phase space analysis of ring current dynamics: Solar wind control of injection and decay, *J. Geophys. Res.*, 105, 7707, 2000.

Rairden, R.L., L.A. Frank, and J.D. Craven, Geocoronal imaging with Dynamics Explorer, *J. Geophys. Res.*, 91, 13613, 1986.

Rasmussen, C.E., S.M. Guiter, and S.G. Thomas, Two-dimensional model of the plasmasphere: refilling time constants, Planet. Space Sci., 41, 35, 1993.

Reeves, G.D., *et al.*, Radial propagation of substorm injections, Intern. Conf. Substorms-3, *Eur. Space Agency Spec. Publ.*, ESA SP-339, 579, 1996.

Richmond, A.D., and Y. Kamide, Mapping electrodynamic features of the high-latitude ionosphere from localized observations: Technique, *J. Geophys. Res.*, 93, 5741, 1988.

Ridley, A.J., and M.W. Liemohn, A model-derived storm time asymmetric ring current driven electric field description, *J. Geophys. Res.*, 107, doi:10.1029/2001JA000051, 2002.

Rowland, D.E., and J.R. Wygant, Dependence of the large-scale, inner magnetospheric electric field on geomagnetic activity, *J. Geophys. Res.*, 103, 14,959, 1998.

Russell, C.T., and R.L. McPherron, Semiannual variation of geomagnetic activity, *J. Geophys. Res.*, 78, 92, 1973.

Schulz, M., and L.J. Lanzerotti, Particle diffusion in the radiation belts, Springer-Verlag, Berlin, 1974.

Sheldon, R.B., and D.C. Hamilton, Ion transport and loss in the Earth's quiet ring current: 1. Data and standard model, *J. Geophys. Res.*, 98, 13491, 1993.

Sheldon, R.B., H.E. Spence, and J.F. Fennell, Observation of the 40 keV field-aligned ion beams, *Geophys. Res. Lett.*, 25, 1617, 1998.

Stern, D.P., The motion of a proton in the equatorial magnetosphere, *J. Geophys. Res.*, 80, 595, 1975.

Takahashi, S., T. Iyemori, and M. Takeda, A simulation of the storm-time ring current, *Planet. Space Sci.*, 38, 1133, 1990.

Thomsen, M.F., *et al.*, Variability of the ring current source population, *Geophys. Res. Lett.*, 25, 3481, 1998.

Thorne, R.M., and R.B. Horne, The contribution of ion-cyclotron waves to electron heating and SAR-arc excitation near the storm-time plasmapause, *Geophys. Res. Lett.*, 19, 417, 1992.

Thorne, R.M., and R.B. Horne, Energy transfer between energetic ring current H^+ and O^+ by electromagnetic ion cyclotron waves, *J. Geophys. Res.*, 99, 17,275, 1994.

Tsyganenko, N.A., A magnetospheric magnetic field model with a warped tail plasma sheet, *Planet. Space Sci.*, 37, 5, 1989.

Turner, N.E., D.N. Baker, T.I. Pulkkinen, and R.L. McPherron, Evaluation of the tail current contribution to *Dst*, *J. Geophys. Res.*, 105, 5431, 2000.

Turner, N.E., D.N. Baker, T.I. Pulkkinen, J.L. Roeder, J.F. Fennell, and V.K. Jordanova, Energy content in the stormtime ring current, *J. Geophys. Res.*, 106, 19149, 2001.

Volland, H., A semiempirical model of large-scale magnetospheric electric fields, *J. Geophys. Res.*, 78, 171, 1973.

Wolf, R.A., The quasi-static (slow-flow) region of the magnetosphere, in *Solar-Terrestrial Physics*, ed. by R.L. Carovillano and J.M. Forbes, pp. 303-368, D. Reidel, Norwell, Mass., 1983.

Wolf, R.A., J.W. Freeman Jr., B.A. Hausmann, R.W. Spiro, R.V. Hilmer, and R.L. Lambour, Modeling convection effects in magnetic storms, in *Magnetic Storms*, Geophys. Monogr. Ser., vol. 98, edited by B.T. Tsurutani *et al.*, pp. 161, AGU, Washington, D.C., 1997.

Wygant, J., D. Rowland, H.J. Singer, M. Temerin, F. Mozer, and M.K. Hudson, Experimental evidence on the role of the large spatial scale electric field in creating the ring current, *J. Geophys. Res.*, 103, 29,527, 1998.

Young, D.T., H. Balsiger, and J. Geiss, Correlations of magnetospheric ion composition with geomagnetic and solar activity, *J. Geophys. Res.*, 87, 9077, 1982.

V.K. Jordanova, Space Science Center, 410 Morse Hall, University of New Hampshire, Durham, NH 03824, USA.

Energetic Particle Losses From the Inner Magnetosphere

Hannu E.J. Koskinen

University of Helsinki, Department of Physical Sciences, Helsinki, Finland
and Finnish Meteorological Institute, Helsinki, Finland

The inner magnetosphere displays many interesting phenomena involving magnetospheric storm dynamics and balancing between particle source and loss processes. In this article the recent progress in two particular loss phenomena are reviewed, namely the relative role of convective and charge exchange losses of energetic ring current ions and the loss of relativistic outer radiation belt electrons. Both are highly relevant for understanding of magnetospheric storms. The former is directly related to the determination of the storm intensity and the latter to the processes through which the storms control the appearance of relativistic electrons that are among the most serious sources of anomalous behavior of satellite electronics. While significant progress has been achieved in modeling and theoretical studies of both the ring current ions and relativistic electrons, this part of magnetospheric physics is suffering of inadequate observational basis. A well-equipped fleet of inner magnetosphere spacecraft observing plasmaspheric composition, ring current and radiation belt particles, and electromagnetic fields including the most critical wave modes is urgently needed to give a more sound empirical foundation for our studies of the inner magnetosphere and to constrain the rapidly evolving theoretical and numerical models.

1. INTRODUCTION

The inner magnetosphere is a complex region containing several different particle species that move under the influence of the nearly dipolar magnetic field of the Earth. The different particle populations are coupled to each other through complicated interactions and full understanding of the inner magnetospheric physics requires understanding of these coupling mechanisms. For example, one might think that the cool (~1 eV) plasmasphere would not play any significant role in the dynamics of the relativistic (several MeV) electrons in the outer radiation belt. However, as will be discussed below, the detailed properties of the plasmasphere determine the characteristics of the waves that dominate the relativistic electron losses. Furthermore, in magnetospheric physics the role of the neutral atoms above the ionosphere is often neglected. However, the neutral exosphere of the Earth is dense enough to dominate the loss of energetic ring current ions from trapped orbits through charge exchange collisions.

For a complete description of particle dynamics in the inner magnetosphere it would be necessary to consider the various source, loss and transport phenomena in a unified way (see, e.g., V.K. Jordanova's article in this issue). In fact, several mechanisms (e.g., wave-particle interactions or electric field pulses) can both act as sources of energetic particles through acceleration and cause loss of particles by moving them to the atmospheric loss cone. It is also useful to note that the same physical agent can have a major impact on several populations as is the case of electromagnetic ion cyclotron waves that can scatter both ring current ions and relativistic outer belt electrons into the loss cone.

Our approach in this article is not to deal with all aspects of particle dynamics. We start from the level of understanding compiled in the International Space Science

The Inner Magnetosphere: Physics and Modeling
Geophysical Monograph Series 155

10.1029/155GM03

Institute (ISSI) book on Magnetospheric Plasma Sources and Losses [*Hultqvist et al.*, 1999] and focus on recent progress in two major and presently very popular loss issues, namely the loss of ring current ions (section 3) and relativistic electrons (section 4). Both of these phenomena are closely related to magnetic storms. Before dwelling into these details we briefly review the basics of general particle losses (section 2). Finally we discuss the urgent need for more comprehensive observations that are needed to constrain the models of the inner magnetosphere.

2. THE INNER MAGNETOSPHERE

With the inner magnetosphere we understand in this article the region from the inner radiation belt to the outer parts of the ring current and the outer radiation belt somewhat beyond the geostationary orbit. The inner magnetosphere contains several different particle populations, which introduces a large variety of significant physical interactions.

The plasmasphere consists of cold (~1 eV) and relatively dense (10^3 cm^{-3}) plasma of ionospheric origin, which co-rotates with the Earth. Its boundary is called plasmapause and it is close to the boundary between closed drift paths of the particles under the influence of the co-rotation electric field and open drift paths determined by the convection electric field. Consequently, the plasmapause is located at L-shells 3-5, depending on the magnetic activity. During disturbed periods the convection electric field is enhanced and pushes the plasmapause closer to the Earth. The plasmasphere is asymmetric with a bulge in the evening sector. The bulge is pushed toward the afternoon during strong convection.

There are two major radiation belts. In the inner belt, mostly at $L < 2$, the radiation is dominated by energetic protons (0.1-40 MeV) whereas the outer belt consists of electrons in the keV-MeV range. There is significant electron population also in the inner belt but in the slot region between the inner and outer belts is most of the time void of energetic electrons. It may occasionally become filled with electrons up to very high energies during particularly strong storms. Once the electrons become trapped at these L-shells they scatter to the atmospheric loss cone very slowly.

The westward drift of energetic ions around the Earth carries the westward ring current. The most important current carriers are protons in the energy range 10-200 keV. During magnetospheric storms this current intensifies and causes a world-wide depression of the north component of the magnetic field measured at mid and low latitudes. This depression is converted to the famous Dst index that is one of the most important measures of the storm strength.

The whole inner magnetosphere is embedded in the gravitationally bound tenuous exosphere of hydrogen atoms that extends far beyond the inner magnetosphere. The exosphere affects magnetospheric dynamics through charge exchange collisions with energetic H^+ and O^+ ions in the ring current. The charge exchange results in a low-energy proton and an energetic neutral atom (ENA), either hydrogen or oxygen, that carries away energy and momentum from the interaction region along a ballistic (practically straight) orbit.

In the inner magnetosphere the magnetic field lines form a closed magnetic bottle and charged particles can remain stably trapped over long periods of time. However, the trapping is not complete. Although infrequent, the Coulomb collisions continuously introduce small changes in the pitch-angles of the particles and some of them are lost to the atmospheric loss cones. Whereas the Coulomb losses are rather slow, the ion-neutral charge exchange collisions are very efficient to transform ring current ions to fast neutrals that escape from the system in all directions. This is the main mechanism to reduce the ring current intensity in the late recovery phases of magnetic storms.

There are always fluctuations in the electromagnetic fields, which scatter particles to the atmospheric loss cones. During strong perturbations the fluctuations become larger and more efficient to remove particles from trapped orbits.

Finally, the solar wind-driven plasma convection sets up a spatially and temporally variable electric field in the magnetospheric coordinate system. The drift paths in the corotation-dominated region are closed whereas they are open in the convection-dominated region. The energy- and species-dependent boundaries between these regions are called the Alfvén layers. Enhanced solar wind driving pushes the Alfvén layers inward and thus the particles coming from the night-side can reach lower L-shells but at the same time previously trapped particles in the day-side can escape and be lost to the magnetopause. As will be discussed in section 3, the amount and significance of energetic ions on open drift paths to the ring current dynamics is one of the presently popular research topics.

The outer boundary of the cool (~1 eV) plasmasphere is roughly equivalent to the Alfvén layer of low-energy particles. The plasmasphere co-rotates with the Earth whereas the hot magnetospheric plasma is forced to convect around this obstacle. Figure 1 is an illustration of the role of the plasmapause to the theme of the present discussion. Note that the shape of plasmapause in this figure indicates strong magnetospheric convection, which shifts the afternoon bulge toward the noon.

The interactions of plasma populations with substantially different characteristics in the vicinity of the plasmapause give rise to a multitude of plasma waves. In the dawn sector, just beyond the plasmapause, right-hand polarized whistler-mode waves are observed over a wide spatial range. In the afternoon sector the left-hand polarized electromagnetic ion

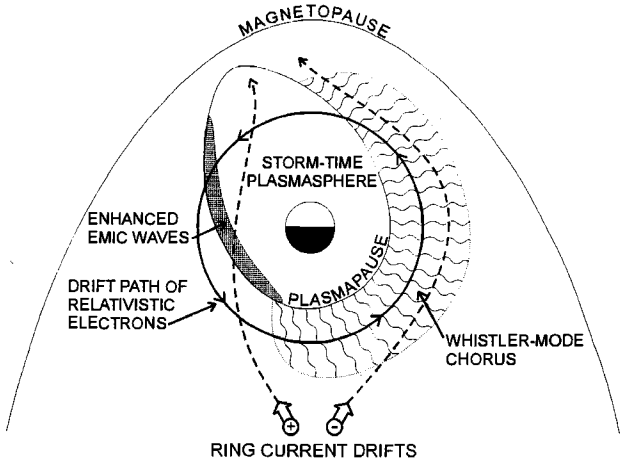

Figure 1. The inner magnetosphere and some of the key elements for energetic particle losses. [*Summers et al.*, 1998].

cyclotron (EMIC) wave amplitudes are strongly enhanced. Note that these waves appear in all local time sectors, but this region of strongly enhanced EMIC waves is particularly significant for the losses of both ring current ions and relativistic electrons.

3. LOSS OF RING CURRENT IONS

3.1. Loss Mechanisms

Already at the dawn of modern magnetospheric physics *Dessler and Parker* [1959] suggested that charge exchange between energetic ions and neutral hydrogen of the exosphere would provide efficient dissipation of ring current energy. As H^+ and O^+ are the dominant ion species in the ring current, the energetic neutral atoms (ENAs) produced by charge-exchange are hydrogen and oxygen atoms. The atom leaves the interaction point along a straight line conserving the momentum of the ion at the moment of electron capture. This makes possible remote sensing of the regions where the charge-exchange is strong enough. While this has been known for some time, it has only recently become possible to observe ENAs with sufficient accuracy for scientific analysis [e.g. *C:son Brandt et al.*, 2002; *Perez et al.*, 2004]. The inversion of the observations is still quite challenging and, in the case of IMAGE ENA observations, limited to the lower end of ring current energies [*Perez et al.*, 2004].

The charge-exchange is the most efficient ion loss mechanism from closed drift paths in the energy range 10-100 keV. The Coulomb collisions also lead to ring current losses, as they transfer energy from energetic particles to thermal plasma and scatter ions to the atmospheric loss cones. As shown by *Fok et al.* [1991], the Coulomb collisions become important for protons below 10 keV and for heavy ions below about 40 keV. The loss of heavier ions is slower than that of protons. Thus it is expected that in the storm recovery phase the protons are more dominant in the energy range above 10 keV wheras the lower energies should be dominated by heavier ions. Note that the modelling of the Coulomb interactions requires knowledge of the average plasmaspheric ion composition.

The models limited to charge exchange and classical Coulomb interactions tend to overestimate the proton fluxes above several tens of keV and produce too flat pitch-angle distributions above 100 keV [*Fok et al.*, 1995]. It is most likely that these features require inclusion of wave-particle interactions in the calculations [e.g., *Fok et al.*, 1996], but due to the lack of sufficiently detailed observations the relative importance of different wave modes is not fully known. For a long time the most promising candidate has been the electromagnetic ion cyclotron (EMIC) mode. It is a left-hand polarized wave mode (*L*-mode) with a frequency below the local ion cyclotron frequency. In multi-ion plasmas the waves appear in frequency bands below the gyrofrequency of each ion species. In the equatorial magnetosphere the mode can be driven unstable by anisotropic ($T_\perp > T_\parallel$) ring current ions in the vicinity of the plasmapause density gradient [*Cornwall*, 1970; *Lyons and Thorne*, 1972]. It still remains to be found out empirically whether the waves are abundant and strong enough in wide enough spatial region to explain the remaining characteristics of energetic ion distributions.

In numerical modeling a self-consistent calculation of the wave amplification is difficult, as it requires knowledge on the detailed ion composition as well as the noise level from which the waves grow. Recent model calculations [*Jordanova et al.*, 2003] discussed in the next section and by V.K. Jordanova in this issue indicate that the EMIC waves really are important for ion losses in the high-energy part of the ring current carriers.

3.2. Convection Losses of Ring Current Ions

When the intensity of the ring current is estimated from the pressure corrected Dst (Dst*) index, the decay of the ring current at the storm recovery phase often indicates two timescales. First the decay is faster and turns later to a slower rate. This feature has been interpreted in terms of the different charge exchange lifetimes of O^+ and H^+ ions. The O^+ lifetime at $L \approx 3$ is about 7-10 hours, whereas the H^+ lifetimes are from one to several days [e.g., *Fok et al.*, 1991]. *Hamilton et al.* [1988] investigated the great storm in February 1986 using AMPTE/CCE observations of the ring current particles. They associated the rapid recovery of the Dst index on February 9 ($\tau \approx 9.3$ hours) with the fast decay of 75-100 keV O^+ ions. *Daglis* [1997] analysed five more

storms near the solar maximum period in 1991 using the CRRES data and came to a similar conclusion.

While it is evident that charge exchange is the dominant loss process of ions on trapped drift paths around the Earth, there is another significant loss mechanism during storm periods. The enhanced convection pushes the Alfvén layers closer to the Earth and previously stably trapped ions find themselves on open drift paths and are lost to the magnetopause. At the same time the convection enhances the ion supply from the plasmasheet but most of these ions are unable to make complete orbits around the Earth and are also lost to the dayside magnetopause. These ions are expected to carry an asymmetric partial ring current from the night sector to the pre-noon sector with a minimum in the post-midnight region, and the current carriers should reflect the plasma composition of the source region. As long as there is sufficient supply of oxygen, there are oxygen ions in the partial ring current. The weakening of both the convection as well as the plasma sheet supply leads to rapid disappearance of this current element and the much slower charge exchange begins to determine the recovery rate. It is, however, quite difficult to determine the relative contributions of the O^+ decay and the weakening of theion current on open drift paths from the rather sparse observational data.

During the last few years this question has been addressed in a number of studies using various versions of the Ring Current-Atmosphere Interaction Model (RAM), where different electric field models are applied to describe the ion drift motion and to determine the open-closed drift boundaries for different ion species. The basic model solves the gyro- and bounce-averaged kinetic equation for the particle phase space distribution functions of different ring current particle species. The applied models include the collisionless drifts, charge exchange, scattering by Coulomb collisions, and the precipitation into the atmosphere and, in some of these studies, also wave-particle interactions at somewhat different levels of sophistication. A critical issue is the inclusion of the electric field model. A simple Volland-Stern [*Volland*, 1973; *Stern*, 1975] model is sufficient to illustrate the main convection losses, but much better model-data agreement is found by using less symmetric electric field models, e.g., the *McIlwain* [1986] model [e.g., *Liemohn et al.*, 2001; *Kozyra et al.*, 2002] or the so-called MACEP procedure, where the electric field is derived using the AMIE technique [*Richmond and Kamide*, 1988], with or without anasymmetric ring current driven penetration electric field at low magnetic latitudes [*Boonsiriseth et al.*, 2001; *Jordanova et al.*, 2003].

Liemohn et al. [2001] modeled three storms (May 15, 1998; September 25, 1998; October 19, 1998) and found that in each case about 80% of the Dst* index at its minimum was due to ions on open drift paths. They also claimed that the rapid decay at the early recovery could not be due to the faster O^+ than H^+ charge exchange, as the observational data indicated much larger H^+ fractions than was the case in the storms analyzed by *Hamilton et al.* [1988] and *Daglis* [1997].

The storms modeled by *Liemohn et al.* [2001] took place near the solar minimum. *Kozyra et al.* [2002] investigated another storm near the solar maximum period on June 5-6, 1991 using the same model. In this case the ring current during the storm main phase was more oxygen-rich and the whole storm was more complicated with two Dst* peaks separated from each other by about 30 min. *Kozyra et al.* [2002] came to the same, although more refined, basic conclusion as *Liemohn et al.* [2001]. More than 80% of the ring current energy during the peak periods of the storm was carried by ions on open drift paths. The rapid early recovery of Dst* was due to rapid convective loss, after which the region of closed drift paths expanded and the later recovery phase was dominated by the much slower charge exchange. Instead of two clearly identifiable time scales after the closure of the drift paths the decay rate of the trapped ions decreased gradually with the changing ion composition and energy content. *Kozyra et al.* [2002] argued that two distinct time scales could be observed only if the two-species ring current would be sharply peaked in energy, pitch angle, and L shell, which according to them has never been observed.

Daglis et al. [2003] compared the charge-exchange and outflow losses during the previously discussed June 1991 and September 1998 storms (Figure 2). They suggested that "charge-exchange appears a more important decay agent in solar maximum storms, which have a dominant O^+ component." While this sounds as a reasonable conclusion, it is quite evident that more detailed direct observations of the ring current ions in different phases of magnetospheric storms are necessary to resolve this issue. The RAM modeling results point out that the role of the O^+ ions in the determination of the fast decay rate in the early recovery phase may be smaller than previously anticipated. Note, however, that in general the role of oxygen in the storm dynamics is a much wider issue, as it is related to the magnetosphere-ionosphere coupling and to the role of substorms in the storm evolution, in particular, in preconditioning of the seed population in the plasma sheet. Thus detailed observational and modeling studies of oxygen are needed in the future as well.

4. LOSS OF RELATIVISTIC ELECTRONS

4.1. Electron Loss Mechanisms

Also low-energy electrons are lost convectively to the dayside magnetopause from the open drift paths. However, the drift paths of electrons at radiation belt energies are closed

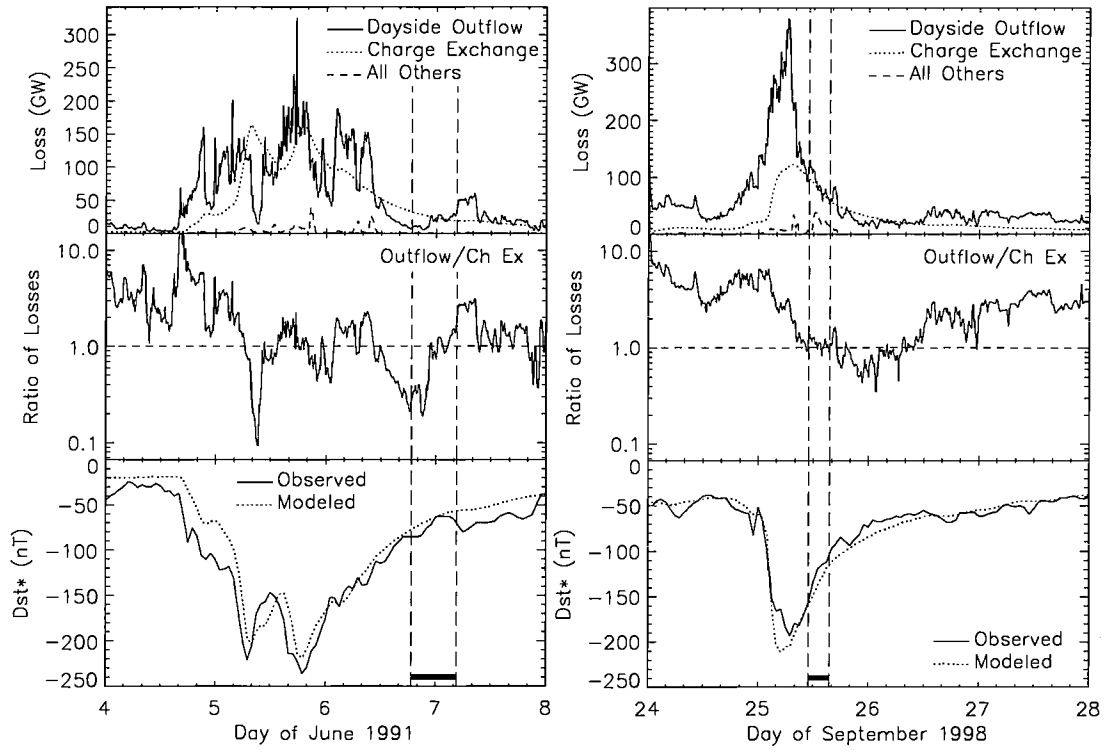

Figure 2. Comparison of modeled ring current losses during two stroms [*Daglis et al.*, 2003]. The upper panels display the dominating loss mechanisms, the middle panels show the relative fractions of outflow and charge exchange, and the bottom panels compare the modeled and observed Dst indices. The dashed time intervals indicate periods when charge exchange lifetimes were possible to calculate from the CRRES data (June 1991 storm) and when POLAR ENA observations were available (September 1998 storm).

except during periods when the magnetopause is compressed close to the geostationary distance.

Coulomb collisions move electrons to the atmospheric loss cone. The lifetimes of the electrons depend on their energies and on the density of collision targets and increase strongly with the L-shell. Figure 3 adapted from *Abel and Thorne* [1998a] illustrates this effect for selected electron energies in the L-range 1.2-4. The Coulomb lifetime is indicated in the figure by the envelope curve denoted by "Coulomb" in each panel. The lifetime of 100-keV electrons exceeds 1 year at $L \approx 1.8$ and reaches 30 years at $L \approx 5$. For the relativistic 1.5-MeV electrons the lifetime is 1 year at $L \approx 1.3$ and 30 years at $L \approx 1.8$. Thus the Coulomb collisions alone are quite inefficient to remove the particles from the radiation belts.

For radiation belt electrons the wave-particle interactions are more important than for ring current ions. The right-hand polarized whistler branch of wave modes is the most obvious agent to scatter the electrons to the loss cone. These modes include the plasmaspheric hiss, lightning-induced whistlers, and man-made VLF signals. The plasmaspheric hiss is the most intense whistler mode wave in the inner magnetosphere. It is confined within the plasmasphere and driven unstable by gyroresonant interaction with energetic electrons [*Thorne et al.*, 1979]. While the driving electrons may be associated to substorm injections, the hiss is detectable also during quiet times. As shown in Figure 3 taking this emission into account leads to significant reduction of electron lifetimes at the L-shells where the curve labeled C/H deviates below the Coulomb curve. Beyond $L \approx 3$ the lifetimes are reduced down to a few tens of days.

At smaller L both lightning-induced whistlers (label C/H/W) and the man-made VLF signals (label C/H/W/VLF) add further to the loss of electrons. For relativistic electrons also the left-hand polarized EMIC waves become important, as discussed in section 4.4.

The lifetime results of *Abel and Thorne* [1998a] depend, of course, on the assumed plasma parameters and wave field intensities. In an accompanying paper [*Abel and Thorne*, 1998b] the authors conducted a parametric study to analyze the sensitivity of their results to model parameters. Each of the investigated wave modes introduces its own range of uncertainty within the L-shell range where it most efficiently reduces the lifetime. However, qualitatively the results

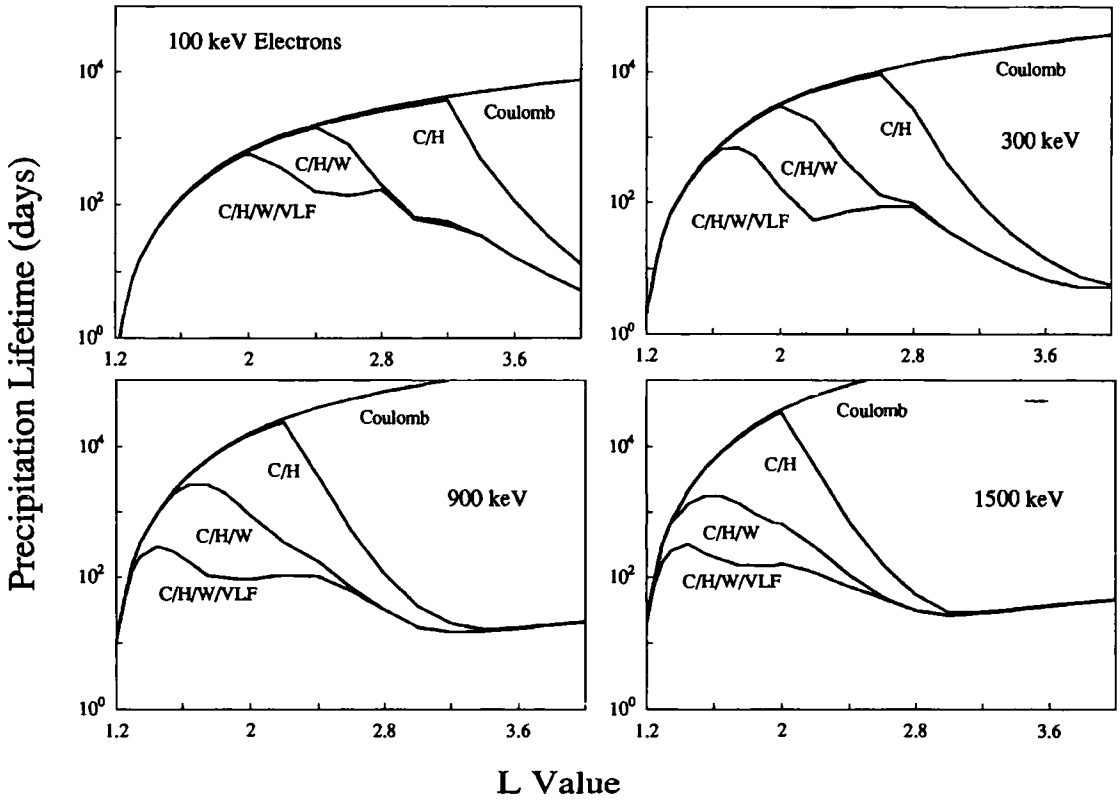

Figure 3. Theoretical calculations of electron lifetimes as a function of L-shell for weakly relativistic (100 and 300 keV) and relativistic (900 and 1500 keV) electrons [*Abel and Thorne*, 1998]. The uppermost envelope in each panel describes the lifetimes calculated using Coulomb collisions alone. Thereafter the effect of plasmaspheric hiss is included (C/H) and the lifetime is seen to drop beyond a given L-shell depending on the energy. Next the lightning-induced whistler mode (C/H/W) and finally the man-made VLF emissions (C/H/W/VLF) are included.

remain the same as in Figure 3, with deviations less than an order of magnitude from the nominal lifetimes of *Abel and Thorne* [1998a].

Note that the whistler-mode chorus outside the post-midnight plasmapause (Figure 1) may be more important for electron acceleration than loss. Chorus waves are excited by cyclotron resonance with anisotropic 10-100-keV electrons in the local time range 2200-0900 magnetic local time [*Tsurutani and Smith*, 1974]. *Summers et al.* [1998] suggested that the waves scatter the relativistic electrons toward pitch angles near 90° and lead to enhanced electron acceleration from a few 100 keV toenergies above 1 MeV.

4.2. Storm Effects on Energetic Electrons

The interplay between the magnetospheric storms and relativistic outer belt electrons is a scientifically interesting and practically important issue because relativistic electrons belong to the major sources of anomalous behavior and even loss of satellites during strongly disturbed conditions. Storms and substorms have traditionally been considered mostly as sources of these electrons but the picture is actually a bit more complicated.

Recently, *Reeves et al.* [2003] published a study of 276 moderate and strong geomagnetic storms during the years 1989-2000. They found that only 53% of the investigated storms increased the relativistic electron fluxes and 19% actually decreased the fluxed. In the remaining 28% of cases the fluxes changed less than a factor of two. This was found to be independent of the L-shell and of the storm strength determined by the minimum Dst. Figure 4 shows examples of each type of events. It was quite noteworthy that there was practically no correlation between pre-storm and post-storm fluxes. Thus the relativistic electron fluxes cannot be predicted based on the history of relativistic electrons alone. A rigorous calculation requires proper inclusion of acceleration, transport, and loss processes.

A further examination by *Reeves et al.* [2003] showed that the storm-associated reductions of the electron fluxes were real losses, and not due adiabatic effects related to the field

[redacted]

[redacted]

[redacted]

[redacted]

[redacted]

[redacted]

[redacted]

[redacted]

energy was typically well above 2 MeV. In localized regions of high plasma density and/or low magnetic field ($\Omega_e^2/\omega_{pe}^2 < 10^{-2}$) the resonant energy can fall below 2 MeV for wave frequencies just below H^+ and He^+ gyrofrequencies. This was found to be the case in about 10% of L-mode observations in the afternoon sector (13-18 MLT) for $L > 4.5$. That the interaction region is limited to a small fraction ($\leq 1\%$) of the orbit of the electrons is rather an advantage than a disadvantage, as this allows for drift-averaged lifetimes from hours to one day. Would the interaction take place within a too wide region, the relativistic electrons would disappear faster than observed.

Meredith et al. [2003] found no clear dependence of the low resonant energy events on the magnetospheric activity. The events were found for almost any value of the Dst index, with a slight tendency to occur more often during moderate or greater storms.

The pitch-angle scattering of relativistic electrons is a prime example of the interconnectedness of the inner magnetospheric particle populations and magnetospheric storms. The plasmapause provides high-enough plasma density (large enough ω_{pe}) and appropriate background ion composition. The storm is needed to supply the ring current ions that drive the EMIC waves unstable [e.g., *Jordanova et al.*, 2001] and finally the waves of the low-energy ion population scatter electrons of relativistic energies.

5. CONCLUDING REMARKS

The increased interests in space weather applications during the last ten years have brought new demand on better modeling schemes of the inner magnetosphere during strongly disturbed periods, space storms. The scientific community has accepted this challenge, which have brought the physics of storms and the inner magnetosphere to the forefront of space physics.

In this review the discussion has been limited to two issues, the loss of ring current ions and relativistic electrons, where significant progress has been achieved both in theoretical and modeling studies. In fact, one may argue that during the recent years the modeling efforts have progressed to a much higher level of sophistication than the observations may really allow. The presently available data coverage is rather sparse in space and time and we can mostly study the effects of the storm-related processes in particle distributions but only seldom the processes themselves. As the most critical region for these studies is the nearly-equatorial magnetosphere within a wide range of L-shells, the 15 months of CRRES observations in 1990-1991 are still among the most useful for detailed analysis of the physical processes.

For the ring current ions the question of processes on open vs. closed drift paths and the associated asymmetries definitely ask for better observational basis. In particular it would be very useful to have simultaneous observations of both waves and particles at several magnetic local times to see the evolution of the ion current on open drift paths and the role of wave-particle interactions thereupon. The emerging remote sensing using ENA techniques may in the future contribute important new means to study this issue, but the presently available data are still too coarse and the inversion methods are still rather immature. Meanwhile it might be useful to look for the signatures of the open drift paths in the asymmetries of the magnetic perturbations measured on ground.

Also the theoretical and modeling results on relativistic electron dynamics require better empirical basis. Here the lack of primary data is perhaps not as bad as in the case of ring current, as several satellites carry energetic electron instruments in the various parts of the magnetosphere. However, if we want to make detailed studies relating the electron observations to local plasma and field conditions in various local time and L-shell regions, we meet the same problem: CRRES data are again the best we have.

The storms clearly behave very individually and analyzing a small number of in situ data is not sufficient for general conclusions. The above considerations strongly argue for a fleet of at least 3 or 4 spacecraft in CRRES-type (nearly GTO) orbits with apogees at different local times. This would allow for synoptic in situ observations of both the primary targets, such as ring current ions and radiation belt particles, and the critical background plasma parameters and actual wave fields. In such a configuration some of the spacecraft would be at a low L-shell at the same time when the others are further away. A wide local time coverage is needed to deal with the significant asymmetries of the plasmasphere, wave occurrence, and the main phase ring current.

Specific missions for this purpose have been proposed to the European Space Agency in 2000 (STORMS, which went through the assessment study but was not selected) and to the Living With a Star program of NASA (Radiation Belt Storm Probes, whose number does not finally appear to more than two). Further progress in the physics of the inner magnetosphere would urgently need such observations. And without solid scientific basis the reliability of the more application-oriented models can be doubted.

Acknowledgments. I am greatful to the organizers of the Chapman Conference on the Physics and Modeling of the Inner Magnetosphere. It provided an excellent forum for exchange of ideas that also strongly influenced the present article.

REFERENCES

Abel, B. and R.M. Thorne, Electron scattering loss in Earth's inner magnetosphere 1. Dominant physical processes, *J. Geophys. Res.*, 103(A2), 2385-2396, 1998a.

Abel, B. and R.M. Thorne, Electron scattering loss in Earth's inner magnetosphere 2. Sensitivity to model parameters *J. Geophys. Res.*, 103(A2), 2397-2407, 1998b.

Boonsiriseth, A., R.M. Thorne, G. Lu, V.K. Jordanova, M.F. Thomsen, D.M. Ober, and A.J. Ridley, A semiempirical equatorial mapping of AMIE convection electric potentials (MACEP) for the January 10, 1997, magnetic storm, *J. Geophys. Res.*, 106, 12,903-12,917, 2001.

Cornwall, J.M., F.V. Coroniti, and R.M. Thorne, Turbulent loss of ring current protons, *J. Geophys. Res.*, 75, 4699, 1970.

C:son Brandt, P., S. Ohtani, D.G. Mitchell, M.-C. Fok, E.C. Roelof, and R. Demajistre, Global ENA observations of the storm main phase ring current: Implications for skewed electric fields in the inner magnetosphere, *Geophys. Res. Lett*, 29 (20), 1954, doi:10.1029/2002GL015160, 2002.

Daglis, I.A., The role of magnetosphere-ionosphere coupling in magnetic storm dynamics, Magnetic Storms, Geophys. Monogr. Ser., vol. 98 edited by B.T. Tsurutani *et al.*, pp. 107-116, AGU, Washington, D. C., 1997.

Daglis, I.A., J.U. Kozyra, Y. Kamide, D. Vassiliadis, A.S. Sharma, M.W. Liemohn, W.D. Gonzales, B.T. Tsurutani, and G. Lu, Intense space storms: Critical issues and open disputes, *J. Geophys. Res.*, 108(A5), 1208, doi:10.1029/2002JA009722, 2003.

Dessler A.J. and E.N. Parker, Hydromagnetic theory of geomagnetic storms, *J. Geophys. Res.*, 64, 2239, 1959.

Fok, M.-C., J.U. Kozyra, A.F. Nagy, and T.E. Cravens, Lifetime of ring current particles due to Coulomb collisions in the plasmasphere, *J. Geophys. Res.*, 96, 7861-7867, 1991.

Fok, M.-C., T.E. Moore, J.U. Kozyra, G.C. Ho, and D.C. Hamilton, Three-dimensional ring current decay model, *J. Geophys. Res.*, 100, 9619-9632, 1995.

Fok, M.-C., T.E. Moore, and M.E. Greenspan, Ring current development during storm main phase, *J. Geophys. Res.*, 101, 15,311-15,322,1996.

Hamilton, D.C., G. Gloeckler, F.M. Ipavich, W. St¸demann, B. Wilken, and G. Kremser, Ring current development during the great geomagnetic storm of February 1986, *J. Geophys. Res.*, 93, 14,343-14,355, 1988.

Hultqvist, B., M. Øieroset, G. Paschmann, and R. Treumann (Eds.) *Magnetospheric Plasma Sources and Losses, Space Sciences Series of ISSI*, Vol.6, Kluwer, Dordrecht, 1999 (Reprinted from *Space Sci. Rev.*, Vol 88, Nos. 1-2, 1999).

Jordanova, V.K., A. Boonsiriseth, R.M. Thorne, and Y. Dotan, Ring currrent asymmetry from global simulations using a high-resolution electric field model, *J. Geophys. Res.*, 108(A12), 1443, doi:10.1029/2003JA009993, 2003.

Jordanova, V.K., C.J. Farrugia, R.M. Thorne, G.V. Khazanov, G.D. Reeves, and M.F. Thomsen, Modeling ring current proton precipitation by EMIC waves during the May 14-16, 1997, storm, *J. Geophys. Res.*, 106, 7, 2001.

Kozyra, J.U., V.K. Jordanova, R.B. Horne, and R.M. Thorne, Modelling of the contribution of electromagnetic ion cyclotron (EMIC) waves to stormtime ring current erosion, in *Magnetic Storms, Geophys. Monogr. Ser.*, vol. 98 edited by B. T. Tsurutani *et al.*, pp. 187-202, AGU, Washington, D. C., 1997.

Kozyra, J.U., M.W. Liemohn, C.R. Clauer, A.J. Ridley, M.F. Thomsen, J.E. Borovsky, J.L. Roeder, V.K. Jordanova, and W.D. Gonzales, Multistep Dst development and ring current composition changes during the 4-6 June 1991 magnetic storm, *J. Geophys. Res.*, 106(A6), 10,883-10,904, 2001.

Liemohn, M.W., J.U. Kozyra, M.F. Thomsen, J.L. Roeder, G. Lu, J.E. Borovsky, and T.E. Cayton, Dominant role of the asymmetric ring current in producing the stormtime Dst*, *J. Geophys. Res.*, 107(A8), doi:10.1029/2001JA000023, 2002.

Lyons, L.R., and R.M. Thorne, Parasitic pitch angel diffusion of radiation belt particles by ion cyclotron waves, *J. Geophys. Res.*, 77, 5608, 1972.

McIlwain, C.E., A Kp-dependent equatorial electric field model, *Adv. Space Res.*, 6(3), 187, 1986.

Meredith, N.P., R.M. Thorne, R.B. Horne, D. Summers, B.J. Fraser, and R.R. Anderson, Statistical analysis of relativistic electron energies for cyclotron resonance with EMIC waves observed on CRRES, *J. Geophys. Res.*, 108(A6), 1250, doi:10.1029/2002JA009700, 2003.

Perez, J.D., X.-X. Zhang, P. C:son Brandt, D.G. Mitchell, J.-M. Jahn, and C.J. Polloc, Dynamics of ring current ions as obtained from IMAGE HENA and MENA ENA images, *J. Geophys. Res.*, 109 A05208, doi:10.1029/2003JA010164, 2004.

Reeves, G.D., K.L. McAdams, and R.H.W. Friedel, Acceleration and loss of relativistic electrons during geomagnetic storms, *Geophys. Res. Lett*, 30(10), 1529, doi:10.1029/2002GL016513, 2003.

Richmond, A.D., and Y. Kamide, Mapping electrodynamic features of the high-latitude ionosphere from localized observations: Technique, *J. Geophys. Res.*, 93, 5741, 1988.

Stern, D.P., The motion of a proton in the equatorial magnetosphere, *J. Geophys. Res.*, 80, 595, 1975.

Summers, D. and R.M. Thorne, Relativistic electron pitch-angle scattering by electromagnetic ion cyclotron waves during geomagnetic storms, *J. Geophys. Res.*, 108(A4), 11143, doi:10.1029/2002JA009489, 2003.

Summers, D., R.M. Thorne, and F. Xiao, Relativistic theory of wave-particle resonant diffusion with application to electron acceleration in the magnetosphere, *J. Geophys. Res.*, 103, 20,487, 1998.

Thorne, R.M. and C.F. Kennel, Relativistic electron precipitation during magnetic storm main phase, *J. Geophys. Res.*, 76, 4446, 1971.

Thorne, R.M., S.R. Church, and D.J. Gorney, On the origin of plasmaspheric hiss: The importance of wave propagation and the plasmapause, *J. Geophys. Res.*, 84, 5241, 1979.

Tsurutani, B.T. and E.J. Smith, Postmidnight chorus: A substorm phenomenon, *J. Geophys. Res.*, 79, 118, 1974.

Volland, H.A., A semiempirical model of large-scale magnetospheric electric field, *J. Geophys. Res.*, 78, 171, 1973.

H.E.J. Koskinen, University of Helsinki, Department of Physical Sciences, P.O.Box 64, FIN-00014 Helsinki. (e-mail: Hannu.E.Koskinen@helsinki.fi)

A Numerical Study on the Resonant Scattering Process of Relativistic Electrons via Whistler-Mode Waves in the Outer Radiation Belt

Yuto Katoh[1], Takayuki Ono, and Masahide Iizima

Department of Geophysics, Graduate School of Science, Tohoku University, Sendai, Miyagi, Japan

Resonant scattering processes of high energy electrons are studied numerically by using a newly developed simulation scheme where cold electrons are treated as a fluid and hot electrons are treated as particles including fully relativistic effects. The present simulation scheme enables us to investigate the resonant energy diffusion process of electrons in the inner magnetosphere, which has been difficult to study by using the PIC code. To verify the accuracy of the present scheme, elementary step of the resonant interaction of high energy electrons with whistler-mode waves are studied. The results of the experiment are consistent with the theoretical predictions and suggest that this simulation scheme has a capability to apply various problem in space physics concerning not only the resonant scattering process of high energetic electrons but the excitation of electromagnetic plasma waves and propagation process in the inhomogeneous media.

1. INTRODUCTION

As has been studied by many workers [e.g. *Baker et al.*, 1994; *Meredith et al.*, 2002], the flux of relativistic electrons in the outer radiation belt once decreases during the main phase of geomagnetic storms and increases again in the recovery phase. Several candidates of the mechanism have been proposed to explain the rebuilding process of the outer radiation belt; especially, the stochastic acceleration process of relativistic electrons by the resonant interaction with the enhanced plasma waves during geomagnetic storms has been studied in detail in the recent works [*Summers and Ma*, 2000; *Miyoshi et al.*, 2003]. These works have their basis on the quasi-linear theory and well explain the temporal and spatial evolution of the flux enhancement. However, there still remains many fundamental physical problems concerning the acceleration processes and a numerical simulation is thought to be an important tool to obtain such physical implications. For the investigation of the elementary process of the resonant interaction, a full particle simulation must be an useful one. However it is difficult to realize the requirement of spatial scale limit for the full particle code to simulate the cyclotron resonant interaction between hot electrons and electromagnetic plasma waves. The difficulty comes from the significant difference of their spatial scale sizes between the wave length of plasma waves and Larmor radius of thermal electrons. Let us consider that the cyclotron resonant interaction between relativistic electrons and electromagnetic plasma waves in the earth's outer radiation belt. The wave length of whistler-mode waves is of the order of 10^3 to 10^4 m, while Larmor radius or Debye length of cold electrons, the medium of propagation of plasma waves, is of the order of 10^0 m. In the study of cyclotron resonant interaction of hot electrons with the electromagnetic plasma waves, both propagation of plasma waves and the motion of cold electrons need to be solved at the same time. Because the grid spacing size must be the order of Debye length for the full particle code (PIC code), namely that $\Delta x \leq 3\lambda_e$ to avoid a nonphysical instability caused by grid spacing [*Birdsall and Langdon*, 1985; *Omura and Matsumoto*, 1993], it is not realistic to treat such a large spatial region to

[1]Now at Research Institute for Sustainable Humanosphere, Kyoto University, Uji, Kyoto, Japan

The Inner Magnetosphere: Physics and Modeling
Geophysical Monograph Series 155

10.1029/155GM04

study the interaction with whistler-mode electromagnetic waves.

To overcome this difficulty, we have developed a new simulation scheme by utilizing a model on the basis of the concept of the hybrid algorithm. In this scheme, plasmas are separated into two components, namely low density, high energy electron component and high density, cold electron component. That is, high energy electrons are treated as relativistic particles while cold electrons are treated as a fluid, considering the difference in the spatial scales of their Larmor radii. By employing this simulation model, we have no constraint on the grid size by the small spatial scale of the gyromotion of cold electrons. This treatment enables us to realize a simulation box with a sufficiently large spatial scale size to investigate the resonant interaction of energetic electrons with plasma waves propagating in the medium of cold electrons. As an example of the initial results, we evaluate the effect of the spectrum of whistler-mode waves by comparing the time variation of the number of the resonant particles. In this paper, we will show initial results of our simulation model and discuss the capability of the model for treating a basic physical process of resonant interaction. The results show that we can treat the acceleration process under the realistic magnetospheric condition by using our simulation model. Hereinafter, we refer to this hybrid model as "Electron Hybrid Model".

2. DETAILS OF THE MODEL

In our newly developed simulation scheme, the high energy electrons are treated as particles and the cold electrons as a fluid. Numerical simulation studies on the basis of similar approaches have been made by *Rathmann et al.* [1978] and *Omura and Matsumoto* [1982], named Long-Time-Scale Code; and *Taguchi et al.* [2001], named Hybrid Darwin Code. Compared with these already established simulation model, our simulation model has several advantages: First, particle motions of high energy electrons are treated including fully relativistic effect. The evolution of the electromagnetic field in time and space are directly solved without any assumptions by using Maxwell's equations. Thus, it can be said that our simulation model describes realistic energy transfer between high energy electrons and plasma waves propagating in the medium of cold electrons. This is one of the most significant advantages given by the present model; this model enables us to treat the wide wavenumber range of plasma waves covering excitation and propagation of free space electromagnetic waves and their cutoff process in inhomogeneous media.

Basic equations in this model to describe the particle motions and electromagnetic fields are as follows:

$$\frac{\partial \boldsymbol{v}_f}{\partial t} = -(\boldsymbol{v}_f \cdot \nabla)\boldsymbol{v}_f + \frac{\boldsymbol{q}}{\boldsymbol{m}_e}(\boldsymbol{E} + \boldsymbol{v}_f \times \boldsymbol{B}), \tag{1a}$$

$$\frac{\partial \rho_f}{\partial t} = -\nabla \cdot (\rho_f \boldsymbol{v}_f), \tag{1b}$$

$$\frac{\partial \boldsymbol{B}}{\partial t} = -\nabla \times \boldsymbol{E}, \tag{1c}$$

$$\frac{\partial \boldsymbol{E}}{\partial t} = \frac{1}{\mu_0 \varepsilon_0}\nabla \times \boldsymbol{B} - \frac{1}{\varepsilon_0}\boldsymbol{J}, \tag{1d}$$

$$\boldsymbol{J} = \boldsymbol{J}_f + \boldsymbol{J}_p, \tag{1e}$$

$$\frac{d\boldsymbol{p}_p}{dt} = q(E + \boldsymbol{v}_p \times \boldsymbol{B}), \tag{1f}$$

$$\frac{d\varepsilon_{kin}}{dt} = \boldsymbol{v}_p \cdot \frac{\boldsymbol{dp}_p}{\boldsymbol{dt}}, \tag{1g}$$

and

$$\mathbf{p}_p = \frac{\mathbf{v}_p}{\mathbf{c}^2}\varepsilon_{kin} \tag{1h}$$

where subscripts f and p denote the quantities associated with the cold (fluid) component and hot (particle) component of electrons, respectively; ε_{kin} is kinetic energy of the hot electron including its rest mass energy; and q and m_e represent charge and mass of electron, respectively. In the present study, we assume that ions are stationary background in the simulation system with a density satisfying quasi-charge-neutrality. Since the time scale in the present study is the order of the electron gyro-period, it is adequate to employ this assumption. The current densities of cold electron J_f and hot electron J_p are calculated separately from the motions of each electron species. A two-step Lax-Wendroff scheme is utilized to calculate the time development of the electromagnetic field and fluid motion of cold electrons. PIC scheme is applied for the hot electron particles and their motions are calculated by using a leap-frog method. To implement the simulation code, each physical value is normalized to be a dimensionless quantity; time is normalized by electron gyro-period T_{ce}, velocity and length are normalized by speed of light c and cT_{ce}, respectively.

Simulation system is separated into three regions as shown in Figure 1; namely, the physical region, the wave source region, and the damping region. High energy electrons are distributed in the physical region by employing a periodic boundary condition. Since the location of the boundary of hot electrons is different from that of cold electrons, to avoid the reflection of waves, a masking method is applied to the electric field caused by the current density of hot electrons near the boundary of the physical region. Plasma waves are assumed to propagate into the physical region from the

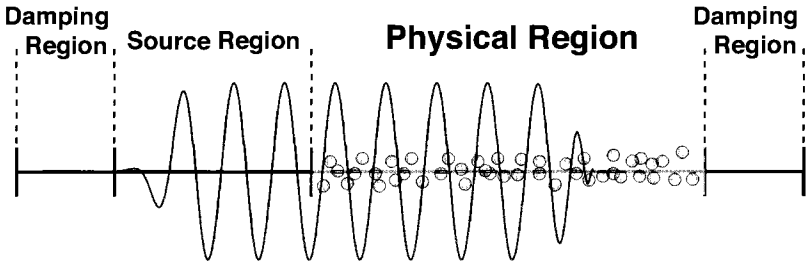

Figure 1. Configuration of the simulation system. High energetic electrons, which are treated as particles, are distributed only in the physical region. Plasma waves generated in the source region propagate into the physical region, and are absorbed in the damping regions.

source region (external source) along the direction of X-axis. In the wave source region, electromagnetic plasma waves are generated by an artificial oscillation of the electric field.

Numerical experiments have mainly been carried out to simulate the basic process of the resonant interaction between high energy electrons and whistler-mode plasma waves. In these simulation runs, we choose the system length of physical region L_x as 4096 Δx aligned to the initial magnetic field direction while grid spacing Δx as $1.0 \times 10^{-2} cT_{ce}$ and time step Δt as $7.5 \times 10^{-3}\ T_{ce}^{-1}$, which satisfy the time and spatial limits necessary for the precise simulation of plasma wave. The validity in the choice of these values are examined through the verification of exact propagation of plasma waves. In the present simulation the plasma parameter f_p/f_c is set to be $f_p/f_c = 1.0$, corresponding to the parameter at the outside region of the plasmapause; these grid spacing and time step width are corresponding to 100 m and 0.268 μsec, respectively, for the real spatial length and time interval.

It is noted that the number of grid points required for a full particle code simulation with the same system length is ten times as large as that of our simulation scheme, since Debye length of cold electrons is 3 m in this case. This advantage of Electron Hybrid Model will be more clearly recognized in the case of 2D or 3D simulation.

3. RESULTS OF NUMERICAL EXPERIMENT

To verify the validity of the present Electron Hybrid Model, test simulations are performed concerning the resonant interaction process of the high energy electrons with whistler-mode waves. To see the basic processes of the resonant interaction at first, the distribution function of high energy electrons is assumed to be a shifted bi-maxwellian type centered at a half of the speed of light corresponding to the energy of 79 keV. They are uniformly distributed in the physical region with their initial pitch angles and gyrophases forming an isotropic distribution (Plate 1). The plasma parameter of the background cold plasma is assumed to be as $f_p/f_c = 1.0$, which represents the typical plasma parameter of the outside region of plasmapause. The number density of high energy electrons is set to be 10^{-6} of the background cold electrons; 1,310,720 super-particles have been used for the calculation of the motion of high energy electrons.

As a first step, we compare the scattering processes by the monochromatic whistler-mode wave and by the whistler-mode wave with a banded spectrum characters. The monochromatic wave has a frequency of $0.5\,\Omega_e$, while the whistler-mode wave with a banded spectrum consists of waves continuously distributed from 0.3 to $0.6\,\Omega_e$. In each case, effective values of the wave amplitudes were set to be 1 mV_{rms}/m. We conducted each experiments up to a time of 7.5×10^3 gyro-cycle of electrons which corresponds to 270 msec time interval in the earth's inner magnetosphere.

The distributions of resonant particles in the velocity space at $7.5 \times 10^3 T_{ce}$ are shown in Plate 2(a) and (b), where these particles are picked up according to the criterion that the speed and pitch angle change from their initial conditions up to a value of 0.1% and 0.1 degree, respectively. In both cases, as shown in Plate 2(a) and (b), resonant particles are distributed on or within the cyclotron resonant curves. We have estimated the resonant curves from $\omega - k_{\|} v_{\|} = \Omega_e/\gamma$, where $v_{\|}$ is field aligned component of the velocity of resonant particles and γ is the Lorentz factor.

Figure 2 represents the variations in the speed of the high energy electrons from their initial speed at 1500, 3750 and 7500 T_{ce}. In early stage of the experiment, velocities of resonant particles in the case of the monochromatic wave show a more rapid change than the banded waves, until reaching a quasi-stationary state at 1500 Ω_e^- (Fig 2(a)). Although the velocity of resonant particles changes moderately in the case of waves with finite band width, the maximum variance in the velocity ($|\delta v| \sim 8.0 \times 10^{-3}\, c$) is rather larger than the monochromatic wave case ($|\delta v| \sim 6.0 \times 10^{-3}\, c$) as shown in Fig 2(c). This result can be explained by the continuous resonant scattering effect due to the broadness of the wave spectrum of

36 [redacted]

[redacted]

v_{ij} [c]

[redacted]

(a) [redacted]

[redacted]

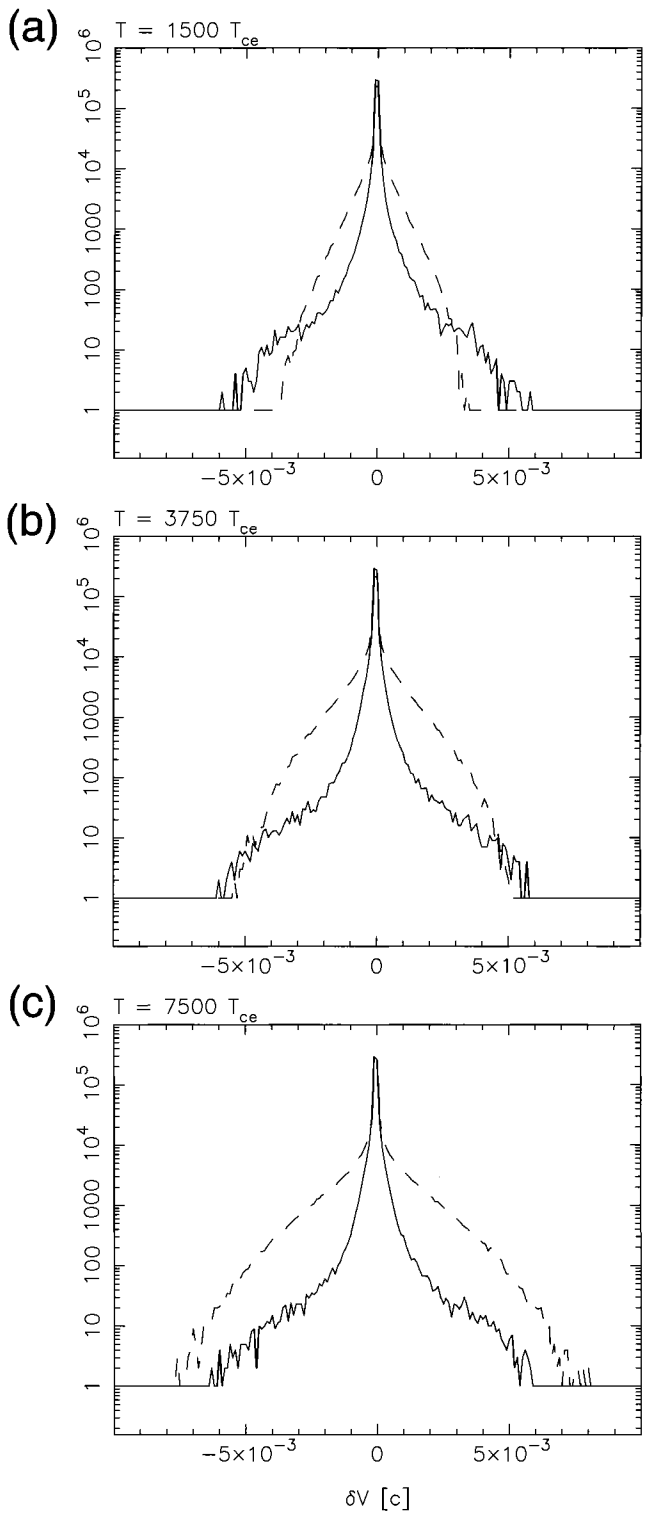

Figure 2. Time evolution of the velocities of the resonant electrons. The variation from the initial speed of electrons is plotted under the wave settings of single wave (solid line) and banded waves (dashed line) at (a) 1500, (b) 3750, (c) 7500 Ω_e^{-1}, respectively. The horizontal scale shows a deviation from the initial speed and the vertical scale shows the number of particles in each range.

whistler-mode wave. The resonant interaction caused by the wave with a frequency of f_a affects resonant particles which satisfy the resonance condition with f_a wave; the resonant particles are then accelerated (decelerated) and deviates from the resonance conditionwith f_a wave. In the case of the banded whistler-mode wave, these deviated particles subsequently interact with another wave with a frequency of $f_b = f_a + \delta f$; the effective acceleration (deceleration) of resonant particles occurs in the case of a wave with a finite band width.

The efficient resonant scattering process for the case of the wave with banded wave spectrum is also indicated in the energy transfer process between whistler-mode waves and energetic particles. In Figure 3, we show the time variations of the kinetic energy density of the energetic electron species for both types of waves. The kinetic energy density of energetic electrons continuously increases by the effect of the successive resonant interaction for the case of banded wave, whereas the kinetic energy slightly decreases for the case of the monochromatic wave. These simulation results suggest a possibility that waves with a finite band width such as turbulent waves induce efficient scattering of resonant particles in the phase space; that is, plasmaspheric hiss is an efficient energy source for the electrons, while man-made, monochromatic transmitter signals actually remove energy from plasma.

4. DISCUSSIONS

On the basis of the present simulation results, it has been demonstrated that our simulation scheme has a enough capability to understand the detailed features of the wave-particle interaction processes in the space plasma. In Fig 2(a), there are 'resonant' particles which are not lying on the resonant curve estimated from the frequency of the injected whistler-mode wave exactly. The existence of 'resonant' electrons can be explained by the effect of the generated plasma waves by the high energy electrons in the physical region. In the present simulation, the velocity distribution function of the high energy electrons is assumed to be the shifted-maxwellian type distribution function, and such electrons act as high energy beams in the simulation space. The beam distribution of electrons possibly excite the plasma waves due to the beam-type instability. To estimate the amplitude of such self-excited plasma waves, we performed another simulation without injecting the whistler-mode waves; the initial parameters of electrons and the condition of the simulation system are set to be the same as those represented in the previous section. Figure 4 shows the $\omega - k$ diagram of the plasma waves generated in the physical region. In the simulation result, whistler-mode waves on the branch of the parallel propagating mode are excited with the wave amplitude up to several $\mu V/m$, while their wave frequencies satisfy the first

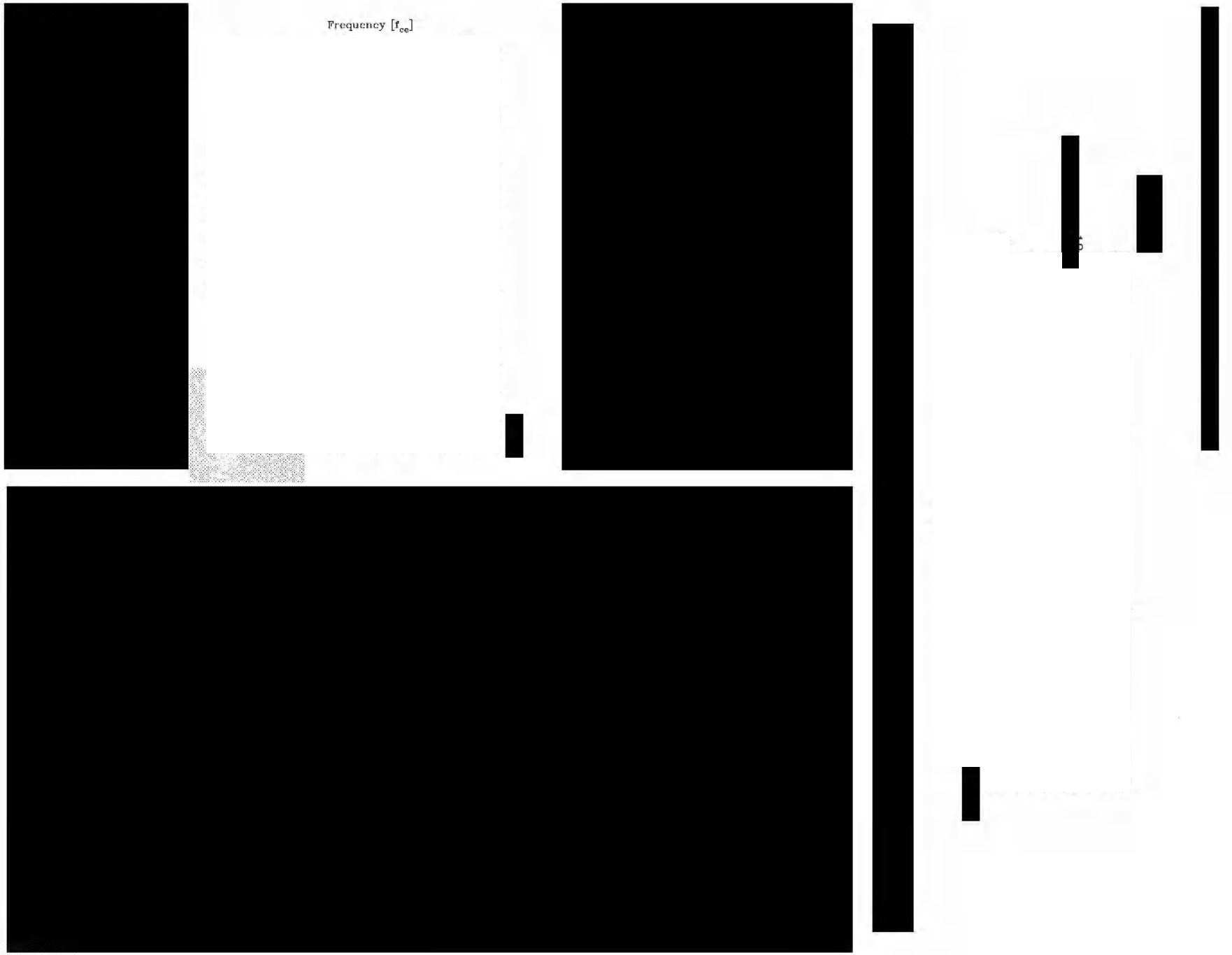
Frequency [f_{ce}]

In this paper, we have presented the results of our newly developed simulation scheme and concluded that the present model accurately simulates the resonant scattering process of high energy electrons. The resonant scattering process via whistler-mode wave is recognized as a strong candidate in the rebuilding process of the outer radiation belt during the geomagnetic recovery phase. Previous theoretical analyses and observational evidences revealed the importance of the effect of resonant interaction. In this current of study, the quantitative estimation of acceleration process and the verification of diffusion coefficients derived from quasi-linear theory have been recognized as an important problem. The diffusion coefficients of high energy particles during resonant interaction with plasma waves has been discussed by various authors on the basis of the quasi-linear theory [e.g., *Lyons*, 1974; *Albert*, 1999]. To understand the details of the properties of pitch angle and energy diffusion processes of energetic particles through the wave particle interactions with the plasma waves, the diffusion coefficient in the phase space is especially important and should be accurately evaluated considering the wave particle interaction processes by using realistic plasma wave parameters. The previous studies explained the response of high energy particles through the resonant scattering with enhanced whistler and ion cyclotron waves by adopting the diffusion coefficient estimated for a high density plasma condition ($\omega_{pe}/\Omega_e)^2 \gg \omega/\Omega_e$) for the region of inner plasmasphere [*Lyons*, 1974]. For the stochastic acceleration processes with whistler-mode waves, however, a condition of low plasma density, which is typical for the case of the outside region of plasmapause, is required for effective acceleration by the whistler-mode waves; therefore it is important to estimate the accurate diffusion coefficients on such realistic plasma parameters as proposed by *Horne et al.* (2003). The results of insitu observation in the inner magnetosphere also reveal the real distribution function and pitch angle distribution of high energy particles which is not the shifted bi-Maxwellian type used in this initial study. To discuss the realistic acceleration process of high energetic electrons, it is necessary to discuss the resonant scattering process by considering the realistic distribution of energetic electrons as well as the realistic plasma parameters as observed in the magnetosphere. By employing the present simulation model, it will be possible to investigate the diffusion process of resonant electrons and estimate their diffusion rate under such a real magnetospheric plasma condition; these works are important for future studies.

Acknowledgements. The Electron Hybrid Code has been developed as a collaboration with Super Computing System, Information Synergy Center, Tohoku University and Research Institute for Sustainable Humanosphere (RISH) at Kyoto University. The authors would like to thank them for their consultation and advice on development of the Electron Hybrid Code. Effort of T. Ono is supported by the 21th Century COE program by the Ministry of Education, Culture, Sports, Science and Technology, Japan.

REFERENCES

Albert, J.M., Analysis of quasi-linear diffusion coefficients, *J. Geophys.* Res., 104, 2429-2441, 1999.

Baker, D.N., J.B. Blake, L.B. Callis, J.R. Cummings, D. Hovestadt, S. Kanekal, B. Klecker, R.A. Mewaldt, and R.D. Zwickl, Relativistic electron acceleration and decay time scales in the inner and outer radiation belts: SAMPEX, *Geophys. Res. Lett.*, 21, 409-412, 1994.

Birdsall, C.K. and A.B. Langdon, *Plasma Physics via Computer Simulation*, McGraw-Hill, New York, 1985.

Horne, R.B., S.A. Glauert, and R.M. Thorne, Resonant diffusion of radiation belt electrons by whistler-mode chorus, *Geophys. Res. Lett.,* 30, 1493-1496, 2003.

Lyons, L.R., Pitch angle and energy diffusion coefficients from resonant interactions with ion-cyclotron and whistler waves, *J. Plasma Phys.,* 12, 417-432, 1974.

Meredith, N.P., R.B. Horne, D. Summers, R.M. Thorne, R.H.A. Iles, D. Heyndreickx, and R.R. Anderson, Evidence for acceleration of outer zone electrons to relativistic energies by whistler mode chorus, Ann. *Geophys.,* 20, 967-979, 2002.

Miyoshi, Y., A. Morioka, T. Obara, H. Misawa, T. Nagai, and Y. Kasahara, Rebuilding process of the outer radiation belt during the 3 November 1993 magnetic storm: NOAA and EXOS-D observations, *J. Geophys. Res.,* 108, 1004-1018, 2003.

Omura, Y. and H. Matsumoto, Computer simulations of basic process of coherent whistler wave-particle interactions in the magnetosphere, *J. Geophys. Res.,* 87, 4435-4444, 1982.

Omura, Y. and Matsumoto, H., KEMPO1: Technical guide to one-dimensional electromagnetic particle code, in *Computer Space Plasma Physics: Simulation Techniques and Software,* Edited by H. Matsumoto and Y. Omura, 103 pp, Terra Scientific Publishing Company, Tokyo, 1993.

Rathmann, C.E., J.L. Vomvoridis, and J. Denavit, Long-time-scale simulation of resonant particle effects in Langmuir and whistler waves, *J. Computational Phys.,* 26, 408-442, 1978.

Summers, D., R.M. Thorne, and F. Xiao., Relativistic theory of wave-particle resonant diffusion with application to electron acceleration in the magnetosphere, *J. Geophys. Res.,* 103, 20487-20500, 1998.

Summers, D. and C.Y. Ma, A model for generating relativistic electrons in the Earth's inner magnetosphere based on gyroresonant wave-particle interactions, *J. Geophys. Res.*, 105, 2625-2639, 2000.

Taguchi, T., J. Thomas, M. Antonsen, C.S. Liu, and K. Mima, Structure formation and tearing of an MeV cylindrical electron beam in a laser-produced plasma, *Phys. Rev. Lett.*, 86, 5055-5058, 2001.

M. Iizima and T. Ono, Department of Geophysics, Graduate School of Science, Tohoku University, Sendai, Miyagi 980-8578, Japan. (e-mail: iizima@stpp1.geophys.tohoku.ac.jp; ono@stpp3.geophys.tohoku.ac.jp)

Y. Katoh, Research Institute for Sustainable Humanosphere, Kyoto University, Uji, Kyoto 611-0011, Japan. (e-mail: yuto@rish.kyoto-u.ac.jp)

Structures of Sub-keV Ions Inside the Ring Current Region

M. Yamauchi[1], R. Lundin[1], L. Eliasson[1], D. Winningham[2], H. Reme[3], C. Vallat[3], I. Dandouras[3] and Cluster-CIS team[1,3-8]

Structured dispersive sub-keV ions inside the ring current region, or so-called wedge-like dispersions, those which have been considered signatures of long-time drift by ***ExB*** and grad-$|\boldsymbol{B}|$ drifts from nightside, are surveyed using the Viking, Freja, Munin, and Cluster satellites. While the ordinary wedge-like dispersion (increasing energy with increasing latitude) is observed mainly in the morning sector at all altitudes (by all spacecrafts), the reversed wedge-like dispersion (decreasing energy with increasing latitude) is observed at different local times by different spacecrafts. The differences between spacecrafts are also found in the H+/O+ ratio and in observation frequency. The observed altitudinal difference indicates that the evolution of drifting particles depends strongly on the mass and mirror altitude.

1. INTRODUCTION

Mid- and low-altitude satellites frequently detect dense trapped sub-keV ions with energy-latitude dispersive structures inside the dayside ring current region [*Yamauchi et al.*, 1996a]. Figure 1 shows examples observed by the Viking satellite [*Lundin et al.*, 1987]. One can recognize two major ion populations: the energetic (>10 keV) ring current component, and the sub-keV component that we study in this paper. Located far equatorward of the auroral region, and clearly separated from the energetic component, the dense sub-keV trapped ions in Figure 1 have energy-latitude dispersive structures as marked by thick curves in the spectrogram. Such structured dense sub-keV ions in the ring current region are well recognized in almost all satellite data as a zoo of various dispersion patterns.

The independence of the sub-keV component from the energetic (>3 keV) component seen in Figure 1 can also be seen in CRRES statistics of average pitch-angle distribution [*Collin et al.*, 1993]. Multiplying the energy by their average number flux, the energy fluxes of sub-keV trapped ions (<30 degree equatorial pitch angle in order to reach the Viking altitude) can often be higher than those of 2-3 keV range ions inside the ring current region (e.g., $5 < L < 6$). Thus the sub-keV ions have different characteristics from the energetic (>5 keV) ions in the ring current region.

Ebihara et al. [2001] made the first attempt to simulate these dispersions seen in Figure 1. Since the drift motion of sub-keV ions are sensitive to both the ***ExB*** drift (eastward, energy independent) and grad-$|\boldsymbol{B}|$/curvature drifts (westward for positive ions, energy dependent), the drift distance for a given elapse time becomes energy-dispersive. When looking at a fixed meridian, a different drift distance means a different L value, resulting in an energy-latitude dispersion. Thus the observed structures of sub-keV ions may directly reflect nightside electromagnetic disturbances, and hence studying the dispersion structures of the sub-keV ring current provides a new and good clue to understanding the dynamics of the inner magnetosphere.

[1] Swedish Institute of Space Physics, Kiruna, Sweden
[2] Southwest Research Institute, San Antonio, Texas
[3] Centre d'Etude Spatiale des Rayonnements, Toulouse, France
[4] Instituto di Fisica dello Spazio Interplanetario, Roma, Italy
[5] Max-Planck-Institut für Extraterrestrischefysik, Garching, Germany
[6] Max-Planck-Institut für Aeronomie, Lindau, Germany
[7] University of New Hampshire, Durham, New Hampshire
[8] Space Science Laboratory, University of California, Berkeley, California

The Inner Magnetosphere: Physics and Modeling
Geophysical Monograph Series 155

10.1029/155GM05

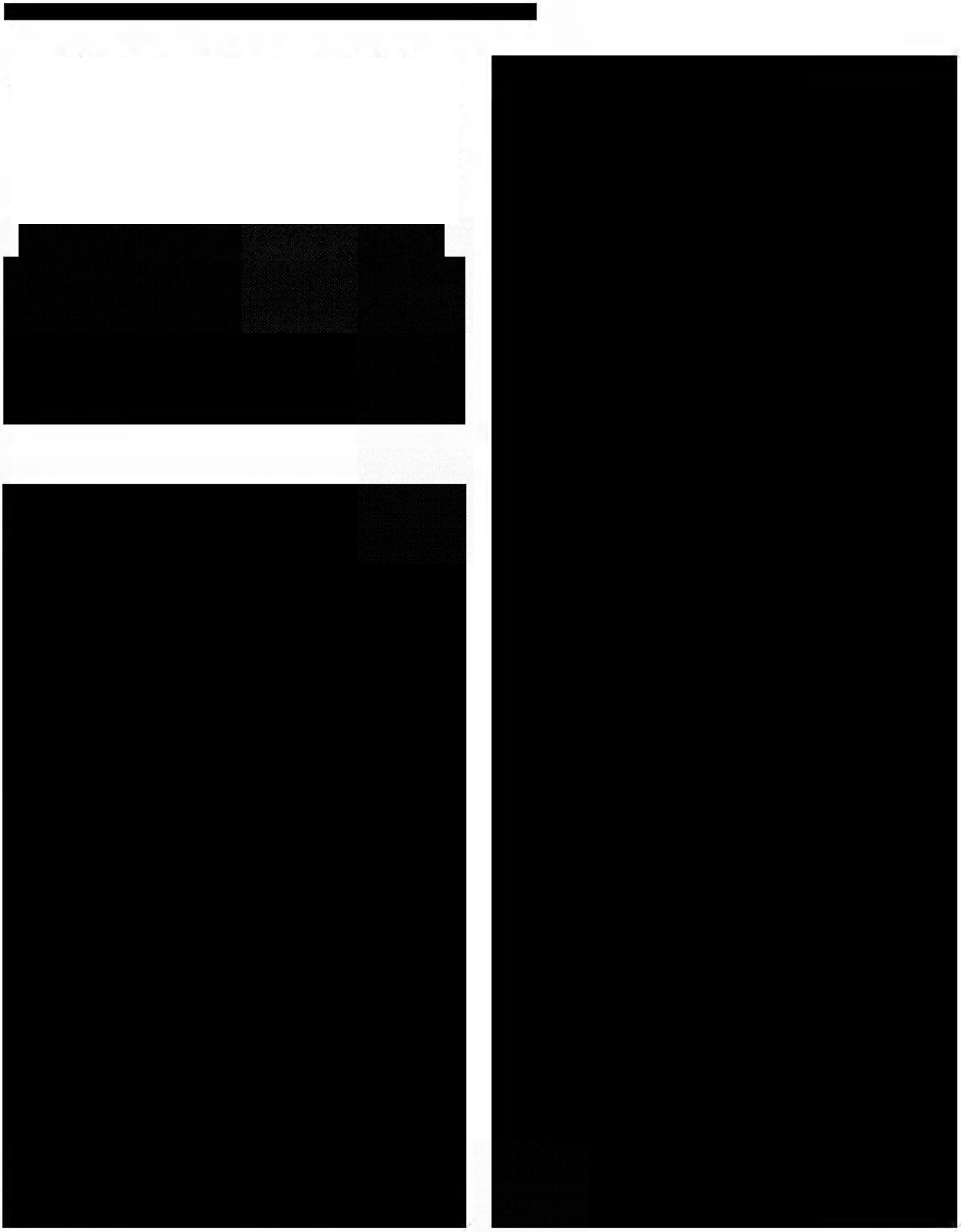

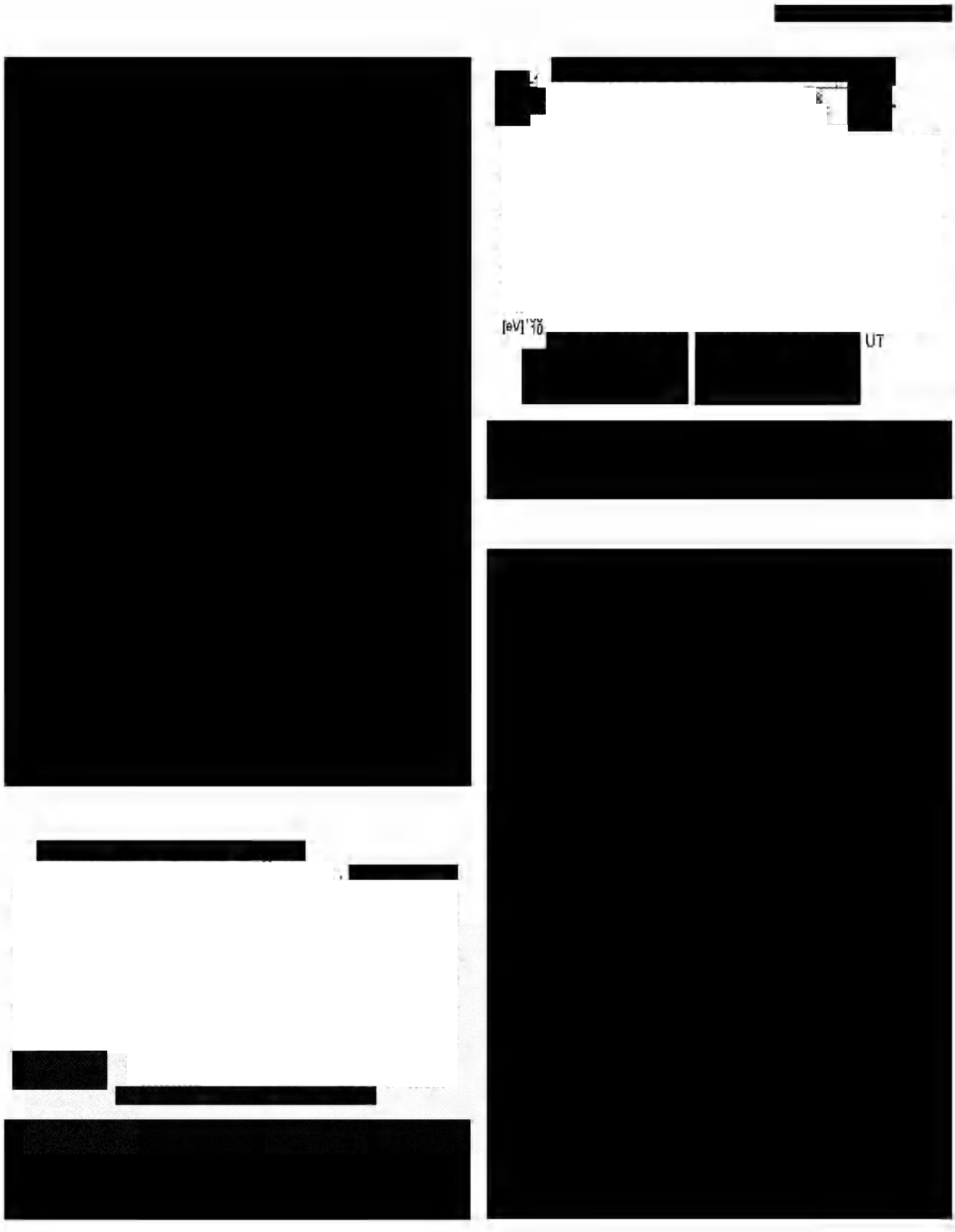
UT

[redacted]

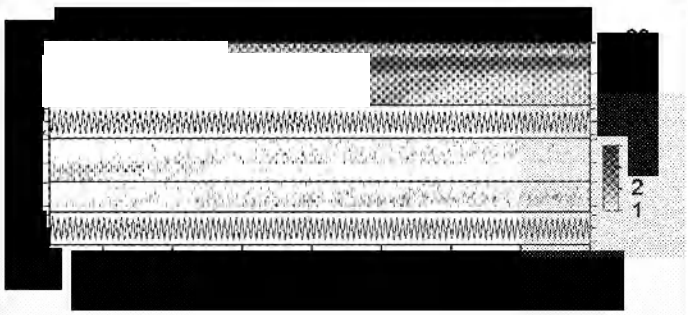

[redacted]

[redacted]

[redacted]

[redacted]

[redacted]

[redacted]

[redacted]

[redacted]

[redacted]

[redacted] [redacted]

[redacted]

[redacted]

[redacted]

To solve these puzzles we definitely need more simulation (with anisotropic source distribution), further data analyses (e.g., fine classification and delay-time analyses versus geomagnetic indices), and analyses of data from different altitudes (FAST, Polar, Interball and new missions).

Acknowledgments. The Viking project is sponsored by the Swedish National Space Board (SNBN). The Freja project is supported by the SNSB and the Deutsche Agentur für Raumfahrtangelegenheiten (DARA). The Munin nano-satellite project was in part carried out within the framework of undergraduate and graduate education, and its SwRI portion was funded by NASA and ONR. The Cluster project is sponsored and performed by the ESA. The Swedish contribution to the project was funded by SNSB and the Wallenberg foundation. The AE index is provided by WDC-C2 for geomagnetism at Kyoto University. We thank Natalia Ganushkina for useful discussion. MY's work is physically assisted by the handicap welfare program in Sweden. This work marks the first step of MY's recovery from a long illness and he thanks all who encouraged him during this illness.

REFERENCES

Chappell, C.R., J.L. Green, J.F.E. Johnson, and J.H. Waite, Jr, Pitch angle variations in magnetospheric thermal plasma: Initial observations from Dynamic Explorer-1, *Geophys. Res. Lett.*, 9, 933, 1982.

Collin, H.L., J.M. Quinn, and J.B. Cladis, An empirical static model of low energy ring current ions, *Geophys. Res. Lett.*, 20, 141, 1993.

Ebihara, Y., M. Yamauchi, H. Nilsson, R. Lundin, and M. Ejiri, Wedge-like dispersion of sub-keV ions in the dayside magnetosphere: Particle simulation and Viking observation, *J. Geophys. Res.*, 106, 29571, 2001.

Ejiri, M., R.A. Hoffman, and P.H. Smith, Energetic particle penetration into the inner magnetosphere, *J. Geophys. Res.*, 85, 653, 1980.

Eliasson, L., O. Norberg, R. Lundin, K. Lundin, S. Olsen, *et al.*, The Freja hot plasma experiment - instrument and first results, *Space Sci. Rev.*, 70, 563, 1994.

Hamilton, D.C., G. Gloeckler, F.M. Ipavich, W. Studemann, B. Wilken, and G. Kremser, Ring current development during the great geomagnetic storm of February 1986, *J. Geophys. Res.*, 93, 14343, 1988.

Høymork, S., M. Yamauchi, Y. Ebihara, Y. Narita, O. Norberg, and D. Winningham, Dense ion clouds of 0.1-2 keV ions inside the CPS-region observed by Astrid-2, *Ann. Geophys.*, 19, 621, 2001.

Lennartsson, W., and R.D. Sharp, A Comparison of the 0.1-17 keV/e ion composition in the near equatorial magnetosphere between quiet and disturbed conditions, *J. Geophys. Res.*, 87, 6109, 1982.

Lundin, R., L. Eliasson, B. Hultqwvist, and K. Stasiewicz, Plasma energization on auroral field lines as observed by the Viking spacecraft, Geophys. Res. Lett., 14, 443, 1987.

Newell, P.T., and C.-I. Meng, Substorm introduction of ≤1 keV magnetospheric ions into the inner plasmasphere, *J. Geophys. Res.*, 91, 11133, 1986.

Quinn, J.M., and C.E. McIlwain, Bouncing ion clusters in the Earth's magnetosphere, *J. Geophys. Res.*, 84, 7365, 1979.

Reme, H., C. Aoustin, J.M. Bosqued, I. Dandouras, B. Lavraud, *et al.*, First multispacecraft ion measurements in and near the Earth's magnetosphere with the identical Cluster ion spectrometry (CIS) experiment, *Ann. Geophys.*, 19, 1303, 2001.

Sauvaud, J.A., J. Crasnier, K. Mouala, R.A. Kovrazhkin, and N.V. Jorjio, Morning sector ion precipitation following substorm injections, *J. Geophys. Res.*, 86, 3430, 1981.

Shelley, E. G., R. G. Johnson, and R. D. Sharp, Satellite observations of energetic heavy ions during a geomagnetic storm, *J. Geophys. Res.*, 77, 6104, 1972.

Smith, P.H., and R.A. Hoffman, Direct observation in the dusk hours of the characteristics of the storm time ring current particles during the beginning of the magnetic storms, *J. Geophys. Res.*, 79, 966, 1974.

Winningham, J.D., J.L. Burch, and R.A. Frahm, Bands of ions and angular V's: A conjugate manifestation of ionospheric ion acceleration, *J. Geophys. Res.*, 89, 1749, 1984.

Vallat, C., I. Dandouras, G.K. Parks, M. Wilber, M. Dunlop, L. Kistler, H. Reme and A. Balogh, New ionic structures observed in the equatorial ring current during CLUSTER perigee passes, presentation at AGU meeting, San Francisco, Dec. 2002.

Yamauchi, M., R. Lundin, L. Eliasson, and O. Norberg, Meso-scale structures of radiation belt/ring current detected by low-energy ions, *Adv. Space Res.*, 17, (2), 171, 1996a.

Yamauchi M., R. Lundin, K. Mursula, G. Marklund, and T.A. Potemra, Dayside Pc5 pulsation detected by Viking ion data at $L = 4$, *Geophys. Res. Lett.*, 23, 2517, 1996b.

Yamauchi, M., O. Norberg, S. Barabash, R. Lundin, and D. Winningham, Mission and science of Munin: The first Swedish nano-satellite, *23rd ISTS proceedings*, 2010, 2002.

I. Dandouras, H. Reme, and C. Vallat, Centre d'Etude Spatiale des Rayonnements, POBox 4346 F-31028 Toulouse, Cedex 4 Toulouse, France.

L. Eliasson, R. Lundin, and M. Yamauchi, Swedish Institute of Space Physics, Box 812, S-98128 Kiruna, Sweden.

D.Winningham, Southwest Research Institute, San Antonio, TX 78228-0510.

Quick Response of the Near-Earth Magnetotail to Changes in the Interplanetary Magnetic Field

Kumiko K. Hashimoto

Department of Environmental Risk Management, Kibi International University, Takahashi, Okayama, Japan

Takashi Kikuchi

Applied Research and Standards Division, National Institute of Information and Communications Technology, Koganei, Tokyo, Japan

We found that the magnetic field at the geosynchronous orbit started to change from the dipole- to tail-like configuration, i.e., plasmasheet thinning in the evening sector six minutes after the onset of development of the ionospheric convection as derived from the ground magnetometers, when the IMF turned southward. The ionospheric plasma convection as observed by SuperDARN started to change simultaneously, and completely changed its pattern from the four-cell to two-cell at the onset of the plasmasheet thinning. The plasmasheet thinning was followed by the development of the partial ring current (PRC) within a few minutes, which implies that the plasma convection was enhanced in the near-earth magnetotail. These results indicate that the convection electric field in the near-earth magnetotail develops concurrently with the large-scale two-cell convection in the ionosphere, suggesting a possible role of the ionosphere in driving the convection in the near-earth magnetotail.

1. INTRODUCTION

Plasma convection in the magnetosphere-ionosphere (M-I) coupled system is controlled by the interplanetary magnetic field (IMF) as demonstrated with the good coherency between the southward IMF and the DP2 currents composed of two-cell current vortices in high latitude extending to the dayside equator [*Nishida*, 1968]. The good correlation implies that the solar wind energy penetrates into the polar ionosphere, and further to the equatorial ionosphere. The transmission of the energy to the equator is nearly instantaneous as suggested by *Kikuchi et al.* [1996]. In the past years, magnetometer networks and SuperDARN observations have shown instantaneous reaction of ionospheric convection on the dayside and nightside [e.g. *Ridley et al.*, 1998; *Ruohoniemi and Greenwald*, 1998; *Murr and Hughes*, 2001; *Lu et al.*, 2002]. The quick response of convection in the nightside polar ionosphere poses an important issue whether the plasma convection responses immediately in the inner magnetosphere and in the near-earth magnetotail after enhancement of magnetic reconnection at the dayside magnetopause. The studies on the quick response of convection to the IMF have been examined mainly for the polar ionosphere, however few studies have been done for the inner magnetosphere.

It has been reported that onset of substorms coincided with northward turning of the IMF [e.g. *Cann et al.*, 1975; *Rostoker*, 1983; *Lyons et al.*, 1995]. *Lyons et al.* [1995] proposed a substorm model in which the substorm was triggered by a reduction in convection electric field due to the northward tuning of the IMF. Based on the GEOTAIL observations, however, *Nishida et al.* [1997] showed that a substorm onset was not accompanied by a reduction in

The Inner Magnetosphere: Physics and Modeling
Geophysical Monograph Series 155

10.1029/155GM06

convection electric field at $x = -19$ Re in the plasmasheet when the IMF turned sharply northward. On the other hand, *Hashimoto et al.* [2002] demonstrated that the partial ring current started to develop a few minutes after growth of the polar cap potential by using global magnetometer networks on the ground and particle simulation of the ring current. They further showed that the partial ring current was reconfigured into more symmetric simultaneously with decrease of the polar cap potential due to northward turning of the IMF. Their results suggested that the convection electric field instantaneously changed at around 4-6 Re in the near-earth magnetosphere with ionospheric convection changes, regardless of the magnetic local time.

The purpose of this paper is to clarify temporal behavior of the near-earth magnetotail at the geosynchronous orbit with respect to the development of ionospheric convection, by comparing the DP2 current, the ionospheric convection observed by SuperDARN and plasma sheet thinning observed by the geosynchronous satellite GOES9. The development of the DP2 currents is a signature of the reconnection at the dayside magnetopause. SuperDARN provides us with a two-dimensional convection pattern in the polar ionosphere. The event we selected indicates that the four-cell convection associated with the northward IMF started to reduce on the dayside just after the DP2 current developed due to the southward IMF, and completed to change into two-cell pattern in six minutes. Although the magnetometer and SuperDARN data were sparse on the nightside, the nightside convection must have been intensified simultaneously with the dayside convection as suggested by *Ridley et al.* [1998], and *Ruohoniemi and Greenwald* [1998]. Consequently, the plasmasheet thinning in the near-earth magnetotail started at the time of the complete change in the ionospheric convection pattern.

2. RESULTS

A southward turning of the IMF was measured by ACE at 10:04 UT on March 26, 1998. Negative By increased and solar wind dynamic pressure was stable during the event (the data is not shown here). Figure 1 shows the D-component of the magnetic field observed at two stations in the polar cap and the X-component at the IMAGE magnetometer network aligned from the high to middle latitudes (geomagnetic latitude of 75–56°) at 13 MLT. Coherent increases in the magnetic field started at 11:00 UT (vertical line) from the polar cap to the dayside middle latitudes. Furthermore, the X-component from CANOPUS and MACCS magnetometer chain observed increases in the eastward and westward currents in the polar cap and auroral latitudes on the dawnside, respectively (data not shown here). These magnetic variations indicate an intensification of the DP2 currents in the polar cap and

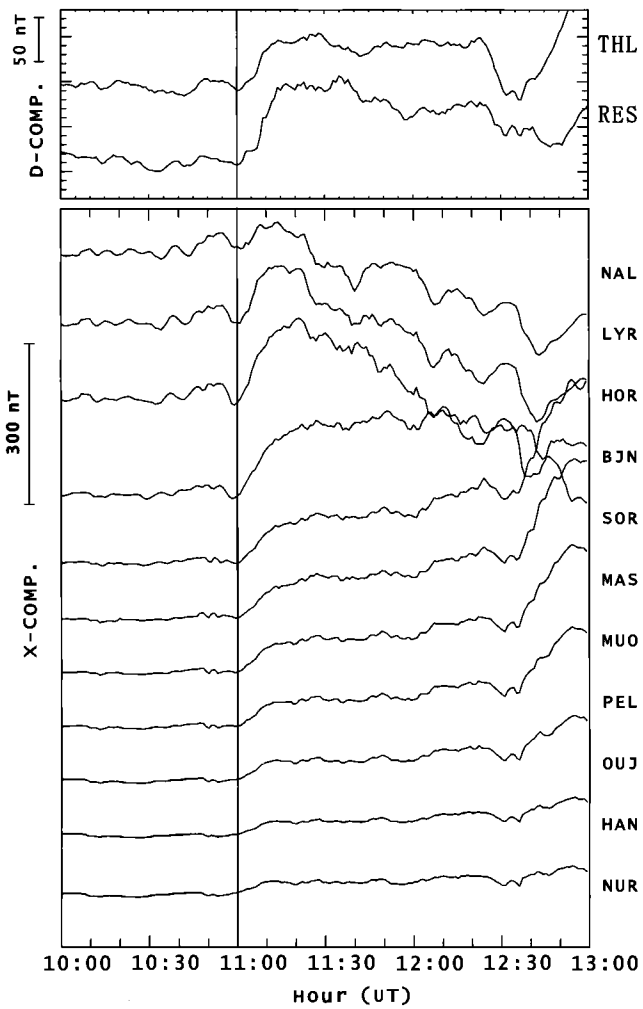

Figure 1. (upper) D-component of the magnetic field from Thule and Resolute Bay in the polar, (lower) X-component from 11 stations at auroral to mid latitudes of the IMAGE magnetometer chain. The vertical solid line presents the onset of the DP2 magnetic perturbation.

auroral latitudes. The convection electric field responsible for the DP2 magnetic variations would propagate instantaneously to the nightside [*Ridley et al.*, 1998; *Lu et al.*, 2002].

Figure 2 shows three components of the magnetic field (He: earthward; Hp: northward parallel to the Earth's rotational axis; Hn: perpendicular to He and Hp) measured by the geostationary satellite GOES 9 that was located at the geomagnetic latitude and longitude of 4.91° and 296.02°, respectively in 00:20 MLT at 11:00 UT. A growth phase signature of an isolated substorm is clearly observed in the Hp-component that decreased gradually with a clear onset at 11:06 UT (dashed line). The He-component, on the other hand, slightly increased in correspondence to the decrease in the Hp.

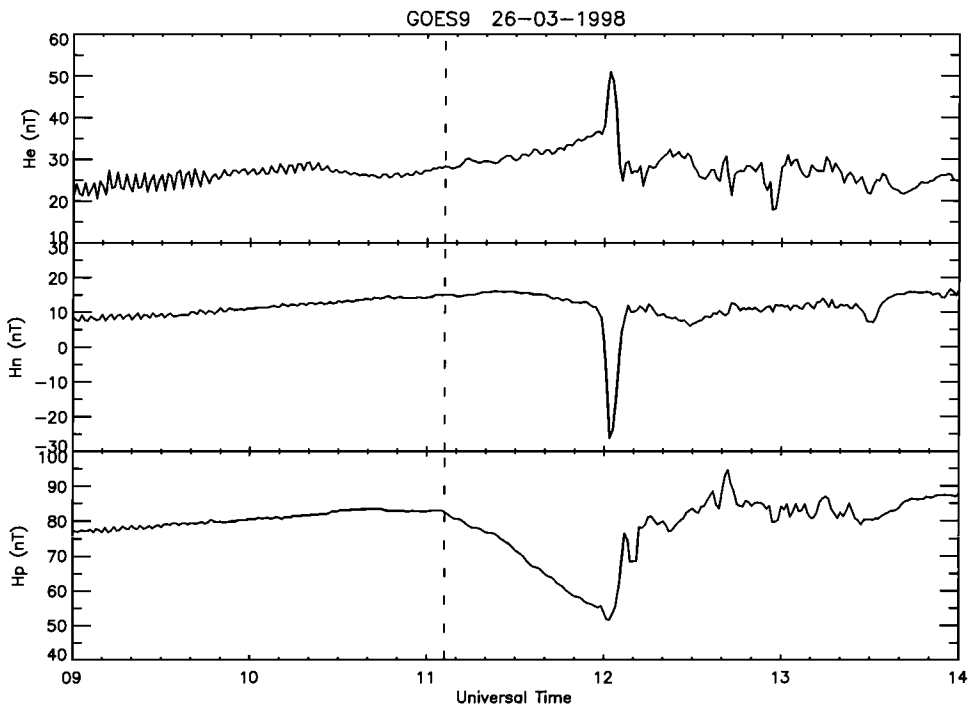

Figure 2. Three components of the magnetic field obtained by GOES-9 that was located in 00:20 MLT at 11:00 UT.

The resultant total magnetic field strength reduced at the geosynchronous orbit. These changes in the magnetic field correspond to the stretching of the magnetic field and thinning of the plasma sheet in the near-earth magnetotail that is characteristic of the substorm growth phase (plasma sheet thinning) [e.g. *Nishida and Hones*, 1974]. This reconfiguration of the magnetic field lines from the dipole may be a result of removal of magnetic fluxes from the magnetotail, which was caused by the dawn-to-dusk convection electric field [*Coroniti*, 1985; and *Tanaka*, 2003].

The growth phase of substorm is also characterized by gradual development of the partial ring current in the nightside magnetosphere [*McPherron*, 1970]. Figure 3 shows the H-component of the magnetic field on the ground at middle to low latitudes in the evening sector (20 MLT at Kakioka). It can be seen that the H-components begin to decrease coherently at 11:11 UT as shown with the vertical line. This indicates that a westward (asymmetrical) ring current has begun to develop in the equatorial plane of the magnetosphere. The ring current is a result of the increased plasma pressure in the inner magnetosphere, which is caused by the development of earthward plasma convection in the nightside magnetosphere [*McEntire et al.*, 1985]. The diamagnetic effects of the high pressure plasma would cause the reduction in magnetic field strength at the geosynchronous orbit as observed by GOES9 (Figure 2). Thus, the magnetic field

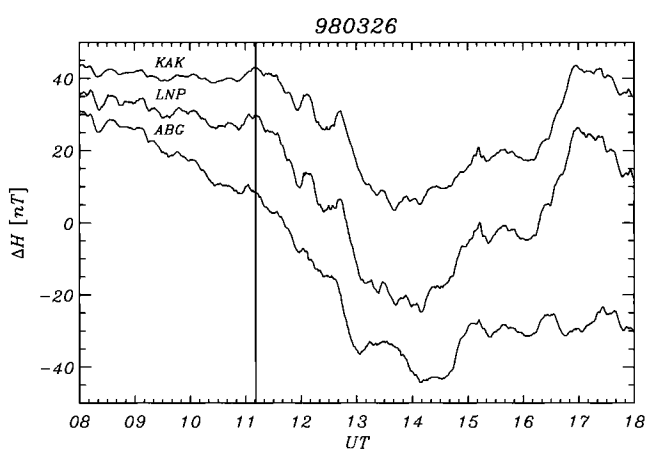

Figure 3. H-component magnetic fields from mid and low latitude stations on the nightside; Kakioka (20 MLT at 11:00 UT), Lunping (19 MLT), Alibag (16 MLT).

observation by GOES-9 indicates that the increase in convection electric field in the nightside near-earth magnetotail began no later than six minutes after the initiation of development of the ionospheric convection.

By applying the potential map model established by the JHU/APL [*Ruohoniemi and Baker*, 1998], the 2-D plasma velocity vectors in the polar ionosphere are derived from

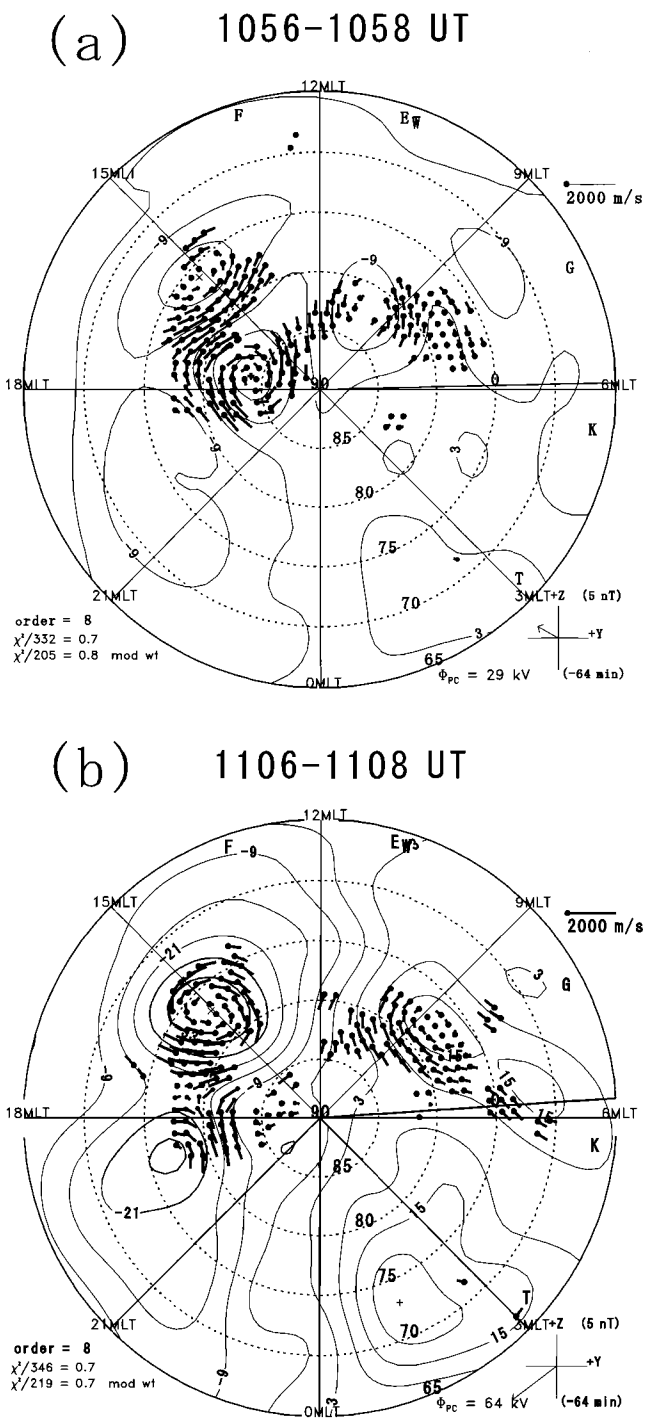

Figure 4. Plasma flow vectors deduced from SuperDARN observations in the northern hemisphere by applying the potential map model (a) at 10:56 –10:58 UT and (b) at 10:06 – 11:08 UT.

the line-of-sight velocities obtained by six HF radars near the auroral belt in Finland, Iceland, Canada, and Alaska for the conditions before (Figure 4a) and after (Figure 4b) the DP2 currents started to grow. It can be seen in Figure 4 (a) that two plasma convection cells are centered around 10 MLT and 17 MLT near the geomagnetic latitude of 83°. The direction of the plasma flow is clockwise and counterclockwise in the morning and afternoon sectors, respectively. Near the noon meridian, the plasma flows sunward. These two convection cells are referred to as the reverse-cell that is a characteristic of plasma convection observed for a due northward IMF [*Bristow et al.*, 1998; and *Huang et al.*, 2000]. A part of the normal two-cell convection, with a center at 15 MLT and the geomagnetic latitude of 75°, is seen on the lower latitude side of the reverse-cell in the afternoon sector. Its plasma flow velocity is comparable to that of the reverse-cell. The convection cells in the morning and afternoon sectors of the reverse-cell infer the upward and downward field-aligned current (FAC) respectively, and these FACs are called NBZ currents. The dynamo for the NBZ currents may be located in the magnetotail lobe, as shown by the three-D MHD simulations [*Tanaka*, 1995; and *Siscoe et al.*, 2000].

Figure 4 (b) shows the plasma convection at the beginning of the plasmasheet thinning in the near-earth magnetotail, as observed by the GOES 9 satellite (Figure 2). It can be seen that the reverse-cell in the polar cap has disappeared, and that a normal two-cell convection has developed with higher velocities. This is attributed to development of the Region 1 FAC due to the southward IMF. The switchover from the four-cell convection pattern to the two-cell convection pattern signifies disappearance of the NBZ currents. As a result, the Region 1 FAC became dominant.

To indicate more clearly the switchover of the convection pattern, we plot in Plate 1 the temporal variations in the line-of-sight velocities measured by the HF radar at Hankasalmi in Finland as a function of latitude on the solid line that traverses the reverse cell as shown in the top panel of Plate 1. The horizontal axis represents time in UT and the vertical axis represents the geomagnetic latitude on the solid line. The color scale shows the line-of-sight velocities of the F layer plasma. The positive and negative velocities correspond to direction toward and away from the radar, respectively. Since the Finland HF radar was located near 13 MLT at 11:00 UT, the plasma flow at latitudes higher than geomagnetic latitude of 84° (shown in blue in Plate 1) corresponded to the sunward plasma flow, which is a part of the reverse-cell.

It can be seen that the velocity of the sunward plasma flow at latitudes higher than the geomagnetic latitude of 84° (shown in blue) begins to decrease at 11:00 UT, simultaneously with the initiation of the growth of the ionospheric convection as observed by the magnetometers (Figure 1). The plasma flow in the polar cap became completely anti-sunward (yellow-green) by 11:06 UT, indicating a complete change in the convection from the four-cell to two-cell pattern. It should be noted that this change was synchronous with the onset of the plasmasheet thinning in the near-earth magnetotail observed by the geostationary satellite (Figure 2).

[redacted]

[redacted]

[redacted]

[redacted]

3. DISCUSSION AND CONCLUSIONS

We examined the relationship between the plasmasheet thinning and the development of ionospheric convection observed with magnetometers and SuperDARN HF radars. We chose the event of the convection development that took place under the condition of well-developed four-cell convection associated with the northward IMF. The event provides the good opportunity to define the initiation of the convection increase in the ionosphere and in the plasma sheet.

The DP2 current identified by the magnetometers started to develop at 11:00 UT, indicating the transmission of potential electric field of the Region-1 FACs to the mid latitude ionosphere [*Kikuchi et al.*, 1996]. Development of the DP2 magnetic field is instantaneous on the dayside and on the nightside in the polar region as shown by *Ridley et al.* [1998], *Murr and Hughes* [2001], and *Lu et al.* [2002]. The plasmasheet thinning was clearly observed in the midnight by GOES-9 no later than six minutes after the development of the DP2 current.

Although the DP2 current started to grow at 11:00 UT, the Region-1 FAC potential electric field may not have been fully developed in the polar ionosphere since the NBZ current system for the northward IMF still remained as observed by SuperDARN. It took approximately six minutes for the NBZ current to be overcome by the Region 1 FACs (11:06 UT). At this moment, the Region 1 FAC potential field strengthened rapidly in the polar ionosphere, which would strengthen the westward electric field in the nightside ionosphere and enhanced the plasma convection in the near-earth magnetotail. As a result, the plasmasheet thinning occurred on the geostationary orbit, followed by the development of the partial ring current as manifested by the decrease in the H-component of the geomagnetic field at low latitudes (Figure 3). This is consistent with the quick development of the partial ring current after the increase in the polar cap potential as demonstrated by *Hashimoto et al.* [2002].

On the other hand, when the cross polar cap potential decreases due to the northward turning of the IMF, the DP2 current decreases simultaneously in the global ionosphere, regardless the magnetic local time. As shown by *Hashimoto et al.* [2002], the high pressure plasma in the inner magnetosphere responsible for the partial ring current started to redistribute instantaneously at the time of the decrease of the DP2 current in the ionosphere, when the IMF turned northward. These observational results indicate that the convection electric field in the inner and near-earth (geosynchronous orbit) magnetosphere changes concurrently with that in the ionosphere. It is interesting to note that the quick response of the near-earth magnetotail at the geosynchronous orbit seems not in agreement with GEOTAIL observation at $x = -19$ Re reported by *Nishida et al.* (1997). Further studies will be needed for the relation between these two locations from the electric field point of view.

In conclusion, we found quick response of the plasmasheet in the near-earth magnetotail to development of the ionospheric convection. There was a time delay of 6 minutes for the plasma sheet thinning from the onset of the DP2 current that signified the development of the Region 1 FAC. However, the potential electric field of the Region 1 FAC completely overcame the preexisted potential electric field of the NBZ FACs in the polar cap at the onset of the plasma sheet thinning. These results suggest that the convection electric field developed concurrently in the ionosphere and near-earth magnetotail.

Acknowledgements. The authors thank the Finish Meteorological Institute for the IMAGE magnetometer data, the institutes responsible for the INTERMAGNET magnetometer array and PIs of SuperDARN for the HF radar data. GOES 9 magnetic field data were provided by H. Singer at NOAA/SEC and data from GOES 9 were obtained from CDAWeb.

REFERENCES

Bristow, W.A., J.M. Ruohoniemi, and R.A. Greenwald, Super Dual Auroral Radar Network observations of convection during period of small-magnitude northward IMF, *J. Geophys. Res.*, 103, 4051-4061, 1998.

Cann, M.N., R.L. McPherron, and C.T. Russell, Substorm and interplanetary magnetic field effects on the geomagnetic tail lobes, *J. Geophys. Res.*, 80, 191,1975.

Coroniti, F.V., Explosive tail reconnection: the growth and expansion phases of magnetospheric substorms, *J. Geophys. Res.*, 90, 7427-7447, 1985.

Hashimoto, K.K., T. Kikuchi, and Y. Ebihara, Response of the magnetospheric convection to sudden interplanetary magnetic field changes as deduced from the evolution of partial ring currents, *J. Geophys. Res.*, 107, 1377, doi:10.1029./2001JA009228, 2002.

Huang C.S., G.J. Sofko, A.V. Koustov, D.A. Andre, J.M. Ruohoniemi, R.A. Greenwald, and M.R. Hairston, Evolution of ionospheric multicell convection during northward interplanetary magnetic field with vertical bar B-z/B-y vertical bar > 1, *J. Geophys. Res.*, 105, 27095-27107, 2000.

Kikuchi, T., H.Lühr, T. Kitamura, O. Saka, and K. Schlegel, Direct penetration of the polar electric field to the equator during a DP2 event as detected by the auroral and equatorial magnetometer chains and the EISCAT radar, *J. Geophys. Res.*, 101, 17161-17173, 1996.

Lu, G., T.E. Holzer, D. Lummerzheim, J.M. Ruohoniemi, P. Stauning, O. Troshichev, P.T. Newell, M. Brittnacher, and G. Parks, Ionospheric response to the interplanetary magnetic field southward turning: Fast onset and slow reconfiguration, *J. Geophys. Res.*, 107(A8), doi:10.1029/2001JA000324, 2002.

Lyons, L.R., A new theory for magnetospheric substorms, *J. Geophys. Res.,* 100, 19069-19081, 1995.

McEntire, R.W., A.T.Y. Lui, S.M. Krimigis, and E.P. Keath, AMPTE/CCE energetic particle composition measurements during the September 4, 1984 magnetic storm, *Geophys. Res. Lett.,* 12, 317-320, 1985.

McPherron, R.L., Growth phase of magnetospheric substorms, *J. Geophys. Res.*, 75, 5592,1970.

Murr, D.L. and W.J. Hughes, Reconfiguration timescales of ionospheric convection, *Geophys. Res. Lett.,* 28, 2145-2148, 2001.

Nishida, A., Coherence of geomagnetic DP2 magnetic fluctuations with interplanetary magnetic variations, *J. Geophys. Res., 73,* 5549-5559, 1968.

Nishida, A., and E.W. Hones, Jr., Association of plasma sheet thinning with neutral line formation in the magnetotail, *J. Geophys. Res.,* 79, 535, 1974.

Nishida, A., T. Mukai, T. Yamamoto, Y. Saito, S. Kokubun, and R.P. Lepping, Response of the near-Earth magnetotail to a northward turning of the IMF, *Geophys. Res. Lett*, 24, 943-946, 1997.

Ridley A.J., G. Lu, C.R. Clauer, and V.O. Papitashvili, A statistical study of the ionospheric convection response to changing interplanetary magnetic field conditions using the assimilative mapping of ionospheric electrodynamics technique, *J. Geophys. Res.,* 103, 4023-4039, 1998.

Rostoker, G., Triggering of expansion phase intensifications of magnetospheric substorms by northward turnings of the interplanetary magnetic field, *J. Geophys. Res.,* 88, 6981, 1983.

Ruohoniemi J.M., Baker K.B, Large-scale imaging of high-latitude convection with Super Dual Auroral Radar Network HF radar observations, *J. Geophys. Res.,* 103, 20797-20811, 1998.

Ruohoniemi, J.M. and R.A. Greenwald, The response of high latitude convection to a sudden southward IMF turning, *Geophys. Res. Lett.,* 25, 2913-2916, 1998.

Siscoe, G.L., N.U. Crooker, G.M. Erickson, B.U.O. Sonnerup, K.D. Siebert, D.R. Weimer, W. White, and N.C. Maynard, Global geometry of magnetospheric current inferred from MHD simulations, in Magnetospheric Current Systems, *Geophys. Monogr. Ser.*, 118, edited by S. Ohtani *et al.*, pp. 41-52, AGU, Washington, D.C., 2000.

Tanaka, T., Generation mechanisms for magnetosphere-ionosphere current systems deduced from a 3-D MHD simulation of the solar wind-magnetosphere-ionosphere coupling processes, *J. Geophys. Res.*, 100, 12057-12074, 1995.

Tanaka, T., Formation of magnetospheric plasma population regimes coupled with the dynamo process in the convection system, *J. Geophys. Res.*,108, 1315, doi:10.1029/2002JA009668, 2003.

hashi@kiui.ac.jp, kikuchi@nict.go.jp

Narrow Plasma Streams as a Candidate to Populate the Inner Magnetosphere

V.A. Sergeev and D.A. Yahnin

Institute of Physics, St. Petersburg State University, St. Petersburg, Russia

K. Liou

John Hopkins APL, Laurel Maryland

M.F. Thomsen and G.D. Reeves

Los Alamos National Laboratory, Los Alamos, New Mexico

Long-duration periods with southward IMF often display a wealth of the fast bursty flows (BBFs) in the plasma sheet, part of them are visible as the auroral streamers and therefore could be monitored by optical means. For couple dozen isolated streamers we confirm statistically the spatial-temporal association of streamer intrusions with the plasma injections to the geostationary orbit. Also, for one long active period with many streamers monitored by Polar UV imager we show that the streamers end their development forming the bright spot in the equatorward oval which continues to exist for several tens minutes drifting eastward and westward as dictated by the convection flow. These results imply that during active times considerable amount of energetic plasma is injected into the inner magnetosphere with the bursty bulk flows. This can have important implications, particularly, for pumping fresh energetic particle population into the radiation belt.

1. INTRODUCTION

Magnetospheric convection, which brings (and accelerates) plasma from the tail plasma sheet to the inner magnetosphere, is undoubtedly the basic process of the magnetic storms. According to observations, the plasma sheet convection contains a strong transient component well-known as the bursty bulk flows (BBFs, after *Angelopoulos et al.* [1992]). Whenever the realistic (in terms of its spatial distribution and magnitude) but large-scale and slowly-varying electric field is used together with the realistic particle (plasma sheet) source to simulate plasma convection and acceleration during magnetic storms, it usually results in a plausible description of resulting medium-energy (keVs-tens keV) plasma distribution and correct prediction of Dst variation [*Ebihara and Eijiri*, 2003]. From this one may conclude that either the bursty appearance disappears in the inner region or it plays no specific role in the plasma acceleration for the bulk of the plasma. However, the acceleration to the high energies (hundreds keV and more) appeared to be more variable and less predictable in their storm-time behaviour (e.g. [*Reeves et al.*, 2003]). The difference with keV plasma is that energetic particles have their Alfven boundaries (boundaries separating open and closed drift trajectories) at large distance, typically outside the inner magnetosphere, so the convection can not normally bring them inward into the radiation belt.

Here specific aspects of the localized transient plasma streams (BBFs) can play their role. Particularly, the BBFs

The Inner Magnetosphere: Physics and Modeling
Geophysical Monograph Series 155

10.1029/155GM07

are typically (1) the plasma-depleted narrow streams with enhanced magnetic field inside it, which (2) has cross-tail size about 2-3 Re, (3) are electrically polarized and (4) generate the region-1 sense field-aligned currents (see [*Sergeev et al.*, 1996a, *Nakamura et al.*, 2001, *Sergeev et al.*, 2004] for observations, [*Chen and Wolf*, 1993] for theory and [*Birn et al.*, 2004] for recent MHD simulation of the plasma bubble evolution). The property (1) implies the existence of inverse (tailward-directed) magnetic field gradient in the leading part of the bubble, where the magnetic drift (the main effect hampering the inward penetration of energetic particle) is considerably reduced or even reversed, allowing a deeper penetration and stronger acceleration of energetic particles. Similar kind of transient electromagnetic structure (although without special reference to the plasma bubbles) was used in the electromagnetic impulse model by [*Li et al.*, 1998, *Sarris et al.*, 2002] which predicts many features of energetic particle injections to the geostationary orbit. Analysis of this model also showed that most effective acceleration is achieved if the electromagnetic pulse was moving inward at unusually low velocity, ranging from roughly a hundred km/s at ~10 Re to a few tens km/s around geostationary orbit. Such speeds are considerably lower than the magneto sonic speed (~1000 km/s), they were not yet explained by any specific mechanism, although such propagation speeds have been reported for magnetic field dipolarization and injection fronts during substorms (e.g. [*Ohtani et al.*, 1998, *Reeves et al.*, 1996]). The plasma bubble model may explain such low velocities, as well as their deceleration inward. Also the general trend of decreasing BBF velocity with decreasing distance (at 10-30 Re) was nicely shown [*Schoedel et al.*, 2001]. The question still remains – how close inward can the BBFs penetrate into the inner region?

In this paper we show the observational arguments indicating that they indeed penetrate deep into the inner magnetosphere and modify the plasma distributions in the latter region.

2. AURORAL STREAMERS AS BBF MONITORS. GENERATION OF LONG-DURATION PLASMA INHOMOGENEITIES IN THE INNER MAGNETOSPHERE

Auroral observations of BBF signatures are the only tool available to monitor the large-scale characteristics and global development of the narrow fast plasma streams. Detailed spatial-temporal association between these two phenomena has been recently established by many authors (see e.g. [*Fairfield et al.*, 1999, *Lyons et al.*, 1999, *Ieda et al.*, 2001, *Nakamura et al.*, 2001] and references therein). According to these studies, a particular form of the auroral response may vary (e.g. the localized brightenings and auroral expansions, bright spots and north-south forms or auroral streamers). Among them a one type, the auroral streamer, has the most obvious connection to the bursty bulk flow. These streamers are common during the intense convection events which are interesting for us. A streamer can best be defined as a transient narrow structure initiated in the poleward oval and propagating towards the equatorial oval boundary – see examples in Plate 1 where the development of four streamers B, C, D, E is easy to discern in this ~10°-wide auroral oval. (According to our experience, the wide oval is the best condition to register the sufficiently long auroral streamers, it occurs most often following the maximal substorm expansion and during recovery phase, as well as during continuously active periods like the steady convection events). The streamer development includes three stages [*Sergeev et al.*, 2001]: (1) auroral brightening in the poleward part of the oval (like C and D as seen at 0458:23 UT), (2) propagation from poleward to equatorward diffuse oval (nicely seen for streamers B, C and D), (3) after contacting the diffuse equatorward oval the streamer leaves here the bright patch (like A and B, C, E in the last frame). In terms of plasma sheet origin, such streamer dynamics and orientation (though not always exactly north-south, see e.g. the streamer D as compared to the streamers B and C) implies a development of some narrow plasma structure in Earthward direction from the distant tail toward the inner magnetosphere. Recent DMSP magnetic and electric field observations above such streamers [*Sergeev et al.*, 2004] confirmed their association with equatorward convection streams and R1-sense double sheet FAC system bordering that stream, with the auroral streamers produced by the precipitation of field-aligned accelerated electrons in the intense upward FAC sheet. The late consequences of the auroral streamer intrusion in the equatorial oval have not yet been systematically studied.

During ~10 hours between 01 and 12 hours UT on December 11, 1998 the Polar UVI instrument monitored the global images at ~36 s time resolution (in two alternating LBHL and LBHS bands) with a good coverage of nightside auroral oval. During this time Kp index was 4 to 5+, Dst declined from –40 nT to –60 nT, and AE index varied between 400 and 800 nT. According to the measurements at Wind and IMP8 spacecraft, the solar wind dynamic pressure varied between 2 and 6 nPa and the IMF was basically southward with the brief northward excursions at around 0340 and 0620 UT. The activity during this time rarely displayed strong large-scale enhancements in both the auroras and auroral electrojet which are typical for the substorms, with exception of a substorm starting at ~0820 UT and possible substorm-like event at around 06 UT. At other times the activity displayed the characteristics of so-called steady convection activity including a lot of localized fluctuations in the ionospheric currents and transient auroral features

[redacted]

[redacted]

[redacted]

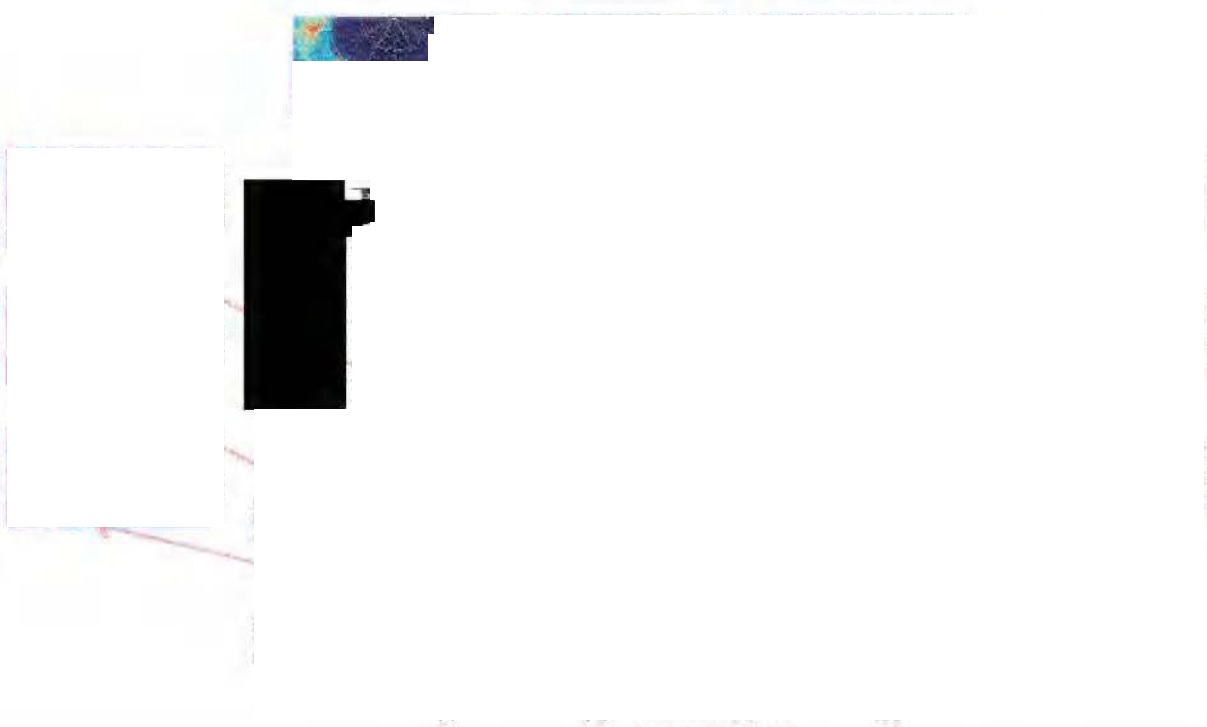

[redacted]

(see e.g. *Sergeev et al.*, 1996b, 2001). The most remarkable was the auroral streamer activity, about two dozen well-defined streamers developing from poleward boundary of wide oval toward its equatorward edge could be clearly observed.

As illustrated in Plate 1, most of streamers (with a few exceptions) have been inclined from NW to SE, they started in premidnight MLT hours and ended in the midnight-postmidnight equatorward diffuse oval (see Figure 1a). Each of them produced here the bright patch which, on many occasions (like bright patch A in Plate 1 formed by the streamer intrusion occurred ~20 min before), could still be discerned in the equatorward oval for several tens minutes after being born by the streamer intrusion (see their lifetime statistics in Fig. 1c). Most of such long-lived auroral patches slowly drifted in longitude at average velocities of a few tenths km/s (Fig. 1b). The MLT-bin-averaged flow is in the westward direction pre-midnight, and in the eastward direction post-midnight. Both the pattern and the flow amplitudes are consistent with the known characteristics of the ionospheric convection. The scale-size, duration, direction and velocity of propagation of (most frequent and strong) morningside auroral patches are similar to those of well-known

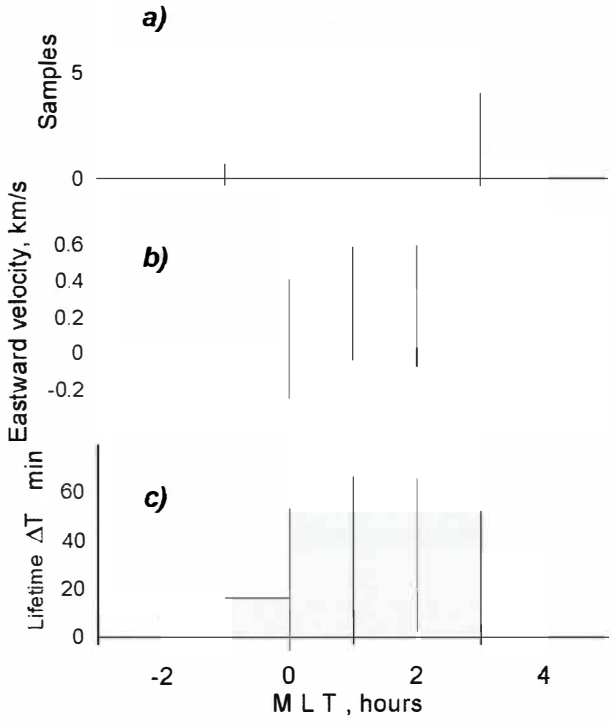

Figure 1. MLT-dependence of streamer-produced auroral patches in the equatorward oval on December 11, 1998, (a) their occurrence (with respect to the MLT of streamer intrusion into the equatorward oval), (b) average azimuthal velocities and, (c) their average lifetime.

omega or torch-like structures which are common in the morning auroral zone (see e.g. [*Opgenoorth et al.*, 1983]). The discussion of their mechanisms as well as the relationship to the substorms (for example, omega-structures are commonly considered as the substorm effects) is outside the scope of our short paper. Here we mostly emphasize the fact that narrow plasma injections (as seen by their auroral images, auroral streamers) generate considerable grainy structure in the inner magnetosphere plasma (reflected in the patchy precipitation observed), which participate in the large-scale convective motion and exist for, at least, several tens minutes.

3. BBF ROLE IN PLASMA INJECTIONS INWARD OF GEOSYNCHRONOUS ORBIT DURING ENHANCED CONVECTION EVENTS

To confirm in the more direct way how deep and how frequently the BBF-related plasma streams can intrude into the inner magnetosphere we, following [*Henderson et al.*, 1998, *Sergeev et al.*, 1999], extend the analysis and consider the observations made at geosynchronous orbit, that is at the entry to the inner magnetosphere. We analysed four long-duration enhanced convection events, when the particle observations were available at the nightside from 3 closely-spaced geostationary spacecraft (LANL-084, -080 and -097, being at midnight at ~17h, `19h and ~23h UT, correspondingly). All these events (December 22, 1996, February 10, 1997, February 17, 1998, December 10, 1998) were characterized by the long-duration southward IMF, by continuously disturbed AE traces (AE ~ 500-1000 nT) which occurred without (or with rare) substorms. The Polar UVI observations were used to confirm the absence of substorms, identify the isolated streamers and determine the times UT and MLT of streamer intrusion into the equatorward oval, which were then compared with geosynchronous observations. At 6.6 Re the energetic particle injections were identified using data from two instruments (SOPA, above 50 keV and MPA, below 32 keV, e.g. *Thomsen et al.* [2001]). Similar to *Thomsen et al.* [2001], the sharp flux increases were categorized into the one of five groups: non-dispersed (simultaneous withing 2 min) particle flux increases (at least by a factor of 2) of both energetic protons and electrons (PE), non-dispersed flux increases of either protons (P) or electrons (E), as well as energy-dispersed (due to magnetic drifts) flux increases of either protons (dP) or electrons (dE).

Particle flux traces at two LANL spacecraft situated near the midnight are shown in Plate 2 during four hours of February 17, 1998 when AE was fluctuating around 600 nT and Dst dropped steadily from –10 nT to –60 nT, showing that the main phase of the moderate (peak Dst ~–100 nT) magnetic storm was in progress. The multiple sharp increases of energetic particles flux (quite typical for the enhanced

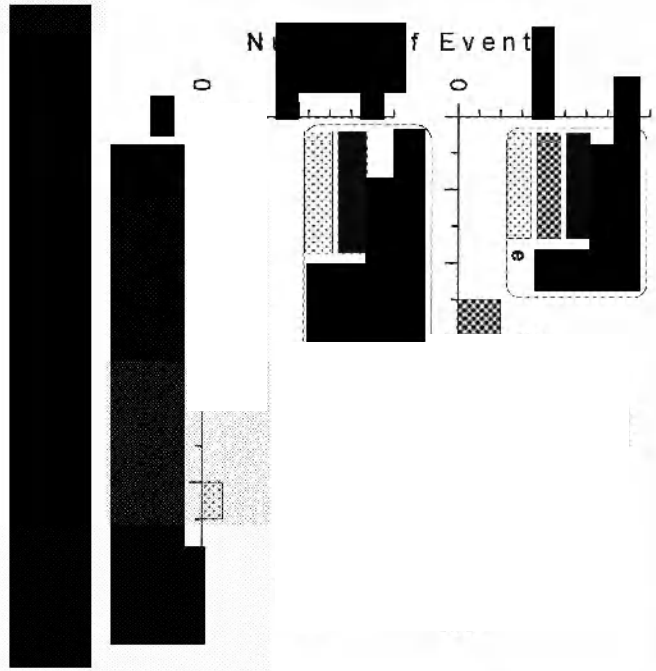
f Event
0
0

Geotail plasma flows and auroral poleward boundary intensifications observed by CANOPUS photometers, *J. Geophys. Res.*, 104, 4485, 1999.

Nakamura, R., W. Baumjohann, R. Schodel, M. Brittnacher, V.A. Sergeev, M. Kubyshkina, T. Mukai, K. Liou, Earthward flow bursts, auroral streamers, and small expansions, *J. Geophys. Res.*, 106, 10791, 2001.

Ohtani, S.-I., Earthward expansion of tail current disruption: Dual-satellite study, *J. Geophys. Res.*, 103, 6815-6825, 1998.

Opgenoorth, H.J., J. Oksman, K.U. Kaila, E. Nielsen, W. Baumjohann, Characteristics of eastward drifting omega bands in the morning sector of the auroral oval, *J. Geophys. Res.*, 88, 9171-9185, 1983.

Reeves, G.D., R.W.H. Friedel, M.G. Henderson, A. Korth, P.S. Mclachlan, R.D. Belian, Radial propagation of substorm injections, in *Substorms-3*, ESA SP-339, 579, 1996.

Reeves, G.D., K.L. McAdams, R.H.W. Friedel, T.P. O'Brien, Acceleration and loss of relativistic electrons during geomagnetic storms, *Geophys. Res. Lett.*, 30, N10, 1529 doi:10.1029/2002GL016513, 2003.

Sarris, E.T., X. Li, N. Tsaggas, N. Paschalidis, Modeling energetic particle injections in dynamic pulse fields with varying propagation speeds, *J. Geophys. Res.*, 107, 10.1029/2001JA900166, 2002.

Schodel, R., R. Nakamura, W. Baumjohann, T. Mukai, Rapid flux transfer and the plasma sheet reconfiguration, *J. Geophys. Res.*, 106, 8381, 2001.

Sergeev, V.A., V. Angelopoulos, C.A. Cattell and C.T. Russell, Detection of localized plasma bubbles in the plasma sheet, *J. Geophys. Res.*, 101, 10817, 1996a.

Sergeev, V.A., M.V. Kubyshkina, K. Liou *et al.*, Substorm and convection bay compared: Auroral and magnetotail dynamics during convection bay, *J. Geophys. Res.*, 106, 18843, 2001.

Sergeev, V.A. K. Liou, P.T. Newell, S.-I. Ohtani, M.R. Hairston, F. Rich, Auroral streamers: Characteristics of associated precipitation, convection and field-aligned currents, *Ann. Geophys.*, 22, 537, 2004.

Thomsen, M.F., J. Birn, J.E. Borovsky, K. Morzinski, D.J. McComas, G.D. Reeves, Two-satellite observations of substorm injections at geosynchronous orbit, *J. Geophys. Res.*, 106, 8405, 2001.

K. Liou, John Hopkins APL, 1100 Johns Hopkins Road, Laurel, Maryland 20723-6099 USA; e-mail: kan.liou@jhuapl.edu; Phone: 443 778-3279

G.D. Reeves, ISR-1, Mail Stop D-466, Los Alamos National Laboratory, Los Alamos, New Mexico, 87545, USA e-mail: reeves@lanl.gov, Phone 505-665-3877,

V.A. Sergeev Institute of Physics, St. Petersburg State University, Petrodvoretz, St. Petersburg 198504, Russia

M.F. Thomsen, Los Alamos National Laboratory, Los Alamos, New Mexico, 875455, USA

D.A. Yahnin, Institute of Physics, St. Petersburg State University, Petrodvoretz, St. Petersburg 198504, Russia

Dynamics of Ions of Ionospheric Origin During Magnetic Storms: Their Acceleration Mechanism and Transport Path to Ring Current

M. Nosé[1], K. Takahashi[2], S. Ohtani[2], S.P. Christon[3], and R.W. McEntire[2]

We investigated the spatial and temporal properties of the 9-210 keV/*e* ion composition in the near-Earth plasma sheet (at geocentric distance, *r*, of 8-15 R_E), using energetic ion flux data acquired by the suprathermal ion composition spectrometer (STICS) sensor of the energetic particle and ion composition (EPIC) instrument onboard the Geotail spacecraft. We analyzed data covering 8.3 years to find the MLT-*r* distribution of the H^+, He^+, and O^+ energy densities (as well as the He^+/H^+ and O^+/H^+ energy density ratios) as a function of the SYM-H index. We obtained the following results: (1) The energy density increases as SYM-H decreases; (2) The energy density change depends on ion mass: the largest change occurs in O^+ and the smallest change occurs in H^+; (3) The energy density shows a dawn-dusk asymmetry when SYM-H < −50 nT, being larger on the duskside than on the dawnside; and (4) The He^+/H^+ and O^+/H^+ energy density ratios in the plasma sheet are similar to those in the ring current. From these results we conclude that ionospheric He^+ and O^+ ions are transported to the plasma sheet, accelerated there by the dawn-to-dusk electric field in a mass-dependent manner (heavier ions gain more energy than lighter ions), and injected into the ring current region. Both the ion flux from the ionosphere and the energy gain in the plasma sheet become large when the geomagnetic disturbance becomes intense.

1. INTRODUCTION

Plasma in the plasma sheet is considered to be an important source of the ring current plasma. Previous simulation studies have shown that changes of the proton density in the plasma sheet have significant effects on development and decay of the ring current [*Kozyra et al.*, 1998; *Ebihara and Ejiri*, 2000, 2001]. *Kozyra et al.* [1998] conducted two numerical simulations of the ring current, one with the plasma sheet proton density fixed at a prestorm value and the other with the density allowed to vary as observed at geosynchronous orbit. They calculated Dst from the simulations and compared it with the observed Dst index. The calculated Dst index in the former simulation was far from the observed Dst, while that in the latter simulation traced the observed Dst fairly well. *Ebihara and Ejiri* [2000, 2001] also found that the Dst derived from a numerical simulation had a large deviation from the observed Dst when the plasma sheet proton density was assumed to have a constant value representative of quiet times. From AMPTE/CCE observations of energetic ions, *Lui et al.* [1986] and *Lui* [1993] concluded that ring current development is explained by inward radial displacement of particle population outside the ring current. By means of model calculation of ion motion, *Nosé et al.* [2001] presented that it is much more likely that

[1]Data Analysis Center for Geomagnetism and Space Magnetism, Graduate School of Science, Kyoto University, Kyoto, Japan
[2]Applied Physics Laboratory, Johns Hopkins University, Laurel Maryland
[3]Focused Research and Analysis, Columbia, Maryland

The Inner Magnetosphere: Physics and Modeling
Geophysical Monograph Series 155

10.1029/155GM08

ions with energy of a few tens of keV in the near-Earth plasma sheet ($L \sim 9$) make a direct contribution to the outer ring current at $L = 5$-7 (the ring current in open drift path).

One of recent outstanding questions concerning the ring current is the dynamics of ions of ionospheric origin (He^+ and O^+), that is, their energization to the ring current energy (20-200 keV) and their transport into the ring current [*Kamide et al.*, 1997]. Since the plasma sheet plays an important role in development and decay of the ring current as shown above, investigation of spatial and temporal change of the energetic (a few keV to a few hundreds of keV) ion composition in the near-Earth plasma sheet will provide us with a vital clue to the above question. If the energetic ion composition in the plasma sheet around midnight is found to be comparable to that in the ring current, it implies that ionospheric ions are transported to the ring current through the plasma sheet where the ions are accelerated to a few hundreds of keV. There have been a large number of studies about ion composition in the low energy range (0.1-30 keV) [e.g., *Peterson et al.*, 1981; *Lennartsson and Sharp*, 1982; *Sharp et al.*, 1982; *Young et al.*, 1982; *Sharp et al.*, 1985; *Lennartsson and Shelly*, 1986]. However, there are no statistical studies on the plasma sheet ion composition in the energy range up to ~200 keV, though case studies have been made by *Ipavich et al.* [1984] and *Nosé et al.* [2001, 2003].

In the present study we perform a statistical study about energetic ion composition change in the near-Earth plasma sheet (a radial distance of 8-15 R_E), using H^+, He^+ and O^+ ion fluxes measured by the Geotail spacecraft. The spacecraft has been placed in the near-Earth orbit (8-9 R_E perigee by ~30 R_E apogee) since the fall of 1994 and is still under operation. Ion flux data in the near-Earth plasma sheet are available for more than 8 years. We examined how ion composition in the plasma sheet changes as a function of the Geotail position and the SYM-H index. From the statistical results we inferred a transport path and an acceleration mechanism for ions of ionospheric origin. The rest of this paper is organized as follows. Section 2 describes the data set. In section 3 we show spatial and temporal changes of distributions of the energy density (and the energy density ratio) in the near-Earth plasma sheet. In section 4 we discuss what mechanisms cause the observed changes of the energy density distributions (and the energy density ratio distributions). The conclusions are presented in section 5.

2. DATA SET

2.1. Geotail/EPIC/STICS and SYM-H Index

The Geotail spacecraft carries the energetic particle and ion composition (EPIC) instrument, which consists of the suprathermal ion composition system (STICS) and the ion composition system (ICS) sensors [*Williams et al.*, 1994]. In the present study we used the EPIC/STICS instrument that provides energetic (9-210 keV/*e*) ion flux with mass and charge information. EPIC/STICS samples ions at eight energy steps evenly spaced in logarithmic scale and has a almost full (~4π sr) directional coverage with six identical telescopes having the polar angles of ± (0°-26.7°), ± (26.7°-53.3°), and ±(53.3°-80.0°) with respect to the spacecraft spin plane. One energy spectrum is obtained every ~24 sec.

Using the differential flux data of H^+, He^+, and O^+ from the EPIC/STICS instrument, we calculated the energy density (ε) in the same manner as *Nosé et al.* [2001, 2003]. After computation of the energy density at a time resolution of ~24 sec (i.e., for each energy spectrum), we took an average of the energy density over ~10 min for statistical significance. We use the 10-min averages in the following statistical analysis.

The SYM-H index, instead of the Dst index, was used to measure geomagnetic disturbance. The SYM-H index is essentially the same as the Dst index but is derived from six mid-latitude stations and has a time resolution of 1 min [*Iyemori et al.*, 1992]. (The Dst index is derived from four stations with a time resolution of 1 hour, which is not short enough to study temporal changes of ion composition here, since we use the 10-min averages of the EPIC/STICS data.) We average the SYM-H index over the same 10-min segments as the EPIC/STICS data.

2.2. Data Coverage

We used the EPIC/STICS and SYM-H data for the period of 1 January 1995 to 10 May 2003, covering about 8.3 years in total. The Geotail spacecraft has a perigee of ~8 R_E, an apogee of 30 R_E, an orbital period of ~5.5 days, and an apsidal period of ~1 year. We limited the Geotail position to magnetic local time (MLT) of 1800-0600 hour and geocentric radial distance (r) of 8-15 R_E, since we are interested in the near-Earth plasma sheet. (Ions in such region can be convected into the ring current region ($r = 3$-6.6 R_E) during storms [*Chen et al.*, 1994, 1998; *Fok et al.*, 1999].) The unique orbit and long uninterrupted operation of Geotail made it possible to examine the spatial and temporal change of ion composition in the plasma sheet.

A criterion for the plasma sheet is taken to be $\varepsilon_{H+} \geq 0.5$ keV/cm^3. Data selected with this criterion had the plasma beta (β) larger than 0.5 for most cases (70.0%), which is a typical β-value of the inner plasma sheet [*Angelopoulos et al.*, 1994]. For almost all (98.8%) of the selected data, β was ≥ 0.1. (We used the plasma moment data of 1995-1997 to derive β, because the plasma moment data after 1998 are under calibration.)

3. OBSERVATIONS

3.1. Energy Density

Plate 1 shows MLT-r distributions of the energy density for H^+, He^+, and O^+, and the energy density ratio for He^+/H^+ and O^+/H^+. From top to bottom of each column we display the distributions for different SYM-H conditions, that is, 10 nT > SYM-H ≥−10 nT (quiet), −10 nT > SYM-H ≥−50 nT (weak disturbance), −50 nT > SYM-H ≥−100 nT (moderate disturbance), and SYM-H < −100 nT (strong disturbance). Data are averaged in 84 MLT-r bins, each covering 1 hour of MLT and 1 R_E of radial distance. The color scale for the energy density or the energy density ratio is displayed at the right of each plate. White bins mean that there were not enough satellite observations for statistics (less than 1 hour or fewer than 6 points of data). In the bottom panels (SYM-H < −100 nT) we see many white bins, because a strongly disturbed interval is generally much shorter than a quiet interval. The numbers in parentheses shown at the bottom-right corner are average values of the energy density or the energy density ratio calculated from colored bins.

The H^+ energy density is shown in Plates 1a-1d. During the quiet and weakly disturbed periods (Plates 1a and 1b), we see smaller energy density as the distance from the Earth becomes larger. The H^+ energy density at $r > 11$ R_E is as small as 2-3 keV/cm^3, while that at $r < 11$ R_E is ~7 keV/cm^3. The energy density distribution is rather symmetric about 0000 MLT. However, when the magnetic storms develop, the energy density at $r > 11$ R_E and 1800-0200 MLT increases greatly (Plate 1c). This causes a dawn-dusk asymmetry. We speculate that the same tendency exists during strong disturbances but cannot substantiate it because data are sparse (Plate 1d). The average energy density changed from 2.98 keV/cm^3 at quiet times to 5.06 keV/cm^3 at strong disturbances, an enhancement by a factor of 1.7.

Plates 1e-1h show the He^+ energy density. The basic behavior of the He^+ energy density is similar to that of H^+. However, for He^+ we see a larger change from low to high storm activity: the average He^+ energy density is 0.041 keV/cm^3 at quiet times and 0.087 keV/cm^3 at strong disturbances, resulting in an enhancement factor of 2.1.

Plates 1i-1l show the O^+ energy density. We also see symmetric distributions of the energy density about the midnight meridian during quiet and weakly disturbed intervals (Plates 1i and 1j). The average of the O^+ energy density is as low as 0.35-0.60 keV/cm^3. As can be seen in Plate 1k, once magnetic storms develop, the energy density exhibits a dawn-dusk asymmetry with larger values on the duskside. The average energy density jumped to 1.79 keV/cm^3. During strong disturbances, the average energy density was enhanced to 3.99 keV/cm^3 (Plate 1l). The enhancement factor of O^+ is 11.4, which is much larger than those of H^+ and He^+.

3.2. Energy Density Ratio

The larger enhancement of the energy density of He^+ and O^+ relative to H^+ can be seen more clearly, if we calculate the energy density ratio of He^+/H^+ and O^+/H^+. Moreover, the energy density ratio is an appropriate quantity to compare the ion composition between the near-Earth plasma sheet and the ring current. Previous studies have reported the energy density ratio in the ring current as will be shown in a later section. Plates 1m-1t show the He^+/H^+ and O^+/H^+ energy density ratios in the MLT-r plane.

From Plates 1m-1p we find that the He^+/H^+ energy density ratio increases slightly as geomagnetic disturbances become intense. Average values of the energy density ratio, which are shown at the bottom-right corner of each plate, indicate a slight increase from 0.014 to 0.020. The O^+/H^+ energy density ratio changes drastically in the course of magnetic storms (Plates 1q-1t). There are strong enhancements in the average energy density ratio from weak to moderate disturbances (from 0.17 to 0.46) as well as from moderate to strong disturbances (from 0.46 to 0.85). It is worth noting that there are some bins having an O^+/H^+ energy density ratio of ~1 during moderate and strong disturbances, which means that the O^+ energy density becomes comparable to the H^+ energy density. In both Plates 1o and 1s we find a dawn-dusk asymmetry, though it is not so clear as that found in Plates 1g and 1k.

4. DISCUSSION

4.1. Comparison of Ion Composition Between Plasma Sheet and Ring Current

We have examined how the He^+/H^+ and O^+/H^+ energy density ratios in the near-Earth plasma sheet change as a function of the SYM-H index. The results are now compared with changes of the energy density ratios in the ring current reported in previous studies.

Plate 2 summarizes observational results of the ring current ion composition by eight previous studies employing the AMPTE/CCE and CRRES spacecrafts. Open circles represent results at quiet intervals and filled circles represent results at storm intervals. (The left part of a vertical dashed line corresponds to a quiet interval.) Blue and red show the He^+/H^+ and O^+/H^+ energy density ratios, respectively. A vertical or horizontal line running through a circle indicates a range of the energy density ratio or a range of the Dst index derived from multi-event analysis. Numbers 1 to 8 indicate references shown at the top-left corner of the plate. A few case studies using the AMPTE/CCE spacecraft found that

[redacted]

[redacted]

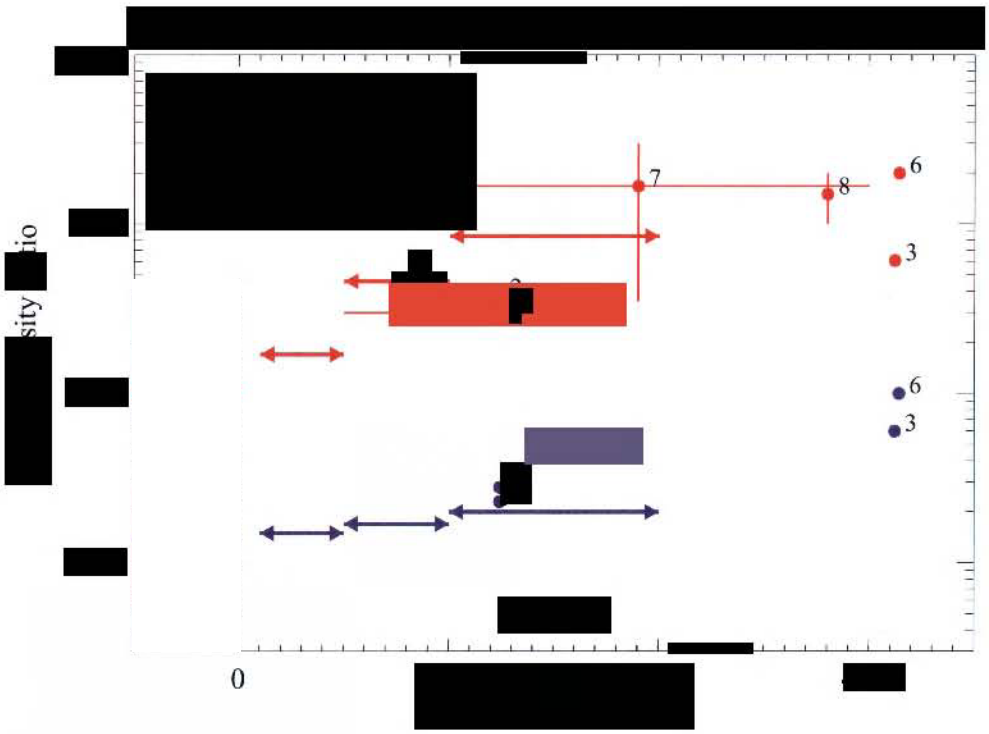

[redacted]

the He^+/H^+ energy density ratio changes from 0.01-0.02 to 0.025-0.06 and the O^+/H^+ energy density ratio changes from 0.01-0.03 to 0.3-0.6 in the outer ring current region of L = 5-7 [*Gloeckler et al.*, 1985; *Krimigis et al.*, 1985; *Hamilton et al.*, 1988; *Feldstein et al.*, 2000]. *Greenspan and Hamilton* [2002] made a statistical analysis of the AMPTE/CCE data and found the O^+/H^+ energy density ratio at L = 2-7 to be ~0.3 during storms. Using data acquired by the CRRES spacecraft, *Roeder et al.* [1996], *Daglis* [1997], and *Daglis et al.* [2000] examined ion composition changes in the ring current. *Roeder et al.* [1996] examined the L range of 3-5, while *Daglis* [1997] and *Daglis et al.* [2000] surveyed the outer ring current region of L = 5-7. The He^+/H^+ energy density ratio was found to change from 0.04 to 0.1, and the O^+/H^+ ratio, from 0.1-0.3 to 0.3-3.0.

We superimposed our Geotail results in the near-Earth plasma sheet over Plate 2. The energy density ratios found in Plates 1m-1t are depicted by horizontal thick arrows. The ratios for SYM-H = 10 nT to −10 nT are shown in the left part of the vertical dashed line. We find a good agreement of the energy density ratios between the near-Earth plasma sheet and the ring current for both He^+/H^+ and O^+/H^+. This implies that the ion composition change in the outer ring current is a direct consequence of the ion composition change occurring in the plasma sheet.

4.2. Flux Increase of Ion Outflow During Magnetic Storms

Moore et al. [1999, 2001] have found that ionospheric plasma outflows promptly respond to disturbances of solar wind dynamic pressure, combining statistical results from the DE-1 data and a case study result from the Polar data. A statistical study with the Polar spacecraft have indicated a direct response of upwelling O^+ escape flux from the cusp/polar cap to the solar wind dynamic pressure [*Elliott et al.*, 2001]. Using the low energy neutral atom (LENA) imager onboard the IMAGE spacecraft, *Fuselier et al.* [2002] reported that episodic bursts of ion outflow were associated with increases in the solar wind density (and therefore the solar wind dynamic pressure). *Cully et al.* [2003a] analyzed data from the Akebono spacecraft and concluded that the solar wind dynamic pressure is one of the important driving factors for ion outflow.

We examined the relation between the solar wind dynamic pressure and geomagnetic disturbances, using the OMNIWeb database (http://nssdc.gsfc.nasa.gov/omniweb/). The result is shown in Figure 1. Horizontal arrows indicate the ranges of the SYM-H index corresponding to those of Plates 1 and 2. A vertical line represents the standard error. We found that solar wind dynamic pressure is constant at 2.0-2.5 nPa during quiet and weak storm intervals, but it increases as the geomagnetic disturbance becomes intense. Since an enhancement

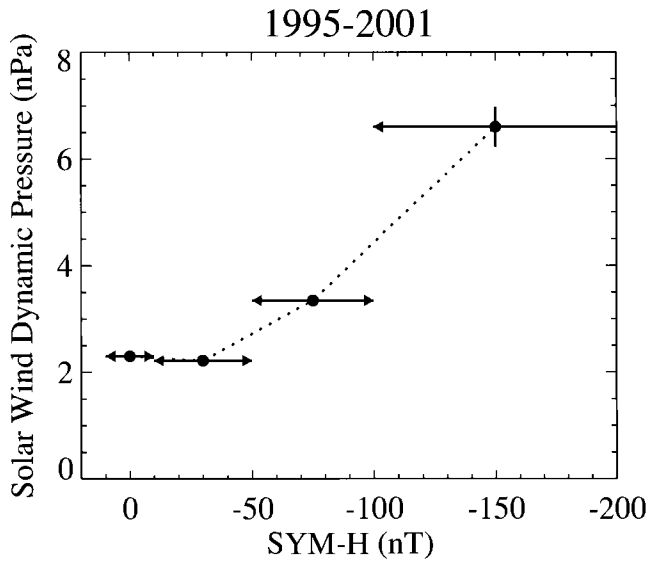

Figure 1. Relation between the solar wind dynamic pressure and geomagnetic disturbances measured with the SYM-H index in the interval of 1995-2001. Horizontal arrows represent ranges of the SYM-H index corresponding to those of Plate 1. A vertical line means the standard error.

in the solar wind dynamic pressure causes a flux increase of ion outflow as reported by previous studies, we argue that the amounts of He^+ and O^+ ions flowing from the ionosphere are generally larger when SYM-H < −50 nT than when SYM-H = 10 nT to −50 nT.

Trajectories of such ions after they have escaped from the ionosphere have been studied using numerical simulations [*Cladis and Francis*, 1985, 1992; *Cladis*, 1986, 1988; *Peroomian and Ashour-Abdalla*, 1996; *Delcourt et al.*, 1999; *Chappell et al.*, 2000; *Cully et al.*, 2003b]. These studies found that most of such ions preferentially move into the plasma sheet through the geomagnetic lobe. Transit time of ions from the ionosphere to the plasma sheet is 1-2 hours if they start from the dayside cusp [*Cladis*, 1986, 1988] or <1 hour if they are originating from the auroral zone in the midnight sector [*Delcourt et al.*, 1999]. These transit times are much shorter than the timescale of magnetic storms (a few days). From the results of these studies and Figure 1, we suggest that more ionospheric ions are transported into the plasma sheet during moderate and intense magnetic storms than during quiet times. In fact, *Nosé et al.* [2003] reported an event in which the O^+ and He^+ number density in the plasma sheet (X ~ −18 R_E) increased at storm maximum, and this magnetic storm was accompanied by a strong enhancement of the solar wind dynamic pressure (see their Figures 5 and 8). The changes of the O^+/H^+ energy density ratio found in our analysis (Plates 1r-1t) can be explained by

the changes of the average solar wind dynamic pressure (Figure 1) that regulates the supply of O^+ ions from the ionosphere to the plasma sheet.

It is worth mentioning briefly influence of solar wind parameters on the Dst index. IMF Bz is widely accepted as the primary parameter to control the Dst index. *O'Brien and McPherron* [2000] and *Temerin and Li* [2002] used IMF Bz and solar wind velocity to model the Dst index. Solar wind dynamic pressure enhancement has been thought to cause an increase in Dst by compressing the magnetopause. However, from the above discussion it is expected that solar wind dynamic pressure enhancement causes a decrease in Dst by delivering ionospheric ions to the plasma sheet (and the ring current). It is left for future studies to reveal how solar wind parameters control the Dst index.

4.3. Acceleration of Ions of Ionospheric Origin During Magnetic Storms

Ionospheric ions injected into the plasma sheet are considered to experience energization by the meandering motion in the current sheet and the dawn-to-dusk convection electric field [*Speiser*, 1965; *Lyons and Speiser*, 1982]. *Nosé et al.* [2001] made a numerical calculation of particle energization in a very simple model of the current sheet and the convection electric field. They found that heavier ions gained more energy than lighter ions, indicating a mass-dependent acceleration.

In order to examine this ion acceleration in a more realistic model, we here performed a numerical calculation of He^+ and O^+ ion trajectories in the modified Tsyganenko 89 geomagnetic field model [*Tsyganenko*, 1989] and the Volland-Stern convection electric field model [*Volland*, 1973; *Stern*, 1975; *Maynard and Chen*, 1975]. Both models have Kp as a parameter. The dipole tilt angle was set to be 0° for simplicity. We assumed that the electrostatic potential is constant along a geomagnetic field line. Ion trajectories were calculated by solving the Lorenz equation of motion numerically with the fourth-order Runge-Kutta method. He^+ and O^+ ions started from (X, Y, Z) = (−30, 0, −1) R_E in the geocentric solar magnetospheric (GSM) coordinate with an initial kinetic energy of 1 keV and a pitch angle of 0°. These initial parameters were chosen to represent ions that originated from the southern ionosphere and were injected into the plasma sheet after traveling through the geomagnetic lobe. Calculation of ion trajectory was terminated when ions reached at X = −3 R_E near the equator ($|Z| \leq 0.3$ R_E). Plate 3 shows the calculation results: Left panels (Plates 3a-3c) are for He^+ and right panels (Plates 3d-3f) are for O^+. From top to bottom, we plotted ion trajectories in the X-Z plane (Plates 3a and 3d) and in the X-Y plane (Plates 3b and 3e), and time profiles of ion kinetic energy (Plates 3c and 3f). Blue and red lines correspond to Kp = 1 and Kp = 4, respectively. The trajectories indicate that injected ions interact with the current sheet and drift duskward. These ions are accelerated because of the convection electric field, reaching energies of 10-100 keV, which is covered by EPIC/STICS, as can be seen in Plates 3c and 3f. In the run for Kp = 1 (blue) the final kinetic energy of He^+ and O^+ is ~15 keV and ~20 keV, respectively. When Kp is 4 (red), O^+ also gains more energy (~60 keV) than He^+ (~40 keV), and the difference of the final energy between He^+ and O^+ becomes larger. These results indicate that the ion acceleration in the current sheet is mass-dependent; that is, the heavier the ion is, the higher the energy gain. This property becomes more evident as the geomagnetic disturbance level becomes higher. Therefore this ion acceleration mechanism can explain the EPIC observations of the dependence of the energy density on SYM-H, ordering of energy density change by ion mass (largest for O^+ and the smallest for H^+ (Plate 1)). We should note that ions gain more energy as they drifted duskward. This will explain the dawn-dusk asymmetry of the energy density (the energy density ratio) distributions found in Plates 1g and 1k (Plates 1o and 1s).

The H^+ ions are considered to have two origins: the ionosphere and the solar wind. *Chappell et al.* [1987] showed that the polar wind is the largest source of ionospheric H^+ to populate the plasma sheet, followed by the auroral zone outflow. *Terasawa et al.* [1997] and *Borovsky et al.* [1997] found a good correlation between the plasma sheet H^+ number density and the solar wind number density. *Fujimoto et al.* [1998] argued that the solar wind plasma enters from the flanks into the plasma sheet. It is difficult to discriminate between terrestrial and solar H^+ ions, and it is controversial which H^+ ions are dominant in the near-Earth plasma sheet [*Moore*, 1991]. *Winglee* [1998] attempted to answer the question by multi-fluid numerical simulation. Whichever origin the H^+ ions have, they are expected to suffer heating in the plasma sheet. The ionospheric H^+ ions are heated when they move from the geomagnetic lobes into the plasma sheet [*Chappell et al.*, 2000]. After the solar wind H^+ ions enter the plasma sheet, they are heated as they move inward and duskward [*Fujimoto et al.*, 2002]. These heating processes might be similar to that for He^+ and O^+ shown above (i.e., interaction with the current sheet), because the energy density distribution of H^+ had the dawn-dusk asymmetry (Plate 1c). Since the heating process is mass-dependent, we can expect that H^+ ions are not accelerated as strongly as He^+ and O^+ ions. This would be one of reasons that the He^+/H^+ and O^+/H^+ energy density ratios were enhanced during magnetic storms.

The above discussions in sections 4.1-4.3 lead us to suppose that ions of ionospheric origin (He^+ and O^+) are transported from the ionosphere to the ring current region through the plasma sheet where ion acceleration is achieved. Flux of

[redacted]

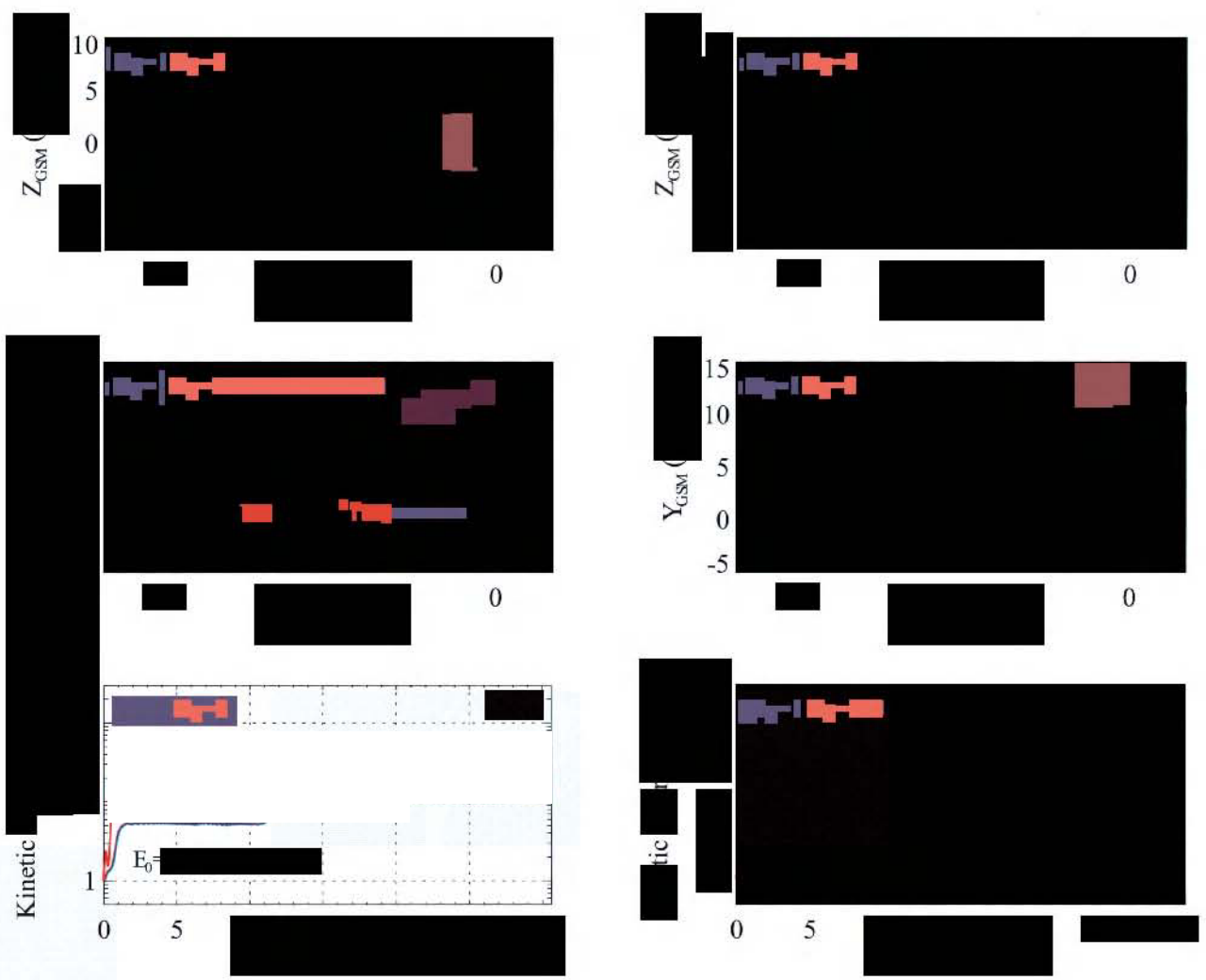

[redacted]

He^+ and O^+ ions flowing from the ionosphere is expected to increase when the solar wind dynamic pressure is enhanced.

4.4. Role of Substorms

It has been demonstrated by numerical calculations that impulsive electric field induced at depolarization (i.e., substorms) can accelerate ions in a mass-dependent manner [*Delcourt et al.*, 1990; *Sánchez et al.*, 1993]. Satellite observations showed that O^+ flux is more enhanced than H^+ flux at substorm onsets [*Möbius et al.*, 1987; *Nosé et al.*, 2000]. Therefore one might argue that ion acceleration at substorm onsets, instead of the ion acceleration in the current sheet, can explain the results shown in Plates 1m-1t, because substorms occur a number of times during magnetic storms. However, recent Geotail observations showed that (1) enhancement of the energy density ratio at substorms is sometimes smaller than the observed changes of the energy density ratio during storms, (2) the enhanced energy density ratio at substorms decays within 1-2 hours, which is much shorter than the timescale of storms, and (3) the energy density ratio increases during storms even if there are no substorm signatures [*Nosé et al.*, 2001, 2003]. These observations suggest that ion acceleration by substorms can enhance the energy density ratio, but it is not responsible for the observed ion composition change during storms.

Fok et al. [1999] showed that substorms are important in pushing the plasma sheet plasma deep into the inner magnetosphere and in creating strong ring current. On the other hand, using the energetic neutral atom (ENA) flux obtained by the IMAGE/HENA (high energy neutral atom) imager, *Ohtani et al.* [2003] found that the O^+ ENA flux increases globally in the ring current region within 10 min or less, which is too short for O^+ ions to be transported from the plasma sheet.

From the present study we cannot derive definite conclusions how important substorms are in ion composition changes of the ring current and the plasma sheet. Further studies are needed to evaluate the role of substorms.

5. CONCLUSIONS

Energetic (9-210 keV/*e*) ion flux data obtained by the EPIC/STICS instrument onboard the Geotail spacecraft were used to examine the spatial and temporal changes of the ion composition in the near-Earth plasma sheet (r = 8-15 R_E). Since the Geotail data were available from January 1995 to May 2003, we could perform a statistical study. We obtained the MLT-r distributions of the H^+, He^+, and O^+ energy densities and the He^+/H^+ and O^+/H^+ energy density ratios in the plasma sheet as a function of the SYM-H index. The main results can be summarized as follows: (1) The H^+, He^+, and O^+ energy densities increased when SYM-H decreased, as expected from the Dessler-Parker-Schopke relationship; (2) The energy density change was ordered by ion mass, being the largest for O^+ and the smallest for H^+; (3) The H^+, He^+, and O^+ energy densities had a dawn-dusk asymmetry when magnetic storms developed, being larger on the dusk-side than on the dawn side; and (4) The He^+/H^+ and O^+/H^+ energy density ratios in the near-Earth plasma sheet were comparable to that in the ring current.

Result 4 suggests that the ion composition change in the ring current is a direct consequence of the ion composition change occurring in the near-Earth plasma sheet.

From a statistical study we found a tendency of high solar wind dynamic pressure during magnetic storms. Combined with results of previous studies, which showed a positive correlation between solar wind dynamic pressure and flux of outflow ions, we supposed that the flux of He^+ and O^+ ions injected into the plasma sheet become high as magnetic storms become intense. This is one explanation for result 1.

We conducted a numerical simulation of ion motion in realistic models of the geomagnetic field and the convection electric field. We found that ions are accelerated in a mass-dependent way and acquire more energy as they move duskward and the geomagnetic disturbance level becomes high. These results may explain results 1-3.

We argue that ionospheric He^+ and O^+ ions are transported into the ring current after traveling through the plasma sheet, where ions undergo mass-dependent acceleration. Solar wind dynamic pressure is considered to control the amounts of ions flowing from the ionosphere.

Acknowledgments. We thank D.J. Williams and S.R. Nylund for their help in analysis of the Geotail/EPIC/STICS data. The SYM-H index was provided by T. Iyemori at WDC for Geomagnetism, Kyoto. The plasma moment data and the magnetic field data from Geotail to calculate plasma beta were supplied by T. Mukai and T. Nagai. A geomagnetic field by the modified Tsyganenko 89 model was calculated with GEOPACK routines developed by N.A. Tsyganenko and the GSFC modeling group. This work was supported by the Atmospheric Science Division of the National Science Foundation (grant ATM-0000255) and the Sasagawa Scientific Research Grant from The Japan Science Society.

REFERENCES

Angelopoulos, V., *et al.*, Statistical characteristics of bursty bulk flow events, *J. Geophys. Res.*, 99, 21,257-21,280, 1994.

Borovsky, J.E., M.F. Thomsen, and D.J. McComas, The superdense plasma sheet: Plasmaspheric origin, solar wind origin, or ionospheric origin?, *J. Geophys. Res.*, 102, 22,089-22,097, 1997.

Chappell, C.R., T.E. Moore, and J.H. Waite, Jr., The ionosphere as a fully adequate source of plasma for the Earth's magnetosphere, *J. Geophys. Res.*, 92, 5896-5910, 1987.

Chappell, C.R., B.L. Giles, T.E. Moore, D.C. Delcourt, P.D. Craven, and M.O. Chandler, The adequacy of the ionospheric source in supplying magnetospheric plasma, *J. Atmo. Solar Terr. Phys.*, 62, 421-436, 2000.

Chen, M.W., L.R. Lyons, M. Schulz, Simulations of phase space distributions of storm time proton ring current, *J. Geophys. Res.*, 99, 5745-5759, 1994.

Chen, M.W., J.L. Roeder, J.F. Fennell, L.R. Lyons, and M. Schulz, Simulations of ring current proton pitch angle distributions, *J. Geophys. Res.*, 103, 165-178, 1998.

Cladis, J.B., Parallel acceleration and transport of ions from polar ionosphere to plasma sheet, *Geophys. Res. Lett.*, 13, 893-896, 1986.

Cladis, J.B., Transport of ionospheric ions in the magnetosphere: Theory and observations, *Adv. Space Res.*, 8, (8)165-(8)173, 1988.

Cladis, J.B., and W.E. Francis, The polar ionosphere as a source of the storm time ring current, *J. Geophys. Res.*, 90, 3465-3473, 1985.

Cladis, J.B., and W.E. Francis, Distribution in magnetotail of O^+ ions from cusp/cleft ionosphere: A possible substorm trigger, *J. Geophys. Res.*, 97, 123-130, 1992.

Cully, C.M., E.F. Donovan, A.W. Yau, G.G. Arkos, Akebono/ Suprathermal Mass Spectrometer observations of low-energy ion outflow: Dependence on magnetic activity and solar wind conditions, *J. Geophys. Res.*, 108(A2), 1093, doi:10.1029/ 2001JA009200, 2003a.

Cully, C.M., E.F. Donovan, A.W. Yau, and H.J. Opgenoorth, Supply of thermal ionospheric ions to the central plasma sheet, *J. Geophys. Res.*, 108(A2), 1092, doi:10.1029/2001JA009457, 2003b.

Daglis, I.A., The role of magnetosphere-ionosphere coupling in magnetic storm dynamics, in *Magnetic Storms*, *Geophys. Monogr. Ser.*, vol. 98, edited by B. T. Tsurutani *et al.*, pp. 107-116, AGU, Washington, D. C., 1997.

Daglis, I.A., Y. Kamide, C. Mouikis, G.D. Reeves, E.T. Sarris, K. Shiokawa, and B. Wilken, "Fine structure" of the storm-substorm relationship: Ion injections during Dst decrease, *Adv. Space Res.*, 25, 2369-2372, 2000.

Delcourt, D.C., J.A. Sauvaud, and A. Pedersen, Dynamics of single-particle orbits during substorm expansion phase, *J. Geophys. Res.*, 95, 20,853-20,865, 1990.

Delcourt, D.C., N. Dubouloz, J.-A. Sauvard, M. Malingre, On the origin of sporadic keV ion injections observed by Interball-Auroral during the expansion phase of a substorm, *J. Geophys. Res.*, 104, 24,929-24,937, 1999.

Ebihara, Y., and M. Ejiri, Simulation study on fundamental properties of the storm-time ring current, *J. Geophys. Res.*, 105, 15,843-15,859, 2000.

Ebihara, Y., and M. Ejiri, Reply, *J. Geophys. Res.*, 106, 6323-6324, 2001.

Elliott, H.A., R.H. Comfort, P.D. Craven, M.O. Chandler, and T.E. Moore, Solar wind influence on the oxygen content of ion outflow in the high-latitude polar cap during solar minimum conditions, *J. Geophys. Res.*, 106, 6067-6084, 2001.

Feldstein, Y.I., L.A. Dremukhina, U. Mall, and J. Woch, On the two-phase decay of the Dst-variation, *Geophys. Res. Lett.*, 27, 2813-2816, 2000.

Fok, M.-C., T.E. Moore, and D.C. Delcourt, Modeling of inner plasma sheet and ring current during substorms, *J. Geophys. Res.*, 104, 14,557-14,569, 1999.

Fujimoto, M., T. Terasawa, T. Mukai, Y. Saito, T. Yamamoto, and S. Kokubun, Plasma entry from the flanks of the near-Earth magnetotail: Geotail observations, *J. Geophys. Res.*, 103, 4391-4408, 1998.

Fujimoto, M., T. Mukai, and S. Kokubun, Cold-dense plasma sheet and hot-dense ions in the inner magnetosphere, *Adv. Space Res.*, 30(10), 2279-2288, 2002.

Fuselier, S.A., H.L. Collin, A.G. Ghielmetti, E.S. Claflin, T.E. Moore, M.R. Collier, H. Frey, and S.B. Mende, Localized ion outflow in response to a solar wind pressure pulse, *J. Geophys. Res.*, 107(A8), doi:10.1029/2001JA000297, 2002.

Gloeckler, G., B. Wilken, W. Stüdemann, F.M. Ipavich, D. Hovestadt, D.C. Hamilton, and G. Kremser, First composition measurement of the bulk of the storm-time ring current (1 to 300 keV/*e*) with AMPTE/CCE, *Geophys. Res. Lett.*, 12, 325-328, 1985.

Greenspan, M.E., and D.C. Hamilton, Relative contributions of H^+ and O^+ to the ring current energy near magnetic storm maximum, *J. Geophys. Res.*, 107(A4), doi:10.1029/ 2001JA000155, 2002.

Hamilton, D.C., G. Gloeckler, F.M. Ipavich, W. Stüdemann, B. Wilken, and G. Kremser, Ring current development during the great geomagnetic storm of February 1986, *J. Geophys. Res.*, 93, 14,343-14,355, 1988.

Ipavich, F.M., A.B. Galvin, G. Gloeckler, D. Hovenstadt, B. Klecker, and M. Scholer, Energetic (>100 keV) O^+ ions in the plasma sheet, *Geophys. Res. Lett.*, 11, 504-507, 1984.

Iyemori, T., T. Araki, T. Kamei, and M. Takeda, *Mid-latitude geomagnetic indices ASY and SYM (Provisional) No. 1 1989*, Data Anal. Center for Geomagn. and Space Magn., Kyoto Univ., Kyoto, Japan, 1992.

Kamide, Y., *et al.*, Magnetic Storms: Current understanding and outstanding questions, in *Magnetic Storms*, *Geophys. Monogr. Ser.*, vol. 98, edited by B.T. Tsurutani, W.D. Gonzalez, Y. Kamide, and J.K. Arballo, pp. 1-19, AGU, Washington, D. C., 1997.

Kozyra, J.U., V.K. Jordanova, J.E. Borovsky, M.F. Thomsen, D.J. Knipp, D.S. Evans, D.J. McComas, and T.E. Cayton, Effects of a high-density plasma sheet on ring current development during the November 2-6, 1993, magnetic storm, *J. Geophys. Res.*, 103, 26,285-26,305, 1998.

Krimigis, S.M., G. Gloeckler, R.W. McEntire, T.A. Potemra, F.L. Scarf, and E.G. Shelley, Magnetic storm of September 4, 1984: A synthesis of ring current spectra and energy densities measured with AMPTE/CCE, *Geophys. Res. Lett.*, 12, 329-332, 1985.

Lennartsson, W., and R.D. Sharp, A comparison of the 0.1-17 keV/e ion composition in the near equatorial magnetosphere between quiet and disturbed conditions, *J. Geophys. Res.*, 87, 6109-6120, 1982.

Lennartsson, W., and E.G. Shelley, Survey of 0.1- to 16-keV/e plasma sheet ion composition, *J. Geophys. Res.*, 91, 3061-3076, 1986.

Lui, A.T.Y., Radial transport of storm time ring current ions, *J. Geophys. Res.*, 98, 209-214, 1993.

Lui, A.T.Y., R.W. McEntire, S.M. Krimigis, and E.P. Keath, Acceleration of energetic oxygen (E>137 keV) in the storm-time ring current, in *Ion Acceleration in the Magnetosphere*

and Ionosphere, *Geophys. Monogr. Ser.*, vol. 38, edited by T. Chang, pp. 149-152, AGU, Washington, D. C., 1986.

Lyons, L.R., and T.W. Speiser, Evidence for current sheet acceleration in the geomagnetic tail, *J. Geophys. Res.*, 87, 2276-2286, 1982.

Maynard, N.C., and A.J. Chen, Isolated cold plasma regions: Observations and their relation to possible production mechanisms, *J. Geophys. Res.*, 80, 1009-1013, 1975.

Möbius, E., M. Scholer, B. Klecker, D. Hovestadt, G. Gloeckler, and F.M. Ipavich, Acceleration of ions of ionospheric origin in the plasma sheet during substorm activity, in *Magnetotail Physics*, edited by A.T.Y. Lui, pp. 231-234, Johns Hopkins Univ. Press, Baltimore, Md., 1987.

Moore, T.E., Origins of magnetospheric plasma, *Rev. Geophys., Supplement*, 1039-1048, 1991.

Moore, T.E., W.K. Peterson, C.T. Russell, M.O. Chandler, M.R. Collier, H.L. Collin, P.D. Craven, R. Fitzenreiter, B.L. Giles, and C.J. Pollock, Ionospheric mass ejection in response to a CME, *Geophys. Res. Lett.*, 15, 2339-2342, 1999.

Moore, T.E., M.O. Chandler, M.-C. Fok, B.K. Giles, D.C. Delcourt, J.L. Horwitz, and C.J. Pollock, Ring currents and internal plasma sources, *Space Sci. Rev.*, 95, 555-568, 2001.

Nosé, M., A.T.Y. Lui, S. Ohtani, B.H. Mauk, R.W. McEntire, D.J. Williams, T. Mukai, and K. Yumoto, Acceleration of oxygen ions of ionospheric origin in the near-Earth magnetotail during substorms, *J. Geophys. Res.*, 105, 7669-7677, 2000.

Nosé, M., S. Ohtani, K. Takahashi, A.T.Y. Lui, R.W. McEntire, D.J. Williams, S.P. Christon, and K. Yumoto, Ion composition of the near-Earth plasma sheet in storm and quiet intervals: Geotail/EPIC measurements, *J. Geophys. Res.*, 106, 8391-8403, 2001.

Nosé, M., R.W. McEntire, and S.P. Christon, Change of the plasma sheet ion composition during magnetic storm development observed by the Geotail spacecraft, *J. Geophys. Res.*, 108(A5), 1201, doi:10.1029/ 2002JA009660, 2003.

O'Brien, T.P. and R.L. McPherron, An empirical phase space analysis of ring current dynamics: Solar wind control of injection and decay, *J. Geophys. Res.*, 105, 7707-7719, 2000.

Ohtani, S., *et al.*, Storm-time energetic O^+ flux variations in the ring current and the plasma sheet: A study of the April 2002 storm event, AGU 2003 Fall Meeting, San Francisco, 2003.

Peroomian, V., and M. Ashour-Abdalla, Population of the near-Earth magnetotail from the auroral zone, *J. Geophys. Res.*, 101, 15,387-15,401, 1996.

Peterson, W.K., R.D. Sharp, E.G. Shelley, R.G. Johnson, and H. Balsiger, Energetic ion composition of the plasma sheet, *J. Geophys. Res.*, 68, 761-767, 1981.

Roeder, J.L., J.F. Fennell, M.W. Chen, M. Schulz, M. Grande, and S. Livi, CRRES observations of the composition of the ring current ion populations, *Adv. Space Res.*, 17(10), 17-24, 1996.

Sánchez, E.R., B.H. Mauk, and C.-I. Meng, Adiabatic vs. non-ádiabatic particle distributions during convection surges, *Geophys. Res. Lett.*, 20, 177-180, 1993.

Sharp, R.D., W. Lennartsson, W., W.K. Peterson, and E.G. Shelley, The origin of the plasma in the distant plasma sheet, *J. Geophys. Res.*, 87, 10,420-10,424, 1982.

Sharp, R.D., W. Lwnnartsson, and R.J. Strangeway, The ionospheric contribution to the plasma environment in near-Earth space, *Radio Sci.*, 20, 456-462, 1985.

Speiser, T.W., Particle trajectories in model current sheets, 1, Analytical solutions, *J. Geophys. Res.*, 70, 4219-4226, 1965.

Stern, D.P., The motion of a proton in the equatorial magnetosphere, *J. Geophys. Res.*, 80, 595-599, 1975.

Temerin, M., and X. Li, A new model for the prediction of Dst on the basis of the solar wind, *J. Geophys. Res.*, 107(A12), 1472, doi:10.1029/ 2001JA007532, 2002.

Terasawa, T., *et al.*, Solar wind control of density and temperature in the near-Earth plasma sheet: WIND/GEOTAIL collaboration, *Geophys. Res. Lett.*, 24, 935-938, 1997.

Tsyganenko, N.A., A magnetospheric magnetic field model with a warped tail current sheet, *Planet. Space Sci.*, 37, 5-20, 1989.

Volland, H. A semiempirical model of large scale magnetospheric electric field, *J. Geophys. Res.*, 78, 171-180, 1973.

Williams, D.J., R.W. McEntire, C. Schlemm II, A.T.Y. Lui, G. Gloeckler, S.P. Christon, and F. Gliem, Geotail energetic particles and ion composition instrument, *J. Geomagn. Geoelectr.*, 46, 39-57, 1994.

Winglee, R.M., Multi-fluid simulations of the magnetosphere: The identification of the geopause and its variation with IMF, *Geophys. Res. Lett.*, 25, 4441-4444, 1998.

Young, D.T., H. Balsiger, and J. Geiss, Correlations of magnetospheric ion composition with geomagnetic and solar activity, *J. Geophys. Res.*, 87, 9077-9096, 1982.

S.P. Christon, Focused Analysis and Research, Columbia, MD 21044, USA.

R.W. McEntire, S. Ohtani, K. Takahashi, Applied Physics Laboratory, Johns Hopkins University, 11100 Johns Hopkins Road, Laurel, MD 20723-6099, USA.

M. Nosé, Data Analysis Center for Geomagnetism and Space Magnetism, Graduate School of Science, Kyoto University, Oiwake-cho, Kitashirakawa, Sakyo-ku, Kyoto 606-8502, Japan. (nose@kugi.kyoto-u.ac.jp)

Particle Acceleration in the Inner Magnetosphere

D.N. Baker, S.R. Elkington, and X. Li

Laboratory for Atmospheric and Space Physics, University of Colorado at Boulder, Boulder, CO

M.J. Wiltberger

High Altitude Observatory, National Center for Atmospheric Research, Boulder, CO

Particle acceleration is an important consequence of eruptive or catastrophic configuration changes in space plasmas. It is also a feature associated with more persistent structures, such as thin boundary layers, which exhibit strong gradients, instabilities, and turbulence. The most important acceleration regions in or near the magnetosphere are the bow shock, the magnetotail, the magnetopause, and the inner magnetosphere. The spatial and temporal properties of accelerated particles are the consequences of motion within the extant magnetic and electric fields. The characteristics of accelerated particles can provide insight into the underlying processes that shape the geomagnetic fields (for instance, magnetic reconnection). On the other hand, identifying the properties of the electric field combined with the magnetic field is a crucial complement to the study of the energetic particles themselves. The electric fields may be quasi-static, induced by magnetic field collapse, or the result of fluctuations related to plasma instabilities. The acceleration may produce suprathermal as well as very energetic particle populations. Highly energetic particles can be detrimental to satellite instrumentation and subsystems. The identification and modeling of acceleration mechanisms is therefore a crucial element in the prediction of energetic particle flux increases and the potential prevention of detrimental "space weather" effects. This review focuses on inner magnetospheric acceleration processes. We address several fundamental questions; (1) What are the main acceleration mechanisms?; (2) What are the particle source populations?; and (3) What determines the spatial and temporal characteristics of the energetic particles?

1. INTRODUCTION

The Earth's magnetosphere has often been likened to a cosmic plasma laboratory. In this relatively accessible volume (see a schematic portrayal in Figure 1), we find many of the most interesting plasma features from an astrophysical point of view: A collisionless shock wave; thin boundary regions (e.g., the magnetopause); auroral regions supporting magnetic field-aligned potential structures; and a strong, stable magnetic dipole field region. In all of these magnetospheric regions, there can be powerful acceleration of particles. The boxes in Figure 1 highlight the general areas where we see evidence of particular types of particle acceleration.

The inner magnetosphere is of special interest from an acceleration standpoint because this is the part of Earth's magnetosphere where particles tend to have the highest characteristic energy and where particles remain confined

The Inner Magnetosphere: Physics and Modeling
Geophysical Monograph Series 155

10.1029/155GM09

[redacted]

[redacted]

[redacted]

[redacted]

[redacted]

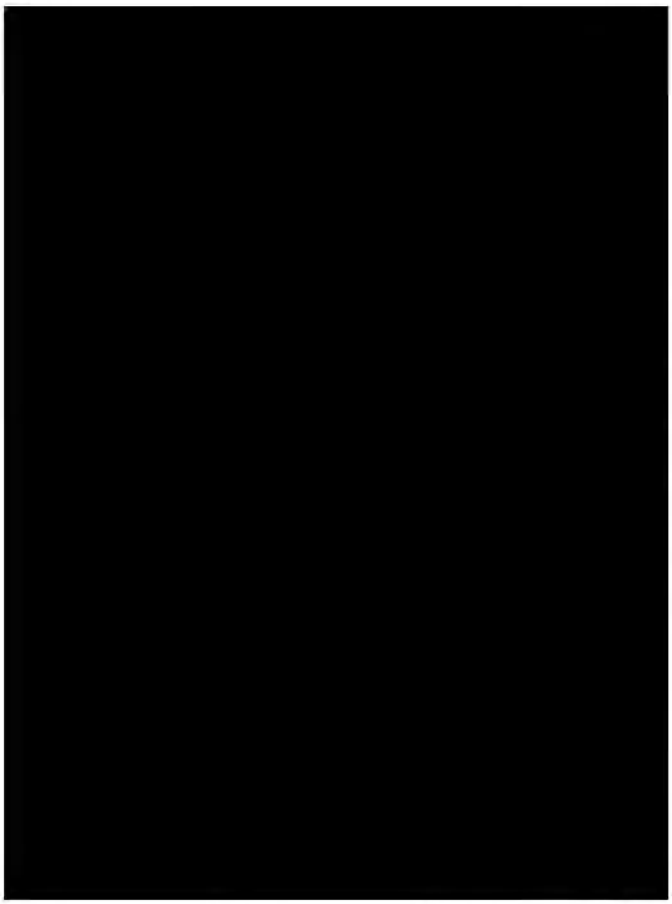

[redacted]

[redacted]

[redacted]

[redacted]

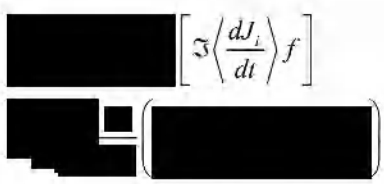

[redacted]

[redacted]

[redacted]

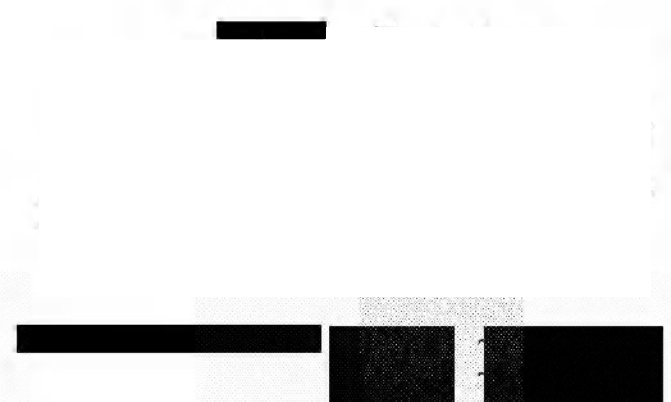

[redacted]

[redacted]

[redacted]

[redacted]

$$W = \frac{MB_0}{L^3} \tag{8}$$

[redacted]

[redacted]

[redacted]

[redacted]

[redacted]

[redacted]

[redacted]

$$\frac{dW}{dt} = q\mathbf{v}_D \cdot \mathbf{E} \qquad (9)$$

[redacted]

[redacted]

[redacted]

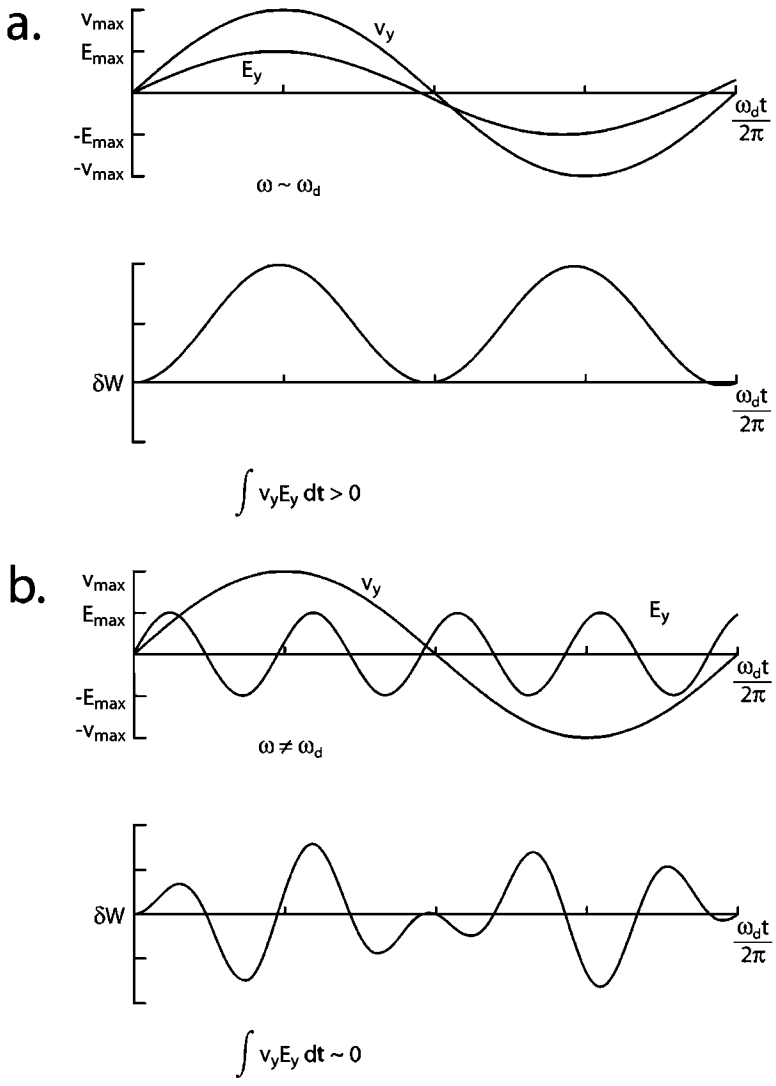

Figure 5. Energization of electron moving in a dipole magnetic field due to ULF waves. (a) For a slowing varying dawn-dusk potential field $E = E_0 \cos(m\phi - \omega t + \xi)$ where the electric field and drift velocity vary together, the particle gains or loses energy. (b) For higher frequency waves, the resonant condition is not met and little net energy gain results.

transport and inductive electric fields in the near-tail region [*Li et al.*, 2003a and references therein]. As suggested by many observations, however, another set of processes must accelerate the majority of electrons with $E > 500$ keV to produce the very 'hard' spectrum seen in the outer radiation belt proper [see Figure 5 of *Baker et al.*, 1998a].

Li et al. [1998; 2003a] have used numerical modeling methods to address the question of how energetic particles are injected from the Earth's magnetotail into the outer radiation belt (trapping) region. It is argued that a pulse is generated at substorm onset which then propagates from the near magnetotail into the inner magnetosphere. A time-varying pulse in the electric and magnetic fields is used to simulate the fields associated with the dipolarization that occurs at the substorm expansion phase onset.

In the work of *Li et al.* [2003a], a particularly well-observed substorm event was simulated. As shown in Figure 6a, there were several spacecraft at geostationary orbit on 27 August 2001 and there also were key spacecraft in the near magnetotail (POLAR and the four spacecraft Cluster constellation). A substorm onset was identified using ground and global auroral imaging methods: This was found to occur at 0409 UT on 27 August. *Li et al.* specified the electric field for the simulated injection as:

$$E = E_0(1 + \cos\phi)^p e^{-\xi^2} \tag{10}$$

where

$$\xi = \frac{r - r_i + v(r)(t - t_0)}{d} \tag{11}$$

Here $v(r)$ is the pulse velocity at a given radial distance, r, and d is the width of the pulse. The associated magnetic field pulse is calculated from

$$\frac{\partial \mathbf{B}}{\partial t} = -\nabla \mathbf{x} \mathbf{E} \tag{12}$$

The guiding center equations are used to express the drift velocity,

$$v_d = c\frac{\mathbf{E}x\mathbf{B}}{B^2} + \frac{M_r c}{\gamma e}\frac{\mathbf{B}x\nabla_\perp B}{B^2} \tag{13}$$

And the time rate of change of the particle energy,

$$\frac{dW}{dt} = -ev_d \cdot E + \frac{M_r}{\gamma}\frac{\partial B}{\partial t} \tag{14}$$

Using an assumed 'kappa' (maxwellian plus power law tail) energy distribution in the plasma sheet, *Li et al.* were able to closely replicate the timing and energy spectrum of substorm-injected electrons at geostationary orbit. This is shown for the 27 August case in Figure 6b. On the left side of Figure 6b are the observations from the three Los Alamos-instrumented spacecraft depicted in Figure 6a. The somewhat "dispersed" pulse of injected electrons was seen at all three spacecraft locations (for the energy range $105 \le E \le 315$ keV). On the right hand side of Figure 6b, we see the simulation results from *Li et al.* [2003a]. There is excellent spatial, temporal, and spectral correspondence between the simulation results and the observations. As shown by the nested elliptical contours in Figure 6a, *Li et al.* [2003a] inferred that the bulk of the injected particles in the 27 August 2001 case originated in a localized region at X~-9 R_E and in the premidnight sector. The initiation of the dipolarization should be farther out. It should be noted that both the model fields and initial particle distribution are adjusted to achieve the excellent agreement with observations. However, for this particular case (27 August 2001), there were multiple-point observations from several spacecraft, which put certain constraints on the model fields and the initial particle distribution [*Li et al.*, 2003a].

The highest energies of electrons produced in the outer radiation belt do not occur in one fell swoop associated with a single substorm event, or similar short-lived episode. Rather, the highly relativistic electrons tend to build up over a few hours to days following the passage of high-speed solar wind streams or coronal mass ejection (CME)-related magnetic clouds [see *Baker et al.*, 1997 and *Reeves et al.*, 1998]. A good example of the latter type of event is shown in Figure 7.

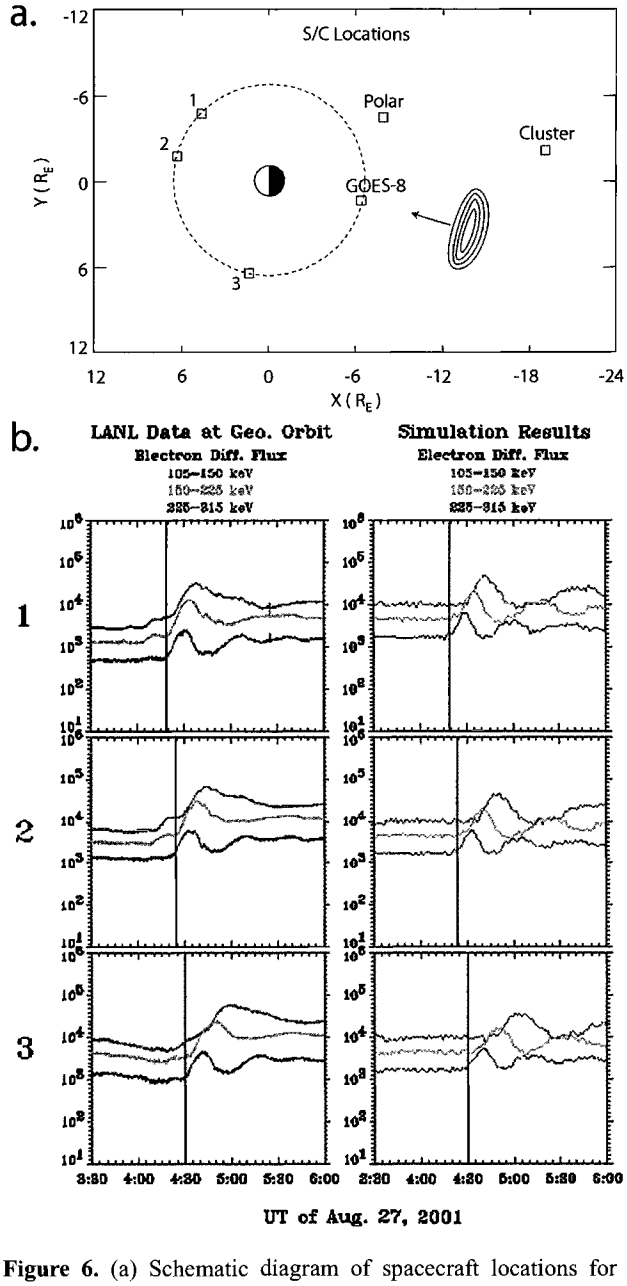

Figure 6. (a) Schematic diagram of spacecraft locations for 27 August 2001 substorm simulation event [*Li et al.*, 2003]. Spacecraft '1' is LANL-97A; spacecraft '2' is LANL 1994-084; spacecraft '3' is LANL 1991-080. (b) Observations (left side) and numerical simulation results (right side) for energetic electrons at geostationary orbit on 27 August 2001 [from *Li et al.*, 2003a].

[redacted]

[redacted]

[redacted]

3

[redacted]

[redacted]

ring of relativistic electrons (Plate 1c) around L~4.0 in the modeled system. This is closely consistent with the observations for this particular event [*Baker et al.*, 2002 and references therein].

It is possible (probable in fact) that other wave-particle interactions of the sort discussed by *Summers et al.* [1998] are acting during events such as the 31 March 2001 storm. Other papers in this volume [*Thorne et al.*; *Meredith et al.*; and *O'Brien et al.*] discuss many of these important acceleration (and loss) processes.

4. ION ACCELERATION IN THE INNER MAGNETOSPHERE

Up to several hundreds of keV kinetic energies, there is often a close analogy between the substorm-related acceleration of ions and that of electrons (as discussed in the last section). As an illustration of this, Figure 8 shows results for the 27 August 2001 substorm event taken from *Li et al.* [2003a].

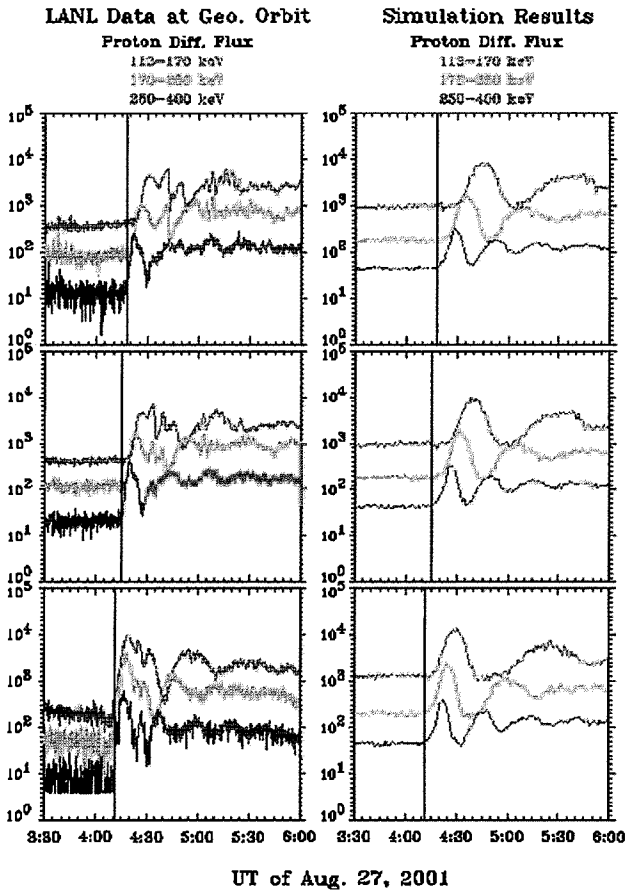

Figure 8. Similar to Fig. 6b for proton observations (left side) and simulation results (right side) during 27 August 2001 substorm [from *Li et al.*, 2003a].

As was shown for electrons in Figure 6b, the left-hand side of Figure 8 shows observations from three LANL-instrumented spacecraft at geostationary orbit.

The substorm expansion phase onset obviously produced a strong pulse of energetic (113 ~400 keV) protons which drifted in azimuth around the Earth. The proton pulses tended to show more spatial and temporal structure than the corresponding electron pulses (see Figure 6b). Using exactly the same model parameters for the ion injection model as was described (Section III) for the electron simulation, *Li et al.* [2003a] obtained the results shown on the right side of Figure 8. The basic timing, pulse amplitude, and dispersion characteristics for the proton simulation compare well with the observations. However, the simulation did not replicate all of the fine structure in the proton time profiles.

Based on simulations such as shown above, it is evident that substorms can inject ions of ring current energies into the inner magnetosphere. Given the 'drift-echo' nature of the pulses seen by sensors at geostationary orbit (Figures 6b and 8), it is also obvious that the energetic particles are drifting azimuthally on trapped orbits. Thus, discrete substorm events must be contributing to the source population of the ring current ions [see the comprehensive review by *Daglis*, 2001]. Yet, a long history of solar wind-ring current comparisons [e.g., *McPherron*, 1997; *McPherron et al.*, this volume] suggests that one can predict *Dst* development without taking detailed cognizance of individual substorm events. This rather paradoxical situation has been explored in previous papers as well [*Pulkkinen and Sharma*, 2000; *Baker*, 2000]. Several papers in this volume use modern observations from the POLAR, IMAGE, and Cluster spacecraft to address ring current dynamics and substorm relationships [e.g., *Vallat et al.*; *Soraas et al.*; and *Antonova*].

An intriguing issue relates to the highest energy ions that often appear in the inner magnetosphere during major geomagnetic storms. An extreme example of this occurred during the great geomagnetic storm of 24 March 1991. This case was modeled by *Hudson et al.* [1997]. Plate 2 shows the observed distribution of energetic ions before a powerful shock wave struck the Earth's magnetosphere (a) and afterward (b). The inductive electric field associated with the compression of the dayside magnetosphere by the shock wave substantially accelerated protons and electrons as well. This compression injected the protons deeply into the inner magnetosphere and increased the flux at tens of MeV energies by several orders of magnitude. This type of acceleration, therefore, corresponds to the notion that solar energetic particles provide a seed population and the shock wave impact produces the induction electric field necessary to accelerate rapidly the ions residing on higher L-shells. This shock-related acceleration is in considerable contrast to the more gradual acceleration of ions by radial diffusion

[e.g., *Spjeldvik*, 1996] which also occurs in the inner magnetosphere.

5. SPACE WEATHER ASPECTS OF INNER MAGNETOSPHERE ACCELERATION

As the presentation above has probably conveyed, the physics associated with particle acceleration in the inner magnetosphere is inherently interesting and it involves quite a wide range of processes. Thus, the intrinsic scientific program of understanding inner magnetospheric particle acceleration is important in the "cosmic laboratory" sense mentioned in the Introduction. However, it is also valuable to bear in mind that the near-Earth magnetosphere is the region in which many (in fact, most) operational and commercial spacecraft fly. Therefore, the particle environment in the inner magnetosphere is of much more than academic interest.

It is interesting to consider the degree to which we can use our physical understanding of particle acceleration in order to specify and forecast the "space weather" of the inner magnetosphere. In fact, there are good reasons to be optimistic that such forecasting can be accomplished both for relativistic electrons and for the energetic ions that constitute the ring current [see *Li et al.*, 2003b]. The work reported by *Li et al.* suggests that electron fluxes at geostationary orbit can be forecast with very high prediction efficiency (80-90%) and also that the *Dst* index can be predicted very well given a knowledge of the upstream solar wind and interplanetary magnetic field. In this sense, our scientific understanding may help society "cope" with some of the principal adverse effects of space weather [*Baker*, 2002].

Forecasts of hours to a day or two [*Li et al.*, 2003b] are important and useful. However, there is a longer term goal of providing even more substantial lead-time predictions. The Center for Integrated Space-Weather Modeling (CISM) is presently developing empirical and physics-based (forward) models that may allow several-day forecasts of radiation belt fluxes, key magnetic indices, and other important space weather parameters. Figure 9 shows schematically how we can use solar boundary measurements and solar wind propagation methods (such as the Wang-Sheeley-Arge kinematic propagation scheme) to give several day forecasts of solar wind mass densities (ρ), speed (V), and magnetic field properties (B). These solar-boundary derived values give a considerably longer lead time than the measurements from an $L1$-monitor such as ACE [*Baker et al.*, 2004].

6. SUMMARY

In this review we have shown examples of relatively rapid and quite powerful acceleration of energetic electrons and ions in the Earth's inner magnetosphere. A variety of physical processes, including radial transport and local wave-particle interactions, probably play key roles in the acceleration that is observed. The Fokker-Planck formalism (as reviewed here) provides a useful framework in which to consider transport, acceleration, and loss.

We have paid particular attention in this review to processes affecting inner magnetospheric electron populations. We have emphasized the key first step represented by magnetospheric substorms which regularly accelerate electrons to tens up to hundreds of keV in energy. These substorm electrons then act as a seed population for subsequent acceleration to several MeV in energy.

We have shown here a specific example of how a global MHD simulation of the solar wind-magnetosphere interaction during a major geomagnetic storm provides a self-consistent picture of electric and magnetic field variations both in space and time. "Particle tracing" within this MHD framework then reveals some of the interesting details of how the initial seed population of electrons gets accelerated to relativistic energies. It appears that ULF wave fluctuations play an important role in the modeled case.

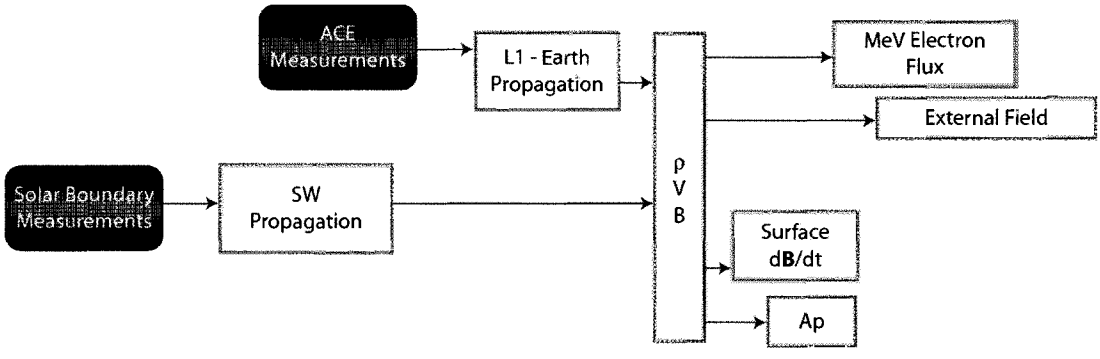

Figure 9. Sun-to-magnetosphere linked models being developed in the Center for Integrated Space Weather Modeling (CISM) [adapted from *Baker et al.*, 2004].

Finally, we noted that particles accelerated in the inner magnetosphere are very important and are of great concern from a space weather standpoint. It is expected that methods being developed today will allow several hour to several day forecasts with the kind of accuracy necessary to meet user requirements.

REFERENCES

Antonova, E., Magnetospheric substorms and the sources of inner magnetosphere particle acceleration, this volume.

Baker, D.N., The role of magnetospheric substorms in high-energy particle production within the Earth's magnetosphere, *Proc. 5th International Conference on Substorms*, 2000.

Baker, D.N., How to cope with space weather, *Science*, 297, 30 Aug 2002.

Baker, D.N., *et al.*, Highly relativistic electrons in the Earth's outer magnetosphere, I. Lifetimes and temporal history 1979-1984, *J. Geophys. Res.*, 91, 4265, 1986.

Baker, D.N., *et al.*, Relativistic electron acceleration and decay time scales in the inner and out radiation belts; SAMPEX, *Geophys. Res. Lett.*, 21, 409, 1994.

Baker, D.N., *et al.*, Recurrent geomagnetic storms and relativistic electron enhancements in the outer magnetosphere: ISTP coordinated measurements, *J. Geophys. Res.*, 102, A7, 14,141-14,148, 1997.

Baker, D.N., *et al.*, Strong electron acceleration in the Earth's magnetosphere, *Adv. Space Res.*, 21, 4, 609-613, 1998a.

Baker, D.N., *et al.*, A strong CME-related magnetic cloud interactions with the Earth's magnetosphere: ISTP observations of rapid relativistic electron acceleration on May 15, 1997, *Geophys. Res. Lett.*, 25, 15, 2975-2978, 1998b.

Baker, D.N., *et al.*, Disturbed space environment may have been related to pager satellite failure, *Eos Trans.* AGU, 79, 40, 477, 482-483, 1998c

Baker, D.N., *et al.*, A telescopic and microscopic view of a magnetospheric substorm on 31 March 2001, *Geophys. Res. Lett.*, 29, 18, 1862, doi: 10.1029/2001GL014401, 2002.

Baker, D.N., *et al.*, Sun-to-Magnetosphere modeling: CISM forecast model development using linked empirical methods, *J. Atmos. Solar Terr. Phys.*, submitted, 2004.

Daglis, I.A., The storm-time ring current, *Space Sci. Rev.*, 98, 343-363, 2001.

Elkington, S.R., *et al.*, Acceleration of relativistic electrons via drift-resonant interaction with toroidal-mode Pc-5 ULF oscillations, *Geophys. Res. Lett.*, 26, 3273, 1999.

Elkington, S.R., *et al.*, Resonant acceleration and diffusion of outer zone electrons in an asymmetric geomagnetic field, *J. Geophys. Res.*, 108, 1116, doi:10.1029/2001/JA009202, 2003.

Elkington, S.R., *et al.*, Injection of energetic ions during the 31 March 0630 substorm, this volume, 2004.

Fei, Y., *et al.*, Radial diffusion simulation of relativistic electron transport by ULF waves in the September 1998 storm, *J. Geophys. Res.*, in press, 2003.

Hudson, M.K., *et al.*, Simulations of radiation belt formation during storm sudden commencements, *J. Geophys. Res.*, 102, A7, 14,087-14,102, 1997.

Hudson, M.K., *et al.*, Simulation of radiation belt dynamics driven by solar wind variations, in Sun-Earth Plasma Connections, AGU *Geophys. Monogr.*, 109, 1999.

Li, X., and M.A. Temerin, The electron radiation belt, *Space Sci. Rev.*, 95, 569-580, 2001.

Li, X., *et al.*, Simulation of dispersionless injections and drift echoes of energetic electrons associated with substorms, *Geophys. Res. Lett.*, 25, 3763, 1998.

Li, X., *et al.*, Simulation of energetic particle injections associated with a substorm on August 27, 2001, *Geophys. Res. Lett.*, 30, 1, 1004, doi: 10.1029/2002GL015967, 2003a.

Li, X., *et al.*, The predictability of the magnetosphere and space weather, *Eos Trans.* AGU, 84, 37, 361-369-370, 2003b.

Liu, W.W., *et al.*, Internal acceleration of relativistic electrons by large-amplitude ULF pulsations, *J. Geophys. Res.*, 104, A8, 17,391-17,407, 1999.

Mathie, R.A., and I. R. Mann, A correlation between extended intervals of ULF wave power and storm-time geosynchronous relativistic electron flux enhancements, *Geophys. Res. Lett.*, 27, 3261, 2000.

Mathie, R.A., and I. R. Mann, Observations of Pc5 field line resonance azimuthal phase speeds: A diagnostic of their excitation mechanism, *J. Geophys. Res.*, 105, 10713, 2001.

McIlwain, C.E., Processes acting upon outer zone electrons, in Radiation Belts: Models and Standards, AGU *Geophys. Monogr.* 97, 1996.

McPherron, R.L., *et al.*, Forecasting the *Dst* index four days ahead, this volume

McPherron, R.L., in Magnetic Storms, AGU *Geophys. Monogr.*, 98, 131, 1997.

Meredith, N.P., *et al.*, Evidence for chorus-driven electron acceleration to relativistic energies from a survey of geomagnetically-disturbed periods, *J. Geophys. Res.*, 108, 1248, doi: 10.1029/2002JA009764, 2003.

Nakamura, R., *et al.*, Relationship between ULF waves and radiation belt electrons during the March 10, 1998, storm, *Adv. Space Res.*, 30, 10, 2163-2168, 2002.

O'Brien, T.P., Energization of relativistic electrons in the presence of ULF power and MeV microbursts; Evidence for dual ULF and VLF accelerations, this volume.

Obara, T., *et al.*, Energetic electron variation in the outer radiation zone during early May 1998 magnetic storm, *J. Atmos. Solar Terr. Phys.*, 62, 15, 1405-1412, 2000.

Pulkkinen, T.I., and A.S. Sharma, Summary of session 5: Storm-substorm relationship, *Proc. 5th International Conference on Substorms*, 2000.

Reeves, G.D., *et al.*, The global response of relativistic radiation belt electrons to the January 1997 magnetic cloud, *Geophys. Res., Lett.*, 25, 17, 3265-3268, 1998.

Roederer, J.G., *Dynamics of geomagnetically trapped radiation*, Springer, Heidelberg, 1970.

Rostoker, G.S., *et al.*, On the origin of relativistic electrons in the magnetosphere, *Geophys. Res. Lett.*, 25, 3701-3704, 1998.

Schulz, M., Canonical coordinates for radiation-belt modeling, in Radiation Belts: Models and Standards, AGU *Geophys. Monogr.* 97, 1996.

Schulz, M. and L.J. Lanzerotti, *Particle diffusion in the radiation belts*, Springer, Heidelberg, 1974.

Soraas, F., *et al.*, Ring current dynamics and local time behavior estimated from low-altitude proton observations, this volume.

Spjeldvik, W.N., Cross field entry of high charge state energetic heavy ions into the Earth's magnetosphere, in Radiation Belts: Models and Standards, AGU *Geophys. Monogr.* 97, 1996.

Summers, D., *et al.*, Relativistic theory of wave-particle resonant diffusion with application to electron acceleration in the magnetosphere, *J. Geophys. Res.*, 103, 20,487, 1998.

Thorne, R.M., R. Horne, N. Meredith, and Y. Shprits, Relativistic electron acceleration and loss during geomagnetic storms, this volume.

Tverskaya, L.V., *et al.*, Storm-time formation of a relativistic electron belt and some relevant phenomena in other magnetospheric plasma domains, *Adv. Space Res.*, in press, 2003.

Vallat, C., *et al.*, Ring current structure and dynamics: Local measurements (CLUSTER/CIS and FGM) and global observations (IMAGE/HENA), this volume.

Vassiliadis, D., *et al.*, Long-term-average, solar cycle, and seasonal response of magnetospheric energetic electrons to the solar wind speed, *J. Geophys. Res.*, 107, 1383, doi: 10.1029/2001JA000506, 2002.

Wiltberger, M.J., *et al.*, Comparison of Magnetohydrodynamic simulations of isolated substorms and those during magnetic storms, this volume.

Daniel Baker, LASP/Univ. of Colorado, 1234 Innovation Drive, Boulder, CO 80303-7814.

Scot Elkington, LASP/Univ. of Colorado, 1234 Innovation Drive, Boulder, CO 80303-7814.

Xinlin Li, LASP/Univ. of Colorado, 1234 Innovation Drive, Boulder, CO 80303-7814.

Michael Wiltberger, NCAR/HAO, 3450 Mitchell Lane, Boulder, CO 80301.

The Energetic Electron Response to Magnetic Storms: HEO Satellite Observations

J.F. Fennell and J.B. Blake

The Aerospace Corporation, Los Angeles, California

R. Friedel

Los Alamos National Laboratory, Los Alamos, New Mexico

S. Kanekal[1]

Catholic University, Washington, District of Columbia

Energetic electron observations from the HEO 97-068 satellite are used to study the electron response to magnetic storms in the inner magnetosphere during 1998-2002. The observations cover L values in the range $2.5 \leq L \leq 6$. The same L values are covered at both high (>2.3 Re) and low (<1.2 Re) geocentric altitudes. The electron flux histories at low and high altitudes are directly compared and are found to track with a high degree of fidelity independent of flux levels and energy for a wide range of L values. The low altitude >1.5 MeV electron fluxes were ~10-16% of the high altitude fluxes for L = 3 - 5.5, except during the rapid post-storm flux rises. The decay of the post storm electron fluxes were examined to obtain the e-folding decay times at L = 3, near the peak of the outer zone. The high-altitude >1.5 MeV electron fluxes were found to have three distinct 1/e decay times of about 5, 10.5, and 17.5 days. The 5 and 10.5 day e-folding times occurred in the first several days after the post-storm fluxes peaked during 2000-2001 and 1998 periods respectively. The longer e-folding times occurred late in the decay history. These results support the view that the acceleration and loss mechanisms are operating essentially simultaneously over much of the outer zone.

INTRODUCTION

Blake et al. [1997] used orbit integrated HEO dose data to infer that the combination of a high speed solar wind stream (HSS) in conjunction with a southward turning of the interplanetary magnetic field (IMF) was key to enhancement in the radiation belt fluxes. They used isolated HSS events in their study to simplify the relationships. They showed that a northward IMF turning negated the HSS and that losses can occur without subsequent flux enhancements. Recent work by *Kanekal et al.* [2001; 1999] has shown that low altitude

[1] Currently at: LASP, University of Colorado, Boulder, Colorado

The Inner Magnetosphere: Physics and Modeling
Geophysical Monograph Series 155

10.1029/155GM10

polar orbiting satellites such as SAMPEX can readily track the responses of the electron radiation to magnetic storms in the inner magnetosphere and that the high altitude and low altitude fluxes track each other closely. *Kanekal et al.* [2001] used Polar, HEO and SAMPEX satellite data to show that the fluxes measured at high and low altitudes tracked well most of the time. They used superposed epoch analyses to show that the delays between flux changes at Polar and SAMPEX were consistent with zero lag. The daily HEO dose at two energies (>1.5 and 3.5 MeV) and fluxes from the SAMPEX 2-6 MeV channel were integrated over the $2.5 \leq L \leq 6.5$ for comparison. While that comparison showed a strong similarity in time history at both HEO and SAMPEX, the different instrument energy responses did not allow for as detailed an intercomparison as was done for the Polar and SAMPEX data. Thus, no previous analyses have compared high and low altitude fluxes using the same set of instrumentation. That is one of the main features of the present paper.

INSTRUMENTATION AND DATA

This study uses data taken by a high Earth orbiting, HEO, satellite in a $\sim 1.15 \times 7.2$ R_E orbit inclined at ~63° with a ~12 hour period. The satellite is designated HEO 1997-086 (or HEO3). HEO3 covers a wide range of L values at both mid to high altitudes and at low altitude. The perigee of HEO3 varied between 1.18 and 1.33 Re geocentric (see Figure 2) during the 1998-2002 period.

The data were obtained using five integral energy sensors that measured electrons with energies >0.23, >0.45, >0.6, >1.5 and >2.9 MeV. The four highest energy sensors make omnidirectional flux measurements. The >0.23 MeV electron data are from a proton-electron telescope with a ~15° conical field of view [*Blake et al.*, 1997]. For much of this study we emphasize the results from the >1.5 MeV electrons because most of the recent results in the literature, concerning electron acceleration and transport in the inner magnetosphere, have emphasized MeV electrons.

We focus on electron data taken during the 1998-2002 period for this report. This includes most of the stormtime events that were highlighted during the Physics and Modeling of the Inner Magnetosphere conference held in Helsinki, Finland. We examine the energetic electron storm responses from two perspectives: (1) the tracking of high and low altitude electron fluxes using the same instrumentation and (2) the post storm decay of the fluxes at L = 3, inside the nominal plasmasphere.

OBSERVATIONS

First, we examine the flux variability taken at high altitudes (>2.5 Re geocentric) for several L values. The top panels in Plate 1 show the daily average >1.5 MeV electron flux history during the April 1998 through March 1999 period at L = 2.5-4. The bottom panel shows a line plot of the estimated minimum daily plasmapause position [*O'Brien and Moldwin*, 2003]. Superimposed on the line plot are colored bars indicating where electron precipitation microbursts [*Lorentzen et al.*, 2001a and 2001b; *O'Brien et al.*, 2003] were observed at $L \leq 4$ (red bars) and $L \geq 4$ (blue bars).

The data in Plate 1 are plotted as line plots instead of in L versus Time spectrogram form so that differences from one L value to the next clearly stand out. Plate 1 shows that the electron fluxes are most variable at large L values with sharp sudden flux drops for short intervals of time. This variability is even greater for $L > 4$ (not shown). The sharp flux drops correspond with periods of magnetic activity, in many cases storm related.

At the lowest L values, one observes sudden electron flux enhancements followed by decay. At L = 2.5 the flux enhancements rise out of the instrument background and are observed only for the storms labeled by the months in which they occurred. At L = 4 there is a series of flux enhancements, most of which are preceded by sharp flux drops as noted above. At the bottom of the panels for each L, we have indicated the occurrence of precipitation microbursts, observed by SAMPEX, as red marks. The thickness of the red marks represents the duration of microburst occurrence for $L \leq 4$. There is a strong association of the flux dropouts and subsequent rapid increases with the appearance of the microbursts. All microbursts caused a flux decrease but not all such decreases were followed by flux enhancements. It is clear that combining such data from SAMPEX, at low altitude, with the HEO data, at high altitude, highlights features of the electron acceleration and loss processes that cannot be garnered from either data set in isolation. These and other microburst associations are discussed, in detail, in a paper by *O'Brien et al.* [2003] and will not be expanded upon here.

Only the strongest storms caused flux enhancements in the electron slot region ($2 < L < 3$). Storms that caused slot region fillings are also associated with strong erosion of the plasmasphere, as shown at the bottom of Plate 1. Each time Dst was <–150 (not shown) and the plasmapause was estimated to be below L = 3, the electron fluxes in the slot showed an increase. This indicates that erosion of the plasmapause to low L is one process that occurs simultaneous with electrons being transported to or accelerated at equally low L. It is not clear from the observations in Plate 1 whether the erosion of the plasmapause is a necessary condition for all low-L electron flux enhancements. Shock acceleration of the type that occurred during the famous March 1991 event [*Li et al.*, 1993; *Blake et al.*, 1992] may occur without plasmapause erosion. However, the relationship between plasmapause erosion and low L electron enhancements needs to be examined in detail.

The IMAGE FUV measurements combined with HEO and SAMPEX data could be used to perform such a study.

High/Low Altitude Flux Comparisons

This preliminary study takes advantage of the fact that the same sensors measure electron fluxes at both high and low altitudes at the same L values because of the highly elliptical orbit of HEO3. This allows us to compare the electron fluxes at different altitudes without worrying about whether the sensor responses are the same.

To show the relationship between the high altitude and low altitude electron fluxes, we first look to Plate 2 where the time history of low (red) and high (black) altitude Ee > 1.5 MeV electron intensities at L = 3 are shown for the 1998-2002 period. This plot shows that the electron fluxes varied over several orders of magnitude at both high and low altitudes and that the fluxes at the two altitudes appear to track very well.

This tracking of the high and low altitude fluxes is further demonstrated in Figure 1, which shows the ratio of the low altitude to high altitude fluxes for multiple L values. Several features are evident in Figure 1. The most striking feature occurs at the highest L values where an annual variation is observed in the ratio. The annual variation results from the fact that we used the IGRF field model for this initial study and it does not contain the day-night asymmetries of the real field that are most prominent at large L, high latitudes and large distances from Earth. The HEO3 database we are using already has all the data in B-L coordinates based on the IGRF and was considered sufficient for this initial low-high altitude comparison. More complicated field models could be used in the future, if warranted. However, no field model does a good job of representing the real field asymmetries at HEO altitudes and latitudes, especially during magnetic storms. The best of the models are compute intensive and not easily applicable to large data sets like the HEO data sets. We have tried the Olson-Pfitzer [*Olson et al.*, 1979], T87 and T96 [*Tsyganenko*, 1996a; 1996b] models for limited periods and found that these models often predicted that HEO3 was on open field lines when the data clearly indicated it was not and vice versa, especially during disturbed periods.

In any case, the peaks in the ratio at large L at the same season from year to year indicates the constancy of the low/high altitude flux ratio. Figure 1 shows that at L ≤ 4.5, the flux ratios are relatively constant independent of the variation in flux levels seen in Plates 1 and 2. The smallest L values show a general rise in the flux ratio from 1998 to 2001 and a decline after that. This variation resulted from the changing perigee altitude of HEO3 with time, as shown in Figure 2. This change in the altitude of the low altitude flux measurement has a greater effect at small L values than large

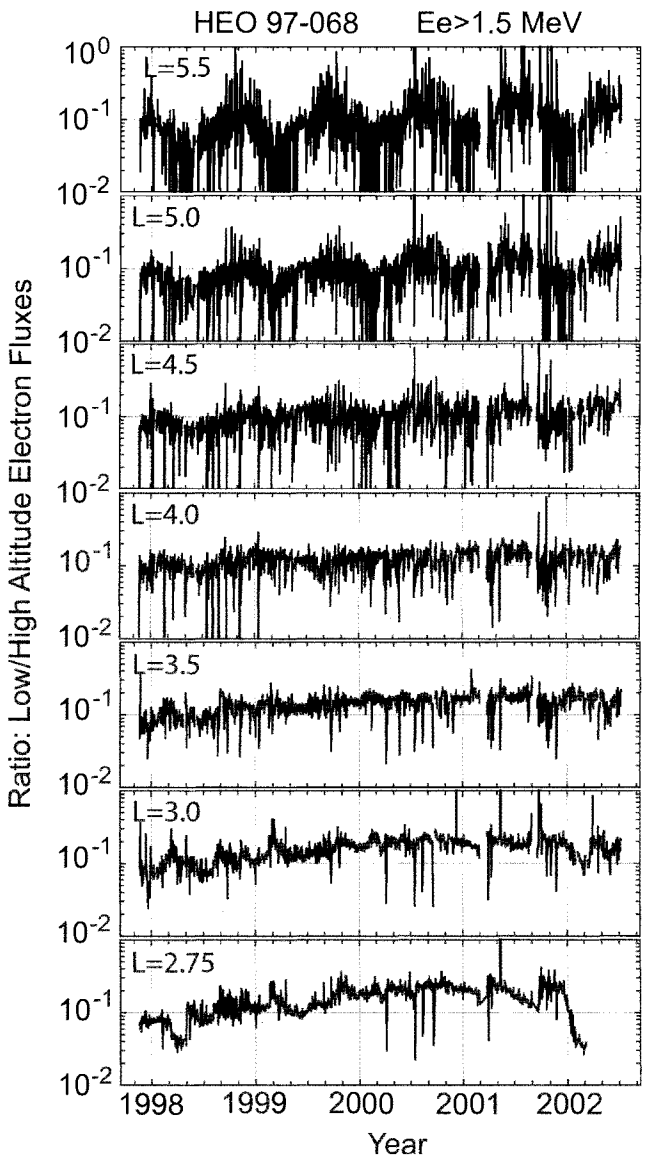

Figure 1. Ratio of four years of low to high altitude Ee > 1.5 MeV electron fluxes from HEO 97-068 for several different L values.

ones because the resultant ratio B_{low}/B_{high} changes most dramatically for the smallest L's.

The other major feature observed in Figure 1 are sharp, short duration decreases in the ratios. These decreases mostly occur at the time of large flux increases. They are consistent with the high altitude fluxes increasing faster than those at low altitudes at the same L. Figure 3 shows an expanded example of one of these downward ratio spikes from the flux increase that occurred in conjunction with a magnetic storm on Sept. 22, 1999. The plot shows that the short-term decrease in the ratio was associated with the difference in the rate of flux increase (here at L = 3) at low and high altitudes.

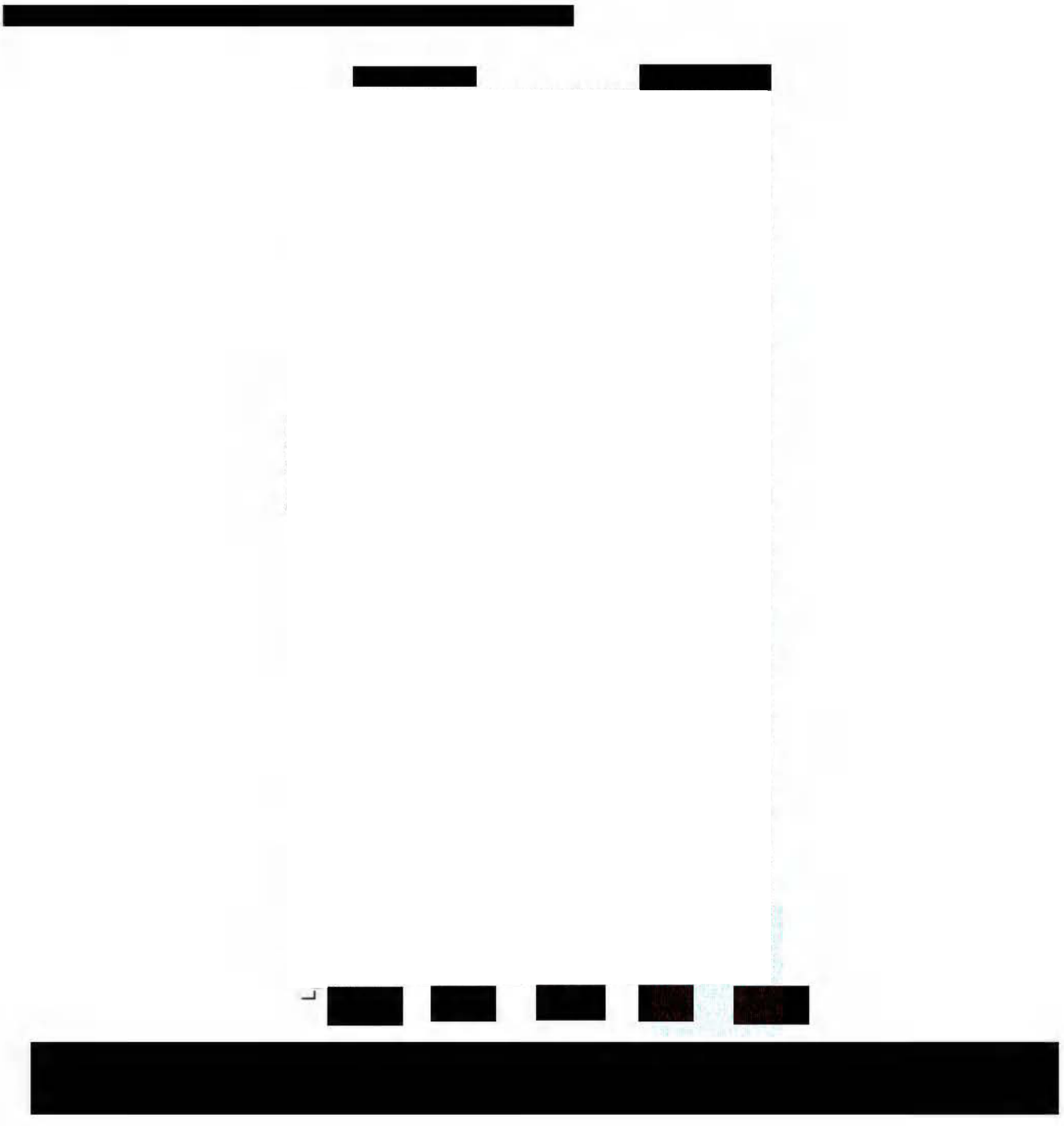

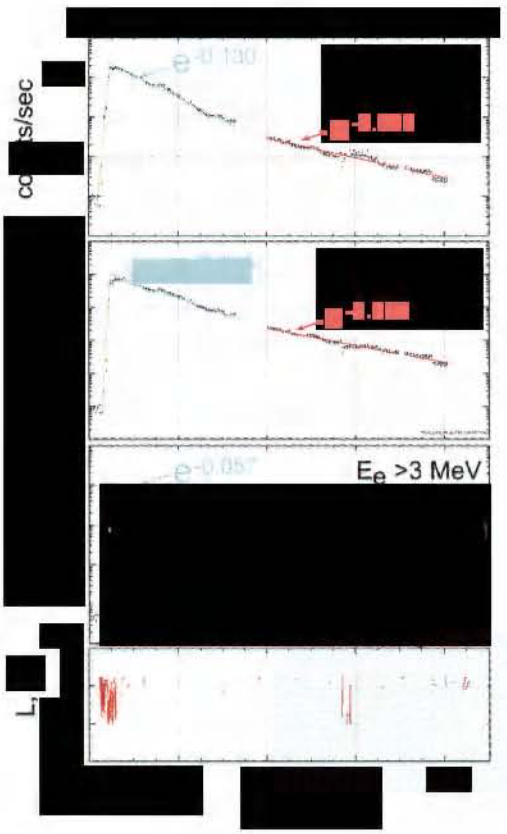
E_e >3 MeV

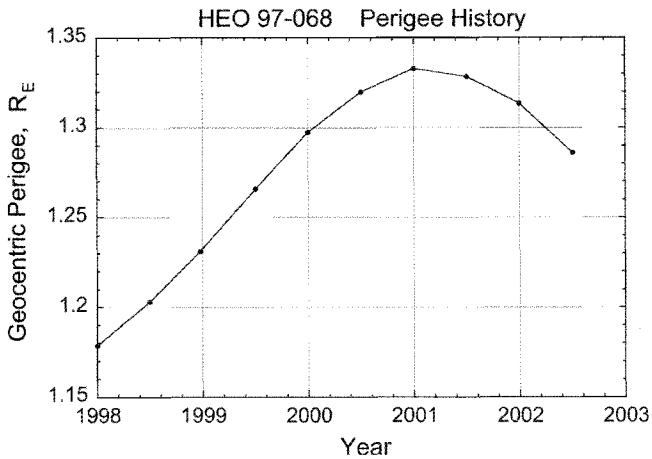

Figure 2. HEO 97-068 perigee altitude history.

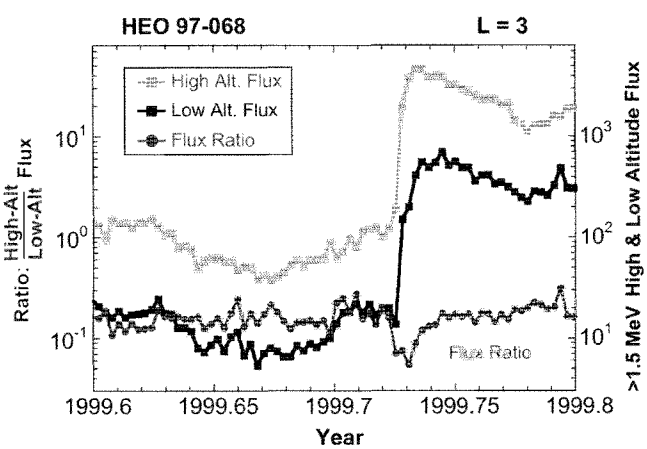

Figure 3. Comparison of low and high altitude HEO3 fluxes and their ratio at L = 3 for the interval around the 22 Sept. 1999 magnetic storm.

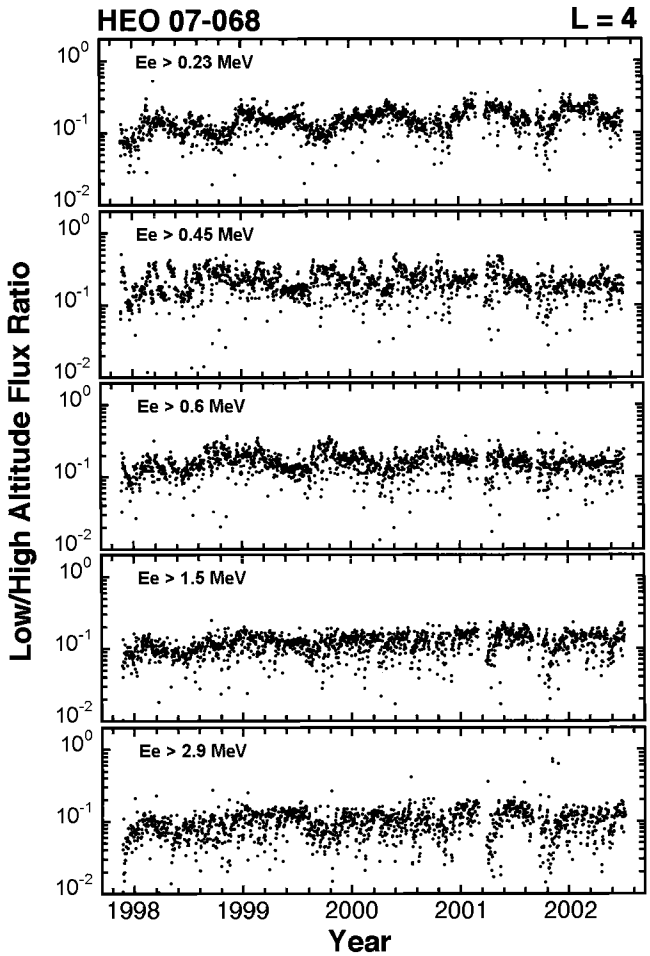

Figure 4. Ratio of four years of low to high altitude electron fluxes from HEO 97-068 L = 4 for several energies.

The ratio returned to its nominal pre-storm value as the fluxes reached their maximum values and started to decay.

Figure 4 shows that the low/high altitude flux ratios at L = 4 are relatively constant for electrons with energies from >0.23 to >2.9 MeV. This is also true for other L values (not shown). Figure 4 indicates that the processes that maintain these low/high altitude electron flux ratios are not strongly energy dependent at least over the energy range measured.

Table 1 shows the statistics for the distributions of >1.5 MeV flux ratios at six different L values. The statistics were obtained from the data shown in Figure 1. The plots of the distributions (not shown) had relatively narrow peaks and the majority were symmetric about the mean. This is evidenced by the fact that the mean and median values are nearly the same. As the table shows, the mean of the low/high altitude flux ratios were in range 0.09 to 0.16 for L = 3-5.5, with the ratio decreasing with increasing L. Thus, the high altitude fluxes were roughly a factor of 6 to 11 higher than those at low altitude.

Plates 1 and 2, Figure 1 and Table 1 emphasize the fact that, independent of the absolute flux levels, the magnetospheric processes that redistribute electrons radially and along the field lines do so efficiently and globally except for short

Table 1. Statistics for Low/High Altitude Flux Ratios.

L	No. Points	Mean	Median	Std. Dev.
3.0	1555	0.159	0.162	0.053
3.5	1559	0.140	0.143	0.043
4.0	1559	0.120	0.121	0.040
4.5	1502	0.100	0.099	0.041
5.0	1507	0.091	0.085	0.049
5.5	1494	0.096	0.082	0.069

intervals during the episodic rapid flux increases associated with magnetic storms (as shown in Figure 3).

Electron Decays at L = 3

At the lower L values, where flux dropouts are rare, the losses are thought to be controlled by coulomb losses (dE/dx losses) and pitch angle scattering of the electrons by interactions with the plasmaspheric Hiss. As Plate 1 shows, the plasma sphere boundary rarely reached L = 3 and then only during storm main and early recovery phases. Thus, we expect the loss rates at L ≤ 3 to be consistent. With this in mind, we examined the electron decay rates at L = 3 to see how they may relate to the near constancy of the low/high altitude flux ratios noted above. Plate 3 sets the stage for this part of the study. It shows the flux rise and subsequent decay following the May 1998 magnetic storm. This storm had a minimum D_{ST} of −205 nT. Plate 3 also shows where SAMPEX observed precipitation microbursts. The microbursts were intense and occurred primarily just before and during the post storm flux increases at all energies.

An exponential fit to the flux decay was done for each energy shown in Plate 3. The Ee >0.6 and >1.5 MeV data could not be fit with a single e-folding value over the full period shown so the period beyond day 40 (9 June 1998) was fit separately. This change in the decay rate late in the decay period is a common feature in the HEO3 data.

Plate 3 is an example of the way L = 3 electron decay data was gathered for the >1.5 MeV electron fluxes for events that occurred between 1 January 1998 and 1 July 2001. Twenty clear electron flux enhancements occurred at L = 3 during this period, as shown in Plate 4. The intervals from a few days after the flux peaked to the next enhancement were piecewise fit to represent the decay history. In Plate 4, the early part of the decay is flagged in blue and the later part in red and/or green where a single fit could not represent the decay. There were intervals where magnetic activity caused sudden drops in the electron flux. These were usually followed by a continuation of the decay with 1/e times somewhat longer than the early decays. These are flagged in red or green and treated as late decay intervals.

The e-folding decay times derived from Plate 4 are plotted in histogram form in Figure 5. The set of e-folding times clustered around three distinct periods: 5, 10.5 and 17.5 days. The error bars are based on a multi-variant error analysis [*Evans et al.*, 2000]. The mean 1/e decay time for all intervals was ~14 days. The enhanced electron fluxes caused by the large storms in May, Sept., Oct. and Nov. 1998 had early 1/e decay periods of 9.5-10.5 days which is very similar to the results obtained with SAMPEX by *Baker et al.* [1994] and consistent with past theoretical modeling [*Lyons and Thorne*, 1973]. The shortest early 1/e decay periods of ~5 days occurred following the flux enhancements in 2000 and 2001. All the secondary or late decay intervals had decay periods longer than the early decays and were more variable. These contributed to the broad peak near 17.5 days in Figure 5.

DISCUSSION

The low/high altitude flux ratio results obtained using the HEO3 data complement and reinforce the results obtained by *Kanekal et al* [1999, 2001] using SAMPEX and Polar data. The fact that the HEO3 ratios were obtained with a single set of instrumentation removes all doubt that the close tracking of the fluxes at low and high altitudes are real. With the HEO3 data, we have shown that the fluxes at the different altitudes are related by a nearly constant multiplier independent of energy and L over a significant range of L values. This means that low altitude satellites could be used to monitor the electron radiation belt fluxes at high altitudes, even near the equator, with a reasonable degree of accuracy. One only needs to determine the scaling factors (i.e. flux rations) between the flux measured at the magnetic equator and at a low altitude platform. Then the observations obtained by a low altitude platform, with its high repeat rate for traversals through a wide range of L values, could be used to represent the time dependent state of the radiation belts. We would suggest that such a platform be somewhat higher than SAMPEX, which spends significant time in both the drift and bounce loss regions. However, it need not be much higher. One to two thousand kilometer altitude circular polar would be a reasonable orbit.

These results show that the processes transporting relativistic electrons from near the equator to low altitudes do so in a manner that keeps the low/high altitude flux ratios constant on time scales of the order of one to a few days, even during periods of extreme flux changes. What we cannot tell from the current study is how these processes work to maintain the flux ratios. Part of the answer lies in the flux decays. The decay times indicate that combined transport and loss process along the field lines matches expectations for wave-particle interaction models of the type discussed by *Lyons and Thorne* [1973] *and Abel and Thorne* [1998]. The processes are primarily ones of pitch angle transport, coulomb drag (energy transport) and atmospheric losses in competition with radial transport. Inside the plasmasphere, we expected the decay rates to be relatively constant. The difference between the initial decay rates in 1998-1999 and those in 2000-2001 may be caused by different levels of average magnetic activity and Hiss production for those periods. This will be examined in a later paper.

Determining exactly how these processes combine to maintain the flux ratios will be a great challenge and will require a set of well designed missions that make the appropriate

[redacted]

[redacted]

[redacted]

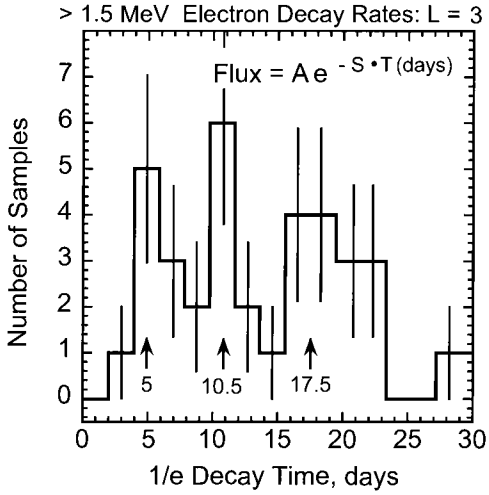

Figure 5. Histogram of e-folding decay times, in days, for the data in Plate 4.

measurements over a range of equatorial L values, at least L = 2.0-6, simultaneous with measurements of electron precipitation at ionospheric altitudes. Hopefully, those missions are the NASA LWS Geospace Storms Investigations [*Kintner et al.*, 2002].

Acknowledgments. The work at Aerospace was supported by NASA LWS grant NAG5-10972 and The Aerospace Corporation MOIE program (via U.S. Air Force under Contract No. FA8802-04-C-0001). The work at Los Alamos was supported by NASA LWS grant W-19957 and DOE OBES. The work at Catholic University was supported by NASA analysis funding for SAMPEX and Polar Ceppad Global Geospace investigations. JFF thanks T. P. O'Brien, J. Roeder and K. Lorentzen for useful discussions.

REFERENCES

Abel, R.W. and R.M. Thorne, Electron scattering loss in Earth's inner magnetosphere, 1: Dominant physical processes, *J. Geophys. Res.*, 103, 2385, 1998.

Baker, D., J. Blake, L. Callis, J. Cummings, D. Hovestadt, S. Kanekal, B. Klecker, R. Mewaldt, and R. Zwickl, Relativistic electron acceleration and decay time scales in the inner and outer radiation Belts: SAMPEX, *Geophys. Res. Lett.*, 21, 409, 1994.

Blake, J.B., D.N. Baker, N. Turner, K.W. Ogilvie, and R. Lepping, Correlation of changes in the outer-zone relativistic-electron population with upstream solar wind and magnetic field measurements, *Geophys. Res. Lett.*, 24, 927, 1997.

Blake, J.B., W. Kolasinski, R. Fillius, and E. Mullen, Injection of electrons and protons with energies of tens of MeV into L < 3 on 24 March 1991, *Geophys. Res. Lett*, 19, 821, 1992.

Evans, M., N. Hastings, and B. Peacock, *Statistical Distributions*, 3rd Ed., John Wiley and Sons, Inc., New York, N.Y., 2000.

Kanekal, S., D. Baker, and J. Blake, Multisatellite measurements of relativistic electrons: Global coherence, *J. Geophys. Res.*, 106, 29721, 2001 (2001JA000070).

Kanekal, S., D. Baker, J. Blake, B. Klecker, R. Mewaldt, and G. Mason, Magnetospheric response to magnetic cloud (coronal mass ejection) events: Relativistic electron observations from SAMPEX and Polar, *J. Geophys. Res*, 104, 24885, 1999 (1999JA900239).

Kintner, *et al.*, The LWS Geospace Storm Investigations: Exploring the Extremes of Space Weather, NASA/TM-2002-211613.

Li, X., I. Roth, M. Temerin, J. Wygant, M.K. Hudson, and J.B. Blake, Simulation of the prompt energization and transport of radiation particles during the March 23, 1991 SSC, *Geophys. Res. Lett.*, 20, 2423, 1993.

Lorentzen, K.R., J.B. Blake, U.S. Inan, and J Bortnik, Observations of relativistic electron microbursts in association with VLF chorus, *J. Geophys. Res*, 106, 6017, 2001a (2000JA003018).

Lorentzen, K.R., M.D. Looper, and J.B. Blake, Relativistic electron microbursts during the GEM storms, *Geophys. Res. Lett.*, 28, 2573, 2001b (2001GL012926).

Lyons, L.R. and R.M. Thorne, equilibrium structure of radiation belt electrons, *J. Geophys. Res*, 78, 2142, 1973.

O'Brien, T.P., M.B. Moldwin, Empirical plasmapause models from magnetic indices, *Geophys. Res. Lett.*, 30, 1152, 2003.

O'Brien, T.P., K.R. Lorentzen, I.R. Mann, N.P. Meredith, J.B. Blake, J.F. Fennell, M.D. Looper, D.K. Milling, and R.R. Anderson, Energization of relativistic electrons in the presence of ULF power and MeV microbursts: Evidence for dual ULF and VLF acceleration, *J. Geophys. Res.*, 108, 1329, 2003.

Olson, W.P., K.A. Pfitzer, and G.J. Mroz, Modeling the magnetospheric magnetic field, in *Quantitative Modeling of Magnetospheric Processes*, W. P. Olson ed., Am. Geophysical Union, 77, 1979.

Tsyganenko, N.A., Quantitative models of the magnetospheric magnetic field: Methods and results, *Space Sci. rev.*, 54, 1 1996.

Tsyganenko, N.A., Effects of the solar wind conditions on the global magnetospheric configuration as deduced from data-based field models, *Eur. Space Agency Spec. Publ., ESA SP-389*, 181, 1996.

J.F. Fennell, The Aerospace Corp., MS: M2-259, P. O. Box 92957, Los Angeles, CA, 90009-2957

J.B. Blake, The Aerospace Corp., MS: M2-259, P. O. Box 92957, Los Angeles, CA, 90009-2957

R.H.W. Friedel, Los Alamos National Laboratory, Los Alamos, NM 87545

S. Kanekal, Catholic University, Washington D. C. 20064

Global View of Energetic Particles During a Major Magnetic Storm

Timo Asikainen[1], Kalevi Mursula[1], Raine Kerttula[1], Reiner Friedel[2], Daniel Baker[3], Finn Søraas[4], Joseph F. Fennell[5] and J. Bernard Blake[5]

We study the global properties of energetic particles during the main and early recovery phase of a major magnetic storm of March 31, 2001, using data of the NOAA-15 and 16 and the CLUSTER satellites. During the storm main phase the ring current energetic electron and ion fluxes were increased by nearly two orders of magnitude, and the flux maxima were shifted to below $L = 3$. The maximum ion fluxes were observed at about 04-07 UT, coinciding with the strongly decreasing *Dst* and maximum Kp. At this time the ring current was dominated by oxygen ions. However, the highest fluxes of energetic electrons were observed at considerably higher L shells and only at about 16-18 UT, in a good correlation with the maximum of the AE index. These observations indicate significant differences in the acceleration of energetic electrons and ions during the storm. We suggest that at least the low energy ring current ion flux maximum at about 04-06 UT is mainly due to the field-aligned acceleration of escaping ionospheric oxygen ions by electromagnetic ion cyclotron waves, whereas the electron maximum at 16-18 UT is due to a large injection from the nightside.

1. INTRODUCTION

During a geomagnetic storm the inflow of solar wind energy into the magnetosphere is significantly enhanced. This is reflected by an intensified ring current (RC) particularly at $L < 4$ [*Smith and Hoffman,* 1973; *Hamilton et al.,* 1988]. The location of the RC energy density maximum is correlated with storm intensity. For a moderate storm with a minimum $Dst = -120$ nT the energy density maximum was found at $L = 3.5$ [*Korth* and *Friedel*, 1997] but for a great storm with a minimum $Dst = -300$ nT it was at $L = 2.5$ [*Hamilton et al.*, 1988]. Also the RC ion content has been found to correlate with storm intensity so that the stronger the storm is, the higher is the ionospheric oxygen contribution to RC. During the main phase of major magnetic storms the oxygen ions can even be the main ion constituent in the ring current [*Hamilton et al.*, 1988; *Daglis,* 1997].

In this paper we will analyse both electron and proton dynamics during the great storm of March 31, 2001, and show that they depict a surprisingly different behaviour during this storm.

2. INSTRUMENTATION

In this study we use particle data from Cluster and NOAA-15 and 16 satellites. The MEPED (Medium Energy Proton and Electron Detector) instrument onboard the NOAA satellites measures ions (no ion mass separation is provided) and electrons in two directions, roughly vertical (the 0° detector) and roughly horizontal (the 90° detector), with 30° field of view. Note that at high (resp. low) latitudes the 0° detector measures mostly precipitating (trapped) particles and vice versa for the 90° detector. The MEPED instrument has six energy channels for ions (from 30-80 keV to >7000 keV)

[1]Department of Physical Sciences, University of Oulu, Finland
[2]Los Alamos National Laboratory, Los Alamos, New Mexico
[3]LASP, University of Colorado at Boulder
[4]University of Bergen, Norway
[5]Aerospace Co., Los Angeles, California

The Inner Magnetosphere: Physics and Modeling
Geophysical Monograph Series 155

10.1029/155GM11

and three energy channels for electrons (from 30 keV to >300 keV). Because the heavier ions require more energy to penetrate into the detector the lower energy limit for heavy ions is slightly higher than the nominal value. For oxygen ions the lower energy limit is estimated to be about 45 keV instead of the nominal 30 keV [*Søraas et al.*, 2002]. NOAA-15 and 16 have polar orbits at an altitude of about 850 km. The orbital plane is 20-08 MLT for NOAA-15 and 14-02 MLT for NOAA-16 (see *Evans and Greer*, 2000, for more details of the MEPED instrument). NOAA auxiliary data include L shell estimates calculated using the IGRF-2000 model, independent of magnetic disturbance level.

Cluster satellites have two instruments for detecting and analyzing ions. The CIS (Cluster Ion Spectrometry) CODIF (COmposition and Distribution Function analyzer) instrument measures the distributions of major plasma ions (H^+, He^+, He^{++} and O^+) in the thermal to suprathermal energy range from 0 to 40 keV/e. (A comprehensive description of the CIS instrument properties is given by *Réme et al.*, 1997.) The RAPID (Research with Adaptive Particle Imaging Detectors) spectrometer for the CLUSTER mission analyzes suprathermal plasma distributions in the energy range from 20-400 keV for electrons, 40-1500 keV for protons and 10-1500 keV/nuc for heavier ion species. The RAPID instrument uses two different and independent detector systems for the detection of nuclei and electrons: IIMS (Imaging Ion Mass Spectrometer) and IES (Imaging Electron Spectrometer). (See [*Wilken et al.*, 1997], for a more detailed description of the RAPID instrument.)

3. OBSERVATIONS

3.1. Storm Overview

On March 31, 2001, the Advanced Composition Explorer (ACE) satellite was measuring interplanetary conditions at about (223, −23, −12) R_E. As shown in Figure 1, IMF Bz(GSM) component was positive from 0030UT until 0240 UT, then fluctuating between negative and positive values until about 0330 UT when the IMF direction changed southwards for about four hours. Strongest negative values of Bz (<−40 nT) were observed around 06 UT. The solar wind (SW) velocity increased between 00 UT and 02 UT in two steps from about 400 km/s to above 750 km/s. Solar wind dynamic pressure, which mainly followed the changes in SW density, showed dramatic variations during the first six hours of the day. At about 0020 UT, SW pressure had a very sharp peak which lasted only about half an hour. Another, longer period of increased pressure lasted roughly from 02 UT to 06 UT. These interplanetary conditions led to the generation of a major (*Dst* about −360 nT; see Figure 1) magnetic storm with a rapid main phase starting at 04 UT and ending at 08 UT. Note that, taking the average SW/IMF time delay of about 30-40 min into account, the positive turning of IMF Bz at about 07 UT corresponds very well with the end of the storm main phase at 08 UT. The extreme geomagnetic conditions were also verified by the LANL geostationary satellite data (not shown here), which indicate that the magnetopause was pushed inside the geosynchronous orbit in the dayside roughly at about 03-08 UT and even in the morning and evening sectors at around 06 UT. After a long period of mainly positive values, the IMF Bz experienced another long interval of negative values at about 14-22 UT which caused a secondary minimum in *Dst* (−285 nT).

The AE index (bottom panel of Figure 1) shows dramatic changes in the intensity of auroral electrojets during the day. The AE index attains fairly high values already in the beginning of the day, exceeding 1000 nT a few times during the first few hours of the day. Note also that the AE index does not depict exceptionally high values during the main phase of the storm, and remains at a rather low level at around 06 UT. The highest values of the AE index of above 2000 nT are observed only after the storm main phase at about 16-21 UT as three enhancements, the first one at about 16-17 UT being the strongest. However, it should be pointed out that during the main phase of a major magnetic storm the auroral currents may descend significantly equatorward of the latitude of AE stations. In this case the AE index underestimates the intensity of auroral electrojet currents. This is also the case at the main phase of the present storm since the Kp index (measured by mid-latitude stations) shows the maximum of 9- around 06 UT.

3.2. NOAA Observations

Figure 2 shows the total energetic ion and electron fluxes measured by the 90° detectors of NOAA-16 on March 30-31, 2001. (The 0° detector shows the same behavior). The ion and electron fluxes at both detectors are increased by nearly two orders of magnitude from the average level of March 30 to their storm time maxima during the next day. As seen in Figure 2, the maximum ion flux is observed at about 04-07 UT, coinciding with the time of the steepest descent of the *Dst* index (and maximum Kp). Instead, the maximum flux of electrons is observed only at 16-18 UT, coinciding well with the largest values of the AE index. A secondary maximum in the ion flux and a secondary minimum in the *Dst* index occur soon thereafter at about 18-19 UT. All these general features are supported by corresponding NOAA-15 data.

Figure 3 shows the 0° and 90° ion flux maxima for the three lowest energy channels of the MEPED instrument during each pass of the NOAA-16 satellite in the post-midnight sector. All channels show two distinct flux enhancements: one around 06 UT and the other at about 1800 UT.

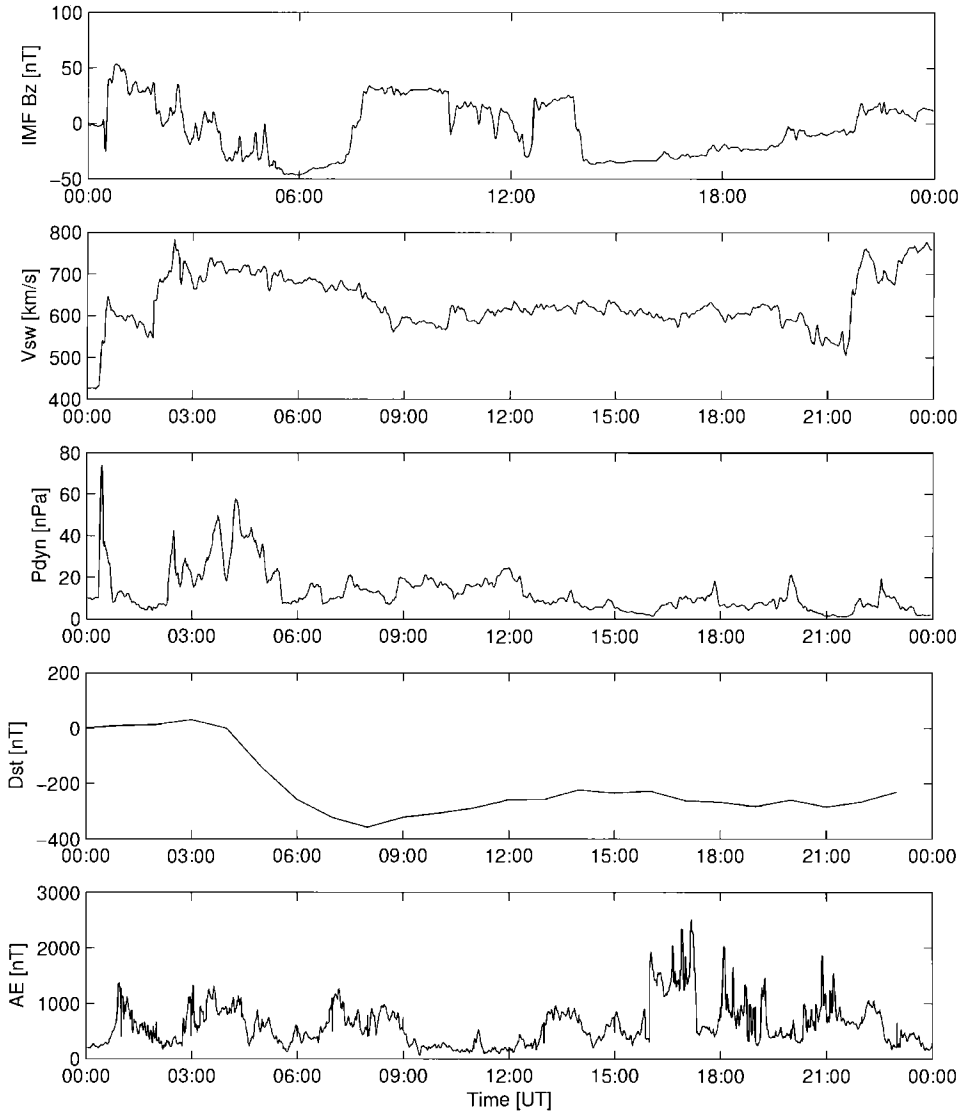

Figure 1. From top to bottom: ACE observations of the IMF Bz(GSM) component, solar wind velocity, solar wind pressure together with *Dst* and AE indices on March 31, 2001.

The first enhancement is considerably stronger than the second one. Note also that the lowest energy channel shows a different behavior during the first enhancement than the higher energies. In the 30-80 keV energy range the ion fluxes grow faster and reach their maximum already at about 0430 UT. At higher energies the fluxes are relatively small and steady until a large spike-like enhancement occurs at about 0630 UT.

The L-shells of the observed ion flux maxima during each NOAA-16 nightside pass are shown in Figure 4. The general behavior of the different energy channels is fairly similar. The L-shell of the maximum flux shifts inwards as the storm main phase progresses until the maximum flux is observed at the lowest L-shell. This rule seems to be valid in detail so that the lowest energy channel reaches its minimum L-shells first, in accordance with its earlier flux maximum. (Note that there are small differences between the 0° and 90° detectors because of temporal evolution. The 0° detector reaches its maximum earlier in the northern hemisphere at a higher L shell, while the 90° detector maximum is later in the southern hemisphere at a lower L shell. Note also that at low L-shells the 90° detector is closer to the precipitating flux.) This leads to the interesting fact that while the L-shells of flux maxima for different energies are ordered normally, e.g., higher L-shells for smaller energies, at 0430 UT the lowest

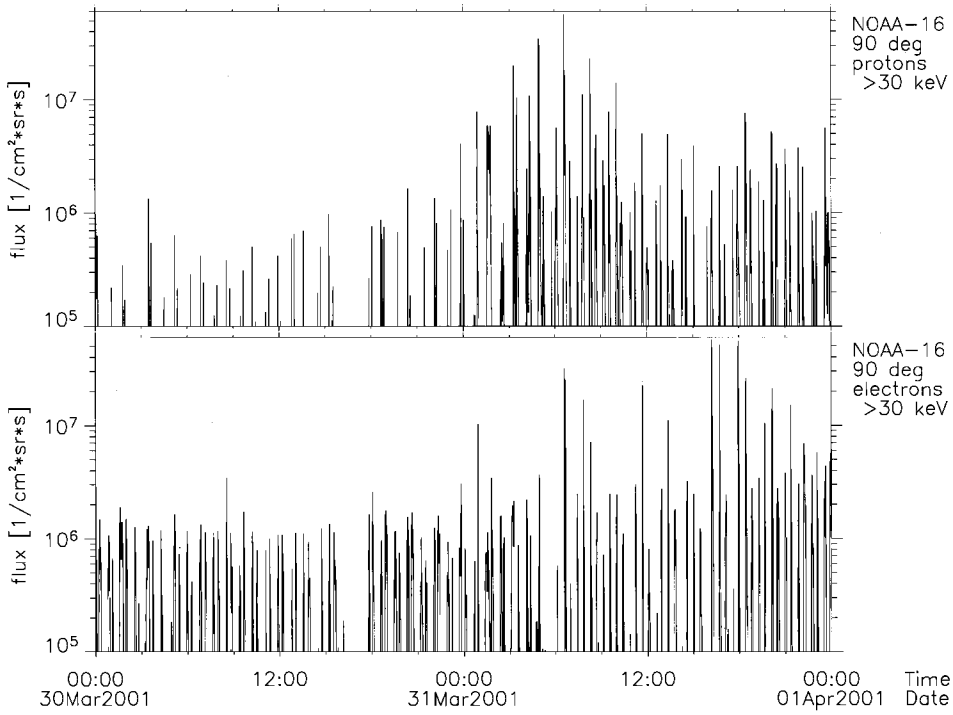

Figure 2. NOAA-16 total ion and electron fluxes on 30-31 March, 2001.

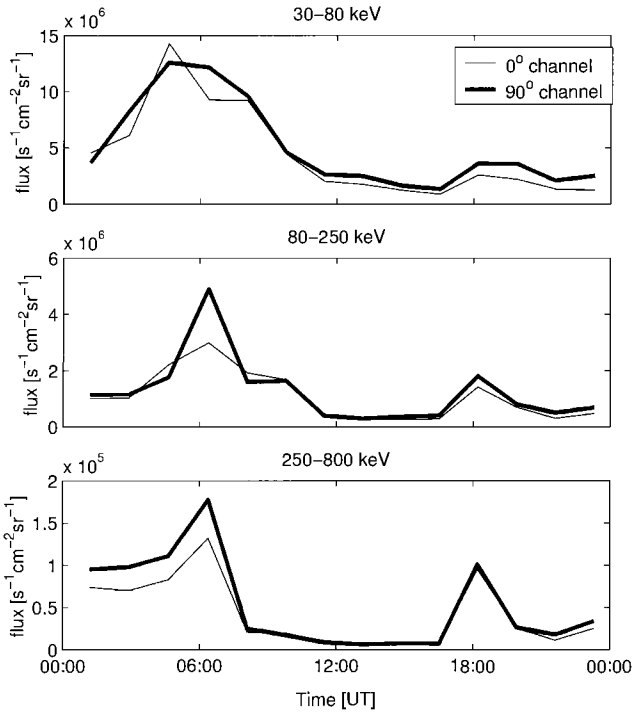

Figure 3. NOAA-16 maximum ion fluxes in the three lowest energy channels. One point denotes the maximum during one night side pass.

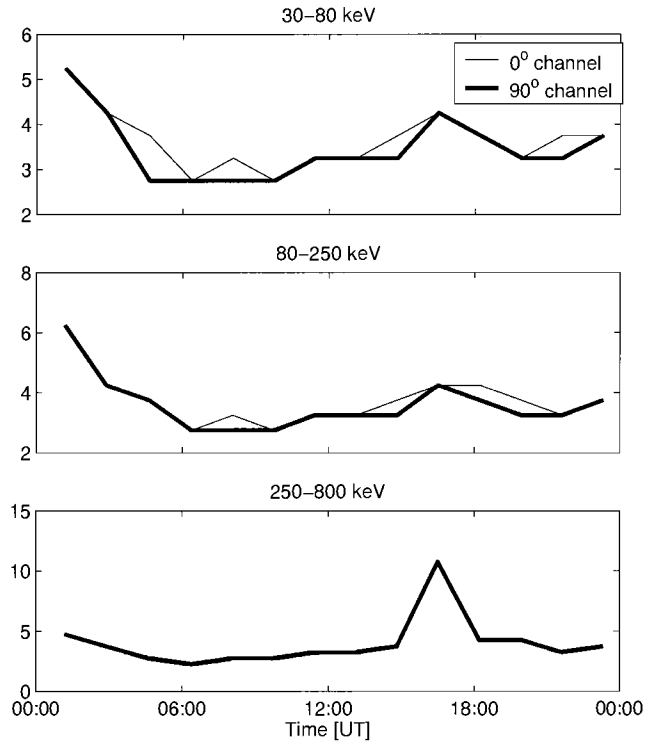

Figure 4. The L values of the maximum flux of NOAA-16 ions in the three lowest energy channels for each nightside pass.

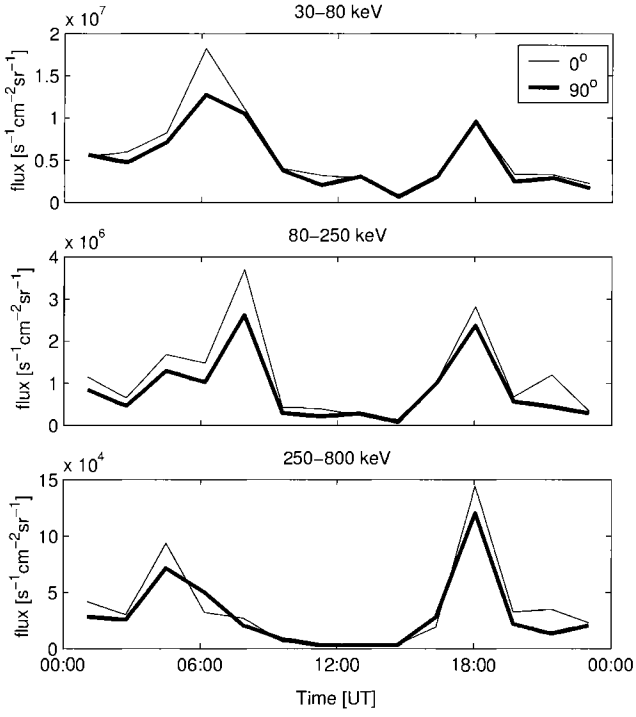

Figure 5. The same for NOAA-15 in the dusk as Figure 3 for NOAA-16 in the nightside.

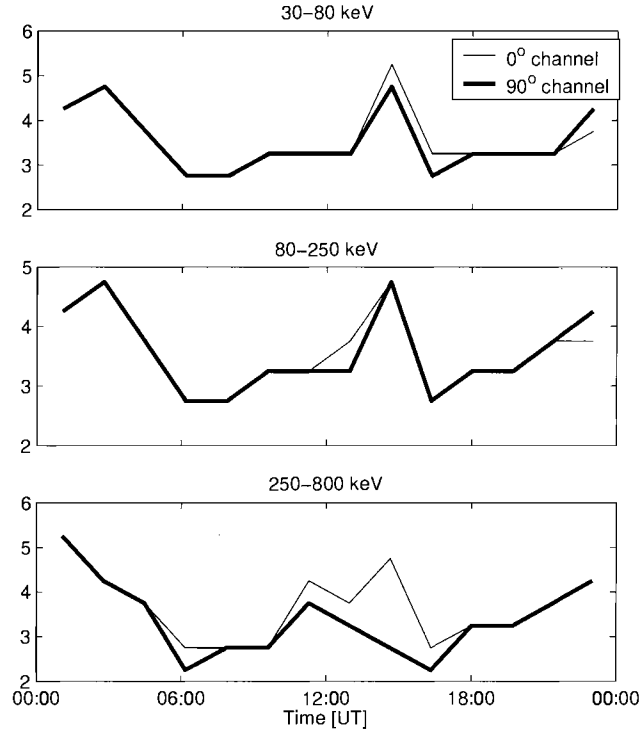

Figure 6. The same for NOAA-15 in the dusk as Figure 4 for NOAA-16 in the nightside.

channel maximum is at lower L-shells than the maxima in the other channels. The normal situation is reached again by the strong enhancement after 06 UT.

Figures 5 and 6 show similar plots for NOAA-15 in the dusk sector as Figures 3 and 4 for NOAA-16. As for NOAA-16 the observed fluxes in NOAA-15 show two broad enhancements: one during the storm main phase and the other at about 18 UT during the recovery phase. Also, as for NOAA-16, interesting differences are found between the three ion energy channels during the main phase. The two highest channels depict a simultaneous enhancement at about 0430 UT that also forms the maximum flux in the highest energy channel during the main phase. This enhancement occurs at about $L = 3.7$. However, the L shell of maximum flux is still decreasing at that time and the final, lowest L shell region is obtained only when the lowest energy channel finds its maximum flux. The other energy channels have their maximum flux L-shells in the same region at the same time, not during their respective flux maxima. The second channel has its flux maximum at about 0730 UT which could well be due to the drift of those ions whose flux maximum was found in NOAA-16 at 0630 UT. (The highest energy ions were mainly missed by NOAA-15 because of their faster drift speed and the coarse sampling time. This is supported by the very fast decline of the flux after 0630 UT at NOAA-16, implying a rather limited injection time.) Note that the final minimum L shell (2.8) is the same in NOAA-15 and NOAA-16, giving strong support for the global nature of the observed changes in the magnetosphere, as well as for the credibility of NOAA observations. Finally, we note that the absolute maximum flux of the highest energy ions at NOAA-15 occurs at about 18 UT and is only slightly lower than the corresponding maximum at NOAA-16 at 0630 UT.

The maximum electron fluxes in the two lowest energy channels observed by NOAA-16 for each nightside pass are shown in Figure 7. The two channels behave very similarly. At about 0630 UT both channels see a distinct increase in the flux. Another nearly identical flux enhancement is seen in the lowest energy channel at about 1130 UT (but not so clearly in the higher energy channel). At about 16 UT the electron fluxes start increasing strongly in both channels reaching maxima around 18 UT. The electron fluxes at NOAA-15 (not shown) remain clearly below those of NOAA-16 but roughly follow the same temporal evolution. In particular, the absolute maximum at NOAA-15 is also seen at about 18 UT. The L shell of maximum electron flux at NOAA-16 (not shown) decreases in the beginning of the day and reaches its minimum already before 06 UT, the lowest energy electron channel interestingly at the same time as the lowest energy ions. On the other hand, the corresponding L shell at

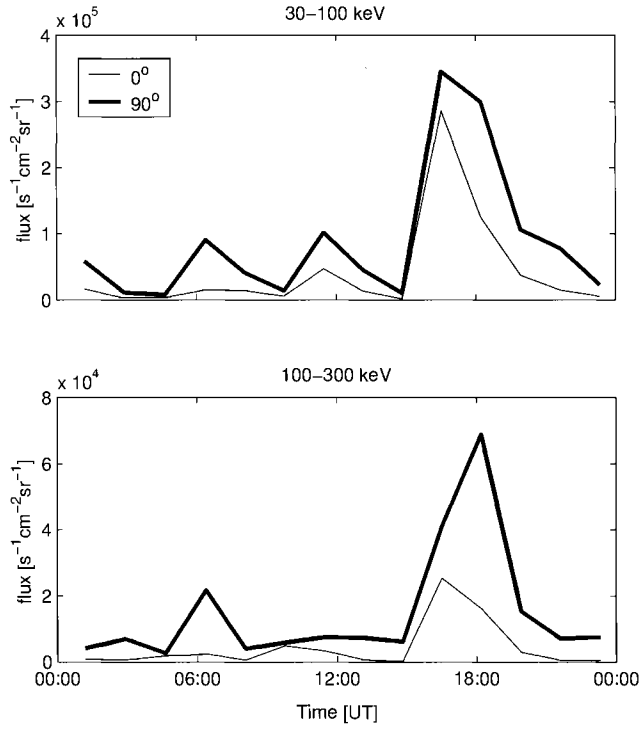

Figure 7. NOAA-16 maximum electron fluxes in the two lowest energy channels. One point denotes the maximum during one night side pass.

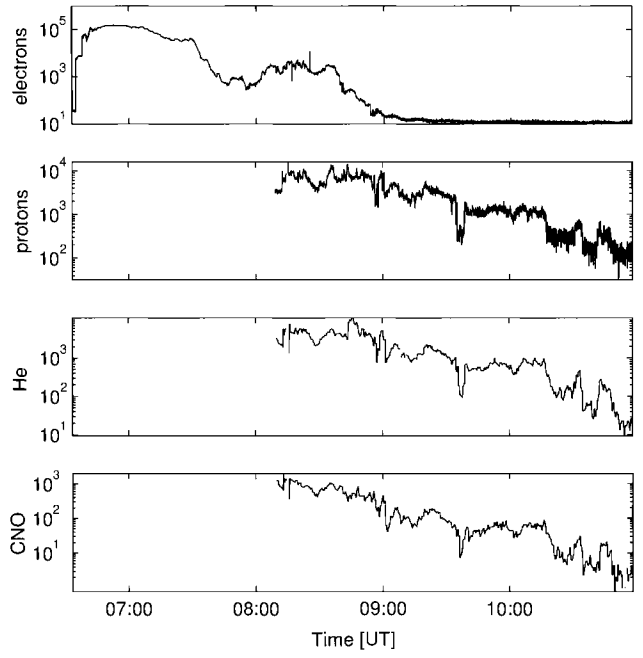

Figure 8. Cluster s/c1 RAPID total fluxes of energetic electrons, protons and oxygen ions ($s^{-1}cm^{-2}sr^{-1}keV^{-1}$).

the absolute flux maximum before 18 UT took place at a significantly higher L shell of about 5-6.

3.3. CLUSTER Observations

The four Cluster satellites had their perigee at about 07 UT on March 31, 2001. The RAPID energetic particle spectrometer [*Wilken et al.*, 1997; 2001] measured the electron fluxes around the perigee since about 0630 UT (see Figure 8) and the three types of ions (protons, heliums and oxygens) since about 0810 UT. Curiously, the Cluster perigee was in the 22 LT sector, i.e., in between the LT sectors of the two NOAA satellites. Cluster observed the highest flux of energetic electrons around the perigee from 0635 UT to 0740 UT which corresponds L-shells from about 4 to 5. This is in an excellent agreement with NOAA-16 and NOAA-15 (see Figures 4 and 6) observations where the highest fluxes were restricted to below $L = 5$. After a weak minimum at about $L = 5$-6 Cluster observed a region of lower fluxes of energetic electrons until about $L = 12$. This structure can also be seen by NOAA-16 at about 05 UT (not shown), as well as at NOAA-15 already at 04 UT and also later at about 08 UT, i.e., at the time of Cluster observations.

Figure 9 shows the ion composition data from the Cluster/CIS instrument which started operating at about 0640 UT when the Cluster satellites were still flying to lower L-shells. The CIS data shows consistent and overwhelming O^+ dominance at $L = 4$-6. The upper energy limit of CIS instrument is 40 keV and the particle spectra (not shown) show that the intensity maximum of oxygen ions is at or above this upper limit. From about 08 UT Cluster satellites are in the plasmasheet where the ions appear in bursty flows and have a lower average energy than in the ring current. However, CIS data shows that also the bursty plasmasheet fluxes are dominated by oxygen ions.

4. DISCUSSION AND CONCLUSIONS

The ring current particle population was found to be greatly intensified from the average quiet time level during the storm. The ion flux maximum was coinciding with the main phase when the *Dst* index was decreasing most rapidly with time. This maximum was seen as particularly strong enhancements of the ion fluxes in the post midnight and dusk sectors around 06 UT. The behavior of the lowest ion energy channel and the CIS ion composition data in the overlapping energy interval confirm that the ring current was dominated by oxygen ions in the main phase of the storm. The NOAA data also show that the outflow of oxygen ions very probably started already in the beginning of the main phase and reached

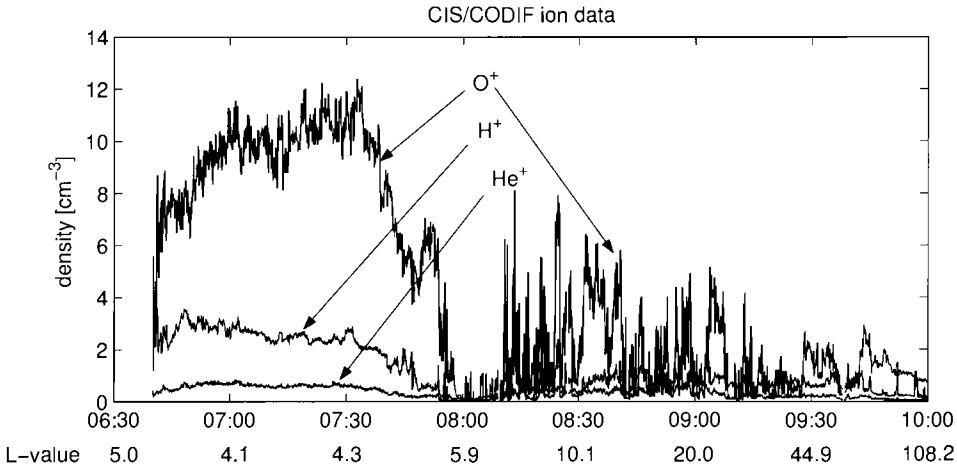

Figure 9. Total number density of Cluster s/c1 CIS protons, helium and oxygen ions.

its maximum at about 0430 UT in the night side and around 06 UT in the dusk sector.

The very intense ion enhancement at the lowest energy channel observed by NOAA-15 at about 0630 UT cannot be only explained by the drift of previously existing population from the night side because the fluxes observed by NOAA-16 are lower than those by NOAA-15. Instead, the enhancement is well in agreement with the simultaneous observation of intense ionospheric outflow of low energy oxygen ions at the dusk by the FAST satellite [see *Baker et al.*, 2002]. Furthermore the Cluster satellites observed an overwhelming O^+ dominance around 40 keV in the pre-midnight sector. All these additional observations give further evidence for the fact that the majority of ions observed by the NOAA satellites during the storm main phase are oxygen ions which dominate at least in the low-energy part of the ring current.

Note also that the NOAA-16 low-energy ions reached their maximum clearly before the higher energy ions. This further implies a different acceleration mechanism for the low-energy ions (oxygens) that most likely are accelerated during their upwelling from the ionosphere and the high-energy ions that rather depict evidence for an injection. The fluxes observed by NOAA-16 at about 0630 UT probably result from a strong dispersionless (at least at this time resolution) substorm injection. This is confirmed by the similar signatures in NOAA-16 ion and electron data (see Figures 3 and 7). This kind of coherent signature is not seen at dusk by NOAA-15. Thus after the injection at 0630 UT in the night side the ions started drifting westwards and electrons eastwards. These injected ions were seen by NOAA-15 at about 0730 UT in the dusk in the energy range of 80-250 keV. The higher energy ions drifted westwards faster and were missed by NOAA-15 which was only flying towards the relevant low L shells.

We would also like to note that NOAA-15 detected a simultaneous strong low-energy ion enhancement in the morning sector at about 07 UT (not shown). This enhancement can not be understood in terms of drift but rather supports the view that it results from the above mentioned ionospheric outflow of oxygen ions. It has been reported [*Daglis*, 1997] that oxygens can be the main ion species in the RC during the main phase of great magnetic storms. Also, the fraction of oxygen in RC is the larger the more intense the storm is. Our observations further emphasize the view that the ionospheric outflow of oxygens is a global phenomenon, and that the observed enhanced ion fluxes had a large oxygen fraction. Also, our results suggest that there is a large contribution to the low-energy part of the ring current during storm main phase which comes directly from the ionosphere instead of a less direct route via storage and acceleration in the tail and subsequent drift.

The particle flux peaks were found to proceed to successively low L shells down to about $L = 2.8$ during the storm main phase. Note that very similar L shells were found for NOAA-16 and NOAA-15 both for ions and electrons. The low L value is also supported by the fact that the AE index was relatively quiet while the Kp index was at its highest during the largest ion fluxes at about 06 UT. Note also that the obtained minimum L value of 2.8 agrees very well with the size of the present storm and the earlier detected relation between storm size and RC flux maxima [*Hamilton et al.*, 1988].

In a dramatic difference to ions, the energetic electrons had their maximum fluxes only in the recovery phase of the storm. The largest electron fluxes were found by NOAA-16 in the night sector. The NOAA-15 fluxes at dawn (not shown) can be well understood in terms of the standard view of eastward drift of electrons. These and other facts suggest that

the flux maxima of low-energy ions and energetic electrons were formed by different mechanisms, the electron flux maxima at 16-18 UT by the standard tailside storage and acceleration, the ion maxima at 06-08 UT mainly by the field-aligned acceleration of ionospheric ions. Note also that the largest values of the AE index at 16-18 UT (see Figure 1) coincide very well with the electron flux maximum. This is also in accordance with the found larger L value of about 5-6 of the maximum fluxes at this time, implying that the injections occurred at L shells higher than the ring current maxima during the main phase. (Note also that this enhancement coincides, taking roughly 1h-delay between ACE and NOAA, with the start of enhanced solar wind pressure and IMF Bz turning slightly less negative after a prolonged period of strongly negative values. These conditions favor substorm occurrence.)

The 06 UT field-aligned acceleration can not be due to a static potential since it would operate similarly with electrons and ions of different masses, and NOAA satellites do not see similar fluxes of energetic electrons at dusk. We suggest that the field-aligned acceleration is caused by the ion cyclotron mechanism which accelerates only ions and prefers heavy ions like oxygens. Equatorially generated ion cyclotron waves (short period Alfvén waves) below the proton gyrofrequency propagate into the ionosphere and cause transverse acceleration of oxygen ions by ion cyclotron instability. This is possible at the fairly low latitudes where the ionospheric gyrofrequency of oxygen ions is close to the equatorial gyrofrequency of protons. Note that this mechanism would mainly accelerate oxygens and less protons, in agreement with our observations. Moreover, it has been found that ion cyclotron wave activity is greatly enhanced during the storm main phase even at ionospheric altitudes [*Bräysy et al.*, 1998], giving support for the existence of these waves and the suggested mechanism.

Acknowledgments. We greatly acknowledge the financial support by the Academy of Finland.

REFERENCES

Baker, D.N., R.E. Ergun, J.L. Burch, J-M. Jahn, P.W. Daly, R. Friedel, G.D. Reeves, T.A. Fritz, and D.G Mitchell, A telescopic and microscopic view of a magnetospheric substorm on 31 March 2001, *Geophys. Res. Lett.*, doi: 10.1029/ 2001GL014491, 2002.

Bräysy, T., K. Mursula and G. Marklund, Ion cyclotron waves during a great magnetic storm observed by Freja double-probe electric field instrument, *J. Geophys. Res.*, 103, 4145, 1998.

Daglis, I.A., The role of magnetosphere-ionosphere coupling in magnetic storm dynamics, *in Magnetic Storms, Geophysical Monograph*, 98, 107, edited by B.T. Tsurutani *et al.*, AGU, Washington, D.C., 1997.

Evans, D.S. and M.S. Greer, Polar orbiting environmental satellite space environment monitor - 2: instrument descriptions and archive data documentation, *NOAA Technical Memorandum OAR SEC-93*, Boulder, Colorado, 2000.

Hamilton, D.C., G. Gloeckler, F.M. Ipavich, W. Stüdemann, B. Wilken, and G. Kremser, Ring current development during the great geomagnetic storm of February 1986, *J. Geophys. Res.*, 102, 14113, 1997.

Korth, A., and R.H.W. Friedel, Dynamics of energetic ions and electrons between L = 2.5 and L = 7 during magnetic storms, *J. Geophys. Res*, 102, 14113, 1997

Réme, H., J.M. Bosqued, J.A. Sauvaud *et al.*, The Cluster Ion Spectrometry (CIS) Experiment, *Space Science Reviews,* 79, 303-350,1997

Smith, P.H., and R.A. Hoffman, Ring current particle distributions during the magnetic storms of December 16-18, 1971, *J. Geophys. Res.*, 78, 4731, 1973

Søraas, F., K. Aarsnes, K. Oksavik and D.S. Evans, Ring current intensity estimated from low-altitude proton observations, *J. Geophys. Res.*, 107, 101029, 2002

Wilken, B., *et al.*, RAPID: The Imaging Energetic Particle Spectrometer on Cluster, *Space Sci. Rev*, 79, 399, 1997

Wilken, B., *et al.*, First results from the RAPID imaging energetic particle spectrometer on board Cluster, *Annales Geophysicae*, 19, 1355, 2001.

Timo Asikainen, Department of Physical Sciences, POBox 3000, FIN-90014, University of Oulu, Finland.

Daniel Baker, Laboratory for Atmospheric & Space Physics, University of Colorado, Boulder 1234 Innovation Drive Boulder CO 80303.

J. Bernard Blake, Mail Stop M2-259, The Aerospace Corp. P.O. Box 92957, Los Angeles, CA 90009.

Joseph F. Fennell, Mail Stop M2-259, The Aerospace Corp. P.O. Box 92957, Los Angeles, CA 90009.

Reiner Friedel, LANL, NIS-2, MS 426, Los Alamos, NM 87544, USA.

Raine Kerttula, Department of Physical Sciences, POBox 3000, FIN-90014, University of Oulu, Finland.

Kalevi Mursula, Department of Physical Sciences, POBox 3000, FIN-90014, University of Oulu, Finland.

Finn Søraas, University of Bergen, Department of Physics, Allegates 55, N-5007 Bergen, Norway.

Magnetospheric Substorms and the Sources of Inner Magnetosphere Particle Acceleration

E.E. Antonova

Skobeltsyn Institute of Nuclear Physics, Moscow State University, Russia

The solution of the problem of the acceleration of relativistic electrons during magnetospheric storms requires the self-consistent analysis of the processes of the formation of the ring current and particle acceleration. The experimental proofs of the substorm particle acceleration before the beginning of the dipolarization provide the new aspects of the problem. The configuration of the high latitude transverse currents is analyzed. It is shown that the near Earth plasma sheet particle domain and its daytime continuation can be considered as the high latitude part of the ring current. The main features of the theory explaining the localization of the magnetospheric substorm expansion phase onset deep inside the magnetopshere on the quasidipolar magnetic field lines (the effect of Akasofu - first auroral arc brightening on the equatorial boundary of the auroral oval) are discussed. The dependence of the value of D_{st} from the position of auroral electrojets is analyzed. It is shown that the formation of the convectively equilibrium distribution of the radial plasma pressure can explain the experimentally obtained dependence. The role of the acceleration of electrons by high frequency electrostatic waves in thin bright auroral arcs is discussed.

1. INTRODUCTION

Resent findings of the role of the plasma pressure gradients in the creation and support of large-scale field-aligned currents (see the review of *Antonova* [2002a]), the localization of the magnetospheric substorm expansion phase onset on the quasidipole magnetic field lines (see *Lyons* [2000], *Stepanova et al.* [2002]) and the experimental supports of the concept of the magnetospheric tail as the turbulent wake (see the reviews of *Borovsky and Funsten* [2003], *Antonova* [2002a]) lead to the definite changes of the main approaches to the description of the magnetospheric processes. One of the aspects of the problem is the configuration of magnetospheric domains and magnetospheric currents. In this paper we try to show that the considerable part of the auroral oval is the ionospheric mapping of the external part of the ring current. We analyze the dependence of the value of D_{st}-variation from the storm time position of auroral electrojets and the region of the acceleration of relativistic electrons. We try to show that experimentally observed dependence is explained by the formation of the plasma pressure profile stable for the interchange disturbances. The processes of the electric field formation during substorm expansion phase is discussed. We analyze the possible role of high frequency electrostatic waves produced by intense electron and ion beams within thin rayed auroral arcs in the formation of the seed population of relativistic electrons.

The Inner Magnetosphere: Physics and Modeling
Geophysical Monograph Series 155

10.1029/155GM12

2. THE TOPOLOGY OF THE MAGNETOSPHERE AND THE CONFIGURATION OF MAGNETOSPHERIC CURRENTS

Traditional point of view considers the auroral oval as the region of the plasma sheet mapping on the ionospheric latitudes. *Newell and Meng* [1992] demonstrate the existence of

the plasma sheet (CPS and BPS) precipitation equatorward from the cusp and cleft. But the picture of *Newell and Meng* [1992] contains the region, which is not identified and is named as void. According to *Starkov et al.* [2002], the region characterized by *Newell and Meng* [1992] as a void, contains, in fact, the plasma sheet-like precipitation. Results of IMAGE observations of cusp position [*Fuselier et al.*, 2002; *Frey et al.*, 2003] support the plasma sheet precipitations to the equator from the cusp. It implies that the plasma sheet-like domain surrounds the Earth. *Hori et al.* [2003] found a drifting population of energetic protons with a fairly long (~several tens of minutes) dispersion at a geocentric distance $>10R_E$ on the base of Geotail data. This observation indicates that energetic particles can lie on a closed drift path around the Earth much farther than the geosynchronous distance (till ~12-13 R_E). The discussed findings mean that the regions of the magnetosphere till 10-12R_E in the nighttime direction and till the low latitude boundary layer (LLBL) in the daytime direction constitute the internal magnetospheric plasma domain. This domain is natural to consider as the continuation of the ring current region.

The transverse current in the traditional ring current region is supported by the radial plasma pressure gradients. The configuration of transverse currents in the high latitude continuation of the ring current can also be supported by plasma pressure gradients. The configuration of plasma pressure distribution on the geocentric distances <9 R_E is investigated due to AMPTE/CCE observations [*Lui and Hamilton*, 1992; *DeMichelis et al.*, 1999]. *Lui and Hamilton* [1992] show that quite time day-night plasma pressure asymmetry is less then 2 and the daytime plasma pressure gradients are directed to the Earth. The daytime magnetic field near the equator is much higher then the nighttime equatorial magnetic field. This means that the daytime equatorial transverse current is much smaller then nighttime current. But it is well known (see *Antonova and Ganushkina* [1997, 2000] and references therein) that the daytime magnetic field has minima on the magnetic field lines far from the equatorial plane, and, therefore, the equatorial plane does not coincide with the region of minimal magnetic field. It implies that the daytime transverse currents comparable in magnitude with the nighttime transverse currents are concentrated at the same geocentric distances far from the equatorial plane. The existence of the closed ring of plasma sheet population surrounding the Earth gives the possibility to suggest that transverse currents in this region are closed inside the magnetosphere and constitutes the external part of the ring current. But the configuration of this external part of the ring current differs from the traditional ring current (see Figure 1) and can be named in accordance with *Antonova and Ganushkina* [2000] the cut-ring current system (CRC). Current lines in the CRC system are concentrated in the equatorial plane on the nightside and at high latitudes near noon (Figure 1).

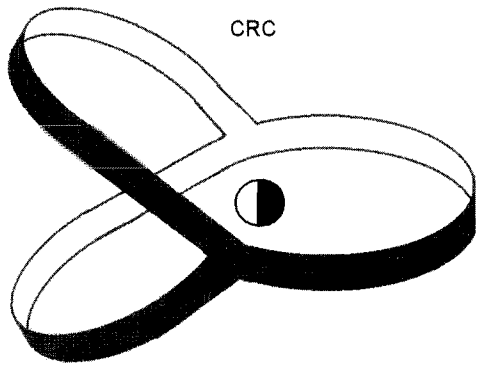

Figure 1. The configuration of currents in the cut-ring (CRC) current system.

CRC system is not included in any of the existing numerical models of the magnetospheric current systems. It is possible to suggest that such inclusion can change the results of the mapping of the daytime magnetospheric domains. *Iijima et al.* [1997] show that the sources of the daytime part of Region 1 currents are located in the regions with comparatively high plasma pressure. *Wing and Newell* [2000] demonstrate the support of Region 1 currents by magnetospheric plasma pressure gradients. These findings show the action of "magnetospheric topology" mechanism of the generation dawn-dusk electric field discussed by *Antonova and Ganushkina* [1997]. The ionospheric divergence of CRC can be considered as the very proper candidate for the source of Region 1 currents of *Iijima and Potemra* [1976]. The disruption and diversion into the ionosphere of the near Earth magnetospheric tail current is considered as one of the main process of the substorm expansion phase onset (see *Lui* [1991]). The introduction of CRC can lead to the correction of this picture. The localization of the region of transverse current disruption at geocentric distances $<8R_E$ can be connected with CRC disruption. The problem of the substorm development becomes the problem of surrounding the Earth current dynamics i.e. the problem of the ring current dynamics. The development of auroral electrojets in such a case is connected with the asymmetry of the ring current (see *Tverskoy* [1972]). It is necessary to mention that the value of current in the substorm Birkeland current loop does not limited by the diversion of the considerable part of the tail current. It determines by the values of local plasma pressure gradients appearing due to substorm particle energization.

Akasofu [1964] shows that substorm onset is characterized by the brightening of the most equatorward auroral arc. Multiple observations show the disturbance motion to the pole after substorm expansion phase onset and auroral bulge formation. The inner boundary of the region of energization is clearly identified as the injection boundary

(*Mauk and Meng* [1983a,b], *Lopez et al.* [1990]). The external boundary of this region in accordance with the results of *Hori et al.* [2003] is observed till $13R_E$. Such observations show the action of the processes of rapid particle acceleration at geocentric distances from ~6-7R_E till ~10-13R_E during isolated substorm. The filling of the CRC region by energized particles and increasing of the plasma pressure take place due to substorm injections. The increase of the plasma pressure leads to the decrease of the earthward plasma pressure gradient and therefore to the decrease of the westward transverse current or to the appearance of the region of antiearthward plasma pressure gradient [*Antonova et al.*, 1999]. The appearance of the antiearthward plasma pressure gradient leads to the formation of the eastward transverse current. This current is localized near the inner boundary of CRC. The results of the work of *Akasofu* [2003] show the importance of the eastward transverse current for the explanation of substorm current dynamics. *Antonova and Ovchinnikov* [2002] show that the magneic field of the eastward current can lead to the formation of the substorm neutral line in the near tail region. Therefore it is necessary to include the eastward transverse current in the model of substorm currents.

One of the main features of the periods of high geomagnetic activity is the auroral oval and electrojet motion to low latitudes. The auroral magnetic stations can become the polar cap stations during great geomagnetic storms. The investigation of geomagnetic disturbances requires using data of many middle latitude magnetic stations (see *Daglis et al.* [2003] and references in this work). Motion of the auroral oval to low latitudes leads to the shift of the substorm activity region to low latitudes and corresponding filling by energetic particles the inner magnetosphere regions. The analysis of the structure of CRC shows that this current can be considered as one of the sources of D_{st}-variation. The first order approximation of CRC contribution can be obtained on the basis of the analysis of the energy content of CRC region suggesting the applicability of Dessler-Parker-Sckopke relation.

3. RADIAL PROFILE OF THE MAGNETOSPHERIC PRESSURE AND D_{st}-VARIATION

The main well-documented process of the storm time activity is the increase of the value of the inner magnetospheric plasma pressure. The information on the distribution of the plasma pressure inside the magnetosphere during magnetospheric storms including latest IMAGE results is quite limited. *Lui et al.* [1987] show that comparatively sharp dropout of the plasma pressure exists on the inner boundary of the storm time ring current. It is also possible to see analyzing Figure 2 and 6 of *Lui et al.* [1987] that the plasma pressure p comparatively quickly decreases with the increase of geocentric distance having maximum at small L. Such results give the possibility to suggest that the formation of the sharp peak of plasma pressure deep inside the magnetosphere can be considered as one of the main features of magnetospheric storm. The stability of the distribution of the plasma pressure depends on the value of the plasma parameter β, where $\beta = 2\mu_0 p / B^2$, μ_0 is the permeability of vacuum, B is the magnetic field. The interchange-like disturbances are the most dangerous ones if $\beta << 1$ and balloon-like disturbances if $\beta \geq 1$. Values of $\beta < 1$ ($\beta \sim 0.1$) were observed by *Lui et al.* [1987]. The experimental results show at the same time that plasma parameter can become larger then unity inside the asymmetric ring current. *Tverskoy* [1972] develops the theory of the magnetospheric susbstorm in accordance with which the auroral electrojets and field-aligned currents are deposited near the inner magnetosphere plasma pressure maximum. The observed value of D_{st}-variation and the dependence of the lowest position of the westward electrojet center during the storm $L_{\max}$ (in the dipole mapping) from the maximal value of D_{st}-variation $|D_{st}|_{\max}$, which has the form [*Tverskaya*, 1986; *Tverskaya, et al.*, 2003]

$$| D_{st} |_{\max} = 2.75 \cdot 10^4 L_{\max}^{-4} \text{nTl}, \qquad (1)$$

give the possibility to evaluate β in the region of the plasma pressure maximum. $L_{\max}$ determines also the position of the peak intensity of fluxes of relativistic electrons, which appear during storm recovery phase. Relation (1) shows that the plasma pressure maximum is positioned at $L_{\max} \sim 3.7$ if $D_{st} \sim 150$ nT and at $L_{\max} \sim 2.6$ if $D_{st} \sim 600$ nT. The distribution of magnetic field inside the current ring is near to homogeneous. The magnetic field inside the ring (due to Earth's skin screening) $B_{rc} = 2 | D_{st}^* | /3$, where D_{st}^* is the value of D_{st} corrected on the magnetopause currents. *Tverskoy* [1997] evaluate the magnetic field in the region $L = L_{\max}$ of the sharp inner boundary of the plasma pressure distribution. It is shown that $B(L_{\max}) = 5B_{rc}/3$. Therefore $\beta(L_{\max}) = (3.06 \cdot 10^4 / B_{eq} L_{\max})^2 \approx 10^{-4} L_{\max}^{-2}$, where $B_{eq} = 0.32 \cdot 10^{-4}$ Tl is the magnetic field near the Earth's equator. Such estimation gives the possibility to use the low β approximation for the description of the processes near the inner magnetospheric pressure maximum during great geomagnetic storms.

The contribution of the ring current to D_{st}-variation is determined by the inner magnetospheric energy content in accordance with Dessler-Parker-Sckopke relation. The nonzero value of plasma pressure at the external boundary of ring current region introduces the correction for this relation [*Antonova*, 2000b; *Liemonhn*, 2003]. The value of this correction is comparatively high only for small geomagnetic storms. The analysis of the section 2 of this paper shows that the energy content of the external part of the ring current (CRC) mapped on the considerable part of the auroral oval is necessary to include in the ring current energy content.

The sources of the formation of the inner magnetospheric part of the ring current (or the traditional ring current) continue to be widely debated [*Daglis et al.*, 2003]. Plasma transport by week large-scale and strong localized electric fields are ordinarily considered as the dominant processes of the inner magnetosphere filling by plasma and energetic particles. The localized fields are mainly responsible for the formation of nose structures [*Ganushkina et al.*, 2000]. The ionosphere is also the powerful source of ring current ions during magnetic storms (see *Pulkkinen et al.* [2001] and references in this paper). The ionospheric source of the increase of the inner magnetospheric plasma pressure is not included in the existing models of ring current formation. But the upper limit of the inner magnetospheric particle feeling exists in spite of the action of different acceleration and transport mechanisms of plasma particles. This limit is determined by the stability of the distribution of the plasma pressure. The stability of the azimuthally symmetric distribution of isotropic plasma pressure in the region of low β is determined by Kadomtsev's [*Kadomtsev*, 1963] criterion: $p < p_{crit}$, where $p = p(W)$, $W = \int dl/B$ is the flux tube volume, $p_{crit} W^{\gamma} = \text{const}$, $\gamma = \text{const}$ equal to 7/4 for the case of the dipole magnetic field. Plasma tongues begin to form if $p > p_{crit}$ and the magnetic trap loses part of plasma population.

The value of D_{st}-variation produced by critically stable plasma pressure distribution is possible to obtained using *Tverskoy* [1997] relation

$$| D_{st}^{*crit} | = \frac{3\mu_0}{4R_E} \int_{W_{in}}^{W_{ex}} p(W) \frac{d}{dW} \frac{W}{L} dW, \qquad (2)$$

where W_{in} and W_{ex} are the values of flux tube volume at the inward and outward boundaries of the ring current, $W = 32R_E L^4/35B_{eq} = W_0 L^4$ in the dipole magnetic field. The accuracy of the relation (2) constitutes 20% for the quasi-dipole magnetic field configuration if the difference of the equatorial magnetic field from the dipole one does not exceed 100% [*Tverskoy*, 1997]. The relation $p(L) = p_{ex}(L_{ex}/L)^7$, where L_{ex} is the position of the outer boundary, p_{ex} is the value of the plasma pressure on $L = L_{ex}$, determines the boundary of the equilibrium pressure distribution in the dipole magnetic field. The interchange instability is developed if the plasma pressure has more steep profile then L^{-7}. The storm time increase of the plasma pressure inside the magnetosphere can continue till the appearance of pressure profile more steep then L^{-7}. Then the interchange instability development leads to losses of plasma in the form of flux tube motion in the radial direction.

The value of the plasma pressure on the external boundary of the ring current (including CRC) is possible to evaluate taking into account the pressure balance across the plasma sheet. The tail lobe magnetic field B_{lobe} has near to constant value at radial distances grater then $L_{ex} \sim 10R_E$. Plasma pressure on the tail axis is equal to $B_{lobe}^2/2\mu_0$. The plasma pressure increase in the earthward direction is observed when $L < L_{ex}$ [*Lui et al.*, 1994]. The change of the plasma pressure slope gives the possibility to suggest that $p_{ex} = B_{lobe}^2/2\mu_0$. Regions of L near L_{in} produce the main contribution to the integral (2). Neglecting the contribution of plasma pressure on the outer boundary of the ring current and suggesting the existence of the sharp inner boundary of the ring current it is possible to obtain

$$| D_{st}^{*crit} | = \frac{27}{70} \frac{\mu_0}{B_{eq}} p_{ex} L_{ex}^7 L_{in}^{-4} = \frac{27}{1400} \frac{B_{lobe}^2}{B_{eq}} L_{ex}^7 L_{in}^{-4} \text{ nTl}, \qquad (3)$$

The dependence (3) coincide with the dependence (1) if $L_{ex} = 10$, $B_{lobe} = 21{,}4$ nTl. *Tverskoy* [1997] obtain the dependence (1) suggesting the existence of the radial adiabatic plasma transport from the external boundary region having fixed value of $p_{ex} W_{ex}^{7/4}$. Any kind of radial plasma transport and the filling of the inner region of the magnetosphere are possible in our analysis. The overfilling of the internal magnetosphere leads to the extraction of the part of the plasma from the trap. The latest results of RICE convection model [*Toffoletto et al.*, this issue] support the possibility of the existence of discussed process.

4. MAGNETOSPHERIC SUBSTORMS AND PARTICLE ACCELERATION

The substorm expansion phase onset is traditionally explained as the result of the development of some kind of the instability. The development of such instability near the equatorial boundary of the auroral oval was the problem for multiple scenarios of substorm expansion phase onset. The results of the observations of plasma sheet turbulence give the comparatively simple explanation of such localization as only a plasma region stable before substorm expansion phase onset can become unstable. It was found (see *Liou et al.* [1999]) that Pi 2 bursts could often lag behind the brightening of the onset arc. This experimental observation shows the development of electrostatic instability as the cause of substorm expansion phase onset. Magnetic field disturbances including transverse magnetospheric current disruption take place ≤1 min later. Particle acceleration till ~50-300 keV is observed about 20 s prior to the substorm onsets by *Lazutin et al.* [2002]. The dispersionless growth of intensity is very fast – from less than one second to about several seconds. The action of the powerful mechanism of particle acceleration ~1 min before the changes of the magnetic field can explain the results of such observations.

The analysis of the part 3 of this work shows that the radial profile of the plasma pressure stable for the development of

the traditional interchange instability is formed. The results of *Stepanova et al.* [2002] of the investigation of the radial plasma pressure profile during growth phase of substorm support this conclusion. *Stepanova et al.* [2002] observe also the latitudinal asymmetry of the inverted V (or LSEA in accordance with the classification of *Newell* [2000]) structures during substorm growth phase. The most equatorward inverted V structure is the most powerful one. It contains the largest field-aligned current and field-aligned potential drop. This means that the maximal ionosphere/magnetosphere decoupling take please during substorm expansion phase on the equatorial boundary of the discrete auroral oval. The ionospheric damping of magnetospheric instabilities is considerably decreased in this region. The properties of the region of strong field-aligned current in the most equatorial inverted V structure can be considered as the proof of the existence of the azimuthal plasma pressure gradients. Therefore the modified interchange instability the source of which is the azimuthal gradient of plasma pressure can be considered as a possible mechanism of the substorm expansion phase onset. The field-aligned current determining the instability threshold in accordance with *Antonova* [2002c], *Stepanova et al.* [2002] is given by the expression

$$| j_{II}^{0} | = \frac{c}{2g^{1/2}} \frac{dW}{d\alpha} \left| \frac{k_\beta}{k_\alpha} \right| \frac{1}{W^\chi} \frac{\partial}{\partial \alpha} (p^0 W^\chi \tag{4}$$

where k_α and k_β are the coordinate of the wave vector (the Euler coordinate system (α, β, l), in which the magnetic field $\mathbf{B} = [\nabla\alpha \times \nabla\beta]$, l is the coordinate along the field line, is used), p^0 is the undisturbed plasma pressure, χ is the polytropic index, $g = \det[g_{i,k}] = \left[\frac{\partial(x,y,z)}{\partial(\alpha,\beta,l)} \right]$ is the determinant of the metric tensor. The relation of the increments of the instability in the regions of upward and downward current is

$$\frac{\gamma^{up}}{\gamma^{dawn}} = 1 + \frac{\Sigma_P T_e^{mag} k_\perp^2}{j^* e}, \tag{5}$$

where $k_\perp^2 = G_{\alpha\alpha} k_\alpha^2 + G_{\beta\beta} k_\beta^2$, $G^{ik} = \int g^{ik} g^{1/2} dl$, e is the electron charge, Σ_P is the integral ionospheric Pedersen conductivity, $j^* = e n_e^{mag} (T_e^{mag})^{1/2} / 2\pi m_e^{1/2}$, n_e^{mag} is the concentration of hot magnetospheric electrons, m_e and T_e^{mag} are the electron mass and temperature, respectively. The increment of the instability is higher when the field-aligned current has upward direction. The instability development leads to the appearance of the localized electrostatic fields. The appearance of localized electric field leads to the penetration of cold ionospheric plasma throw the boundary of the region of the acceleration of magnetospheric electrons forming the inverted V structure. Directed to the Earth cold field-aligned electron beam is formed on the boundary of inverted V. Cold field-aligned upward directed ion beam is formed simultaneously The flux in the electron beam is 1-2 orders of magnitude larger than the flux of accelerated magnetospheric electrons ($\sim 10^{10}$-10^{11} cm^{-2}s^{-1}). Electrons of the cold beam produce the thin rayed arc, intense bursts of X-rays and auroral kilometric radiation. The time scale of the process of the acceleration is less then 20 c. The thickness of the current layer is ~100 m-1 km. Current density is $\sim 10^{-4}$-10^{-3} A/m^2. The energy of electrons is ~1 keV.

The existence of very bright thin auroral forms during the time of the substorm expansion phase is supported by the results of multiple observations. The regions inside very thin lists of intense electron and ion beams and field-aligned currents can be considered as the possible regions of the acceleration of the seed population of relativistic electrons. Really, the Langmuir wave generation is the most typical effect of electron beam relaxation. The amplitudes of Langmuir waves in rayed arcs must be very high. The amplitudes of Langmuir wave of several hundred mV/m are observed by *Kintner et al.* [1995] on Frejia satellite. *Stasiewicz et al.* [1996] observe the amplitude of Langmuir wave as high as 1 V/m. The process of strong nonlinear wave-wave interactions of Langmuir waves well investigated in the laboratory plasma produces the wave spectra necessary for the quick acceleration of electrons till hundreds of keV.

The storm time relativistic electrons are accelerated deep inside the magnetosphere in the ring current region (see the review of *Friedel et al.* [2002]). The connection of the action of the mechanisms of relativistic electron acceleration with the recovery phase of the geomagnetic storm is widely accepted. The region of the formation of rayed arcs coincides with the region of auroral electrojets. The relation (1) shows that during great geomagnetic storm the region of the acceleration of relativistic electrons coincides with the lowest position of the westward electrojet center and the region of the generation of discrete forms of aurora. It is ordinarily suggested that the electron acceleration has two-step character. Substorm disturbances provide the initial seed populations of electrons with energies hundreds of keV [*Baker et al.* 1997] and then electrons are accelerated till relativistic energies. The interaction of the seed population with chorus driven and ULF waves is considered as the very probable mechanism of relativistic electron acceleration. But such mechanisms require the comparatively long time of the acceleration (~ dayes). *Tverskaya* [2000] at the same time shows that the characteristic time of the acceleration can be smaller then 1 hour. The coincidence of the region of the appearance of relativistic electrons with the region of plasma pressure maximum and therefore the magnetic field depression gives the preference for the adiabatic acceleration of the seed population The magnetic field increase due to the decay

of the ring current leads to the betatron acceleration of the seed population.

5. SUMMARY

The relativistic electrons are frequently called "satellite killers". They sporadically appear during recovery phases of magnetospheric storms. The analysis of the position and geometry of the region of the acceleration and the selection of the mechanisms responsible for the acceleration are very important for the solution of the problem. The conducted analysis shows that the near Earth part of the plasma sheet and its daytime continuation is the external part of the plasma ring surrounding the Earth. This structure can be considered as the high latitude part of the ring current. The stability of the plasma pressure distribution inside the magnetosphere during storm time is analyzed. It is shown that the suggestion of the formation of plasma pressure profile stable for the interchange disturbances give the possibility to explain the experimentally obtained dependence of D_{st}-variation from the position of auroral electrojets. The peak intensity of fluxes of relativistic electrons, which appear during storm recovery phase, is observed at the same L-shells as the lowest position of the westward electrojet center during the storm. Such dependence can help to understand the mechanisms of electron acceleration. The process of the formation of the seed population of relativistic electrons is discussed. It is suggested that the interaction of electrons with high frequency electrostatic waves inside very thin bright auroral arcs can lead to the formation of the seed population of relativistic electrons.

Acknowledgments. The work is supported by RFBR grants and the program Universities of Russia.

REFERENCES

Akasofu, S.-I., The development of the auroral substorm, *Planet. Space Sci.*, 12(4), 273-282, 1964.

Akasofu, S.-I., A source of auroral electrons and the magnetospheric substorm current systems, *J. Geophys. Res.*, 108(A4), 8006, doi:10.1029/2002JA009547, 2003.

Antonova, E.E., and N.Yu. Ganushkina, Azimuthal hot plasma pressure gradients and dawn-dusk electric field formation, *J. of Atmospheric and Solar-Terrestrial Physics*, 59(11), 1343-1354, 1997.

Antonova, E., V.F. Bashkirov and N.Yu. Ganyshkina, Quite time plasma pressure distribution in the Earth's magnetospheric trap calculated on the basis of the existing models of trapped radiation, *Radiation measurements*, 30, 523-527, 1999.

Antonova, E.E., and N.Yu. Ganushkina, Inner magnetospheric currents and their role in the magnetosphere dynamics, *Phys. Chem. Earth(C)*, 25(1-2), 23-26, 2000.

Antonova, E.E., Magnetostatic equilibrium and turbulent transport in Earth's magnetosphere: A review of experimental observation data and theoretical approach, *International Journal of Geom. and Aeronomy*, 3(2), 117-130, 2002a.

Antonova, E.E., Plasma pressure distribution in the inner magnetosphere and the applicability of Dessler-Parker-Sckopke relation to storm time magnetic disturbance description, *Adv. Space Res.*, 25(12), 2357-2360, 2000b.

Antonova, E.E., The results of INTERBALL/Tail observations, the innermagnetosphere substorm onset and particle acceleration, *Adv. Space Res.*, 30(7), 1671-1676, 2002c.

Antonova, E.E., and I.L. Ovchinnikov, Reconnection in the conditions of developed turbulence, *Adv. Space Res.*, 29(7), 1063-1068, 2002.

Baker, D.N., X. Li, J.B. Blake and S. Kanekal, Strong electron acceleration in the earth's magnetosphere, *Adv. Space Res.*, 21, 609-613, 1997.

Borovsky, J.E., and H.E. Funsten, MHD turbulence in the Earth's plasma sheet: Dynamics, dissipation and driving, *J. Geophys. Res.*, 107(A7), 1284, doi: 10.1029/2002JA009625, 2003.

Ganushkina, N.Yu., T.I. Pulkkinen, V.A. Segeev, M.V. Kubyshkina, D.N. Baker, N.E. Turner, M. Grande, B. Kellett, J. Fennell, J. Roeder, J.-A. Sauvaud and T.A. Fritz, Entry of plasma sheet particles into the inner magnetosphere as observed by Polar/CAMMICE, *J. Geophys. Res.*, 105(A11), 25205-2519, 2000.

Daglis, I.A., J.U. Kozyra, Y. Kamide, D. Vassiliadis, A.S. Sharma, M.W. Liemohn, W.D. Gonzales, B.T. Tsurutani and G. Lu, Intense space storms: Critical issues and open disputes, *J. Geophys. Res.*, 108(A5), 1208, doi:10,1029/2002JA009722, 2003.

DeMichelis, P., I.A. Daglis and G. Consolini, An average image of proton plasma pressure and of current systems in the equatorial plane derived from AMPTE/CCE-CHEM measurements, *J. Geophys. Res.*, 104(A12), 28615-28624, 1999.

Frey, H.U., S.B. Mende, S.A. Fuselier, T.J. Immel, N.Ø. Stgaard, Proton aurora in the cusp during southward IMF, *J. Geophys. Res.*, 108(A7), 1277, doi:10.10291/2003JA009861, 2003.

Friedel, R.H.W., G.D. Reeves and T. Obara, Relativistic elecron dynamics in the inner magnetosphere – a review, *J. Atmospheric and Solar-Terrestrial Physics*, 64(2), 265-282, 2002.

Fuselier, S.A., H.U. Frey, K.J. Trattner, S.B. Hende, J.L. Burch, Cusp auroral dependence on interplanetary magnetic field Bz, *J. Geophys. Res.*, 107(A7),10.1029/2001JA900165, 2002.

Hori, T., S. Ohtani, A.T.Y. Lui, R.W. McEntire, K. Maezawa, Y. Sato and T. Mukai, A substorm associated drift echo of energetic protons observed by Geotail: Radial density gradient structure, *Geophys. Res. Lett.*, 30(6), 1330, doi:10.1029/ 20002GL016137, 2003.

Iijima, T., and T.A. Potemra, The amplitude distribution of field-aligned currents at northern high latitudes observed by Triad, *J. Geophys. Res.*, 81(13), 2165-2174, 1976a.

Kadomtsev, B.B., Hydrodynamic stability of plasma, *Problems of plasma theory*, ed. M.A. Leontovich, 2, 132-176, 1963.

Kintner, P.M., J. Bonnell, S. Powell and Jan-Erik Wahlund, First results from the Frejia HF Snapshot Receiver, *Geophys. Res. Lett.*, 22(3), 287-300, 1995.

Lazutin, L., A. Korth, and T. Kozelova, Fast bursts of high energy protons and their role in triggering of the substorm onset instability, Sixth International Conference on Substorms University of Washington, Seattle, Washington, USA March 25-29, pp. 340-346, 2002.

Liou, K., C.-I. Meng, A.T.Y. Lui, P.T. Newell, M. Brittnacher, G. Parks, G.D. Reeves, R.R. Anderson and Y. Yumoto, On relative timing in substorm onset signatures, *J. Geophys. Res.*, 104(A10), 22807-22817, 1999.

Liemon, M.W., Yet another caveat to using Dessler-Prker-Sckopke relation,, *J. Geophys. Res.*, 108(A6), 1251, doi:10.1029/2003JA009839, 2003.

Lopez, R.E., D.G. Sibeck, R.W. McEntire and S.M. Krimigis, The energetic ion substorm injection boundary, *J. Geophys. Res.*, 95(A1), 109-117, 1990.

Lui, A.T.Y., R.W. McEntire and S.M. Crimigis, Evolution of the ring current during two geomagnetic storms, *J. Geophys. Res.*, 92(A7), 7459-7470, 1987.

Lui, A.T.Y., Extended consideration of a synthesis model for magnetospheric substorms, *Magnetospheric substorms*, ed. by J.R. Kan *et al.*, Geophysical Monograph 64, AGU, 43-60, 1991.

Lui, A.T.Y., and D.C. Hamilton, Radial profile of quite time magnetospheric parameters, *J. Geophys. Res.*, 97(A12), 19325-19332, 1992a.

Lui A.T.Y., H.E. Spence and D.P. Stern, Empirical modeling of the quiet time nightside magnetosphere, *J. Geophys. Res.*, 99(1), 151-157, 1994.

Lyons, R.L., Determination of relative timing of near Earth substorm onset and tail reconnection, in *Proceedings of the 5th International conference on Substorms, St. Peterburg, Russia, 16-20 May 2000, Eur. Space Agence Spec. Publ., ESA SP-443*, 255-262, 2000.

Mauk, B.H., and C.-I. Meng, Characterization of the geostationary particle signatures based on the "injection boundary" model, *J. Geophys. Res.*, 88(A4), 3055-3071, 1983a.

Mauk, B.H., and C.-I. Meng, Dynamical injections as the source of near geostationary quite time particle spatial boundaries, *J. Geophys. Res.*, 88(A12), 10011-10020, 1983b

Newell, P.T., and C.-I. Meng, Mapping the dayside ionosphere to the magnetosphere according to particle precipitation characteristics, *Geophys. Res. Lett*, 19(6), 609-612, 1992.

Newell, P.T., Reconsidering the inverted-V particle signature: Relative frequency of large-scale electron acceleration events, *J. Geophys. Res.*, 105(A7), 15779-15794, 2000.

Pulkkinen, T.I., N.Yu. Ganushkina, G.N. Baker, N.E. Turner, J.F. Fennell, J. Roeder, T.A. Fritz, M. Grande, B. Kellett and G. Kettmann, Ring current ion composition during solar minimum and rising solar activity: Polar/CAMMICE/MICS results, *J. Geophys. Res.*, 106(A9), 19131-19147, 2001.

Starkov, G.V., B.V. Rejenov, V.G. Vorobiev, Ya. I. Feldstein and L.I. Gromova, The structure of auroral precipitations in the dayside sector, *Geomagn. Aeronomy*, 42, 186-194, 2002, (in Russian).

Stasiewicz, K., B. Holback, V. Krasnoselskikh, M. Boehm, R. Bostrom and P.M. Kintner, Parametric instabilities of Langmuir waves observed by Frejia, *J. Geophys. Res.*, 101(A10), 21515-2155, 1996.

Stepanova, M.V., E.E. Antonova, J.M. Bosqued, R.A. Kovrazhkin and K.R. Aubel, Asymmetry of auroral electron precipitations and its relationship to the substorm expansion phase onset, *J. Geophys. Res.*, 107(A7), 10.1029/2001JA003503, 2002.

Tverskaya, L.V., On the boundary of electron injection into the magnetosphere, Geomagnetism and Aeronomy, 26(5), 864-865, 1986, (in Russian).

Tverskaya, L.V., Diagnosing the magnetospheric plasma structure using relativistic electron data, *Phys. Chem. Earth (C)*, 25(1-2), 39-42, 2000.

Tverskaya, L.V., N.N. Pavlov, J.B. Blake, R.S. Selesnick and J.F. Fennell, Predicting the L-position of the storm-injeced relativistic electron belt, *Adv. Space Res.*, 31(4), 1039-1044, 2003.

Tverskoy, B.A., Electric fields in the magnetosphere and the origin of trapped radiation, *Solar-Terrestrial Physics*, edited by E.R. Dyer, Dordrecht, Holland, 297-317, 1972.

Tverskoy, B.A., Formation mechanism for the structure of the magnetic storm ring current, *Geomagn. and Aeronomia*, 37(5), 555-559, 1997, (in Russian).

Wing S., and P.T. Newell, Quite time plasma sheet ion pressure contribution to Birkeland currents, *J. Geophys. Res.*, 105(A4), 7793-7802, 2000.

E.E. Antonova, Skobeltsyn Institute o Nuclear Physics Moscow State University, Moscow, 119992, Russia, e-mail: antonova@orearm.msk.ru

Energization of the Inner Magnetosphere by Solar Wind Pressure Pulses

W. William Liu

Space Science Program, Canadian Space Agency, Ottawa, Canada

Geomagnetic storms involve the entry of a prodigious amount of energy into the inner magnetosphere. Despite decades of research, there remain serious, if often overlooked, gaps in our understanding of how energy transport is effected in the storm process. A minimal theory of storm energization must explain the following observations: 1) The timescale of energization is shorter than that of radial diffusion and perhaps also convection; 2) the energization favors the ring current region ($L \leq 5$); and 3) the transferred energy is of a significant magnitude, on the order of 10^{15} J or more. Resonant magnetospheric coupling with solar wind pressure pulses has been considered in the past as a candidate mechanism for the energy transfer; however, this view has not been elaborated quantitatively to show that the mechanism is powerful enough to meet the energy requirement of a storm. In this paper, we construct a theoretical model to show that pressure pulse coupling can attain the requisite magnitude to provide for storm-time energization.

INTRODUCTION

The Dessler-Parker-Sckopke formula predicts that the inner magnetosphere experiences substantial energization during a magnetospheric storm. Quantitatively, 2.8×10^{15} J of energy is required for ring-current energization for every 100 nT of *Dst*. To appreciate the magnitude of this energy requirement, we quantify the problem in terms of the Perreault-Akasofu parameter [*Perreault and Akasofu*, 1978], which, taken by many as a proxy of reconnection energy transfer, has a typical active-time value of 2×10^{11} W [*Tanskanen et al.*, 2002]. At this rate, more than 3 hours of uninterrupted energization would be needed, just to build up the ring current to the required intensity. However, because of its earthward location, the inner magnetosphere is not ideally situated to receive energy from reconnection. The reasons are several. First, convection takes time (min ~1 h) to transport energy to the inner magnetosphere. Second, the energy transferred through reconnection is siphoned off on its way to the inner magnetosphere (by ionospheric dissipation and substorms, for example). Third, the ionosphere polarization (i.e., the region-2 current system) exerts a significant shielding effect on convection so that only a fraction of convection electric field can penetrate the inner magnetosphere. Fourth, the Alfvén layer effect deflects a large amount of charged particles, before they have a chance to reach the inner magnetosphere. These considerations expose the need for a paradigm other than reconnection which can meet the energy needs of the inner magnetosphere.

The inner magnetosphere, of late, has been seen as a more dynamic region than previously thought. For example, there is a growing belief that relativistic electrons are accelerated locally in the inner magnetosphere by ULF waves [e.g., *Liu et al.*, 1999]. The IMAGE satellite has returned tantalizing pictures of the rapidly changing plasmasphere and ring current features. All these processes require energy.

A theory of inner magnetospheric energization must meet some simple but stringent demands concerning time, space, and power. The main phase of storms suggests that ring current energization occurs over a time of hours. This rules out

The Inner Magnetosphere: Physics and Modeling
Geophysical Monograph Series 155

10.1029/155GM13

the slow radial diffusion process. Magnetospheric convection, while capable of meeting the time requirements, suffer the drawback that the increase in cross-tail potential drop, the limit to energization, rarely exceeds a factor of two above the average, whereas ring current energy density can increase by two orders of magnitude. On spatial requirement, the energization mechanism should be invulnerable to 'poaching' by outer regions of the magnetosphere, i.e., it should deliver energy preferentially to the inner magnetosphere. In terms of power, the mechanism should have enough capacity to generate energy on the order 10^{15} J.

The paradigm which best meets these requirements is the so-called pressure pulse model [*Sibeck*, 1989, 1990; *Lee and Lysak*, 1989; *Southwood and Kivelson*, 1990; *Lysak and Lee*, 1992]. The basic reasoning of the pressure pulse model is simple: As the solar wind experiences an increase in dynamic pressure, it does work on the magnetosphere, and leads to an internal energy gain in the magnetosphere. Empirically, the pressure pulse model is supported by the observation of correlation between storms and large solar wind dynamic pressure events. However, compression is only a necessary first, but not sufficient step. The idea of work against the magnetosphere does not solve the key problem of energy retention; that is, as the magnetosphere rebounds, it will do work against the solar wind, giving back whatever energy it has gained in the compressional phase. Consequently, there ought to be some irreversible element leading to the absorption of energy by the magnetosphere.

Field line resonance is invoked to facilitate the requisite energy retention (absorption). It is postulated that the buffeting of the magnetopause launches compressional MHD waves toward the inner magnetosphere. At locations where the compressional wave frequency matches that of the standing Alfvén mode of the field line, a resonant conversion of energy from compression to shear oscillation takes place [*Southwood*, 1974; *Chen and Hasegawa*, 1974]. The shear mode, with its Poynting flux parallel to the closed magnetic field, can be considered an energy sink, since the energy flow path does not intersect the solar wind. The proposed scenario is fast, as the fast-mode speed, greatly exceeding radial diffusion and convection in alacrity, controls the rate of energization. The resonant interaction favors locations well inside the magnetopause. The question whether the mechanism is powerful enough is of a quantitative nature and will be dealt with presently. We will develop a simple, but instructive, theoretical model to provide some initial answers in quantitative terms; in so doing, we intend to establish the feasibility of pressure pulse absorption as a major energy source of magnetic storms.

MODEL

A one-dimensional Radoski-type [*Radoski*, 1971] model is used to represent the magnetosphere. The magnetic field is uniform and straight. The plasma inside the magnetosphere is cold. As an extension to the most common version of this model [see, for example, *Zhu and Kivelson*, 1989], we add two regions adjacent to the magnetosphere (see Figure 1). On the left-hand side of the magnetopause, we add a uniform, warm solar wind with the plasma density n_0, temperature T_0, and magnetic field B_0. Within the magnetosphere, the temperature is zero, and the plasma density varies linearly as

$$n_m(x) = 1 - x \tag{1}$$

The decrease of density toward Earth is used to compensate for the constant magnetic field restriction of the box model.

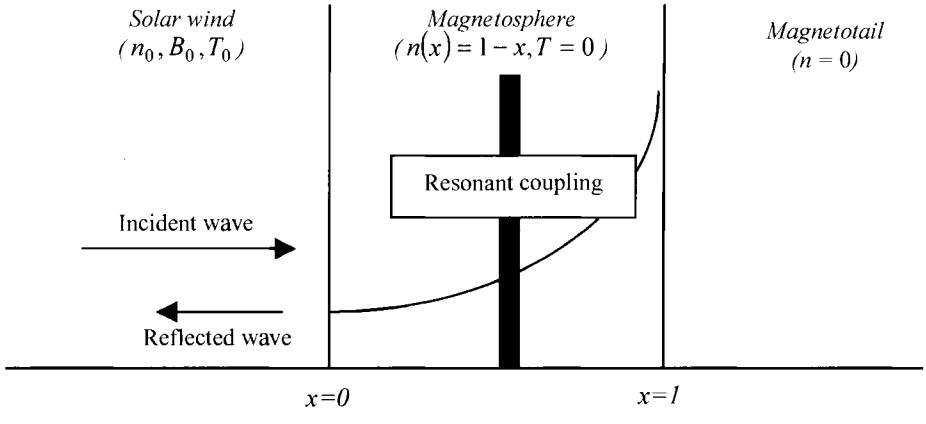

Figure 1. The box model used to calculate the energy absorption. Resonant interaction results in part of the compressional wave incident from the solar being converted to the shear Alfvén mode in the shaded column. The difference between the incident and reflected wave amplitudes indicates the strength of energy absorption.

The goal is to achieve a Alfvén speed profile that is increasing toward Earth. For the magnetotail region ($x > 1$), we choose $n = 0$. In writing (1), we have normalized the magnetospheric density at the magnetopause ($x = 0$) as 1, as well as the distance between the subsolar point and Earth ($x = 1$). With the freedom to set a velocity unit, we choose the Alfvén speed on the magnetospheric side of the subsolar point to be 1. Under this normalization scheme, time is expressed in the physical unit of $L_0/v_A(0)$, where L_0 is the physical distance of the subsolar point, and $v_A(0)$ the physical value of Alfvén speed at the subsolar point. In the zeroth order, the total pressure is balanced across the magnetopause, giving,

$$2n_0T_0 + B_0^2 = 1 \tag{2}$$

where we have set physical constants k and μ_0 equal to unity.

Taking z axis to be upward and y axis to be dawnward, we consider the case where a compressional wave of the form $\delta x = \delta x_> \exp(ik_z z + ik_y y + ik_x x - i\omega t)$ is incident on the magnetopause from the solar wind, where δx is the longitudinal plasma displacement associated with the wave, and the subscript $>$ indicates the wave is right-going. Upon interaction with the magnetopause and the dayside magnetosphere, there is a reflected compressional wave traveling in the opposite (left) direction, $\delta x_< = \exp(ik_z z + ik_y y - ik_x x - i\omega t)$. The overall solution in the solar wind is the linear sum of the two wavelets. The fast-mode dispersion relation in the solar wind gives the following relationship

$$k_x = \left[\frac{\omega^4 - k_\perp^2 v_{f0}^2 \omega^2 + k_z^4 v_{s0}^2 v_{A0}^2}{\omega^2 v_{f0}^2}\right]^{1/2} \tag{3}$$

where $k_\perp^2 = k_y^2 + k_z^2$ and v_s, v_A, and v_f denote sound, Alfvén, and fast speed in the solar wind, respectively. In contrast, in the magnetotail region ($x > 1$), the Alfvén speed is infinite, and the wave solution is evanescent, $\delta x = \delta x_T \exp(-k_\perp x)$. In the magnetosphere, there is usually a quantization on k_z, in order to satisfy the ionospheric boundary condition. This effect can be accommodated into the present theory without any change on the formalism or on the main conclusions (except k_z can only take discrete values). This consideration is taken to be implicitly understood in the following discussion.

By construction, our model has the absorption of solar wind pressure pulses occurring only in the dayside magnetosphere, $0 < x \leq 1$, a reasonable first approximation given the expectation that most energy absorption should occur on the dayside. To an observer standing at the left end of the system, a measurement of the amplitudes of the right-going (incident) and left-going (reflected) waves will generally yield a smaller $\delta x_<$ than $\delta x_>$, the difference being the result of resonant energy conversion to the shear mode in the magnetosphere. On a relative basis, we define

$$K = 1 - \left|\frac{\delta x_<}{\delta x_>}\right|^2 \tag{4}$$

as the energy absorption coefficient, which measures the fraction of incident pressure-pulse energy that is absorbed by the magnetosphere.

In the dayside magnetosphere, the differential equation describing the magnetic field perturbation b_z is

$$\frac{\partial}{\partial x}\left[\frac{1}{\omega^2(1-x) - k_z^2}\frac{\partial b_z}{\partial x}\right] + \frac{\omega^2(1-x) - k_\perp^2}{\omega^2(1-x) - k_z^2} b_z = 0 \tag{5}$$

with the plasma displacement given by

$$\delta x = \frac{1}{\omega^2(1-x) - k_z^2}\frac{\partial b_z}{\partial x} \tag{6}$$

The numerical solution of (5) has been treated by a number of authors before (see *Zhu and Kivelson*, [1989], and references therein). Without repeating the mathematical procedure, we note that there are two independent solutions to (5), one regular at the resonant point, $x_r = 1 - k_z^2/\omega^2$, and the other having a logarithmic singularity. As demonstrated by *Southwood* [1974], the mathematical singularity has the physical significance of a mode conversion, whereby some of the compressional energy is absorbed into shear oscillations of field lines.

The procedure of finding the energy absorption coefficient K is described below. We start from the rightmost region (the model magnetotail), with an evanescent solution $b_z = b_T \exp(-k_\perp x)$. At $x = 1$, both b_z and its first derivative must continue into the dayside magnetosphere. The first continuity results from the requirement that the total pressure perturbation in the cold plasma, $b_z/2$, must be balanced on the two sides, and the second continuity from the fact that normal plasma motion is equal on the two sides (see (6)). These continuity conditions will lead to the solution of the coefficients of the two independent solutions of (5). At the magnetopause ($x = 0$), the continuity of total pressure changes slightly in form, because the solar wind has a finite pressure. After some manipulation, we obtain

$$-\frac{(\gamma p_0 + B_0^2)\omega^2(\omega^2 - k_z^2 v_{A0}^2)}{\omega^4 - k_\perp^2 v_{f0}^2 \omega^2 + k_z^2 v_{s0}^2 v_{A0}^2}\frac{\partial \delta x}{\partial x} = b_z \tag{7}$$

where the left and right-hand sides of the equation are evaluated on the solar wind and magnetospheric sides, respectively. Recall that δx in the solar wind is the sum of $\delta x_>$ and $\delta x_<$. The application of the two continuity conditions, of displacement and total pressure, will lead to the solution of $\delta x_>$ and $\delta x_<$ in terms, ultimately, of the magnetotail amplitude b_T. In forming the ratio $\delta x_</\delta x_>$, b_T is eliminated, and the energy absorption coefficient is thus shown to be uniquely determined by incident wave frequency (ω), wavenumbers (k_y and k_z), and solar wind and magnetospheric parameters.

ENERGY ABSORPTION SPECTRUM

In Figure 2, we show the energy absorption coefficient as a function of wave frequency and wavenumbers. The most striking feature is the pronounced concentration of absorption in two narrow high-absorption bands (additional, weaker bands are present, if the plot is extended in frequency range). A closer examination reveals that, within these bands, the absorption coefficient attains very high values. For example, the maximum in the primary band in Figure 2 has a value of 0.73; that is, 73% of the free energy embedded in a solar wind pressure pulse at the corresponding frequency-wavenumber combination will be absorbed by the magnetosphere. The discrete band structure is in stark contrast to the absorption coefficient shown in *Kivelson and Southwood* [1986], who used the method *Budden* [1961] developed for ionospheric wave absorption to obtain a magnetospheric absorption spectrum by analogy. The spectrum of *Kivelson and Southwood* [1986] has a broad distribution, with a single maximum 0.5. The difference of our result from *Kivelson and Southwood* [1986] relates to the fact that our model magnetosphere has a finite size and is limited by boundaries at $x = 0$ and 1, whereas the Kivelson-Southwood model assumes effectively a magnetosphere of infinite size. The delimitation of the magnetosphere resulted in quasi-eigenmodes of absorption, whereby waves bouncing back and forth between boundary points give rise to strong absorption where there is a constructive interference at the resonant point.

It is instructive to consider the frequency of the primary maximum absorption in physical unit. For a subsolar distance 10 R_E, and a typical Alfvén speed of 1000 km/s we find the normalization unit of frequency $f_0 = v_A(0)/2\pi R_s = 2.4$ mHz. Referring to Figure 2, we find that significant absorption occurs for $\omega \geq 3$, which in physical unit corresponds to the first maximum at $f \approx 8$ mHz. This is consistent with the observation of the Alfvén continuum on the dayside [*Waters et al.*, 1995]. The characteristic diurnal variation observed in the Alfvén continuum (the maximum frequency decreases away from noon) is strictly beyond the description by a 1D theory, but the following conjecture might be useful. In a realistic magnetosphere, the size of the magnetospheric cavity increases from noon to the flanks; this means that the fundamental frequency of the cavity mode decreases toward the dawn and dusk sector. For a theory based on a normalized unit, this means that the frequency unit in Figure 2 decreases as one moves away from

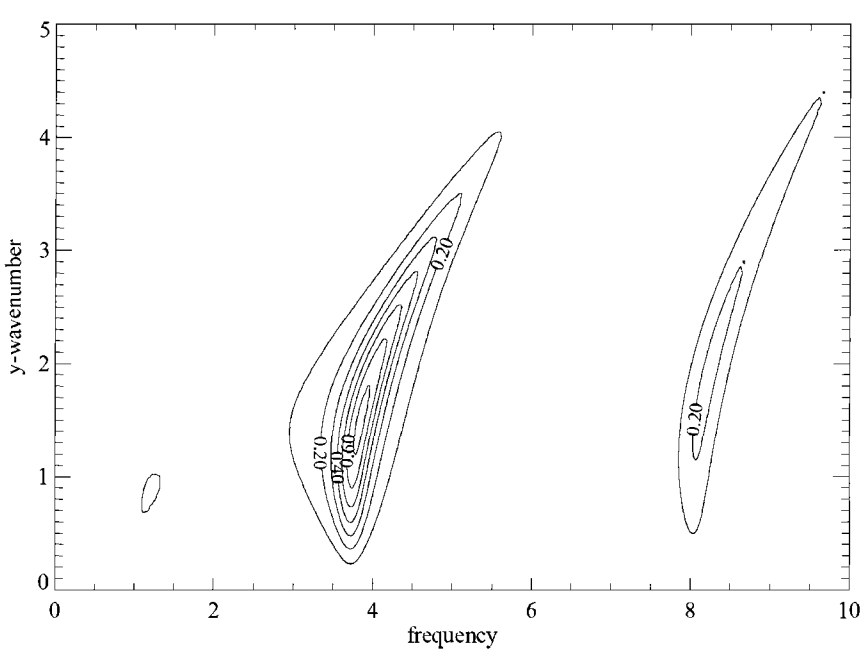

Figure 2. Energy absorption as a function of frequency ω and wavenumber k_y. The fixed parameters in the plot are $k_z = 1$, $n_0 = 5$, and $\beta_0 = 2n_0T_0/B_0^2 = 10$. The frequency and wave numbers are normalized according to the discussion in the text.

noon, resulting in a shift of the absorption spectrum to smaller frequencies in physical unit. This shift is consistent with the observed diurnal variation of the Alfvén continuum.

DISCUSSION

Although the 1D geometry used in our model is idealized, historically this geometry has played a very important role in elucidating the physics of global MHD waves in the magnetosphere. Likewise, we believe that the present model has captured certain fundamental physics to warrant further discussion in relation to inner magnetospheric dynamics.

Our results support the notion that pressure-pulse coupling is a faster and potentially more powerful mechanism to energize the inner magnetosphere than convective transport associated enhanced reconnection. The mechanism is expected to be faster, because compressional waves associated with pressure pulses travel at a faster speed than that of convection and have a much shorter distance to cover. The strength of pressure pulse coupling is manifested in the high energy absorption coefficient that can be achieved in the absorption bands. As a comparison, we note that the typical rate of energy transfer attributed to reconnection has a magnitude of about 2%. This estimate is based on the Perreault-Akasofu parameter ε divided by the solar wind bulk flow energy flux integrated over the magnetospheric cross section intercepting the solar wind. Although high rate of absorption occurs only in restricted bands in the pressure coupling theory, there can be special circumstances in which the solar wind energy spectrum matches the absorption, resulting in anomalous energy transfer. A more interesting and broadly applicable scenario, however, is a solar wind bulk pressure enhancement of arbitrary shape and a limited duration (i.e., a pulse). Although, under this condition, the average energy absorption coefficient will be lower than the maxima in Figure 2, there is still a significant amount of energy that can be transferred. It can be shown that the total energy coupled into the magnetosphere is

$$E = C\int |p(\omega)|^2 K(\omega)\, d\omega \tag{8}$$

where C is a constant. The time-averaged absorption coefficient K is given by

$$\langle K\rangle = \frac{\int |p(\omega)|^2 K(\omega)\, d\omega}{\int |p(\omega)|^2 d\omega} \tag{9}$$

We consider a pressure pulse of a form represented by,

$$\Delta p = \Delta p_0 \exp\,[-t/\tau + ik_y y + ik_z z];\ t \geq 0 \tag{10}$$

with $k_y = k_z = 1$. The Fourier transform of (10) is

$$|p(\omega)|^2 = \frac{C'}{1+\omega^2\tau^2} \tag{11}$$

Suppose the energy flux enhancement is ΔF_0. It can be shown that the total energy transfer is given by

$$E = \frac{1}{2}\Delta F_0 A_m \langle K\rangle \tau \tag{12}$$

where A_m is the cross-section area of the magnetosphere perpendicular to the solar wind flow. Consider a typical event in which the solar wind speed increases from 400 km/s to a peak of 600 km/s, and the density increases from 5 cm^{-3} to a peak of 10 cm^{-3}. The peak energy flux enhancement for this hypothetical event is 3.3×10^{-3} J · $m^{-2} \cdot s^{-1}$. Assuming a magnetospheric cross-sectional area of 4×10^{16} m^2 (equivalent to a tail radius of about 17 R_E), we calculate and plot the resulting energy transfer as a function of τ in Figure 3. It is seen that, after a sharp rise, the total energy absorption function asymptotes to a constant value of about 2.1×10^{14} J. There is no apparent advantage to have long-duration events (τ large), since such events would have wave-energy concentrated in low frequencies far off the absorption maxima, offsetting the advantage of more integrated incident energy. Also shown in Figure 3 is the average energy absorption coefficient $\langle K\rangle$, which as expected, falls off as τ tends to large values.

It is interesting to note that the proposed coupling mechanism operates mainly in the inner magnetosphere, as the maximal coupling occurs well inside the magnetopause. Our geometrical simplification, however, does not permit us to pinpoint the exact location of maximal energy absorption. A rough comparison with empirical work can help constrain the location. *Waters et al.* [1995] found that the primary absorption peak identified here (~8 mHz) is located near the CANOPUS Gillam station. On the dayside Gillam maps to a distance of between 5 and 6 R_E [Eric Donovan, private communications]. It is further noted that, since the absorption bands shown in Figure 2 are narrow, the radial distribution of energy, at least initially, is expected to concentrate in a fairly restrictive range.

The numerical value of energy absorption in Figure 3 for a typical event is interesting and warrants further comment. Apparently, the amount of energy is about one-tenth of that required to generate a 100 nT *Dst* event (the value will be greater, if we assume a stronger solar wind event than the fairly moderate pressure enhancement used here). Therefore, one single pressure pulse, at least according to our theory, cannot cause a major storm. As suggested in Figure 3, prolonging the event will not help the matter. We note, however, that it is

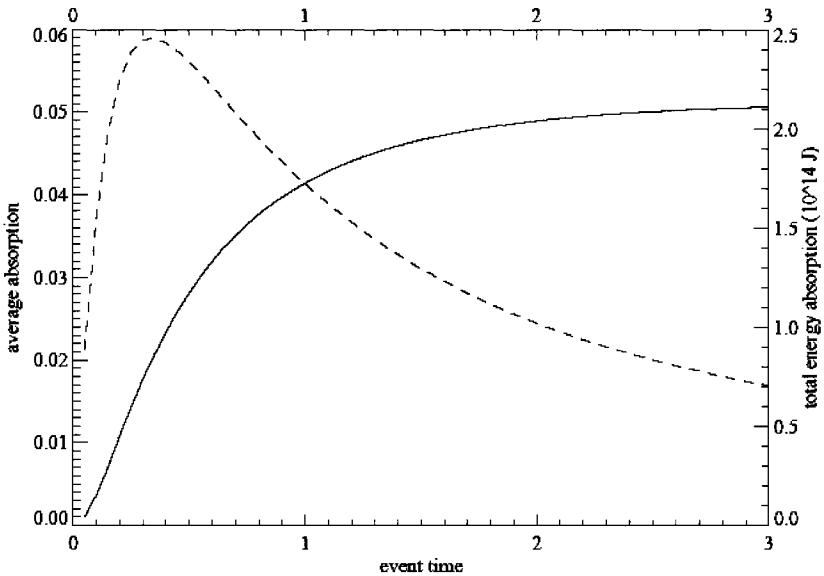

Figure 3. Total energy absorption (solid) and time-averaged energy absorption coefficient (dashed) for an exponential pressure pulse. The time unit is approximately 1 min.

generally the case that a major solar wind perturbation contains more than just one pulses. If the magnetopause is impacted by a series of 10 or more pulses of the kind used to produce Figure 3, a major storm results as a product of cumulative action. This logic leads us to suggest that stronger storms are more likely to result from spiky solar wind pressure variations than for a monolithic one-up-one-down affair. This suggestion can be tested against observations. To the extent that the main-phase profile of *Dst* serves as a proxy of ring-current energization, we observe that the energy build-up takes several hours to reach the maximum; this seems to favor multiple pulses spanning over several hours, than a single pulsing action.

We point out that the average energy absorption coefficient, in the range shown in Figure 3, is comparable to or larger than the typical reconnection rate, calculated by dividing the Perreault-Akasofu parameter with the integrated energy flux on the magnetopause. This suggests that pressure pulse coupling can rival reconnection as an energy source to the magnetosphere, when solar wind perturbations are comparable to quiet-time base values.

We have not addressed the question how the absorbed energy, in the form of shear Alfven waves initially, is further degraded to ring current particle energy, which is what ultimately accounts for *Dst*. In order for our theory to work as intended, this conversion should occur on the timescale of the main phase. There exists theoretical work showing that such transfer is possible [e.g., *Liu and Rostoker,* 1995]. We will consider the problem in detail as part of a future simulation study.

CONCLUSION

We have demonstrated that resonant interaction between solar wind pressure pulses and the magnetosphere can supply the energy need of a magnetic storm. Qualitatively, the coupling is fast (controlled by MHD wave speeds in the magnetosphere, instead of the slower convection speed or glacial radial diffusion), correlates well with known precursors to geomagnetic storms (large fluctuations in solar wind dynamic pressure), and concentrates energy in the inner magnetosphere where it is needed. The major original contributions of this research are quantitative calculation and discussions surrounding Figures 2 and 3. We showed that the so-called energy absorption efficiency is high (at more than 2×10^{14} J per pulse), though not high enough for a single pressure pulse to supply the energy need of a major storm. Consequently, we suggested that a major storm is a product of the cumulative work of a series of pressure pulses.

Acknowledgments. The author thanks David Sibeck, Eric Donovan and Robert Rankin for discussions during the course of this research.

REFERENCES

Budden, K., *Radio Waves in the Ionosphere*, p. 4479, Cambridge University Press, New York, 1962.

Chen, L., and A. Hasegawa, A theory of long-period magnetic pulsations 2. Impulse excitation of surface eigenmode, *J. Geophys. Res.*, 79, 1033, 1974.

Kivelson, M.G., J. Etcheto, and J. Trotignon, Global compressional oscillations of the terrestrial magnetosphere, The evidence and a model, *J. Geosphys. Res.*, 89, 9851, 1984.

Kivelson, M.G., and D.J. Southwood, Coupling of global magnetospheric MHD eigenmodes to field line resonances, *J. Geophys. Res.*, 91, 4345, 1986.

Lee, D.H., and R.L. Lysak, Magnetospheric ULF wave coupling in the dipole model: the impulsive excitation, *J. Geophys. Res.*, 94, 17,097, 1989.

Liu, W.W., G. Rostoker, and D.N. Baker, Internal acceleration of relativistic electrons by large-amplitude ULF pulsations, *J. Geophys. Res.*, 104, 17391, 1999.

Liu, W.W., and G. Rostoker, Energization of ring-current particles by recurring substorm cycles, *J. G.eophys. Res.*,100, 21,897, 1995.

Lysak, R.L., and D.-H. Lee, Response of the dipole magnetosphere to pressure pulses, *Geophys. Res. Lett.*, 19, 937, 1992.

Perreault, P., and S.I. Akasofu, A study of geomagnetic storms, *Geophys. J.R. Astr. Soc.* 54, 547, 1978.

Radoski, H.R., A note on the problem of hydromagnetic resonances in the magnetosphere, *Planet Space Sci.*, 19, 1012, 1971.

Sibeck, D.G., A model for the transient magnetospheric response to sudden solar wind dynamic pressure variations, *J. Geophys. Res.*, 95, 3755, 1990.

Sibeck, D.G., W. Baumjohann, and R.E., Lopez, Solar wind dynamic pressure variations and transient magnetospheric signatures, *Geophys. Res. Lett.*, 16, 13, 1989.

Southwood, D.J., Some features of field line resonances in the magnetosphere, *Planet. Space Sci.*, 22, 482, 1974.

Southwood, D.J., and M.G. Kivelson, The magnetohydrodynamic response of the magnetospheric cavity to changes in the solar wind pressure, *J. Geophys. Res.*, 95, 2301, 1990.

Tanskanen, E.I., T.I. Pulkkinen, H.E.J. Koskinen, and J.A. Sauvaud, Substorm energy budget near solar minimum and maximum, 1997 and 1999 compared, *J. Geophys. Res.*, 107(A7), 1086, doi:10.1029/2001JA900153, 2002.

Waters, C.L., J.C. Samson, and E.F. Donovan, The temporal variation of the frequency of high-latitude field line resonances, *J. Geophys. Res.*, 100, 7987, 1995.

Zhu, X., and M.G., Kivelson, Analytical formulation and quantitative solutions of the coupled ULF problem, *J. Geophys. Res.*, 93, 8602, 1989.

W. William Liu, Space Science Program, Canadian Space Agency, 100 Sussex Dr, Ottawa, Ontario K1L 8E3, Canada.

Energetic Trapped Proton and Electron Flux Variations at Low Altitudes Measured Onboard CORONAS-F Satellite During 2001, August-December, Their Connection with the Particle Flux Variations in Geostationary Orbit

Sergey N. Kuznetsov and Irina N. Myagkova

Skobeltsyn Institute of Nuclear Physics, Lomonosov Moscow State University, Moscow, Russia.

Trapped energetic particle variations at altitudes of ~500 km were studied using data obtained in the experiment onboard the «CORONAS-F» satellite (launched in July, 2001). Results of analysis of proton (1-5 MeV) and electron (0.6-1.5 MeV) flux variations at different L-shells (from 3 to 5.5) from August to December, 2001 are presented. Connection of these particle flux variations with particle flux dynamics measured onboard the «GOES» satellite were analysed. We found strong correlation between proton fluxes measured onboard the «CORONAS-F» satellite and ones measured onboard the «GOES» satellite without any time lag and significant correlation during quiet time periods for electron flux with different time lag for different L-shell values (about 5 days for $L = 3$ and about 1 day for L from 4 to 5).

1. INTRODUCTION

The Earth's radiation belts dynamics is important for the near-Earth's space environment. The energetic particle population trapped in the Earth's radiation belts is known to be highly variable. Now it is commonly accepted that the main energetic particle sources are located near the last closed L-shell trajectory. There is a lot of publications on this problem. For example, in [*Baker*, 1987] it was shown that fluxes of electrons with the energies of some hundreds keV in geostationary orbit correlated with solar wind flow speed V for the time interval from 1979 to 1985. We have reported about similar studies of electron ($E_e > 2$ MeV) and proton ($E_p > 1$ MeV) fluxes measured onboard the «GOES» satellite during 1986-1997 in [*Kuznetsov*, 2002a]. The connection between electron ($E_e = 100$ keV) fluxes measured at $L = 4$-6 in the experiment onboard the «Electron» satellite during one year (1964) was studied in [*Kuznetsov*, 1968]. It was shown that the best correlation between electron flux variations at $L = 4$ and $L = 6$ was obtained with time lag of ~5 days (variations at $L = 4$ were observed later than at $L = 6$).

We have investigated the variations of energetic trapped protons (1-4.5 MeV) and electrons (> 2 MeV) measured in the experiment onboard the «CORONAS-I» satellite, the first satellite of «CORONAS» satellites series, with the altitude ~500 km and inclination ~83 degrees [*Kuznetsov*, 2002b]. We have found the correlation between electron fluxes measured onboard the «CORONAS-I» satellite and those measured onboard the «GOES» satellite with different time lag for different L-shell values (about 5 days for $L = 3.5$ and about 1 day for L from 4 to 5). For proton any correlation was not found So it is clear that this problem has not been solved yet.

2. EXPERIMENTAL DATA

The energetic trapped proton and electron flux variations obtained in the experiment onboard the «CORONAS-F» satellite during August-December 2001 are investigated. The Russian solar space observatory «CORONAS-F», the second

The Inner Magnetosphere: Physics and Modeling
Geophysical Monograph Series 155

10.1029/155GM14

satellite of «CORONAS» series, was launched on July 31, 1994 into a circular orbit with altitude of 500 km and a 83° inclination. The satellite is oriented towards the Sun and is equipped with a set of instruments for studies of solar flares and corresponding SEP phenomena [*Kuznetsov*, 2002b]. Protons (E_p = 1-5 MeV) and electrons (E_e = 0.6-1.5), which were used for the analysis in this paper, were measured by the instrument with the geometry factor $G = 0.65$ cm^2 sr. The charged particle detectors were oriented during the measurements in anti-Sunward direction. The trapped electron and proton fluxes were measured at L = 3; 3.5; 4; 4.5; 5 and 5.5 only in the Southern hemisphere (above the Southern part of the Atlantic Ocean) for one, two or three successive orbits. We use only those parts of the «CORONAS-F» satellite's orbits where measured particles were really trapped - the magnetic field B in 500 km (the altitude of the «CORONAS-F» satellite's orbit) for chosen parts should be smaller than minimal B_0 for this L in altitude 100 km.

We also use for our analysis the electron ($E_e > 2$ MeV) and proton ($E_p > 1$ MeV and $E_p > 10$ MeV) flux variations measured onboard the «GOES-10» satellite. These data are presented in the Space Physics Interactive Data Resource database from 1986 up to the present time.

The figures 1 and 2 show the variations of proton flux (E_p = 1-5 MeV) and of electron one (E_e = 0.6-1.5 MeV) measured onboard the «CORONAS-F» satellite at L = 3.5, 4.5 and 5.5 during August-December 1, 2001, and variations of proton flux ($E_p > 1$ MeV and > 10 MeV) and electron one ($E_e > 2$ MeV) measured during the same time interval onboard the «GOES» satellite. All used data have been averaged over a one day time period are presented.

3. RESULTS

We examine the correlation between trapped particle fluxes measured onboard «CORONAS-F» and «GOES» for electrons and protons using different time lags between the particle flux values obtained at the geostationary altitudes and ones measured deep inside the radiation belts. The fact that we search for the correlation between the particles with the same energies

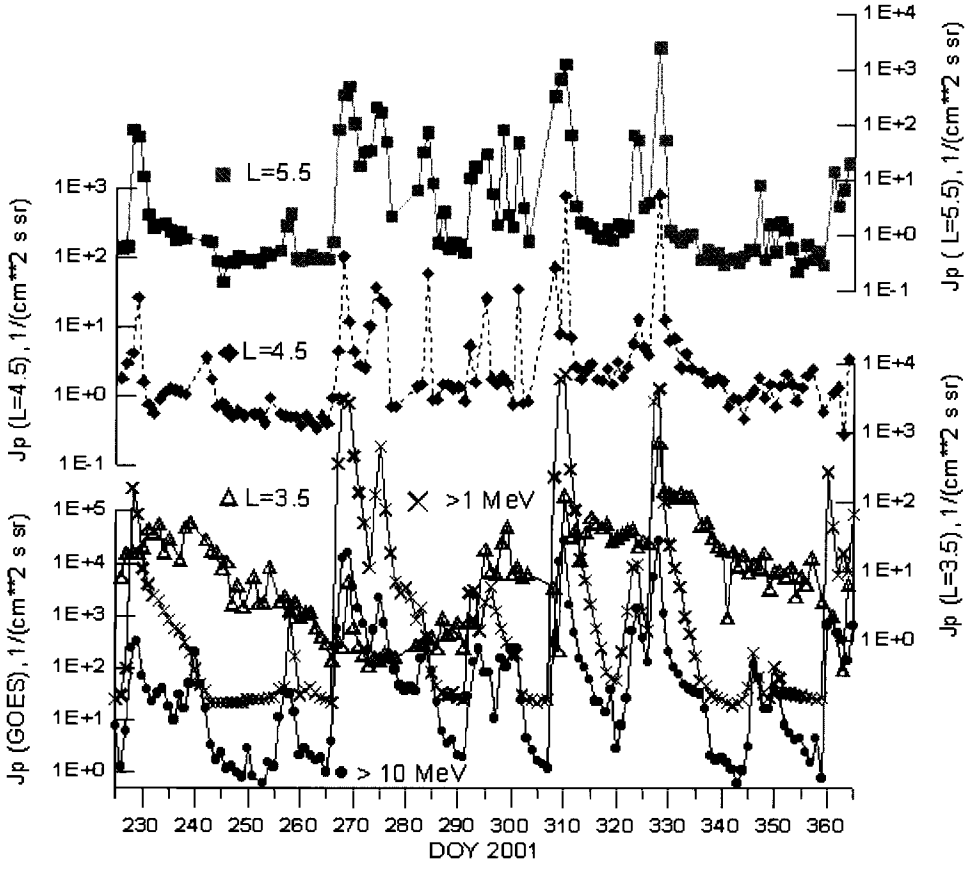

Figure 1. The proton (E_p = 1-5 MeV) flux variations measured in the experiment onboard the «CORONAS-F» satellite at L = 3.5 (open triangles), 4.5 (closed diamonds), 5.5 (closed grey squares) during 2001, August-December 2001 and those measured onboard «GOES-10» satellite for >1 MeV (closed circles) and >10 MeV (crosses).

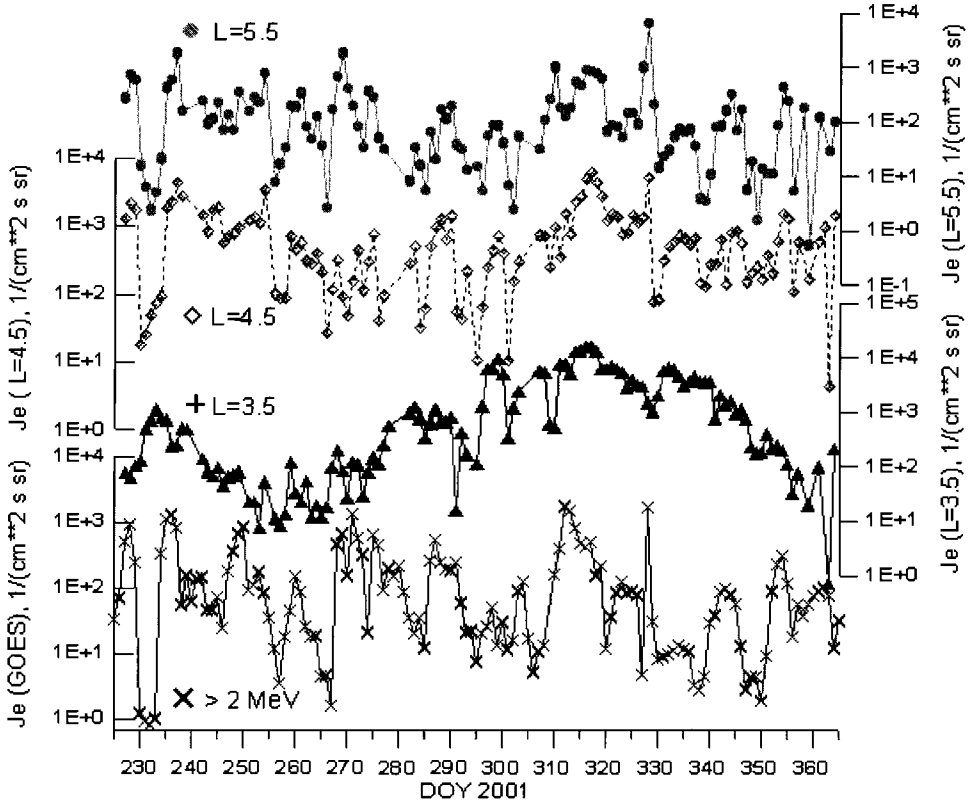

Figure 2. The electron (E_e = 0.6-1.5 MeV) flux variations measured in the experiment onboard the «CORONAS-F» satellite at L = 3.5 (closed triangles), 4.5 (open diamonds), 5.5 (closed circles) during August-December 2001 and those measured onboard the «GOES-10» satellite for > 2 MeV (crosses).

is one of the difficulties of our analysis. The variations of the proton fluxes with the energies E_p = 1 MeV at L = 3 should be connected with the variations of the protons with the energies E_p = 100 keV at L = 6.6; and the variations of the electrons with the energies E_e = 600 keV at L = 3 should be connected with those of the electrons with the energies about E_e = 85 keV at L = 6.6 due to the diffusion across the drift shells. Only under the assumption that the particle spectrum in the source was constant (or its changes were small) our analysis is possible. We recognize that this underlying assumption may only be necessary for the present limited analysis.

We have searched for the correlation between charged particle fluxes measured onboard the «GOES» satellite and ones variations measure onboard the «CORONAS-F» at different L-shells using different time lags. The correlation analysis permit us to estimate this correlation numerically.

The correlation coefficients of proton and electron flux measured onboard the «CORONAS-F» and the «GOES» satellites obtained using different time lags are presented in Figure 3. The correlation coefficients for L = 3 are marked as closed grey triangles, for L = 3.5 – as open triangles, for L = 4 – as open diamonds, for L = 4.5 – as closed diamonds, for L = 5 – as open squares and for L = 5.5 – as closed grey squares.

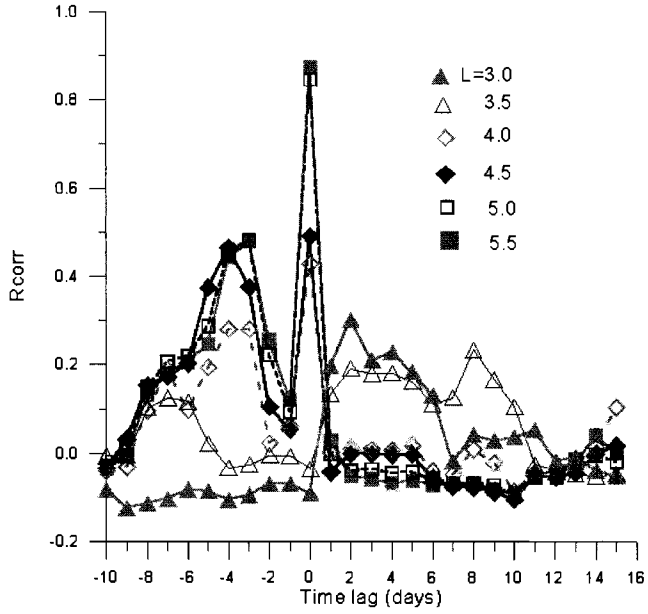

Figure 3. The correlation coefficients between proton flux variations measured onboard the «CORONAS-F» satellite at L = 3 (closed circles), L = 3.5 (open circles), L = 4 (closed diamonds) L = 4.5 (open diamonds), L = 5 (closed squares) and L = 5.5 (open squares) and onboard the «GOES» one.

Table 1. The Correlation Coefficients between the Proton (E_p = 1-5 MeV) Flux Variation Onboard the «CORONAS-F» Satellite at the Different L-shells and those Measured Onboard the «GOES» Satellite.

Time Period	Rcorr for p at L = 3, %	Rcorr for p at L = 3.5, %
September, 24-October, 2	67	76
November, 4-November, 13	75	77
November, 23-December, 2	96	98

The time lags are positive if data onboard the «CORONAS-F» satellites were obtained later than onboard the «GOES» satellite. From Figure 3 we can see the strong correlation for trapped protons with the energies 1-5 MeV measured onboard the «CORONAS-F» and ones (E_p > 1 MeV) measured onboard the «GOES» satellite at L > 3.5 (without any time lag) during all time period 2001, August-December and even at L = 3.0 and 3.5 for some time periods during and after strong magnetic storms (see Table 1.) We assume that founded correlation of proton fluxes with zero time lag is a consequence of the rapid injection of solar energetic particles inside the Earth's magnetosphere during strong magnetic storms connected with large solar flares. Figure 1 shows that the strongest correlation for protons with energies > 1 MeV exists when SEP are observed (see protons E_p > 10 MeV in Figure 1).

Comparing Figures 1 and 2 we can see the significant difference in the results obtained for the proton and electron flux variations. In contrast to the strong correlation finding for energetic proton fluxes, Fig. 4 shows that the electron (E_e = 0.6–1.5 MeV) fluxes measured onboard the «CORONAS-F» satellite at different L-shells correlate with ones measured onboard the «GOES» satellite significantly worse. Strong correlation (without any time lag) was found for trapped electrons measured onboard the «CORONAS-F» with electrons measured onboard the «GOES» satellite at L = 4 and higher L-shells (R_{corr} = 0.7 for L = 4 and R_{corr} > 0.95 for L = 4.5, 5 and 5.5) only for rather short time period 2001, November, 22-26 during strong magnetic disturbances (Dst = −221 nT).

To investigate more exactly the correlation between electron fluxes onboard the «CORONAS-F» and the «GOES» satellites we excluded time periods when SEP fluxes (E_p > 10 MeV) were higher when 100 (cm^2 s sr)$^{-1}$. Obtained correlation coefficients with different time lags during the quiet time periods are presented in Figure 5. We have found that electron flux variations measured onboard the «CORONAS-F» at L = 3 and 3.5 are delayed in comparison with ones measured onboard the «GOES» with time lags ~5 and ~3 days. We assume that time lags Δt_i of electron flux variations measured at low L in comparison with ones in the source at L_0 can be expressed as

$$\Delta t_i = (L_0/L_i)^n \quad (1)$$

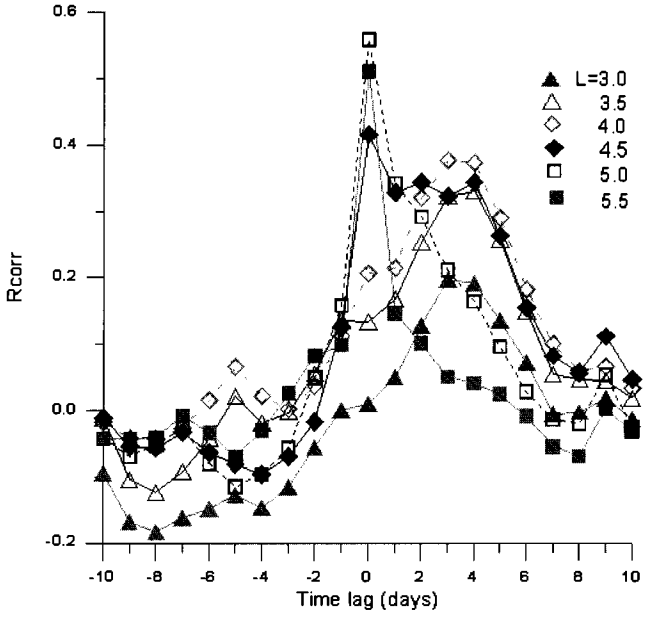

Figure 4. The correlation coefficients between electron flux variations measured onboard the «CORONAS-F» satellite at L = 3 (closed circles), L = 3.5 (open circles), L = 4 (closed diamonds) L = 4.5 (open diamonds), L = 5 (closed squares) and L = 5.5 (open squares) and onboard the «GOES» one.

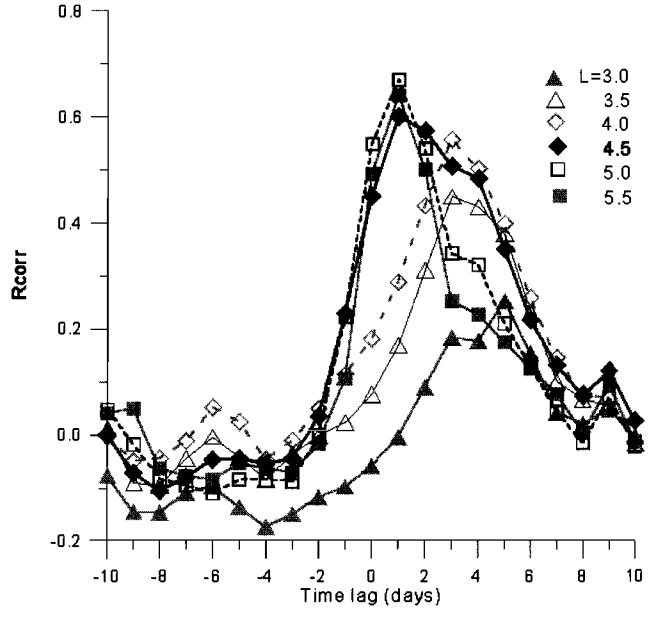

Figure 5. The correlation coefficients between proton flux variations measured in quiet time onboard the «CORONAS-F» satellite at L = 3 (closed circles), L = 3.5 (open circles), L = 4 (closed diamonds) L = 4.5 (open diamonds), L = 5 (closed squares) and L = 5.5 (open squares) and onboard the «GOES» one.

Table 2. The Best Correlation Coefficients between the Electron Flux Variation Onboard the «CORONAS-F» Satellite at the Different L-shells and those Measured Onboard the «GOES» Satellite and their Time Lags (Experimental and Calculated).

L	3	3.5	4	4.5	5	5.5
R_{corr}(CORONAS-F-GOES), %	25	45	56	60	72	67
Δt_{ie} (CORONAS-GOES), days	5	3	3	1	1	1
Δt_{ic} (CORONAS-GOES), days	–	–	1-3.2	0.5-2.7	0.2-2.5	0.1-2

according to radial diffusion theory. Comparing the time lag values at $L = 3$ and 3.5 we have obtained $n = 1.5$-6 and calculated Δt_{ic} for $L = 4$-5.5. The best correlation coefficients obtained with different time lags, these time lags (experimented) and calculated ones with the help of (1) are presented in the Table 2.

4. DISCUSSION

We can see that electron flux variations measured onboard the «CORONAS-F» satellite are delayed in comparison with those measured onboard the «GOES» satellite with time lags ~5 and 1-3 days, correspondingly. Comparing the time lag values at $L = 3$ and 3.5 we obtained $n = 1.5$-6 and calculated Δt_i for $L = 4$-5.5.

Our earlier data obtained in the experiment onboard «CORONAS-I» (1994, March-May) [*Kuznetsov,* 2002b] show that at the L-shells from 6 to 4 the time lag values are 1-2 days, and ones increases to 4-6 and 16 days for $L = 3.5$ and 3. It permit us to conclude that diffusion coefficient during the time period with high level of solar activity (2001 year) is higher than one during the decreasing phase of the solar activity (1994 year).

5. CONCLUSIONS

The following conclusions can be derived from the analysis of the «CORONAS-F» data:

1. We have found the strong correlation between proton fluxes measured onboard the «CORONAS-F» satellite with ones measured onboard the «GOES» satellite at $L > 3.5$ all time period 2001, August-December at $L = 3.0$ and 3.5 during and after strong magnetic storms (without any time lag). We assume that founded correlation of proton fluxes with zero time lag is a consequence of the rapid injection of solar energetic particles inside the Earth's magnetosphere.
2. Significant correlation was found for trapped electron measured onboard the «CORONAS-F» with ones measured onboard the «GOES» at $L > 3.5$ during time periods without large SEP
3. The obtained time lag values are equal to ~1 day at the L-shells from 5.5 to 4.5, and increased to ~ 3 and ~ 5 days for $L = 3.5$ and 3, in agreement with radial diffusion theory.
4. Diffusion coefficient during the time period with high level of solar activity (2001 year) is higher than one during the decreasing phase of the solar activity (1994 year).

REFERENCES

Baker D.N., J.B.Blake, D.J. Gorney, P.R. Higbie, R.W. Klebesadel, and J.H. King, Highly relativistic electrons: A role in coupling to the middle atmosphere, *Geophysical Research Letters*, 14, 1027-1039, 1987.

Kuznetsov S.N., I.N.Myagkova I.N., and B.Yu. Yushkov "Relationship of Energetic Particle Fluxes at Geostationary orbit with Solar Wind Parameters and Cosmic Ray Fluxes" *in Proc. of Space Radiation Environment Workshop*, edited by D.Rodgers, S.Clucas, K.Hunter and C.Dyer, v. 8, pp 1-4, British National Space Centre,:Farnborough,UK, 2002.

Kuznetsov S.N., and I.N. Myagkova "Energetic trapped proton and electron flux variations at low altitudes measured onboard «CORONAS-I» satellite their connection with the particle flux variations in geostationary orbit", Adv. Space Res., 30, N10, 2319-2323, 2002.

Vernov S.N., S.N. Kuznetsov S.N., Yu.I.Logachev Yu.I., and V.G. Stolpovsky "The radial diffusion of the electrons with the energy 100 keV in the Outer Radiation belt" *Geomagnetizm and Aeronomy*, 8, N3, 402-411, 1968.

irina@srd.sinp.msu.ru
kuznets@srd.sip.msu.ru

Dynamics of the Earth's Radiation Belts During the Time Period April 14-24, 2002 – Experimental Data

Irina N. Myagkova, Sergey N. Kuznetsov, Boris Yu. Yushkov, Yury I. Denisov, and Ekaterina A. Murav'eva

Skobeltsyn Institute of Nuclear Physics, Lomonosov Moscow State University, Moscow, Russia

Joseph Lemaire

Institute d'Aeronomie Spatiale, 3, Avenue circulaire, Brussels, Belgium

We analysed the variations of radiation belt electrons observed during 14-24 April 2002 obtained on board CORONAS-F satellite (polar orbit at altitude of ~500 km). Measurements of April 14 and 16 correspond to the quiet state of the radiation belts before a magnetic storm. The first storm connected with the M1/CME which occurred April 15 was observed near noon of the following day, next magnetic storm, connected with M2/CME which took place April 17, occurred April 19. As consequence the short time interval between both events strong changes have been observed in the Earth's radiation belt. Significant decrease of electron fluxes in wide energy range was observed in the outer radiation belt April 17 and early morning April 18. During April 18 and 19 the electron flux intensity increased in the outer radiation belt and the location of the peak flux shifted from 4.5 to 3.2 in the nightside and from 5 to 3.5 in the dayside. The next increase of electron flux was observed after the next magnetic storm during April 19-20 both in the inner and outer radiation belts.

1. INTRODUCTION

It is now commonly accepted that the most significant energetic particle flux variations take place in Earth's radiation belts during strong magnetic storms (see for example [*Emel'yanenko et al.*, 1978; *West et al.*, *Li and Temerin*, 2001]. From the analysis of outer belt variations observed simultaneously at high and low altitudes it was shown [*Emel'yanenko et al.*, 1978], that these variations are qualitatively similar, though there are significant different in the magnitude of the observed flux changes. We analyse below the changes in high energy electron fluxes measured at low altitudes in the inner and outer belts during the complicated magnetic disturbances for the period of ten days (14-24 April 2002), when two geomagnetic storms were observed.over the short time interval.

The Inner Magnetosphere: Physics and Modeling
Geophysical Monograph Series 155

10.1029/155GM15

2. EXPERIMENT

CORONAS-F was launched on July 30th, 2001 in a polar orbit at an altitude of ~500 km and an inclination of ~83°. The data analysed here were obtained by a telescope consisting of two semiconductor detectors with thickness equal to 0.05 mm (D1) and 2.0 mm (D2), as well as with a CsI crystal (D3) whose thickness is equal to 1.0 cm. The latter was surrounded by an anti-coincidence plastic scintillator with thickness equal to 0.5 cm. The threshold of the anti-coincidence pulse generation corresponds to an energy release of 0.5 MeV. The detected particles are assumed to be an electron if the energy release in D1 is less than 0.5 MeV. The energy channel E_e of detected electrons depends on the energy release ΔE in D2 and D3 (see Table 1, LE means "low energy",

Table 1. The energy release and coincidence logic for the different detector channels.

E_e, MeV	ΔE (D2), MeV	ΔE (D3), MeV
0.3-0.6 (LE)	0.2-0.5	No
0.6-1.5 (ME)	0.5-1.5	No (<0.5)
1.5-3 (HE)	0.5-1.5	0.5-2

ME - "middle energy", HE - "high energy"). The minimum thickness of the telescope passive shielding corresponds to proton energy ~40 MeV and electron energy ~3 MeV. The minimum thickness of the telescope passive shielding corresponds to proton energy ~40 MeV and electron energy ~3 MeV. The geometry factor of the telescope is equal to 0.4 $cm^2 \cdot sr$ and the aperture is equal to ~23°. The recording efficiency was calculated by taking account backscatter of electrons. The telescope was continuously oriented in the anti-sunward direction.

3. RESULTS

In Figure 1. we show the *Dst*-variation (black) and the distance to the subsolar point of the magnetopause X_0 (grey) measured in Earth radii R_E; the value of X_0 calculated from the solar wind (*SW*) and interplanetary magnetic field (*IMF*) parameters in the following way [*Kuznetsov and Yushkov*, 2000a]:

$$X_0 = 8.51/P^{0.19} + 3.45/P^{0.22} \exp(-(|B_z| - B_z)^2/200\, P^{0.15}), \quad (1)$$

where P is the *SW* dynamic pressure (measured in nPa) and B_z is the *IMF* component (in nT). This is a useful index to characterise the size of the magnetosphere as a function of *SW* parameters.

At the altitude of ~500 km the satellite penetrates the trapped radiation regions only above the South Atlantic Anomaly. During the period of interest CORONAS-F was in the outer belt every day at ~12-13 UT at ~ 11-12 MLT and ~24-00 UT at ~ 22-24 MLT. The high altitude flux of electrons with $E_e > 2$ MeV is recorded at geosynchronous GOES-8. The changes of the electron fluxes measured by GOES-8 and CORONAS-F are similar but electron fluxes measured by GOES-8 are of course significantly higher than ones measured by CORONAS-F. It can be seen that the magnetosphere had a minimum size near noon of April, 17th, at the time when the first two orders of magnitude enhancement in two orders were detected by CORONAS-F in the polar caps.

Electron fluxes measured April 14-24th, 2002 during crossing of CORONAS-F through the radiation belt are presented in Figures 2a and 2b. The data averaged over 14 seconds were used here and in the following of this study. LE electrons marked as black solid line, ME ones as grey solid line and HE ones as black dashed line. The radiation belt structure, intensity and L-distribution are different in the midday and midnight local sectors. This difference is connected with the fact that axis of the detector had different orientation to magnetic field lines in midday and midnight sectors. Data of midday sectors during 15th and 16th were not obtained due to

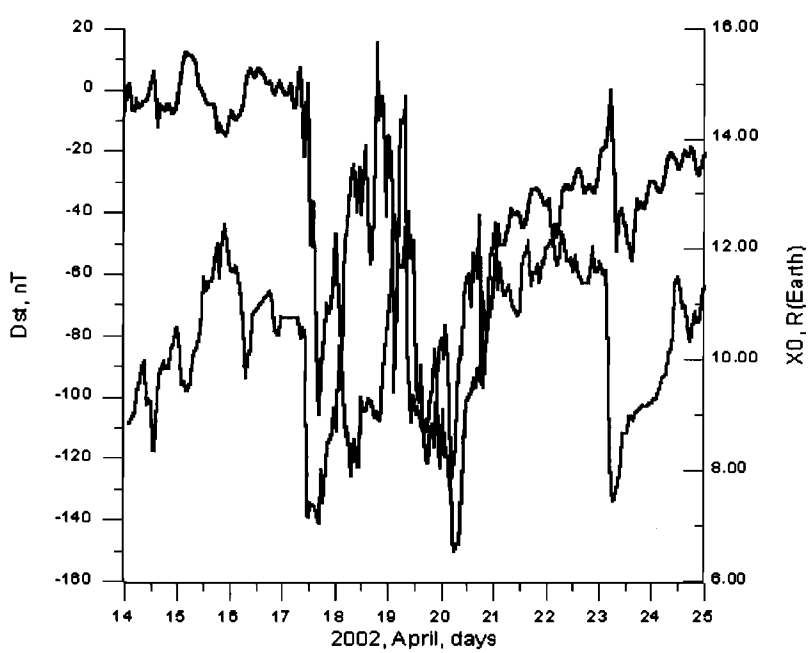

Figure 1. *Dst*-variation (black line) and the distance to the magnetopause nose point X_0 (grey line) during 2002, April, 14-24.

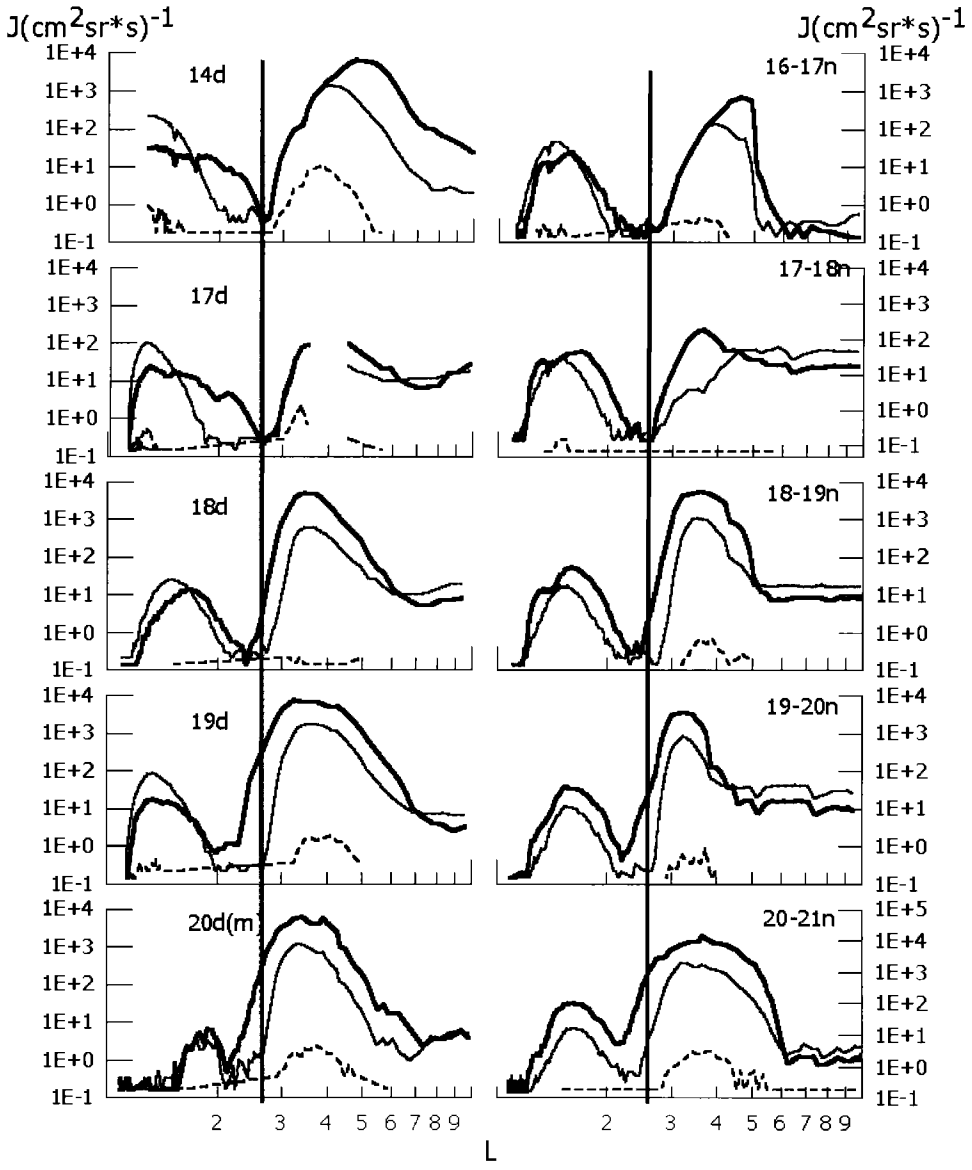

Figure 2a. Radiation belt profiles (2002, April, 14-20) for LE electrons (black solid), ME (grey solid) and HE (black dashed). On the panels shown the days of measurement, the letter "d" corresponds to the day MLT sector and letter "n" - to the night MLT sector, letters 'm' and 'e' means "morning" and "evening" MLT sectors.

the lack of telemetry. On April 14th and 16-17th, 2002 the belt was observed during magnetically quiet and weakly-disturbed conditions: the *SW* velocity was about 300-400 km/s, *SW* pressure 1-2 nPa, Earth's magnetosphere size about 10 R_E in the subsolar direction The maximum flux of the outer belt for LE electrons was located at 4.5-5, for ME ones it was at $L = 3.5$-4.0, and at $L = 4$ for HE ones. The slot region was located at $L = 2.3$-2.6 for LE electrons and at $L = 2.0 \div 2.6$ for ME ones. Its position for the LE electrons before the magnetic storms is marked by thin solid line in Figures 2a and 2b.

After 12 UT on April 17th *Dst* gradually decreased from 0 to −106 nT over the time 6 hours, *Bz* reached −20 nT, and the subsolar equatorial distance of the magnetopause shrank to ~7 R_E, the polar cap was filled with solar energetic particles. Therefore it is difficult to make a detailed analysis distribution of trapped particles at the outer edge of the belt until April 18th due to flux of solar energetic protons, recorded by the telescope outside its aperture. At the beginning of the *Dst* variation decrease near the noon of April 17th the peak the outer belt shifted to $L = 2.8$-3.3, and J_e at $L = 3.3$ was equal to each other for LE and ME electrons.

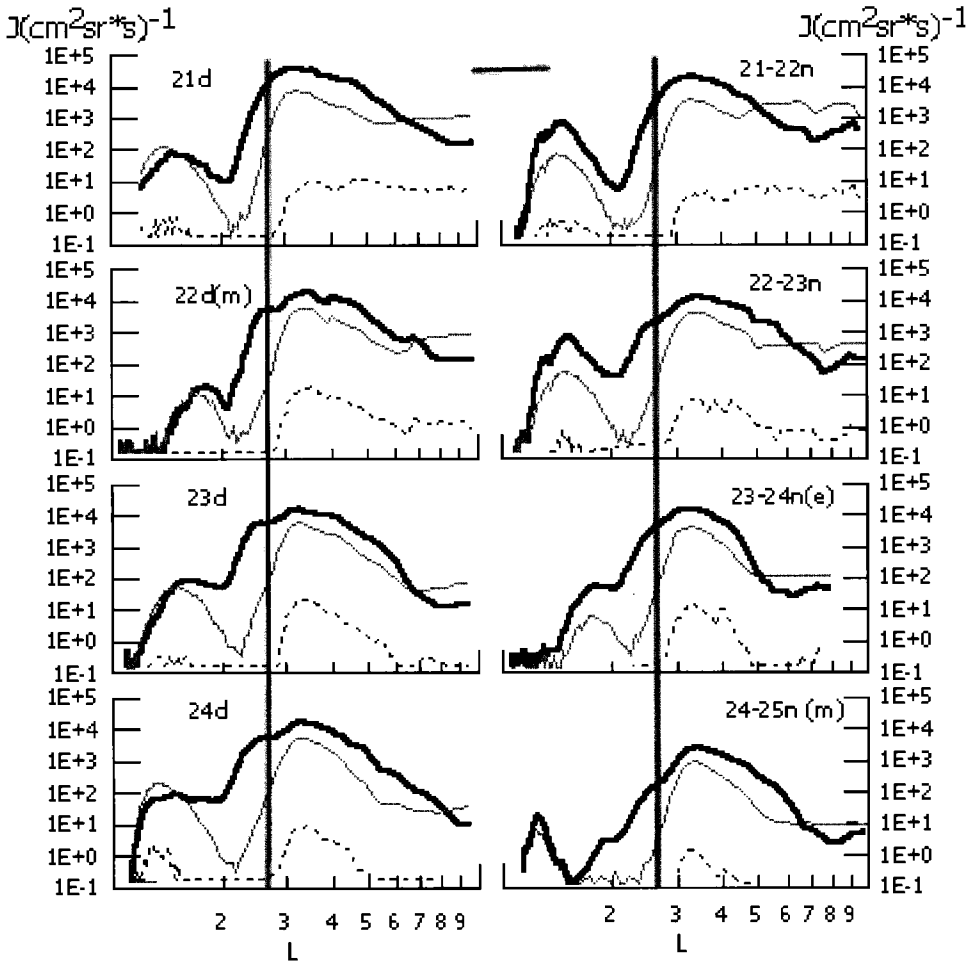

Figure 2b. Radiation belt profiles (2002, April, 21-24) for LE electrons (black solid), ME (grey solid) and HE (black dotted).

During the second half of April 17th the main phase of magnetic storm was 'interrupted': indeed the *Dst* variation increased until 24:00 UT, then *Dst* variation decreased again until 12:00 UT of April 18th. It should be noted that during this 24 hours period from noon to noon the size of magnetosphere grew up from 7 to 14 R_E and remained abnormally large till 06 UT of April 19th.

CORONAS-F crossed the belt April 17-18th in the night MLT sector at ~24 UT. The peak of the outer belt was located at $L = 3.4$-3.6 for LE electrons. In that time electron spectra became significantly softer, the flux of ME electrons was equal $J_e = 5$ $(cm^2sr{\cdot}s)^{-1}$, i.e. the outer radiation belt practically disappeared in energy range 0.6-1.5 MeV. The similar drops of the electron flux intensity were described in [*Buhler and Desorgher*, 2002]. The ME electrons began to appear again in the outer belt only at ~05:30 UT April 18thT also in night MLT sector (22 h MLT) in very narrow L interval 3.5-3.8.

The intensity of ME electrons increased during April 18th, the peak was observed near $L = 3.5$ and slot region shifted to 2.2 for both MLT sectors. Electron spectra at L-shells 2.5-4 became softer than before the magnetic storm. At these L-shells fluxes of LE and ME electrons were equal before the storm. The flux of ME electrons increased subsequently above that of ME electrons by more than order of magnitude.

Unfortunately due lack of telemetry we could not to capture the detail time variation in the noon MLT of April, 17th, i.e. when the first sharp decrease of the *Dst* magnitude began and when the electron outer belt started to change in the MLT midday sector. We can only say that solar energetic electrons were indeed detected in polar caps at 12:05 UT (when CORONAS-F was at $L = 12$) but at them time structure of radiation belts was unchanged in that moment - the outer radiation belt maximum was at $L = 5$, the slot was at $L = 2.5$. Next crossing was lost. The following crossing at 15:00 UT April 17th we can see in Figure 2a. Due to the data gap near the peak value and its position could not be measured exactly, but one can guess that the peak shifted to $L = 3.5$-4.5, while position of the slot region did not change significantly.

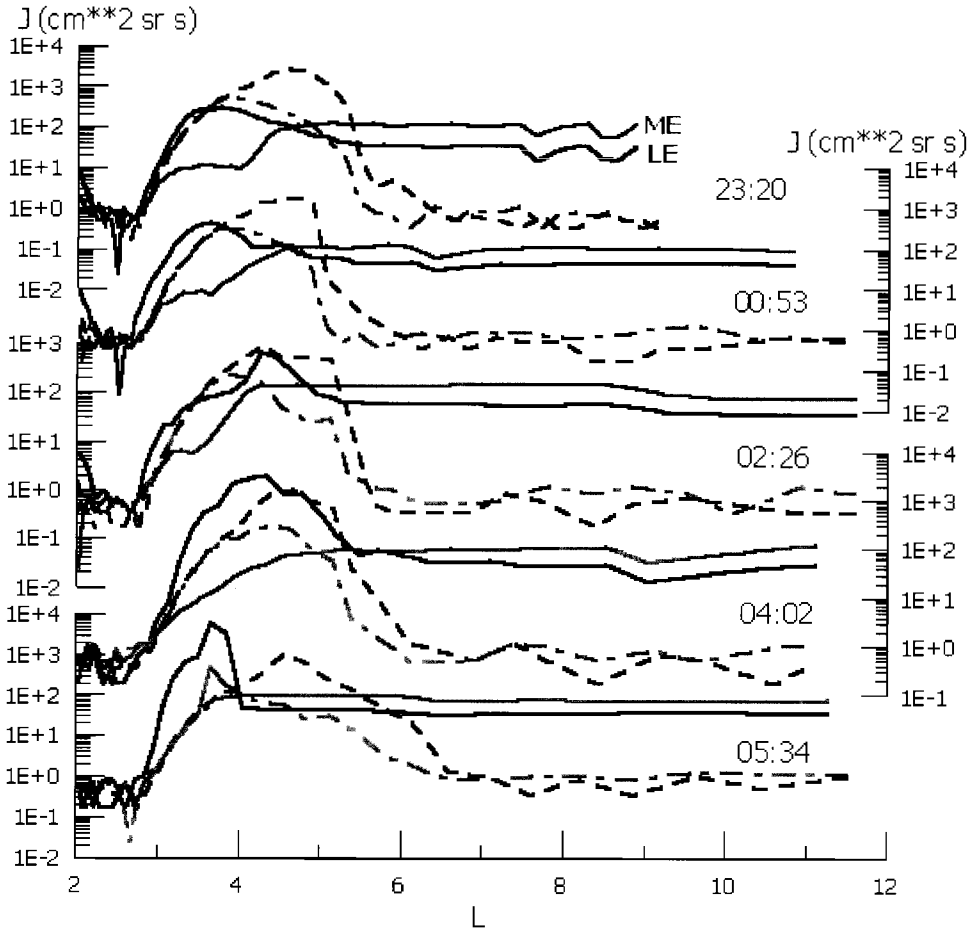

Figure 3. Profiles of the outer radiation belt in the night MLT sector LE (black) and ME (grey). The dashed lines correspond to April, 16-17th data, solid lines - to April, 17-18th.

Already in that time solar energetic electron were recorded at $L > 9.5$.

An example of belt detailed variations of electron flux in night MLT sector illustrated in Figure 3, obtained in the midnight April 17-18th. Background fluxes (17-18th) are shown by dashed lines, black for LE, grey for ME.

At 23:20 UT on April 17th the intensity of electrons at the outer edge of the belt was equal to the intensity recorded on April 16th. Solar energetic protons were already recorded at that time for $L > 4.5$. It was already after the beginning of the magnetic storm, and the boundary of the solar energetic electron flux, was located also at $L = 4.5$, i.e. at the same L-shell as where the maximum of the belt was observed on April 16th ($L = 4.5$).

At the inner boundary of the belt a mixture of trapped electrons and solar energetic protons was recorded. This remained practically unchanged during the next three crossings at 00:53 UT, 02:23 UT and 04:02 UT, the boundary of the penetration of solar energetic electrons was detected during these crossings near $L = 4.5$. As for ME electrons (marked grey) one can see that their peak intensity decreased in two orders of magnitude. At the beginning of the next *Dst* increasing (05:32 UT) we observed for the first time the belt of ME electrons with energies 0.6-1.5 MeV. The peak of the outer electron belt was formed at $L \sim 3.5$.

The penetration boundary of solar energetic electron corresponded to the polar cap boundary of open magnetic field lines on the day-side and the boundary of the plasma sheath on the night-side [*Antonova et al.*, 1989]. During the *Dst* decrease near noon of April 17th the boundary of solar energetic electron penetration was located at $L \sim 10$ ($\Lambda \sim 72°$) for MLT 10-12 h. The plasmasheath inner boundary was at $L \sim 8.5$ ($\Lambda \sim 70°$) for MLT 22-24 h. During the next *Dst* decrease after the midnight April 17-18th, the dayside polar cap boundary of solar energetic electron penetration was located at $L \sim 6$ ($\Lambda \sim 66°$) for MLT 13 h, and the plasmasheath inner boundary was at $L \sim 4.5$ ($\Lambda \sim 62°$) for MLT = 20-21 h. It is likely that such a shift of the boundary

of solar energetic electron penetration which was associated with very the quick decrease of the magnetosphere size means that a significant part of the field lines, which originally belonged to the outer belt, are transferred to the tail and the plasmasheath during the main phase of the magnetic storm. The particles, located on these field lines, are transferred either into the magnetotail, or escape into the interplanetary space outside the magnetopause. During the 'interruption' of the main phase of the storm in the second half of April 17th the size of magnetosphere became abnormally large and the outer radiation belt was formed anew with the peak at L near 3.2 and a significantly softer energy spectrum.

We assume that the re-appearance of new particles in the outer belt corresponds to the recovery of the magnetosphere structure. Now the *Dst* is mostly governed by strong ring current. The soft spectrum of energetic electrons in the new outer belt is controlled by the interplay between particle convection, electric drift velocity and magnetic drift velocities. Later, slow diffusion processes can play a significant role in the dynamics of the outer belt. From the panels 18-19n, 19d, 19-20n in Figure 2 it can be seen that maximum of outer radiation belt shifted to $L = 3$-3.2 and the slot minimum shifted to 2-2.2, the peak electron flux intensity did not change significantly, but spectra of the electrons at $L = 2.5$ became softer.

The next magnetic storm, which was connected with M2 flare accompanied by a CME occurred on April, 19th. The minimum $Dst = -150$ was observed April, 20th. The peak of the magnetic storm occurred from 00:00-09:00 UT in association with strong transient *SW* flow (see Figure 4). The level of geomagnetic activity weakened to mostly active during the next 9 hours, consistent with the slow return of *SW* flow to nominal levels.

Near noon April, 20th only available the crossing of the radiation belt for more earlier MLT than other (i.e. MLT = 10 h), There are then no significant changes in outer radiation belt structure.

At night April, 20-21th (during the recovery phase, when the magnetosphere size X_0 increased up to 11.5 R_E) we observed that with of the outer radiation belt increased from $\Delta L = 2.2$ to 6 for LE electrons and from 2.5 to 5.5., electron flux increased then by order of magnitude both in the outer radiation belt and in the slot. At night MKL on April, 20-21th the structure of the outer belt for HE electrons has recovered; the wide maximum LE electrons was observed at $L \sim 3.3$-4 after magnetic

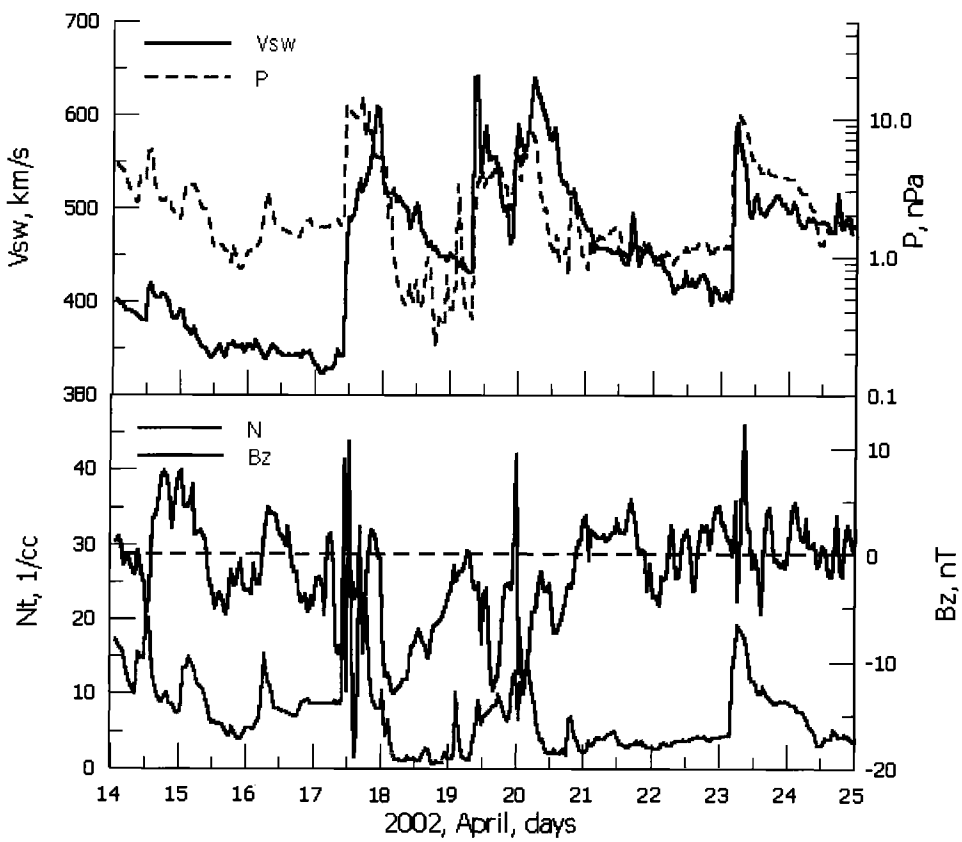

Figure 4. Solar wind velocity, pressure (top panel), density of solar wind and *Bz* (bottom panel) during 2002, April, 14-24.

storm with $Dst = -150$. According to empirical expression presented in [*Tverskaya*, 1996]) for such *Dst* values the maximum of the increased electron fluxes should be located at $L > 3.59$.

Large solar particle event (SEP) were observed in the early morning of April, 21st. According to Figure 2b the electron flux increased at this time at $L > 3.5$ for all three energy intervals. The dayside penetration boundary of solar HE electron penetration was located at $L \sim 3.5$ ($\Lambda \sim 58°$) for 11 h MLT, and the nightside one at $L \sim 6$ ($\Lambda \sim 66°$) for 20:30 h MLT. During April, 22-23th the high electron flux intensity in the outer belt was stable, while the slot region shifted to $L = 2$ for nightside and electron flux intensity the slot increased by three orders magnitudes above those April, 16-17th. Furthermore, from the midday crossing on April, 22nd we can see in Figure 2b the tendency of formulation of a second peak of the outer radiation belt with a much soft spectrum at $L = 2.3$-2.4. The intensity of LE electrons in the slot was equal to one in the inner belt dayside for April, 23rd and 24th.The slot was not observed till the night of April, 24-25th. This might be connected with the quick changes of the size of magnetosphere in the morning of April, 23rd. that was caused by the strong transient solar wind flow. Indeed, solar wind velocity was about 600 km/s, solar wind pressure −10 nPa, X_0 changed them from 11.5 R_E to 7.5 R_E within four hours.

4. DISCUSSION

The comparable roles of slow and fast transport processes in the dynamics of the electron radiation belts can be studied using the data on electron fluxes measured with the CORONAS-F detector from 14th till 24th of April presented in Figures 2a and 2b. The hour-averaged values of the *IMF* components *Bz*, the *SW* velocity, density and pressure are given in Figure 4. The *Dst*-variation and the distance to the magnetopause nose point X_0 are shown in Figure 1. The results illustrated in Figures 1, 2, and 4 indicate that besides the particle flux variations in the outer belt there was a noticeable decrease of electron fluxes with $E_e > 0.3$ MeV on $L > 2.8$ connected with the magnetic storm of April, 17th. The electron flux decrease was accompanied by the slot shift to $L \sim 2.5$. We conclude that it is the consequence of cross-*L* diffusion similar to one observed on March 24, 1991 [*Blake et al.*, 1992] and January 11, 1997 [*Kuznetsov et al.*, 2000b].

The *SW* velocity *V* was maximum (~630 km/s) in the end of April, 17th. At the beginning of April, 18th a rapid decrease of *V* to 500 km/s was observed. During the first half of April, 18th *Dst* was equal −120-130 nT, $Bz = -10$-15 nT. Since disturbed structure existed during 12 h. We guess that it connected with a strong current in plasma sheath. It continued till noon April, 19th when $V = 440$ km/s. *SW* pressure became high (about 10 nPa) earlier, near noon of April, 17th. On April, 19th *V* value sharply increased to ~ 650 km/s and *P* became about 5 nPa. During April 19-20th there was a noticeable increase of LE electrons in the slot region, whereas the electron flux in the inner belt did not change. The most rapid increase of the electron flux was observed at $L = 2$-3 during the magnetic storm recovery phase prior to April 20-22nd. Later, until April 23rd, *P* was practically constant ~1 nPa, and the belt of electrons at $L \sim 3$ continued to became wider. An additional peak of belt for LE electron flux was formed at $L = 2.3$-2.5, where the slot was situated earlier.

The following information can be derived from the analysis of the CORONAS-F data, obtained during April, 14-24th. After main phase of the magnetic storm April, 17th the significant decreasing of electron flux in the outer belt was observed in the early morning of April, 18th. The outer belt practically disappeared in energy range 0.6-1.5 MeV for during the time period more then 6 h. The restoring of the outer radiation belt closer to the Earth (with significantly softer spectrum) was observed only after 10 UT of April, 18th when the *Dst* has reached its minimum value. The decrease of the electron flux in the outer radiation belt during this magnetic storm was accompanied by a particularly reduction in the size of the magnetosphere. It is possible that magnetic field lines of outer radiation belt extended into the magnetotail and plasmasheath.

Let us discuss the variation of these electron flux variations on the basis of currently accepted acceleration mechanisms [*Li and Temerin*, 2001]. Based on the results published in [*Lyons and Williams*, 1984] we should consider two types of closed drift shells. The first type of drift shells during quiet times is located totally inside the plasmasphere (the inner radiation belt), the other type is partially (on the morning side) located outside the plasmasphere (the outer belt). The plasmapause is located closest to the Earth on the post-midnight and morning side on $L = 3 \div 3.5$. A strong magnetic storm is the result of a strong ring current enhancement and of the injections of particles into the quiet plasmasphere region. The peak of ring current flux should be located at $L = (3075/|Dst|)^{0.37}$ [*Kuznetsov*, 1996]. For $Dst = -106$ nT, L_{RC} should be equal to 3.7, and for $Dst = -150$, $L_{RC} = 3.05$. The post-storm evolution of particles in the inner and outer belts should be considered separately. The variations of radiation belts observed after magnetic storm April 19-20th strongly distinguished from ones 17-18th. There was no decreasing of electron flux observed after storms April 19-20th. A significant increase of the fluxes of electrons of all energies was observed in the inner belt April 21-22th, during the recovery phase of the second magnetic storm, but it was not observed after April, 17th magnetic storm. We propose that this sequence of events can be explained by particle acceleration due to the radial diffusion and their scattering in the loss cone due to interactions with the whistler mode of electromagnetic waves.

5. CONCLUSIONS

The low altitude observations of the relativistic electrons fluxes from the CORONAS-F mission discussed in this paper illustrate how the inner and outer radiation belts and the slot region change during a sequence of magnetic storms which occurred between 2002 April, 14 and 25. The two first storm events were separated by a time difference of only 12 hours. It is known from earlier observations that this are the most favourable conditions to obtain the largest enhancement of ring current intensity, and therefore in the strongest variation of the *Dst* geomagnetic index; this are also the most favourable conditions to produce the most drastic changes in the cross-*L* distribution of the trapped relativistic electrons fluxes: i.e. changes of the maximum flux intensity and position, as well as of the slope of the energy spectrum for these electrons. Isolated geomagnetic storm do not produce as large *Dst* minimum, nor as larger changes in the peak intensities and positions. It is also during successive geomagnetic storms separated by short delay times that the slot region can be filled up, and does almost disappear as it was observed during the event of 24 March 1991 [*Blake et al.*, 1992].

The results presented here confirm in many respect those presented in [*Kuznetsov et al.*, 2003], which were obtained for the sequence of geomagnetic storms of November 2001. In all cases it was found that geomagnetic storms are initiated when the *IMF* turns southward with *Bz* decreasing for an extended period of a few hours. But the second key condition for having a geomagnetic storm, instead of a "substorm" of relatively small effect on the structure of the radiation belts, is that the solar wind velocity has to be larger (>500 km/s) at the time of the southward turning of the interplanetary magnetic field.

Much of the adiabatic and non-adiabatic changes in the distribution of relativistic electron fluxes observed in the equatorial region of the outer belt during geomagnetic storms and reported in the paper by [*McIlwain*, 1996] are also observed at low altitudes by CORONAS-F during geomagnetic storms.

It is also worthwhile to point out that our observations confirm those recently published for example in the paper [*Buhler and Desorgher*, 2002]: i.e. that the relativistic electron intensity drops during the main phase of a magnetic storm. The question of flux levels during the recovery phase is more complicated - many storms show little or no increase in flux levels, as were discussed in the paper [*Reeves et. al.*, 2003], but in other cases the electron intensity subsequently enhanced during the recovery phase. This recovery may lead to higher fluxes of relativistic electrons after the storm than before.

REFERENCES

Antonova, E.E., S.N. Kuznetsov, and A.V. Suvorova, Determination of some geomagnetic field characteristics from the low-orbiting satellite data, *Geomagnetizm & Aeronomia*, 29, 556-562, 1989.

Blake, J.B., W.A. Kolasinski, R.W. Fillius, and E.G. Mullen, Injection of electrons and protons with energies of tens of MeV into $L < 3$ on March 24, 1991, *Geophys. Res. Lett.*, 19, 821-824, 1992.

Buhler, H. and Desorgehr L, relativistic electron enhancements, magnetic storm and substorm activity, *J. Atmos. Solar Terr. Phys.*, 64, N5-6, 593-599, 2002.

Emel'yanenko, S.P., S.N. Kuznetsov, and V.G. Stolpovsky, Investigation of captured radiation on Kosmos-426. V. The behavior of the outer radiation belt after the magnetic storm of December 17, 1971, *Cosmic Res. (USA)*, 15, 129-132, 1977.

Kuznetsov, S.N., A model of ring current based on the Dessler-Parker-Sckopke theorem, *Radiation Measurements*, 26, 403-404, 1996.

Kuznetsov, S.N., and B.Yu.Yushkov, Magnetopause position dependence on the interplanetary magnetic field *Bz*-component. Analysis of the pressure balance equation, *Phys. Chem. Earth (C)*, 25, 165-168, 2000a.

Kuznetsov, S.N., A.V. Bogomolov, Yu.I. Denisov, G.Ya. Kolesov, M.I. Kudryavtsev, I.N. Myagkova and S.I. Svertilov, Change in structure of the Earth's outer radiation belt under the action of the magnetic disturbance of January 10-11, 1997, *Geomagn. Aeron. (Russia)*, 40, 300-306, 2000b.

S.N. Kuznetsov, B.Yu. Yushkov, K. Kudela, J. Lemaire I.N. Myagkova, L.I. Starostin, and Yu.I. Denisov " Evolution of outer radiation belt during the month of november 2001, according to relativistic electron observations from the CORONAS-F mission, *in ISEC2003 Abstract book* (2-5 September, 2003, Toulouse, France),. 19-20., 2003.

Li, X. and M.A. Temerin, The electron radiation belt, *Space Sci. Rev.*, 95, 569-580, 2001.

Lyons, L.R. and D.J. Williams, *Quantitative aspects of magnetospheric physics*, 231, D.Reidel Publ. Comp., Dordrecht, 1984.

McIlwain C.E., Processes acting upon outer zone electrons, *in "Radiation Belts: Models and Standards". Geophysical Monograph 97*, editeds. by J.F. Lemaire, D. Heynderickx, D.N. Baker, pp.15-26, AGU, Washinton DC, USA, 1996.

Reeves, G.D., K.L. McAdams, R.H.W. Friedel, and T.P. O'Brien, Acceleration and loss of relativistic electrons during geomagnetic storms, *Geophys. Res. Lett.*, 30(10), 1529, doi: 10.1029/2002GL016513, 2003.

Tverskaya, L.V., The latitude position dependence of the relativistic electron maximum as a function of Dst, *Adv. Space Res.*, 18, 135-138, 1996.

West, A.I., R.M. Buck, and G.T. Davidson, The dynamics of energetic electrons in the Earth's outer radiation belt during 1968 as observed by the Lawrence Livermore National Laboratory's spectrometer on OGO-5, *J. Geophys. Res.*, 86, 2111-2142, 1981.

irina@srd.sinp.msu.ru
kuznets@srd.sip.msu.ru

Drivers of the Inner Magnetosphere

Natalia Yu. Ganushkina

Finnish Meteorological Institute, Geophysical Research, Helsinki, Finland

This paper addresses the role of the electric fields in the inner magnetosphere dynamics by reviewing observations and model results, especially whether the stormtime ring current intensification is generated by large-scale convection alone or together with substorm-associated variations. It is discussed that in addition to the large-scale convection electric field partially generated in the magnetospheric boundary layers via reconnection and viscous interaction, there can exist a mechanism for its generation in the magnetotail via plasma pressure gradients. We review the models for this large-scale convection field. One type of these models describe the electric field by the ionospheric potential pattern associated with the solar wind and IMF behavior and then mapped to the magnetotail along the magnetic field lines. The other adjusts the intensity of the model convection field in the tail to the overall level of magnetic activity. It is concluded that these models describe the system only in an average sense. Observations show that particle transport occurs in flow bursts, and that while ions in the energy range 20-80 keV contribute most to the ring current energy density during the storm main phase, during the recovery phase the contribution from the high-energy ions (above 80 keV) becomes dominant. It is argued that during inward particle motion, the final energy and the lowest L-shell reached depend on the intensity of the large-scale convection and smaller-scale substorm-associated electric fields, and that only the addition of the substorm-associated electric fields made it able to produce the observed fluxes of high-energy particles.

1. INTRODUCTION

Already *Gold* [1959] noted that the large scale flow of magnetospheric plasma is analogous to thermal convection. Later *Axford and Hines* [1961] used the term "convection" to describe large-scale circulation inside the magnetosphere. *Axford and Hines* [1961] and *Dungey* [1961] developed first theories of magnetospheric convection to explain the observed pattern of plasma circulations in the polar cap [*Davis*, 1962]. The large-scale convection electric field in the magnetosphere is considered to be a potential field with rather homogeneous structure, which can be mapped to the ionosphere.

The Inner Magnetosphere: Physics and Modeling
Geophysical Monograph Series 155

10.1029/155GM16

These theories have been questioned in several studies. *Parker* [1996] in his alternative paradigm for magnetospheric physics stressed that the concept of equipotential field lines is not applicable to nonsymmetric and time-dependent circumstances of magnetospheric activity. The interplanetary electric field can not be mapped along the magnetic field lines to the magnetosphere and ionosphere, unless the ionospheric convection keeps up with the field line convection at the magnetopause such that the field is stationary. *Antonova and Ganushkina* [1997] suggested that the magnetospheric system is driven by internal forces related to plasma pressure and by external forces exerted by the solar wind plasma flow.

The basic transport and acceleration process for ions moving from the magnetotail plasma sheet to the inner magnetosphere is the $\mathbf{E} \times \mathbf{B}$ drift imposed by the large-scale convection electric field in the nightside magnetosphere. In the drift approximation, the magnetotail particles gain

energy while they move from regions of weaker to stronger magnetic field, conserving their first adiabatic invariant. While approaching the inner magnetosphere, the particles are transported across the magnetic field lines primarily by the gradient and curvature drifts, as well as by the $\mathbf{E} \times \mathbf{B}$ drift. During disturbed conditions particles move under a complicated combination of potential and induction electric fields and time-varying magnetic field associated with substorms. Recent studies have shown that earthward transport of plasma and magnetic flux occurs in the form of short-duration, high-speed plasma flows, rather than as a slow, steady convection [*Baumjohann et al.*, 1990; *Angelopoulos et al.*, 1992]. Both simulation studies [*Brin et al.*, 1997; *Li et al.*, 1998] and observations of substorm-associated electric fields [*Aggson et al.*, 1983; *Maynard et al.*, 1996; *Tu et al.*, 2000] coincident with the braking of the fast flows have suggested that these fields are the driving force of the particle injections.

The main portion of the Earth's ring current is carried by geomagnetically trapped energetic ions in the energy range of 10-200 keV. The main effect of space storms is the injection of energetic particles from the near-Earth magnetotail into the inner magnetosphere, which results in a significant growth of the ring current. The net westward-flowing ring current, containing the eastward-flowing component at the inner edge, decreases the horizontal component of the geomagnetic field at the Earth's surface. The Dst index constructed from ground magnetic measurements is commonly considered as a measure of space storm intensity. Recent studies [*Liemohn et al.*, 2001] have shown that the contribution of non-trapped particles, consisting the partial ring current, to the Dst is very important, even dominant, during storms.

Earlier studies by *Chapman* [1962] and *Akasofu* [1966] regarded storms as superpositions of successive substorms. During substorm expansion phase induction electric fields accelerate magnetospheric particles and inject them into the inner magnetosphere, where they become trapped and form the ring current. Later studies have stated that the substorm occurrence is incidental to the main phase of storms [*Kamide*, 1992]. Usually it is assumed that storm-time substorms do not differ from non-storm substorms, but it was noted that ions are energized more and penetrate deeper in the inner magnetosphere during storms than during isolated substorms [*Daglis et al.*, 1998]. Furthermore, *Pulkkinen et al.*, [2002] showed that during magnetic storms, there are several distinct categories of substorm-like activations, which are not similar to each other or to isolated substorms.

For many years, the significance of the ionosphere as a source of ring current ions was considered negligible. The AMPTE mission demonstrated that magnetospheric O+ ions originating in the ionosphere are important terrestrial agents in the storm-time geospace dynamics. *Hamilton et al.*, [1998] have shown a dominance of O+ in the inner ring current, during one magnetic storm. *Daglis et al.*, [1994] demonstrated the occurrence of fast ionospheric ion feeding to the inner magnetosphere during substorms. *Daglis et al.*, [1997] showed that O+ ions were not only important in the storm-time geospace, but actually dominated throughout the ring current during the main phase of all intense storms observed by CRRES in 1990-1991.

The purpose of this paper is to discuss the formation of the large-scale electric field and the consequent convection pattern in the magnetosphere. It is then demonstrated that in addition to these processes, the smaller-scale substorm-associated electric fields play a key role in magnetospheric dynamics during magnetic storms. The paper is organized as follows: Section 2 describes the generation of the large-scale convection electric field. Section 3 discusses the existing models of the large-scale convection electric field. The different ways of particle transport in the inner magnetosphere such as large and small-scale flows are addressed in Section 4. Section 5 presents the observations and models of substorm-associated electric fields and Section 6 discusses their role in the particle transport and acceleration and the ring current formation. The last section contains concluding remarks.

2. GENERATION OF LARGE-SCALE CONVECTION ELECTRIC FIELD

Axford and Hines [1961] used the concept of a "closed" magnetosphere, where all terrestrial magnetic field lines are confined inside a cavity in the solar wind. In their convective flow pattern, plasma was carried tailward along the flanks and was returned by sunward flow near the tail center. They suggested that such a flow could be caused by a viscous-like momentum transfer from the solar wind to adjacent regions of the tail. If this flow pattern is mapped along field lines to the polar ionosphere, it produces a two-cell flow pattern, with plasma flowing to the nightside across the pole and returning to the dayside at lower latitudes. The frozen-in concept, $\mathbf{E} = -\mathbf{v} \times \mathbf{B}$ in an ideal magnetized plasma, where $\mathbf{v}$ is the steady bulk flow velocity, $\mathbf{E}$ is the electric field and $\mathbf{B}$ is the magnetic field, can be interpreted as particles moving with field lines. If $\mathbf{E} = -\nabla V$, where V is the electric potential, plasma flow lines are lines of constant electric potential, suggesting a dawn-to-dusk electric field across the polar cap.

Dawn-dusk electric fields were observed both directly by low-altitude polar orbiting satellites such as Injun 5 [*Cauffman and Gurnett*, 1971] and OGO-6 [*Heppner*, 1972a] and indirectly using "driftmeters" by Atmospheric Explorer C (*Spiro et al.*, [1978] and references therein) and Dynamics Explorer 2 [*Heelis et al.*, 1981]. The observations confirmed the two-cell pattern and obtained typical voltage drops of 40-70 kV. The two-cell pattern is most stable when the IMF

$B_z < 0$, and it contains asymmetries correlated with the IMF B_y [*Heppner*, 1972b]. When the IMF $B_z > 0$, the two-cell pattern becomes distorted and the electric field is time-varying. More complex patterns may also develop, such as the four-cell [*Burke et al.*, 1979].

Dungey [1961] applied the concept of reconnection to magnetospheric physics in his theory of convection. He proposed that an X-type neutral line at the front of the magnetosphere enables terrestrial field lines to link up with interplanetary ones and produce "open" field lines, with one end tied to earth and the other reaching to distant space. The convection flow and electric field pattern resulting from this motion in the polar ionosphere is similar to that in the viscous-like interaction. Furthermore, the reconnection process leads to formation of field-aligned currents between the boundary layers and the ionosphere in the Region 1 sense. In Dungey's approach, the magnetopause is identified as a sharp discontinuity in the magnetic field with a small component (0.5-1 nT) perpendicular to the magnetopause. Because this perpendicular component is so small, it is difficult to distinguish Dungey's scenario from the Axford and Hines picture from in situ magnetic field observations. The finding [*Fairfield*, 1967] that the level of magnetospheric activity and energy transfer from the solar wind to the magnetosphere depend strongly on the IMF B_z component was a major support for Dungey's theory.

Thus, in these two theories, an external electric field is either produced by the MHD dynamo in the magnetospheric boundary layers or penetrated from the solar wind. This electric field is then applied on the polar cap and governs the inner magnetosphere dynamics. The boundary layer mechanism requires the existence of finite conductivity or finite and comparatively large viscosity. Although the introduction of such parameters in the collisionless plasma meets with certain difficulties, many observational and theoretical studies such as, for example, ISEE observations of flux transfer events [*Paschmann*, 1982] and magnetopause reconnection [*Sonnerup et al.*, 1981], study of viscous processes [*Tsurutani and Thorne*, 1982], were done to prove the mechanisms of electric field generation.

In Dungey and Axford and Hines theories all Region 1 field-aligned currents were connected to the boundary layers. The mapping of the magnetospheric domains [*Elphinstone et al.*, 1991; *Feldstein and Galperin*, 1985] suggested that the auroral oval, Region 1 field-aligned currents, and convection reversal boundary are all projected into the plasma sheet, while the magnetospheric boundary layers are projected into a narrow region near the cusp. *Tsyganenko et al.*, [1993] searching for the signatures of field-aligned currents in the magnetotail in the large sets of the spacecraft magnetic field data showed that the significant portion of Region 1 field-aligned currents comes from the plasma sheet. Similar idea was proposed by *Karty et al.*, [1984] and *Yang et al.*, [1994]. *Antonova and Ganushkina* [1997] developed the idea that Region 1 field-aligned currents can be produced in the plasma sheet by the existence of azimuthal plasma pressure gradients as in the inner magnetosphere $j_{\|} \propto \nabla W \times \nabla p$ [*Vasyliunas*, 1970; *Tverskoy*, 1982]. If the curvature of the flux tube volume W isolines is larger than that of the transverse current lines, ∇p will have a projection on the W-surface, which generates the Region 1 field-aligned currents (Figure 1, see review by *Antonova* [2002]). The closure of the field-aligned currents in the ionospheric dynamo region provides a quasi-stationary electric field [*Tverskoy*, 1982] $\nabla \cdot \hat{\Sigma} \nabla \Phi^i = j_{\|}$, where $\hat{\Sigma}$ is the ionospheric conductivity tensor and Φ^i is the ionospheric potential. This equation has been examined in detail (see, for example, *del Pozo and Blanc* [1994] and references therein) in order to solve the generation of Region 2 field-aligned currents. This quasistationary electric field when mapped to the magnetotail represents a possible additional source for the large-scale electric field in the magnetotail.

Suggesting the possibility of the electric field appearance in the magnetotail due to the internal distribution of plasma pressure, this mechanism does not exclude solar wind driving and therefore is not in the direct opposition to the Dungey and Axford and Hines pictures. The distribution of the plasma pressure necessary for Region 1 field-aligned current generation needs to be maintained. If there is no solar wind driving and no energy is coming to the system as a momentum transfer from the solar wind to adjacent regions of the tail, the described cycle will stop, since the ionosphere is a dissipative

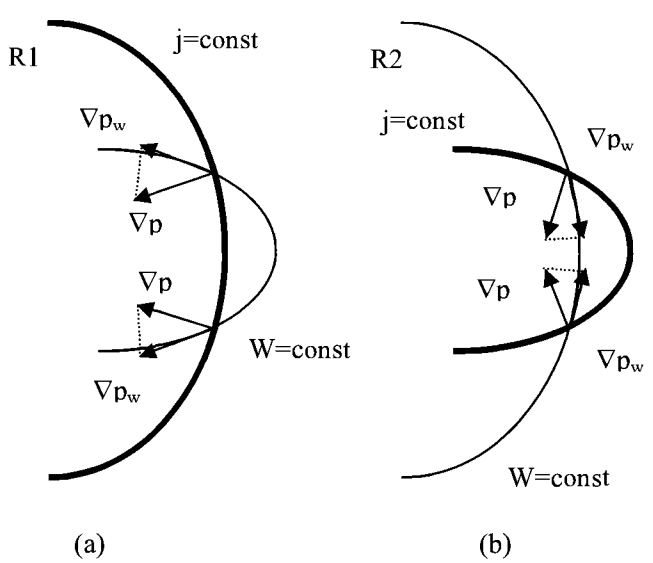

Figure 1. Crossing of transverse current lines (thick) and magnetic flux tube volume isolines (thin) that corresponds to (a) Region 1 and (b) Region 2 field-aligned current generation (after *Antonova and Ganushkina* [1997]).

system. There should be a momentum transfer from the solar wind to adjacent regions of the tail.

The generation of Region 1 currents in the plasma sheet can be verified directly if the distributions of the magnetic field and plasma pressure are known. However, direct verification is difficult, as there are still not sufficiently detailed measurements of the plasma pressure which would allow to produce instantaneous distributions and to obtain plasma pressure gradients. The possible first-step check could be performed by using empirical models of the magnetospheric plasma (for example, *De Michelis et al.*, [1999], *Milillo et al.*, [2001]. Moreover, *W*-isolines were calculated using the empirical models of the magnetic field, which represent quite average magnetic field distribution [*Ganushkina et al.*, 2002]. Furthermore, during storms the observations are even more sparse and the state of the magnetosphere more complex and structured.

Although the main driver of the large-scale convection is solar wind, it is still unclear what portion of the large-scale convection electric field can be created by internal distribution of plasma and external sources and how they are related under different conditions.

3. MODELS OF LARGE-SCALE CONVECTION ELECTRIC FIELD

Several models have been proposed for the large-scale convection electric field. One of the widely used convection electric field models is the Volland-Stern model [*Volland*, 1973; *Stern*, 1975]. The electric potential is given by $\Phi_{conv} = AL^{\gamma} sin\ (\phi - \phi_0)$, where A is the factor determining the intensity of the convection electric field, L is the McIlwain L-value, γ is the shielding factor, ϕ is the magnetic local time, and ϕ_0 is the offset angle from the dawn-dusk meridian. *Maynard and Chen* [1975] obtained a *Kp*-dependent function of A based on data of plasmapause crossings. Figure 2 shows schematically the equipotential lines in the equatorial plane given by Volland-Stern model with $Kp = 2$ together with corotation electric field.

Several functions have been constructed to couple the polar cap potential with the solar wind parameters [*Boyle et al.*, 1997]. Parameterized empirical electric field models have been constructed using data from low and high altitude satellites [*McIlwain*, 1986; *Heppner and Maynard*, 1987; *Richmond and Kamide*, 1988; *Weimer*, 2001]. For example, in the E3 model [*McIlwain*, 1986] the *Kp*-dependent electric potential was expressed by a set of 120 functions with approximately Gaussian forms based on particle data from geosynchronous satellites. *Weimer* [2001] proposed a model for electric potential which was fitted to a spherical harmonic function depending on the solar wind velocity and IMF clock angle using the electric field data from the DE 2 satellite.

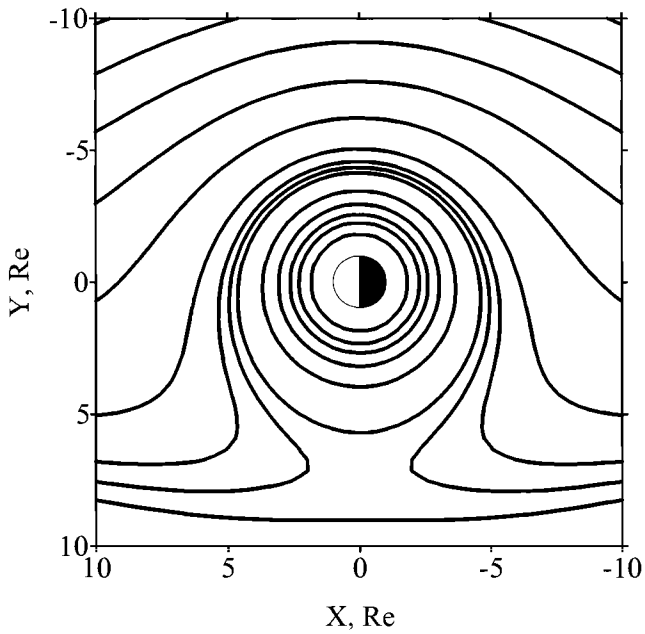

Figure 2. Equipotential lines in the equatorial plane given by Volland-Stern convection electric field model with $Kp = 2$ together with corotation electric field.

The Rice Convection Model (RCM) describes plasma electrodynamics in the inner and middle magnetosphere and its coupling to the ionosphere [*Wolf et al.*, 1982; *Spiro et al.*, 1981]. The RCM represents the plasma distribution in terms of multiple fluids. Its equations and numerical methods have been specifically designed for treatment of the inner magnetosphere, including the flow of electric currents along magnetic field lines to and from the conducting ionosphere. The model computes these currents and the associated electric fields self-consistently.

However, these models do not give an answer on the nature of large-scale convection electric field. Models, where the polar cap potential is directly dependent on solar wind parameters [*Boyle et al.*, 1997] and is then mapped to the magnetosphere, are constructed by assuming an external source of the electric field (i.e., viscous interaction or reconnection at the magnetopause). On the other hand, the Volland-Stern and McIlwain models depend only on *Kp*, so that the conditions in the magnetotail do not depend on the solar wind parameters or magnetopause reconnection, and thus the electric field could be viewed as an internal magnetotail property (i.e., generated by plasma pressure gradients). In reality, both external and internal sources are probably responsible for generation of the large-scale convection.

During geomagnetic disturbances the enhanced convection in the night time sector was found to differ significantly from the standard Volland-Stern type two-cell pattern. Penetration

of strong electric field at $L < 4$ was reported based on CRRES observations [*Rowland and Wygant*, 1998]. A common feature of many empirical convection models is a lack of accuracy in representation of the subauroral electric fields in the region equatorward of 55° invariant latitude. Observations of SAID (subauroral ion drifts) events, seen as latitudinally narrow westward convection with 500 m/s speed equatorward of the auroral oval predominantly in the pre-midnight sector (see, for example overview by *Anderson et al.*, [2001]), and SAPS (subauroral polarization stream) events, which include latitudinally broader and persistent secondary westward convection peak [*Foster and Vo*, 2002], make it important to include subauroral electric fields for the ring current formation during disturbed conditions.

4. PARTICLE TRANSPORT IN THE INNER MAGNETOSPHERE: LARGE AND SMALL SCALES

Large-scale convection electric field models were constructed either as steady-state models (Volland-Stern, McIlwain models) or by assuming perfect mapping between the ionosphere and the magnetosphere along equipotential magnetic field lines (Weimer, RCM models). Neither of these assumptions are valid during magnetospheric activity such as substorms, when the magnetic field changes cannot be considered small.

Recent studies have shown that earthward transport of plasma and magnetic flux occurs in the form of short-duration, high-speed plasma flows, rather than as slow, steady convection. High-speed flows in the inner central plasma sheet were first reported by *Baumjohann et al.*, [1990] and later studied in detail by *Angelopoulos et al.*, [1992]. The flow velocity exhibits peaks of very large amplitude (100-400 km/s) with a characteristic time scale of the order of one minute, which are usually associated with magnetic field dipolarizations and ion temperature increases. *Sergeev et al.*, [1996] confirmed that short-term flux transfer events, which have the basic properties of bubbles, occur in the midtail plasma sheet. These bubbles are underpopulated plasma flux tubes of small cross-tail size of about 1-3 R_E, which may intrude earthward [*Chen and Wolf*, 1993]. Recent Cluster 4-spacecraft observations have revealed the association of a magnetic flux rope and bursty bulk flow in the central plasma sheet [*Slavin et al.*, 2002] as well as the connection of the evolution of the dipolarization front across the tail and the fast flow [*Nakamura et al.*, 2002].

The fine structuring of the flows in the magnetotail into bursty bulk flows and bubbles is an internal magnetotail process. It is difficult to picture a direct influence of the solar wind parameters in the generation of such flows, as the solar wind conditions can control whether this fine structuring occurs, but not in detail where it is created. Thus, internal characteristics such as magnetotail structure and plasma pressure distribution, are very important for the creation of the fast flows.

5. PARTICLE INJECTIONS AND ELECTRIC FIELDS DURING SUBSTORMS: OBSERVATIONS AND MODELS

The sharp increase of energetic (a few tens to hundreds of keV) particle flux in the near-Earth tail is one of the most important manifestations of the substorm expansion phase [*Arnoldy and Chan*, 1969; *Baker et al.*, 1982; *Reeves et al.*, 1991]. If the measurements are taken close to the injection site, injections are dispersionless, i.e. fluxes of electrons and ions at different energies are enhanced at the same time.

Moore et al., [1981] investigated injections using two radially separated satellites. They found that dispersionless injections and associated magnetic field signatures occur earlier at the outer satellite. *Russell and McPherron* [1973] estimated a propagation speed of 150 km/s in the compressed magnetic field configuration. *Moore et al.*, [1981] proposed an injection front model, in which an injection corresponds to a compressional wave front that propagates earthward from a disturbance occurring in the magnetotail. Particles are transported towards the Earth by the compressional wave. *Birn et al.*, [1997] performed test particle simulations and found that betatron acceleration provides the necessary energization by moving particles into a stronger magnetic field by a time-dependent electric field predominantly in the dawn-to-dusk direction. Analysis of single-particle dynamics in simulations of magnetospheric field reconfigurations has revealed prominent acceleration of plasma sheet ions during the substorm expansion phase [*Delcourt*, 2002].

Thus, electric field behavior is important in understanding how the energetic particle injections are formed and how the particles are accelerated. Observations show that substorm-associated electric fields usually display a very complicated behavior [*Maynard et al.*, 1996]. Large, transient electric fields appear in the plasma sheet during the substorm expansion phase [*Aggson et al.*, 1983; *Cattell and Mozer*, 1984]. The enhanced electric fields are impulsive with amplitudes of up to 20 mV/m, which is more than three times the largest convection electric field, and coincident with the braking of the fast flows and correlated with the magnetic field dipolarization in the inner central plasma sheet [*Tu et al.*, 2000 and references therein].

The origin of strong transient electric fields at substorm onset and their detailed relationship to the magnetic field dipolarization is still an open question. However, several models have been proposed to explain particle injections [*Li et al.*, 1998; *Zaharia et al.*, 2000; *Sarris et al.*, 2002]. In the *Li et al.*, [1998] model the time varying fields are associated with a dipolarization, during which the northward magnetic

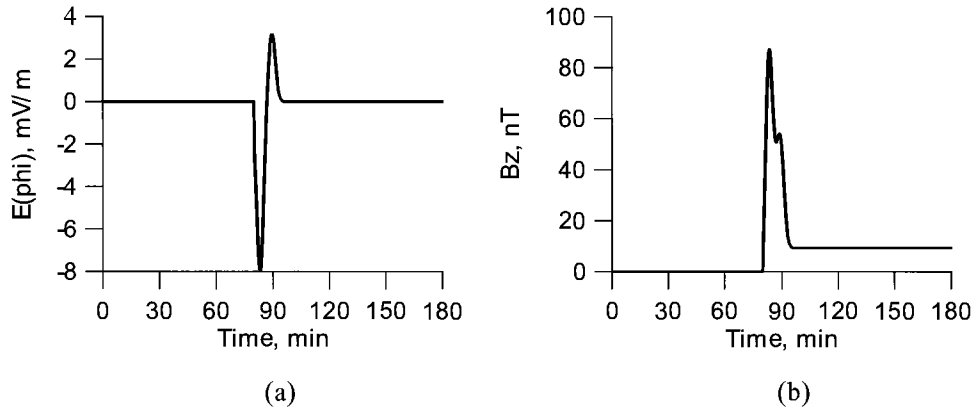

Figure 3. Behavior of the (a) electric field E_ϕ and (b) magnetic field B_z components in the *Li et al.*, [1998] electromagnetic pulse model.

field in the equatorial plane increases due to a temporally and spatially varying electric field predominantly westward. The perturbed fields propagate from the tail earthward. The electric field is modeled as a time-dependent Gaussian pulse with a purely azimuthal electric field component that propagates radially inward, decreases away from midnight, and is partially reflected near the plasmapause. The modeled magnetic field dipolarization, determined from Faraday's law, occurs first at midnight and subsequently at other longitudes. Figure 3 shows the behavior of the electric field E_ϕ and magnetic field B_z components. The model gives good agreement with the observed dispersionless electron injections at geostationary orbit. The model is built on the idea that a perturbation farther out in the magnetotail propagates inward, probably in the form of bursty bulk flows, and produces dipolarization and dispersionless injections. *Sarris et al.*, [2002] introduced a pulse velocity decreasing with radial distance. Figure 4a shows the influence of the electric field pulse with amplitude of 1 mV/m on the trajectories of 3 keV protons at 8 R_E, which move in Volland-Stern electric and dipole magnetic field models for $Kp = 2$. The pulse shifts protons inward by 2 R_E within 15 min. Figure 4b illustrates the changes of the 3 keV proton energy and radial distance. The pulse energizes the proton up to 42 keV.

Ganushkina et al., [2000, 2001] studied the penetration of the plasma sheet ions deep into the inner magnetosphere.

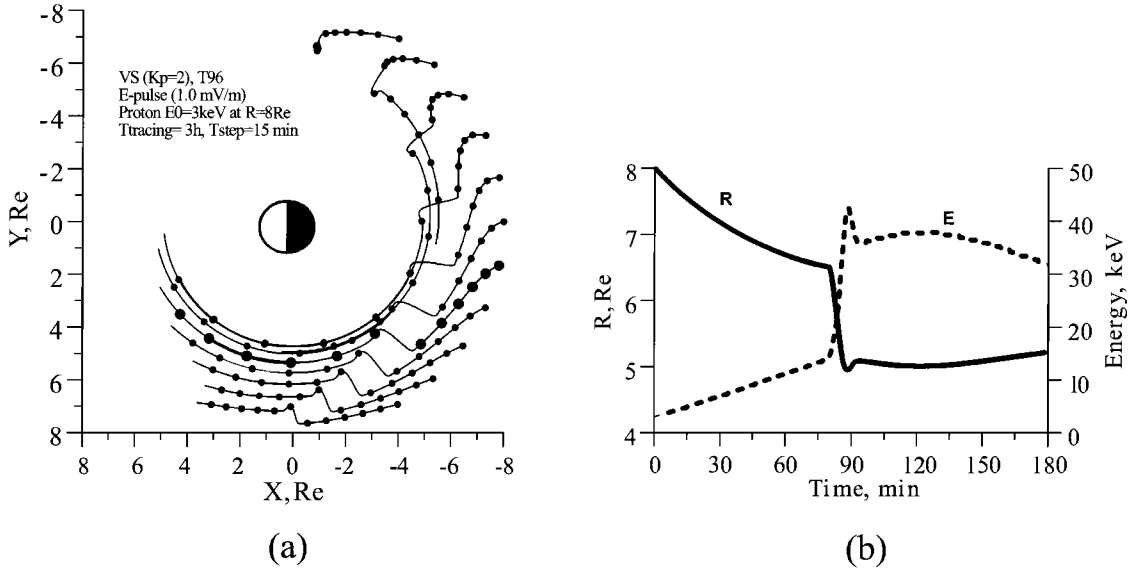

Figure 4. (a) Influence of the electric field pulse with amplitude of 1 mV/m on the trajectories of 3 keV protons at 8 R_E, which move in Volland-Stern electric and Tsyganenko T96 magnetic field models. (b) Changes of the 3 keV proton energy (dashed line) and radial distance (solid line).

These structures are called intense nose events, owing to their characteristic structure in energy-time spectrograms. The *Li et al.*, [1998] model was used together with large-scale electric and magnetic fields for particle tracing. It was shown that the inward displacement of the intense nose structure can occur under short-lived pulse electric fields combined with the convection electric field. Large scale convection alone leads to the regular nose structure formation which takes several (>5) hours during quiet periods [*Buzulukova et al.*, 2003].

As observations and modeling have shown, the substorm-associated electric fields are effective in the particle transport and energization. There is a great need to get more realistic models for the electric field. Likewise, there is an equal need for better and more comprehensive electric field observations that could be used to constrain such models both for the large-scale convection and smaller-scale temporally evolving structures.

6. RING CURRENT DEVELOPMENT: CONVECTION OR SUBSTORM PARADIGM

The relative importance of the large-scale convection electric field and the substorm-associated electric fields in the energization and transport of ions into the ring current is still an open question.

Many storms have been simulated based on the convection paradigm [*Lee et al.*, 1983; *Takahashi et al.*, 1990; *Kozyra et al.*, 1998; *Ebihara and Ejiri*, 2000; *Jordanova et al.*, 2001; *Liemohn et al.*, 2001]. In these calculations the magnetic field was in most cases a dipole, and the electric field was taken to be the Volland-Stern or other empirical convection electric field model. These authors concluded that the ion transport into the ring current can be accomplished by the enhanced large-scale convection electric field, and that the role of the substorm-associated electric field in developing the ring current is only to enhance the intensity of the convection electric field [*Ebihara and Ejiri*, 2003].

Other studies have concluded that concurrent action of global convection and substorm-associated dipolarization and electric field variations inject plasma closer to the Earth than either one would do individually [*Fok et al.*, 1999; *Pulkkinnen et al.*, 2000; *Ganushkina and Pulkkinen*, 2002]. Especially, *Ganushkina and Pulkkinen* [2002] studied the role of electric field pulses in the ring current formation by tracing protons numerically in the guiding center approximation in Volland-Stern large-scale convection electric field and Tsyganenko T96 [*Tsyganenko*, 1995] magnetic field models. In addition, they introduced substorm-associated variations as electric field pulses, similar to *Li et al.*, [1998], at substorm onsets. It was shown that the large-scale convection alone can transport the ions to the observed ring current location, but that the electric field pulses were necessary to get the observed energy spectrum peaking at several tens of keV. The formation of the ring current is thus a combination of convection and pulsed inward shifts and consequent energization.

In order to evaluate the energy range, which is most important for the ring current energy content during storms, *Ganushkina et al.*, (manuscript submitted to Annales Geophysicae, 2004) analyzed Polar CAMMICE MICS particle data during 27 storms. The energy density and total energy of ring current protons were computed in the low (1-20 keV), medium (20-80 keV), and high (80-200 keV) energy ranges. The statistical results showed that the medium energy protons contributed most to the total ring current energy during the storm main phase. During the recovery phase, the high energy protons played a dominant role.

Further development of the particle tracing procedure described by *Ganushkina and Pulkkinen* [2002] made it possible to trace protons with arbitrary pitch angles, assuming conservation of the 1st and 2nd invariants, in different time-dependent magnetic and electric fields (Figure 5). For May 2-4, 1998 storm, using stationary Volland-Stern electric field model, the results showed that the main contribution to the ring current energy comes from protons with medium energies of 20-80 keV during the entire storm (Figure 5a). The contribution from the high energy protons was very small. Using other empirical electric field models, such as *Boyle et al.*, [1997] polar cap potential applied to Volland-Stern type convection electric field, or varying the plasma sheet number density and/or temperature in the initial distribution showed similar results (Figure 5b). However, when the substorm activity was represented by incorporating the time varying fields associated with dipolarization in the magnetotail (similar to *Sarris et al.*, [2002] pulse model), the contribution from the high energy protons became dominant during the storm recovery phase (Figure 5c).

Although these results are related to a question of storm-substorm relationship, it does not give an exact answer. Dst index is usually considered as a measure of storm ring current. The absence of further decrease in Dst (rather Dst increase) when a substorm occurs during storm [*Iyemori and Rao*, 1996; *Siscoe and Petschek*, 1997] argues against the important role of substorms in storm ring current development [*McPherron*, 1997]. From the other hand, Dst index contains contributions from other current systems, and their relations depend on the storm intensity and phase. During moderate storms the contribution from the tail current during storm main phase can be comparable to that of the ring current [*Ganushkina et al.*, 2004]. The modeled Dst index can be in a very good agreement with the observed one [*Ebihara and Ejiri*, 2003] but the energy density of the ring current which constitutes in the Dst index consists mainly from medium energy ions when large-scale electric fields are only considered. High energy ions provide a significant part

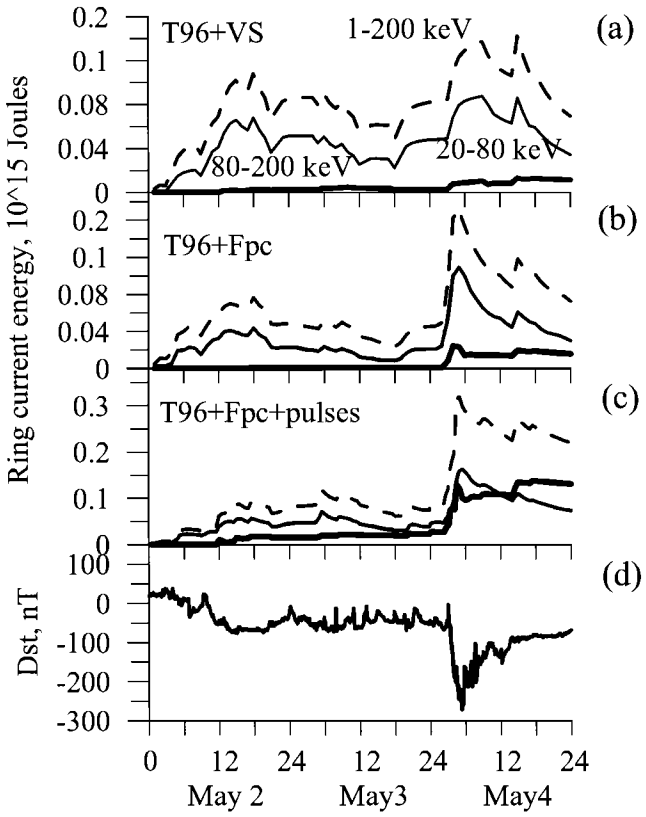

Figure 5. Calculated proton ring current energy in Joule for total (1-200 keV, dashed lines), medium (20-80 keV, thin solid lines) and high energies (80-200 keV, thick solid lines) while tracing in (a) Tsyganenko T96 magnetic field and Volland-Stern electric field, (b) T96 and *Boyle et al.,* (1997) polar cap potential applied to Volland-Stern model, and (c) with addition of electric field pulses at substorm onsets, together with the measured Dst index (d) for May 2-4, 1998.

of the ring current, energy density and electric current and they can be indeed created by acceleration by the substorm-associated pulse electric fields.

7. CONCLUDING REMARKS

In this paper the role of the electric fields in the inner magnetosphere dynamics was discussed. While the magnetospheric magnetic field is relatively well-known and several empirical models exist, the electric field observations are much fewer and the separation of the large-scale properties and the smaller scale structures is much less clear. The main issues raised in this paper can be summarized as follows:

1. The generator of the large-scale convection electric field is partly in the magnetospheric boundary layers and partially in the magnetotail. The solar wind magnetosphere interaction can generate this electric field either by reconnection (Dungey model) or viscous interaction (Axford and Hines model). On the other hand, while the primary driver is the solar wind, the regions where the plasma pressure gradient is at an angle to the magnetotail current flow lines, the resulting field-aligned current can be the source for the additional tail electric field.
2. Large scale convection models describe the electric field either by associating the solar wind and IMF behavior to the ionospheric potential pattern and via mapping to the tail (reconnection or viscous interaction as possible generators) or by adjusting the intensity of the convection field to the overall level of magnetic activity (plasma pressure gradients as possible generators). Both types of models yield large-scale stationary or slowly varying tail electric field pattern. It is important to include subauroral electric fields for the ring current formation during disturbed conditions.
3. Detailed tail observations have shown that the plasma transport in the magnetotail occurs in sporadic, intense flow bursts, which are associated with magnetic field dipolarization, high flow speeds, and highly fluctuating electric fields. It is thus clear that the models described in point (2) represent only a crude average of reality.
4. Particle injections into the inner magnetosphere are associated with fast plasma flow, magnetic field dipolarization and fluctuating electric fields. Empirical models can be used to show that the final ion energy and the lowest L-shell reached depend on the intensity of the convection and substorm associated electric fields.
5. Observations show that during storms, the ions in the energy range 20-80 keV dominate the ring current energy density during the storm main phase, but that during the recovery phase the contribution from the high-energy ions (above 80 keV) becomes dominant. Several tests using empirical models showed that such behavior of the ion distribution cannot be obtained by simply using variable intensity of the large-scale convection electric field. Only the substorm-associated electric fields were strong enough to yield the observed fluxes of high-energy (above 80 keV) particles.

As summarized above, the present state of our understanding of the magnetospheric dynamics is quite advanced. Thus, gaining new understanding will necessarily require complex models of the electromagnetic fields and particle motion. This will require combination and coupling of multiple sources as well as large-scale and small scale processes. The relative significance of these is still an open issue and calls for detailed as well as synoptic observations, preferably simultaneously.

Acknowledgments. The author would like to thank Prof. Tuija Pulkkinen and Prof. Hannu Koskinen for the most valuable discussion when writing this paper. The work was supported by the Academy of Finland.

REFERENCES

Aggson, T.L., J. Heppner, and N. Maynard, Observations of large magnetospheric electric fields during the onset phase of a substorm, *J. Geophys. Res.*, 88, 3981-3990, 1983.

Akasofu, S.-I., The development of geomagnetic and auroral storms, *J. Geomag. Geoelect.*, 18, 109-123, 1966.

Anderson, P.C., D.L. Carpenter, K. Tsuruda, T. Mukai, and F.J. Rich, Multisatellite observations of rapid subauroral ion drifts (SAID), *J. Geophys. Res.*, 106, 29,585-29,599, 2001.

Angelopoulos, V., W. Baumjohann, C.F. Kennel, *et al.*, Bursty bulk flows in the inner central plasma sheet, *J. Geophys. Res.*, 97 4027-4039, 1992.

Antonova, E.E., Magnetostatic equilibrium and turbulent transport in Earth's magnetosphere: A review of experimental observation data and theoretical approaches, *Int. J. Geomagn. and Aeron.*, 3, 117-130, 2002.

Antonova, E.E., and N. Yu. Ganushkina, Azimuthal hot plasma pressure gradients and dawn-dusk electric field formation, *J. Atmos. Terr. Phys.*, 59, 1343-1354, 1997.

Arnoldy, R.L., and K.W. Chan, Particle substorms observed at the geostationary orbit, *J. Geophys. Res.*, 74, 5019-5028, 1969.

Axford, W., and C. Hines, A unifying theory of high-latitude geophysical phenomena and geomagnetic storms, *Canad. J. Phys.*, 39, 1433-1464, 1961.

Baker *et al.*, Observations and modeling of energetic particles at synchronous orbit on July 29, 1977, *J. Geophys. Res.*, 87, 5917-5932, 1982.

Baumjohann, W., G. Paschmann, and H. Luehr, Characteristics of high-speed ion flows in the plasma sheet, *J. Geophys. Res.*, 95 3801-3809, 1990.

Birn, J., M.F. Thomsen, J.E. Borovsky, *et al.*, Substorm ion injections: Geosynchronous observations and test particle orbits in three-dimensional dynamic MHD fields, *J. Geophys. Res.*, 102, 2325-2341, 1997.

Boyle, C.B., P.H. Reiff, and M.R. Hairston, Empirical polar cap potentials, *J. Geophys. Res.*, 102, 111-125, 1997.

Burke, W.J., M.C. Kelley, R.C. Sagalyn, *et al.*, Polar cap electric field structure with northward interplanetary magnetic field, *Geophys. Res. Lett.*, 6, 21-24, 1979.

Buzulukova, N. Yu., R.A. Kovrazhkin, A.L.Glazunov, *et al.*, Stationary nose structures of protons in the inner magnetosphere: Observations by the ION instrument onboard the Interball-2 satellite and modeling, *Cosmic Research*, 41, 3-12, 2003.

Cattell, C.A., and F.S. Mozer, Substorm electric fields in the Earth's magnetotail, in *Magnetic Reconnection in Space and Laboratory Plasmas, Geophys. Monogr. Ser., vol.* 30, edited by E.W. Hones Jr., p. 208-215, AGU, Washington, D.C., 1984.

Cauffman, D.P., and D.A. Gurnett, Double-probe measurement of convection electric fields with the Injun 5 satellite, *J. Geophys. Res.*, 76, 6014-6027, 1971.

Chapman, S., Earth Storms: Retrospect and Prospect, *J. Phys. Soc. Japan*, 17, 6-16, 1962.

Chen, C.X., and R.A. Wolf, Interpretation of high-speed flows in the plasma sheet, *J. Geophys. Res.*, 98, 21,409-21,419, 1993.

Daglis, I.A., S. Livi, E.T. Sarris, *et al.*, Energy density of ionospheric and solar wind origin ions in the near-Earth magnetotail during substorms, *J. Geophys. Res.*, 99, 5691-5703, 1994.

Daglis, I.A., The role of magnetosphere-ionosphere coupling in magnetic storm dynamics, in: *Magnetic Storms, Geophys. Monogr. Ser., vol.* 98, edited by B.T. Tsurutani, W.D. Gonzalez, Y. Kamide, and J.K. Arballo, pp. 107-116, American Geophysical Union, Washington, DC, 1997.

Daglis, I.A., Y.Kamide, G. Kasotakis, C. Mouikis, B. Wilken, E.T. Sarris, and R. Nakamura, Ion composition in the inner magnetosphere: Its importance and its potential role as a discriminator between storm-time substorms and non-storm substorms, in: *Fourth International Conference on Substorms (ICS-4)*, edited by S. Kokubun and Y. Kamide, Terra/Kluwer Publications, Tokyo, pp. 767-772, 1998.

Davis, T.N., The morphology of the auroral displays of 1957-1958, 2. Detail analyses of Alaska data and analyses of high-latitude data, *J. Geophys. Res.*, 67, 75-110, 1962.

Delcourt, D.C., Particle Acceleration by Inductive Electric Fields in the Inner Magnetosphere, *J. Atm. Solar Terrest. Phys.*, 64, 551-559, 2002.

del Pozo, C.F., and M. Blanc, Analytical self-consistent model of the large-scale convection electric field, *J. Geophys. Res.*, 99, 4053-4068, 1994.

De Michelis, P., I.A. Daglis, and G. Consolini, An average image of proton plasma pressure and of current systems in the equatorial plane derived from AMPTE/CCE-CHEM measurements, *J. Geophys. Res.*, 104, 28,615-28,624, 1999.

Dungey, J.W., Interplanetary magnetic field and the auroral zones, *Phys. Rev. Letters*, 6, 47-48, 1961.

Ebihara, Y., and M. Ejiri, Simulation study on fundamental properties of the storm-time ring current, *J. Geophys. Res.*, 105, 15,843-15,860, 2000.

Ebihara, Y., and M. Ejiri, Numerical simulation of the ring current: Review, *Space Sci. Rev.*, 105, 377-452, 2003.

Elphinstone, R.D., D. Hearn, J.S. Murphree, and L.L. Cogger, Mapping using the Tsyganenko long magnetospheric model and its relationship to Viking auroral images, *J. Geophys. Res.*, 96 1467-1480, 1991.

Fairfield, D.H., Polar magnetic disturbances and the interplanetary magnetic field, *Space Research VIII*, 107-119, 1967.

Feldstein, Ya.I., and Yu.I. Galperin, The auroral luminosity structure in the high-latitude upper atmosphere: Its dynamics and relationship the large-scale structure of the Earth's magnetosphere, *Rev. Geophys.*, 23, 217-275, 1985.

Fok, M.-C., T.E. Moore, and D.C. Delcourt, Modeling of inner plasma sheet and ring current during substorms, *J. Geophys. Res.*, 104, 14,557-14,569, 1999.

Foster, J.C., and H.B. Vo, Average characteristics and activity dependence of the subauroral polarization stream, *J. Geophys. Res.*, 107, 1475, DOI: 10.1029/2002JA009409, 2002.

Ganushkina, N. Yu., and T.I. Pulkkinen, Particle tracing in the inner Earth's magnetosphere and the formation of the ring current during storm times, *Adv. Space Res.*, 30, 1817-1820, 2002.

Ganushkina, N. Yu., T.I. Pulkkinen, V.A. Sergeev, *et al.*, Entry of plasma sheet particles into the inner magnetosphere as observed by Polar/CAMMICE, *J. Geophys. Res.*, 105, 25,205-25,219, 2000.

Ganushkina N. Yu., T.I. Pulkkinen, V.F. Bashkirov, D.N. Baker, and X. Li, Formation of intense nose structures, *Geophys. Res. Lett.*, 28, 491-494, 2001.

Ganushkina, N. Yu., T.I. Pulkkinen, M.V. Kubyshkina, *et al.*, Modeling the ring current magnetic field during storms, *J. Geophys. Res.*, 107, 10.1029/2001JA900101, 2002.

Ganushkina, N. Yu., T.I. Pulkkinen, M.V. Kubyshkina, *et al.*, Long-term evolution of magnetospheric current systems during storms, *Ann. Geophys.*, 22, 1317-1334, 2004.

Gold, T., Motions in the magnetosphere of the Earth, *J. Geophys. Res.*, 64, 1219-1224, 1959.

Hamilton, D.C., G. Gloeckler, F.M. Ipavich, *et al.*, Ring current development during the great geomagnetic storm of February 1986, *J. Geophys. Res.*, 93, 14,343-14,355, 1988.

Heelis, R.A., W.B. Hanson, C.R. Lippincott, *et al.*, The ion drift meter for Dynamics Explorer B, *Space Sci. Instrum.*, 5, 511-521, 1981.

Heppner, J.P., Electric field variations during substorms: OGO 6 measurements, *Planet. Space Sci.*, 20, 1475-1498, 1972a.

Heppner, J.P., Polar cap electric field distributions related to the interplanetary magnetic field direction, *J. Geophys. Res.*, 77, 4877-4887, 1972b.

Heppner, J.P., and N.C. Maynard, Empirical high-latitude electric field models, *J. Geophys. Res.*, 92, 4467-4489, 1987.

Iyemori, T., and D.R.K. Rao, Decay of the Dst field of geomagnetic disturbances after substorm onset and its implication to storm-substorm relation, *Ann. Geophys.*, 14, 608-618, 1996.

Jordanova, V.K., L.M. Kistler, C.J. Farrugia, and R.B. Torbert, Effects of inner magnetospheric convection on ring current dynamics: March 10-12, 1998, *J. Geophys. Res.*, 106, 29,705-29,720, 2001.

Kamide, Y., Is substorm occurrence a necessary condition for a magnetic storm?, *J. Geomagn. Geoelectr.*, 44, 44, 109-117, 1992.

Karty, J.L., R.A. Wolf, and R.W. Spiro, Region one Birkeland currents connecting to sunward convecting flux tubes, In: Magnetospheric currents; Chapman Conference, Irvington, VA, April 5-8, 1983, Selected Papers (A84-45751 22-46), Washington, DC, AGU, pp. 269-275, 1984.

Kozyra, J.U., V.K. Jordanova, J.E. Borovsky, *et al.*, Effects of a high-density plasma sheet on ring current development during the November 2-6, 1993, *J. Geophys. Res.*, 103, 26,285-26,305, 1998.

Lee, L.C., G. Corrick, and S.-I. Akasofu, On the ring current energy injection rate, *Planet. Space Sci.*, 31, 901-911, 1983.

Li, X., D.N. Baker, M. Temerin, *et al.*, Simulation of dispersionless injections and drift echoes of energetic electrons associated with substorms. *Geophys. Res. Lett.*, 25, 3763-3766, 1998.

Liemohn, M.W., J.U. Kozyra, M.F. Thomsen, *et al.*, Dominant role of the asymmetric ring current in producing the stormtime Dst. *J. Geophys. Res.*, 106, 10,883-10,904, 2001.

McPherron, R.L., The role of substorms in the generation of magnetic storms, in: *Magnetic Storms, Geophys. Monogr. Ser., vol.* 98, edited by B.T. Tsurutani, W.D. Gonzalez, Y. Kamide, and J.K. Arballo, pp. 131-147, American Geophysical Union, Washington, DC, 1997.

Maynard, N.C., *et al.*, Dynamics of the inner magnetosphere near times of substorm onsets. *J. Geophys. Res.*, 101, 7705-7736, 1996.

Maynard, N.C., and A.J. Chen, Isolated cold plasma regions: Observations and their relation to possible production mechanisms, *J. Geophys. Res.*, 80, 1009-1013, 1975.

McIlwain, C.E., A *Kp*-dependent equatorial electric field model, *Adv. Space Res.*, 6, 187-197, 1986.

Milillo, A., S. Orsini, and I.A. Daglis, Empirical model of proton fluxes in the equatorial inner magnetosphere: Development. *J. Geophys. Res.*, 106, 25,713-25,730, 2001.

Moore, T.E., R.L. Arnoldy, J. Feynman, and D.A. Hardy, Propagating substorm injection fronts, *J. Geophys. Res.*, 86, 6713-6726, 1981.

Nakamura, R., W. Baumjohann, B. Klecker, *et al.*, Motion of the dipolarization front during a flow burst event observed by Cluster, *Geophys. Res. Lett.*, 29, CiteID 1942, DOI 10.1029/2002GL015763, 2002.

Parker, E.N., The alternative paradigm for magnetospheric physics, *J. Geophys. Res.*, 101, 10,587-10,625, 1996.

Paschmann, G., G. Haerendel, I. Papamastorakis, N. Sckopke, S.J. Bame, J.T. Gosling, C.T. Russell, Plasma and magnetic field characteristics of magnetic flux transfer events. *J. Geophys. Res.*, 87, 2159-2168, 1982.

Pulkkinen, T.I., N. Yu. Ganushkina, V.F. Bashkirov, *et al.*, Ring current enhancement due to substorm-associated inductive electric fields, *Proc. 5th Int. Conf. Substorms*, ESA Publications Division, Special Publication SP-443, pp. 451-454, 2000.

Pulkkinen, T.I., H.E.J. Koskinen, K.E.J. Huttunen, *et al.*, Effects of magnetic storms on substorm evolution, *Proc. 6th Int. Conf. Substorms*, edited by R.M. Winglee, pp. 464-471, 2002.

Reeves, G.D., R.D. Belian, and T. Fritz, Numerical tracing of energetic particle drifts, *J. Geophys. Res.*, 96, 13,997-14,008, 1991.

Richmond, A.D., and Y. Kamide, Mapping electrodynamics features of the high-latitude ionosphere from localized observations: Technique, *J. Geophys. Res.*, 81, 5741-5759, 1988.

Rowland, D.E., and J.R. Wygant, Dependence of the large-scale, inner magnetospheric electric field on geomagnetic activity, *J. Geophys. Res.*, 103, 14,959-14,964, 1998.

Russell, C.T., and R.L. McPherron, The magnetotail and substorms, *Space Sci. Rev.*, 15, 205, 1973.

Sarris, T.E, X. Li, N. Tsaggas, and N. Paschalidis, Modeling energetic particle injections in dynamic pulse fields with varying propagation speeds, *J. Geophys. Res.*, 107, CiteID 1033, DOI 10.1029/2001JA900166, 2002.

Sergeev, V.A., V. Angelopoulos, J.T. Gosling, C.A. Cattell, C.T. Russell, Detection of localized, plasma-depleted flux tubes or bubbles in the midtail plasma sheet, *J. Geophys. Res.*, 101, 10,817-10,826, 1996.

Siscoe, G.L. and H.E. Petschek, On storm weakening during substorm expansion phase, *Ann. Geophys.*, 15, 211-216, 1997.

Slavin, J.A., R.P. Lepping, J. Gjerloev, J., *et al.*, Cluster electric current density measurements within a magnetic flux rope in the plasma sheet, *Geophys. Res. Lett.*, 30, CiteID 1362, DOI 10.1029/2002GL016411, 2002.

Sonnerup, B.U.O., G. Paschmann, I. Papamastorakis, N. Sckopke, G. Haerendel, S.J. Bame, J.R. Asbridge, J.T. Gosling, C.T. Russell, Evidence for magnetic field reconnection at the earth's magnetopause, *J. Geophys. Res.*, 86, 10049-10067, 1981.

Spiro, R.W., R.A. Heelis, and W.B. Hanson, Ion convection and the formation of the mid-latitude F region ionization trough, *J. Geophys. Res.*, 78, 4255-4264, 1978.

Spiro, R., W.M. Harel, R.A. Wolf, and P.H. Reiff, Quantitative simulation of a magnetospheric substorm. III - Plasmaspheric electric fields and evolution of the plasmapause, *J. Geophys. Res.*, 86, 2261-2272, 1981.

Stern, D.P., The motion of a proton in the equatorial magnetosphere, *J. Geophys. Res.*, 80, 595-599, 1975.

Takahashi, S., T. Iyemori, and M. Takeda, A simulation of the storm-time ring current, *Planet. Space Sci.*, 38, 1133-1141, 1990.

Tsurutani, B.T. and R.M., Thorne, Diffusion processes in the magnetopause boundary layer, *Geophys. Res. Lett.*, 9, 1247-1250, 1982.

Tsyganenko, N.A., Modeling the Earth's magnetospheric magnetic field confined within a realistic magnetopause, *J. Geophys. Res.*, 100, 5599-5612, 1995.

Tverskoy, B.A., On the field-aligned currents in the magnetosphere, *Geomagn. Aeron.*, 22, 991-994, 1982.

Tu, J.-N., K. Tsuruda, H. Hayakawa, A. Matsuoka, T. Mukai, I. Nagano, and S. Yagitani, Statistical nature of impulsive electric fields associated with fast ion flow in the near-Earth plasma sheet, *J. Geophys. Res.*, 105, 18,901-18,907, 2000.

Vasyliunas, V.M., Mathematical models of magnetospheric convection and its coupling to the ionosphere, in *Particles and Fields in the Magnetosphere*, B.M. McCormac, ed., D. Reidel, p. 60-71, 1970.

Volland, H., A semi-empirical model of large-scale magnetospheric electric field, *J. Geophys. Res.*, 78, 171, 1973.

Weimer, D.R., An improved model of ionospheric electric potentials including substorm perturbations and application to the geospace environment modeling November 24, 1996 event, *J. Geophys. Res.*, 106, 407-416, 2001.

Wolf, R.A., R.W. Spiro, G.-H. Voigt, *et al.*, Computer simulation of inner magnetospheric dynamics for the magnetic storm of July 29, 1977, *J. Geophys. Res.*, 87, 5949-5962, 1982.

Yang, Y.S., R.W. Spiro, and R.A. Wolf, Generation of region 1 current by magnetospheric pressure gradients, *J. Geophys. Res.*, 99, 223-234, 1994.

Zaharia, S., C.Z. Cheng, and J.R. Johnson, Particle transport and energization associated with substorms, *J. Geophys. Res.*, 105, 18,741-18,752, 2000.

N. Yu. Ganushkina, Finnish Meteorological Institute, Geophysical Research, PO Box 503, Helsinki, FIN-00101 Finland. (email: Nataly.Ganushkina@fmi.fi)

Injection of Energetic Ions During the 31 March 0630 Substorm

Scot R. Elkington and Daniel N. Baker

Laboratory for Atmospheric and Space Physics, University of Colorado, Boulder

Michael Wiltberger

National Center for Atmospheric Research/High Altitude Observatory, Boulder, Colorado

The geomagnetic storm beginning on March 31, 2001 was characterized by high solar wind speeds and long intervals of strongly-southward interplanetary magnetic field. These conditions led to high levels of magnetospheric convection and significant distortion in the inner magnetosphere. During a period of particularly intense driving by the solar wind, an ~0630 UT substorm onset was observed to inject energetic particles into relatively low L-values in the premidnight regions of the inner magnetosphere. In this work we present the results of MHD/particle simulations of the storm, focusing on the period immediately surrounding the 0630 substorm. We analyze the characteristics of the global field prior to onset, and the evolution and effect of the subsequent dipolarization on the keV protons injected from the plasma sheet into the inner magnetosphere. We find good qualitative agreement between global observations of the injection event and the results of the MHD/particle simulations, and suggest that a weak field region in the near-Earth tail may have served as a source region for the more energetic particles injected in the premidnight regions of the magnetosphere.

1. INTRODUCTION

Transient processes affecting the field configuration in the near-Earth tail can have a direct effect on the energetic particle population in the plasma sheet and inner magnetosphere. In particular, magnetospheric substorms can inject energetic ions and electrons inside geosynchronous orbit [*Reeves and Henderson*, 2001], into the trapped particle region, energizing particles participating in the injection process. Such particles can potentially enhance the ring current, increasing the storm-time magnetic disturbance at the surface of the Earth [*McPherron*, 1997], and may be a contributing source of energetic electrons populating the outer zone radiation belts [*Kim et al.*, 2000; *Ingraham et al.*, 2001]. Energization of magnetospheric particles during a substorm may occur through some combination of betatron and Fermi acceleration processes [*Williams et al.*, 1990].

Observations of magnetospheric fields and particles during substorm events has provided much insight into the phenomenology of substorm particle injections [*Baker et al.*, 1996]. However, our understanding of substorms' affect on global particle dynamics may be furthered through direct simulation of the particle trajectories moving under the influence of representative electric and magnetic fields. For example, *Li et al.* [1998b] used analytic field models to examine the dispersionless injection of electrons into geosynchronous altitudes during a substorm dipolarization, and found that the bulk of the energization could be explained in terms of betatron acceleration as the particles were moved by the impulse into regions of stronger magnetic field strength. In that study, the idealized field model consisted of a gaussian electric pulse propagating through a dipole magnetic field, with a corresponding magnetic

The Inner Magnetosphere: Physics and Modeling
Geophysical Monograph Series 155

10.1029/155GM17

disturbance satisfying Faraday's law. *Birn et al.* [1997a] and *Kim et al.* [2000] similarly examined the detailed dynamics of plasma sheet ions and electrons moving under the influence of an idealized substorm onset, using a physically-based magnetohydrodynamic (MHD) simulation of the near-Earth tail.

Many aspects of substorm particle injections may be considered in the same terms as other types of impulsive injection events, e.g. particles injected during a storm sudden commencement (SSC) [*Li et al.*, 1998a]. The dynamical characteristics of the injection front is an important contributing factor in determining the extent to which a given particle population is affected by the substorm. Relevant characteristics include the amplitude of the induced electric fields seen by the particles, as well as the azimuthal and radial extent and propagation velocities of the injection front. For example, *Elkington et al.* [2002] used an analysis of an injection of particles during the March 24, 1991 sudden commencement to show that coherent, impulsive injections were drift resonant in nature, i.e. those particles that saw the greatest energization were those with drift velocities that allowed them to stay "in sync" with the injection front as it propagated radially inward and spread azimuthally about the Earth. *Sarris et al.* [2002] undertook a parametric study of substorm injections using an analytic field model. That work suggested that observations of dispersionless particle injections were best explained in terms of an impulsive injection model that begins as a high-speed, Earthward-directed event in the magnetotail, slowing to under 100 km/s as the disturbance propagates into the inner magnetosphere.

The March 31, 2001 geomagnetic storm was characterized by significant dynamic pressures in the solar wind and notable levels of magnetospheric distortion, with the D_{ST} index dropping below –380 nT and the magnetopause, and perhaps even the bow shock, driven at times inside geosynchronous orbit [*Baker et al.*, 2002]. Intervals of southward interplanetary magnetic field as low as –50 nT led to intense magnetospheric convection, and significant activity in the magnetotail and premidnight/duskward regions of the magnetosphere [*Skoug et al.*, 2003]. In particular, an intense, isolated substorm was observed at 0630 UT on March 31. Multisatellite observations of the injection process gave an unprecedented view of the characteristics of this substorm. Notably, the bulk of the substorm injection was centered on the premidnight sector of the magnetosphere, with the injection front approaching as close as 4 R_E and dispersionless particle signatures seen at geosynchronous as far into the dusk sector as 20 LT [*Baker et al.*, 2002]. Global images of energetic neutral atoms (ENA) injected during the event are indicated in Plate 1, where protons with energies above 27 keV are seen to be enhanced primarily in the post-dusk, premidnight sector of the magnetosphere.

In this work we analyze the global field configuration as given by MHD simulations of the magnetosphere during the growth and onset of the 0630 magnetospheric substorm. We examine properties of the injection region, including the speed and evolution of the injection front during the substorm onset and particle injection. Test particle simulations are conducted within the MHD fields, and show consistency with global observations of the newly injected particles.

INJECTION FRONT ANALYSIS

Magnetohydrodynamic simulations of the the March 31, 2001 geomagnetic storm were undertaken using the Lyon-Fedder-Mobarry MHD code [*Lyon et al.*, 1998; *Fedder and Lyon*, 1995]. The LFM consists of a coupled ionosphere magnetosphere model, solving the MHD equations on a 3D grid subject to upstream solar wind conditions. The LFM includes in a self-consistent fashion (within the limits of the MHD approximation, see [*Sturrock*, 1994]) physical effects relevant to the study of substorm initiation and propagation, including reconnection, convection, and variable wave propagation speeds. The driving solar wind conditions were taken in this case from measurements conducted by the ACE solar wind monitor, lying at the L_1 point approximately ~240 R_E upstream of the Earth, and ballistically propagated to the forward boundary of the simulation domain. The time period simulated encompasses the storm sudden commencement (SSC) occurring late on March 30, 2001, through the storm main phase and into the recovery phase on April 2. Further details of this particular simulation, including the MHD signatures of the 0630 dipolarization, are described in *Wiltberger et al.* [2004] (this volume).

Results from the MHD simulation are indicated for the solar-magnetic equatorial plane in Plate 2, for the period (a) prior to and (b) during the substorm onset. Dashed circles concentric about the origin indicate radial distance in the equatorial plane at increments of 3, 5, 7,... R_E. Contours indicate magnetic field strength, arrows indicate the direction and magnitude of plasma flow, and the color scale gives the plasma density in the equatorial plane. To the right of the equatorial figures are the solar wind conditions driving the simulation (from top: B_Z (nT), B_y (nT), $v_s w$ (km/s), and plasma density (cm^{-3})), with a vertical line indicating the time at which the simulation snapshots were taken. For reference, the positions of four geosynchronous spacecraft (NOAA GOES-8 and 10; LANL 1991-080 and 1994-084) are indicated in the figure.

Stretching and distortion of the geomagnetic field is observed about 15 R_E downtail in the period prior to the 0630 onset. This can be seen in the top panel of Plate 2, where the magnetic field contours indicate a local minimum in the magnetic field strength just east of the noon-midnight meridian.

[redacted]

[redacted]

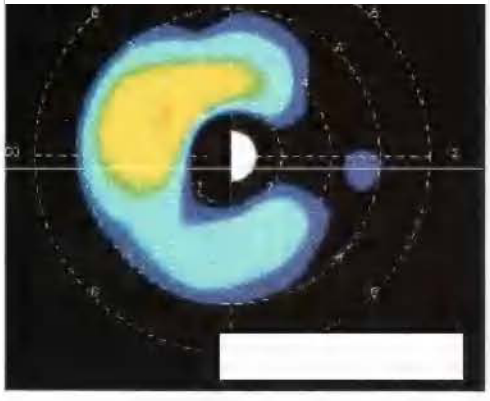

[redacted]

While such a weakening of magnetic field strength may be an indication of a local reconnection region, Earthward-directed plasma flow vectors at the tailward edge of the figure indicate reconnection is occurring further down tail.

Shortly after 0630, the MHD simulation shows a collapse of the cross-tail current Earthward of the region of maximum magnetic distortion, whereupon the field relaxes to a more dipolar configuration. Concurrent with this, plasma flow velocities increase Earthward throughout the pre-midnight sector, as indicated in the lower panel of Plate 2. This jump in plasma flow velocity is seen to extend inside geosynchronous orbit.

We wish to examine the location and evolution of the injection front throughout the dipolarization process. As a preliminary means of identifying the location of the front, we focus on the amplitude of the cross-tail electric field. This is the component of the electric field which would be responsible for the Earthward transport of energetic protons during the injection process. Figure 1 shows the E_y profile along the $y = 3R_E$ axis at selected times during the injection. The peak observed in the profile initially increases in amplitude as it propagates inward in association with the dipolarization, subsequently decreasing in magnitude as it approaches the inner magnetosphere. The peak electric field amplitude seen in this region of the simulation, ~30 mV/m, is consistent with substorm electric fields seen observationally (e.g. *Fairfield et al.* [1998]) and within previous MHD substorm simulations [*Birn et al.*, 1997a].

In Figure 2 we use a simple differencing method applied to the location of the maximum cross-tail field (indicated in the selected profiles illustrated in Figure 1 by the arrow at the peak of the evolving electric field) to gain some information about the propagation speed of the injection front. Though somewhat noisy due to the simplicity of the method used in tracking the front, the figure does indicate some of the general characteristics of the time evolution of the injection region. The peak rapidly accelerates early in the dipolarization process when the injection front was furthest downtail, and slows as the front arrives and breaks in the inner magnetosphere. Throughout most of the midtail region the front appears to propagate Earthward with a velocity between 100-150 km/s, slowing to under 100 km/s as it moves into the inner magnetosphere. Both the speed of Earthward motion and the inward deceleration are consistent with observations of substorm-induced injection fronts [e.g. *Russell and McPherron*, 1973].

PARTICLE INJECTION

The MHD flow velocities indicated in Plate 2 correspond to cold plasma flows, i.e. those particles whose motion is dominated by the local electric field. To investigate the effect of this injection process on more energetic particles, where magnetic drifts may also become important, we conduct test particle simulations of particles in the injection region during substorm onset. The technique used to track the particles is generally that described in [*Elkington et al.*, 2002, 2004], whereby individual particles are traced in the MHD under a guiding center approximation in the equatorial plane. Those particles failing the adiabaticity criterion corresponding to

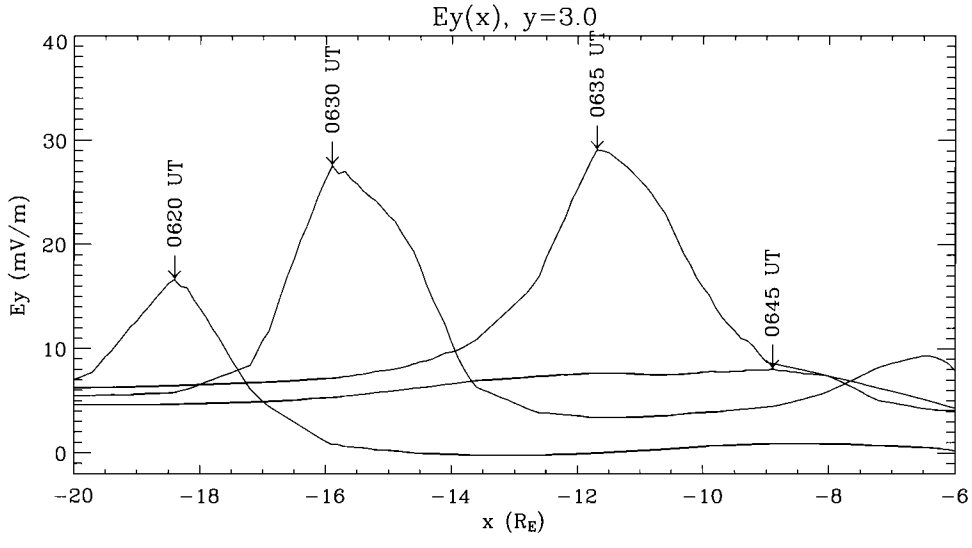

Figure 1. E_y (mV/m) in the equatorial plane at $y = 3$ at four successive times during the injection event. The arrows indicate points of maximum E_y at each time.

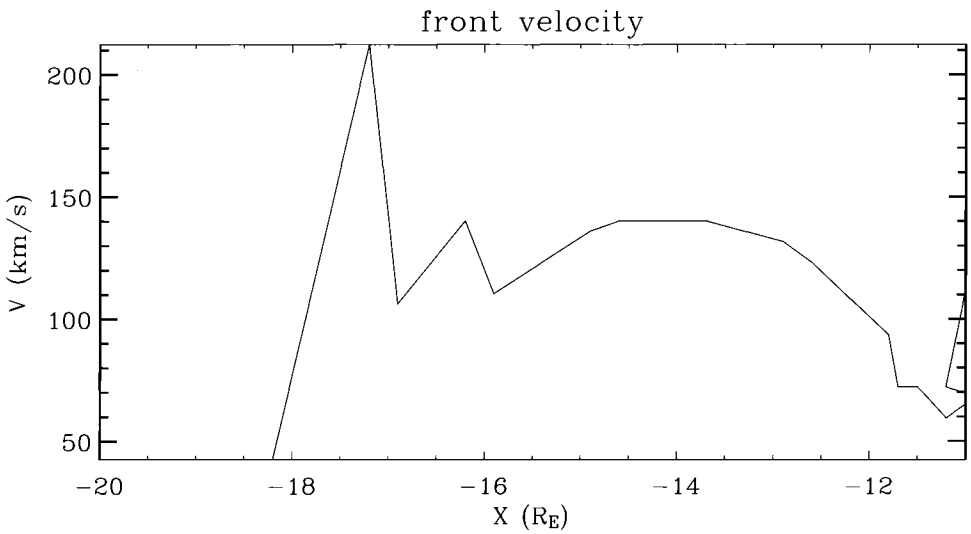

Figure 2. Velocity of the peak of the injection front as a function of distance downtail.

guiding center motion (see, for example, *Hudson et al.* [1998]) are removed from the simulation.

We initially focus on those protons that might have formed the seed population for the > 27 keV protons depicted in Plate 1. In the panel (a) of Plate 3, we begin with a population of 5 keV protons distributed in the equatorial plane throughout the tail region. The grey bar at the bottom of the panel indicates the total number of particles initially (lower) and instantaneously (upper) within the simulation. In a fashion similar to Plate 2, magnetic field strength is indicated with solid contours, and each test particle is given a color according to its first adiabatic invariant, M. Here $M = p^2/2m_0B$, where p is the relativistic momentum perpendicular to the local magnetic field, m_0 is the particle rest mass, and B is the magnitude of the local magnetic field. In a dipole field in the equatorial plane, M for a given energy particle increases as the third power of the radial distance from the center of the Earth.

Since the particles are moving under a guiding center approximation, M is conserved and serves to identify the bulk motion of different populations. Those 5 keV protons lying in the region of minimum magnetic field strength are seen to initially have a higher first invariant than those particles at similar radial distances but outside the local magnetic field minimum.

Plate 3(b) shows the particle configuration a few minutes after the substorm onset. The grey bar numbering the total particles within the simulation indicates that a few of the simulated protons are lost in the injection process, either through failure to conserve the first invariant during the onset of reconnection, or lost on open drift trajectories that pass through the sunward or flank magnetopause regions. However, most particles starting closer to the noon-midnight meridian, and in particular, those protons in the island of minimum magnetic field strength at the beginning of the injection, are efficiently moved inside geosynchronous and into the stable trapping region.

In Plate 4 we show the same protons depicted in Plate 3, here color coded by energy rather than first adiabatic invariant. Comparing Figures 3 and 4, we see that those protons initially within the local magnetic field minimum are heated to substantially higher energies than those outside the local minimum. This is due to the higher initial first adiabatic invariant of this particle population. As the particles are injected inward to regions of higher magnetic field strength, the perpendicular energy increases as a result of conservation of M. Following the injection, we find those particles initially within the local magnetic field minimum largely confined to the premidnight sector inside geosynchronous orbit. In Plate 4(c), we plot only those particles which have been heated to energies > 27 keV. The spatial distribution of these > 27 keV protons is similar to that of the injected particles observed by HENA, as illustrated in the middle panel of Plate 1.

DISCUSSION AND CONCLUSION

In this work we have examined characteristics of the substorm and resulting particle injection that occurred at 0630 on March 31, 2001. Using MHD simulations of the geomagnetic field prior to onset, we discussed the global magnetic field configuration in the region of the tail which may have served as a source region for keV protons injected during the substorm dipolarization. Simulations show significant distortion and stretching of the field in the near-Earth tail during the growth phase of the substorm, which leads to enhanced

plasma flows into the premidnight region during the dipolarization. Test particle simulations conducted in the MHD fields show evidence that the ~27 keV duskside injection of protons observed by the HENA instrument aboard IMAGE (Plate 1) corresponded to a seed population of particles with energies of a few keV, injected from the weakened field region that formed ~$15R_E$ downtail during the growth phase of the substorm.

Correlations between magnetospheric simulations and global observations of this substorm (*Baker et al.* [2002], *Skoug et al.* [2003]; see also *Wiltberger et al.* [2004], this volume) suggest that further insight may be gained through more detailed examination of this event as a an example of a storm-driven substorm. Understanding the nature and origin of the current systems that lead to the magnetic weakening and distortion in the premidnight tail may provide insight into the evolution of the magnetosphere during strongly-driven conditions such as exhibited during this storm. Further, a more detailed examination should made of the implications of these weak-field regions for those particles heated to highest energies during a substorm injection.

The analysis of the injection front characteristics seen in this MHD simulation, though preliminary, suggests good agreement with the propagation characteristics seen in other substorms. This includes both the electric field amplitude [*Fairfield et al.*, 1998], as well as the velocity and [*Russell and McPherron*, 1973] and characteristic deceleration [*Reeves et al.*, 1996; *Shiokawa et al.*, 1997] of the injection region as it approaches the inner magnetosphere. Inasmuch as the azimuthal extent and propagation characteristics of a general injection disturbance contribute to the details of the particle energization [*Birn et al.*, 1997b; *Elkington et al.*, 2002], future work should extend the analysis from the single axis examined here work to include a global picture of the characteristics and evolution of the injection front.

Although the premidnight injection of keV particles shown in these simulations suggests a specific source region and population, a more detailed examination of the characteristics of the injected particles should be undertaken in the context of a broader study. The equatorial approximation used in this work is sufficient to demonstrate the general adiabatic motion of a population of particles, but cannot include effects out of the equatorial plane or those that result from bounce motion of the particles. The simulations should also extend the comparison to other energies to allow comparison of the dispersive nature of the injection, and include the self consistent evolution and weighting of the particle populations in the weakened field region in contrast to those in the rest of the tail.

In conclusion, this study represents the first look at the March 31, 2001 substorm from the perspective of a substorm's effect on energetic particles in the near-Earth magnetotail. The use of real solar wind conditions to drive the LFM produces a substorm which agrees well with observed onset time and characteristics of the actual event. Using the MHD magnetic and electric fields to drive the particle simulation produces a proton injection into the inner magnetosphere which shows qualitative correspondence to global observations. We feel our techniques, and this event in particular, are well-suited for further study examining the details of the substorm injection process.

Acknowledgments. Work has been supported by grants ATM-0303209, NAG5-11576, and NAG5-10108 at the University of Colorado; ATM-0101375 at NCAR/HAO; and ATM-9977411 at Dartmouth College. The National Center for Atmospheric Research is sponsored by the National Science Foundation. Computational work was completed with the aid of NPACI computers. The authors would like to thank T. E. Sarris for useful discussion.

REFERENCES

Baker, D.N., T.I. Pulkkinen, V. Angelopoulos, W. Baumjohann, and R. L. McPherron (1996), Neutral line model of substorms: Past results and present view, *J. Geophys. Res.*, 101(A6), 12,975, doi:10.1029/95JA03753.

Baker, D.N., R.E. Ergun, J.L. Burch, J.-M. Jahn, P.W. Daly, R. Friedel, G.D. Reeves, T.A. Fritz, and D.G. Mitchell (2002), A telescopic and microspcopic view of a magnetospheric substorm on 31 March 2001, *Geophys. Res. Lett.*, 29(18), 1862, doi:10.1029/2001GL014491.

Birn, J., M.F. Thomsen, J.E. Borovsky, G.D. Reeves, D.J. McComas, and R.D. Belian (1997a), Characteristic plasma properties during dispersionless substorm injections at geosynchronous orbit, *J. Geophys. Res.*, 102(A2), 2309, doi:10.1029/96JA02870.

Birn, J., M.F. Thomsen, J.E. Borovsky, G.D. Reeves, D.J. McComas, R.D. Belian, and M. Hesse (1997b), Substorm ion injections: Geosynchronous observations and test particle orbits in three-dimensional dynamic MHD fields, *J. Geophys. Res.*, 102(A2), 2325, doi:10.1029/96JA03032.

Elkington, S.R., M.K. Hudson, M.J. Wiltberger, and J.G. Lyon (2002), MHD/Particle simulations of radiation belt dynamics, *J. Atmos. Solar Terr. Phys.*, 64, 607.

Elkington, S.R., M. Wiltberger, A.A. Chan, and D.N. Baker (2004), Physical models of the geospace radiation environment, *J. Atmos. Solar Terr. Phys.*, 66, 1371, doi:10.1016/j.jastp.2004.03.023.

Fairfield, D.H., *et al.* (1998), Geotail observations of substorm onset in the inner magnetotail, *J. Geophys. Res.*, 103(A1), 103, doi:10.1029/97JA02043.

Fedder, J.A. and J.G. Lyon (1995), The Earth's magnetotail is 165 R_E long: Self-consistent currents, convection, magnetospheric structure, and processes for northward interplanetary magnetic field, *J. Geophys. Res.*, 100, 3623.

Hudson, M.K., V.A. Marchenko, I. Roth, M. Temerin, J.B. Blake, and M.S. Gussenhoven (1998), Radiation belt formation during storm sudden commencements and loss during main phase, *Adv. Space Res.*, 21, 597.

Ingraham, J.C., T.E. Cayton, R.D. Belian, R.A. Christensen, R.H.W. Friedel, M.M. Meier, G.D. Reeves, and M. Tuszewski (2001), Substorm injection of relativistic electrons to geosynchronous orbit during the great magnetic storm of March 24, 1991, *J. Geophys. Res.*, 106, 25,759, doi:10.1029/2000JA000458.

Kim, H.-J., A.A. Chan, R.A. Wolf, and J. Birn (2000), Can substorms produce relativistic electrons?, *J. Geophys. Res.*, 105(A4), 7721, doi:10.1029/1999JA900465.

Li, X., D.N. Baker, M. Temerin, G.D. Reeves, and R.D. Belian (1998a), Simulation of dispersionless injections and drift echoes of energetic electrons associated with substorms, *Geophys. Res. Lett.*, 25, 3763, doi:10.1029/1998GL900001.

Li, X., *et al.* (1998b), Energetic electron injections into the inner magnetosphere during the January 10-11, 1997 magnetic cloud event, *Geophys. Res. Lett.*, 25, 2561, doi:10.1029/98GL00036.

Lyon, J.G., R.E. Lopez, C.C. Goodrich, M. Wiltberger, and K. Papadopoulos (1998), Simulation of the March 9, 1995, substorm: Auroral brightening and the onset of lobe reconnection, *Geophys. Res. Lett.*, 25(15), 3039, doi:10.1029/98GL00662.

McPherron, R.L. (1997), The role of substorms in the generation of magnetic storms, in *Magnetic Storms*, vol. 98, edited by B.T Tsurutani, W.D. Gonzalez, Y. Kamide, and J.K. Arballo, p. 131, AGU, Washington, D.C.

Reeves, G.D. and M.G. Henderson (2001), The storm-substorm relationship: Ion injections in geosynchronous measurements and composite energetic neutral atom images, *J. Geophys. Res.*, 106(A4), 5833, doi:10.1029/2000JA003017.

Reeves, G.D., R.W.H. Friedel, M.G. Henderson, A. Korth, P.S. McLachlan, and R.D. Belian (1996), Radial propagation of substorm injections, in *International Conference on Substorms* 3, vol. ESA SP-339, p. 579, European Space Agency Special Publications.

Russell, C.T. and R.L. McPherron (1973), The magnetotail and substorms, *Space Sci. Rev.*, 15, 205.

Sarris, T.E., X. Li, N. Tsaggas, and N. Paschalidis (2002), Modeling energetic particle injections in dynamic pulse fields with varying propagation speeds, *J. Geophys. Res.*, 107(A3), 1033, doi:10.1029/2001JA900166.

Shiokawa, K., W. Baumjohann, and G. Haerendel (1997), Braking of high-speed flows in the near-Earth tail, *J. Geophys. Res.*, 24(10), 1179, doi:10.1029/97GL01062.

Skoug, R.M., *et al.* (2003), Tail-dominated storm main phase: 31 March 2001, *J. Geophys. Res.*, 20, 23-1, doi:10.1029/2002JA009705.

Sturrock, P.A. (1994), Plasma Physics, 335 pp., Cambridge Univ. Press, Cambridge.

Williams, D.J., D.G. Mitchell, C.Y. Huang, L.A. Frank, and C.T. Russell (1990), Particle acceleration during substorm growth and onset, *Geophys. Res. Lett.*, 17(5), 587.

Wiltberger, M., S.R. Elkington, D.N. Baker, T. Guild, J.G. Lyon, and R.E. Lopez (2004), Comparison of MHD simulations of isolated and storm time substorms, in *Physics and modeling of the inner magnetosphere*, edited by T. Pulkkinen, N. Tsyganenko, and R. Friedel, AGU, Washington, D.C., (this volume).

S.R. Elkington and D.N. Baker, Laboratory for Atmospheric and Space Physics, University of Colorado, Boulder, CO 80303; email: scot.elkington@lasp.colorado.edu

M. Wiltberger, NCAR/HAO, POB 3000, 80307

Storm-Substorm Coupling During 16 Hours of *Dst* Steadily at -150 nT

T.I. Pulkkinen[1], N. Yu. Ganushkina[1], E. Donovan[2], X. Li[3], G.D. Reeves[4], C.T. Russell[5], H.J. Singer[6], and J.A. Slavin[7]

We examine storm-time solar wind – magnetosphere – ionosphere coupling during October 21-22, 2001. This event showed atypically long-lasting, steady depression of the *Dst* index driven by both the solar wind and the magnetotail dynamics. It is demonstrated that the solar wind pressure plays a role in the magnetospheric energy budget. It is also shown that the magnetotail response to solar wind driving depends on the tail configuration and its history, which then affects the inner magnetosphere observations by changing the tail current contribution to *Dst*. It is concluded that the effects of solar wind driving to the inner magnetosphere dynamics may vary depending on the tail configuration, which limits our capability to categorize storm events using indices only.

1. INTRODUCTION

The traditional view of solar wind – magnetosphere coupling asserts that substorms are key elements in the ring current intensification during storms [e.g., *Chapman*, 1940], while many later studies indicate that the ring current response is a function of the solar wind electric field only [e.g., *Burton et al.*, 1975]. Two points highlight the importance of storm-time substorms: (1) convection alone cannot energize particles to the observed energies [*Pulkkinen et al.*, 2000; *Ganushkina, this volume*], and (2) a large part of the energy is dissipated in the ionosphere during stormtime substorms [*Lu et al.*, 1998]. It is important to note that all substorm-like activations during storms do not have characteristics similar to isolated substorms [*Pulkkinen et al.*, 2002].

For magnetic storms, the *Dst* index gives an estimate of the ring current intensity. This index, and the high-time-resolution SYM-H, are defined as the average of the disturbance at several low-latitude stations weighted by a function of the station latitude. While these indices constitute long time series and as such highly valuable data sets, their interpretation in terms of the solar wind driver is still under discussion [e.g., *Häkkinen et al.*, 2003]. The uncertainty is caused by both the complexity of the solar wind – magnetosphere interaction and the sources other than ring current (e.g., magnetopause, magnetotail, field-aligned currents) that contribute to the indices.

While a variety of solar wind drivers cause "typical" magnetic storms, specific features in the driver can cause unusual magnetospheric response: Steady convection events arise from weak but steady driving [*Sergeev et al.*, 1996], while the HILDCAA events occur as a response to strong Alfvénic fluctuations in the interplanetary magnetic field (IMF) [*Tsurutani and Gonzalez*, 1987]. Here we analyze magnetospheric activity during a storm during which the *Dst* index was steady over an extended period of time and compare the results with substorm-like activity during typical storms.

2. EVENT DESCRIPTION

The storm initiated when the sheath region of an interplanetary magnetic cloud reached the magnetosphere at

[1]Finnish Meteorological Institute, Helsinki, Finland
[2]Department of Physics and Astronomy, University of Calgary, Canada
[3]University of Colorado, Boulder, CO
[4]Los Alamos National Laboratory, Los Alamos, NM
[5]Institute for Geophysics and Planetary Physics, UCLA, Los Angeles, CA
[6]Space Environment Center, Boulder, CO
[7]NASA Goddard Space Flight Center, Greenbelt, MD

The Inner Magnetosphere: Physics and Modeling
Geophysical Monograph Series 155

10.1029/155GM18

1645 UT on Oct 21, 2001 (Figure 1). The shock was associated with a velocity jump from about 400 to 600 km/s. In the sheath, the IMF B_Z was variable but mostly negative, and plasma pressure pulses reached above 40 nPa. The following magnetic cloud (0140-1915 UT on Oct 22) had a large negative B_X and slowly rotating B_Y and B_Z. The leading edge of the cloud had near-zero B_Z; negative B_Z dominated the latter part of the cloud passage.

Figure 1 shows magnetic field data from both Advanced Composition Explorer (ACE) and Wind. The measurements are nearly identical even though the spacecraft were far apart: Wind was at (43.3, −7.5, 6.5) R_E at the shock onset and moved to (22.3, 7.0, −0.1) R_E by the end of Oct 22 while ACE moved from (220.9, 4.7, 26.2) R_E to (220.7, 11.1, 25.3) R_E (GSM coordinates). The average travel times from the satellite position to the magnetopause were 4.5 min for Wind and 36.7 min for ACE, assuming only motion in the X direction. These time shifts are included in all figures.

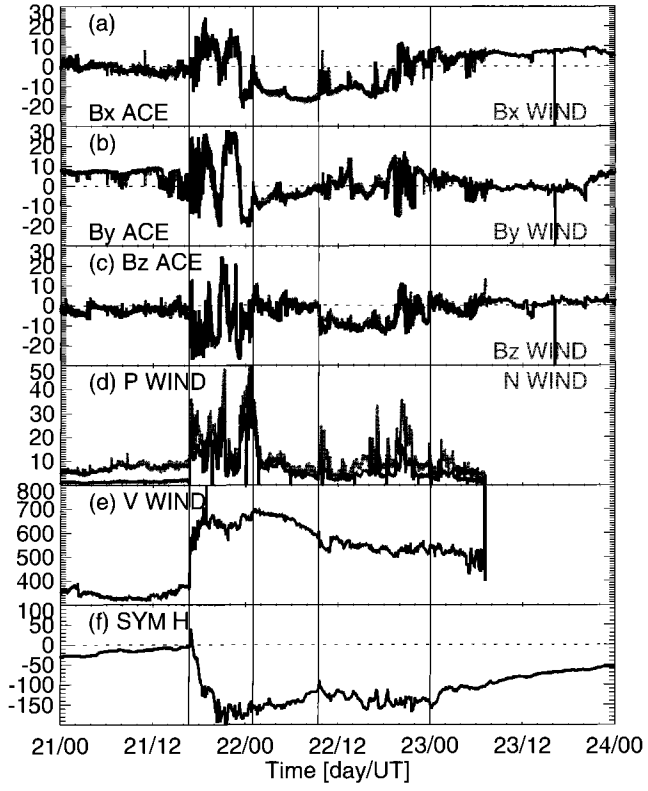

Figure 1. Interplanetary magnetic field measurements from WIND (gray dotted line) and ACE (black solid line) (a) B_X, (b) B_Y, (c) B_Z in units of nT. (d) Solar wind pressure in nPa (black solid line) and density in cm^{-3} (grey dotted line). (e) Solar wind speed in km/s. Time shifts taking into account the solar wind travel times 4.5 min for Wind and 36.7 min for ACE are introduced in the data. (f) SYM-H index in nT.

The expected solar wind energy input into the magnetosphere can be estimated using the ϵ parameter

$$\epsilon = 10^7 V B^2 l_0^2 \sin^4\left(\frac{\theta}{2}\right) \quad (1)$$

[*Akasofu*, 1981], where V is the solar wind velocity, B the IMF, $L_0 = 7R_E$ an empirical scaling parameter, and $\theta = tan^{-1}(B_Y/B_Z)$ the IMF clock angle. The ϵ parameter rose to above storm level (10^3 GW) immediately after the shock (Figure 2). It stayed at about 10^4 GW level almost throughout the sheath

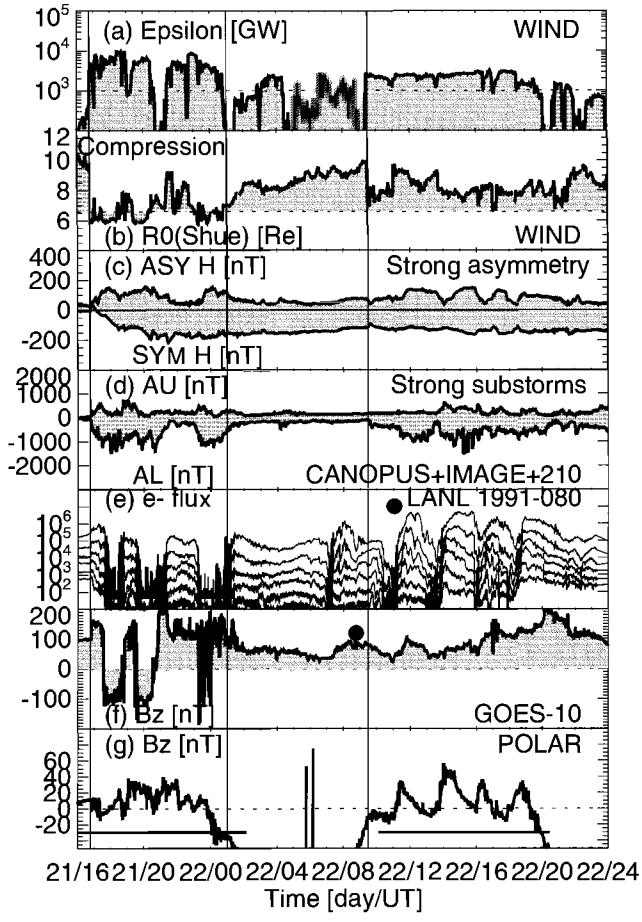

Figure 2. (a) Epsilon-parameter computed using data from Wind. (b) Subsolar magnetopause distance in R_E computed using data from Wind and model by *Shue et al.* [1998]. (c) SYM-H and ASY-H indices. (d) AU and AL indices computed using data from IMAGE, CANOPUS, and 210-meridian magnetometer chains. (e) Geosynchronous energetic electron observations. Differential fluxes for channels 50-75 keV, 75-105 keV, 105-150 keV, 150-225 keV, 225-315 keV, and 315-500 keV from s/c 1991-080. (f) B_Z in nT from GOES-10. (g) B_Z in nT from POLAR (horizontal bars mark periods when $X \leq -6R_E$). Large filled circles mark local midnight at the geosynchronous spacecraft.

encounter, but decreased at the cloud arrival to about 10^3 GW, being still near storm level at the end of Oct 22. Based on the driver properties, the Oct 21-22 storm interval is divided into three periods: (1) The sheath region (1600-0100 UT), (2) early part of the magnetic cloud with weak driving (0100-0930 UT), and (3) late part of the magnetic cloud with strong driving (0930-2400 UT). These periods are later referred to as "sheath", "weak driving", and "strong driving" periods.

The pressure pulses pushed the magnetopause to geosynchronous orbit during 1650-2030 and 2300-0030 UT on Oct 21-22. Figure 2b shows the subsolar magnetopause location computed from the solar wind and IMF using the *Shue et al.* [1998] model. The SYM-H index showed a strong positive peak beginning at 1645 UT on Oct 21, 2001, followed by a decrease to −130 nT by 1830 UT. After a period of strong activity there was a slow recovery during 0100-0930 UT, after which SYM-H stayed at about constant level for another 15 hours. The substorm activity as measured by the auroral electrojet indices in the ionosphere was strong outside a quieter period during 0100-0930 UT on Oct 22. AL/AU-type indices were created using three meridional magnetometer chains, the CANOPUS chain in Canada, the IMAGE magnetometer array in Scandinavia, and the 210 meridian chain in Eastern Asia.

The Los Alamos instruments onboard geostationary satellites showed intense substorm activity (Figure 2). During the strong driving period, particle injections were mostly clear and distinct and the electron fluxes at different local times increased almost at the same time. Thus, the entire inner magnetosphere responded in a coherent fashion. As GOES 8 and GOES 10 moved to the nightside during early Oct 22, they recorded several substorm dipolarizations. The magnetotail field was taillike with strong B_X and depressed B_Z indicating that the cross-tail current was intensified and its inner edge reached geostationary orbit. Polar further out in the magnetotail at 8 R_E and 2230 MLT observed dipolarizations that occurred simultaneously with the geostationary orbit dipolarizations and injections.

3. ENERGY DISSIPATION

The ionospheric energy dissipation can be estimated using AE-based proxies for Joule heating and particle precipitation using

$$P_{JH}[W] = 2 \cdot 1.9 \cdot 10^8 AE[nT] \quad (2)$$

$$P_{PREC}[W] = 2 \cdot 10^9 \left(4.4\sqrt{(AL[nT])} - 7.6\right). \quad (3)$$

[e.g., *Tanskanen et al.*, 2002], [*Ahn et al.*, 1983; *Østgaard et al.*, 2002]. Using this formulation, during the sheath encounter (storm main phase), the combined Joule heating and precipitation powers totalled about 900 GW, while during the weaker driving, the energy dissipation was at the level of about 200-300 GW (Figure 3).

Figure 4 shows a scatter plot of the driver-response correlation. The left and right panels show the dependence of the ionospheric power on the solar wind electric field and the solar wind dynamic pressure. The data resolution shown is 2 min; the results remain the same even for 30-min averaging. There is a tendency for weaker ionospheric power for weaker E_Y; the correlation is best during the strong driving. During the weak driving, the ionospheric dissipation has a linear dependence on the solar wind dynamic pressure with a correlation coefficient of 0.79; there is an indication of a similar tendency for the sheath encounter also.

The *Burton et al.* [1975] model has been revisited by *O'Brien and McPherron* [2000], who give a formulation for the pressure-corrected Dst^* ($= Dst - 7.26\sqrt{P_{SW}} + 11.0$), in terms of the solar wind E_Y

$$dDst^*/dt = Q(t) - Dst^*/\tau \quad (4)$$

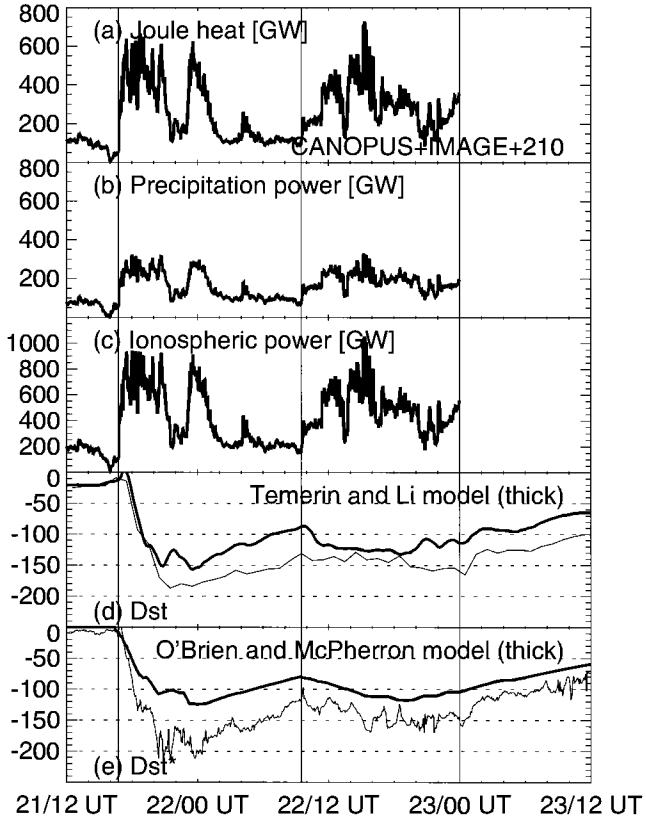

Figure 3. (a) Joule heat in GW, (b) particle precipitation power in GW, and (c) total ionospheric power in GW. (d) *Dst* index from Kyoto and model [*Temerin and Li*, 2002], (e) Pressure corrected *Dst** and model [*O'Brien and McPherron*, 2001].

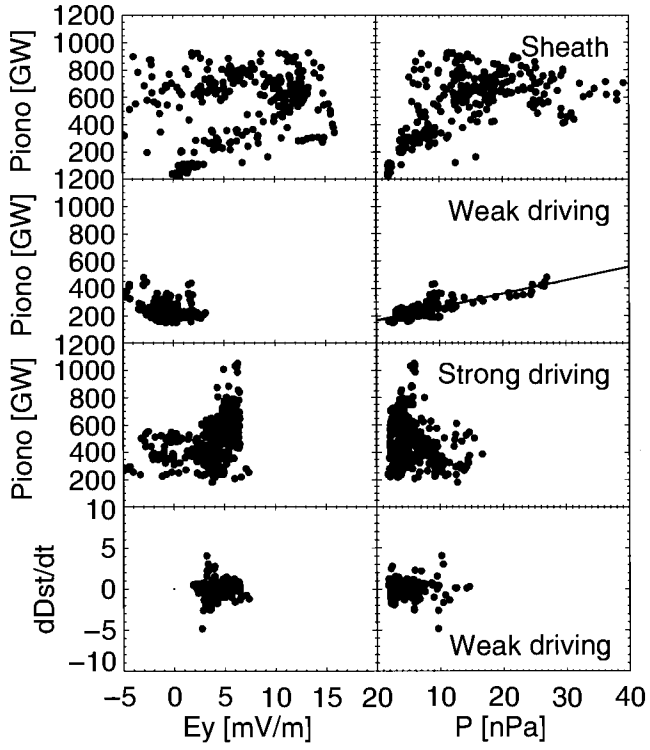

Figure 4. Scatter plots showing the dependence of the ionospheric and ring current power dissipation on (left) the solar wind electric field and (right) the solar wind dynamic pressure. For ionospheric power, three periods are shown: From top to bottom: Sheath encounter, weak driving, and strong driving. The bottom panel shows the time derivative of SYM-H as a proxy for ring current power for the weak driving period.

where $Q(t) = -4.4(VB_S - E_C)$ nT/h is the driver (zero for $VB_S \leq E_C$), $E_C = 0.49$ mV/m, and the ring current decay time is $\tau = 2.40 \exp(9.74/(4.69 + VB_S))$ h.

Figure 3e shows the pressure-corrected *Dst** and the O'Brien and McPherron model. Pressure correction yields a deeper minimum during the first main phase, and there now is a *Dst**-recovery during 00-09 UT on Oct 22. The model predicts a two-phase storm with two almost equal maxima. Thus, the E_Y-based model produces a smaller ring current during the sheath encounter than was recorded by *Dst**, and overall lower level of activity.

During the latter part of the cloud passage and strong driving, the inner magnetosphere was close to a steady state where the solar wind energy feeding to the ring current was just enough to compensate for its losses. If the input is steady at a level of τQ at a time when $Dst^*(t) = \tau Q$, the Burton equation produces a constant *Dst** with neither growth nor recovery. For this case, when the IMF turned southward again at 0930 UT, the parameters were $V = 540$ km/s and $B = 15$ nT, which give $\tau Q = -133$ nt, close to the observed *Dst**, and thus the system was left close to a steady state.

A recent model developed by *Temerin and Li* [2002] describes the *Dst* evolution using six complex terms formed as combinations of the solar wind and IMF, and about 30 parameters. Figure 3e gives the Kyoto *Dst* index and the *Temerin and Li* [2002] model. The model predicts a two-phase storm with a clear recovery in between. The model reproduces the observations quite well during the sheath encounter, but the faster than observed decay of the model leads to underestimation of the index throughout the second activation.

4. DISCUSSION

The classical energy coupling studies assert that the energy dissipation in the ionosphere and magnetosphere depends mainly on the solar wind E_Y, while the pressure plays only a minor role. However, this event reveals a dependence of the ionospheric dissipation on the solar wind pressure, most clearly during the weaker driving, but also during the sheath encounter (see Figure 4). As the *Dst** does not show similar dependence, this indicates that increasing the solar wind pressure increases the relative portion of energy dissipated in the ionosphere. Such pressure dependence has also been found in observations [*Boudouridis et al.*, 2003] and in MHD simulations (M. Palmroth, private communication).

The E_Y-based model [*O'Brien and McPherron*, 2000] showed weaker activity than observed, especially the first maximum did not reach the observed values. On the other hand, the *Temerin and Li* [2002] model using all solar wind and IMF data predicted the sheath encounter period well. The recovery after the first activation was faster than observed, which led to underestimation of the second activation. This indicates that not only the E_Y but also its fluctuations (see also *Tsurutani and Gonzalez* [1987]) and solar wind pressure effects contribute to *Dst* and *Dst**, and probably also to the ring current enhancement. (Exact correspondence is difficult to obtain, as proxies of both input and output contain large uncertainties, including pressure correction of the *Dst* index during high solar wind pressure).

During the sheath encounter, the strong pressure caused a positive contribution to the *Dst* index (Figure 5), and thus the *Dst* minimum was not as deep as it would otherwise have been. During the weaker driving, the almost linearly decreasing pressure partially compensated the *Dst* change arising from ring current decay (pressure correction changed from ~10 nT to zero). Furthermore, the magnetotail energy was increasing (decreasing B_Z in the tail), which brought a negative component to the *Dst* index, and also compensated for the ring current decay. (The quiet-time field [*Tsyganenko*, 1995] subtracted from observations is constant over time, which means that variations from zero reflect changes in tail current when the s/c is in the nightside and in the magnetopause current when the s/c is in the dayside). It is often

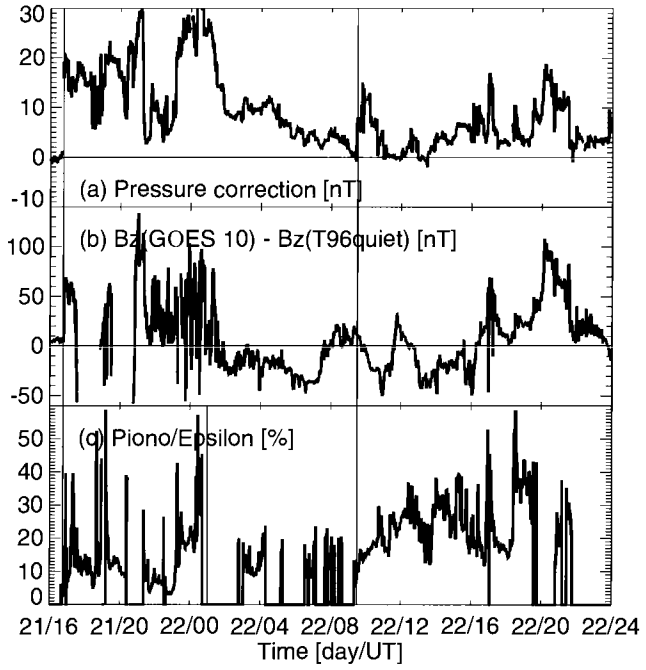

Figure 5. (a) Pressure correction term 7.26 $\sqrt{P_{SW}}$ − 11 for *Dst**; (b) Tail magnetic field change Bz(GOES-10)-Bz(T96quiet); (c) Portion of solar wind energy dissipated in the ionosphere.

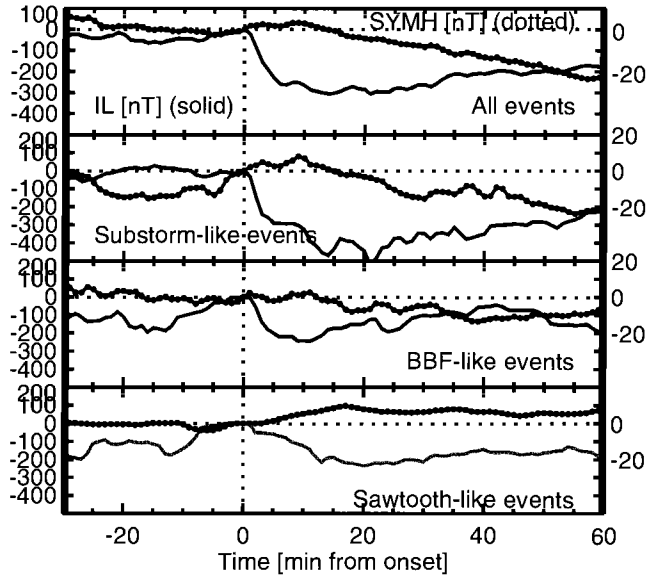

Figure 6. Superposed epoch analysis of stormtime electrojet enhancements. IL (local AL index from IMAGE magnetometer chain, shown solid) and SYM-H (dotted). (a) All events; (b) substorm-like events with poleward expansion and particle injections; (c) BBF-like events with equatorward electrojet expansion and no particle injections; (d) sawtooth-like events from strong driving period during Oct 22, 2001.

assumed that the tail field contribution to *Dst* remains approximately constant at about 20% level [*Turner et al.*, 2002], but this event would indicate that depending on the appearance of substorms, this ratio may vary over time. This can also be demonstrated by examining the energy dissipated in the ionosphere: It was smaller during weak driving and larger during strong driving (Figure 5). Thus, the absence of substorms in the ionosphere led to storage of the solar wind energy in the tail as enhanced cross-tail current. The lack of recovery after the main phase is a balance between the ring current decay, decreasing solar wind pressure, and increasing magnetotail currents in the absence of substorms.

The above suggests that not only the solar wind driver, but also the internal magnetospheric dynamics affect the ring current and ionospheric energy deposition. In a study of about 40 activations during 5 storms, *Pulkkinen et al.* [2002] argued that there are distinct types of stormtime activations in the magnetotail, which all have their typical characteristics and response to the SYM-H index (Figure 6). Those activations resembling isolated substorms had a clear positive change of SYM-H that started well before onset and maximized about 10 min after onset, which was interpreted as decreasing the cross-tail contribution to SYM-H at the current disruption time. Another class of events resembled large bursty bulk flows (BBFs) with equatorward propagating ionospheric electrojet activation. These showed no consistent response in the SYM-H index. Finally, the quasi-steady oscillations causing sawtooth-like behavior in the particle injections [*Reeves et al.*, 2002] observed in the strong driving period (Figure 3) caused a clear positive response to the SYM-H index. This period had a large ASY-H (Figure 3). The strong asymmetry and its dependence on the tail field characteristics was also pointed out by *Le et al.* [2004]. As all these events occur during storms, the variance in the superposed epoch analysis is quite large, but the typical behavior can be identified as well in individual events as in the means.

In summary of the results here and in *Pulkkinen et al.* [2002], the tail response to external driving depends on the tail configuration and its recent history: If the tail is near its nominal configuration, a normal substorm may develop. If strong driving continues after plasmoid release, the tail may not have time to recover, and the driving re-activates the post-plasmoid plasma sheet flows creating a strong flow channel in a dipolarized tail. The substorm-like and BBF-like events occurred alternatingly at about 1-hour time intervals [*Pulkkinen et al.*, 2002], which supports the above scenario. If the driving is steady (this event), strong saw-tooth oscillations can follow one another for extended periods. All together this then implies that substorms do not occur independent of storms, but that the storm phase, driver, and tail characteristics all affect magnetotail dynamics.

Results discussed here indicate that activity indices have limited capability to describe the nature of the activity during storms: The AE-indices are a useful proxy for the amount of energy dissipated in the ionosphere, but do not reflect properties of the concurrent tail activity. Similarly, the *Dst* behavior is a complex function of the magnetospheric current systems, of the type of magnetotail activity, and of the solar wind driving properties. This unfortunately limits our capability to categorize storm events using simple indices only.

5. CONCLUSIONS

1. Solar wind pressure enhancements increase ionospheric energy dissipation during storms;
2. Magnetopause reconnection is important means for energy transfer, but solar wind and IMF properties other than E_Y are also important for *Dst* dynamics;
3. Magnetospheric dynamics affect *Dst* by changing the tail current contribution to *Dst*;
4. The complex driver – response relationship limits our capability to categorize storms using indices only.

These results and our previous analysis [*Pulkkinen et al.*, 2002] indicates that, as the magnetotail response to the solar wind driving depends on the tail configuration and its history, the effects of particular solar wind and IMF conditions to the inner magnetosphere also depend on the past and present tail configuration.

Acknowledgments. The 210° Magnetic Observation Group is acknowledged for their kind cooperation and continuous supply of coordinated magnetic field data. The Solar-Terrestrial Environment Laboratory, Nagoya University, supports construction of the 210° MM database.

REFERENCES

Ahn, B.-H., S.-I. Akasofu, and Y. Kamide, The Joule heat production rate and the particle energy injection rate as a function of the geomagnetic indices AE and AL., *J. Geophys. Res.*, 88, 6275, 1983.

Akasofu, S.-I., Energy coupling between the solar wind and the magnetosphere, *Space Sci. Rev.*, 28, 121, 1981.

Baker, D.N., How to cope with space weather, Science, 297, 30 Aug 2002.

Boudouridis, A., E. Zesta, L.R. Lyons, P.C. Anderson, and D. Lummerzheim, Effect of solar wind pressure pulses on the size and strength of the auroral oval, *J. Geophys. Res.*, 108, A4, 8012, doi:10.1029/2002JA009373, 2003.

Burton, R.K., R.L. McPherron, and C.T. Russell, An empirical relationship between interplanetary conditions and *Dst*, *J. Geophys. Res.*, 80, 4204, 1975.

Chapman, S., and V.C.A. Ferraro, A new theory of magnetic storms, *Terr. Mag. Atmosph. Electr.*, 36, 77, 1931.

Ganushkina, N. Yu., Drivers of the inner magnetosphere, this volume.

Häkkinen, L.V.T., T.I. Pulkkinen, R.J. Pirjola, H. Nevanlinna, E.I. Tanskanen, and N.E. Turner, Seasonal and diurnal variation of geomagnetic activity: revised *Dst* vs. external drivers, *J. Geophys. Res.*, 108, A2, 1060, doi:10.1029/2002JA009428, 2003.

Le, G., C.T. Russell, and K. Takahashi, Morphology of the ring current derived from magnetic field observations, *Ann. Geophys*, in press, 2004.

Lu, G., et al. Global energy deposition during the January 1997 magnetic cloud event, *J. Geophys. Res.*, 103, 11685, 1998.

O'Brien, T.P., and R.L. McPherron, An empirical phase space analysis of ring current dynamics: Solar wind control of injection and decay, *J. Geophys. Res.*, 105, 7707, 2000.

Østgaard, N.R., R. Vondrak, J.W. Gjerloev, and G.A. Germany, A relation between the energy deposition by electron precipitation and geomagnetic indices during substorms, *J. Geophys. Res.*, 107(A9), SMP 16, DOI 10.1029/2001JA002003, 2002.

Pulkkinen, T.I., N.Yu. Ganushkina, V.F. Bashkirov, D.N. Baker, J.F. Fennell, J. Roeder, T.A. Fritz, M. Grande, B. Kellett, and G. Kettmann, Ring current enhancement due to substorm-associated inductive electric fields, in: Proceedings of the Fifth International Conference on Substorms, ESA SP-443, p. 451-454, 2000.

Pulkkinen, T.I., H.E.J. Koskinen, K.E.J. Huttunen, K. Kauristie, E.I. Tanskanen, M. Palmroth, G.D. Reeves, Effects of magnetic storms on substorm evolution, Sixth International Conference on Substorms, edited by R.M. Winglee, University of Washington, Seattle, 2002, pp. 464-471.

Reeves, G.D., M.G. Henderson, R.M. Skoug, M.F. Thomsen, J.E. Borovsky, H.O. Funsten, P. C:son Brandt, D.J. Mitchell, J.-M. Jahn, C.J. Pollock, D.J. McComas, and S.B. Mende, IMAGE, POLAR, and geosynchronous observations of substorm and ring current ion injection, AGU Monograph on the Storm-Substorm Relationship, in press, 2002.

Sergeev, V.A., T.I. Pulkkinen, and R.J. Pellinen, Steady magnetospheric convection: A review of recent results, *Space Sci. Rev.*, 75, 551, 1996.

Shue, J.-H., P. Song, C.T. Russell, J.T. Steinberg, J.K. Chao, G. Zastenker, O.L. Vaisberg, S. Kokubun, H.J. Singer, T.R. Detman, and H. Kawano, Magnetopause location under extreme *J. Geophys. Res.*, 103, 17 691, 1998.

Tanskanen, E.I., T.I. Pulkkinen, H.E.J. Koskinen, Substorm energy budget near solar minimum and maximum: 1997 and 1999 compared, *J. Geophys. Res.*, 107, A6, 10.1029/ 2001JA900153, 2002.

Temerin, M. and Li, X., A new model for the prediction of *Dst* on the basis of the solar wind, *J. Geophys. Res.*, 107, A12, 1472, doi:10.1029/2001JA007532, 2002.

Tsurutani, B.T., and W.D. Gonzalez, The cause of high-intensity long-duration continuous AE activity (HILDCAAs): interplanetary Alfven wave trains, *Planet. Space Sci.*, 35, 405, 1987.

Tsyganenko, N.A., Modeling the Earth's magnetospheric magnetic field confined within a realistic magnetopause, *J. Geophys. Res.*, 100, 5599, 1995.

Turner, N.E., D.N. Baker, T.I. Pulkkinen, and R.L. McPherron, Evaluation of the tail current contribution to *Dst*, *J. Geophys. Res.*, 105, 5431-5440, 2000.

E. Donovan, Department of Physics and Astronomy, University of Calgary, Alberta, Canada, T2N 1N4. e-mail eric@clearwater.phys.ucalgary.ca

N. Yu. Ganushkina and T.I. Pulkkinen, Finnish Meteorological Institute, POBox 503, FIN-00101 Helsinki, Finland. e-mail tuija.pulkkinen@ fmi.fi

X. Li, Laboratory for Atmospheric and Space Physics, University of Colorado, 1234 Innovation Drive, Boulder, CO 80303. e-mail lix@paracel.colorado.edu

G.D. Reeves, Mail Stop D-436, Los Alamos National Laboratory, Los Alamos, NM 87545. e-mail reeves@lanl.gov

C.T. Russell, Institute of Geophysics and Planetary Physics, UCLA, Los Angeles, CA 90024-1567. e-mail ctrussel@igpp.ucla.edu

H.J. Singer, NOAA Space Environment Ctr, 325 Broadway, Boulder, CO 80303. e-mail howard.singer@noaa.gov

J.A. Slavin, NASA Goddard SFC, Code 696, Greenbelt, MD 20771. e-mail James.A.Slavin@nasa.gov

On the Relation Between Sub-Auroral Electric Fields, the Ring Current and the Plasmasphere

P.C. Brandt[1], J. Goldstein[2], P.C. Anderson[3], B.J. Anderson[1], R. DeMajistre[1], E.C. Roelof[1] and D.G. Mitchell[1]

Large electric fields in the sub-auroral, dusk side ionosphere have long been inferred from observations of fast (>1000 m/s) sun ward ion drifts. Extreme Ultraviolet (EUV) images of the plasmasphere obtained by the EUV camera on board the IMAGE satellite, suggest that the dusk side plasmapause can be eroded by these strong sub-auroral electric fields. Ring current models, that self-consistently compute the electric field, can reproduce the observed phenomena qualitatively, and they indicate that the electric field is driven by the closure of the Region 2 (R2) pressure-driven field aligned currents (FAC) through the dusk side, sub-auroral low-conductance ionosphere. We investigate the temporal and spatial relation between global ring current images and the onset of sub-auroral electric fields by using data from the High Energetic Neutral Atom (HENA) imager on board the IMAGE satellite, Ion Drift Meter (IDM) data from the Defense Meteorological Satellite Program (DMSP), and field-aligned currents (FACs) derived from Iridium magnetometer data. We find that the ring current pressure is enhanced about 30 min before an erosion of the plasmapause is first observed. We compute the correlation between the Region 2 FAC obtained by Iridium multiplied by the size of the low-conductance gap and the sub-auroral potential drop (SAPD) and find that it is 0.79 for the period 16-23 April 2002. These results show that there is a correlation between the FAC, the size of the low-conductance gap and strength of the SAPD.

1. INTRODUCTION

The convection electric field of the inner magnetosphere is related directly to the transport and energization of plasma. Several semi-empirical models of the electric field are in contemporary use: for example the Weimer (*Weimer*, 1995) and Volland-Stern (*Volland*, 1973) models. A few kinetic ring current models, such as the models developed by *Wolf* (1970) and *Fok et al.* (2001), derive the electric field in a self-consistent way by computing the currents driven by the plasma pressure distribution and closing it through an ionospheric model. Only the ring current models computing the electric field self-consistently are consistent with global ring current observations by the HENA imager on board IMAGE. Specifically, the model results reported by *Fok et al.* (2001) agreed well with the IMAGE/HENA observations reported by *C:son Brandt et al.* (2002), in which the peak of the <100 keV proton ring current was located in the post-midnight sector, rather than around dusk as is expected from ring current models utilizing the semi-empirical electric field models.

Observations have shown large enhancements of the magnetospheric electric field on the dusk side into extremely low L shells (between 2 to 4) during large storms

[1] The Johns Hopkins University Applied Physics Laboratory, Laurel, Maryland.
[2] Southwest Research Institute, San Antonio, Texas.
[3] Space Science Applications Laboratory, The Aerospace Corporation, El Segundo, California.

The Inner Magnetosphere: Physics and Modeling
Geophysical Monograph Series 155

10.1029/155GM19

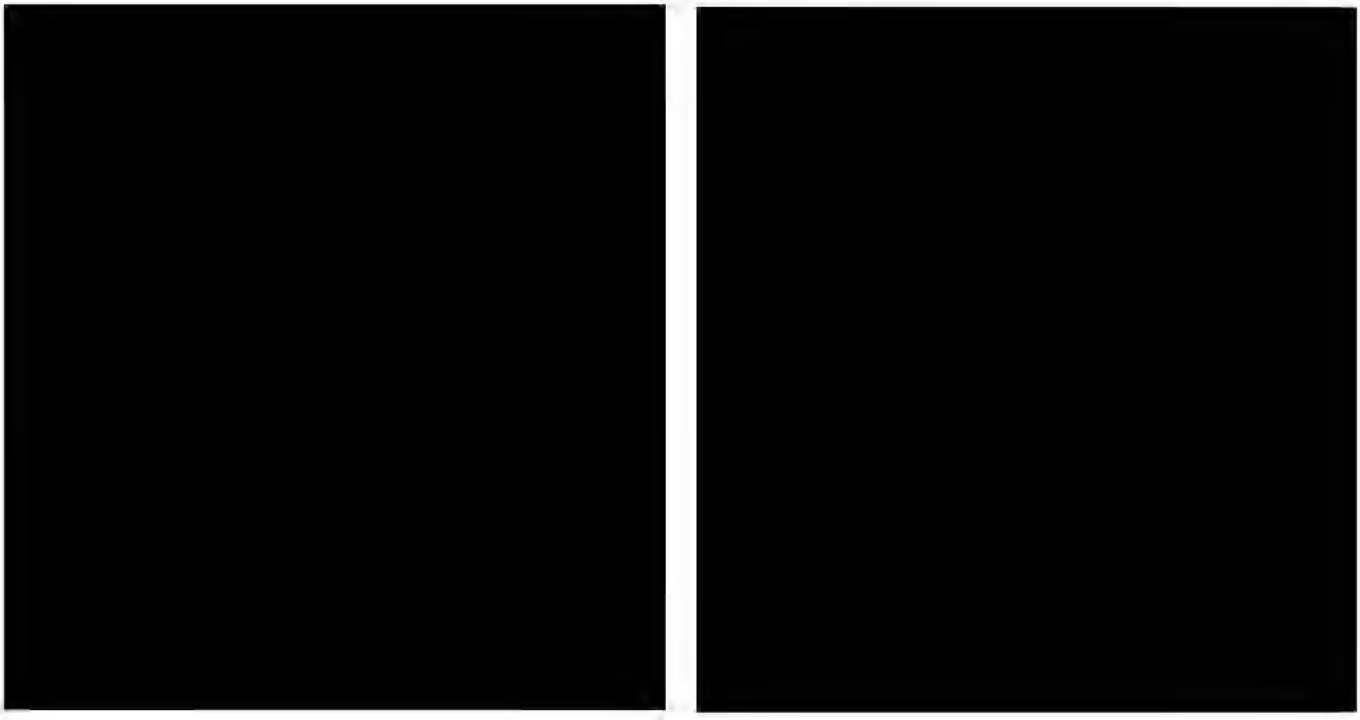

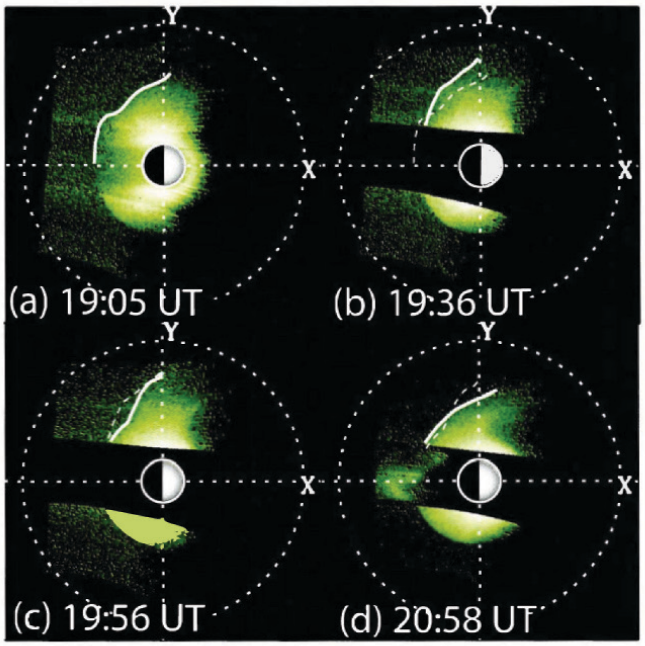

Plate 1. Sequence of EUV images of the plasmasphere from 17 April 2002 obtained from above the north pole by the EUV imager on board the IMAGE satellite. The white outline is a manual trace of the plasmapause in the evening sector. The dashed line in each image (except the first one) is the plasmapause outline from the previous image.

the gap. In order to test this hypothesis, we take the Iridium derived Region 2 current, integrated over the dusk side. This current is then multiplied with the latitudinal separation between the equator ward auroral boundary and the equator ward edge of the SAPD. We find a statistically significant correlation between these two quantities of 0.79. However, the correlation including SAPDs larger than about 20 kV, significantly decreases, which indicate that the hypothesis needs modification for high potential drops.

2. OBSERVATIONS

At around 19:30 UT on 17 April 2002, the EUV imager on board IMAGE observed a rather peculiar motion of the dusk side plasmapause. Plate 1 shows a sequence of EUV images illustrating this motion. The EUV images for this event have been analyzed in more detail by *Goldstein et al.* (2004). The evening side plasmapause bulged slightly radially outward at around 19:26 UT and then an inward (sun ward) motion commenced around 19:36 UT. The outline of the plasmpause for each instant is marked with a solid white line. The outline from the previous image in the sequence is over plotted with a thin, dashed line. *Goldstein et al.* (2003b) showed EUV observations of the plasmasphere during a substorm injection event. During that event the plasmaspheric bulge on the dusk side formed a remarkably thin and narrow plume. This feature could be reproduced by adding a SAPS-like electric field to a regular convection electric field. A SAPS electric field was observed simultaneously by DMSP, strongly suggesting that the SAPS electric field was responsible for the additional modification of the plasmapause.

The event discussed in this paper displays the same behavior as the event reported by *Goldstein et al.* (2003b) and occur during the same conditions: A dusk-side erosion of the plasmapause occurred at the time of enhanced SAPS electric field as observed by DMSP/IDM. In addition, an enhancement of the ring current pressure is observed during the same time.

Plates 2a-2c show the hydrogen ENA images during this period obtained by the HENA imager on board IMAGE in the 27-39 keV range. The ENA images are 10 min integrations. The lower panels (Plates 2d-2f) shows the equatorial proton distribution in the same energy range derived by using the inversion technique developed by *DeMajistre et al.* (2004) and validated by *Vallat et al.* (2004). We see that there is a sudden increase of ion intensity in the ring current, that can be associated with an auroral substorm onset occurring at around 19:05 UT (not shown here).

There are several cases where plasmapause motion is observed in conjunction with ring current increases. The question is whether the plasmapause motion is an effect of the ring current increase, or, if they are both effects of something else. There are clear cases when the plasmapause motion can be associated with convection enhancements, that would lead to an increase in the ring current too (*Goldstein et al.*, 2003a). However, (*Goldstein et al.*, 2003b) showed that the ionospheric sub-auroral electric fields on the dusk side directly affect the plasmapause shape, which implies that the simultaneous occurrence of ring current pressure enhancement and plasmapause erosion is more than a coincidence.

In order to investigate how the ring current relates to the sub-auroral electric fields via Region 2 FAC as proposed by *Anderson et al.* (1993), we use the HENA data to derive a proxy for the Region 2 FAC. This can be done by using the retrieved ion fluxes to compute the partial pressure and then use the force balance equation $\mathbf{J} \times \mathbf{B} = \nabla \mathbf{P}$ to derive the partial current. This method assumes an isotropic pitch-angle distribution and dipole field. Results have been reported by *C:son Brandt et al.* (2004); *Roelof et al.* (2004).

It has to be kept in mind that the FAC proxy obtained this way is by no means a quantitative measure of the true Region-2 FAC intensity. First, the HENA derived pressures are only partial pressures obtained from hydrogen ENA images in the 10-81 keV, which is roughly 50% of the total pressure of the ring current (*Krimigis et al.*, 1985). Second, we assume pitch angle isotropy, while statistical observations show that the pressure anisotropy during storms is about 2 (*De Michelis et al.*, 1999). Therefore, we may underestimate the pressure due to the viewing geometry from the high latitude vantage point of IMAGE. Third, and perhaps most severe, we assume a dipole magnetic field during an event of a *Dst* of about −80 nT. This assumption underestimates the current intensity by several factors. The reason for this is that in a pure dipole magnetic field, FAC intensity depends only on the azimuthal pressure gradients. In a non-dipolar field the misalignment between the constant pressure contours and the constant magnetic field contours is stronger. We are currently improving the technique, but those results will not be covered here.

The purpose of the derived FAC proxy is to shed light on how the ring current development relates to the current intensity, and in turn affects the SAPD. A more accurate picture of the total large-scale Region 2 FAC system can be derived from Iridium magnetometer data (*Anderson et al.*, 2000), but the current data set limits the time resolution to 30 min, at best, and normally 60 min, for strong current systems, whereas the HENA derived proxy provides a typical resolution of 10 min. Moreover, the Iridium derived currents do not directly tell us what is driven by the ring current.

Plate 3 shows the integrated strength of the potential drop in the 12-24 MLT sector in the sub-auroral region obtained by DMSP/IDM. The red line is the downward FAC intensity derived from Iridium magnetometer data integrated over the 12-24 MLT region and below 75°. The blue line is

the computed FAC proxy from IMAGE/HENA data using hydrogen 10-min ENA images (spaced 2 min apart) in the 10-81 keV range.

The technique used to derive the potential drops has been used in a number of studies (*Hairston and Heelis*, 1990; *Rich and Hairston*, 1994). The in-track electric field is calculated from the DMSP ion drift measurements and integrated along the orbit track. The limits of the integration on the evening and morning sides of the auroral oval are identified as the locations where the horizontal ion drift goes to zero or, in the cases where a small drift still exists (<100 m/s), where the drift reaches an asymptote with respect to zero. Such small drifts can be due to neutral wind drag or errors in the absolute measurement of the drift. This integration typically produces a potential curve with a minimum on the evening side and a maximum on the morning side. The difference between the potential minimum and maximum is the polar cap potential (PCP). The SAPD is calculated on the evening side between the equatorial edge of the electron auroral oval determined using the SSJ/4 energetic particle data and the low-latitude limit used for the calculation.

There are a number of errors inherent in the calculation of the potential drops. Integration is always from the evening side to the morning side and the potential does not always return to zero on the morning side probably due to time-varying changes in the global electric field pattern during the 25-minute traversal between the integration limits. This offset is typically less than 20 kV. Authors of prior studies (*Rich and Hairston*, 1994) apply a linear correction to the potential curve to remove this offset; we choose not to do this in this study to avoid the uncertainties this may introduce. Note that the mean value of the offset in the potential for all potential calculations in this study is 11.5 kV. The time-varying changes in the electric field pattern affect the calculation of the SAPD much less than the calculation of the PCP due to the shorter integration time (<5 min) of the SAPD. Identification of the limits of the integration at too high a latitude because the drift did not go to zero, can introduce a small error. A cross-track drift of 100 m/s corresponds to an along-track electric field of ~5 mV/m; this contributes less than 3 kV integrated over 5° of latitude. Errors in the absolute value of the measured drift (<40 m/s) similarly introduce a relatively small error. This error depends on the distance the satellite travels in the sub-auroral region for the SAPD and between the convection reversals for the PCP. Integration in the sub-auroral region over 15° (on the order of the largest distance used) produces an absolute error in the SAPD of less than 3.5 kV.

Although the time resolution of the DMSP/IDM data is about one hour (orbital period of the satellite), Plate 3 indicates that there is a dramatic rise of the SAPD between 18:00 UT and 21:00 UT. The black vertical line indicates 19:36 UT when the first motion of the plasmapause could be detected. We see that the Iridium-derived FACs (red line) rise until 19:30 UT and then decrease gradually through 22:00 UT. The HENA-derived FAC proxy (blue line) implies that there is a sharp peak of Region 2 FAC on the dusk side between 19:20 and 19:30 UT. This implies that the pressure driven FACs closing through the dusk side ionosphere increased just some ten minutes before the observed plasmapause motion.

Large sub-auroral electric fields and their effects have been seen in much more detail from ground radar data and in total electron content (TEC) maps (*Foster and Vo*, 2002; *Foster et al.*, 2002), where they display a tongue of relatively enhanced ionospheric densities extending from post-dusk local times to higher latitudes toward noon. This tongue of enhanced electron density was reported by *Foster* (1993) and was shown to merge with anti-sun ward flow of enhanced ionization over the polar cap.

3. DISCUSSION

Models indicate that the SAPD is produced by the closure of the Region-2 FACs poleward through a low-conductance gap. The Region-2 FACs are driven by the ring current pressure distribution. Therefore, to a first approximation the SAPD should be directly related to the resistance of the low-conductance gap multiplied by the current flowing through it.

To test the validity of this hypothesis, let us take the Region-2 current density into the ionosphere, integrated over the dusk side sub-auroral region. This will then represent the total current (A) that may close through the low-conductance gap. It is, of course, true that all this current may not close poleward through the low-conductance gap, but it is not unreasonable to assume that whatever current is closing through the gap is closely related to the total Region-2 FAC.

If the conductance across the gap is constant, we can futher assume that the resistance is proportional to the spatial length scale of the gap. *Anderson* (2004) defined the poleward edge of the gap as the equator ward edge of the electron auroral oval, which can be found from DMSP precipitating electron data. The equator ward extent of the SAPD is difficult to quantify because of uncertainties in where to identify the equator ward SAPS boundary. Therefore we take the equator ward edge as the latitude where the SAPD (counting from the pole toward lower latitudes) reaches 90% of its value. The separation can then be taken as the difference in these two latitudes. The correlation between the potential drop U and the product between the current intensity and the separation should indicate whether or not the hypothesis is realistic.

In Figure 2 we have plotted the integrated current intensity multiplied by the separation distance in radians D as defined above versus the SAPD for the time period 16 April through 23 April 2002. We find a statistically significant correlation

[redacted]

[redacted] cor-

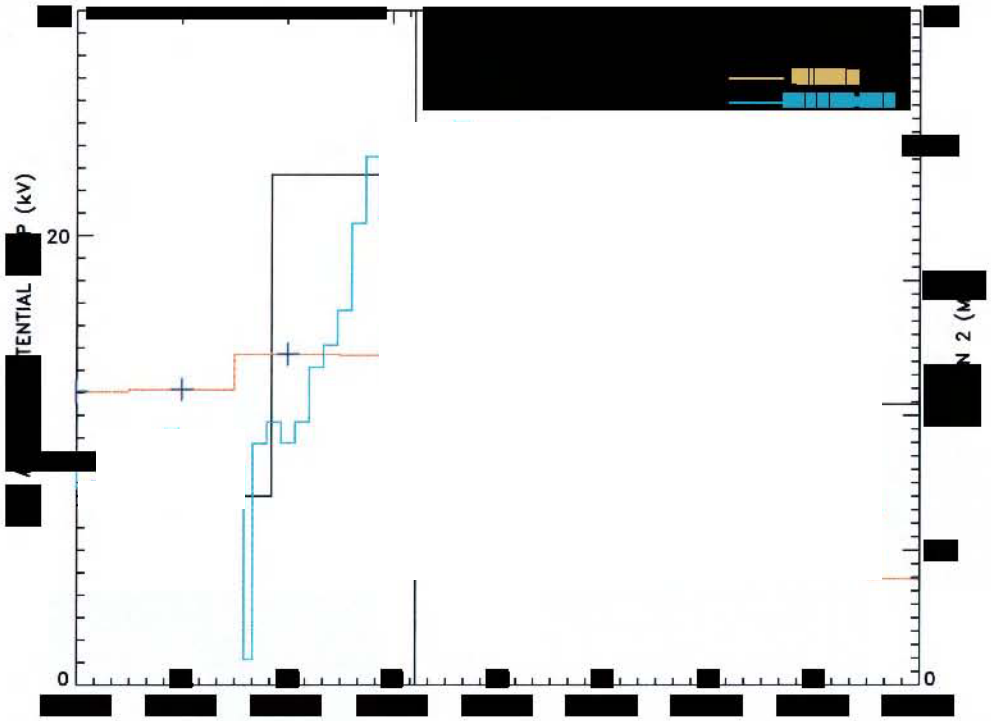

[redacted]

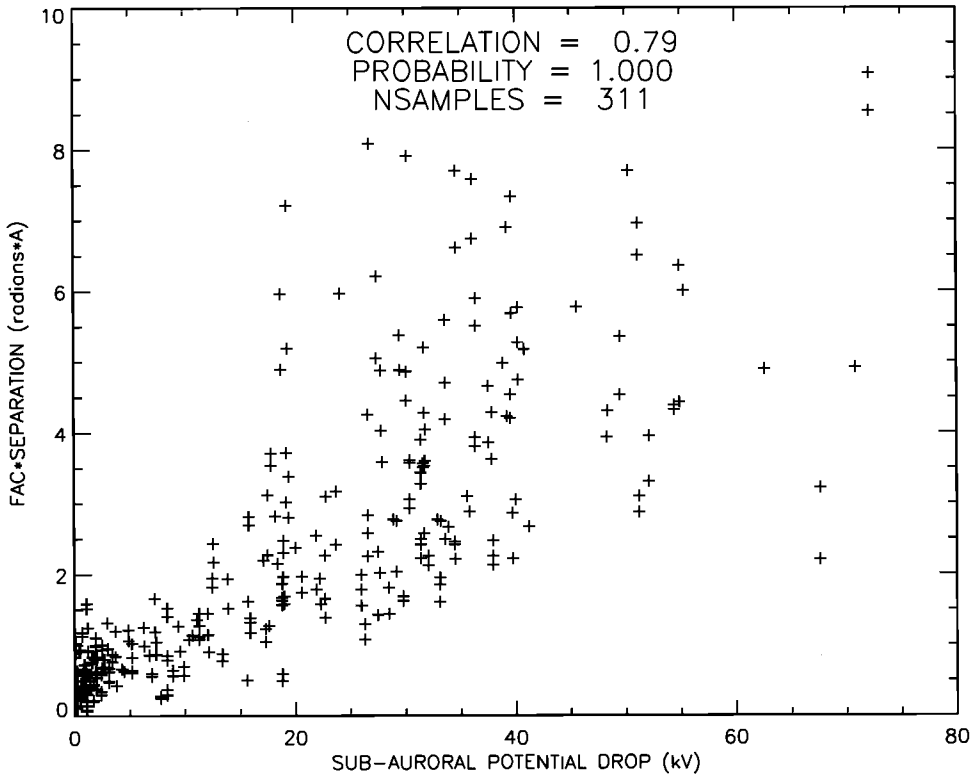

Figure 2. The correlation between the SAPD and the product between the dusk side integrated Region 2 FAC and separation between the SAPD and the auroral zone. The correlation coefficient of 0.79 was found to be statistically significant.

of 0.79 between these two quantities. The two quantities were tested for the probability that they have significantly different means. The probability value found is very close to one, and therefore the correlation is statistically significant. The correlation becomes insignificant (with a level of significance of 0.05) if only samples with potential drops less than 1.5 kV are included. Furthermore, the 0.79 correlation was the highest found and found only when all samples were included.

We notice that the spreading in current times distance becomes large for higher SAPDs. For potentials higher than 20 kV the correlation decreases to 0.46, and for samples with potentials less than 20 kV the correlation is 0.70. This suggests that there may be other factors that need to be taken into account for SAPDs higher than 20 kV, and the hypothesis needs to be modified.

Several aspects of the relations between the sub-auroral electric field, the ionospheric conductance and the ring current have not been covered here. For example, the ionospheric conductance is increased by the ionospheric flows associated with the sub-auroral electric fields (*Anderson et al.*, 1993). An increased ionospheric conductance would lead to a weaker shielding field, which would allow the ring current to penetrate closer to the Earth and perhaps weaken due to an increased charge exchange.

4. SUMMARY

This preliminary study has been an attempt to investigate the validity of a hypothesis for the production mechanism of the strong dusk side SAPD observed frequently by DMSP/IDM. In this hypothesis the SAPD is produced by the closure of the Region-2 current, poleward through the low-conductance gap equator ward of the auroral zone.

In order to investigate the relation in detail between the ring current and sub-auroral electric fields, we derived a proxy for the Region 2 FAC from global proton pressure distributions during 17 April 2002. The pressure distributions were retrieved from global hydrogen ENA images in the 10-81 keV range obtained by the HENA imager on board IMAGE. We found that the dusk side HENA-derived FACs increased in intensity about 10 min before the first detectable motion of the dusk side plasmapause observed by the EUV camera on board IMAGE. DMSP/IDM data implied that the sub-auroral electric field during this period became enhanced. Although the inferred electric fields from

DMSP/IDM have a coarse time resolution of about one hour, these observations are consistent with the scenario proposed by *Anderson et al.* (1993), in which the ring current pressure gradients drive Region 2 FACs downward in the dusk side, sub-auroral ionosphere, where they close with the poleward Region 1 through a low-conductance gap via Pedersen currents. This will translate into a radially outward electric field in the equatorial ring current/plasmapause region that in turn will enhance the azimuthal drift of the plasmasphere and thus erode the plasmapause.

In order to test the validity of the hypothesis, we investigated how the SAPD (measured by DMSP/IDM) relates to the dusk side Region-2 current and the size of the low-conductance gap. In a first order approximation, the SAPD should be the product between the resistance of the gap and the current intensity flowing through it. As the gap resistance we took the latitudinal distance between the equator ward edge of the auroral electron precipitation and the low-latitude point where the SAPD reached 90% of its total integrated value. The current was approximated by the dusk side Region-2 FAC (obtained by Iridium) integrated over the dusk side. For the period of 16-23 April 2002, we found a correlation of 0.79 between the two quantities. This result is consistent with the scenario put forth by *Anderson et al.* (1993), and indicates that there are more factors affecting the SAPD, than this simple hypothesis suggests. A more detailed analysis of additional factors are currently being pursued.

Acknowledgements. This work was supported by NASA grant NAG5-12772 and NSF grants ATM-0000268 and ATM-0302529.

REFERENCES

Anderson, B.J., K. Takahashi, and B.A. Toth, Sensing global Birkeland currents with Iridium engineering magnetometer data, *Geophys. Res. Lett.*, 27(24), 4045-4048, 2000.

Anderson, P.C., Subauroral electric fields and magnetospheric convection during the April 2002 geomagnetic storms, *Geophys. Res. Lett.*, 31(L11801), doi:10.1029/2004GL019588, 2004.

Anderson, P.C., W.B. Hanson, R.A. Heelis, J.D. Craven, D.N. Baker, and L.A. Frank, A proposed production model of the rapid sub-auroral ion drifts and their relationships to substorm evolution, *J. Geophys. Res.*, 98(A4), 6069-6078, 1993.

C:son Brandt, P., S. Ohtani, D.G. Mitchell, M.C. Fok, E.C. Roelof, and R. DeMajistre, Global ENA observations of the storm mainphase ring current: Implications for skewed electric fields in the inner magnetosphere, *Geophys. Res. Lett.*, 29(20), 1954, doi:10.1029/2002GL015160, 2002.

C:son Brandt, P., E.C. Roelof, S. Ohtani, D.G. Mitchell, and B. Anderson, IMAGE/HENA: Pressure and current distributions during the 1 October 2002 storm, *Adv. Space Res.*, 33/5, 719-722, doi:10.1016/S0273-1177(03)00633-1, 2004.

De Michelis, P., I.A. Daglis, and G. Consolini, An average image of proton plasma pressure and of current systems in the equatorial plane derived from AMPTE/CCE-CHEM measurements, *J. Geophys. Res.*, 104(A12), 28,615-28,624, 1999.

DeMajistre, R., E.C. Roelof, P. C:son Brandt, and D.G. Mitchell, Retrieval of global magnetospheric ion distributions from high energy neutral atom (ENA) measurements by the IMAGE/HENA instrument, *J. Geophys. Res.*, 109(A04214), doi:10.1029/2003JA010322, 2004.

Fok, M.C., R.A. Wolf, R.W. Spiro, and T.E. Moore, Comprehensive computational model of Earth's ring current, *J. Geophys. Res.*, 106(A5), 8417-8424, 2001.

Foster, J.C., Storm time plasma transport at middle and high latitudes, *J. Geophys. Res.*, 98(A2), 1675-1689, 1993.

Foster, J.C. and W.J. Burke, SAPS: A new categorization for sub-auroral electric fields, *EOS Transactions*, 83(36), 393-394, 2002.

Foster, J.C. and H.B. Vo, Average characteristics and activity dependence of the subauroral polarization stream, *J. Geophys. Res.*, 107(A12), SIA 16-1 to SIA 16-10, 2002.

Foster, J.C., P.J. Erickson, A.J. Coster, J. Goldstein, and F.J. Rich, Ionospheric signatures of plasmaspheric tails, *Geophys. Res. Lett.*, 29(13), 1-1, 2002.

Goldstein, J., B.R. Sandel, W.T. Forrester, and P.H. Reiff, IMF-driven plasmasphere erosion of 10 July 2000, *Geophys. Res. Lett.*, 30(3), doi:10.1029/2002GL016,478, 2003a.

Goldstein, J., B.R. Sandel, and P.H. Reiff, Control of plasmaspheric dynamics by both convection and sub-auroral polarization stream, *Geophys. Res. Lett.*, 30(24), 2243, doi:10.1029/2003GL018,390, 2003b.

Goldstein, J., B.R. Sandel, M.R. Hairston, and S.B. Mende, Plasmapause undulation of 17 April 2002, *Geophys. Res. Lett.*, 31(L15801), doi:10.1029/2004GL019959, 2004.

Hairston, M.R. and R.A. Heelis, Model of the high-latitude ionospheric convection pattern during southward interplanetary magnetic field using DE 2 data, *J. Geophys. Res.*, 95(A3), 2333-2343, 1990.

Krimigis, S.M., G. Gloeckler, R.W. McEntire, T.A. Potemra, F.L. Scarf, and E.G. Shelley, Magnetic storm of September 4, 1984: A synthesis of ring current spectra and energy densities measured with AMPTE/CCE, *Geophys. Res. Lett.*, 12(5), 329-332, 1985.

Rich, F.J., and M. Hairston, Large-scale convection pattern observed by DMSP, *J. Geophys. Res.*, 99(A3), 3827-3844, 1994.

Roelof, E.C., P.C. Brandt, and D.G. Mitchell, Derivation of currents and diamagnetic effects from global pressure distributions obtained by IMAGE/HENA, *Adv. Space Res.*, 33/5, 747-751, doi:10.1016/S0273-1177(03)00633-1, 2004.

Rowland, D.E., The electrodynamics of the inner magnetosphere during major geomagnetic storms, Ph.D. thesis, University of Minnesota, 2002.

Vallat, C., I. Dandouras, P. C:son Brandt, and D.G. Mitchell, First comparison between ring current measurements by Cluster/CIS and IMAGE/HENA, *J. Geophys. Res.*, 109(A04213), doi:10.1029/2003JA010224, 2004.

Volland, H., A semiempirical model of large-scale magnetospheric electric fields, *J. Geophys. Res.*, 78, 171, 1973.

Weimer, D.R., Models of high-latitude electric potentials derived with a least error fit of spherical harmonic coefficients, *J. Geophys. Res.*, 100, 19,595-19,607, 1995.

Wolf, R.A., Effects of ionospheric conductivity on convective flow of plasma in the magnetosphere, *J. Geophys. Res.*, 75(25), 4677-4698, 1970.

Wygant, J., D. Rowland, H.J. Singer, M. Temerin, F. Mozer, and M.K. Hudson, Experimental evidence on the role of the large spatial scale electric field in creating the ring current, *J. Geophys. Res.*, 103(A12), 29,527-29,544, 1998.

Yeh, H.C., J.C. Foster, F.J. Rich, and W. Swider, Storm time electric field penetration observed at mid-latitude, *J. Geophys. Res.*, 96(A4), 5707-5721, 1991.

P.C. Brandt, B.J. Anderson, The Johns Hopkins University Applied Physics Laboratory, 11100 Johns Hopkins Rd., Laurel, MD 20723

J. Goldstein, Southwest Research Institute, 6220 Culebra Rd San Antonio, TX 78238

P.C. Anderson, The Aerospace Corporation, 2350 E. El Segundo Blvd., El Segundo, CA 90245

Transmission Line Model for Driving Plasma Convection in the Inner Magnetosphere

Takashi Kikuchi

National Institute of Information and Communications Technology, 4-2-1, Nukui-Kitamachi, Koganei, Tokyo, Japan

The plasma convection in the inner magnetosphere reacts quickly after a growth of the polar cap potential, as revealed by the quick onset of the development of the partial ring current as demonstrated by *Hashimoto et al.* [2002]. In order to explain the quick response of the inner magnetosphere, we apply the Earth-ionosphere waveguide (transmission line) model developed by *Kikuchi and Araki* [1979b]. In this paper, we examine how the TM0 mode is excited in the waveguide by the electric potential transported along with the field-aligned currents, and show that the electric potential is transmitted horizontally at the speed of light in the Earth-ionosphere waveguide. We then evaluate the attenuation of the TM0 mode by calculating the Poynting flux transported upward from the Earth-ionosphere waveguide into the conducting ionosphere. A fraction of the Poynting flux is further transported into the magnetosphere when the Alfvén conductance of the magnetosphere is not very small compared with the ionospheric conductance. The upward transportation of the Poynting flux causes a loss of the horizontally transmitting energy, resulting in the attenuation of the TM0 mode, but it is not substantial compared to the geometrical attenuation due to the finite size of the polar electric field. We stress that the electric field associated with the ionospheric current is mapped upward into the magnetosphere by the Alfvén mode, which drives the plasma convection in the inner magnetosphere. We note that the ionosphere is not a generator but constitutes a transmission line for the electromagnetic energy to be transported into the inner magnetosphere.

1. INTRODUCTION

SuperDARN and magnetometer observations have demonstrated that the ionospheric convection developed nearly instantaneously at the dayside and nightside polar ionosphere [*Ridley et al.*, 1998; *Ruohoniemi and Greenwald*, 1998]. The prompt propagation of the convection electric field to the nightside ionosphere has been interpreted by means of the fast mode waves in the magnetosphere [e.g., *Ridley et al.*, 1998; *Slinker et al.*, 2001].

The Inner Magnetosphere: Physics and Modeling
Geophysical Monograph Series 155

10.1029/155GM20

Hashimoto et al. [2002], on the other hand, demonstrated that the partial ring current developed a few minutes after the development of the polar cap potential, based on the magnetometer observations at low latitudes as well as in the polar cap. *Hashimoto and Kikuchi* [2005] further demonstrated that the plasmasheet thinning in the nightside geosynchronous orbit started simultaneously with the development of the two-cell ionospheric convection observed by SuperDARN. These results imply that the plasma convection in the near-earth magnetosphere developed concurrently with the ionospheric convection. *Hashimoto et al.* [2002] discussed that the fast mode may not play a role since it just reduces an imbalance in the magnetic pressure distribution and hardly drives rotational motion of plasma. They suggested that the ionosphere played

a crucial role in driving the convection in the inner magnetosphere. However, the mechanism for transmission of the convection electric field to the inner magnetosphere has been a question to be answered.

Horizontal transmission of the polar electric field to low latitudes was studied by *Kikuchi et al.* [1978] and *Kikuchi and Araki* [1979b], to explain the simultaneous onset of the preliminary reverse impulse (PRI) of the geomagnetic sudden commencement as shown by *Araki* [1977]. *Kikuchi and Araki* [1979b] showed that the zeroth-order transverse magnetic (TM0) mode could transmit the polar electric field to low latitudes at the speed of light. The attenuation of the TM0 mode was negligibly small under the daytime ionospheric parameters. *Kikuchi and Araki* [1979b] also indicated that the transmitted electric field was mapped upward into the magnetosphere with no significant attenuation. The instantaneous transmission of the polar electric field was applied to explain the coherent occurrence of the DP2 magnetic fluctuations [*Kikuchi et al.*, 1996]. Although the TM0 mode successfully explained the simultaneous onset of the PRI and the excellent coherency of the DP2 at high latitudes and at the dayside dip equator, questions have not been answered on the excitation of the TM0 mode and the attenuation of the TM0 mode due to the finite conductivity of the ionosphere, particularly for the nighttime condition.

The purpose of this paper is to examine how the TM0 mode is excited and transmitted to the nightside ionosphere with no significant attenuation. Then we apply the TM0 mode propagation to explain the quick response of the convection in the inner magnetosphere. In the following sections, we first examine how the TM0 mode is excited by the electric potential carried along the field-aligned currents from the dynamo in the outer magnetosphere. We then evaluate attenuation of the TM0 mode due to finite conductivity for the nighttime condition, and Poynting flux escaping into the magnetosphere from the ionosphere. We finally conclude that the electric field transmitted from the ionosphere drives the convection in the inner magnetosphere.

2. THREE-LAYERED MODEL

2.1. Equations and Solutions

Kikuchi and Araki [1979b] solved equations in the three-layered waveguide composed of the vacuum, conducting ionosphere and fully ionized magnetosphere (MHD) terminated below by the perfectly conducting Earth as schematically shown in Figure 1. The propagation is assumed to be in the x-z plane, and the model is assumed to be uniform in y-direction. The electric and magnetic fields in the vacuum region are governed by the Maxwell equations shown below.

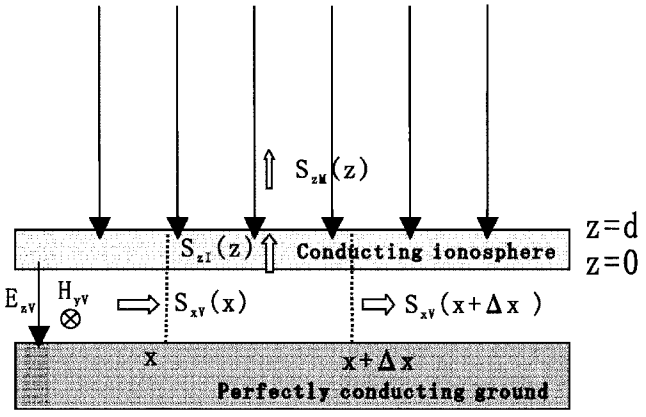

Figure 1. Three-layered Earth-ionosphere waveguide composed of MHD medium (magnetosphere), conductor (ionosphere) and vacuum (neutral atmosphere), which is terminated below by the perfectly conducting ground. The TM0 mode in the waveguide is characterized by the transverse magnetic field, H_{yV} and the vertical electric field, E_{zV}. The electric and magnetic fields provide the Poynting flux, S_{xV}, transmitting in the x-direction. A fraction of energy escapes into the ionosphere (S_{zI}) and the magnetosphere (S_{zM}), causing the attenuation of the TM0 mode.

$$\nabla \times \boldsymbol{E}_V = -\mu_0 \frac{\partial \boldsymbol{H}_V}{\partial t}, \tag{1}$$

$$\nabla \times \boldsymbol{H}_V = \varepsilon_0 \frac{\partial \boldsymbol{E}_V}{\partial t}, \tag{2}$$

where $\boldsymbol{E}$ and $\boldsymbol{H}$ denote the electric and magnetic field vectors, respectively, and μ_0 and ε_0 the magnetic permeability and electric permitivity, respectively. The suffix V refers to the vacuum region.

In the ionosphere, we have similar equations with conducting currents as shown below.

$$\nabla \times \boldsymbol{E}_I = -\mu_0 \frac{\partial \boldsymbol{H}_I}{\partial t}, \tag{3}$$

$$\nabla \times \boldsymbol{H}_I = \sigma \cdot \boldsymbol{E}_I, \tag{4}$$

where σ denotes the conductivity of the ionosphere, and I refers to the ionosphere. The ionospheric conductivity is assumed to be isotropic. If the Hall conductivity is taken into account, the transverse electric (TE) mode is produced by the TM0 mode. However, no significant modification is made on the propagating TM0, since the TE mode is an evanescent mode in the Earth-ionosphere waveguide [*Kikuchi and Araki*, 1979b].

In the fully ionized magnetosphere, the electromagnetic fields are transmitted by the magnetohydrodynamic (MHD)

waves, which accompany motion of the magnetized plasma. Thus, the basic equations include the equation of plasma motion and the relation for the frozen-in condition.

$$\nabla \times \boldsymbol{E}_M = -\mu_0 \frac{\partial \boldsymbol{H}_M}{\partial t}, \tag{5}$$

$$\nabla \times \boldsymbol{H}_M = \boldsymbol{J}, \tag{6}$$

$$\boldsymbol{E}_M + \boldsymbol{u} \times \boldsymbol{B}_0 = 0, \tag{7}$$

$$\rho \frac{\mathrm{d}\boldsymbol{u}}{\mathrm{dt}} = \boldsymbol{J} \times \boldsymbol{B}_0, \tag{8}$$

where $\boldsymbol{u}$ and $\boldsymbol{J}$ denote the velocity of the plasma and electric current, respectively. The suffix, M refers to the magnetosphere. As we focus our attention on the inner magnetosphere, particularly the MHD region above the conducting ionosphere, we ignored the pressure of the plasma in the equation of motion (8). As was done by *Kikuchi and Araki* [1979b], we solve the equations as an initial-boundary-value problem. For this purpose, we use the Laplace transformation with respect to time in the above listed basic equations. The Laplace transform of H_y is defined as below.

$$h_y(x,s) = \int_0^\infty H_y(x,t)\, e^{-st} dt, \tag{9}$$

where s denotes a complex parameter. The inverse Laplace transform of h_y is given by

$$H_y(x,t) = \frac{1}{2\pi \cdot j} \int_{a-j\infty}^{a+j\infty} h_y(x,s)\, e^{st} ds, \tag{10}$$

where a is a real number. As we describe in section 2, the transverse magnetic field H_y is transmitted into the Earth-ionosphere waveguide through the polar ionosphere. The transmitted magnetic field is assumed to be the boundary condition at one end of the waveguide, which would excite the TM0 mode in the Earth-ionosphere waveguide. Since the boundary condition is fixed, we can apply the Fourier sine transform with respect to x to the magnetic field as below.

$$\overline{h_y(\beta,s)} = \sqrt{\tfrac{2}{\pi}} \int_0^\infty h_y(x,s) \sin(\beta \cdot x) dx, \tag{11}$$

where β denotes a real parameter. The inverse Fourier transform is given below,

$$h_y(x,s) = \sqrt{\tfrac{2}{\pi}} \int_0^\infty \overline{h_y(\beta,s)} \sin(\beta \cdot x) d\beta. \tag{12}$$

The governing equations for the transverse magnetic field are readily obtained after Laplace and Fourier transformations are applied, which are given below for the vacuum, conductor and MHD medium, respectively.

$$\frac{d^2 \overline{h_{yV}}}{dz^2} - \left(\beta^2 + \frac{s^2}{c^2}\right) \overline{h_{yV}} = -\sqrt{\frac{2}{\pi}} \beta \cdot h_{yV}(0) = -H_{y0} \sqrt{\frac{2}{\pi}} \frac{\beta}{s} \tag{13}$$

$$\frac{d^2 \overline{h_{yI}}}{dz^2} - (\beta^2 + \mu_0 \sigma \cdot s) \cdot \overline{h_{yI}} = -\sqrt{\frac{2}{\pi}} \beta \cdot h_{yI}(0) = -H_{y0} \sqrt{\frac{2}{\pi}} \frac{\beta}{s} \tag{14}$$

$$\frac{d^2 \overline{h_{yM}}}{dz^2} - \frac{s^2}{V_A^2} \overline{h_{yM}} = 0, \tag{15}$$

where c denotes the light speed. In deriving the equations (13)-(15), we assumed a stepwise increase in the magnetic field as a function of time at x = 0 in the vacuum and conducting media, of which Laplace transform is expressed as

$$h_{yV} = H_{y0} \frac{1}{s}, \tag{16}$$

where $1/s$ represents the Laplace transform of the Heaviside unit function of time, $\mathrm{U}(t)$ and H_{y0} the intensity of the magnetic field at the boundary. Since the transverse magnetic field propagates along the field line in the MHD medium, we give $H_y = 0$ at x = 0 in (15). Thus we have solutions of (13), (14) and (15) and the accompanying horizontal electric fields as

$$\overline{h_{yV}} = H_{y0} \sqrt{\frac{2}{\pi}} \frac{\beta}{s\left(\beta^2 + \frac{s^2}{c^2}\right)} + A_{V1} e^{-z\sqrt{\beta^2 + \frac{s^2}{c^2}}} + A_{V2} e^{z\sqrt{\beta^2 + \frac{s^2}{c^2}}}, \tag{17}$$

$$\overline{e_{xV}} = \frac{1}{\varepsilon_0 s} \sqrt{\beta^2 + \frac{s^2}{c^2}} \left(A_{V1} e^{-z\sqrt{\beta^2 + \frac{s^2}{c^2}}} - A_{V2} e^{z\sqrt{\beta^2 + \frac{s^2}{c^2}}} \right) \tag{18}$$

in the vacuum,

$$\overline{h_{yI}} = \sqrt{\frac{2}{\pi}} \frac{\beta}{s(\beta^2 + \mu_0 \sigma \cdot s)} + A_{I1} e^{-z\sqrt{\beta^2 + \mu_0 \sigma s}} + A_{I2} e^{z\sqrt{\beta^2 + \mu_0 \sigma s}} \tag{19}$$

$$\overline{e_{xI}} = \frac{\sqrt{\beta^2 + \mu_0\sigma \cdot s}}{\sigma}\left(A_{I1}e^{-z\sqrt{\beta^2+\mu_0\sigma s}} - A_{I2}e^{z\sqrt{\beta^2+\mu_0\sigma s}}\right) \quad (20)$$

in the conductor, and

$$\overline{h_{yM}} = A_{M1}e^{-\frac{(z-d)}{V_A}s} + A_{M2}e^{\frac{(z-d)}{V_A}s} \quad (21)$$

$$\overline{e_{xM}} = \mu_0 V_a\left(A_{M1}e^{-\frac{(z-d)}{V_A}s} - A_{M2}e^{\frac{(z-d)}{V_A}s}\right) \quad (22)$$

in the MHD medium, where the coefficients A's represent constants. The coefficients are determined by boundary conditions at the interfaces between the different media; the horizontal electric and magnetic fields are continuous at the interfaces, the horizontal electric field vanishes at the surface of the ground, and the electric and magnetic fields vanish at the infinite z.

2.2. TM0 Mode in The Vacuum Region

The first term of the solution in the vacuum (17) represents a mode propagating in the x-direction with uniform intensity in the z-direction. This mode is the zeroth-order transverse magnetic (TM0) mode studied by *Kikuchi and Araki* [1979b], of which inverse-Fourier and -Laplace transforms are given below.

$$h_{yV} = H_{y0}\frac{2}{\pi}\frac{1}{s}\int_0^\infty \frac{\beta}{\beta^2 + \frac{s^2}{c^2}}\sin(\beta x)d\beta = H_{y0}\frac{1}{s}e^{-\frac{x}{c}s} \quad (23)$$

$$H_{yV} = H_{y0}\mathrm{U}\left(t - \frac{x}{c}\right). \quad (24)$$

As indicated in (24), the TM0 mode propagates at the speed of light, without suffering attenuation. On the other hand, the second and third terms of (17) represent secondary magnetic fields depending on z produced at the interface between the vacuum and the conductor, which causes attenuation of the TM0 mode. The secondary magnetic fields are obtained by determining all the coefficients in (17)-(22) coupled with each other through continuity equations of the horizontal electric and magnetic fields at the interfaces.

In the followings, we derive the attenuation of the TM0 mode from the loss of the horizontally transported Poynting flux, instead of solving the equations simultaneously. The TM0 mode does not accompany the horizontal electric field, E_x, but accompany the vertical electric field E_z as obtained from (2) and (23) as below.

$$e_{zV} = H_{y0}\frac{1}{\varepsilon_0 s}\frac{\partial h_{yV}}{\partial x} = -Z_0 H_{y0}\frac{1}{s}e^{-\frac{x}{c}s}. \quad (25)$$

The inverse transform is given as follows.

$$E_{zV} = -Z_0 H_{y0}\mathrm{U}\left(t - \frac{x}{c}\right). \quad (26)$$

The result, (26) indicates that the vertical electric field is transmitted at the speed of light in the x-direction in the same way as the transverse magnetic field. Since the electric potential of the ionosphere with respect to the ground is defined by E_z multiplied by the height of the ionosphere (100 km), we obtain an important result that the ionospheric potential is transmitted at the speed of light by the TM0 mode in the Earth-ionosphere waveguide if the attenuation is ignored.

In the conductor, the horizontally propagating mode expressed by the first term of (19) represents the diffusion of the magnetic field through the conductor. As discussed by *Kikuchi and Araki* [1979a], the one-dimensional propagation through the ionospheric E-region never plays a role in transmitting the electric field horizontally because of a time lag of the order of an hour. The second and third terms of (19) represent magnetic fields determined by the boundary conditions at the interfaces. These terms represent electromagnetic fields excited by the TM0 mode at the lower boundary of the conducting ionosphere.

In determining the electromagnetic fields in the ionosphere, we first evaluate a transient time for the electric and magnetic fields in the ionosphere to reach a quasi-steady state in which the electromagnetic fields are well controlled by the boundary conditions at the interface with the magnetosphere. If we let the conductivity and thickness of the ionosphere be 2 10^-4 mho/m and 30 km for the daytime condition, we obtain 1 sec for the transient time in which the skin depth is equal to the width of the ionosphere. Thus, if we focus our attention to the time greater than 1 sec, the electromagnetic fields in the ionosphere do not depend on time, and are determined by the magnetospheric and ionospheric parameters, as expressed below.

$$H_{yI}(x) = \left(1 - \frac{\sigma z}{\Sigma_A + \Sigma_I}\right)H_{yV}(x), \quad (27)$$

$$E_{xI}(x) = \frac{1}{\Sigma_A + \Sigma_I}H_{yV}(x), \quad (28)$$

where Σ_A and Σ_I denote the Alfvén conductance of the magnetosphere and height-integrated ionospheric conductivity, respectively, which are given below.

$$\Sigma_A = \frac{1}{\mu_0 V_A}, \quad \Sigma_I = \sigma \cdot d, \tag{29}$$

where d represents the thickness of the ionosphere.

In the magnetosphere, the transverse magnetic field is transmitted upward along the magnetic field lines by the Alfvén waves. The magnetic field and the associated electric field are expressed as below.

$$H_{yM}(x) = \frac{\Sigma_A}{\Sigma_A + \Sigma_I} H_{yV}(x) \cdot U\left(t - \frac{z}{V_A}\right), \tag{30}$$

$$E_{xM}(x) = \frac{1}{\Sigma_A + \Sigma_I} H_{yV}(x) \cdot U\left(t - \frac{z}{V_A}\right). \tag{31}$$

Here we note that the electric field in the ionosphere is uniform in the ionosphere, and is transmitted at the Alfvén speed upward along the field lines in the magnetosphere. The solutions (27) and (30) imply that a part of the electric currents flow at the front of the Alfvén wave, carrying the transverse magnetic field (30) behind. In an extreme case of negligibly small Alfvén conductance, most currents flow in the ionosphere, and the electric field in the magnetosphere is determined by ionospheric currents and ionospheric conductance as discussed by *Kikuchi and Araki* [1979b].

3. EXCITATION OF THE TM0 MODE

Tanaka [1995], based on a global MHD simulation, demonstrated that the Region-1 field-aligned currents are generated around the cusp, where the magnetic stress energy is converted to the internal energy of hot plasma and then to the electromagnetic energy transmitted along the field lines. The potential electric field is transmitted along the field lines to the polar ionosphere, and is partly reflected at the conducting ionosphere. We here assume that the field lines are replaced by a transmission line [*Watanabe et al.*, 1986] with the intrinsic impedance, Z_1, terminated by the conducting ionosphere with the impedance, Z_2 (1/height-integrated conductivity). We here assume that the magnetosphere-ionosphere-ground system is axi-symmetric as shown in Figure 2, so that a pair of the field-aligned currents has a positive and negative potential V as shown in Figure 2. If we assume that the center of the magnetospheric transmission line is of null potential and that the potential of the ground is null, the dashed line can be replaced by a perfectly conducting plane. Then we have a bent transmission line composed of the magnetospheric transmission line and the Earth-ionosphere waveguide with load ionosphere inserted in between (Figure 2). If we let the intrinsic impedance of the Earth-ionosphere transmission line be Z_3, the reflection coefficient at the surface of the ionosphere and the transmission coefficient are expressed as follows.

$$r = \frac{Z_2 Z_3 - Z_1(Z_2 + Z_3)}{Z_2 Z_3 + Z_1(Z_2 + Z_3)}, \tag{32}$$

$$t = \frac{2Z_2 Z_3}{Z_2 Z_3 + Z_1(Z_2 + Z_3)}, \tag{33}$$

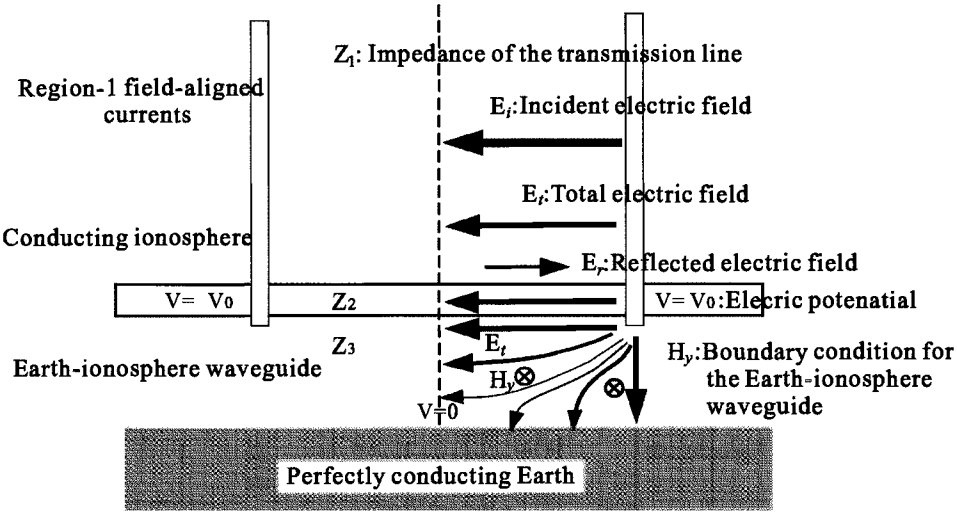

Figure 2. Magnetosphere-ionosphere-ground transmission system composed of magnetic field lines and the Earth-ionosphere waveguide. The TM0 mode is excited in the waveguide by an energy transmitted through the ionosphere. The dashed line indicates null-potential, which separates the system into two bent transmission lines (see text).

where the intrinsic impedances are defined as below.

$$Z_1 = \mu_0 V_A$$
$$Z_1 = 1/\Sigma_I \tag{34}$$
$$Z_3 = Z_V = \sqrt{\mu_0/\varepsilon_0}.$$

We here take the parameters of the magnetosphere, ionosphere and vacuum as

$$V_A = 1000\ km/s$$
$$\Sigma_P = 5\ mho$$
$$Z_V = 377\ ohm.$$

Then we have $t = 0.27$. It should be stressed that 27 percent in strength of the incident electric field is transmitted into the Earth-ionosphere transmission line (waveguide). The transmitted electric field should accompany a transverse magnetic field of which intensity is determined by the following relation.

$$H_y = E_x / Z_3. \tag{35}$$

If we let this transverse magnetic field be the boundary condition for the Earth-ionosphere waveguide, the TM0 mode will be excited as shown above.

4. ATTENUATION OF THE TM0 MODE IN THE WAVEGUIDE

We here evaluate the attenuation of the TM0 mode in the Earth-ionosphere waveguide by calculating loss of the horizontally transported Poynting flux instead of determining all the coefficients in (17)-(22). We assume that the loss of the Poynting flux should be equal to that transported upward through the ionosphere, which is calculated using the results obtained above, (27)-(28).

As shown in Figure 1, we let the Poynting flux flowing across the section at x be $S_{xV}(x)$. The Poynting flux in the x-direction is derived from the transverse magnetic field (24) and the vertical electric field (26) as shown below.

$$S_{xV} = E_{zV} \times H_{yV} = Z_0 H_{y0}^2 U\left(t - \frac{x}{c}\right). \tag{36}$$

The energy transported through the waveguide across $x = x$ is obtained from (36) by multiplying the height of the ionosphere (h) as expressed below.

$$W_x(x) = h \cdot S_{xV}(x). \tag{37}$$

The upward propagating Poynting flux in the conductor is derived from (27) and (28) as expressed below,

$$S_{zI}(x,z) = \frac{\Sigma_A + \Sigma_I - \sigma \cdot z}{(\Sigma_A + \Sigma_I)^2} H_{yV}^2(x). \tag{38}$$

The Poynting flux penetrating upward across the lower edge of the ionosphere is given by,

$$S_{zI}(x, z=0) = \frac{1}{\Sigma_A + \Sigma_I} H_{yV}^2(x), \tag{39}$$

and the Poynting flux transported into the magnetosphere is given below,

$$S_{zM}(x,z) = \frac{\Sigma_A}{(\Sigma_A + \Sigma_I)^2} H_{yV}^2(x) \cdot U\left(t - \frac{z}{V_A}\right). \tag{40}$$

We assume that energy is not produced inside the section bounded at x and $x + \Delta x$ (Figure 1), the energy leaked into the ionosphere is derived from the divergence of energy transported in the waveguide. Thus, we have

$$h[S_{xV}(x) - S_{xV}(x + \Delta x)] = \Delta x S_{zI}(x, z=0). \tag{41}$$

This equation leads to a differential equation described as below.

$$\frac{\partial S_{xV}(x)}{\partial x} = -\frac{1}{h} \frac{1}{Z_0(\Sigma_A + \Sigma_I)} S_{xV}(x). \tag{42}$$

We here define the ratio of the Poynting flux at x to that at $x = 0$ as follows,

$$\overline{S_{xV}}(x) = \frac{S_{xV}(x)}{S_{xV}(0)} = e^{-\frac{x}{h} \frac{1}{Z_0(\Sigma_A + \Sigma_I)}} = e^{-\frac{0.0265x[\mathrm{Mm}]}{(\Sigma_A + \Sigma_I)}} \tag{43}$$

or the ratio of the electric field is

$$\overline{E_{zV}}(x) = \frac{E_{zV}(x)}{E_{zV}(0)} = e^{-\frac{x}{2h} \frac{1}{Z_0(\Sigma_A + \Sigma_I)}} = e^{-\frac{0.0133x[\mathrm{Mm}]}{\Sigma_A + \Sigma_I}}, \tag{44}$$

and alternatively

$$\overline{E_{zV}}[\mathrm{dB}] = -0.116 \frac{x[\mathrm{Mm}]}{(\Sigma_A + \Sigma_I)}. \tag{45}$$

If we use the parameters used before ($V_A = 1000$ km/s, $\Sigma_I = 5$ mho, $x = 10000$ km), we obtain the ratio of the electric field as 0.98. The result indicates no appreciable attenuation for the transmission of the ionospheric potential over 10000 km for the daytime condition. For the nighttime condition, the ionospheric conductance is usually smaller than the Alfvén conductance. In the extreme case of poorly conducting ionosphere, null-conductance, the ratio is 0.85. Thus, the attenuation is not significant compared with the geometrical attenuation as shown by *Kikuchi and Araki* [1979b]. The curvature of the Earth would make some

modification on the propagation of the TM0 mode. However, we should recall that the TM0 mode is characterized by the electric field perpendicular to the walls of the waveguide. This condition would be valid even when the waveguide is curved. It should be noted that the waveguide model is assumed to be horizontally semi-infinite, and that the propagation time of the TM0 mode over 10000 km is only 0.03 sec. In the actual situation, the waveguide has a finite length in the x-direction, say, 10000 km. Although the finite length of the waveguide causes drastic changes in the ionospheric potential and currents [*Kikuchi*, presented at AGU2004 fall meeting], the semi-infinite model provides us with a fundamental nature of the transmission of the ionospheric potential toward low latitudes and further to the inner magnetosphere.

5. DISCUSSION AND CONCLUSION

There are several possible propagation modes or mechanisms that could be applied to the transmission of the convection electric field from the dayside outer magnetosphere to the nightside inner magnetosphere. If we assume that an accumulation of the FTEs causes the global convection, it would take a long time (> 30 min) for the nightside convection to be completed [e.g., *Walker et al.* 1993], which is inconsistent with the observed quick development of the nightside ionospheric convection as demonstrated by *Ridley et al.* [1998] and *Ruohoniemi and Greenwald* [1998]. The magnetosonic wave hardly drives a rotational motion of plasma, since it only reduces an imbalance in the magnetic pressure distribution. The shear Alfvén waves are generated from the magnetosonic wave if there is a strong inhomogeneity in the distribution of the Alfvén speed. However, this mechanism works only for time scales of the ULF wave [*Kivelson and Southwood*, 1988]. The convective motion of the plasma can be driven by shear Alfvén waves, but the Alfvén waves never propagate to the nightside magnetosphere across the magnetic field lines. Thus, we apply the TM0 mode in the Earth-ionosphere waveguide [*Kikuchi and Araki*, 1979b] proposed to explain the instantaneous transmission of the polar electric field to the dayside dip equator, explaining the simultaneous onset of the preliminary impulse of the SC at high and equatorial latitudes. In this paper, we examined how the waveguide mode is excited by the electric potential impressed from the magnetosphere, and showed that the TM0 mode can carry the ionospheric electric potential to the nightside without significant loss due to the finite conductivity of the ionosphere. We further showed that the ionospheric electric field propagates upward into the magnetosphere along magnetic field lines. As a result, the electric field transmitted from the ionosphere drives the plasma convection in the magnetosphere. Finally, we point out that the ionosphere never creates electromagnetic energy but transmits the Poynting flux from the dayside to the nightside, further to the inner magnetosphere.

REFERENCES

Araki, T., Global structure of geomagnetic sudden commencements, *Planet. Space Sci.*, 25, 373-384, 1977.

Hashimoto, K.K., T. Kikuchi, and Y. Ebihara, Response of the magnetospheric convection to sudden interplanetary magnetic field changes as deduced from the evolution of partial ring currents, *J. Geophys. Res.*, 107, A11, 1337, doi:10.1029/2001JA009228, 2002.

Hashimoto, K., and T. Kikuchi, Quick Response of the near-Earth Magnetotail to Changes in the Interplanetary Magnetic Field, *AGU Monograph*, 2005, this issue.

Kikuchi, T., and T. Araki, Transient response of uniform ionosphere and preliminary reverse impulse of geomagnetic storm sudden commencement, *J. Atmosph. Terrest. Phys.*, 41, 917-925, 1979a.

Kikuchi, T. and T. Araki, Horizontal transmission of the polar electric field to the equator, *J. Atmosph. Terrest. Phys.*, 41, 927-936, 1979b.

Kikuchi, T., T. Araki, H. Maeda, and K. Maekawa, Transmission of polar electric fields to the equator, *Nature*, 273, 650-651, 1978.

Kikuchi, T., H. Lühr, T. Kitamura, O. Saka, and K. Schlegel, Direct penetration of the polar electric field to the equator during a DP2 event as detected by the auroral and equatorial magnetometer chains and the EISCAT radar, J. Geophys. Res., 101, 17161-17173, 1996.

Kivelson, M.G. and D.J. Southwood, Hydromagnetic waves and the ionosphere, *Geophys. Res. Lett.*, 15, 1271-1274, 1988.

Ridley A.J., G. Lu, C.R. Clauer, and V.O. Papitashvili, A statistical study of the ionospheric convection response to changing interplanetary magnetic field conditions using the assimilative mapping of ionospheric electrodynamics technique, *J. Geophys. Res.*, 103, 4023-4039, 1998.

Ruohoniemi, J.M. and R.A. Greenwald, The response of high latitude convection to a sudden southward IMF turning, *Geophys. Res. Lett.*, 25, 2913-2916, 1998.

Slinker, S.P., J.A. Fedder, J.M. Ruohoniemi, and J.G. Lyon, Global MHD simulation of the magnetosphere for Novemver 24, 1996, *J. Geophys. Res.*,106, 361-380, 2001.

Tanaka, T., Generation mechanisms for magnetosphere-ionosphere current systems deduced from a three-dimensional MHD simulation of the solar wind-magnetosphere-ionosphere coupling processes, *J. Geophys. Res.*, 100, 12057-12074, 1995.

Walker, R.J., T. Ogino, J. Raeder, and M. Ashour-Abdalla, A global magnetohydrodynamic simulation of the magnetosphere when the interplanetary magnetic field is southward: The onset of magnetotail reconnection, *J. Geophys. Res.*, 98, 17235-17249, 1993.

Watanabe, K., M. Ashour-Abdalla, and T. Sato, A Numerical Model of Magnetosphere-Ionosphere Coupling: Preliminary Results, *J. Geophys. Res.*, 91, A6, 6973-6978, 1986.

kikuchi@nict.go.jp

Advances in Inner Magnetosphere Passive and Active Wave Research

James L. Green and Shing F. Fung

Goddard Space Flight Center, Greenbelt, Maryland

This review identifies a number of the principal research advancements that have occurred over the last five years in the study of electromagnetic (EM) waves in the Earth's inner magnetosphere. The observations used in this study are from the plasma wave instruments and radio sounders on Cluster, IMAGE, Getotail, Wind, Polar, Interball, and others. The data from passive plasma wave instruments have led to a number of advances such as: determining the origin and importance of whistler mode waves in the plasmasphere, discovery of the source of kilometric continuum radiation, mapping AKR source regions with "pinpoint" accuracy, and correlating the AKR source location with dipole tilt angle. Active magnetospheric wave experiments have shown that long range ducted and direct echoes can be used to obtain the density distribution of electrons in the polar cap and along plasmaspheric field lines, providing key information on plasmaspheric filling rates and polar cap outflows.

1. INTRODUCTION

Within the magnetosphere there are more then 40 plasma wave emissions that have been classified [see the excellent review by *Shawhan,* 1979]. It is well known that space plasmas can support a variety of EM wave modes. To illustrate, Figure 1 shows various propagation modes for a point in the magnetosphere in which the local electron gyrofrequency is less than the local electron plasma frequency ($f_g < f_p$; i.e. the plasmasphere). As the frequency increases (from Hz to kHz) plasma waves can propagate in the whistler, Z, and the L-O and R-X modes. The frequency range of each mode has been shaded to easily distinguish between them. These modes have lower and, sometimes, upper frequency limits to their propagation that are called cutoffs or resonances as described by *Stix* [1992]. The left hand ordinary (L-O) and the right-hand extraordinary (R-X) modes are called the free space modes [using the terminology of Stix, 1992] since they only have lower frequency cutoffs (f_R for R-X mode and f_p for L-O mode as shown in Figure 1) and at sufficiently high frequencies can propagate into the solar wind once they are generated in the magnetosphere. The Z and whistler mode emissions are referred to as trapped emissions since they have well defined upper frequency limits that confine these emissions to specific regions in space.

Due to space limitations it is impossible to review all the progress made in understanding magnetospheric processes from EM waves, so the authors will concentrate on a few selected topics that have undergone rapid advances in the last five years in both trapped and free space portions of the spectrum. Recent missions such as Cluster and the Imager for Magnetopause-to-Aurora Global Exploration (IMAGE) satellites, along with older spacecraft such as Geotail, Wind, Polar, and Interball that routinely orbit the Earth, have provided a wealth of new data for analysis. In addition to passive measurements, the long range EM sounder capability on IMAGE and the short-range sounders on the four Cluster spacecraft are producing unique types of data. The purpose of this paper is to review a number of important advances in our understanding of inner magnetospheric processes from passive and active wave measurements. The paper will first concentrate on passive measurements consisting of trapped waves (Section 2) and escaping waves (Section 3) and then on active magnetospheric sounder measurements (Section 4).

The Inner Magnetosphere: Physics and Modeling
Geophysical Monograph Series 155

10.1029/155GM21

2. TRAPPED WAVES IN PLASMASPHERE

The index of refraction in the whistler mode is such that these EM waves have a natural tendency to travel along a magnetic field. In the plasmasphere, whistler mode waves make repeated journeys from northern to southern hemisphere and vice versa. Since the upper frequency of the whistler mode is the local f_p or f_g (see Figure 1) whichever is less, these waves are largely confined or trapped in the higher density plasmasphere region around the Earth.

There are four basic whistler mode waves generated in the plasmasphere as summarized in Figure 2 as a function of their frequency range. From 10-50 kHz, Earth-based transmitters dominate the spectrum. The authors have identified over 100 stations generating emissions at more than 60 discrete frequencies, and there are quite likely many more. Chorus emissions, observed from the plasmaspause outward typically in the frequency range from 0.3-12 kHz, can be found extending from the magnetic equator to mid-latitudes, and generally intensify during storm periods. Plasmaspheric hiss is observed in the plasmasphere at frequencies typically between 0.3-3 kHz and is believed to be responsible

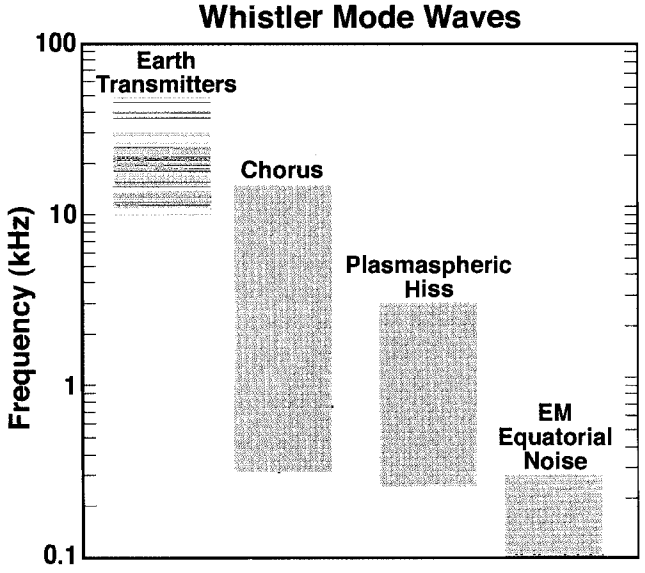

Figure 2. A summary of the four whistler mode waves in the inner magnetosphere as a function of their frequency range that are reviewed in this paper.

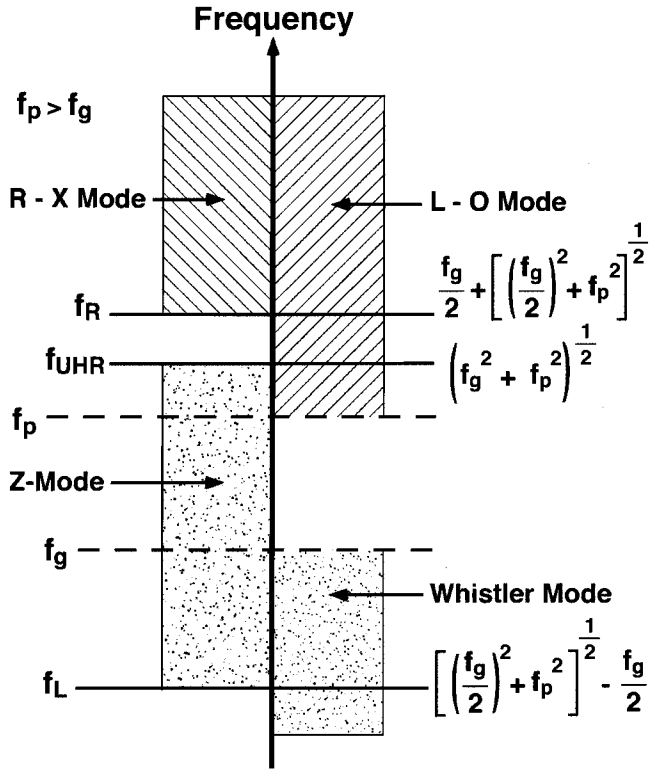

Figure 1. Trapped and escaping waves modes in a plasma in which the $f_p > f_g$ illustrating the upper and lower frequency cutoffs and resonances.

for electron precipitation in the slot region ($L \sim 2.5$) between the inner and outer radiation belts. Electromagnetic (EM) equatorial waves are typically found from a few Hz to about 300 Hz and are confined to the magnetic equator (typically within 1 R_E) within the plasmasphere. Lightning whistlers are also observed in the plasmasphere (not shown in Figure 2) and they have the frequency range of from about 0 to 10 kHz.

The average magnetic wave field spectral density measurements, as a function of frequency and L value, from the Plasma Wave Instrument (PWI) on Dynamics Explorer -1 (hereafter DE) is shown in Plate 1 [adapted from *André et al.*, 2002]. The top and bottom panels of Plate 1 are from quiet and disturbed conditions respectively, use the same intensity levels, and show the dramatic increase in intensity of the whistler mode wave spectrum in the plasmasphere (except for the transmitters) during disturbed conditions. The longitudinal distributions, where the whistler mode waves are the most intense in the plasmasphere, are shown in Figure 3. Most of the whistler mode wave research in the last 5 years has dealt with various aspects of plasmaspheric hiss and chorus. Resent results of plasmaspheric hiss research will be discussed in this review since chorus is well covered by another paper in this monograph [see *Meredith et al.*, 2004].

Although found essentially everywhere in the plasmasphere at some intensity level, plasmaspheric hiss is most intense throughout the local afternoon sector (see Figure 3) and on L shells which contain the slot region in the electron

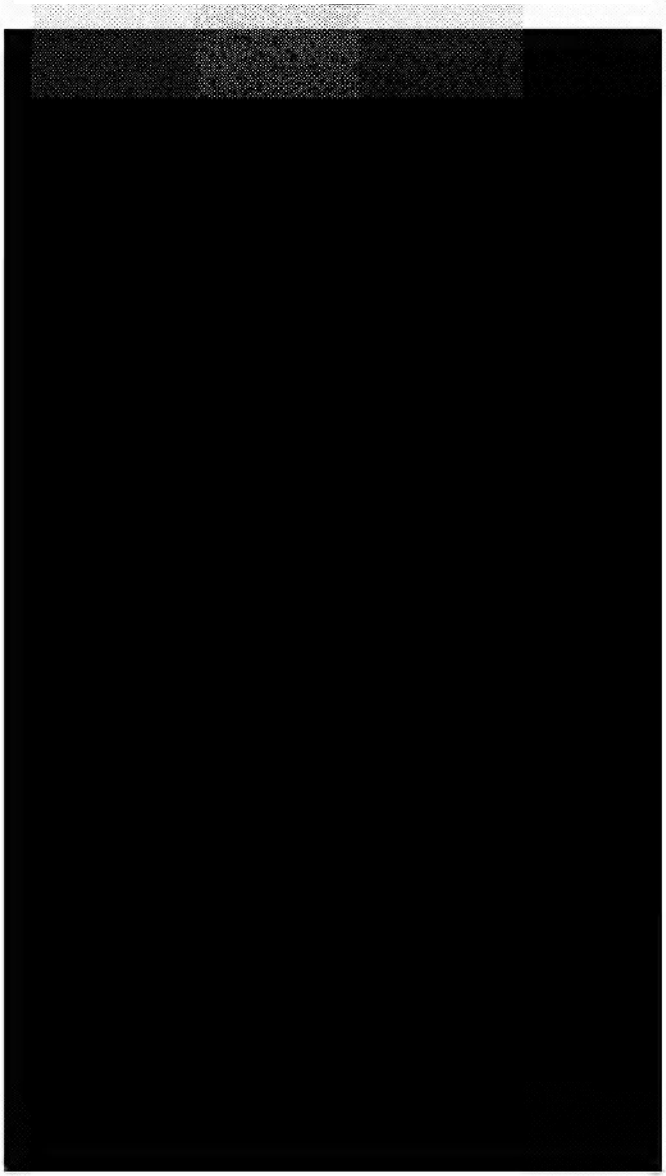

1 [redacted]

by a mode conversion process, converting electrostatic Z mode emissions to the electromagnetic L-O mode, over the entire frequency range of the emission (see Figure 1). The two classes of mode conversion mechanisms that have been considered are linear [e.g., *Jones*, 1976 and *Budden*, 1980] and non-linear [e.g., *Melrose*, 1981; *Fung and Papadopoulos*, 1987].

3.1.1. Normal Continuum Radiation. At frequencies less than the magnetopause plasma frequency (~30 kHz), the continuum radiation has been referred to as the "trapped" component [*Gurnett and Shaw*, 1973] since it is observed primarily in the magnetospheric density cavity between the plasmapause and magnetopause (Plate 2 lower left). The trapped continuum spectrum is observed as a broad-band emission with very little frequency structure. The broadband structure of the trapped continuum spectrum is believed to be produced from a series of narrow band emissions at slightly different frequencies from an extended source region at the plasmapause whose emission then mixes due to multiple reflections (with some Doppler broadening) in the magnetospheric density cavity.

Continuum radiation at frequencies above the magnetopause plasma frequency has been referred to as the "escaping" component [*Kurth et al.*, 1981] since it propagates from the Earth's plasmapause to well outside the magnetosphere (Plate 2 upper left). A common characteristic of all the escaping continuum radiation is that it has narrow frequency bands of emissions showing that the name continuum is not entirely descriptive of the radiation in this frequency range. Continuum radiation below 100 kHz is typically generated at the plasmapause in the pre-noon sector (06-12 LT) and has been called "normal continuum" by a number of authors [e.g., *Kasaba et al.*, 1998; *Hashimoto et al.*, 1999].

Plate 3 has been adapted from Figure1 and Plate 3 of *Green and Boardsen* [1999] and shows the observed emission cone of the normal continuum radiation by combining four years of Hawkeye plasma wave data overlaid with ray tracing calculations at that same frequency. These authors found that normal continuum radiation was generated in the pre-noon sector and is beamed into broad cones (half width of ~35°) at low frequencies (~30 kHz). When modeled with ray tracing calculations, the resulting radiation pattern is such that the trapped continuum radiation does not completely fill the magnetospheric cavity as previously believed. In addition, the trapped continuum component that consists of multiple reflections between the magnetopause and the plasmapause, as shown in Plate 3 (labeled as "trapped rays"), is confined to only ~10° in latitude about the magnetic equator.

Direction finding measurements from all four of the Cluster spacecraft from spin modulated Whisper data have confirmed many of the general properties of continuum radiation such as the plasmapause source regions [see *Décréau et al.*, 2004]. Near source region measurements have revealed new properties such as the importance of small-scale density irregularities in the local amplification of normal continuum and the possible role wave ducting may play in its generation.

Normal continuum radiation at frequencies near the magnetopause plasma frequency has also been used to be an indicator of the global scale magnetosheath electron density. *Nagano et al.* [2003], using data from PWI on Geotail, observed a portion of the normal continuum spectrum that was trapped within the magnetsheath. The upper frequency was controlled by the f_p in the solar wind after taking into account a time delay. The upper frequency was termed the transition frequency since it was the frequency at which the radiation changed from isotropic (due to multiple reflections in the magnetosheath randomizing its direction of arrival) to anisotropic (having a preferred direction). These authors found that a 0-3 hour time delay in the variation in the transition frequency of the normal continuum relative to the upstream f_p may suggest that the magnetosheath plasma relaxes at the local Alfven speed rather than the convection speed of the solar wind.

3.1.2. Continuum Enhancement. Large variations in continuum intensity over the 20-80 kHz frequency range lasting for up to 2 hours have been observed primarily in the midnight to dawn sector and were first reported by *Gough* [1982]. This distinct feature in the continuum emission spectrum has been called "continuum enhancement" by *Kasaba et al.* [1998]. The characteristic emission spectrum of continuum enhancement is shown in Plate 2 upper right spectrogram. *Kasaba et al.* [1998], using simultaneous Geotail and Wind observations, showed that the normal continuum emissions in the pre-noon sector appeared to follow continuum enhancement events. This relationship has lead these authors to suggest that a series of storm time electron injections are generating both types of emissions.

3.1.3. Kilometric Continuum. Kilometric continuum (KC) is a major component of the escaping continuum radiation in the 100-800 kHz frequency range. *Hashimoto et al.* [1999] have rediscovered this component of the emission and has sparked considerable interest in further understanding various aspects of this radiation that make it different from its lower frequency trapped and escaping (<100 kHz) counterpart generated in the pre-noon sector and discussed in the previous section. The lower right hand panel of Plate 2 clearly shows the discrete emissions bands of KC extending from 17-24UT. The frequency range for kilometric continuum is approximately the frequency range of auroral kilometric

radiation (AKR), but as shown in the Plate 2 lower right panel, there are significant differences that can be used to easily distinguish between these two emissions. KC has a narrow band structure over a number of discrete frequencies while AKR is observed to be a broadband and sporadic emission and can be seen from 16-17:00 and from 21:30 to 24:00 UT in that spectrogram.

Kilometric continuum has been observed at all local times, although it has been difficult to make a positive identification of the emission during the times when Geotail was in the late evening or early morning local time sector when AKR was active [*Hashimoto et al.,* 1999]. From Geotail and IMAGE observations *Hashimoto et al.* [1999] and *Green et al.* [2004a] have found that kilometric continuum is confined to a narrow latitude range of approximately ±15° about the magnetic equator. Although these characteristics make it different from the lower frequency continuum discussed in Section 3.2, the similar spectral characteristics of the emission and its relationship to the plasmapause supports the conclusion by *Menietti et al.* [2003] from Polar observations that the radiation is generated by the same mechanism.

At lower frequencies, beaming of continuum radiation around the magnetic equator to latitudes as high as 50° has also been observed by *Jones et al.* [1987] (from 80 to 100 kHz), *Morgan and Gurnett* [1991] (from 45 to 154 kHz), and by *Green and Boardsen* [1999] (from 24 to 56 kHz) as discussed above. The narrow beaming of kilometric continuum in magnetic latitude has made this emission difficult to observe routinely or for only short periods of time except for equatorial orbiting spacecraft with the proper instrumentation, such as Geotail.

The source region for KC was originally identified by *Carpenter et al.* [2000] as coming from plasmaspheric cavities, but more recently *Green et al.* [2002] and *Green et al.* [2004a] clearly identified KC as being generated at the plasmapause, deep within plasmaspheric notch structures that corrotate with the Earth. Plate 4 has been adapted from Figure 8 of *Green et al.* [2002] and Figure 1 of *Green et al.* [2004a] and illustrates the location of the KC source region and resulting emission cone pattern of the radiation to be consistent with the observations. Panel A of Plate 4 is a frequency-time spectrogram from the PWI instrument on GEOTAIL showing the banded structure of KC. Panel B shows the magnetic longitude versus the equatorial radial distance of the plasmapause (derived from the inserted EUV image of the plasmasphere) and the position of GEOTAIL during the KC observations of panel A. Panel C is a ray tracing analysis which shows that the structure of the plasmaspheric notch has a significant effect on the shape of the resulting emission cone through refraction. The process by which the notch structure is produced in the plasmasphere is not completely understood at this time.

3.2. Auroral Kilometric Radiation

Over 35 papers have been published in the last 5 years on auroral kilometric radiation (AKR) demonstrating that after the classic paper by *Gurnett* [1974], AKR is, arguably, still the most intensely studied magnetospheric emission. It is beyond the scope of this brief review to discuss all these results. Significant progress in understanding various aspects in the generation of AKR has been made in the areas of seasonal and solar cycle variations, polarization measurements, fine structure, and source region location. AKR research continues to be an important aspect of ionospheric-magnetospheric coupling during the substorm processes.

The cyclotron maser instability [*Wu and Lee*, 1979] is believed to be the basic mechanism for the generation of AKR. For generation of AKR near the local electron gyrofrequency, the cyclotron maser instability requires a source of free energy in the electron distribution and the following condition:

$$f_p/f_g < 0.3 \quad (1)$$

The observation that the AKR emission frequency is very near the local f_g in the auroral zone density cavity [e.g., *Hilgers et al.*, 1991] where the electron distribution function has a number of sources of free energy [*Delory et al.,* 1998; *Ergun et al.*, 1998; *Ergun et al.*, 2000; *Fung and Vinas*, 1994] is the strongest observational evidence supporting the cyclotron maser instability.

The AKR emission spectrum, in general terms, is observed over a broad frequency range from ~30 to ~700 kHz with the peak intensity around 250 kHz. *Kumamoto and Oya* [1998] noted a seasonal difference in the AKR intensity from Akebono plasma wave data with increases in intensity in the winter polar region over the summer polar region. *Kumamoto et al.* [2003] expanded on these results and showed seasonal and solar cycle variations in the vertical distribution of the occurrence probability of AKR emissions from low altitude Akebono measurements. Using Polar and IMAGE wave data, *Green et al.* [2004b] used the observed AKR spectrum to estimate the altitude range of the source region as suggested by *Lee et al.* [1980] by mapping the observed frequency to the f_g in the auroral density cavity. In both these studies, ionospheric density variations were believed to be mainly responsible for large-scale changes in the AKR source location.

Using two years of IMAGE Radio Plasma Imager (RPI) and one and a half years of Polar PWI data *Green et al.* [2004b], found a dramatic frequency shift in the average AKR spectrum (intensity normalized to 8 R_E) with dipole tilt. Panel A of Plate 5 clearly shows two main seasonal effects on the average AKR spectrum as observed by the IMAGE RPI

[redacted]

[redacted]

[redacted]

[redacted]

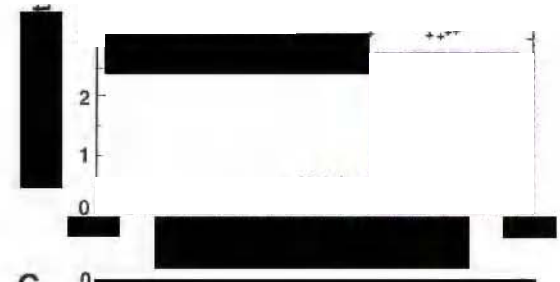

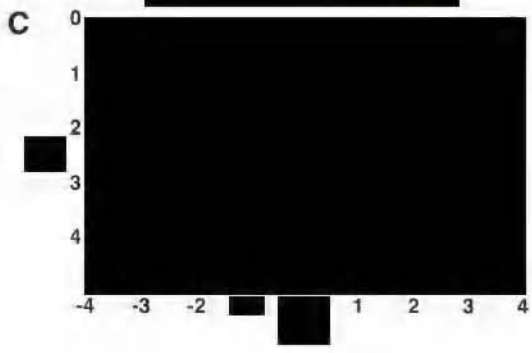

[redacted]

[redacted]

[redacted]

[redacted]

[redacted]

[redacted]

[redacted]

[redacted]

[redacted]

[redacted]

[redacted]

instrument: 1) the AKR emission spectrum shifts down in frequency with increasing dipole tilt, and 2) the emission spectrum extends over a larger frequency range for negative dipole tilt angles than for positive dipole tilt angles. Panel B of Plate 5 is a qualitative illustration of the AKR spectrum, from panel A, mapped into contours of f_p/f_g for a 70° invariant auroral field line. *Green et al.* [2004b] found that the source region during extreme negative dipole tilt angles (winter) shows the auroral zone density cavity stretching from a region where f_g = 500 kHz to nearly f_g = 80 kHz. In contrast, for extreme positive dipole tilt angles the source region extent is much smaller, has moved further up the field line, and has a lower frequency boundary of 60 kHz and an upper frequency boundary near 250 kHz. In addition, *Green et al.* [2004b] also found an overall solar cycle effect with the average AKR intensity lowered by as much as an order of magnitude during solar maximum. These results are consistent with *Newell et al.* [1996] who showed that there is a significant suppression of discrete aurora by sunlight and that ionospheric conductivity is a key factor in controlling the occurrence of discrete aurora. It was *Gurnett* [1974] who first clearly showed that AKR was closely correlated with discrete auroral arcs.

The Polrad instrument on Interball 2 has made detailed polarization measurements of AKR distinguishing between L-O and R-X polarization components. Plate 6, adapted from *Hanasz et al.* [2003], show a frequency time spectrogram of AKR from Polrad (top panel) and the polarization (middle panel) derived from determining the Stokes parameters [technique described by *Hanasz et al.*, 2000] and by factoring in the trajectory of the spacecraft relative to the source region (bottom panel). *Hanasz, et al.* [2003] has found that L-O polarized AKR, observed to be coming from dayside sources, is about three times more frequent than L-O polarized night side sources which are observed about 10% of the time. In addition, *Hanasz et al.* [2003] was able to distinguish two classes in the circular polarized AKR spectrum. The "regular" AKR is dominated by the R-X mode and observed in the upper frequency portion of the spectrum and a weak L-O mode in the lower portion as shown in Plate 6. The "irregular" AKR is somewhat patchy with the two polarizations interwoven randomly over the whole frequency range. The reason for this variation in polarization is unknown.

Another new spectral feature of AKR recently discovered by *de Feraudy et al.* [2001] and *Hanasz et al.* [2001] is an intense, nearly simultaneous broad frequency burst of AKR in as short as 6 s and as long as a few minutes that is generated during the fast expansion of the auroral bulge. These bursts of emission extend from 100 to 800 kHz and last for only a few tens of minutes. What remains to be explained is how the free energy for these waves be created so rapidly along such a large section of the source field line.

The AKR emission spectrum also contains narrow band fine structure referred to as striations. *Menietti et al.* [2000] have analyzed a semi-random sample of the AKR spectrum using the high-resolution wideband instrument on the Polar satellite. New results from that survey show that the AKR fine structure, consisting of very narrow band emissions, is observed predominantly in the 40-215 kHz range and drifts in frequency with time. Negative drifting fine structures bands (decreasing frequency with time) are observed approximately 6% of the time, while the positive sloping (increasing in frequency with time) striations are observed at a much lower rate. The typical drift rate of the fine structure is observed to be between –8 kHz/s and –2 kHz/s and, for the positive sloping fine structure, between 5 or 6 kHz/s. In addition, there was a general decrease in drift rate with increasing frequency. Although the origin of the AKR fine structure is not known, it has been pointed out that the frequency dependence of the drift rate is consistent with AKR production stimulated by an upward propagating electromagnetic ion cyclotron wave [*Menietti et al.,* 1996].

Applying a very long baseline interferometry (VLBI) technique to simultaneous observations from the four Cluster spacecraft, *Mutel et al.* [2003 and 2004] determined the source locations, at selected frequencies, of individual AKR bursts. The VLBI technique involves precise timing of measured wave fronts from two or more locations separated by great distances. Six baselines can be formed from the four spacecraft yielding, when combined with the knowledge that the AKR emission is very close to the local gyrofrequency in the source region, source positions within an error of ~200 km from individual burst events. From several thousand observed burst events, *Mutel et al.* [2003] found that the AKR sources were confined to the night side auroral oval and that the distribution of AKR auroral source footprints, during the same storm period (1-3 hours long), had an overall spatial scale from 1000 to 2000 km. This is entirely consistent with a number of other earlier studies [e.g., *Kurth et al.,* 1975; *Gallagher and Gurnett*, 1979; and *Panchenko*, 2003]. As an example of the "pin-point" accuracy that this new technique has yielded, Plate 7 shows source locations from AKR burst at 125 kHz (red), 250 (green), and 500 kHz (blue) from two substorms. Panel A shows AKR burst locations during a southern hemisphere (positive dipole tilt) pass while panel B show the sources from a northern hemisphere (negative dipole tilt) pass. A clear shift in local time in AKR source region extent is seen in Plate 7 which is consistent with the results by *Green et al.* [2004b] that AKR sources are near dusk during times of negative dipole tilt (northern winter) and near midnight during times of positive dipole tilt (northern summer). This effect is attributed to AKR source regions preferring the lower density cavity regions that develop along field lines whose foot is not illuminated by the sunlight.

During times of negative dipole tilt a greater portion of the auroral oval is in darkness (AKR sources near dusk) with the opposite effect occurring during times of positive dipole tilt (AKR sources near midnight). It is important to point out that seasonal variations in the production of AKR were also found in an earlier study by *Kasaba et al.* [1997] from GEOTAIL/PWI observations. These authors showed that AKR is more active in the winter hemisphere for higher frequencies (500 kHz) representing lower latitude source regions.

4. ACTIVE PROBES

Plasma waves offer invaluable means for probing remote plasma regimes that are not readily or conveniently accessible to *in situ* measurements. Using the propagation characteristics such as cutoffs and resonances of different wave modes [*Stix*, 1992], it is possible to ascertain plasma environment parameters, such as density and magnetic field strength profiles, with accuracies that rival or are even superior to those measured by *in situ* instrumentations. An advantage of active probing by plasma waves over conventional passive observation techniques is that a large volume of the target plasma regime can be probed simultaneously. In this section, we review recent advances in active remote sensing of magnetospheric plasmas.

4.1. Brief Historical Development

The earliest applications of active probing of space plasmas were soundings of the ionosphere by radio waves [*Appleton and Barnett*, 1925; *Breit and Tuve*, 1926]. In fact, much of our current knowledge about the structures of the ionosphere has been derived from active radio measurements [e.g., *Davies*, 1990; *Hunsucker*, 1992]. Because of ionospheric shielding, ground-based radio observations of the magnetosphere are not possible except by whistler waves [*Storey*, 1953; *Helliwell*, 1988.]. Nevertheless, active magnetospheric sounding has been proposed for many years [*Franklin and Maclean*, 1969; *Ondoh et al.*, 1978; *Calvert*, 1981]. Because of the long ranges and uncertainties involving magnetospheric plasma targets, the practicality of magnetospheric radio sounding had been subject of investigations [*Green et al.,* 1993; *Calvert et al.*, 1995; *Calvert et al.*, 1997; *Greenwald*, 1997a,b]. The first successful long-range magnetospheric sounder experiment is the RPI [*Reinisch et al.*, 2000] onboard the IMAGE satellite [*Burch*, 2000], launched on March 25, 2000.

4.2. Active Radio Techniques

Active probing by radio waves involves transmitting radio waves into a plasma target, and receiving the signals (echoes) returned after the incident waves interacted with the target. Classification of different probing techniques depends on the mechanisms by which signals are returned to the receivers, and thus on the frequencies of the probing waves. The instrument that performs active radio probing of plasmas is called a sounder or radar.

4.2.1. Incoherent Scattering. As mentioned above, radio probing has been used most extensively in ionospheric studies. Notable instrumentations used in these studies include bottom-side (ionosondes) and topside (space-based) radio sounders, and incoherent and coherent scatter radars [*Kelley*, 1989]. An incoherent scatter radar (ISR) operating at high frequencies (>few hundred MHz) transmits waves with wavelengths that are typically small compared to the Debye length, $\lambda_{De} = v_e/f_p$ (where v_e is the thermal speed and f_p is the plasma frequency) of the intervening medium and the target plasma. The ISR-transmitted waves can therefore interact with individual charged particles and thus be Thomson scattered, i.e., absorbed and re-radiated. A small amount of the scattered wave energy can always return to the receiver as echoes. Signals from different ranges can be selected by different delay times. The ISR turns out to be a very useful tool for studying the ionosphere above the E and F layers where the densities are higher than the densities in the layers above.

It should be noted, however, that when ISR was first constructed to observe the ionosphere, the detected signal strengths were found to be much stronger and concentrated in much narrower bandwidths than expected from incoherent backscattering [*Bowles*, 1958]. It was then found that the observed scattered signals at frequencies <few 100 MHz were due to backscattering from ion acoustic waves, a process that is more akin to coherent scattering to be discussed next [e.g., *Dougherty and Farley*, 1960].

4.2.2. Coherent Scattering. Ionospheric and magnetospheric plasmas are filled with irregularities of various scale sizes [e.g., *Fejer and Kelley*, 1980; *Hanuise*, 1983; *Fung et al.,* 2000; *Fung et al.*, 2003]. When the wavelengths of the probing radio waves are larger than the local Debye length and become comparable to certain plasma irregularity scales, the waves can be effectively scattered by plasma collective effects according to

$$\mathbf{k}_i = \mathbf{k}_s + \mathbf{k}_{ir} \tag{2}$$

where $\mathbf{k}_i$, $\mathbf{k}_s$, and $\mathbf{k}_{ir}$ are the incident, scattered, and plasma irregularity wave vector, respectively. A special case of coherent scattering of this type is backscattering, in which $\mathbf{k}_s \approx -\mathbf{k}_i$, so that equation (2) gives $\mathbf{k}_{ir} \approx 2\mathbf{k}_i$. This is the well-known aspect-sensitive backscattering condition that the scattering irregularity scale is half the probing wavelength.

[redacted]

A

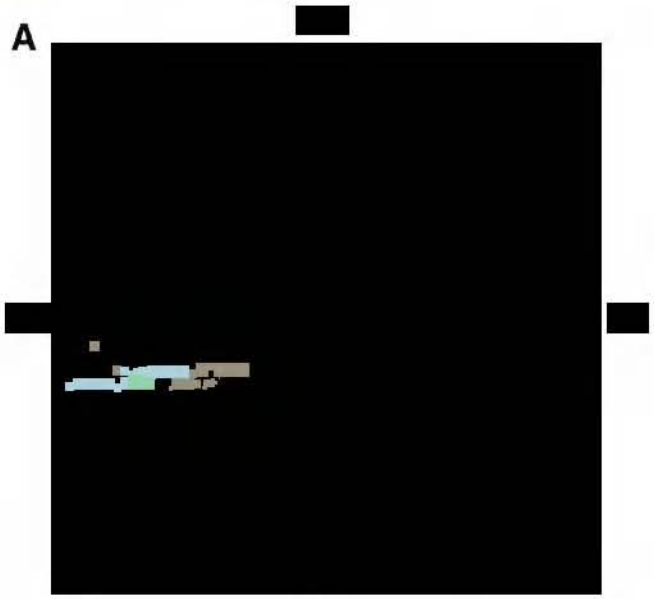
[redacted]

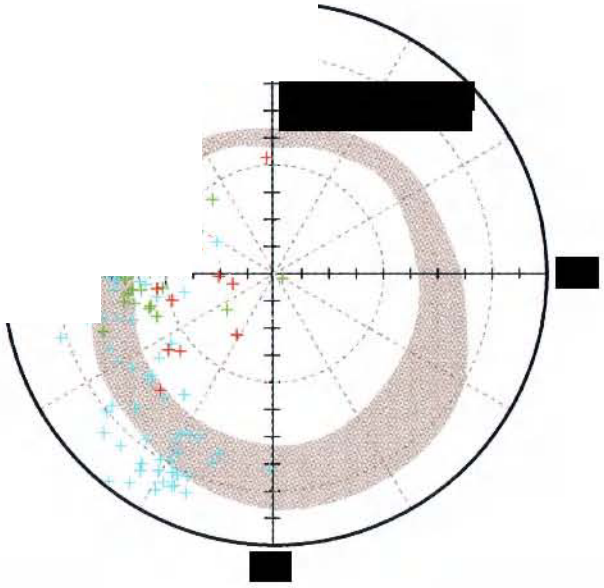
[redacted]

[redacted]

Coherent scatter radars (CSR) and aspect-sensitive scattering are particularly useful for measuring the occurrences of plasma instabilities and determining plasma irregularities, such as spread F [*Fejer and Kelley*, 1980; *James*, 1989].

4.2.3. Relaxation Sounding. Like any object, a plasma has a number of "ring tones" or resonances that are characteristic of the plasma density and embedded magnetic field strength. Plasma resonances have been explained in terms of sounder-stimulated electrostatic waves that propagate to short distances from the sounder and are reflected by local gradients back to the sounder receiver [*Muldrew*, 1972]. To learn about the local properties of a plasma medium, a relaxation sounder can be used to send out small amount of wave energy to stimulate resonances in the plasma nearby to the sounder [*e.g., Etcheto and Bloch*, 1978; *Etcheto et al.*, 1983; *Trotignon et al.,* 1986; *Oya and Ono,* 1987; *Oya et al.,* 1990]. This technique has been used by the Alouette-ISIS topside sounder satellites [*Jackson*, 1986] to produce many valuable studies of ionospheric resonances [e.g., *Benson*, 1971; 1977; 1996; *Warnock*, 1969; *Warren and Hagg*, 1968; *Muldrew*, 1972]. Typical plasma resonances observed in the ionosphere and magnetosphere include the electron gyroharmonic resonances nf_g, electron plasma resonance f_p, and the upper hybrid resonance f_{uhr},

$$f_g\,(\text{kHz}) = 0.028\ B\ (\text{nT}) \tag{3}$$

$$f_p\,(\text{kHz}) \approx 8.97\ [N_e\ (\text{cm}^{-3})]^{1/2} \tag{4}$$

$$f_{uhr} = (f_g^2 + f_p^2)^{1/2} \tag{5}$$

As shown in *Benson et al.* [2003], gyroharmonic and other plasma resonances (see equations (4) and (5)) are useful for deriving local magnetic field strengths and densities (to within a few percent or less), particularly when there are no other in situ observations of such parameters.

In addition, there exist "$(n + 1/2)f_g$" resonances that occur between successive gyroharmonics and have been referred to as the Q_n and D_n resonances, depending on whether they are observed above or below the upper hybrid resonance f_{uh} [equation (5)] [e.g., *Benson et al.*, 2003]. Assuming a thermal electron plasma distribution, *Warren and Hagg* [1968] obtained an expression for the Q_n frequencies,

$$f_{Qn} = f_g\,[n + (0.464/n^2)\,(f_p/f_g)^2] \tag{6}$$

For $n \geq 1$, the Q_n resonances can be weak and not easily distinguishable from gyroharmonic resonances when $(f_p/f_g)^2 < 1$ [*Perraut et al.,* 1990]. Frequency splitting of Q_n resonances has also been observed [e.g., *Trotignon et al.*, 1986; *Canu et al.*, 2001; *Trotignon et al.*, 2001].

The identification and interpretation of magnetospheric D_n resonances has been somewhat controversial [*LeSager et al.*, 1998; *Benson et al.*, 2001; *Canu*, 2001a,b]. D_n resonances were first identified in topside ionospheric sounding data [*Nelms and Lockwood*, 1967; *Oya*, 1970], but there had not been any first-principle explanation for their mode of propagation. *Osherovich* [1987; 1989] and *Osherovich and Benson* [1991] have found, however, the eigen-frequencies derived from an electromagnetic force-free analysis of a cylindrical plasma volume to match the observed D_n resonances quite successfully, yielding

$$f_{Dn} = 0.95(f_g f_p)^{1/2}\ n^{1/2} \tag{7}$$

$$f_{Dn}^{+} = (f_{Dn}^2 + f_g^2)^{1/2} \tag{8}$$

$$f_{Dn}^{-} = (f_{Dn}^2 - f_g^2)^{1/2} \tag{9}$$

While equations (7)-(9) seem to allow an independent means to determine the local f_g and f_p, particularly when the plasma and gyroharmonic resonances are not otherwise observed, their origin remain to be explained theoretically based on realistic plasma distributions.

4.2.4. Long-Range Sounding. As implied by its name, long-range (LR) sounding uses radio waves to probe plasma regimes at a distance. This differs from the other techniques mentioned so far in that target ranges in LR sounding can be more than an Earth radius ($1\ R_E \approx 6378$ km). The long sounding ranges would normally require higher transmission powers to overcome the long distances. Special digital techniques, such as pulse compression and spectral integration, however, are used by RPI on IMAGE to lower the transmission power requirements so that LR sounding of the magnetosphere can become possible [*Benson et al.*, 1998; *Reinisch et al.*, 2000].

After a sounder pulse is transmitted, different types of echoes are received, depending on the structure of the medium and irregularities present in the target region [*Fung et al.,* 2000]. Figure 4 illustrates the different types of possible echoes from a magnetospheric sounder. As discussed above, short-range echoes from local resonances (e.g., f_p and nf_g) are due to electrostatic waves excited by the sounder pulse [*Muldrew*, 1972; *Benson et al.*, 2003 and references therein]. In LR magnetospheric sounding, due to the generally low transmission power involved, only specular reflected or coherently backscattered signals are detectable over long distances. Incoherent scatter signals are too weak to be observed.

Radio waves transmitted at frequencies above the local cutoffs (f_R or f_P, see Figure 1) can propagate freely in all directions. When the wave propagates into a refractive index


fp

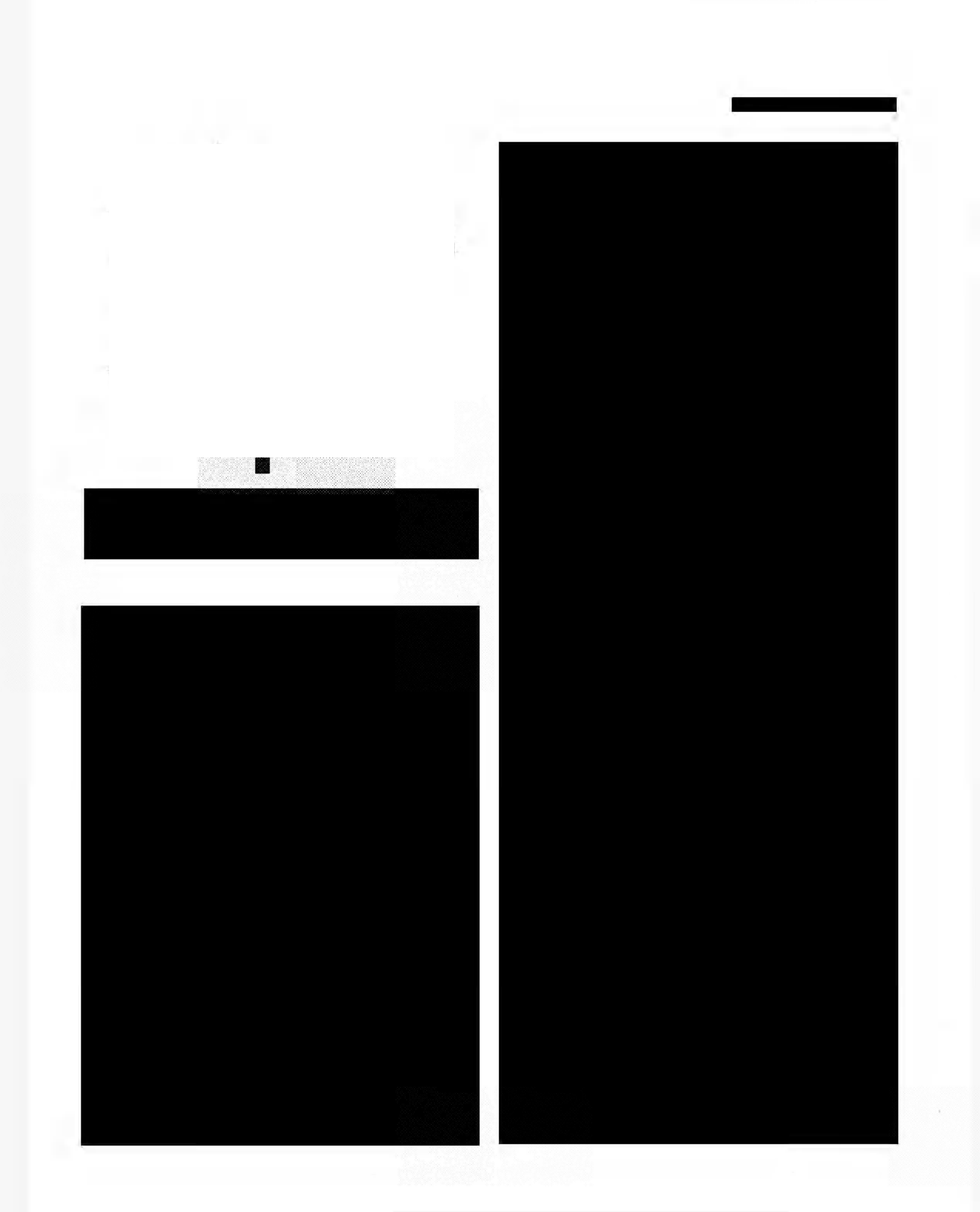

[redacted]

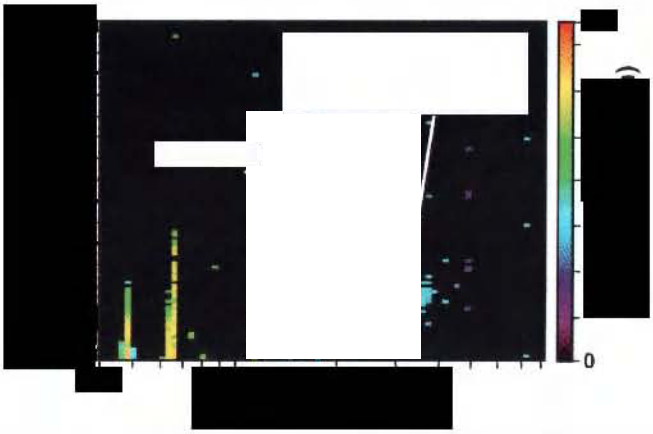

[redacted]

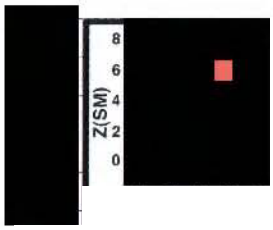

[redacted]

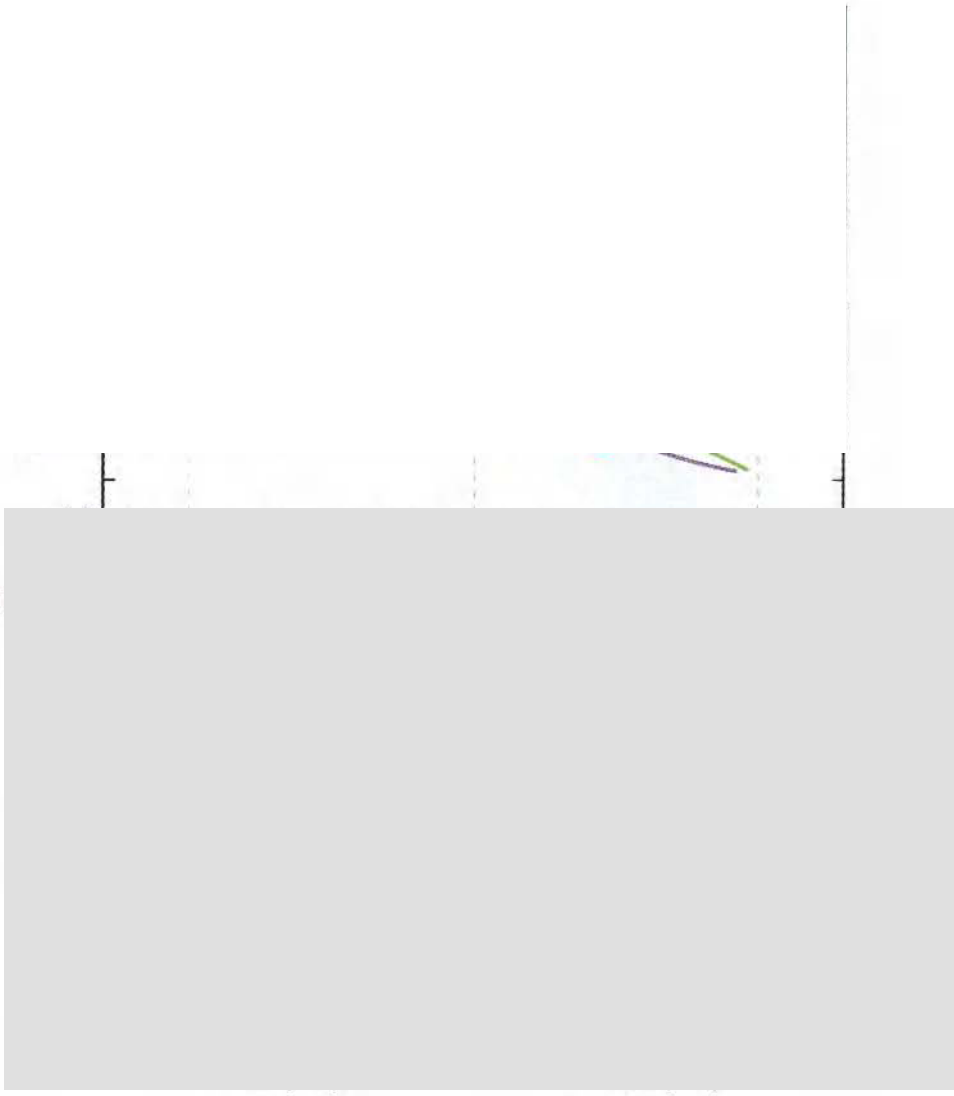

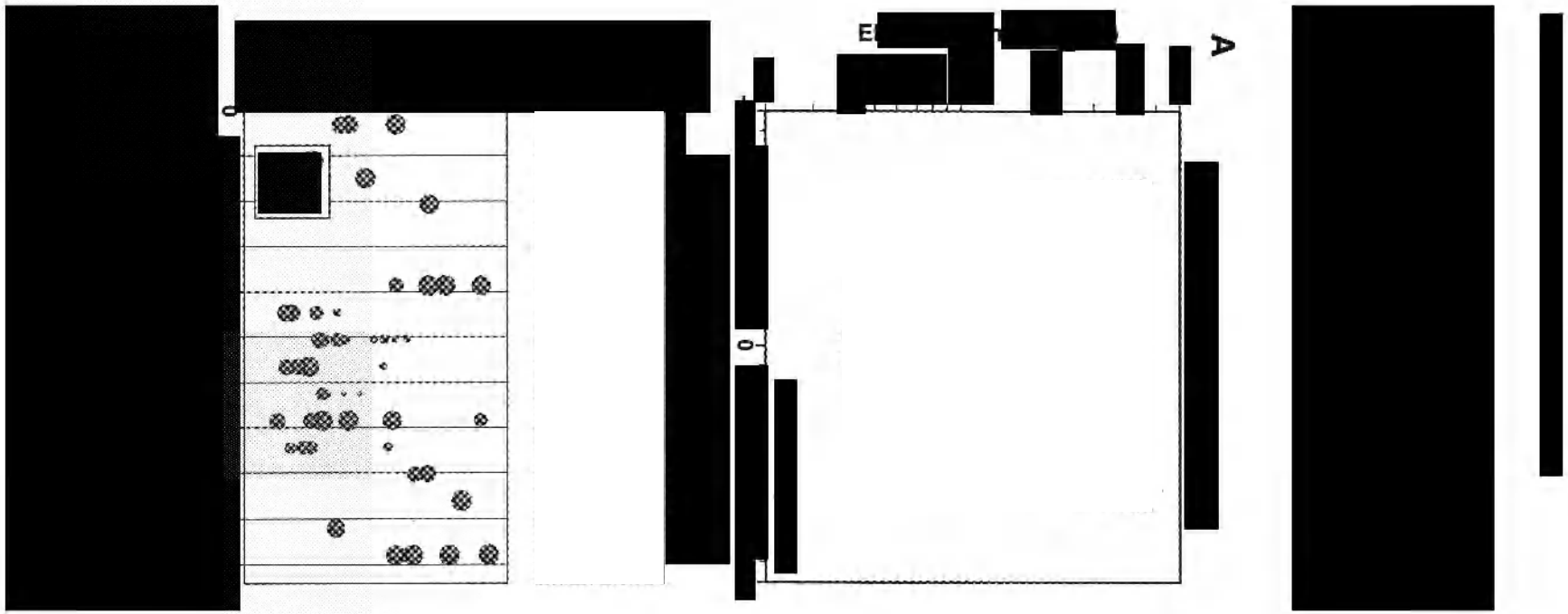

4. From direct and ducted magnetospheric sounder waves, the density structure and evolution of the plasmasphere and polar cap have been determined providing the observations needed to understand the processes of plasmaspheric filling and the variability of polar cap outflows.

Acknowledgments. The authors will like to gratefully acknowledge discussions with W.W.L. Taylor and for allowing us to consult his comprehensive list of VLF ground transmitters. The National Aeronautics and Space Administration supported this research under proposal SECGIP03-0085.

REFERENCES

Abel, B., and R.M. Thorne, Electron scattering loss in Earth's inner magnetosphere: 2. Sensitivity to model parameters, *J. Geophys. Res.*, 103, 2397-2407, 1998.

André, R., F. Lefeuvre, F. Simonet, and U.S. Inan, A first approach to model the low-frequency wave activity in the plasmasphere, *Annales Geophys.*, 20, 981-996, 2002.

Appleton, E.V. and M.A.F. Barnett, On some direct evidence for downward atmospheric reflection of electric rays, Proc. R. Soc. Lond., 109A, 621-641, 1925.

Benson, R.F., Alouette 2 observations supporting the oblique echo model for the plasma frequency resonance, *J. Geophys. Res.*, 76, 1083-1087, 1971.

Benson, R.F., Stimulated plasma waves in the ionosphere, *Radio Sci.*, 12, 861-878, 1977.

Benson, R.F., Ionospheric investigations using digital Alouette/ ISIS topside ionograms, in 1996 Ionospheric Effects Symposium, edited by J.M. Goodman, pp. 202-209, Alexandria, Virginia, 1996.

Benson, R.F., V.A. Osherovich, J. Fainberg, B.W. Reinisch, Classification of IMAGE/RPI-stimulated plasma resonances for the accurate determination of magnetospheric electron-density and magnetic-field values, *J. Geophys. Res.*, 108(A5), 1207, doi:10.1029/2002JA009589, 2003.

Benson, R.F., J. Fainberg, R.A. Hess, V.A. Osherovich, and R.G. Stone, Comment on "Observation of long-duration gyroharmonic resonances: A refutation of the short-duration explanation for interpreting the anomalous URAP sounder spectra observed in the Io torus" by P. Canu, *Radio Sci.*, 36, 1649-1652, 2001.

Benson, R.F., J.L. Green, S.F. Fung, B.W. Reinisch,W. Calvert, D.M. Haines, J.-L. Bougeret, R. Manning, D.L. Carpenter, D.L. Gallagher, P.H. Reiff, and W.W.L. Taylor, Magnetospheric radio sounding on the IMAGE Mission, *The Radio Science Bulletin*, 285, Union Radio-Scientifique Internationale (URSI), 9-20, 1998.

Born, Max and Emil Wolf, *Principles of Optics*, Cambridge University Press, Cambridge, UK, 1999.

Bortnik, J., U.S. Inan, and T.F. Bell, Energy distribution and lifetime of magnetospherically reflecting whistlers in the plasmasphere, *J. Geophys. Res.*, 108(A5), 1199, doi:10.1029/2002JA009316, 2003.

Bowles, K.L., Observations of vertical incidence scatter from the ionosphere at 41 Mc/sec, *Phys. Rev. Lett.*, **1**, 454, 1958.

Breit, G. and M.A. Tuve, A test for the existence of the conducting layer, *Phys. Rev.*, 28, 554-575, 1926.

Budden, K.G., The theory of radio windows in the ionosphere and magnetosphere, *J. Atoms. Terr. Phys.*, 42, 287-298, 1980.

Burch, J.L. ed., *The IMAGE Mission*, Reprinted from *Space Science Review*, 91, Nos. 1-2, 2000.

Calvert, W., The detectability of ducted echoes in the magnetosphere, *J. Geophys. Res.*, 86, 1609-1612, 1981.

Calvert, W., R.F. Benson, D.L. Carpenter, S.F. Fung, D.L. Gallagher, J.L. Green, D.M. Haines, P.H. Reiff, B.W. Reinisch, M.F. Smith, and W.W.L. Taylor, The feasibility of radio sounding in the magnetosphere, *Radio Sci.*, 30, 1577-1595, Sep.-Oct. 1995.

Calvert, W., R.F. Benson, D.L. Carpenter, S.F. Fung, D.L. Gallagher, J.L. Green, D.M. Haines, P.H. Reiff, B.W. Reinisch, M. F. Smith, and W.W.L. Taylor, Reply to Comment on "The feasibility of radio sounding in the magnetosphere", *Radio Sci.*, 32 (1), 281-284, Jan.-Feb. 1997.

Canu, P., Observation of long-duration gyroharmonic resonances: A refutation of the short-duration explanation for interpreting the anomalous URAP sounder spectra observed in the Io torus, *Radio Sci.*, 36, 171-181, 2001a.

Canu, P., Reply, *Radio Sci.*, 36, 1645-1647, 2001b.

Canu, P., *et al.*, Identification of natural plasma emissions observed close to the plasmapause by the Cluster-Whisper relaxation sounder, *Ann. Geophysicae*, 19, 1697-1701, 2001.

Carpenter, D.L., R.R. Anderson, W. Calvert, and M.B. Moldwin, CRRES observations of density cavities inside the plasmasphere, *J. Geophys. Res.*, 105, 23323-23338, 2000.

Carpenter, D.L., M. Spasojevic, T.F. Bell, U.S. Inan, B.W. Reinisch, I.A. Galkin, R.F. Benson, J.L. Green, S.F. Fung, and S.A. Boardsen, Small-scale field-aligned plasmaspheric density structures inferred from RPI on IMAGE, *J. Geophys. Res.*, 107(A9), 1258, doi:10.1029/2001JA009199, 2002.

Davies, K., *Ionospheric Radio*, Peter Peregrinus Ltd., London, U.K., 1990.

Décréau, P.M.E., *et al.*, Observation of continuum radiations from the CLUSTER fleet: first results from direction finding, *Annales Geophysicae*, in press, 2004.

de Feraudy, J. Hanasz, R. Schreiber, G. Parks, M. Brittnacher, S. Perraut, J.A. Sauvaud, F. Lefeuvre, and M.M. Mogilevsky, AKR bursts and substorm field line excitation, *Phys. Chem, Earth*, 26, 151-159, 2001.

Delory, G.T., R.E. Ergun, C.W. Carlson, L. Muschietti, C.C. Chaston, W. Peria, J.P. McFadden, and R. Strangeway, FAST observations of electron distributions within AKR source regions, *Geophys. Res. Lett.* 25, 2069-2072, 1998.

Dougherty, J.P., and D.T. Farley, A theory of incoherent scattering of radio waves by a plasma, *Proc. Roy. Soc. (London)*, A259, 79, 1960.

Ergun, R.E., C.W. Carlson, J.P. McFadden, F.S. Mozer, G.T. Delory, W. Peria, C.C. Chaston, M. Temerin, R. Elphic, R. Strangeway, R. Pfaff, C.A. Cattell, D. Klumpar, E. Shelly, W. Peterson, E. Moebius, L. Kistler, FAST satellite wave observations in the AKR source region, *Geophys. Res. Lett.*, 25, 2061-2065, 1998.

Ergun, R.E., C.W. Carlson, J.P. McFadden, G.T. Delory, R.J. Strangeway, and P.L. Pritchett, Electron-cyclotron maser driven by charged-particle acceleration from magnetic field-aligned electric fields, *Astrophys. J.*, 538, 456-466, 2000.

Etcheto, J. and J.J. Bloch, Plasma density measurements from the GEOS-1 relaxation sounder, *Space Science Reviews*, 22, 597-610, 1978.

Etcheto, J., G. Belmont, P. Canu, and J.G. Trotignon, Active sounder experiments on GEOS and ISEE, in *Active Experiments in Space, Proceedings of an International Symposium held at Alpbach, Austria 24-28 May 1983*, 39-46, European Space Agency, Noordwijk, Netherlands, 1983.

Fejer, B.G. and M.C. Kelley, Ionospheric irregularities, *Rev. Geophys. Space Phys.*, 18, 401-454, 1980.

Franklin, C.A. and M.A. Maclean, The design of swept-frequency topside sounders. *Proc. IEEE*, 57, 897-929, 1969.

Fung, S.F. and A.F. Vinas, Excitation of high frequency electromagnetic waves by energetic electrons with an effective loss cone distribution, *J. Geophys. Res.*, 99, 8671-8686, 1994.

Fung, S.F. and K. Papadopoulos, The emission of narrow-band Jovian kilometric radiation, *Journal of Geophysical Research*, 92, 8579-8593, 1987.

Fung, S.F., R.F. Benson, D.L. Carpenter, B.W. Reinisch, and D.L. Gallagher, Investigations of irregularities in remote plasma regions by radio sounding: applications of the Radio Plasma Imager on IMAGE, *Space Sci. Rev.*, 91, 391-419, 2000.

Fung, S.F., R.F. Benson, J.L. Green, B.W. Reinisch, D.M. Haines, I.A. Galkin, J.-L. Bougeret, R. Manning, P.H. Reiff, D.L. Gallagher, D.L. Carpenter, and W.W.L. Taylor, Observations of Magnetospheric Plasmas by the Radio Plasma Imager on the IMAGE Mission, *Advances in Space Research*, 30, 2259-2266, 2002.

Fung, S.F., R.F. Benson, D.L. Carpenter, J.L. Green, V. Jayanti, I.A. Galkin, and B.W. Reinisch, Guided Echoes in the Magnetosphere: Observations by Radio Plasma Imager on IMAGE, *Geophys. Res. Lett*, 30(11), 1589, doi:10.1029/2002GL016531, 2003.

Gallagher, D.L. and D.A. Gurnett, Auroral kilometric radiation: Time-averaged source location, *J. Geophys. Res.*, 84, 6501-6509, 1979.

Gough, M.P., Nonthermal continuum emissions associated with electron injections: Remote plasmapause sounding, *Planet. Space Sci.*, 30, 657, 1982.

Green, J.L., R.F. Benson, W. Calvert, S.F. Fung, P.H. Reiff, B.W. Reinisch, and W.W.L. Taylor, A Study of Radio Plasma Imaging for the proposed IMI mission, NSSDC Technical Publication, February 1993.

Green, J.L. and S.A. Boardsen, Confinement of non-thermal continuum radiation to low latitudes, *J. Geophys. Res.*, 104, 10307-10316, 1999.

Green, J.L., B.R. Sandel, S.F. Fung, D.L. Gallagher, and B.W. Reinisch, On the origin of kilometric continuum, *J. Geophys. Res.*, 107(A7), 10.1029/2001JA000193, 2002.

Green, J.L., S.A. Boardsen, S.F. Fung, H. Matsumoto, K. Hashimoto, R.R. Anderson, B.R. Sandel, and B.W. Reinisch, Association of kilometric continuum radiation with plasmaspheric structures, *J. Geophys. Res.*, A03203, doi:10.1029/2003JA010093, 2004a.

Green, J.L., S.A. Boardsen, L. Garcia, S.F. Fung, and B.W. Reinisch, Seasonal and solar cycle dynamics of the AKR source region, *J. Geophys. Res.*, 109, *A05223*, doi:10.1029/2003JA010311, 2004b.

Greenwald, R.A., Comment on "The feasibility of radio sounding in the magnetosphere" by W. Calvert *et al.*, *Radio Sci.*, 32, 277-280, 1997a.

Greenwald, R.A., Rebuttal to reply by W. Calvert *et al.*, *Radio Sci.*, 32, 877-879, 1997b.

Gurnett, D.A., The Earth as a radio source: Terrestrial kilometric radiation, *J. Geophys. Res.*, 79, 4227-4238, 1974.

Gurnett, D.A., The Earth as a radio source: The nonthermal continuum, *J. Geophys. Res.*, 80, 2751-2763, 1975.

Gurnett, D.A. and R.A. Shaw, Electromagnetic radiation trapped in the magnetosphere above the plasma frequency, *J. Geophys. Res.*, 78, 8136-8148, 1973.

Gurnett, D.A. and L.A. Frank, Continuum radiation associated with low-energy electrons in the outer radiation zone, *J. Geophys. Res.*, 81, 3875- 3885, 1976.

Gurnett, D.A., W. Calvert, R.L. Huff, D. Jones, and M. Sugiura, The polarization of escaping terrestrial continuum radiation, *J. Geophys. Res.*, 93, 12817-12825, 1988.

Hanasz, J., M.Y. Boudjada, R. Schreiber, Z. Krawczyk, M. Malycha, M.M. Mogilevsky, H.O. Rucker, and T.V. Romantsova, Dynamic spectra of the Stokes parameters for the dayside and night side auroral kilometric radiation, *Geophys. Res. Lett.*, 27, 1631-1634, 2000.

Hanasz, J., H. de Feraudy, R. Schreiber, G. Parks, M. Brittnacher, M.M. Mogilevsky, T.V. Romantsova, Wideband bursts of auroral kilometric radiation and their association with UV auroral bulges, *J. Geophys. Res.*, 106, 3859-3871, 2001.

Hanasz, J., M. Panchenko, H. de Feraudy, R. Schreiber, and M.M. Mogilevsky, Occurrence distributions of the auroral kilometric radiation ordinary and extraordinary wave modes, *J. Geophys. Res.*, 108(A11), 1408, doi:10.1029/2003JA010093, 2003.

Hanuise, C., High-latitude ionospheric irregularities: a review of recent radar results, *Radio Sci.*, 18, 1093-1121, 1983.

Hashimoto, K., W. Calvert, and H. Matsumoto, Kilometric continuum detected by Geotail, *J. Geophys. Res.*, 104, 28645-28656, 1999.

Helliwell, R.A., VLF wave stimulation experiments in the magnetosphere from Siple Station, Antarctica, *Rev. Geophys.*, 26, 551-578, 1988.

Hilgers, A., A. Roux, and R. Lundin, Characteristics of AKR sources; a statistical description, *Geophys. Res. Lett.*, 18, 1493-1496, 1991.

Hunsucker, R.D., *Radio Techniques for Probing the Terrestrial Ionosphere*, Vol. 22, Phys. Chem. Space, Springer-Verlag, Berlin, 1992.

Huang, X. and B.W. Reinisch, Automatic calculation of electron density profiles from digital ionograms 2. True height inversion of topside ionograms with the profile-fitting method, *Radio Sci.*, 17, 837-844, 1982.

James, H.G., ISIS 1 measurements of high-frequency backscatter inside the ionosphere, *J. Geophys. Res.*, 94, 2617-2629, 1989

Jackson, J.E., Alouette-ISIS Program Summary, NSSDC Report 86-09, National Space Science Data Center, Greenbelt, Maryland, 1986.

Jackson, J.E., The reduction of topside ionograms to electron-density profiles, *Proc. IEEE*, 57, 960-976, 1969.

Jones, D., Source of terrestrial non-thermal continuum radiation, *Nature*, 260, 686-689, 1976.

Jones, D., W. Calvert, D.A. Gurnett, and R.L. Huff, Observed beaming of terrestrial myriametric radiation, *Nature*, 328, 931-394, 1987.

Kasaba, Y., H. Matsumoto, and K. Hashimoto, The angular distribution of auroral kilometric radiation observed by the GEOTAIL spacecraft, *Geophys. Res. Lett.*, 20, 2483-2486, 1997.

Kasaba, Y., H. Matsumoto, K. Hashimoto, R.R. Anderson, J.-L. Bougeret, M.L. Kaiser, X.Y. Wu, and I. Nagano, Remote sensing of the plasmapause during substorms: GEOTAIL observation of nonthermal continuum enhancement, *J. Geophys. Res.*, 103, 20389-20405, 1998.

Kelley, M.C., *The Earth's Ionosphere*, Academic Press, San Diego, CA, 425-434, 1989.

Kennel, C.F. and H.E. Petschek, Limit on stably trapped particle fluxes, *J. Geophys. Res.*, 71, 1-28, 1966.

Kumamoto, A. and H. Oya, Asymmetry of occurrence frequency and intensity of AKR between summer polar region and winter polar region, *Geophys. Res. Lett.*, 25, 2369-2372, 1998.

Kumamoto, A., T. Ono, M. Iizima, and H. Oya, Seasonal and solar cycle variations of the vertical distribution of occurrence probability of auroral kilometric radiation sources and of upflowing ion events, *J. Geophys. Res.*, 108(A1), doi:10:1029/2002JA009522, 2003.

Kurth, W.S., M.M. Baumback, and D.A. Gurnett, Direction-finding measurements of auroral kilometric radiation, *J. Geophys. Res.*, 80, 2764-2770, 1975.

Kurth, W.S., J.D. Craven, L.A. Frank, and D.A. Gurnett, Intense electrostatic waves near the upper hybrid resonance frequency, *J. Geophys. Res.*, 84, 4145, 1979.

Kurth, W.S., D.A. Gurnett, and R.R. Anderson, Escaping nonthermal continuum radiation, *J. Geophys. Res.*, 86, 5519-5531, 1981.

Lee, L.C., J.R. Kan, and C.S. Wu, Generation of Auroral Kilometric Radiation and the structure of the auroral acceleration region, *Planet. Space Sci.*, 28, 703-711, 1980.

LeSager, P., P. Canu, and N. Cornilleau-Wehrlin, Impact of the Ulysses velocity on the diagnosis of the electron density by the Unified Radio and Plasma Wave sounder in the outskirts of the Io torus, *J. Geophys. Res.*, 103(A11), 26667-26677, 1998.

Meredith, N.P., R.B. Horne, R.M. Thorne, D. Summers, M.C. Cain, and R.R. Anderson, Evidence for Chorus-driven electron acceleration to relativistic energies from a survey of geomagnetically-disturbed periods, this monograph, 2004.

Melrose, D.B., A theory for the nonthermal radio continua in the terrestrial and Jovian magnetospheres, *J. Geophys. Res.*, 86, 30-36, 1981.

Menietti, J.D., H.K. Wong, W.S. Kurth, D.A. Gurnett, J. Grandroth, and J.B. Groene, Discrete, stimulated auroral kilometric radiation observed in the Galileo and DE-1 wideband data, *J. Geophys. Res.*, 101, 10673, 1996.

Menietti, J.D., A.M. Persoon, J.S. Pickett, D.A. Gurnett, Statistical study of auroral kilometric fine structure striations observed by Polar, *J. Geophys. Res.*, 105, 18857-18866, 2000.

Menietti, J.D., R.R. Anderson, J.S. Pickett, D.A. Gurnett, and H. Matsumoto, Near-source and remote observations of kilometric continuum radiation from multispacecraft observations, *J. Geophys. Res.*, 108(A11), 1393, doi:10.1029/2003JA009826, 2003.

Morgan, D.D. and D.A. Gurnett, The source location and beaming of terrestrial continuum radiation, *J. Geophys. Res.*, 96, 9595-9613, 1991.

Muldrew, D.B., Electron resonances observed with topside sounders, *Radio Sci.*, 7, 779-789, 1972.

Mutel, R.L., D.A. Gurnett, I.W. Christopher, J.S. Pickett, and M. Schlax, Locations of auroral kilometric radiation bursts inferred from multispacecraft wideband Cluster VLBI observations. 1: Description of technique and initial results, *J. Geophys. Res.*, 108(A11), 1398, doi:10.1029/2003JA010011, 2003.

Mutel, R.L., D.A. Gurnett, and I.W. Christopher, Spatial and temporal properties of AKR burst emissions derived from Cluster WBD VLBI studies, *Ann. Geophys.*, Accepted for publication, 2004.

Nagano, I., X.-Y. Wu, H. Takano, S. Yagitani, H. Maatsumoto, K. Hashimoto, and Y. Kasaba, Remote sensing the magnetosheat by the spin modulation of terrestrial continuum radiation, *J. Geophys. Res.*, 108(A6), 1224, doi:10.1029/2002JA009691, 2003.

Nelms, G.L. and G.E.K. Lockwood, Early results from the topside sounder in the Alouette II satellite, in *Space Research VII*, edited by R.L. Smith-Rose, North-Holland Publishing Co., Amsterdam, 604-623, 1967.

Newell, P.T., Ching-I Meng, and K.M. Lyons, Suppression of discrete aurorae by sunlight, *Nature*, 381, 766-767, June 27, 1996.

Nsumei, P.A., X. Huang, B.W. Reinisch, P. Song, V.M. Vasyliunas, J.L. Green, S.F. Fung, R.F. Benson, and D.L. Gallagher, Electron density distribution over the northern polar region deduced from IMAGE/RPI sounding, *J. Geophys. Res.*, 108(A2), 1078, doi: 1.1029.2002JA/009616, 2003.

Ondoh, T., Y. Nakamura, and T. Koseki, Feasibility of plasmapause sounding from a geostationary satellite, *Space Sci. Instrum.*, 4, 57-71, 1978.

Osherovich, V.A., Physical nature of the diffuse plasma resonances in the ionosphere, *J. Geophys. Res.*, 92, 316-320, 1987.

Osherovich, V.A., The physical nature of the upper subsidiary diffuse resonances, *J. Geophys. Res.*, 94, 5530-5532, 1989.

Osherovich, V.A. and R.F. Benson, The lower subsidiary diffuse plasma resonances and the classification of radio emissions below the plasma frequency, *J. Geophys. Res.*, 96, 19331-19341, 1991.

Oya, H., Sequence of diffuse plasma resonances observed on Alouette 2 ionograms, *J. Geophys. Res.*, 75, 4279-4285, 1970.

Oya, H., A. Morioka, K. Kobayashi, M. Iizima, T. Ono, H. Miyaoka, T. Okada and T. Obara, Plasma wave observation and sounder experiments (PWS) using the Akebono (EXOS-D) satellite - Instrumentation and initial results including discovery of the high altitude equatorial plasma turbulence, *J. Geomagn. Geoelectr.*, 42, 411-442, 1990.

Oya, H. and T. Ono, Stimulation of plasma waves in the magnetosphere using satellite JIKIKEN (EXOS-B). Part II: Plasma density across the plasmapause, *J. Geomagn. Geoelectr.*, 39, 591-607, 1987.

Panchenko, M., Direction finding of AKR sources with three orthogonal antennas, *Radio Sci.*, 28(6), 1099, doi:10.1029/2003RS002929, 2003.

Perraut, S., H.d. Feraudy, A. Roux, P.M.E. Kelley, J. Paris, and L. Matson, Density measurements in key regions of the Earth's magnetosphere: Cusp and auroral region, *J. Geophys. Res.*, 95, 5997-6014, 1990.

Reinisch, B.W., D.M. Haines, K. Bibl, G. Cheney, I.A. Galkin, X. Huang, S.H. Myers, G.S. Sales, R.F. Benson, S.F. Fung, J.L. Green, W.W.L. Taylor, J.-L. Bougeret, R. Manning, N. Meyer-Vernet, M. Moncuquet, D.L. Carpenter, D.L. Gallagher, and P. Reiff, The Radio Plasma Imager investigation on the IMAGE spacecraft, *Space Science Reviews*, 91, 319-359, February, 2000.

Reinisch, B.W., X. Huang, P. Song, G.S. Sales, S.F. Fung, J.L. Green, D.L. Gallagher, and V.M. Vasyliunas, Plasma density distribution along the magnetospheric field: RPI observations from IMAGE, *Geophys. Res. Lett.*, 28, 4521-4524, 2001a.

Reinisch, B.W., X. Huang, D.M. Haines, I.A. Galkin, J.L. Green, R.F. Benson, S.F. Fung, W.W.L. Taylor, P.H. Reiff, D.L. Gallagher, J.-L. Bougeret, R. Manning, D.L. Carpenter and S.A. Boardsen, First results from the Radio Plasm Imager on IMAGE, *Geophys. Res. Lett.*, 28, 6, 1167-1170, 2001b.

Reinisch, B.W., X. Huang, P. Song, S.F. Fung, J.L. Green, V.M. Vasyliunas, D.L. Gallagher, and B.R. Sandel, Plasmaspheric Mass Loss and Refilling as a Result of a Magnetostorm, *J. Geophys. Res., J. Geophys. Res.*, 109(A1), A01202, doi:10.1029/2003JA009948, 2003.

Rodger, C.J., M.A. Cilverd, and R.J. McCormick, Significance of lightning-generated whistlers to inner radiation belt electron lifetimes, *J. Geophys. Res.*, 108(A12), 1462, doi:10.1029/2003JA009906, 2003.

Santolik, O., M. Parrot, L.R.O. Storey, J.S. Pickett, and D.A. Gurnett, Propagation analysis of plasmaspheric hiss using Polar PWI measurements, *Geophys. Res. Lett.*, 28, 1127-1130, 2001.

Shawhan, S.D., Magnetospheric plasma wave research 1975-1978, *Rev. Geophys.* & Sp. Phys., 705-724, June 1979.

Stix, T.H., *Waves in Plasmas*, AIP Press, New York, 1992.

Storey, L.R.O., An investigation of whistling atmospherics, *Phil. Trans. Roy. Soc.*, 246, 113-141, 1953.

Storey, L.R.O. and F. Lefeuvre, The analysis of 6-component measurements of a random electronmagnetic wave field in a magnetoplasma, 1: The direct problem, *Geophys. J. R. Astron. Soc.*, 56, 255-270, 1979.

Storey, L.R.O., F. Lefeuvre, M. Parrot, L. Cairo, and R.R. Anderson, Initial survey of the wave distribution functions for plasmaspheric hiss observed by ISEE 1, *J. Geophys. Res.*, 96, 19469-19489, 1991.

Thorne, R.M., S.R. Church, and D.J. Gorney, On the origin of Plasmaspheric hiss: The importance of wave propagation and the plasmapause, *J. Geophys. Res.*, 84, 5241-5247. 1979.

Trotignon, J.G., *et al.*, How to determine the thermal electron density and the magnetic field strength from the Cluster/Whisper observations around the earth, *Ann. Geophysicae*, 19, 1711-1720, 2001.

Trotignon, J.G., J. Etcheto, and J.P. Thouvenin, Automatic determination of the electron density measured by the relaxation sounder on board ISEE 1, *J. Geophys. Res.*, 91 (A4), 4302-4320, 1986.

Warnock, J.M., Sideband structure observed by topside sounders, *Proc. IEEE*, 57, 1135-1139, 1969.

Warren, E.S. and E.L. Hagg, Observation of electrostatic resonances of the ionospheric plasma, *Nature*, 220, 466-468, 1968.

Wu, C.S. and L.C. Lee, A theory of the terrestrial kilometric radiation, *Astrophys. J.*, 230, 621-626, 1979.

J.L. Green and S.F. Fung, NASA/Goddard Space Flight Center, Space Science Data Operations Office, Greenbelt, Maryland, 20771, USA. (email: james.green@nasa.gov)

Probabilistic Forecasting of the Dst Index

Robert L. McPherron

Institute of Geophysics and Planetary Physics, University of California Los Angeles, Los Angeles California

George Siscoe and Nancy U. Crooker

Center for Space Physics, Boston University, Boston, Massachusetts

Nick Arge

Phillips Lab, Hanscom Air Force Base, Boston, Massachusetts

The Dst index can be predicted by an autoregressive moving average filter that transforms the solar wind electric field and dynamic pressure into changes in the index. Integration of these changes gives Dst. The maximum lead time possible is less than 60 minutes. Longer lead times are probably unobtainable due to the stochastic nature of IMF Bz. In this paper we use photospheric observations of the solar magnetic field to predict Dst. Our technique uses the Wang-Sheeley-Arge (W-S-A) model to forecast the time variations of solar wind speed, IMF polarity, and IMF strength at Earth four days in advance. Since the waveform of Bz is incalculable from solar observations we make use of air mass climatology. In this technique the cumulative probability distribution is determined as a function of time relative to a stream interface. During the declining phase of the solar cycle persistent coronal holes create high speed streams. The interface between these streams and slower speed solar wind ahead provides a reference time that can be used to organize the cumulative probability distributions determined from historic data (climatology). We then use the predicted arrival of an interface and the associated cumulative distributions to predict the probability that |Dst| will fall within a range of values. This technique works best for small to moderate storms occurring during the declining phase of the solar cycle. CMEs are not predictable by this model hence we do not expect this approach to work as well at solar maximum.

1. INTRODUCTION

The Dst index is the primary indicator of the state of the inner magnetosphere. Traditionally it has been associated with the strength of the symmetric ring current. The DPS theorem [*Dessler and Parker*, 1959; *Sckopke*, 1966] establishes a relation between the total kinetic energy of ring current particles and the magnetic perturbation they cause at the center of the Earth. The Dst index is an approximation to this perturbation calculated from a local time average of disturbances in the horizontal component of the magnetic field on the Earth's surface. More recently it has been recognized that there are many magnetospheric currents that contribute to the Dst index [*Campbell*, 1996] and that throughout the main phase of a storm it in unlikely that the ring current is symmetric [*Kamide et al.*, 1997; *Sharma et al.*, 2002]. None-the-less as shown by [*Carovillano*

The Inner Magnetosphere: Physics and Modeling
Geophysical Monograph Series 155

10.1029/155GM22

and McGuire, 1968] the relationship holds approximately for asymmetric currents. If it were possible to predict this index some time in advance it would provide useful warnings of hazards to technological systems dependent on the space environment.

The Dst index has been found to be remarkably easy to forecast empirically on a short-term [*McPherron and O'Brien*, 2001; *Temerin and Li*, 2002]. The latter authors claim nearly 95% prediction efficiency using a scheme involving about 35 terms that transforms solar wind observations into the Dst index. Unfortunately, all such schemes require the solar wind velocity and interplanetary magnetic field (IMF-Bz) to drive the prediction model. At the present time the furthest upstream of the Earth that we can measure these parameters provides only 30-60 minutes advance warning. Any attempt to utilize a monitor further upstream is unlikely to be successful. The IMF Bz is a turbulent variable with a median time between zero crossings of about six minutes. The fluctuations in Bz are produced by a variety of processes in the solar wind including large-scale structures, stream interactions, and Alfven waves. As the solar wind flows from the upstream monitor towards the Earth waves enter or leave the stream, and stream interactions change Bz from what was measured at the monitor.

Even though the deterministic approach is likely to fail it is still possible to use probabilistic methods. In particular we have advocated the use of air mass climatology [*McPherron and Siscoe*, 2004]. In this approach one utilizes predictable properties of the solar wind (the air mass) to organize probability distribution functions for solar wind and magnetospheric variables. For example, during the declining phase of the solar cycle the solar wind is dominated by recurrent high speed streams. These streams overtake slow solar wind ahead of them and create an interface responsible for disturbances in the magnetosphere. It is possible to use past observations of the type and level of activity caused by these interfaces to construct probability distributions for magnetic indices as a function of time relative to the interface. Then if some method exists to predict the arrival of the interface some time in advance one can use the distributions to predict the range of activity expected at various times relative to the interface.

In this paper we describe a procedure for medium-term prediction (2-4 days in advance) of the Dst index. The technique utilizes observations of the photospheric magnetic field of the Sun to predict the solar wind velocity on a source surface around the Sun [*Wang and Sheeley*, 1990]. This velocity is then propagated to the Earth [*Arge and Pizzo*, 2000] and processed to detect stream interfaces. Knowing the time of arrival of an interface, probability distributions for Dst are used to forecast the expected level of activity. We apply this technique to data acquired during the last solar minimum in 1995 and discuss the problems found in implementing the technique.

2. HIGH-SPEED SOLAR WIND STREAMS

Two typical high-speed streams observed in January of 1995 are presented in Figure 1. Four panels show the velocity, density, temperature and azimuthal flow direction of the solar wind plasma. Labeled vertical dashed lines show the times of three interfaces between high and low velocity streams. The interface is clearly defined by the behavior of the four variables. The velocity increases rapidly from a low value of order 300 km/s to a high value of order 700 km/s. The density changes in the opposite direction increasing slowly from moderate to high value before the interface. Then, just at the interface, it drops rapidly to a low value. As the density drops the temperature rises. In the bottom panel the azimuthal flow angle switches from positive values, an outward flow westward of radial (in the direction of solar rotation), to an eastward value. The time most easily identified on higher resolution plots is the zero crossing of the flow angle. Below we use this time as the reference time in a superposed epoch analysis of solar wind and magnetospheric variables.

Other solar wind variables including the IMF Bz are organized by stream interfaces. Below we show that during 1995 the IMF Bz was biased negative and had large fluctuations for a day centered on nearly every interface. After the interface the combination of high velocity and occasional strong negative Bz drives geomagnetic activity and produces moderate magnetic storms.

3. SUPERPOSED EPOCH ANALYSIS

The behavior of the solar wind velocity for ten days centered on a stream interface is shown in Figure 2. The figure presents the results of a superposed epoch analysis of the solar wind velocity measured by Wind spacecraft during 1995. Epoch zero in this analysis was defined by an interactive procedure in which traces of the velocity, density, and azimuthal flow angle were displayed on a high resolution plot. First the plot of velocity was examined for a transition from a low to high speed solar wind stream. Then the density trace was examined near the time of the velocity transition to identify intervals of slow increase in density. Finally, the azimuthal flow angle was examined just after a rapid decrease in density. A positive to negative zero crossing of the flow angle was used to precisely define the stream interface. Ten-day segments of data centered on the time of each stream interface were then selected and stored as rows of an ensemble array. The figure illustrates the results obtained for velocity in the year 1995. Each row of

[redacted]

[redacted]

[redacted]

[redacted]

[redacted]

[redacted]

[redacted]

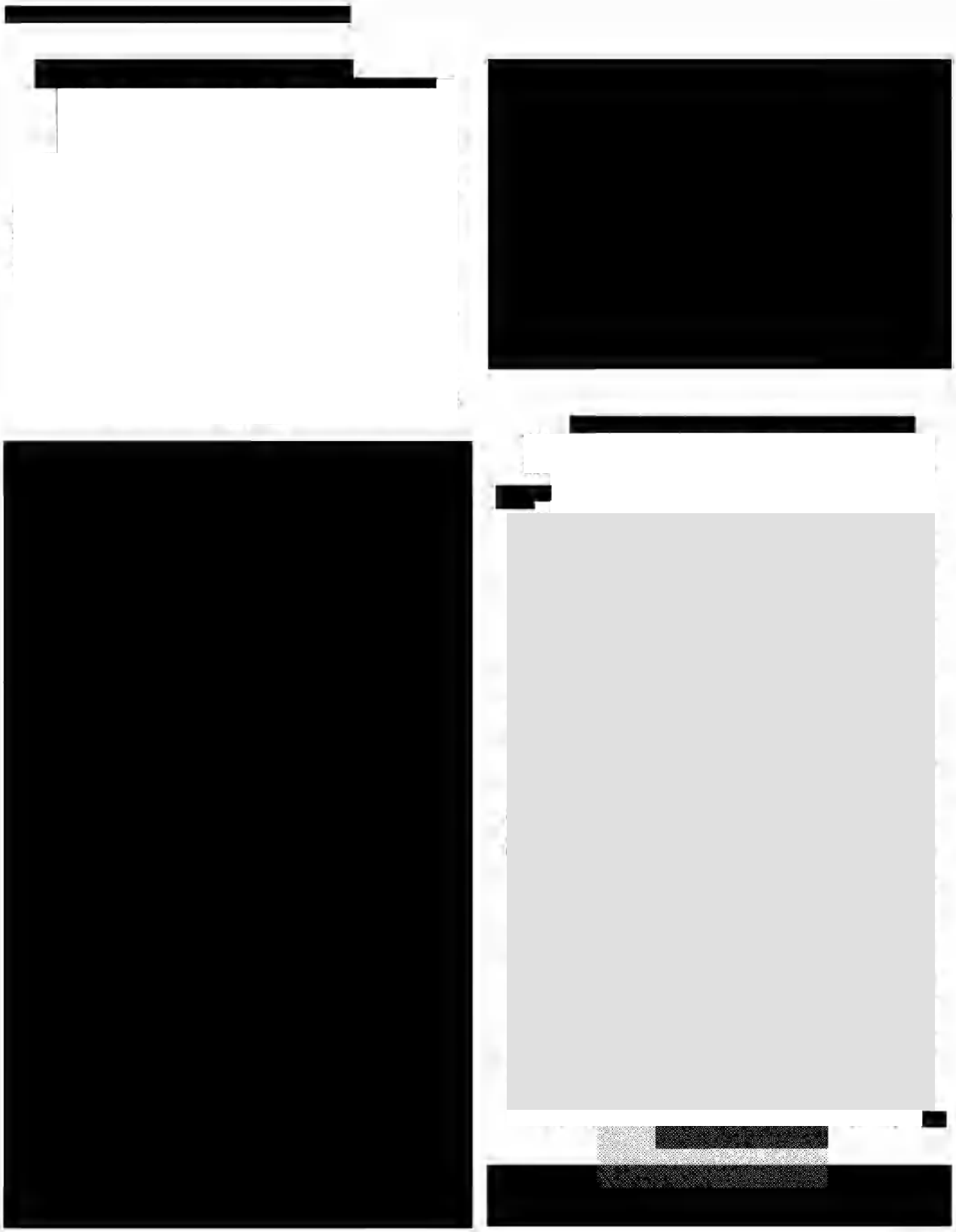

enhanced. As a consequence interface storms in 1996 were weaker than in 1995 Note also in Figure 4 that for several days after the interface the median electric field was slightly negative and the separation of the quartiles was larger than before the interface. This is primarily due to amplification of Bz fluctuations by the higher velocity occurring at this time. The consequence of this behavior is evident in the third panel which shows quartiles of the 3-hr ap index ensemble. Magnetic activity is strongest at the interface but decays slowly for many days. The fourth panel shows the quartiles of sym-H already discussed. It is apparent that the electric field around the interface produces the main phase of these weak magnetic storms, and then the prolonged decay of the electric field after the interface produces the linear recovery. Apparently the ring current is in quasi-equilibrium with injection nearly matching decay during the storm recovery phase. The fourth panel presents a measure of Pc 5 power determined from ground observatories. This maximizes at the interface and then decays even more slowly than the ap index. These waves are highly correlated with large increases in the flux of relativistic electrons at synchronous orbit [*Green and Kivelson*, 2001; *O'Brien et al.*, 2001] and hence are though to play a role in the acceleration of these electrons [*Hudson et al.*,; *Liu et al.*, 1999].

That this is the case is demonstrated in the bottom panel. Here it is seen that for a day prior to the interface the flux of relativistic electrons decreases. About six hours after the interface, coincident with the beginning of the storm recovery the fluxes begin to increase. The increase continues reaching a maximum about four days after the interface. The median increase is at least a factor of 10 above the pre-interface fluxes.

5. A STREAM INTERFACE DETECTOR

To predict magnetospheric activity associated with storms two things are needed. The first is a method of predicting the solar wind velocity profile several days in advance of its arrival at the Earth. The second is a method for identifying the stream interface from the predicted velocity profile. The technique for predicting the solar wind velocity at 1 AU 2-4 days in advance has been described elsewhere [*Arge and Pizzo*, 2000; *Wang and Sheeley*, 1990] and because of space limitations we do not repeat this here. For our purposes we assume that a real time procedure generates the solar wind velocity time series about three days in advance. We process this series with the stream interface detector described next.

The detector is based on simple pattern recognition. We start with the shape of the median velocity profile for two days centered on the interface. We remove the mean and normalize the patterns so the sum of the absolute value of the points is 1.0. Then we standardize the predicted time series by removing the mean and dividing by the standard deviation. We next convolve the pattern with the standardized velocity. When the shape of the two curves is similar the output of the convolution approaches 1.0. We take the center of the time interval in which the response is greater than 0.5 as the time of the interface. In practice the predictions are made approximately every 8 hours so we resample both series to precisely 8-hour cadence. This reduces the interface pattern to seven points. Note that at least one day beyond the interface is required to identify the position of the interface. This reduces the advance warning by one day.

The 7-point pattern appears to work well identifying a large number of stream interfaces at a point midway along the rising ramp of predicted velocity. However, a comparison with the interfaces detected manually in high resolution data shows that the W-S-A interfaces are systematically early. Statistically the bias is –0.25 days. This appears to be a characteristic of the predicted time series and not a bias of the detector. Apparently additional work is needed to optimize the W-S-A predictions. In 1995 there were eight manual interfaces not detected by our automatic procedure. Four of these appear to be the consequence of missing data. Another seems to be a poor manual choice of an interface. At least one miss is a result of an outright failure of the solar wind model to predict a rise in velocity in early March of 1995.

6. EXAMPLE PREDICTIONS

Using the stream interface detector we predict the arrival of a stream interface two days in advance. Knowing this we use climatology of the Dst index relative to the interface to predict the quartiles of expected activity. The simplest climatology for the years 1995-1996 depending only on time relative to the interface is illustrated in Figure 5.

Since the time resolution of the W-S-A predictions is roughly 8 hours we have chosen to create cumulative probability distributions (cdfs) averaged over nine hour intervals. To provide some smoothing we overlap these estimates by three hours - the resolution of the ap index. Using the 16 day ensemble shown in Figure 3 we produced 125 distribution functions centered about epoch zero. There is a significant difference between the distributions two days before the interface (heavy line on right side) and ¼ day after the interface (heavy line on left side). For example, the probability that Sym-H will be below –50 nT two days before an interface is zero! In contrast, there is a 4% probability that it will be below –100 nT ¼ day after the interface. These distributions provide the "climatology" used to make a probabilistic forecast of the Sym-H index. In the following we have chosen the upper and lower quartiles of these distributions as a function of time relative to an interface to bracket the expected value of Sym-H.


Speed (km/s)

arrived 0.25 days early. We have not removed this bias in the predictions because it is less than a single sample interval. In addition there is a random error in the predicted arrival times of about 1.3 days. This is significant to the potential users of the forecasts. Also this model does not predict the occurrence of coronal mass ejections (CME) that are responsible for much larger magnetic storms than those caused by the recurrent high-speed streams. Since CMEs also occur at solar minimum it is inevitable that there will be events not anticipated by our procedure.

It is possible to make a number of improvements in this procedure. First, data from more than one solar observatory could be used to eliminate problems caused by missing data at one location. Also this would have the advantage of using features in the solar field that are seen at all observatories rather than just one. Second it is possible to improve the quality of the predicted speed on the solar source surface using a more complex model that includes location of the sub-Earth point relative to a coronal hole as well as the flux tube expansion factor [*Arge and Pizzo*, 2000]. It is also likely that the kinematic model for the propagation and interaction of high speed streams can be improved by parameterizing the model and then optimizing these parameters with historical data.

It may also be possible to improve the detection of the stream interfaces in the predicted velocity. We have used a centered pattern to convolve with the series. A pattern containing only data before the interface might add several 9-hour samples of advance warning. Another possible improvement would use precursors in the measured solar wind. For example the solar wind density (not shown here) begins to increase about two days before a stream interface, and is obviously elevated one day before. About 12 hours before the interface a variety of indicators including density, azimuthal flow angle, and magnetic field strength all show significant perturbations. A probabilistic stream interface detector utilizing all of these parameters could be developed. Such a detector could be used to refine the W-S-A predicted interface arrival times.

Another way to improve predictions is to include two other parameters predictable by W-S-A. These are the polarity of the IMF either towards or away from the Sun, and the strength of the IMF (not implemented). The polarity is important for the Russell-McPherron effect [*Russell and McPherron*, 1973] which increases the strength of activity significantly when the IMF satisfies the rule "spring to and fall away". The second is to make the cdfs functions of the velocity and field strength. At the current time these improvements are difficult to implement because of insufficient solar wind data.

Acknowledgments. Support for this work has been provided by a NSF Space Weather Grant ATM 02-08501 and by NASA grants NAG 5-11898 and NNG 04GA93G. Wind magnetic field data were obtained from the NASA National Space Science Data Center courtesy of the Wind/MFI team (Ronald Lepping, PI). Wind plasma data from the NSSDC are courtesy of Keith Olgive and Al Lazarus. Magnetic indices were obtained from the WDC-B in Kyoto, Japan.

8. REFERENCES

Arge, C.N., and V.J. Pizzo, Improvement in the prediction of solar wind conditions using near-real time solar magnetic field data, *Geophysical Research Letters*, 105 (A5), 10,465-10,4709, 2000.

Campbell, W.H., Geomagnetic storms, the Dst ring-current myth and lognormal distributions, *Journal of Atmospheric and Terrestial Physics*, 58 (10), 1171-1187, 1996.

Carovillano, R.L., and J.J. McGuire, Magnetic energy relationships in the magnetosphere, in *Physics of the Magnetosphere*, edited by R.L. Carovillano, J.F. McClay, and H.R. Radoski, pp. 290-300, D. Reidel, Norwell, Mass., 1968.

Dessler, A.J., and E.N. Parker, Hydromagnetic theory of magnetic storms, *Journal of Geophysical Research*, 64 (12), 2239-2259, 1959.

Green, J.C., and M.G. Kivelson, A tale of two theories: how the adiabatic response and ULF waves affect relativistic electrons, *Journal of Geophysical Research*, 106 (A11), 25777-91, 2001.

Hudson, M.K., S.R. Elkington, J.G. Lyon, and C.C. Goodrich, Increase in relativistic electron flux in the inner magnetosphere: ULF wave mode structure, *Advances in Space Research*, 25 (12), 2327-2337, 2000.

Kamide, Y., W. Baumjohann, I. Daglis, W.D. Gonzalez, M. Grande, J.A. Joselyn, R.L. McPherron, J.L. Phillips, G. Reeves, G. Rostoker, A.S. Sharma, H. Singer, B.S. Tsurutani, and V.M. Vasyliunas, Current understanding of magnetic storms: Storm/substorm relationships, *Journal of Geophysical Research*, 103 (A8), 17,705-17,728, 1997.

Liu, W.W., G. Rostoker, and D.N. Baker, Internal acceleration of relativistic electrons by large-amplitude ULF pulsations, *Journal of Geophysical Research*, 104 (A8), 17391-407, 1999.

McPherron, R.L., and T.P. O'Brien, Predicting Geomagnetic Activity: The Dst Index, in *Space Weather*, edited by P. Song, G.L. Siscoe, and H. Singer, pp. 339-345, American Geophysical Union, Clearwater, FL, 2001.

McPherron, R.L., and G.L. Siscoe, Probabilistic forecasting of geomagnetic indices using solar wind air mass analysis, *Space Weather*, 2, S01001, doi:10.1029/2003SW000003, 2004.

O'Brien, T.P., and R.L. McPherron, An empirical phase-space analysis of ring current dynamics: solar wind control of injection and decay, *Journal of Geophysical Research*, 105 (A4), 7707-7719, 2000.

O'Brien, T.P., R.L. McPherron, D. Sornette, G.D. Reeves, R. Friedel, and H.J. Singer, Which magnetic storms produce relativistic electrons at geosynchronous orbit?, *Journal of Geophysical Research*, 106 (A8), 15533-44, 2001.

Russell, C.T., and R.L. McPherron, Semiannual variation of geomagnetic activity, *Journal of Geophysical Research*, 78 (1), 92-108, 1973.

Sckopke, N., A general relation between the energy of trapped particles and the disturbance field over the earth, *Journal of Geophysical Research*, 71 (13), 3125-3130, 1966.

Sharma, A.S., D.N. Baker, M. Grande, Y. Kamide, G.S. Lakhina, R.L. McPherron, G.D. Reeves, G. Rostoker, R. Vondrak, and L. Zelenyi, Storm-substorm relationship: Current understanding and outlook, in *Disturbances in Geospace: The Storm-Substorm Relationship*, edited by Y. Kamide, pp. 1-14, American Geophysical Union, Lonavala, India, 2002.

Temerin, M., and X. Li, A new model for the prediction of Dst on the basis of the solar wind, *Journal of Geophysical Research*, 107 (A12), 1472, doi:10.1029/2001JA007532, 2002.

Wang, Y.M., and N.R. Sheeley, Jr., Solar wind speed and coronal flux-tube expansion, *Astrophysical Journal*, 355 (2), 726-32+1 plate, 1990.

Robert L. McPherron, Institute of Geophysics and Planetary Physics, University of California Los Angeles, Los Angeles, CA 90095-1567, USA, e-mail:rmcpherron@igpp.ucla.edu

George Siscoe, Center for Space Physics, Boston University, Boston, Massachusetts, 02215, USA, siscoe@bu.edu

Nancy Crooker, Center for Space Physics, Boston University, Boston, Massachusetts, 02215, USA, siscoe@bu.edu

Nick Arge, AFRL/VSBXS29 Randolph Rd, Hanscom Afb, MA 01731-3010, USA, nick.arge@hanscom.af.mil

Testing the Hypothesis That Charge Exchange Can Cause a Two-Phase Decay

M.W. Liemohn and J.U. Kozyra

Atmospheric, Oceanic, and Space Sciences Department, University of Michigan, Ann Arbor

We test the hypothesis that a two-phase decay of the ring current energy content can be produced by the differential charge exchange loss rates of hot O^+ and hot H^+. Results are presented from idealized simulations of ring current decay and show that, for realistic plasma boundary conditions, a two-phase decay can only be created by the transition from flow-out to charge exchange dominance of ring current loss. Differential charge exchange between hot ($E > 40$ keV) O^+ and hot H^+ cannot produce the observed two-phase decay signature for several reasons. First, there are always significant levels of low-energy ($E < 10$ keV) H^+ present in the injected plasma, which charge exchanges rapidly and makes the H^+ loss rate comparable to or greater than the O^+ loss rate. Second, the ring current is spread over a wide range of L values, and the total charge exchange loss rate is an integral value that does not suddenly change. Third, this integral loss rate is too slow (at least in the results presented here) to create a rapid loss of ring current energy content. Other possible causes of two-phase decay signatures in the storm-time *Dst* index are briefly discussed.

1. INTRODUCTION

For many years, it was commonly believed that the main phase of a magnetic storm rapidly produced a symmetric ring current that provided a majority fraction of the *Dst* index decrease [e.g., *Lyons and Williams*, 1980; *Lee et al.*, 1983]. More specifically, the ring current is the dominant contributor to the *Dst** index, which is *Dst* with the influences from the magnetopause current, quiet time offset, and induced Earth currents removed. Loss of the trapped ring current energy (and thus recovery of the *Dst** index toward zero) was believed to occur dominantly through charge exchange with the neutral hydrogen geocorona, with minor contributions from Coulomb drag energy loss and scattering of particles into the loss cone by wave-particle interactions [see the review by *Daglis et al.*, 1999]. In fact, the two-phase decay of large magnetic storms was believed to be the result of the large differences between the charge exchange lifetimes of oxygen and hydrogen ions with energies above 50 keV [*Tinsley and Akasofu*, 1982; *Hamilton et al.*, 1988]. The much more rapid removal of oxygen ions was thought to be the cause of the fast loss lifetimes during the early recovery phase. By the end of the early recovery phase, the ring current was significantly depleted in oxygen relative to protons. The long charge-exchange lifetimes of the proton component dominated the late recovery phase. The preferential removal of oxygen ions by charge exchange with the hydrogen geocorona in the early recovery phase was thought to drive the observed dramatic composition changes that are correlated closely with the ring current recovery [*Hamilton et al.*, 1988; *Daglis*, 1997].

It is now understood, however, that the partial ring current far exceeds the symmetric ring current throughout the entire main phase of magnetic storms (which typically last from several hours to more than a day) and into the early recovery phase. This has been shown both theoretically [e.g., *Takahashi et al.*, 1990, 1991; *Ebihara and Ejiri*, 1998, 2000;

The Inner Magnetosphere: Physics and Modeling
Geophysical Monograph Series 155

10.1029/155GM23

Jordanova et al., 1998; *Liemohn et al.*, 1999, 2001a, b; *Kozyra et al.*, 2002] as well as observationally [e.g., *Greenspan and Hamilton*, 2000; *Jorgensen et al.*, 2001; *Pollock et al.*, 2001; *Mitchell et al.*, 2001; *Reeves and Spence*, 2001; *Soraas et al.*, 2002, 2003]. A major symmetric ring current component only appears in the late recovery phase. The partial ring current is formed as energetic ions in the inner plasma sheet are convected deep into the dipolar regions under the action of an enhanced convection electric field. These particles move on open drift paths that intersect the dayside magnetopause and thus rapid particle loss occurs through this boundary [*Liemohn et al.*, 1999]. Of course, the removal of ions from these open drift paths by charge exchange interactions and precipitation (which results from nonadiabatic scattering of the ions moving along highly stretched magnetic field lines) decreases the ring current lifetime even further; but these are secondary effects [c.f., *Kozyra et al.*, 1998, 2002; *Liemohn et al.*, 1999]. As the early recovery phase of the storm begins, the convection electric field weakens. This decrease drives the conversion of open to closed drift paths; in other words, the conversion from a partial to a symmetric ring current. Time scales in the late recovery phase are dominated by charge exchange losses of high-energy protons and thus are long compared to those in the early recovery phase.

The changeover from rapid removal at the dayside magnetopause during the main and early recovery phases to much-slower charge-exchange removal of trapped ring current particles during the late recovery phase accounts for the two distinctly different lifetimes that dominate the ring current recovery [*Jordanova et al.*, 2003; *Kozyra and Liemohn*, 2003]. That is, continued convection into the recovery phase causes the initial fast recovery of the ring current, and a rapid shut-off of this flowout suddenly stops this loss process, allowing the slower loss processes to dominate the recovery time scale. The timing of the convection decrease relative to the plasma sheet density decrease is critical. The density reduction must happen first for a rapid decay phase to occur. During a period of high convection and low source population intensity, the high-density plasma injected during the main phase is quickly flushed from the inner magnetosphere, being replaced by less-dense plasma.

The debate remains alive, however. For instance, *Feldstein et al.* [2000] and *Ohtani et al.* [2001] argue that a rapid shut off the tail current can cause a significant recovery of the *Dst* index. *Walt and Voss* [2001] found that particle precipitation causes fast loss lifetimes that might be responsible for the two-phase decay of the ring current. *O'Brien et al.* [2002] statistically analyzed the recovery rate of *Dst* for storms with rapid shut-off of the convection strength versus those with gradual shut-off (continued convection). They found that the two groups of storms had statistically identical decay rates. *Daglis et al.* [2003] argued that differential charge exchange loss between hot O^+ and H^+ is a major factor in the two-phase decay recovery for some storms.

This study addresses the relationship between charge exchange losses and flowout out losses. A series of numerical experiments are conducted with idealized input conditions to parametrically examine the relative importance of flowout and charge exchange to the decay rate of the ring current total energy content. In particular, the study will assess the validity of the hypothesis that the differential charge exchange rates between energetic O^+ and H^+ is sufficient to produce a two-phase decay. The other possibilities for two-phase decay production mentioned above will be discussed but not quantitatively investigated. In addition, a list of caveats to the interpretation and application of these results is given.

2. NUMERICAL APPROACH

This study uses results from the Michigan version of the ring current-atmosphere interaction model (RAM), a kinetic transport code that solves the gyration and bounce-averaged Boltzmann equation inside of geosynchronous orbit. *Fok et al.* [1993] was the first to publish results from this model, and she continues to maintain a version of this code [e.g., *Fok et al.*, 2003]. The code remained at Michigan as well, and the next development series began with *Jordanova et al.* [1996], who also continues to use the code [e.g., *Jordanova et al.*, 2003]. The version used for the present study is described by *Liemohn et al.* [2001a, 2004]. It uses second-order accurate numerical schemes to determine the hot ion phase-space distribution in the inner magnetosphere as a function of time, equatorial plane location, energy, and equatorial pitch angle. Sources are specified by geosynchronous orbit plasma data across the nightside outer boundary. Loss mechanisms include the flow of plasma out the dayside outer boundary, precipitation of particles into the upper atmosphere, pitch angle scattering and drag from Coulomb collisions with the plasmasphere (using the *Ober et al.* [1997] thermal plasma code), and charge exchange with the neutral hydrogen geocorona (using the *Rairden et al.* [1986] geocoronal model). A dipole magnetic field is assumed. The magnetopause is not explicitly defined in these simulations. Therefore, flow-out losses are losses through the dayside outer boundary, which is at geosynchronous altitude.

For the present study, idealized inputs were specified for each simulation. The electric field description chosen for these experiments is the Volland-Stern two-cell convection model [*Volland*, 1973; *Stern*, 1975], with nominal shielding ($\gamma = 2$) and the Kp-dependent activity parameter defined by *Maynard and Chen* [1975]. While this is a very simplistic field model, it has been used effectively to reproduce

the inner magnetospheric plasma dynamics with reasonable accuracy [e.g. *Jordanova et al.*, 1998, 2003; *Kozyra et al.*, 1998; *Ebihara and Ejiri*, 1998, 2000]. Furthermore, statistical analyses of inner magnetospheric plasma observations have found that the shielded Volland-Stern electric field is very good at reproducing the observations [*Korth et al.*, 1999; *Friedel et al.*, 2001]. In the simulations conducted for this study, artificial "Kp" time series were created for each numerical experiment, with step-function changes in the activity level separating intervals of constant convection strength.

The second half of the idealized input specification is the nightside outer boundary condition for the hot ions. A kappa distribution (with $\kappa = 5$) is assumed with identical characteristics at all local times. The near-Earth plasma sheet characteristic energy (E_{PS}) is held constant throughout the simulation (7 keV unless specified), while the density (N_{PS}) is changed at certain times in each run (again, with step function changes separating intervals of constant density). The chosen values are typical for the near-Earth plasma sheet [*McComas et al.*, 1993; *Birn et al.*, 1997; *Borovsky et al.*, 1998]. The composition of the boundary condition plasma is specified to be equal densities of H^+ and O^+ (each equal to N_{PS}). Because the hot ion species are not coupled for these simulations (that is, the electric field is specified rather than self-consistently calculated), the run for each species can be conducted separately and the results added later. This also allows for an arbitrary combination of the two species.

In the present study, step-function changes in Kp and N_{PS} are applied. After a 24-hour interval of quiescent values (Kp = 2, $N_{PS} = 0.5$ cm^{-3}), both parameters are increased to disturbed-condition values (Kp = 6.5 or 9, $N_{PS} = 4$ cm^{-3}). These high values are held constant for 12 hours of run time to reach a quasi-steady-state level in the inner magnetosphere. This is the initial condition for all of the numerical experiments shown below. The down-step for Kp and N_{PS} is then applied at either the 1-hour or the 4-hour mark (sometimes together, other times staggered), dropping the parameters back to their quiescent levels.

The chosen boundary and input conditions are not particularly realistic. For instance, ion distributions are not identical across the nightside, the magnetic field is not dipolar, factor of 8 step-function changes in density and convection are rare, and the inner magnetospheric electric field is modulated by the hot ion pressures in this region. The simulation results are thought to be useful, though, because they demonstrate the relative dominance of flow-out versus charge-exchange losses in modulating the recovery of the ring current. More on these caveats to the study results are given below in the Discussion.

Kp is a quasi-logarithmic index, and so a more useful quantity to discuss is the westward convection electric field at midnight at the outer simulation boundary. Figure 1 shows

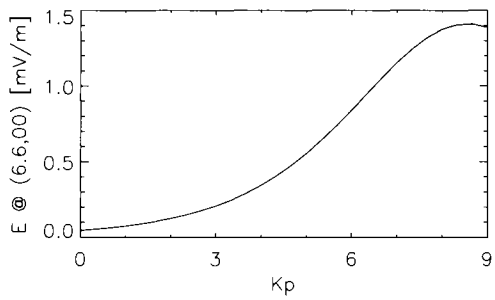

Figure 1. Electric field strength at $R = 6.6$ R_E at magnetic local midnight with respect to Kp for the shielded Volland-Stern electric potential description with the Maynard-Chen activity dependence.

the relationship between this electric field value and Kp for a shielded Volland-Stern description. For Kp = 2, the electric field is 0.125 mV/m. For Kp = 6.5, the electric field is 1.0 mV/m. This Kp step produces a factor of 8 increase in the convection strength, matching the factor of 8 increases applied to N_{PS}. Two cases use Kp = 9, which yields an electric field of 1.4 mV/m. This is more than 11 times bigger than the Kp = 2 electric field, and represents extreme geomagnetic activity.

3. RESULTS

The purpose of this study is to examine the ability of flowout loss and charge exchange loss to produce a two-phase decay. While there are many other loss mechanisms acting on the storm-time ring current, these two are the largest [e.g., *Liemohn et al.*, 1999; *Kozyra et al.*, 2002] and they are the center of the controversy around the two-phase-decay phenomenon [e.g., *Daglis and Kozyra*, 2002; *Daglis et al.*, 2003].

3.1. Down-Step Experiments

Figure 2 shows results from a simulation in which N_{PS} drops 3 hours before Kp. Figures 2a and 2b show the time series of N_{PS} and the midnight outer boundary electric field, respectively. This is an example of continued convection, but with decreased plasma sheet density, during the recovery phase of a magnetic storm.

The total energy of the hot ion population inside of geosynchronous orbit E_{RC} is shown in Figure 2c, along with the totals for H^+ and O^+ separately. The solid curve in Figure 2c has the appearance of a two-phase decay. It begins at 10.1 PJ, decreasing to 4.93 PJ by $t = 4$ h, and eventually dropping to 3.24 PJ by $t = 12$ h. There is a definite kink in the E_{RC} curve at $t = 4$ h, with the loss rate becoming much smaller after the down-step of the electric field. The two species have very

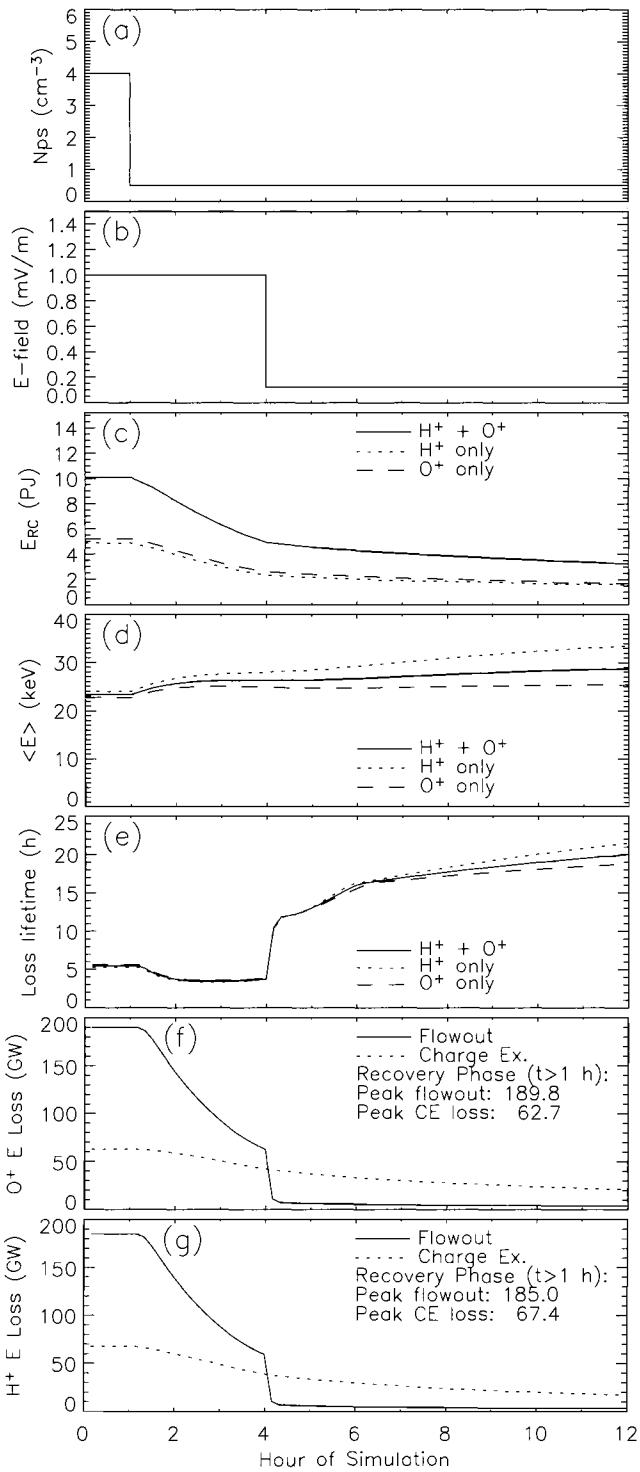

Figure 2. Simulation inputs and results from a numerical experiment in which the plasma sheet density decreases before the convection strength. Shown are the following: (a) plasma density applied at the outer simulation boundary (the same for both H^+ and O^+); (b) the midnight outer boundary electric field strength; (c) the total energy content in the ring current; (d) the average energy of a ring current ion; (e) the pure-loss lifetime for the total energy content; (f) the particle loss rate for O^+ from flowout and charge exchange; and (g) the particle loss rate for H^+ from flowout and charge exchange.

similar total energy values throughout the simulation, with the O^+ curve beginning 0.3 PJ higher than the H^+ value and ending 0.1 PJ higher than H^+ at $t = 12$ h.

Figure 2d presents the average particle energy during the simulation (total amount of energy divided by total number of particles). This is an interesting quantity because both loss processes are dependent on it. Flowout is affected because the drift paths through the inner magnetosphere are influenced by the gradient-curvature drift, which is directly proportional to energy. Charge exchange has energy dependence in both the cross section and the number of targets ($v\Delta t$, the flight distance per time increment). The average energy (H^+ and O^+ together) begins at a steady 23 keV, and then slowly increases to 29 keV by $t = 12$ h. The average energy for H^+ is slightly higher than that for O^+ throughout the simulation.

Liemohn and Kozyra [2003] discussed the calculation of loss lifetimes from ring current simulations. A "pure-loss" time scale can be calculated by dividing the total energy content by the energy loss rate from all processes. For example, at the end of the simulation ($t = 12$ h), the total energy content of the hot ions is 3.24 PJ (1.57 PJ carried by H^+ and 1.67 PJ carried by O^+). The total loss rate from the system at this time is 45.2 GW (20.4 GW departing from the H^+ content and 24.9 GW from O^+). Dividing the latter into the former yields a pure-loss lifetime of 20.0 hours (for H^+ and O^+, the pure-loss lifetimes are 21.5 hours and 18.8 hours, respectively). The "pure-loss" qualifier is added because this loss lifetime is only observed if there is no energy input to the ring current, which is not the case, even during quiet times. Nevertheless, it is useful quantity because it tells about the relative magnitude of the energy loss (compared to the total energy).

Figure 2e shows this pure-loss lifetime from the simulation results. At $t = 0$ h, the loss lifetime is ~5.5 hours. It then decreases to a minimum value of ~4 hours at $t = 3$ h. At $t = 4$ h, there is a sudden jump in the loss lifetime up to ~12 hours, and the lifetime slowly increases to 20 hours by $t = 12$ h. In this latter part of the simulation, the O^+ and H^+ lifetimes split apart a little, with H^+ ending with a loss lifetime of 21.5 hours and O^+ at 19 hours. That is, the total energy of O^+ is being lost slightly faster than that of H^+ (relative to the total energy for each species). This is reflected in the convergence of the dashed and dotted lines in Figure 2c.

The magnitudes of the hot ion losses for O^+ and for H^+ are shown in Figures 2f and 2g, respectively. Only the two

dominant loss processes of dayside flowout and charge exchange are plotted. The peak values during the recovery phase ($t > 1$ h) are listed for each process in each figure. It is seen that flowout energy loss is 3 to 4 times larger than charge exchange at the beginning of the recovery phase (just after $t = 1$ h), and remains larger than charge exchange through the early recovery period (until $t = 4$ h). Once the convection electric field is reduced (at $t = 4$ h), flowout drops to less than 10 GW for each of the species, a level below that for charge exchange at this time (~40 GW). The losses from charge exchange do not show such a dramatic change. Instead, they gradually decrease throughout the recovery phase. While both charge exchange loss rates (H^+ and O^+) end near 20 GW (at $t = 12$ h), they begin at slightly different values, with O^+ starting at 60 GW and H^+ starting at 70 GW.

Note that the energy loss rates are significantly different from the particle loss rates. Because flowout occurs at the outer simulation boundary while charge exchange occurs deep within the simulation domain, the average energies of the particles lost by these two processes are quite different. Therefore, the ratio of flowout-to-charge exchange particle losses is ~8 at $t = 1$ h, dropping to ~4 just before $t = 4$ h, and the two particle loss rates are roughly equal throughout the late recovery phase. The energy loss rate is more applicable to this study, and therefore it is shown in Figure 2.

Figure 3 presents a similar sequence of plots for the opposite ramp-down case, in which the convection electric field is reduced 3 hours prior to the plasma sheet density (see figures 3a and 3b). The resulting total energy content carried by the hot ions in the inner magnetosphere is shown in Figure 3c. There is no visible kink in the curves at $t = 4$ h, or in fact anywhere past $t = 1$ h. The average energy is shown in Figure 3d, again showing that O^+ is slightly cooler than H^+ and that the two are diverging slowly throughout the recovery phase. The pure-loss lifetimes are given in Figure 3e. There is a step-function change from 5 to 15 hours at the time when the electric field is reduced ($t = 1$ h). After this, the loss lifetime slowly increases above 20 hours by the end of the simulation. The magnitudes of the loss rates are shown in the final two panels (Figures 3f and 3g), again showing that the flowout loss rate is much bigger than charge exchange during high convection ($t < 1$ h) but drops below the charge exchange loss rate when the convection strength is reduced ($t > 1$ h). The late recovery phase ($t > 4$ h) flowout energy loss rates for both species are larger for this simulation than for the simulation results presented in Figure 2. This is because of the much lower energy loss rate during the first three hours of the recovery. Therefore, flowout loss is roughly a factor of 2 to 3 less than charge exchange throughout the recovery phase. As in Figure 2, the charge exchange loss rates decrease slowly throughout the simulation, with no sudden changes in the loss rate for either species.

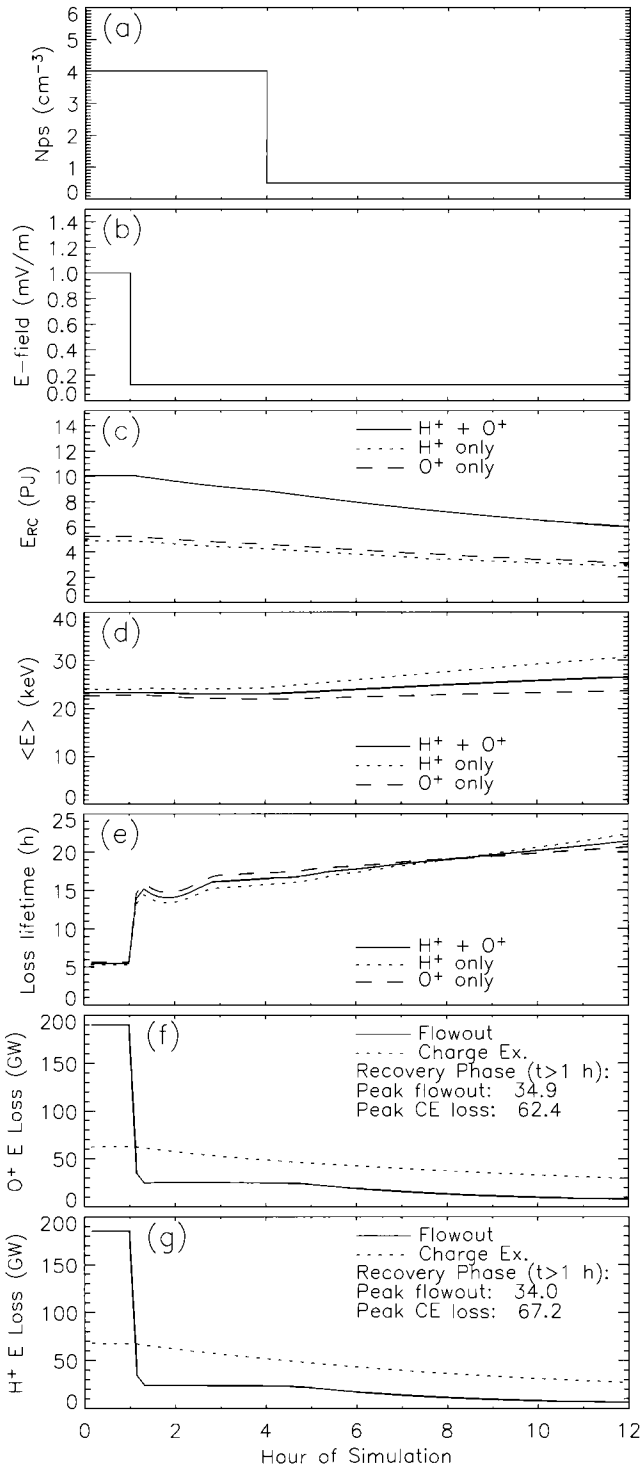

Figure 3. Same as Figure 2 except for a numerical experiment in which the convection strength decreases before the plasma sheet density.

Figure 4 presents a third case in which the electric field and N_{PS} are both reduced simultaneously (Figures 4a and 4b). There is no kink evident in the total energy content of the hot ions for this simulation (Figure 4c), and the ion average energies slowly increase at different rates for the two species (Figure 4d). As in the previously discussed simulation, the loss lifetime shows a sudden increase at $t = 1$ h followed by a slow increase for the rest of the simulation (Figure 4e). The sudden increase in the loss lifetime corresponds to the sharp drop in flowout loss (Figures 4f and 4g), and the subsequent slow rise in the loss lifetime is caused by the slow decrease in the loss rates for both flowout and charge exchange during the rest of the simulation.

3.2. *High-Convection Experiments*

The results presented thus far are for simulations with Kp ramping down from 6.5 to 2. While Kp = 6.5 is a storm-time value, this isn't the highest value for the index. Stronger convection allows for deeper injection of the plasma sheet ions into the inner magnetosphere. Because the hydrogen geocoronal density increases closer to the Earth, the charge exchange losses should be bigger. Furthermore, the adiabatic acceleration of the particles as they convect radially inward should create more high-energy ring current particles. It is at the high energies that O^+ is preferentially removed via charge exchange. Thus, a higher magnetospheric convection rate should result in more charge exchange loss of O^+, yielding the best opportunity (of the selected numerical experiments) for a charge-exchange-driven two-phase decay of the ring current.

Figure 5 shows results for a ramp-down from Kp = 9, which corresponds to a midnight outer boundary convection electric field strength of 1.4 mV/m. Both input parameters (electric field and N_{PS}) are reduced simultaneously (Figures 5a and 5b). It is seen that the total energy content of the ring current ions has no visible kink (Figure 5c). While the average energies are higher for this simulation than the previous ones (Figure 5d), the loss lifetimes are still quite close early in the recovery phase and diverge rather slowly throughout the simulation (Figure 5e). The loss rates shown in Figures 5f and 5g are very similar to those presented in Figures 4f and 4g, respectively, with slightly higher magnitudes for the charge exchange losses, as expected.

A final numerical experiment to be discussed is a simulation with the plasma sheet characteristic energy E_{PS} set to 20 keV, instead of 7 keV as in the previous 4 runs. Otherwise, the set up is identical to the previous run, with the high convection set to Kp = 9 and both input parameters decreasing simultaneously. This simulation is the most favorable of all of those presented for creating a charge-exchange-driven two-phase decay. The results are shown in Figure 6. The average particle energy is indeed higher than in any of the other

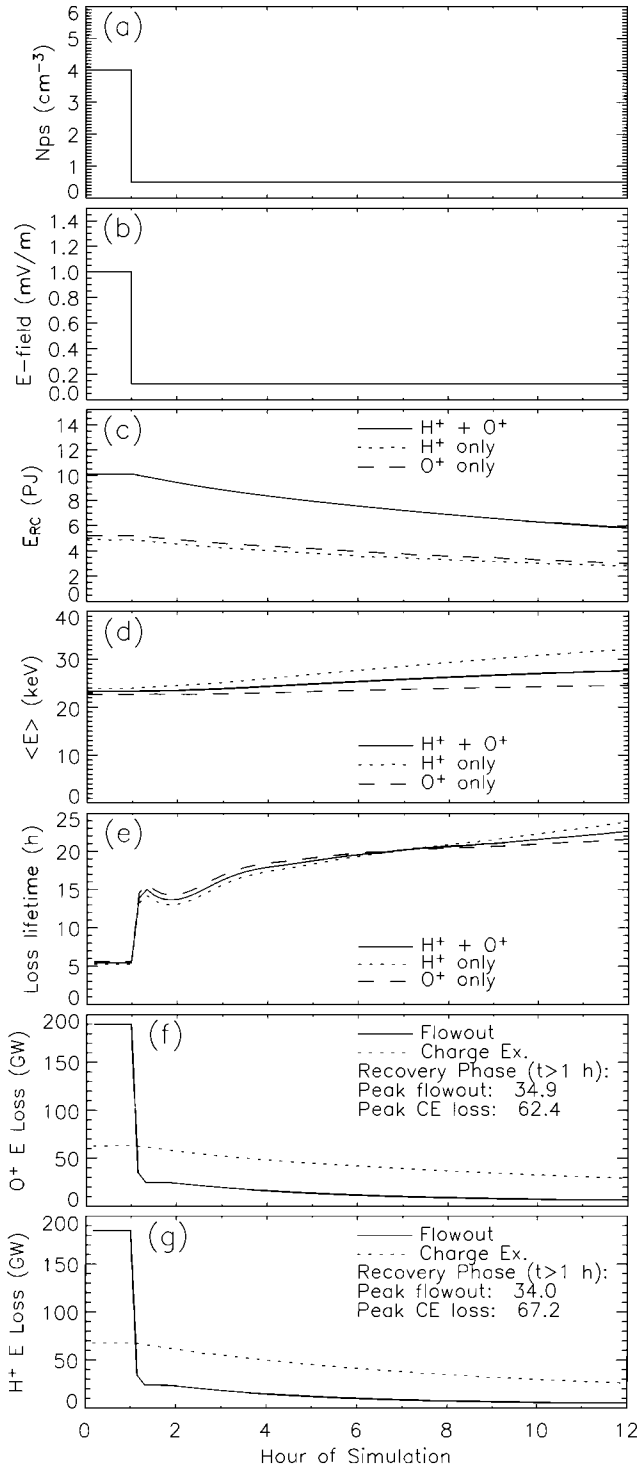

Figure 4. Same as Figure 2 except for a numerical experiment in which the convection strength and plasma sheet density decrease simultaneously.

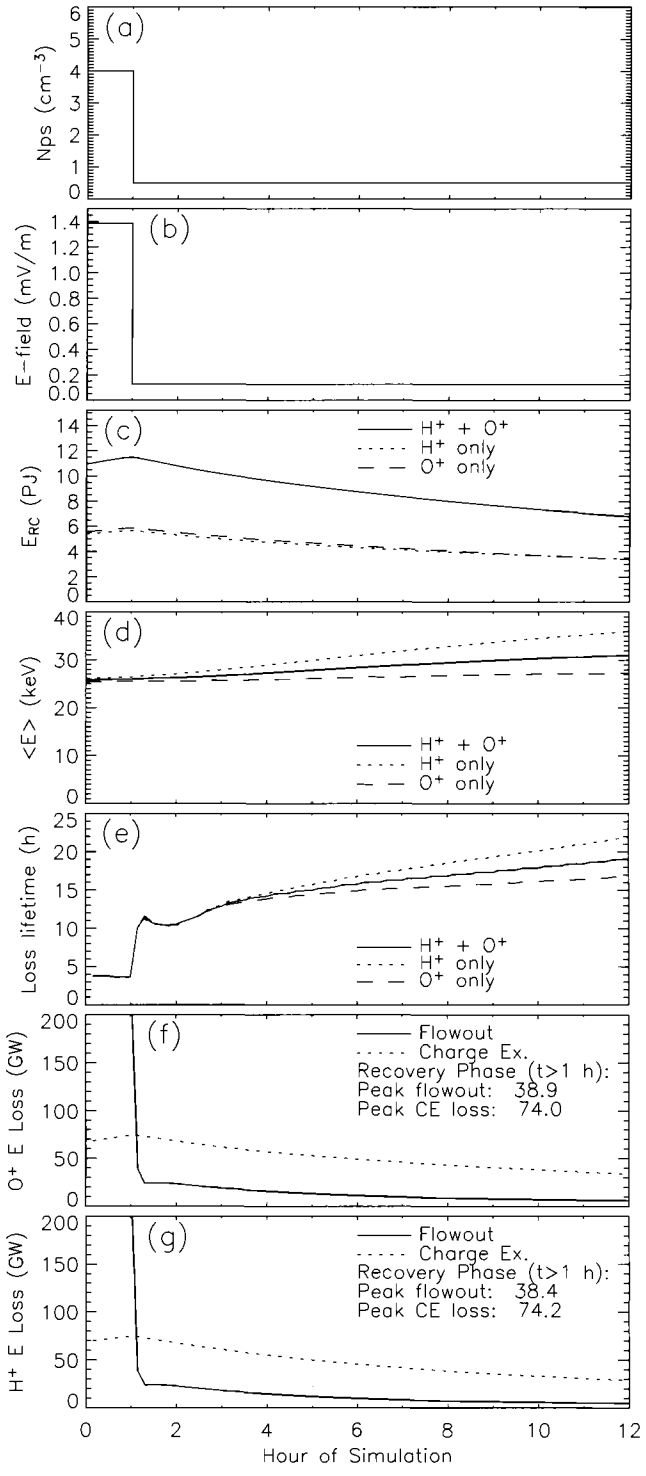

Figure 5. Same as Figure 4 except for a numerical experiment in which the peak convection strength is set to Kp = 9 instead of Kp = 6.5.

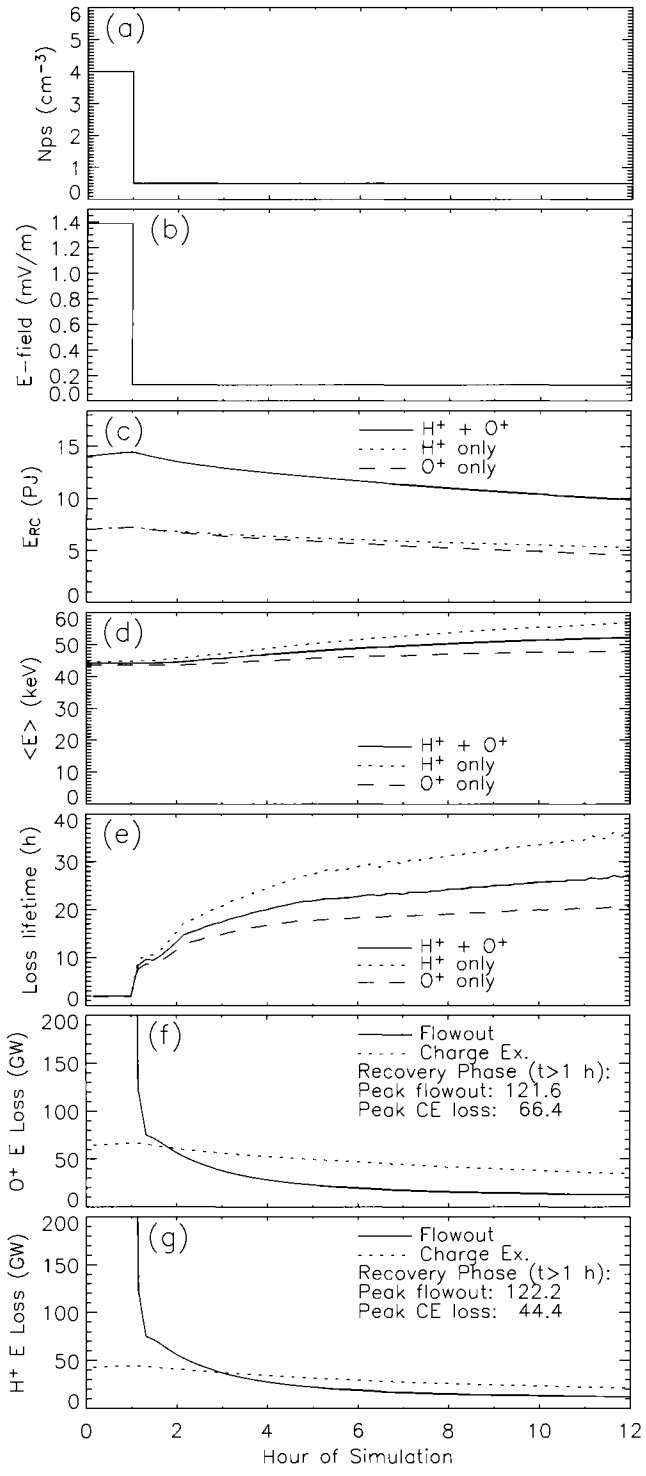

Figure 6. Same as Figure 5 except for a numerical experiment in which the characteristic energy of the plasma sheet is 20 keV instead of 7 keV.

simulations (Figure 6d), but the total energy content still does not show a two-phase decay signature (Figure 6e). In fact, the charge exchange loss rates are less than in the previous run with $E_{PS} = 7$ keV (compare Figures 6f and 6g with 5f and 5g). The peak O^+ charge exchange energy loss rate in Figure 6f is 90% of the peak value in Figure 5f, but the peak H^+ charge exchange rate in Figure 6g is only 65% of the peak value in Figure 5g. So, even though the ratio of the O^+ charge exchange loss rate to that of H^+ is larger for this "hot" simulation (Figure 6) than for the nominal E_{PS} run (Figure 5), the total loss from charge exchange is less, and thus no two-phase decay is produced.

3.3. Composition Experiments

The results thus far have discussed an equal N_{PS} value for H^+ and O^+, resulting in nearly equal energy contents for the two hot ion species. It is useful, however, to assess the compositional dependence of two-phase decay formation. Because the simulations use an imposed electric field description, the results for H^+ and O^+ may be arbitrarily scaled and summed to yield other boundary composition ratios. Figure 7 shows the results of such a calculation, using the results from three of the previously discussed simulations. The plots in the first column (Figures 7a-7d) use the results shown in Figure 4c, in which Kp steps down from 6.5 to 2 simultaneously with the N_{PS} drop. The plots in the second column (Figures 7e-7h) use the results from Figure 5c, where Kp starts at 9 and drops to 2. The plots in the third column (Figures 7i-7l) use the results from Figure 6c, which not only has a Kp drop from 9 to 2 but also has a characteristic energy at the outer boundary of 20 keV (instead of 7 keV). The rows are as follows: the top row shows E_{RC} for H^+ plus half of the O^+ energy content; the second row shows E_{RC} for H^+ plus a tenth of the O^+ energy content; the third row shows E_{RC} for O^+ added to half of the H^+ energy content; and the last row shows E_{RC} for O^+ and a tenth of the H^+ energy content.

It is seen in Figure 7 that none of these compositional combinations for these simulations produce a visible two-phase decay signature in the total energy content of the hot

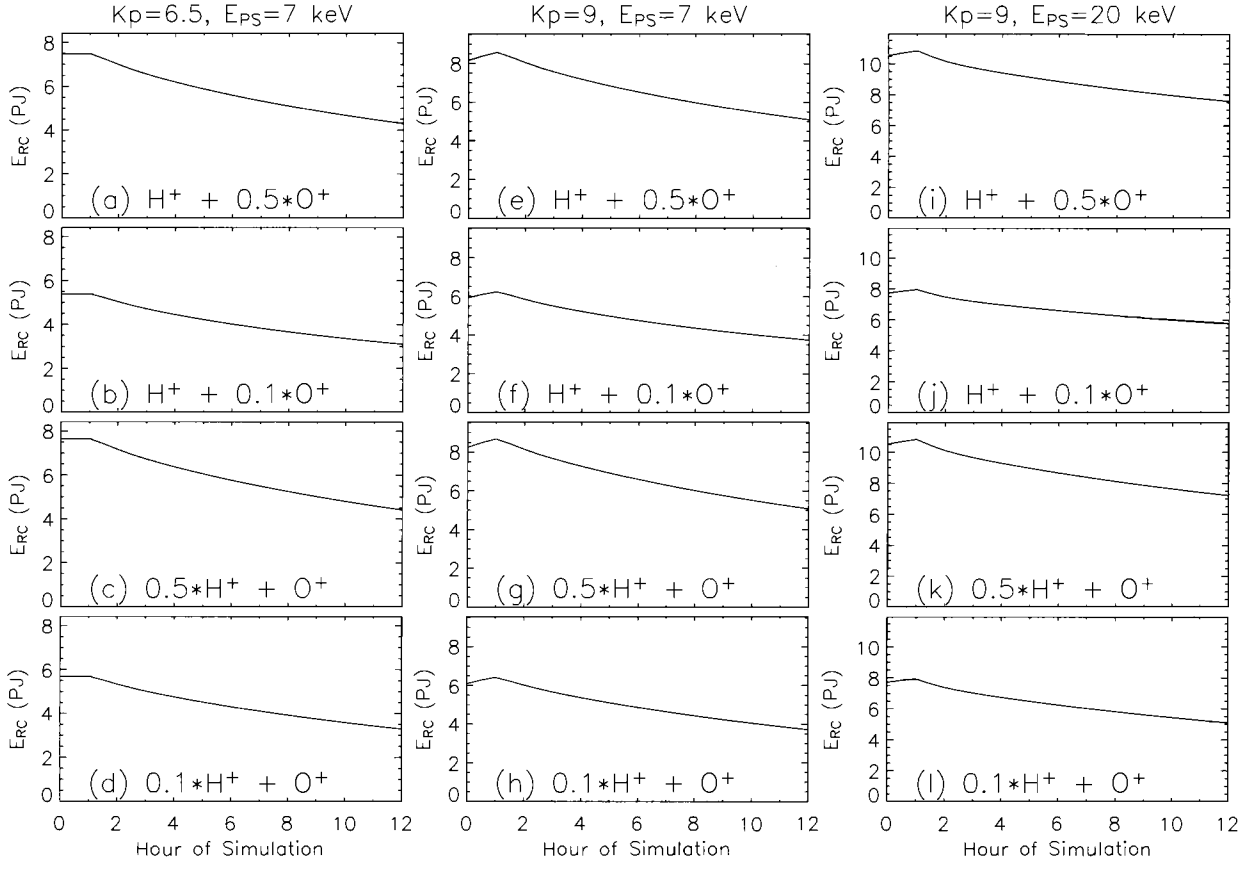

Figure 7. Total energy content for three of the numerical experiments (the 3 columns) with various combinations of the H^+ and O^+ contributions, as marked in each panel.

ions. While the slope of E_{RC} changes throughout the recovery phase in each panel of Figure 7, there is never a sharp transition from a fast to a slow loss rate. It is always a gradual conversion from fast loss to slow loss, regardless of either the ring current boundary conditions (temperature or composition) or the storm-time convection intensity.

3.4. Decay Rate Analysis

In order to quantitatively analyze the structure of the ring current total energy content decay, it is useful to consider ratios of E_{RC} at various times during the simulations. Table 1 presents these ratios for the simulation results presented in Figures 2c, 3c, 4c, 5c, and 6c (from the solid lines in each plot), as well as for each panel in Figure 7. The first column is the fraction that E_{RC} dropped in the first 3 hours of the decay phase. The simulation with high convection continuing after the density decrease (Figure 2c) had a ~50% drop in energy content, while the other simulations had drops in the ~15% range. The simulation with high density continuing after the convection strength reduction (Figure 3c) had the highest fraction remaining, followed by the simulation with the abnormally hot plasma sheet (Figure 6c). The ratios from Figure 7a-7d show that the fraction remaining after 3 hours is smaller when there is relatively more H^+ than O^+, while the fraction is larger when there is relatively more O^+. The next set of numbers (from Figures 7e-7h) show a similar trend, but the fractions are much closer to each other. The third set (from Figures 7i-7l) has the opposite trend, with a higher O^+ relative content producing a lower fraction.

The next two columns of Table 1 show the ratios of E_{RC} after 6 and 9 hours of recovery, respectively, to the peak E_{RC} value just before the recovery began (at $t = 1$ h). The ratios from Figure 2c are well below those from the other simulations. The other simulations continue in their relatively slow decay from the peak E_{RC} value, with the ratios from Figure 6c being the highest in both columns. This is because the high-density source has now turned off for the simulation shown in Figure 3c, and the lower average energy (compare Figures 3e and 6e) leads to a faster recovery rate. The fractions for the plots in Figure 7 continue the trends seen in the first column of numbers.

The final two columns in Table 1 present E_{RC} ratios for 3-to-6 hours into the recovery and 6-to-9 hours into the recovery, respectively. All of these values are quite similar, ranging between 0.82 and 0.93. This shows that all of the simulation results are decreasing at roughly the same pace from $t = 4$ h through $t = 10$ h. Both input parameters are at their quiescent values during this period (in all of the simulations), so any differences in the ratios are primarily caused by different charge exchange loss rates. The slight increase in the values between the fourth and fifth columns in Table 1 is because the particles with faster charge exchange lifetimes are being preferentially removed, leaving only the longer lifetime particles. The fact that the increases in these ratios are slight (1-5%) indicates that the ring current is undergoing a rather slow conversion from fast lifetime dominance to slow lifetime dominance in the decay rate.

4. DISCUSSION

The results presented in Figures 2-7 imply that a two-phase decay is caused by a decrease in the plasma sheet density

Table 1. Ring Current Total Energy Content Ratios.

	$(t = 4\text{ h})/(t = 1\text{ h})$	$(t = 7\text{ h})/(t = 1\text{ h})$	$(t = 10\text{ h})/(t = 1\text{ h})$	$(t = 7\text{ h})/(t = 4\text{ h})$	$(t = 10\text{ h})/(t = 7\text{ h})$
Figure 2c	0.488	0.402	0.350	0.823	0.870
Figure 3c	0.878	0.747	0.646	0.851	0.864
Figure 4c	0.830	0.716	0.626	0.862	0.875
Figure 5c	0.838	0.726	0.639	0.867	0.879
Figure 6c	0.863	0.784	0.720	0.909	0.918
Figure 7a	0.828	0.713	0.625	0.862	0.876
Figure 7b	0.825	0.710	0.623	0.861	0.877
Figure 7c	0.832	0.718	0.628	0.863	0.874
Figure 7d	0.835	0.721	0.630	0.864	0.873
Figure 7e	0.837	0.728	0.642	0.869	0.882
Figure 7f	0.837	0.729	0.646	0.871	0.886
Figure 7g	0.838	0.725	0.636	0.866	0.876
Figure 7h	0.838	0.724	0.631	0.864	0.872
Figure 7i	0.868	0.794	0.734	0.915	0.924
Figure 7j	0.876	0.809	0.754	0.923	0.933
Figure 7k	0.858	0.774	0.706	0.903	0.911
Figure 7l	0.850	0.760	0.685	0.894	0.902

associated with a continued large electric field, followed by a subsequent decrease in the electric field. The decrease in N_{PS} starts the early recovery phase, while the decrease in electric field starts the late recovery phase. The corollary of this conclusion is that charge exchange is incapable of producing a two-phase decay.

4.1. Charge Exchange

The hypothesis was that the charge exchange loss rates for H^+ and O^+ were sufficiently different above ~40 keV to cause a two-phase decay signature. In other words, the transition between the initial rapid loss of hot O^+ and the much slower loss of hot H^+ would create a kink in the total energy content of the ring current. In the kinetic transport model, the influence of charge exchange on the distribution function f is included via an attenuation factor [*Jordanova et al.*, 1996],

$$f_{t+dt} = f_t \exp\left(-v\Delta t \sigma_{CE} \langle n_H \rangle\right) \tag{1}$$

where v is the hot ion velocity, Δt is the time step of the simulation, σ_{CE} is the charge exchange cross section, and $\langle n_H \rangle$ is the bounce-averaged neutral hydrogen density. Equation (1) can be rewritten with a loss lifetime parameter τ_{CE},

$$f_{t+dt} = f_t \exp\left(-\frac{\Delta t}{\tau_{CE}}\right) \tag{2}$$

where

$$\tau_{CE} = \frac{1}{v\sigma_{CE}\langle n_H \rangle} \tag{3}$$

is a function of hot ion energy, equatorial pitch angle, radial distance, and hot ion species. Figure 8 presents a few curves of τ_{CE} (in hours) versus hot ion energy (in keV) for H^+ and O^+ at several L values. All of these results are for an equatorial pitch angle of 45°. Figure 8 shows that τ_{CE} can vary over several orders of magnitude as these parameters are changed. Most notably, τ_{CE} for H^+ is always lower than τ_{CE} for O^+ at energies below 40 keV. At $L = 6.5$, this crossover value is above 100 hours (more than 4 days). For $L = 4.5$, the crossover value is ~40 hours, and for $L = 2.5$, H^+ and O^+ have equal τ_{CE} values at ~9 hours. The H^+ loss lifetime quickly rises above 40 keV, but the O^+ loss lifetime is relatively flat at these higher energies. Thus, there is a large disparity in the loss lifetime at high energies, and the hot O^+ ions should be preferentially removed long before the hot H^+ ions are depleted.

The problem is the magnitude of the loss lifetime. The entire ring current must reside at $L = 2.5$ in order to get a charge

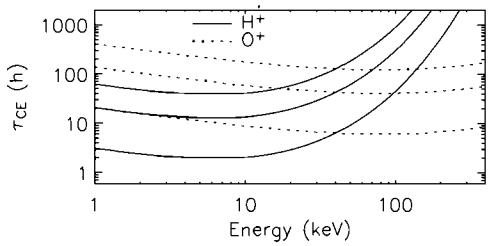

Figure 8. Charge exchange loss lifetimes versus hot ion energy as a function of radial distance and species. The solid curves show the values for H^+ and the dotted curves show the values for O^+. For each species, there are 3 curves. The highest curve is for $L = 6.5$, the middle curve is for $L = 4.5$, and the lowest curve is for $L = 2.5$. All results are for a hot ion equatorial pitch angle of 45°.

exchange loss lifetime for the total energy content below 10 hours. Moving the ring current just one Earth radius (R_E) outward doubles the O^+ τ_{CE} value (from 10 to 20 hours), and moving it out another R_E doubles the O^+ τ_{CE} again (up to 40 hours). It was shown in Figures 5 and 6 that, even with the application of the largest possible convection strength from the *Maynard and Chen* [1975] activity relationship for the shielded Volland-Stern field, charge exchange can only yield a 10-15 hour loss lifetime for the early recovery phase of the ring current. Conversely, flowout loss is capable of producing a 4-hour loss lifetime with only a moderately high Kp value (see Figure 2).

Compare this with the *O'Brien et al.* [2002] study. They concluded that the recovery of *Dst* is statistically identical for storms with or without continued high convection. This conclusion is compatible with the conclusion of the present study. The important difference is that the plasma sheet density must be dramatically reduced prior to the reduction in convection. If the density reduction is only slight, then there will be significant injection of new plasma into the inner magnetosphere. The rapid removal of the high-density partial ring current must be accompanied by a very weak injection from the tail in order to produce a two-phase decay. When the two input parameters are decreased simultaneously, a two-phase decay is not produced.

Another issue is the relative magnitudes of the H^+ and O^+ charge exchange loss rates. The expectation was that O^+ would have a larger loss rate because of the short loss lifetimes at high energies. This was not observed in the results presented in the previous section. The reason for this is that H^+ is rapidly removed via charge exchange at energies below 40 keV. In the 5-10 keV energy range, the loss lifetime for H^+ at $L = 6.5$ is ~25 hours and at $L = 2.5$ it is less than 2 hours. The O^+ τ_{CE} values are nearly an order of magnitude larger at these energies. The relatively fast removal of H^+ in the low-energy range significantly contributes to the total loss rate. In fact, it accounts for a majority of the H^+ charge exchange loss rate. Because

there are more particles in the low-energy range than the high-energy range, H^+ has a higher charge exchange loss rate than O^+ in all of the simulation results presented in this study.

4.2. Energy Content Recovery

Table 1 highlights this disparity in the loss rate between flowout and charge exchange. The fastest drop in the total energy content of the ring current occurs during a flowout-dominated period. This fast drop only occurs when convection is strong and the plasma sheet density is low. The fractional decrease in the total energy content is much slower during all of the periods when charge exchange was either comparable to or greater than the flowout loss rate (which only occurs during low convection times).

Figure 7 and Table 1 presented results for E_{RC} recovery as a function of boundary condition composition. All of the plots showed a relatively slow conversion from shorter loss lifetimes to longer loss lifetimes, and therefore did not produce a two-phase decay. The rate of recovery, however, is slightly different for each plot. Figures 7a-7d (and the corresponding fractions in Table 1) showed a trend of more H^+ resulting in faster decay. This is because of the E_{PS} value (7 keV) for this simulation. There is an abundance of low-energy H^+ leaving the system through charge exchange, resulting in a higher energy loss rate for H^+ than for O^+.

Figures 7e-7h had the same trend as Figures 7a-7d, but with loss rates that were much closer together. The fractions of remaining E_{RC} (the first 3 columns in Table 1) are also higher than the fractions from Figures 7a-7d, indicating that the energy loss was slower. Both of these trends are because of the higher convection strength, which has several effects. First, it injects the plasma deeper. The ions undergo more adiabatic energization, resulting in a bigger differential between the H^+ and O^+ charge exchange rates. Secondly, charge exchange is faster because of the higher geocoronal density closer to the Earth. The third influence is that the particles are swept through the inner magnetosphere faster, resulting in less total attenuation of the ions due to charge exchange. All three of these effects produce more O^+ charge exchange loss relative to H^+ charge exchange. The third effect is responsible for the overall decrease in the charge exchange loss rate, resulting in the higher fractions in Table 1.

Figure 7i-7l showed the opposite trend from the previous two sets of results. That is, a higher relative O^+ energy content resulted in a faster recovery. This is because of the unusually high E_{PS} value (20 keV) for this simulation as well as the high convection strength during the main phase. These two effects produce a much higher average energy of the ring current ions than for the other simulations (compare Figure 6d with Figures 4d and 5d). The differential charge exchange loss lifetime between O^+ and H^+ for $E > 40$ keV results in an O^+-dominated ring current yielding a faster decay rate than an H^+-dominated one.

This brings up the issue of average ion energy in the numerical experiments. Figures 2-6 show average energy <E> ranging from 20 keV to 60 keV. In general, <E> is 2-3 times higher than E_{PS} during the main phase, and this ratio increases to 3-5 by $t = 12$ h. Note that this is an average over the entire simulation domain, and therefore the large flux tubes in the outer simulation domain can significantly contribute to the average energy. This is true even though the equatorial plane density and pressure are much lower here than at the peak of the ring current (which is typically inside of 4 R_E) [e.g., *Liemohn et al.*, 2001a, b]. Because of adiabatic energization, the local average energy is much higher at the peak of the ring current than out near the simulation boundaries.

A logical question to ask is whether there is observational evidence for step-function-like decreases in either convection or plasma sheet density, particularly the case of the density decreasing before the convection. An excellent example of this is the September 25, 1998 storm, which has this pattern of input decreases and also exhibits a clear two-phase *Dst** decay [see *Liemohn et al.*, 1999, 2001a]. Whether this is a typical case or a rare occurrence is unknown. However, the authors of the *O'Brien et al.* [2002] study are pursuing a follow-up to their statistical analysis of *Dst* decay [T.P. *O'Brien*, personal communication, 2004]. Specifically, they are investigating the timing of plasma sheet versus convection shut-offs and the resulting *Dst* time series. The result should be an observational test of this hypothesis.

4.3. Comparisons and Caveats

It should be noted that the total ion energy content of the hot ions in the inner magnetosphere can be related to the magnetic perturbation at Earth through the Dessler-Parker-Sckopke (DPS) relation [*Dessler and Parker*, 1959; *Sckopke*, 1966]. For the Earth, this relation is one nT of southward magnetic deflection for every 0.04 PJ of energy content (that is, multiply the energy content numbers by –25 to yield magnetic perturbation in nT). Because this introduces an extra layer of assumptions into the model results, the conversion is not performed here. Furthermore, the energy content results are relative numbers because the magnitude is scalable by the plasma sheet density for each hot ion species. Many studies use the DPS formula, however, with success at reproducing the observed magnetic perturbation [e.g., *Kozyra et al.*, 1998, 2002; *Jordanova et al.*, 1998, 2003; *Greenspan and Hamilton*, 2000; *Liemohn et al.*, 2001a]. Therefore, a two-phase decay in the ring current total energy content most likely produces a two-phase decay in the *Dst* index.

Figures 2-6 showed energy loss rates from the various numerical experiments. It was noted that the particle loss

rates have a different relative relationship between flowout and charge exchange. In general, the energy loss rate is a more relevant quantity because it can be directly related to a change in *Dst* (through the DPS relation). However, the particle loss rate is sometimes important, especially when interpreting energetic neutral atom observations. Therefore, care must be taken to not confuse these two loss rates because they are not directly interchangeable.

Walt and Voss [2001] concluded that wave-particle interactions elevate particle precipitation losses to a level capable of producing a rapid initial recovery of the ring current. Other studies have shown that wave-induced particle precipitation is a minor component of the total loss rate from the ring current [e.g., *Jordanova et al.*, 1998, 2001; *Soraas et al.*, 2002, 2003; *Khazanov et al.*, 2002, 2003b]. In fact, particle precipitation losses on the nightside from the injection process are often larger than the losses from wave-particle interactions [e.g., *Jordanova et al.*, 2001; *Soraas et al.*, 2002]. The present study does not address wave-particle interactions as a source of two-phase decay, but if precipitation is able cause this phenomenon, it is most likely only under rare and special circumstances.

An alternative explanation for two-phase decay formation is the rapid reduction of the tail current. It has been shown that the tail current contributes up to a 25 nT decrease in the *Dst* index [e.g., *Turner et al.*, 2000], which can be a significant (but minor) fraction of the total perturbation during a magnetic storm. A sudden decrease in the tail current can therefore cause a sudden recovery of the *Dst* index [e.g., *Feldstein et al.*, 2000; *Ohtani et al.*, 2001]. Observationally, these recoveries from abrupt changes in the tail current are on the order of 20 nT [*Friedrich et al.*, 1999; *Ohtani et al.*, 2001]. During a major storm with the minimum *Dst* at −200 nT or below, this is a minor perturbation to the overall recovery rate. It is significant, however, when examining the rapid fluctuations of the *Dst* index (or its one-minute-resolution counterpart, SYM-H). Furthermore, *Liemohn* [2003] showed that the commonly used DPS relation implicitly includes a truncation current when the plasma pressure just inside the outer boundary of the integration volume is nonzero. This truncation current is a crude approximation of the tail current, but the real issue is that the DPS relation overpredicts the perturbation from the currents inside the integration volume, and that this overprediction varies with time. Therefore, great care must be taken in equating changes in the *Dst* index with changes in the ring current. Specifically for this study, a two-phase decay in the *Dst* index may not be a two-phase decay in the ring current.

It is necessary to explain some caveats to the general applicability of these results. For instance, the initial condition for the presented simulations was essentially a steady-state solution for constant, high convection and high plasma sheet density. This neglects the radial diffusion of the high-energy particles into the inner magnetosphere from electric field fluctuations [e.g., *Chen et al.*, 1993, 1994; *Khazanov et al.*, 2004a, b]. Inclusion of this process would increase the high-energy portion of the ring current ion distribution in the inner magnetosphere, and would alter the charge exchange loss lifetime (lowering it if O^+ is dominant, raising it if H^+ is dominant). The application of identical ion characteristics across the nightside is also not correct, but the injected ion flux is actually not identical because the radial drift at the outer boundary is local time dependent. In addition, even though the Volland-Stern model has been used successfully in modeling the storm-time ring current, more robust electric field models exist that include flow channels and other features for rapid access of the plasma sheet to the inner magnetosphere [e.g., *Chen et al.*, 2003; *Khazanov et al.*, 2003a; *Jordanova et al.*, 2003; *Fok et al.*, 2003]. Moreover, *Wygant et al.* [1998] reported inner magnetospheric electric field measurements of up to 6 mV/m during storms, and substorm-associated amplitudes of up to 20 mV/m. The former is probably from partial ring current - driven feedback on the electric field [e.g., *Ridley and Liemohn*, 2002; *Fok et al.*, 2003], and the latter is probably from the magnetic field reconfiguration [e.g., *Li et al.*, 1998]. The peak electric field of 1.4 mV/m is therefore small compared to these observed peak values. A more sophisticated electric field description that includes rapid access to the inner magnetosphere might yield a different distribution for the hot ions, resulting in a different loss rate. The *Daglis et al.* [2003] conclusion that O^+ can significantly contribute to a two-phase decay of the ring current is, therefore, compatible with the conclusion of this study given the proper electric field description in the inner magnetosphere. For the description chosen for this study, charge exchange is clearly not capable of producing a two-phase decay. Even with these caveats about the electric field model, the Kp = 9 simulation essentially fills the simulation domain with ring current ions, and there was still no sign of a two-phase decay in the total energy content time series. Another caveat to mention is the use of a static dipole magnetic field in these simulations. This is certainly not correct, especially for large storms [e.g., *Tsyganenko et al.*, 2003]. Inflation of the field will change the particle trajectories and energies, and therefore alter the loss rates. However, by applying the boundary condition at geosynchronous orbit, it is felt that a dipole field is not prohibitively incorrect. The results presented above, therefore, are qualitatively demonstrative of the relative contributions of flow-out and charge exchange to the decay of the storm-time ring current.

5. CONCLUSIONS

It was shown that a two-phase decay (a sharp transition between fast and slow recovery rates) of the ring current total

energy content is produced when the plasma sheet density is dramatically reduced several hours prior to a sudden reduction in the magnetospheric convection strength. The reverse situation, a convection strength reduction prior to a plasma sheet density decrease, does not produce a two-phase decay signature. A two-phase decay is not visible in the results for simultaneous reduction of these two input parameters. Moderate and strong convection strengths were applied, as well as a typical plasma sheet characteristic energy and an elevated energy (that is, a hot plasma sheet).

The hypothesis was that the differential charge exchange rates between hot O^+ (fast) and hot H^+ (slow) can produce a two-phase decay in the ring current. The modeling results presented in this study refute this hypothesis. It was shown that a two-phase decay is formed when the loss lifetime is initially short (less than 10 hours) for some interval at the beginning of the recovery phase, followed by a sudden transition to a much longer loss lifetime (at least double the previous value). Flowout loss was found to be the only process with sufficient intensity and variability to cause a sudden increase in the ring current energy loss lifetime. While charge exchange can yield loss lifetimes below 10 hours (for special configurations of the ring current), is not capable of producing a rapid transition in the loss lifetime. Charge exchange is an exponential attenuation of the distribution, with the shorter loss lifetime particles being removed first, followed by a gradual shift to dominance by the longer lifetime particles. This process cannot cause a sudden jump in the total loss lifetime.

An additional finding is that the O^+ and H^+ charge exchange loss rates are often very similar, and the H^+ loss rate is actually larger than the O^+ loss rate in many of the simulation results. This is because of the short loss lifetime for H^+ at low energies (below 40 keV), which are actually faster than the high-energy O^+ loss lifetimes. Low-energy H^+ ions are therefore rapidly removed from the inner magnetosphere at a rate that is equal to or higher than the rapid loss of high-energy O^+ ions. This balance between the H^+ and O^+ charge exchange loss lifetimes further refutes the hypothesis that differential charge exchange can produce a two-phase decay. Even a delta-function in energy for the incoming plasma sheet particles would most likely not produce significant differential loss, because the L-shell dependence of the charge exchange loss lifetimes would yield a gradual transition in the total loss lifetime for the ring current energy content.

Acknowledgments. The authors would like to thank the sources of funding for this study: NASA grants NAG5-10297 and NAG-10850 and NSF grant ATM-0090165. We would also like to thank the organizing committee of the Chapman Conference on Inner Magnetospheric Modeling for inviting M.W. Liemohn to give a presentation at the meeting.

REFERENCES

Birn, J., M.F. Thomsen, J.E. Borovsky, G.D. Reeves, D.J. McComas, and R.D. Belian, Characteristic plasma properties during dispersionless substorm injections at geosynchronous orbit, *J. Geophys. Res.*, 102, 2309, 1997.

Borovsky, J.E., M.F. Thomsen, and R.C. Elphic, The driving of the plasma sheet by the solar wind, *J. Geophys. Res.*, 103, 17,617, 1998.

Chen, M.W., M. Schulz, L.R. Lyons, and D.J. Gorney, Stormtime transport of ring current and radiation belt ions, *J. Geophys. Res.*, 98, 3835, 1993.

Chen, M.W., L.R. Lyons, and M. Schulz, Simulations of phase space distributions of storm time proton ring current, *J. Geophys. Res.*, 99, 5745, 1994.

Chen, M.W., M. Schulz, G. Lu, and L.R. Lyons, Quasi-steady drift paths in a model magnetosphere with AMIE electric field: Implications for ring current formation, *J. Geophys. Res.*, 108(A5), 1180, doi: 10.1029/2002JA009584, 2003.

Daglis, I.A., The role of magnetosphere-ionosphere coupling in magnetic storm dynamics, in *Magnetic Storms, Geophys. Monogr. Ser., vol. 98*, edited by B. T. Tsurutani *et al.*, pp. 107-116, AGU, Washington, D. C., 1997.

Daglis, I.A., and J.U. Kozyra, Outstanding issues of ring current dynamics, *J. Atmos. Solar-Terr. Physics*, 64, 253-264, 2002.

Daglis, I.A., R.M. Thorne, W. Baumjohann, S. Orsini, The terrestrial ring current: origin, formation and decay, *Rev. Geophys.*, 37, 407-38, 1999.

Daglis, I.A., J.U. Kozyra, Y. Kamide, D. Vassiliadis, A. S. Sharma, M.W. Liemohn, W.D. Gonzalez, B.T. Tsurutani, and G. Lu, Intense space storms: Critical issues and open disputes, *J. Geophys. Res.*, 108(A5), 1208, doi: 10.1029/2002JA009722, 2003.

Dessler, A.J., and E.N. Parker, Hydromagnetic theory of geomagnetic storms, *J. Geophys. Res.*, 64, 2239, 1959.

Ebihara, Y., and M. Ejiri, Modeling of solar wind control of the ring current buildup: A case study of the magnetic storms in April 1997, *Geophys. Res. Lett.*, 25, 3751, 1998.

Ebihara, Y., and M. Ejiri, Simulation study on fundamental properties of the storm-time ring current, *J. Geophys. Res.*, 105, 15,843, 2000.

Feldstein, Y.I., L.A. Demukhina, U. Mall, and J. Woch, On the two-phase decay of the Dst-variation, *Geophys. Res. Lett.*, 27, 2813, 2000.

Fok, M-C., J.U. Kozyra, A.F. Nagy, C.E. Rasmussen, and G.V. Khazanov, A decay model of equatorial ring current and the associated aeronomical consequences, *J. Geophys. Res.*, 98, 19,381, 1993.

Fok, M.-C., *et al.*, Global ENA image simulations, *Space Sci. Rev.*, 109, 77, 2003.

Friedel, R.H.W., H. Korth, M.G. Henderson, M.F. Thomsen, and J.D. Scudder, Plasma sheet access to the inner magnetosphere, *J. Geophys. Res.*, 106, 5845, 2001.

Friedrich, E., G. Rostoker, and M.G. Connors, Influence of the substorm current wedge on the Dst index, *J. Geophys. Res.*, 104, 4567-4575, 1999.

Greenspan, M.E., and D.C. Hamilton, A test of the Dessler-Parker-Sckopke relation during magnetic storms, *J. Geophys. Res.*, 105, 5419, 2000.

Hamilton, D.C., G. Gloeckler, F.M. Ipavich, W. Studemann, B. Wilkey, and G. Kremser, Ring current development during the great geomagnetic storm of February 1986, *J. Geophys. Res.*, 93, 14343-55, 1988.

Jordanova, V.K., L.M. Kistler, J.U. Kozyra, G.V. Khazanov, and A.F. Nagy, Collisional losses of ring current ions, *J. Geophys. Res.*, 101, 111, 1996.

Jordanova, V.K., C.J. Farrugia, L. Janoo, J.M. Quinn, R.B. Torbert, K.W. Ogilvie, R.P. Lepping, J.T. Steinberg, D.J. McComas, and R.D. Belian, October 1995 magnetic cloud and accompanying storm activity: Ring current evolution, *J. Geophys. Res.*, 103, 79, 1998.

Jordanova, V.K., C.J. Farrugia, R.M. Thorne, G.V. Khazanov, G.D. Reeves, and M.F. Thomsen, Modeling ring current proton precipitation by EMIC waves during the May 14-16, 1997, storm, *J. Geophys. Res*, 106, 7, 2001.

Jordanova, V.K., L.M. Kistler, M.F. Thomsen, and C.G. Mouikis, Effects of plasma sheet variability on the fast initial ring current decay, *Geophys. Res. Lett.*, 30(6), 1311, doi: 10.1029/2002GL016576, 2003.

Jorgensen, A.M., M.G. Henderson, E.C. Roelof, G.D. Reeves, and H.E. Spence, Charge exchange contribution to the decay of the ring current, measured by energetic neutral atoms (ENAs), *J. Geophys. Res.*, 106, 1931, 2001.

Khazanov, G.V., K.V. Gamayunov, V.K. Jordanova, and E.N. Krivorutsky, A self-consistent model of the interacting ring current ions and electromagnetic ion cyclotron waves, initial results: Waves and precipitating fluxes, *J. Geophys. Res.*, 107(A6), 1085, doi: 10.1029/2001JA000180, 2002.

Khazanov, G.V., M.W. Liemohn, T.S. Newman, M.-C. Fok, and R.W. Spiro, Self-consistent magnetosphere-ionosphere coupling: Theoretical studies, *J. Geophys. Res.*, 108(A3), 1122, doi: 10.1029/2002JA009624, 2003a.

Khazanov, G.V., K.V. Gamayunov, and V.K. Jordanova, Self-consistent model of magnetospheric ring current and electromagnetic ion cyclotron waves: The 2-7 May 1998 storm, *J. Geophys. Res.*, 108(A12), 1419, doi: 10.1029/ 2003JA009856, 2003b.

Khazanov, G.V., M.W. Liemohn, T.S. Newman, M.-C. Fok, and A.J. Ridley, Magnetospheric convection electric field dynamics and stormtime particle energization: Case study of the magnetic storm of 4 May 1998, *Ann Geophys.*, 22, 497, 2004a.

Khazanov, G.V., M.W. Liemohn, M.-C. Fok, T.S. Newman, and A.J. Ridley, Stormtime particle energization with high time resolution AMIE potentials, *J. Geophys. Res.*, doi: 10.1029/2003JA010186, in press, 2004b.

Korth, H., M.F. Thomsen, J.E. Borovsky, and D.J. McComas, Plasma sheet access to geosynchronous orbit, *J. Geophys. Res.*, 104, 25,047, 1999.

Kozyra, J.U., and M.W. Liemohn, Ring current energy input and decay, *Space Sci. Rev*, 109, 105, 2003.

Kozyra, J.U., M.C. Fok, E.R. Sanchez, D.S. Evans, D.C. Hamilton and A. F. Nagy, The role of precipitation losses in producing the rapid early recovery phase of the great magnetic storm of February 1986, *J. Geophys. Res.*, 103, 6801, 1998.

Kozyra, J.U., M.W. Liemohn, C.R. Clauer, A.J. Ridley, M.F. Thomsen, J.E. Borovsky, J.L. Roeder, and V.K. Jordanova, Two-step Dst development and ring current composition changes during the 4-6 June 1991 magnetic storm, *J. Geophys. Res.*, 107(A8), 1224, doi: 10.1029/ 2001JA000023, 2002.

Lee, L.C., G. Corrick, and S.-I. Akasofu, On the ring current energy injection rate, *Planet. Space Sci.*, 31, 901, 1983.

Li, X., D.N. Baker, M. Temerin, G.D. Reeves, and R.D. Belian, Simulation of dispersionless injections and drift echoes of energetic electrons associated with substorms, *Geophys. Res. Lett.*, *25*, 3763, 1998.

Liemohn, M.W., Yet another caveat to the Dessler-Parker-Sckopke relation, *J. Geophys. Res.*, 108(A6), 1251, doi: 10.1029/2003JA009839, 2003.

Liemohn, M.W., and J.U. Kozyra, Lognormal form of the ring current energy content, *J. Atmos. Solar-Terr. Phys.*, 65, 871, 2003.

Liemohn, M.W., J.U. Kozyra, V.K. Jordanova, G.V. Khazanov, M.F. Thomsen, and T.E. Cayton, Analysis of early phase ring current recovery mechanisms during geomagnetic storms, *Geophys. Res. Lett.*, 25, 2845, 1999.

Liemohn, M.W., J.U. Kozyra, M.F. Thomsen, J.L. Roeder, G. Lu, J.E. Borovsky, and T.E. Cayton, Dominant role of the asymmetric ring current in producing the stormtime Dst*, *J. Geophys. Res.*, 106, 10,883, 2001a.

Liemohn, M.W., J.U. Kozyra, C.R. Clauer, and A.J. Ridley, Computational analysis of the near-Earth magnetospheric current system, *J. Geophys. Res.*, 106, 29,531, 2001b.

Liemohn, M.W., A.J. Ridley, D.L. Gallagher, D.M. Ober, and J.U. Kozyra, Dependence of plasmaspheric morphology on the electric field description during the recovery phase of the April 17, 2002 magnetic storm, *J. Geophys. Res.*, 109(A3), A03209, doi: 10.1029/2003JA010304, 2004.

Lyons, L.R., and D.J. Williams, A source for the geomagnetic storm main phase ring current, *J. Geophys. Res.*, 85, 523, 1980.

Maynard, N.C., and A.J. Chen, Isolated cold plasma regions: Observations and their relation to possible production mechanisms, *J. Geophys. Res.*, 80, 1009, 1975.

McComas, D.J., S.J. Bame, B.L. Barraclough, J.R. Donart, R.C. Elphic, J.T. Gosling, M.B. Moldwin, K.R. Moore, and M.F. Thomsen, Magnetospheric plasma analyzer: initial three-spacecraft observations from geosynchronous orbit, *J. Geophys. Res.*, 98, 13,453, 1993.

Mitchell, D.G., K.C. Hsieh, C.C. Curtis, D.C. Hamilton, H.D. Voss, E.C. Roelof, and P. C:son Brandt, Imaging two geomagnetic storms in energetic neutral atoms, *Geophys. Res. Lett.*, 28, 1151, 2001.

Ober, D.M., J.L. Horwitz, and D.L. Gallagher, Formation of density troughs embedded in the outer plasmasphere by subauroral ion drift events, *J. Geophys. Res.*, 102, 14,595, 1997.

O'Brien, T.P., R.L. McPherron, and M. W. Liemohn, Continued convection and the initial recovery of Dst, *Geophys. Res. Lett.*, 29(23), 2143, doi: 10.1029/2002GL015556, 2002.

Ohtani, S., M. Nosé, G. Rostoker, H. Singer, A.T.Y. Lui, and M. Nakamura, Storm-substorm relationship: Contribution of the tail current to *Dst*, *J. Geophys. Res.*, 106, 21,199, 2001.

Pollock, C.J., *et al.*, First medium energy neutral atom (MENA) images of Earth's magnetosphere during substorm and stormtime, *Geophys. Res. Lett.*, 28, 1147, 2001.

Rairden, R.L., L.A. Frank, and J.D. Craven, Geocoronal imaging with Dynamics Explorer, *J. Geophys. Res.*, 91, 13,613, 1986.

Reeves, G.D., and H.E. Spence, Charge exchange contribution to the decay of the ring current measured by energetic neutral atoms (ENAs), *J. Geophys. Res.*, 106, 1931-1937, 2001.

Sckopke, N., A general relation between the energy of trapped particles and the disturbance field near the Earth, *J. Geophys. Res.*, 71, 3125, 1966.

Søraas, F., K. Aarsnes, K. Oksavik, and D.S. Evans, Ring current intensity estimated from low altitude proton observations, *J. Geophys. Res.*, 107, 1149, doi: 10.1029/2001JA000123, 2002.

Søraas, F., K. Oksavik, K. Aarsnes, D.S. Evans, and M.S. Greer, Storm time equatorial belt—an "image" of RC behavior, *Geophys. Res. Lett.*, 30(2), 1052, doi: 10.1029/ 2002GL015636, 2003.

Stern, D.P., The motion of a proton in the equatorial magnetosphere, *J. Geophys. Res.*, 80, 595, 1975.

Takahashi, S., T. Iyemori, and M. Takeda, A simulation of the storm-time ring current, *Planet. Space Sci.*, 38, 1133-1141, 1990.

Takahashi, S., M. Takeda, and Y. Yamada, Simulation of storm-time partial ring current system and the dawn-dusk asymmetry of geomagnetic variation, *Planet. Space Sci.*, 39, 821, 1991.

Tinsley, B.A., and S.-I. Akasofu, A note on the lifetime of the ring current particles, *Planet. Space Sci.*, 30, 733, 1982.

Tsyganenko, N.A., H.J. Singer, and J.C. Kasper, Storm-time distortion of the inner magnetosphere: How severe can it get?, *J. Geophys. Res.*, 108(A5), 1209, doi: 10.1029/ 2002JA009808, 2003.

Turner, N.E., D.N. Baker, T.I. Pulkkinen, and R.L. McPherron, Evaluation of the tail current contribution to Dst, *J. Geophys. Res.*, 105, 5431, 2000.

Volland, H. A semiempirical model of large-scale magnetospheric electric fields, *J. Geophys. Res.*, 78, 171, 1973.

Walt, M., and H.D. Voss, Losses of ring current ions by strong pitch angle scattering, *Geophys. Res., Lett.*, 28, 3839, 2001.

Wygant, J., D. Rowland, H.J. Singer, M. Temerin, F. Mozer, and M.K. Hudson, Experimental evidence on the role of the large spatial scale electric field in creating the ring current, *J. Geophys. Res.*, 103, 29,527, 1998.

J.U. Kozyra and M.W. Liemohn, Atmospheric, Oceanic, and Space Sciences Department, University of Michigan, 2455 Hayward St., Ann Arbor, MI 48109-2143 (liemohn@umich.edu, jukozyra@umich.edu).

Substorm Associated Spikes in High Energy Particle Precipitation

E. Spanswick[1], E. Donovan[1], W. Liu[2], D. Wallis[3], A. Aasnes[4], T. Hiebert[1], B. Jackel[1], M. Henderson[4], and H. Frey[5]

Using data from the 13 instrument CANOPUS riometer array in north-central Canada, we have examined a large number of substorm events. Here, we focus on a substorm associated transient "spike" of significant absorption. We present a statistical analysis of temporal structure, propagation characteristics, and relative occurrence of absorption spikes seen with the CANOPUS array. We also present examples of both isolated transient spike events and a single propagating event. Seen from any one station, the spike lasts several minutes. More globally, it typically takes tens of minutes to propagate across the CANOPUS array. The propagation is in general a combination of azimuthal (ie., East or West) and poleward motion. Spikes are associated with the vast majority of substorms and at least some pseudobreakups. Simultaneous X-ray images confirm that the spike is a spatially localized region of high-energy precipitation and not, for example, a boundary. We discuss possible magnetospheric sources of this precipitation.

1. INTRODUCTION

There is contention over the nature of almost every major aspect of the onset. An important question is whether formation of the Near Earth Neutral Line (NENL) leads or follows Current Disruption (CD) in the inner magnetosphere [see eg., *Baker et al.*, 1996; *Lui et al.*, 1996]. That this remains unresolved reflects the difficulty in the interpretation of existing substorm onset observations. Onset takes place on the timescale of seconds. Onset is localized to some magnetospheric location, so the paucity of *in situ* observations means that we are almost always getting information from the "wreckage" that follows onset, rather than the onset itself. The macroscale topological evolution in the late growth and early expansive phase sees major changes in precipitation, convection, currents, and other parameters on a time scale of minutes, which is unfortunately comparable to information communication times between different magnetospheric (ie., the CD and NENL) regions, and between the magnetosphere and the ionosphere. Thus even though we often have essentially global information from the ionospheric projection of substorm activity, and even when there is a clear sequence of recognized ionospheric onset signatures such as Pi2s, auroral breakup, and negative H-bays, it is not clear that this provides an unambiguous picture of the order of events in the magnetosphere. This is exacerbated by uncertainties in both the magnetic mapping and our understanding of the magnetospheric processes that give rise to those ionospheric signatures.

Closure of the onset question is a fundamental objective in space science. An important research avenue in this context is to unambiguously identify the magnetospheric processes that correspond to various ionospheric signatures. During the time around onset, there are dramatic changes in both the high energy magnetospheric charged particle population, as well as high energy electron precipitation [eg., *Baker et al.*, 1981; *Håland et al.*, 1999]. Many onset related phenomena, such as current disruption and dipolarization, Bursty Bulk Flows (BBFs), thin current sheets, reconnection, and flux

[1]Department of Physics and Astronomy, University of Calgary, Calgary, AB
[2]Canadian Space Agency, Ottawa, ON
[3]Magnametrics, Ottawa, ON
[4]Los Alamos National Laboratory, Los Alamos, NM
[5]Space Science Laboratory, University of California Berkeley, CA

The Inner Magnetosphere: Physics and Modeling
Geophysical Monograph Series 155

10.1029/155GM24

ropes, can be expected to impact the transport, acceleration, and precipitation of high energy electrons. Tracking the evolution of the high energy magnetospheric charged particle population and high energy electron precipitation on a near global scale, as well as connecting any changes to onset related processes, is an important part of our arsenal of tools for attacking the substorm question.

A Relative Ionospheric Opacity Meter (riometer) is a ground-based instrument that measures the intensity of cosmic radio noise. Riometers typically operate at 20 to 60 MHz. Significant absorption of the cosmic radio noise is indicated by a weaker than normal signal at a given right ascension, declination, and frequency. Absorption is attributed directly to enhanced ionization at altitudes where electron motion is collision dominated, and hence controlled in part by precipitation of high energy (in the case of e^-, >20 keV) particles. *Baker et al.* [1981] used Los Alamos National Laboratories (LANL) Charged Particle Analyzer satellite data and magnetically conjugate riometer data to demonstrate that during substorm injections, provided conditions for strong pitch angle scattering were met, riometer absorption is an excellent proxy for the geosynchronous >30 keV electron flux. Thus, while riometers lack the energy resolution of in situ particle detectors, they can provide more global coverage of substorm injections giving, for example, the radial extent and azimuthal evolution of the changes in the high energy electron population.

Another prominent substorm signature in riometer data is the "absorption spike" (herein referred to as the "spike"). These events are characterized by a rapid and intense increase in absorption lasting for ~2-3 min at or around onset [see eg., *Hargreaves et al.*, 1979; *Nielsen et al.*, 1980; *Baker et al.*, 1981; *Hargreaves et al.*, 2001]. *Hargreaves et al.* [1997] used imaging riometer data to argue that spikes are spatially localized, elongated in the East-West direction, and have average ionospheric dimensions of roughly 150 km by 70 km. For one event, *Nielsen et al.* [1982] showed that the spike was associated with a strong field aligned bi-directional anisotropy in GEOS-2 <100 keV electron fluxes. There have been a number of geosynchronous observations of field-aligned tens of keV electron beams [*Parks et al.*, 1977; *Kremser et al.*, 1988]. For the few events studied in those two papers, the geosynchronous particle flux spike was at the beginning of an injection at the same satellite, and lasted several minutes. Although the temporal characteristics of these beams and their association with substorm onsets are reminiscent of the riometer spikes, a one to one correspondence between the two phenomena has not been made. Previous studies of the spikes have utilized data from single imaging riometers or closely spaced broad-beam riometers with fields of view small in comparison to the spatial extent of the auroral substorm. The temporal characteristics of the spike as seen from an individual station have been explored with a limited number of events in earlier papers [see eg., *Nielson* 1978, *Ranta et al.* 1981]. Using imaging riometers, the propagation has been explored on a local scale by, for example *Hargreaves et al.* [1979] and *Nielsen et al.* [1980]. These studies led to contradictory conclusions, the first (*Hargreaves et al.*) being that the spike does not propagate, and the second that the predominant motion of the spike is northward.

Here, we utilize data from the geographically extended CANOPUS array of single-beam (also called integrating) riometers to explore the temporal and spatial evolution of this substorm phenomenon. We use single station riometer data from a large number of substorms to examine the temporal characteristics of the spike as seen at one station and the temporal relationship between the spike and injections and other onset related phenomena. We use multiple station data to explore the propagation of the spike across distances comparable with mesoscale auroral substorm features (ie., several hours of local time and ten or more degrees of latitude). We also demonstrate, for one event, that the precipitation causing the spike is also detectable via satellite X-ray images. As we use a large number of substorms identified in more than a decade of CANOPUS riometer data, our statistical results are more comprehensive than those of previous studies (ie., the single station results, relationship to onset features) and our observations of the large-scale propagation of this feature are new.

2. DATA

We rely heavily on data from the single beam (ie., integrating) CANOPUS riometers. These instruments are operated at 13 sites in north-central Canada (see map in Figure 1). Key components of the array are an East-West chain which extends roughly 4 hours of Magnetic Local Time (MLT) at roughly 67° invariant latitude, and a north-south chain (the "Churchill line") with coverage between ~60° and ~80° invariant latitude. Details about the location and instrument complement of the CANOPUS sites are widely available (see eg., *Rostoker et al.* [1995]). These riometers are dual dipole broad-beam (~60°) antennae, operate at 30 MHz, and collect data at 1 sample per second. The final data is post-processed down to a cadence of 1 sample every 5 seconds. The raw 5 second data (signal strength in volts or dB) must be converted to dB absorption if comparison of the relative importance of two absorption sources (ie. spikes vs. injection) is required (we present data in both formats). The bottom panel of Figure 1 is a stack plot of riometer data (raw signal in dbs) from five CANOPUS stations. The spike is the transient feature highlighted by the gray swath and is

[redacted]

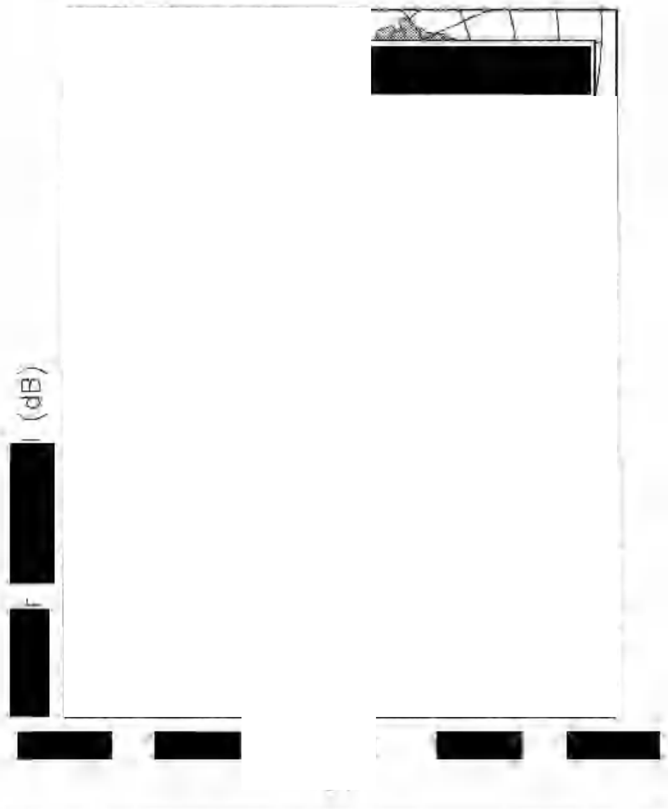

[redacted]

[redacted]

[redacted]

[redacted]

[redacted]

[redacted]

[redacted]

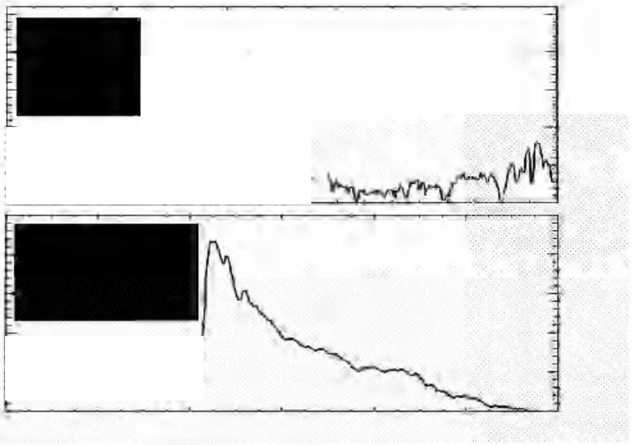

[redacted]

[redacted]

[redacted]

within the CANOPUS array for the vast majority of these substorms. In this section we present specific examples of absorption spikes and explore their general temporal structure, propagation characteristics, and MLT occurrence statistics.

3.2. Case Studies

We present data from two events. For the first event, we show three spikes observed by the Gillam riometer during a sequence of 2 pseudobreakups followed by an onset. For the second event, we show a spike as seen in 5 riometers and the PIXIE X-ray imager. The onset in the second event was preceded by a pseudobreakup. For our purposes, our operational definition of a pseudobreakup is a small activation which has some features of an onset, but lacks all the elements of a global substorm. In both cases, for example, the final activation that we call the onset results in a significant dipolarization seen at GOES at several hours or more away from the onset meridian. This definition is consistent with the definition of *McPherron* [1991].

On September 29, 1996, there was a sequence of two pseudobreakups, followed by an onset. The stack plot (Plate 1) shows data from the Gillam MSP, the CANOPUS Churchill line magnetometers, GOES 8, and the Gillam riometer. The two pseudobreakups occur at ~0505 and ~0525 UT, while the onset occurs at roughly ~0537 UT. As can be seen from the 557 nm Gillam MSP and Churchill line magnetometer data, auroral brightenings and electrojet enhancements accompany the pseudobreakups and the onset. There are at least four Pi2 bursts (Pinawa data, second panel from bottom), two of which accompany the pseudobreakups and a third the onset. The others (one occurs between ~0515 and ~0523) likely indicate pseudobreakups away from the Churchill Meridian. GOES 8 is located about two hours MLT East of the Churchill line. Comparison of the magnetic inclination at GOES 8 (in black) with its median value for the same local time and time of year (in red) shows stretching until 0540, after which there is a dipolarization back to (ostensibly) normal values. This, together with the Canadian Geological Survey magnetic field data from Poste-de-la-Baleine Quebec (not shown), is our basis for calling the 0537 UT activation an onset rather than a pseudobreakup. The bottom panel of Plate 1 shows the Gillam riometer data (db absorption). Gillam was the only station in the CANOPUS array to observe spikes. There are three spikes, each corresponding to the auroral brightenings. Again, two accompany pseudobreakups and the third the onset. There is no spike accompanying the large Pi2 burst between ~0515 and ~0523. The third spike is definitely followed by, and possibly preceded by, injection related absorption.

In contrast to the transient localized spikes illustrated in the 960929 event, it is more typical to observe spike events propagating across the CANOPUS array. On May 25, 1998 there was a pseudobreakup at approximately 0635 UT followed by an onset. Onset appears clearly in the Fort Simpson magnetometer (#2 in Plate 2) around 0642 UT. It is associated with Pi2 bursts in the Victoria magnetometer (subauroral and in the same meridian as #2), and an auroral brightening seen in Polar UVI data (not shown). In GOES 9, there is a small dipolarization around the pseudobreakup, which stalls (there is even a brief period of increased stretching) and is followed by a larger one that starts at around 0642. Dipolarization is seen later in GOES 8.

The top two panels of Plate 2 summarize the riometer and PIXIE X-ray data for this event. PIXIE observed an isolated region of precipitation over Fort Simpson at precisely the time of an absorption spike, this is also the exact time and location of onset. Another spike event is evident over the Churchill line some 10 minutes later when PIXIE again observed a localized patch of X-ray aurora. While the riometer signatures in the intervening time stretch our definition of what we call a spike, there appears to be a propagation of a spike-like feature from Fort Simpson towards the Churchill line. Indeed the few PIXIE images from this time period (6:44 and 6:51) show little evidence of the spike. However the riometer signature suggests that there may have been a spatial and/or intensity change in the spike, both of which would cause it to fall out of PIXIE's observable range.

Together, these two events highlight the following: (1) spikes accompany at least some pseudobreakups and onsets; (2) spikes propagate azimuthally over 100's of kilometers; (3) spikes are a consequence of spatially localized precipitation.

3.3. Spike Characteristics

During this study we compiled various data sets tailored to specific characteristics of the spike. In each case, we manually identified spikes as sudden bursts of precipitation that were distinctly separate from the nominal absorption. All spikes were selected from time spans between 18 and 6 MLT. Every spike we have examined in detail is associated with a pseudobreakup or onset activation (note: this does not preclude spikes not associated with substorms [see eg. *Hargreaves et al.*, 1997]).

Our first data set was adapted to investigate the temporal evolution of the spike. We selected 92 unambiguous events from the Gillam riometer and found that on average the "ramp up" time is around one minute. Some spikes can reach their maximum absorption in as little as 15 seconds, rendering them among the fastest developing signatures in riometer data. Typically spike related absorption will last for 1-2 minutes and then decay at the same rate at which it

[redacted]

[redacted]

[redacted] [redacted] [redacted]

[redacted]

[redacted]

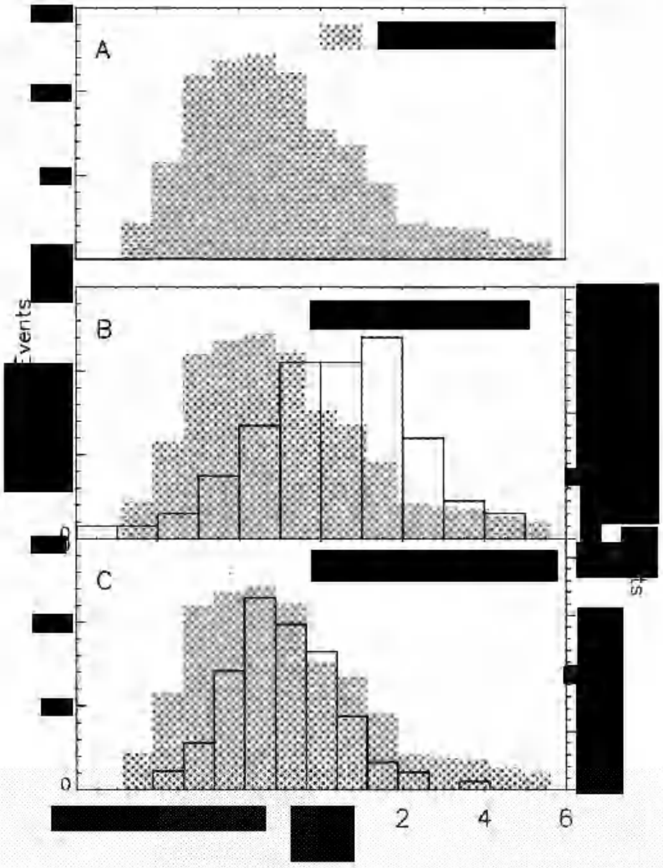

[redacted]

[redacted]

[redacted]

prior to local midnight but there is still a substantial population of events which occur outside this region. When compared to the occurrence of dispersionless electron injection regions [*Thomsen et al.*, 2001], which we loosely associate with the onset of injections in the riometers (ie. as per the results of *Baker et al.* [1981]), there is a distinct difference in the shape of the two distributions (see B in Figure 4). Dispersionless electron injections peak in the hours after midnight whereas the spikes are distinctly a pre-midnight phenomena. In contrast, the occurrence of substorm onset appears to be contained within the distribution of spike occurrence (see Figure 4). Remember that our spike occurrence contains those events which were isolated as well as those which propagated to a particular location. It is not unlikely that the source region of the spike is in fact the substorm onset region and the broadened wings represent propagation. To test this hypothesis we sampled 40 events from the wings of the occurrence distribution, 19 from the dusk side and 21 from dawn. From these events, 17 of them exhibited clear propagation. In all cases the propagation was away from the midnight meridian, implying a motion of the spike away from substorm onset.

4. DISCUSSION

Using data from the 13 station CANOPUS riometer array we have examined a large number of spike events. The bulk properties of absorption spikes reported in this paper are summarized in the table below.

Riometer spikes are associated with the majority of substorms and at least some pseudobreakups. Although we have not established a connection to the pseudobreakup, we have found clear examples of events where there is a one-to-one correspondence. We have found that for single injection events, the riometer signature can be classified in terms of this spike (see Figure 2) which is a repeatable phenomena and distinctly separate from the typical riometer injection signature. In a single riometer, spikes appear as sudden bursts of absorption reaching their maximum in approximately one minute (72 event avg.). This absorption will last for ~1-2 minutes before decaying. Spike events in general, may be isolated transient signatures (see Plate 1), or features that propagate across great distances (see Plate 2, Figure 1). X-ray images confirm that the spike is a spatially localized region of precipitation and corroborate the propagation from riometer-to-riometer. We found that average azimuthal velocities of the spike are ~2-3 km/sec, at 90 km altitude (75 events: 200 samples). When projected to the equatorial plane for a dipole field, velocities are comparable to those reported by *Liou et al.* [2002] for the dipolarization front at geosynchronous orbit. We have also found that the MLT occurrence of spikes for a single riometer (813 spikes observed [1989-1999]) peaks in the premidnight sector but with a significant number of spikes observed towards dawn and dusk. Spikes in this flank population display motion away from the midnight meridian in all cases where propagation was detected. Comparison of spike occurrence to that of dispersionless electron injections reveals a westward shift of the spikes which is inconsistent with the notion of a typical riometer injection signature. The distribution of substorm onsets, however, appears to be encompassed in the spike occurrence (Panels B & C of Figure 4).

Riometer Spike Properties

Occurrence	- accompany the majority of substorms (also associated w/pseudobreakups)
Spatial Scale	- ~100 km × 70 km [*Hargreaves et al.* 1997] - associated w/localized X-ray emissions (PIXIE)
Temporal Structure	- average "ramp up" time ~1 min. - average lifetime ~2-3 min. (single station view)
Propagation Characteristics	- exclusively east-west and poleward - can propagate across 100's of km - avg. east-west speed ~2-3 km/s at 90 km altitude

We postulate that the riometer spike is in fact an onset related phenomena. The overlap in spike and onset occurrence conceivably represents the spike "source region". Spikes created in this fashion are also most likely those with the shortest ramp up times. Materializing in as little as 15 seconds, these spikes constitute the fastest signature associated with the substorm (*J. Borovsky private communication*). It also appears, from the few events we have looked at in detail, that the first occurrence of the spike is associated with the onset. In the simplest of events (ie. a single spike), this spike either decays quickly (see Plate 1) or propagates away from the onset region azimuthally and poleward (see Plate 2). Observations of Pi2 bursts, which also accompany at least some pseudobreakup and onset spikes (see Plate 4), as well as the similarity in propagation speed to that of the dipolarization front are all consistent with this hypothesis.

Placing the spike at the time and location of onset adds this phenomena to the list of dynamic processes occurring during the substorm but provides little insight into possible magnetospheric sources. A number of processes could be responsible for producing a spatially localized disturbance of high energy electron precipitation, which then propagates away from the onset region. Major contenders are the dipolarization, thin current sheets, reconnection, turbulence, and BBFs. The dipolarization, for example, involves the shortening of flux

tubes on a time scale of several minutes which is long compared to gyro and bounce periods of higher energy electrons. It can be shown that all electrons in this flux tube end up closer to field-aligned after the dipolarization, and that this should transport previously trapped electrons into the loss cone on a time scale comparable to the shortening of the flux tube. All of these electrons will precipitate, so a several minute long burst of high energy precipitation (seen at the footpoint of the flux tube) would follow. We have compared the passage of the spike over the fields of view of our MSPs (Fort Smith and Gillam), focussing our attention on the 486 nm proton auroral emissions. *Donovan et al.* [2003] have argued that poleward motion of the equatorward boundary of those emissions indicates dipolarization in that meridian. Though we have not shown these results here (we plan a detailed study of a number of events as the basis for a follow up paper), we have found that the spike and poleward motion of the proton aurora do happen relatively close in time, but often separated by several or more minutes.

The two case studies we presented support a connection between the spike and Pi2s in onsets and pseudobreakups. One phenomenological picture is that mid-tail reconnection spawns BBF-type flows that brake in the inner magnetosphere, initiating Pi2s, substorm current wedge, and other near-Earth phenomena (see eg., *Shiokawa et al.*, [1998] and *Fairfield et al.*, [1999]). The spike then, could be connected to reconnection, thin-current sheets, or some facet of the BBF flow structure. If this is the case, then the azimuthal propagation and radial localization of the spikes will provide valuable information in terms of our ultimate understanding of the connection between the mid-tail and inner magnetosphere during substorms.

It is also possible that the spike is the same phenomena identified in geosynchronous particle data by *Kremser et al.* [1988], and *Parks et al.* [1977]. Again, this connection is attractive because of the similarity in behavior in time between the riometer and geosynchronous particle spike, and because the latter consists of field-aligned beams of high energy electrons and so should give a riometer signature. Again, this connection is weak at first glance because in the few events presented in those two papers the geosynchronous spike appeared to be at the very beginning of injections seen at the same satellite, and we sometimes see the spike embedded (temporally) in the riometer signature of an injection (see Figure 2). It may be that a more comprehensive statistical study of the geosynchronous data will lead to similar examples in the geosynchronous spike. Further, we should be able to identify events where a satellite with pitch angle resolved high energy particle data is in the inner magnetosphere and magnetically conjugate to a riometer at the time of a spike observation (CRESS is one possibility that we will follow up, and there are others). Such conjugate observations would allow for a firm connection between the geosynchronous and riometer phenomena (or strong evidence to the contrary).

Clearly future work on this phenomena is required. In addition to the CRESS-type study mentioned in the previous paragraph, we intend to follow this study up with an analysis of 10 or more events where the spike can be placed in time and space relative to other onset features (Pi2s, dipolarization seen in MSP and GOES data, injections, etc). Further work on this problem must involve simulations to explore specific mechanisms at play in the magnetosphere in terms of their ability to produce spatially and temporally localized high energy precipitation. Our overarching question is "what magnetospheric substorm associate process is most directly tied to the spike?". We believe that question is closeable with the results of a tractable amount of work. We further believe that this substorm feature is an important piece of the puzzle and warrants much more attention than it has received in recent years.

Acknowledgements. The Canadian Space Agency provided financial and operational support for the CANOPUS program (riometers, magnetometers and photometers). GOES data was provided by Howard Singer.

REFERENCES

Baker *et al.*, Near equatorial, high-resolution measurements of electron precipitation and L ≅ 6.6, *J. Geophys. Res.*, 86, 2295, 1981.

Baker *et al.*, Neutral line model of substorms: Past results and present view, *J. Geophys. Res.*, 101, 12975-13010, 1996.

Donovan *et al.*, Ground-based optical determination of the b2i boundary: a basis for an optical MT-index, *J. Geophys. Res.*, 108, doi:10.1029/2001JA009198, 2003.

Fairfield *et al.*, Earthward flow bursts in the inner magnetotail and their relation to auroral brightenins, AKR intensifications, geosynchronous particle injections and magnetic activity, *J. Geophys. Res.*, 104, 355-370, 1999.

Hargreaves *et al.*, A study of substorm associated nightside spike events in auroral absorption using imaging riometers, *J. Atmos. Terr. Phys.*, 59, 853, 1997.

Hargreaves *et al.*, Properties of spike events in radio absorption, *J. Geophys. Res.*, 84, 4245, 1979.

Hargreaves *et al.*, Temporal fine structure of nighttime spike events in auroral radio absorption, studied by a wavelet method, *J. Geophys. Res.*, 106, A11, 24621-24636, 2001.

Håland *et al.*, Magnetospheric and ionospheric response to a substorm: Geotail HEP-LD and Polar PIXIE observations, *J. Geophys. Res.*, 104, A12, 28459-28474, 1999.

Imhof *et al.*, The Polar Ionospheric X-ray Imaging Experiment (PIXIE), *Space Sci. Rev.*, 71, 385, 1995.

Kremser *et al.*, Field-aligned beams of energetic electrons (16 keV < E ≲ 80 keV) observed at geosynchronous orbit at substorm onset, *J. Geophys. Res.*, 93, 14453-14463, 1988.

Liou *et al.*, Magnetic dipolarization with substorm expansion onset, *J. Geophys. Res.*, 107, 2002.

Lui, A.T.Y, Current disruption in the Earth's magnetosphere: Observations and models, *J. Geophys. Res.*, 101, 13067, 1996.

McPherron R.L., Growth Phase of Magnetospheric Substorm, *J. Geophys. Res.*, 75, 5592-5599, 1970.

McPherron *et al.*, Satellite studies of magnetospheric substorms on August 15, 1968, 9. Phenomenological model for substorms, *J. Geophys. Res.*, 78, 3131-3149, 1973.

McPherron, R.L., Physical processes producing magnetospheric substorms and magnetic storms, *in Geomagnetism*, 4, 593-739, 1991.

Nielsen *et al.*, Variations in ionospheric currents and electric fields in association with absorption spikes during the substorm expansion phase, *J. Geophys. Res.*, 83, 5645-5654, 1978.

Nielsen, E., Dynamics and spatial scale of auroral absorption spikes associated with the substorm expansion phase, *J. Geophys. Res.*, 85, 2092, 1980.

Nielsen *et al.*, The electron pitch angle distribution at geosynchronous orbit associated with absorption spikes during the substorm expansion phase, *J. Geophys. Res.*, 87, 887-894, 1982.

Parks *et al.*, Characteristics of magnetospheric particle injection deduced from events observed on August 18, 1974, *J. Geophys. Res.*, 82, 5208, 1977.

Ranta *et al.*, Development of the auroral absorption substorm: studies of pre-onset and sharp onset using an extensive riometer network, *Planet. Space Sci.*, 29, 1287-1313, 1981.

Rostoker *et al.*, CANOPUS - A ground based instrument array for remote sensing the high latitude ionosphere during the ISTP/CGS program, *Space Sci. Rev.*, 71, 743, 1995.

Shiokowa *et al.*, High-speed ion flow, substorm current wedge, and multiple Pi 2 pulsations, *J. Geophys. Res.*, 103, 4491-4507, 1998.

Thomsen *et al.*, Two-satellite observations of substorm injections at geosynchronous orbit, *J. Geophys. Res.*, 106, 8405-8416, 2001.

E. Spanswick, E. Donovan and T. Hiebert, Department of Physics and Astronomy, University of Calgary, Calgary, T2N 1N4. (e-mail: emma@phys.ucalgary.ca; eric@phys.ucalgary.ca; tbhieber@ucalgary.ca)

W. Liu, Canadian Space Agency, (e-mail: William.Liu@space.gc.ca)

A. Aasnes, Los Alamos National Laboratory, (e-mail: aasnes@lanl.gov)

D. Wallis, Magnametrics, (e-mail: dwallis@eisa.com)

H. Frey, Space Science Laboratory, University of California Berkeley, CA (e-mail: hfrey@ssl.berkeley.edu)

Ring Current Behavior as Revealed by Energetic Proton Precipitation

F. Søraas, K. Aarsnes, and D.V. Carlsen

Department of Physics and Technology, University of Bergen, Norway.

K. Oksavik

Department of Physics, University of Oslo, Norway.

D.S. Evans

NOAA Space Environment Center, Boulder, Colorado, USA.

The precipitation of energetic ions and electrons into the upper atmosphere is a direct manifestation of their acceleration and pitch angle scattering in the magnetosphere. Electric fields inject/convect the particles from the tail plasma sheet towards the earth, and when closer to the Earth they spread in local time due to magnetic field forces. The electrons drift towards the morning sector and the ions towards the evening sector thus creating the ring current. Certain aspects of the ring current behavior can be revealed by the precipitating energetic protons. From these particles a proxy for the energy injection rate into the ring current can be estimated, and a ring current index which correlates highly with the pressure corrected D_{st}* can be calculated. The pitch angle distribution of the precipitating ring current protons is either isotropic with a filled loss cone, or anisotropic with an almost empty loss cone. In the isotropic zone the ring current protons are stable to wave growth. In the anisotropic zone, however, the protons are unstable to wave growth. Thus, there exists a fairly wide L-value interval equatorward of the isotropic zone with ample conditions for EMIC (electromagnetic ion-cyclotron) wave generation. In the anisotropic zone a number of wave-particle phenomena linked to the precipitating protons take place: enhanced proton pitch angle scattering manifested as intensity peaks at mid-latitudes, SAR arc formation, Pc1 and IPDP wave generation, and increased loss of relativistic electrons. An important decay process for the ring current protons is through charge exchange. The ENAs (Energetic Neutral Atoms) from this process create a well defined belt or region of ENA and protons observed at low altitudes along the geomagnetic equator. This belt reveals important aspects of the ring current such as: the ring current injection region, the drift of ring current particles, and convection losses of the ring current particles to the dayside magnetopause, and its asymmetric and symmetric behavior.

The Inner Magnetosphere: Physics and Modeling
Geophysical Monograph Series 155

10.1029/155GM25

1. INTRODUCTION

The aurora is created when energetic electrons and ions excite the atoms and molecules in the upper atmosphere. These atoms and molecules then emit light and aurora is displayed on the dark sky. The energetic charged particles in the magnetosphere are governed/take part in a number of processes. All these processes imprint their mark on the particle population. Thus by examining the particles, their energy and pitch angle distribution and their behavior in time and space, it is possible to gain some insight into the physical mechanisms that are operating.

The main physical cause for the ground magnetic perturbations at low latitudes, D_{st}, is the variability of the ring current composed of energetic ions and electrons encircling the Earth at altitudes of several Earth radii. Due to their larger mass the ions contribute by far the most to the ring current energy density. There have been many suggestions on how the ring current particles are injected. For a review see *Tsurutani and Gonzalez* [1997] and *McPherron* [1997]. It is generally believed that the ring current is created by a combination of substorm particle injection and enhanced convection. When injected from the plasma sheet into the ring current, ions will be accelerated and precipitate to the atmosphere. During their injection ions are subjected to intense pitch angle scattering in the region of strong field line curvature that scatters or "demagnetizes" the protons [*Sergeev et al.*, 1983]. An isotropic pitch angle distribution with a filled loss cone is the result. This process is most intense in the midnight/evening sector. Using the "splash-catcher" model advocated by *O'Brien* [1964], where the loss cone is populated by some of the protons which are injected into the ring current, *Søraas et al.* [2002] used the intensity of these precipitating protons as a measure for the ring current energy injection rate.

Low altitude satellite observations give a magnified view of processes taking place within and close to the atmospheric loss cone. In the following we will concentrate on protons and discuss how observations of these particles at low altitudes can reveal information on the ring current (RC).

2. INSTRUMENTATION

The present study uses observations from the MEPED instrument on board the NOAA 12 and 15 satellites. Protons with angles 10° and 80° with the local vertical are measured in three energy channels ranging from 30 to 800 keV, and electrons above 30, 100 and 300 keV are measured at the same angles. The MEPED instrument cannot distinguish between different ion types. We therefore use the term protons in this study. The NOAA 12 satellite DOME instrument can detect relativistic electrons with energies above about 1.5 MeV whenever high energy protons with energies above 13 MeV are not dominant. The orbits of both spacecraft are circular at an altitude of about 850 km. At this altitude the atmospheric loss cone above 50° geographic latitude is around 50°. The 10°detector thus looks well into the loss cone, while the 80°detector looks at trapped protons. A full description of the satellites and their instrumentation are given by *Raben et al.* [1995] and *Evans and Greer* [2000].

3. PROTON INJECTION AND THE RING CURRENT INDEX

Figure 1 shows data from a typical NOAA satellite pass during the recovery phase of a storm in March 1998. Protons with angles 10° (solid line) and 80° (dashed line) to the local vertical are each measured in three energy channels 30-80, 80-250 and 250-800 keV.

Both the 10° and 80° protons have a well defined poleward boundary, where the particle intensities drop two orders of magnitude when the satellite enters the polar cap. On the equatorward side the 10° protons exhibit a clear boundary. The region where the proton intensities at 10° and 80° are about equal is well defined and marks the isotropic precipitation zone. The equatorward border of this zone is called the isotropic boundary (IB). Protons in the isotropic zone are subjected to intense pitch angle scattering and those inside the loss cone will penetrate into the atmosphere and be lost. The protons thus exhibit two precipitation zones, one poleward zone where the pitch angle distribution is isotropic, and an equatorward one where the pitch angle distribution is anisotropic, that is with a partly filled loss cone. This precipitation pattern has been described in a number of papers [*Hauge and Søraas*, 1975; *Lundblad and Søraas*, 1978; and others].

Plate 1 shows the intensity (color-coded) of protons precipitating into the evening sector from October 7 to November 6 in 1998. The measured proton intensities in each NOAA 15 pass are plotted vs. ILAT (invariant latitude) and time. The three top panels show protons well within the loss cone for three different energy channels. The three next panels show the same energy channels for the 80° detector, and the bottom panel shows D_{st}. The data refer to evening/midnight, as this is the MLT (magnetic local time) sector that most directly exhibits the injection of protons into the ring current.

The time period considered contains one large (−111 nT) and two smaller (−60 and −55 nT) geomagnetic storms. The intensity and latitudinal extent of the protons correlates with the D_{st}. Note that during every negative deviation in D_{st} there is increased proton precipitation and an equatorward movement of the precipitation zone, indicating a deeper injection of protons into the magnetosphere. As the size of the disturbance increases the equatorward border moves to lower latitudes and the intensity of the precipitation increases.

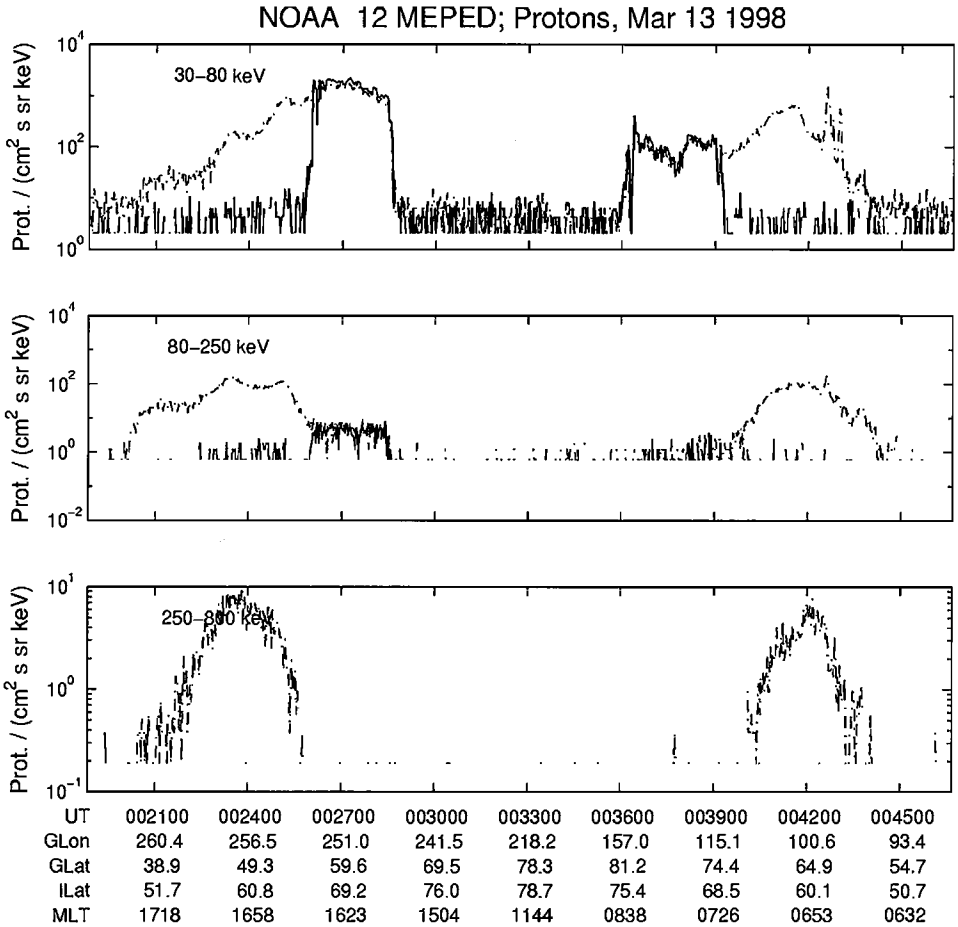

Figure 1. Typical dusk-to-dawn NOAA pass in the Northern Hemisphere. Protons with angles 10° and 80° with the vertical are measured in three energy channels ranging from 30 to 800 keV. The intensity of the 80° protons is shown by a dashed line, and the intensity of the 10° protons is shown by a solid line.

As seen from the three top panels the precipitating protons exhibit a clear IB. Poleward of this boundary the precipitation is isotropic, and equatorward of it the proton pitch angle distribution is anisotropic. Plate 1 gives a clear picture of the two-zone structure of the protons observed at low altitudes.

From Plate 1 it is seen that the intensity for both the 10° and 80° detectors exhibit a daily modulation, most prominent in the 80° detector. This behavior is due to the magnetic field control of the particles and that a satellite in low orbit observes particles on the same L-shell at different magnetic field strengths during the course of the day [*Berg and Søraas*, 1972].

Søraas et al. [2002] showed that the protons precipitating within the isotropic zone in the evening/midnight quadrant can be used as a proxy for the particle injection into the ring current. The injection rate Q(t) is not based upon solar wind parameters but directly on the observed proton precipitation rate. This is done under the assumption that the proton intensity in the loss cone follows the rate at which protons are injected into the ring current. The protons in the loss cone do not merely represent a loss from the ring current but are, in fact, a measure of the proton injection rate into the ring current. From the precipitating protons, *Søraas et al.* [2002] derived a RC index (ring current index) which is not influenced by magnetic fields generated by magnetopause, field-aligned, and tail currents (as D_{st} is). The RC index should give a "true" picture of the proton energy content in the ring current.

We will now show how the low altitude observations obtained during the larger October 1998 storm relate to D_{st} and the solar wind parameters measured by the Wind satellite. The relations between the different parameters are illustrated in Plate 2.

[redacted]

[redacted]

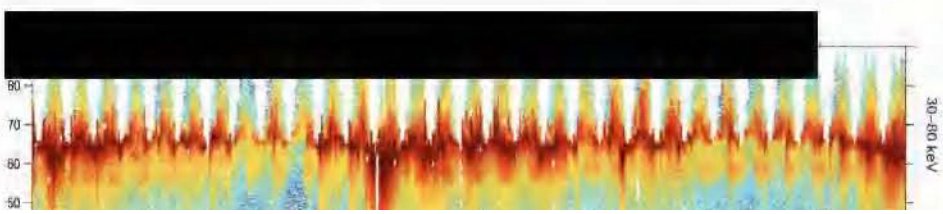

[redacted]

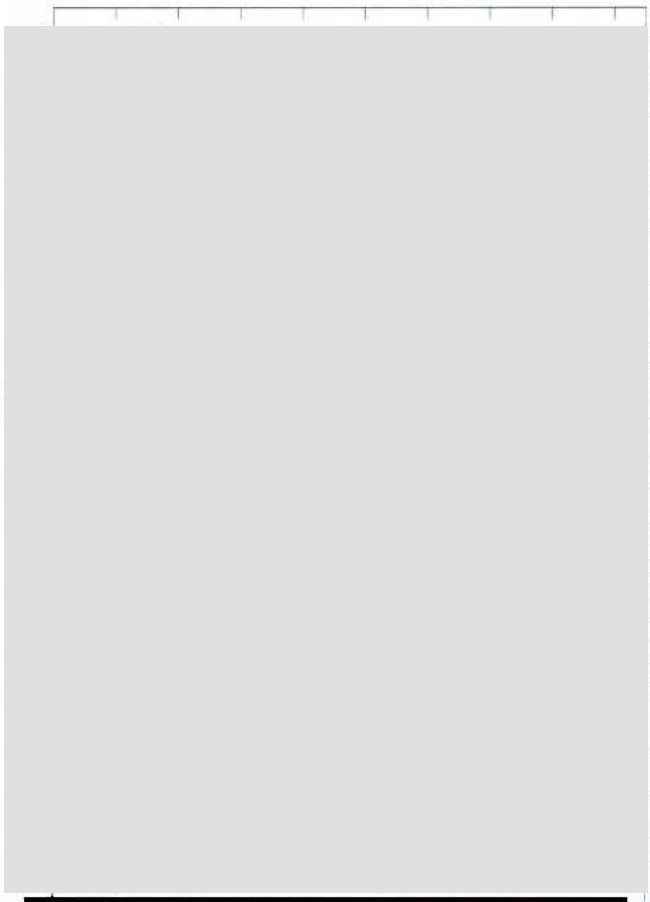

In the top panel of Plate 2 the D_{st}* (the pressure corrected D_{st}) and the RC index are shown. The correlation between the two ring current estimates is 0.94 for this 20-days period. The RC index is normalized to have the same average value as the D_{st}*. The two indices follow each other very well, and the six injection events taking place in the storm recovery phase are clearly seen in both indices.

In panel two the injection rate Q(t) as estimated from NOAA 15 satellite observations is shown. There is a small increase in Q(t) on day 290 coinciding with a small decrease in D_{st}*. One day later there is a similar increase in the injection rate and a decrease in D_{st}*. On day 292 there are two large increases in the injection rate, and the D_{st}* decreases to -111 nT in the storm main phase. The storm has an initial fast recovery back to -50 nT during this period when the injection rate is reduced. It could be argued that this initial fast recovery of the D_{st}* reflects a contribution from the cross tail current, which has a rapid dynamic [*Alexeev et al.*, 1996]. Subsequently the storm exhibits a slow recovery with multiple proton injections each followed by a decrease in D_{st}*. During the 10-days recovery there are six distinct injection events with increased Q(t), each followed by a decrease in D_{st}*. The slow recovery of this storm is due to a HILDCAA (High Intensity Long Duration AE Activity) event [*Tsurutani and Gonzalez*, 1987], characterized by the prolonged AE activity displayed in panel three. This event and its HILDCAA behavior have been discussed by *Sandanger et al.* [2004]. The AE activity is often taken as a measure for substorm activity. The AE activity and the injection rate Q(t) have very similar time development and both increase for every one of the six decreases in D_{st}* during the storm recovery phase.

In the next four panels of Plate 2 the interplanetary electric field component E_y, the IMF B_z component, the solar wind density N_{sw}, and velocity V_{sw} are shown. Notice the large positive E_y component and the intense AE activity during the storm main phase. This increased electric field and high substorm activity transport particles from the plasma sheet and deep into the magnetosphere creating the main-phase ring current.

3.1. Summary Ring Current Index

The calculated RC index gives a good estimate for the D_{st}*. The correlation between the two quantities is high, indicating that they vary in concert and that the ring current energy is for a large part due to protons being injected from the plasma sheet. It further shows that the corrected D_{st}* is a direct measure of the particle energy content in the ring current. The absolute energy content in the ring current, however, cannot be calculated by our method. In order to obtain the same average value as D_{st}* our estimate has to be normalized. Nevertheless, the normalizing factor calculated for different times is almost invariant. This indicates that the ring current and the proton precipitation are intimately connected. Due to the good correlation between the estimated and measured D_{st}, it would be possible to use observations from the NOAA satellites to derive a space-based equivalent of the D_{st} index in near real-time without many of the problems associated with the ground-based D_{st} currently in use [*Søraas et al.*, 2002].

4. THE STORM TIME EQUATORIAL BELT

The production of ENAs by charge exchange of ring current ions with neutral hydrogen in the geocorona was predicted by *Dessler et al.* [1961] and is an important loss process for the ring current. The energy range 20-200 keV includes the carriers of the major part of the ring current energy. The first observational data on ENA precipitation giving rise to low latitude protons was obtained in 1969 and 1970 from the AZUR satellite [*Moritz*, 1972; *Hovstadt et al*, 1972]. *Moritz* [1972] suggested that these ions at low L-values near the equatorial plane come from ENAs born in charge exchange of ring current ions. The ENAs originating from higher L-values may reach low altitudes where they are reionized by charge exchange and become energetic ions trapped by the magnetic field. *Tinsley* [1981] has given a comprehensive review of these equatorial ions and some of their consequences for the equatorial atmosphere.

Søraas et al. [2003] studied the STEB (Storm Time Equatorial Belt) for a number of geomagnetic storms. In this report we will consider the STEB behavior during a major geomagnetic storm. The intense ($D_{st} = -358$ nT) geomagnetic storm starting on March 31, 2001, is an example of such a storm. Figure 2 display the observations of the particles measured at the magnetic equator arranged by the local time (LT) of observation.

In the main phase of the storm the low L-value particles exhibit a clear LT asymmetry. The intensity in the midnight/evening sector is markedly higher than in the postnoon/morning sector (two top panels). A delay in the appearance of the particles with LT is also apparent. The (30 to 80 keV) particles appear simultaneously at 02 and 19 LT. There is, however, a delay before they appear in the morning sector (14 and 07 LT). As seen from the D_{st} index, the March storm exhibits the double main phase depression typical for large storms. This double structure is also clearly seen in the intensity of the low-latitude particles. It appears that the ring current injection region is more widespread in LT during the first RC injection than in the second one. The intensity in the first injection is about equal at 02 and 19, but the second injection is more concentrated around 19 LT. In the bottom panel the ratio between the intensities measured at

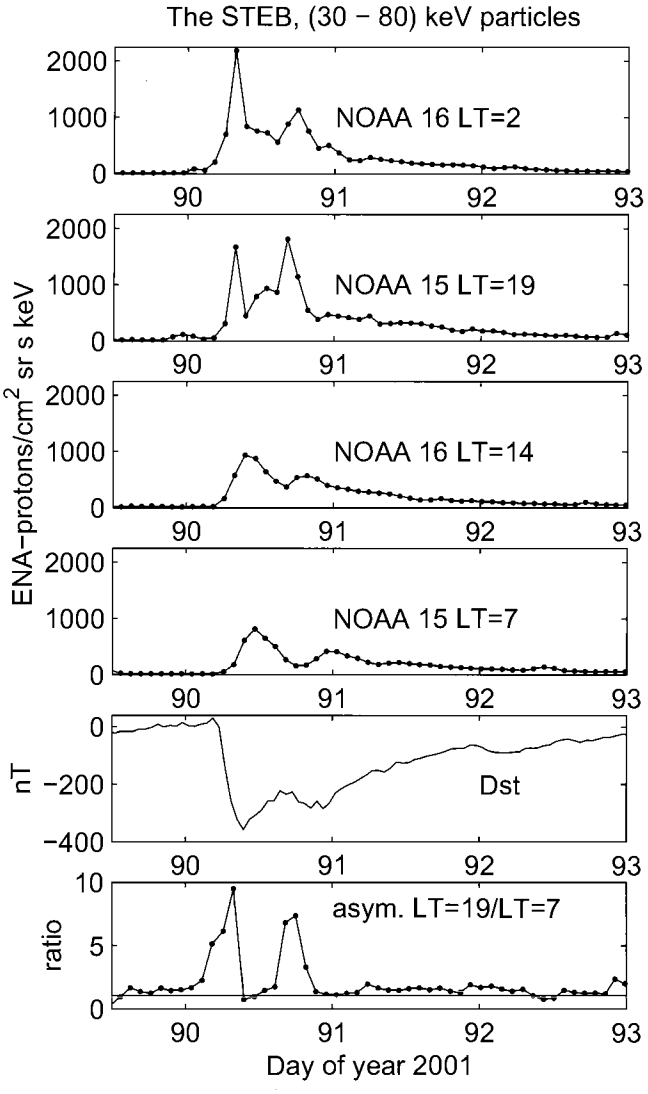

Figure 2. The top four panels show how the intensity of trapped protons in the energy range 30 to 80 keV varies with time at low L-values through the March 31 storm. Each panel refers to a different local time (LT), and data from both NOAA 15 and 16 are shown. The D_{st} index is in the fifth panel, and the bottom panel gives the ratio of the intensities measured at LT 19 and LT 07. To guide the eye a straight line is drawn at a ratio of 1 in the bottom panel.

19 and 07 LT is shown. This ratio (an asymmetry indicator) exhibits large values at 06 and 18 UT on day 90 concurrent with the injection event seen in the D_{st} index. This occurs simultaneous with the large values of the asymmetry indicator shown in panel five. The STEB thus responds to the asymmetric ring current. In the storm recovery phase the intensities at all local times decay in a similar fashion with about equal intensities, even though the evening intensity is slightly above the morning intensity. This probably indicates that there is a continuous injection of energy into the ring current also during the storm recovery phase.

4.1. Summary STEB

In Plate 3 the different aspects of our STEB observations have been illustrated. It shows how the particles in the storm main phase are injected from the tail and gradient/curvature drift through the midnight/evening sector to produce the asymmetric part of the ring current. While they drift and charge exchange, some ENAs are sent towards the low-altitude equatorial region of the Earth, where they are ionized forming the STEB. During this phase of the storm the ring current is subjected to heavy convection loss. As time progresses the convection field disappears and the ring current develops into a symmetric belt that decays through charge exchange and wave-particle interaction. The ENA flux is a function of ring current intensity and its spatial distribution.

The protons at low L-values will experience a rapid decay due to charge exchange processes in the dense geocorona. Because of their fast decay and slow azimuthal drift the proton intensity in the STEB is determined by their source, the charge exchange of ring current protons at larger L-values. The LT extension and intensity of the low latitude belt is thus an "image" of the ring current. From observations of the STEB the ring current injection region, its evolution through the evening/afternoon and into the morning sector, its asymmetry during the initial and main phases, and its development into a symmetric ring current in the recovery phase of the storm can all be clearly seen and followed.

Observations of STEB at several local times provide unique opportunities to follow the build up and decay of the ring current. Multiple satellites makes it possible to get a fair time resolution of the STEB and thus of the ring current.

5. WAVE-PARTICLE INTERACTION

During the recovery of geomagnetic storms, highly localized regions of enhanced proton (ion) precipitation can appear at mid-latitudes well inside the anisotropic precipitation zone. The particle pitch angle distribution in these enhanced regions is most often anisotropic with maximum intensity perpendicular to the magnetic field [*Søraas et al.*, 1999].

In Figure 1 an example of increased proton intensity at mid-latitudes is shown. Such enhanced regions of precipitation embedded in the anisotropic zone are most likely due to protons scattered by resonant wave-particle interaction at or near the plasmapause, as discussed by *Lundblad and Søraas* [1978], and represent a loss of ring current particles in the recovery phase of a geomagnetic storm. They further showed, using data from the ESRO I satellite, that these regions with

[redacted]

increased proton precipitation were closely connected with SAR arc formation.

Yahnina et al. [2003] have done studies relating these mid-latitude enhancements to geomagnetic pulsations of Pc1 and the IPDP (Intervals of Pulsations with Diminishing Periods) types. Both Pc1 and IPDP pulsations are believed to be the electromagnetic ion-cyclotron waves generated in the equatorial plane by the unstable proton angular distribution. These waves scatter energetic protons in pitch angle, so those authors concluded that the precipitation patterns at mid-latitudes are the particle counterparts of ion-cyclotron waves.

These observations of particles and waves support the *Cornwall et al.* [1970, 1971] theory for the generation of ion-cyclotron waves and SAR arc formation. It was suggested by *Thorne and Kennel* [1971] that ion-cyclotron waves can precipitate relativistic electrons in the E ~1 MeV range. If this theory is applicable, one would expect to observe relativistic electrons collocated with the increased proton precipitation taking place in the anisotropic zone.

An example of such a collocation of protons and relativistic electrons is shown in Figure 3. The event took place on day 207 during the recovery phase of a −50 nT geomagnetic storm that had its main phase on day 204. The three panels in the figure display from the top: electrons with energies >30 keV, relativistic electrons with energies >1500 kev, and protons in the energy range 30 to 80 keV. The protons shown in the bottom panel exhibit the mid-latitude enhancement typical for the storm recovery phase. This enhancement occurred in both hemispheres at the same ILAT (63°) and at approximately the same MLT (~ 06).

The >1500 keV electrons exhibit increased precipitation in the region of anisotropic proton precipitation. The relativistic electron precipitation starts immediately equatorward of the IB (isotropic boundary) in both hemispheres and is confined within the region of anisotropic proton precipitation. In the Southern Hemisphere the relativistic electrons exhibited a very narrow peak displaying a sudden intensity increase of nearly an order of magnitude above its uniform background

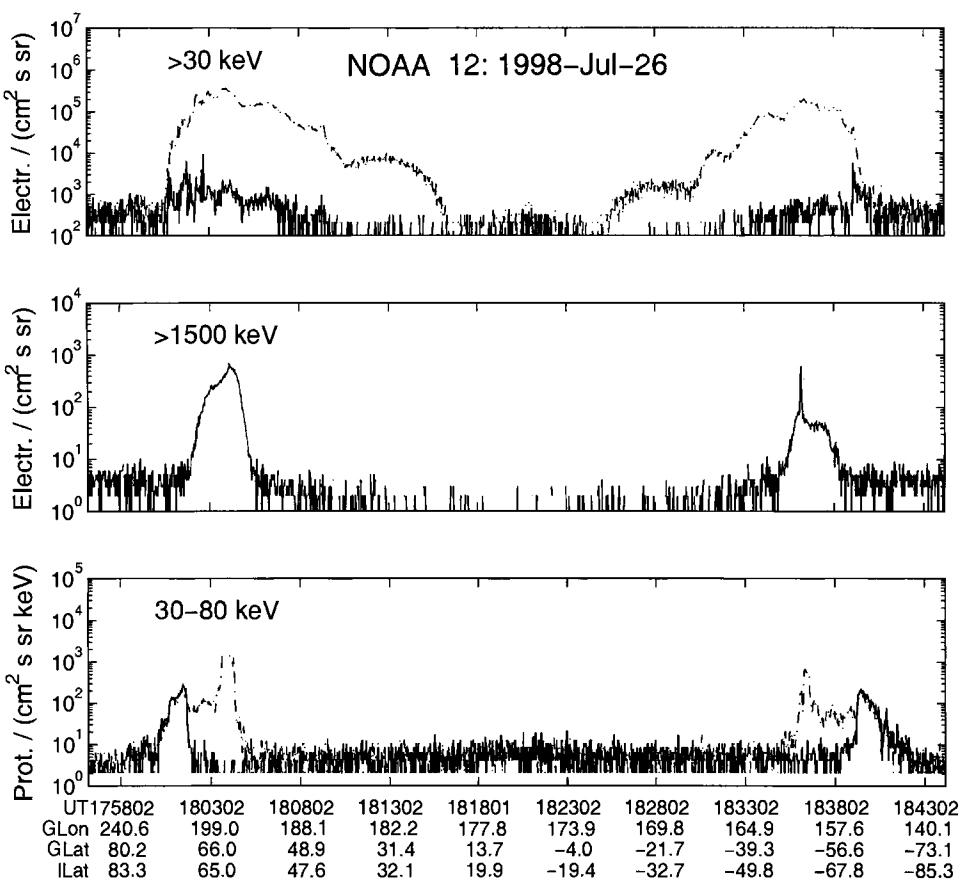

Figure 3. Morningside NOAA 12 pass from north to south (crossing the Equator). The three panels display from the top; electrons with energies >30 keV, omnidirectional relativistic electrons with energies >1500 keV, and protons in the energy range 30 to 80 keV. In panels one and three the flux of 80° particles is shown with a dashed line, and the 10° particles with a solid line.

precipitation level. In the Northern Hemisphere the relativistic electrons also exhibit a peak in precipitation, but not as pronounced as in the conjugate hemisphere. The increased precipitation of relativistic electrons is coincident with the increased loss of protons. The >30 keV electrons show no direct spatial resemblance to the protons or the >1500 keV relativistic electrons.

5.1. Summary Waves and Particles

Relativistic electrons execute nearly circular drift orbits around the Earth in the L-value range 3 to 7. These orbits are within the region of the ring current protons. Both the isotropic and the anisotropic zones are traversed by these electrons during their drift. Observations support the conclusion that there is an almost one-to-one correspondence between the precipitation (loss) of relativistic electrons and the anisotropic proton precipitation.

In the anisotropic zone the protons are unstable to wave growth. The instability causes pitch angle diffusion, particle precipitation and the generation of ion-cyclotron waves. Thus there exists a fairly wide L-value range equatorward of the isotropic zone with ample conditions for EMIC wave generation. According to *Thorne and Kennel* [1971] one should expect relativistic electrons to be parasitically scattered into the loss cone by ion-cyclotron waves generated at or near the plasmapause by the unstable proton population. It is in the midnight/evening MLT sector that the proton drift paths intersect the plasmapause and they are expected to be strongly unstable. Our observations show that there can be intense precipitation of relativistic electrons collocated with the proton precipitation peak also in the morning sector, and it is interesting to observe that the relativistic electron precipitation can take place over the whole anisotropic proton zone; a fairly wide region in L-value.

Proton precipitation in the anisotropic zone can also exist without any evidence of relativistic electron precipitation, but on the other hand, whenever relativistic electron precipitation is present it is always embedded in the anisotropic proton zone. The close correspondence between protons and relativistic electrons suggests that the electrons are scattered into the loss cone by EMIC waves. Spatial peaks in proton precipitation have been shown to be associated with SAR arc formation [*Lundblad and Søraas*, 1978], the plasmapause, and Pc1 and IPDP wave generation [*Yahnina et al.*, 2003]. During the recovery phase of the storm the location of the proton peak moves towards higher ILAT in accordance with the plasmapause [*Søraas et al.*, 1999]. This later observation further strengthens the connection between precipitation of relativistic electrons and EMIC waves generated at the plasmapause and in the anisotropic proton zone.

Acknowledgments. The authors thank the Norwegian Research Council for financial support. Furthermore, we thank the Wind spacecraft team and CDA Web for providing solar wind data.

REFERENCES

Alexeev, I.I., E.S. Belenkaya, V.V. Kalegaev, Y.I. Feldstein, and A. Grafe, Magnetic storms and magnetotail currents, *J. Geophys. Res.*, 101 (A4), 7737-7748, 1996.

Berg, L.E., and F. Søraas, Observations suggesting weak pitch angle diffusion of protons, *J. Geophys. Res.*, 77, 34, 1972.

Cornwall, J.M., F.V. Coroniti, and R.M. Thorne, Turbulent loss of ring current protons, *J. Geophys. Res.*, 75, 4699, 1970.

Cornwall, J.M., F.V. Coroniti, and R.M. Thorne, Unified theory of SAR arc formation at the plasmapause, *J. Geophys. Res.*, 76, 4428, 1971.

Dessler A.J., W.B. Hanson, and E.N. Parker, Formation of the geomagnetic storm main-phase ring current, *J. Geophys. Res.*, 66, 3631, 1961.

Evans, D.S., and M.S. Greer, Polar orbiting environmental satellite space environment monitor - 2: Instrument descriptions and archive data documentation, *NOAA Technical Memorandum OAR SEC-93*, Boulder, Colorado, 2000.

Hauge, R., and F. Søraas, Precipitation of >115 keV protons in the evening and forenoon sectors in relation to magnetic activity, *Planet. Space Sci.*, 23, 1141, 1975.

Hovstadt, D., B. Hausler, and M. Scholer, Observation of energetic particles at very low altitudes near the geomagnetic equator, *Phys. Rev. Lett.*, 28, 1340, 1972.

Lundblad J.Å., and F. Søraas, Proton observations supporting ion cyclotron wave heating theory of SAR arc formation, *Planet. Space Sci.*, 26, 245-254, 1978.

McPherron, R.L., The role of substorms in the generation of magnetic storms, in *Magnetic Storms*, edited by B.T. Tsurutani *et al.*, Geophysical Monograph 98, American Geophysical Union, 1997.

Moritz, J., Energetic protons at low equatorial altitudes: A newly discovered radiation belt phenomenon and its explanation, *Z. Geophys.*, 38, 701, 1972

O'Brien, B.J., High-latitude geophysical studies with satellite Injun 3, 3, Precipitation of electrons into the atmosphere, *J. Geophys. Res.*, 69, 13, 1964.

Raben, V.J., D.S. Evans, H.H. Sauer, S.R. Sahm, and M. Huynh, TIROS/NOAA satellite space environment monitor data archive documentation: 1995 update, *NOAA Technical Memorandum ERL SEL-86*, Boulder, Colorado, 1995.

Sandanger, M.I., F. Søraas, K. Aarsnes, K. Oksavik, D.S. Evans, and M.S. Greer, Proton injection into the ring current associated with B_z variations during HILDCAA events, in Geophysical Monograph, this issue, 2004.

Sergeev, V.A., E.M. Sazhina, N.A. Tsyganenko, J.Å. Lundblad, and F. Søraas, Pitch-angle scattering of energetic protons in the magnetotail current sheet as the dominant source of their isotropic precipitation into the nightside ionosphere, *Planet. Space Sci.*, 31, 1147, 1983.

Søraas, F.,K. Aarsnes, J.Å. Lundblad, and D.S. Evans, Enhanced pitch angle scattering of protons at mid-latitudes during geomagnetic storms, *Phys. Chem. Earth* (C), 24, 287-292, 1999.

Søraas, F., K. Aarsnes, K. Oksavik, and D.S. Evans, Ring current intensity estimated from low-altitude proton observations, *J. Geophys. Res.*, 107 (A7), 1149, doi:10.1029/ 2001JA000123, 2002.

Søraas, F., K. Oksavik, K. Aarsnes, D.S. Evans, and M.S. Greer, Storm time equatorial belt - an "image" of ring current behavior, *Geophys. Res. Lett.*, 30 (2), 1052, doi:10.1029/ 2002GLO15636, 2003.

Thorne R.M., and C.F. Kennel, Relativistic electron precipitation during magnetic storm main phase, *J. Geophys. Res.*, 76, 4446, 1971.

Tinsley, Brian, A., Neutral atom precipitation—a review, *J. Atmos. Terr. Phys.*, 43 (5/6), 617-632, 1981.

Tsurutani, B.T., and W.D. Gonzalez, The cause of high intensity long duration continuous AE activity (HILDCAA's): Interplanetary Alfvén waves trains, *Planet. Space Sci.*, 35, 405, 1987.

Tsurutani, B.T., and W.D. Gonzalez, The interplanetary cause of magnetic storms: A Review, in *Magnetic Storms*, edited by B.T. Tsurutani *et al.*, Geophysical Monograph 98, American Geophysical Union, 1997.

Yahnina, T.A., A.G. Yahnin, J. Kangas, J. Manninen, D.S. Evans, A.G. Demekhov, V. Yu. Trakhtengerts, M.F. Thomsen, G.D. Reeves, and B.B. Gvozdevsky, Energetic particle counterpart for geomagnetic pulsations of Pc1 and IPDP types, *Ann. Geophysicae,* 21, 2281-2292, 2003.

F. Søraas, K. Aarsnes, and D.V. Carlsen, Department of Physics and Technology, University of Bergen, AllÈgaten 55, N-5007 Bergen, Norway. (E-mail: finn.soraas@ift.uib.no; kjell.aarsnes@ift.uib.no)

K. Oksavik, Department of Physics, University of Oslo, P.B. 1048 Blindern, N-0316 Oslo, Norway. (E-mail: kjellmar.oksavik@fys.uio.no)

D.S. Evans, NOAA Space Environment Center, 325 Broadway, Boulder, CO 80305, USA. (E-mail: David.S.Evans@noaa.gov)

Proton Injections Into the Ring Current Associated With B_z Variations During HILDCAA Events

M.I. Sandanger, F. Søraas, and K. Aarsnes

University of Bergen, Norway

K. Oksavik

University of Oslo, Norway

D.S. Evans and M.S. Greer

NOAA Space Environment Center, Colorado, USA

The variation of Earth's magnetic field at the equator, as monitored by the *Dst* index, can stay below its quiet day value for days. This can happen after storms resulting in a very slow recovery of the *Dst* index, or it can happen in the absence of a storm. Such "anomalous" behaviour is observed during periods with continuous auroral activity called High-Intensity Long-Duration Continuous AE Activity—HILDCAA. NOAA satellite data is used to investigate the radial depth of particle injections into the ring current and its dependence on fluctuations in the interplanetary magnetic field. It is found that the particle injections are sufficient to delay the recovery of the *Dst* during HILDCAA events. It is further found that the particle injections during HILDCAA events are closely connected with Alfvén fluctuations in the interplanetary magnetic field B_z component.

1. INTRODUCTION

The HILDCAA phase of the storm is characterized by fluctuations in the solar wind magnetic field B_z component simultaneous with continuous high *AE* activity through the recovery phase of the storm or during no storm periods with reduced *Dst*. During HILDCAA events the *Dst* index does not exhibit the "normal" recovery back to its quiet-day zero-level value. A working definition of a HILDCAA event is; a maximum of $AE > 600$ nT, continuous $AE > 200$ nT, duration > 2 days, and the event is not associated with the storm main phase [*Tsurutani and Gonzalez,* 1987].

The Inner Magnetosphere: Physics and Modeling
Geophysical Monograph Series 155

10.1029/155GM26

Variations of Earth's magnetic field at the equator, is measured with the *Dst* index, which can stay negative for several days. The depression is mostly attributed to the ring current, but it also depends on other current systems in the magnetosphere such as magnetopause, tail and auroral currents. It is well established that the magnetic effect of the ring current is proportional to the energy content of the charged particles generating it [*Dessler and Parker,* 1959; *Sckopke,* 1966]. *Søraas et al.* [2002] have developed a ring current index based on the precipitation of protons into the evening side upper atmosphere. The precipitating protons give a good estimate of the ring current injection rate. By comparing the newly developed ring current index with the pressure corrected *Dst** index, *Søraas et al.* [2004] determined that the depressed *Dst** index during HILDCAAs could to a large degree be accounted for by the ring current alone, not influenced by other current systems.

In this paper we will use NOAA (National Oceanic and Atmospheric Administration) satellite data to determine the depth of the particle injections into the RC and its relation to B_z variations during three HILDCAA events.

2. DATA SOURCES

We will use solar wind data from the ACE satellite, geomagnetic activity indices provided by the World Data Center in Kyoto, and proton data from the low-altitude satellite NOAA-12. The polar satellite NOAA-12 is orbiting Earth at an altitude of 815 km. The orbital plane of NOAA-12 is in the local evening/morning sector (see Figure 1). The orbital period is around 103 minutes. We are using data from the MEPED (Medium Energy Proton and Electron Detector) instrument. MEPED measures protons and electrons at angles of 0° and 90° with the local vertical. We are concentrating the analysis on precipitating protons as observed by the 0° detector. A full description of the NOAA spacecraft and the MEPED instrument is given by *Raben et al.* [1995].

The precipitating protons observed at low altitude reflect the proton intensities at higher altitude at various locations in the radiation belt. The precipitating protons that the 0° proton detector observe at high geomagnetic latitudes, originate from the inner part of the ring current. In both cases the intensity of the precipitating protons mirrors the proton population in the magnetosphere, and their variations reflect injections of protons into the ring current.

3. THREE HILDCAA-EVENTS IN 1998

Figure 2 displays observations during two geomagnetic storms from April 1998, Figure 3 displays a storm from August 1998, and Figure 4 shows a storm in October 1998. All these storms exhibit HILDCAA activity. The three Figures all have four panels. The first panel gives the B_z component of the solar wind magnetic field measured by the ACE spacecraft. The second and third panels give the *AE* and *Dst* indices. The last panel exhibit the precipitating proton data from the NOAA-12 satellite. Each satellite pass is plotted versus L and time, and the observed proton flux is plotted with a logarithmic gray scale code. The proton flux from channel 1 (30-80 keV) illustrate the depth and intensity of proton penetration in the $L = 3$ to $L = 9$ range.

3.1. HILDCAA Event in April 1998

The period covers the days 113 to 120 in year 1998 (April 23 to April 30). The *Dst* index has two minima during this period, one on day 114 and the other on day 116. The *Dst* index reaches −70 nT on day 114 and −60 nT on day 116. The main phase of the first magnetic storm is at the beginning of day 114. The recovery phase starts at the end of day 114, but the *Dst* index shows a very slow recovery and stays almost constant at −40 nT for about two days. After the second storm at the end of day 116, the *Dst* index requires almost three days to recover to the quiet day value.

The *AE* index is high and variable through the recovery phase of both storms and these periods are marked 'HILDCAA' at the top panel of Figure 2. The interplanetary magnetic field B_z component fluctuates around zero with several intervals as low as −7 nT throughout the first HILDCAA period. Through the second HILDCAA period, B_z is also fluctuating but with −3 nT as the lowest value.

During the main phase of the two storms the protons are injected deep into the evening side magnetosphere as evident from the intensity observed inside $L = 4$. It is only during

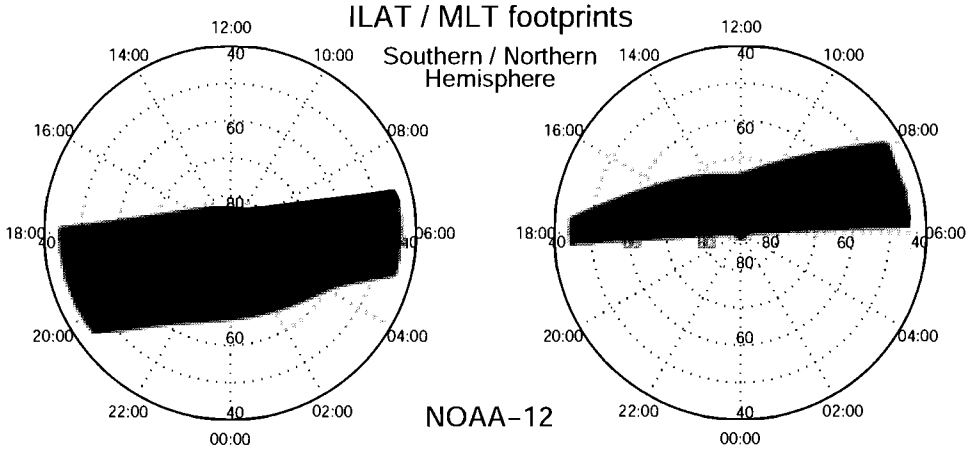

Figure 1. ILAT/MLAT footprint of the NOAA-12 spacecraft. Southern Hemisphere to the left, and Northern Hemisphere to the right.


Log Proton Flux
0
1
2
3
4

[redacted]

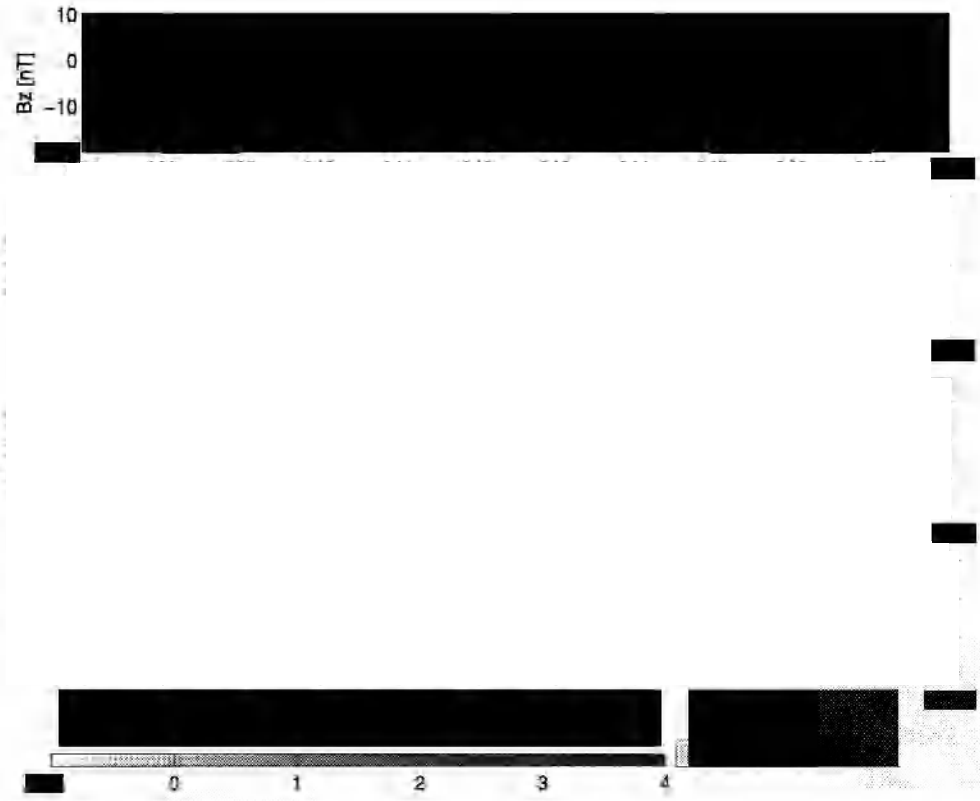

[redacted]

[redacted]

[redacted]

[redacted]

[redacted]

[redacted]

[redacted]

[redacted]

[redacted]

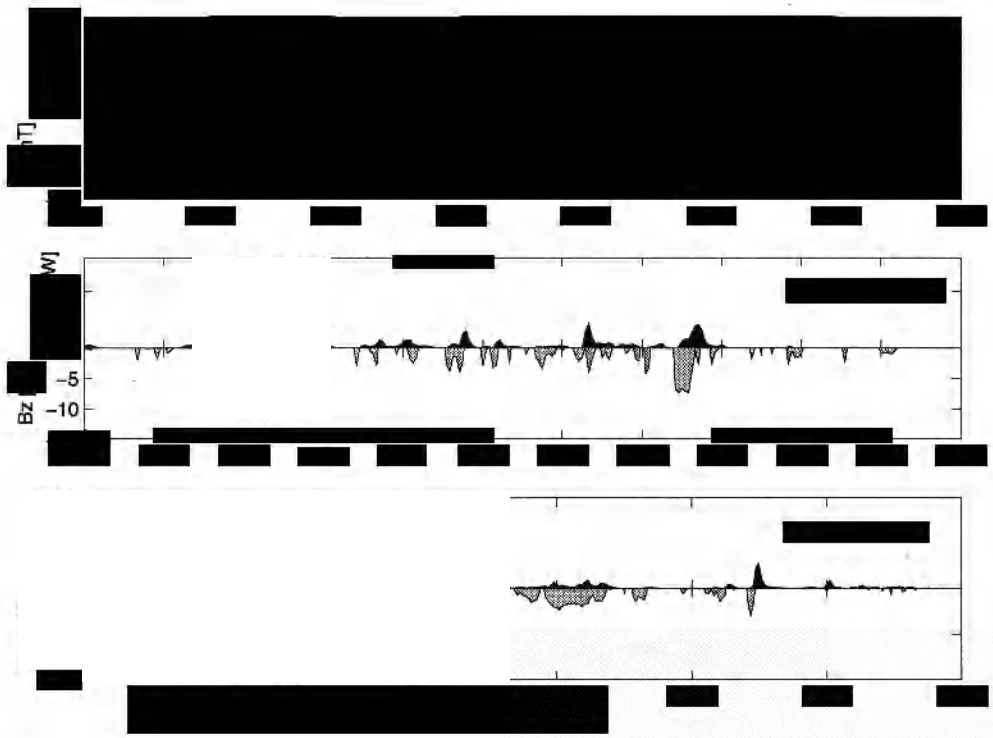

[redacted]

[redacted]

[redacted]

[redacted]

Dessler, A.J., and E.N. Parker, Hydromagnetic theory of magnetic storms. *J. Geophys. Res.*, 64, 2239, 1959.

Hollweg, J.V., Some physical processes in the solar wind. *Rev. Geophys. Space Phys.*, 16, 689 pp., 1978.

Raben, V.J., D.S. Evans, H.H. Sauer, S.R. Sahm and M. Huynh, TIROS/NOAA Satellite Space Environment Monitor Data Archive Documentation: 1995 Update. *NOAA Technical Memorandum ERL SEL-86, Boulder, Colorado.*, 1995.

Sckopke, N., A general relation between the energy of trapped particles and the disturbance field near the Earth, *J. Geophys. Res.*, 71, 3125 pp., 1966.

Søraas, F., K. Aarsnes, K. Oksavik, and D.S. Evans, Ring current intensity estimated from low altitude proton observations, *J. Geophys. Res.*, 107, 1149 pp., doi:10.1029/2001JA000123, 2002.

Søraas, F., K. Aarsnes, K. Oksavik, M.I. Sandanger, D.S. Evans, and M.S. Greer, Evidence for particle injection as the cause of *Dst* reduction during HILDCAA events, *J. Atm. Solar-Terr. Phys.*, 66, 2, 177 pp., 2004.

Tsurutani, B.T., and W.D. Gonzalez, The cause of high intensity long duration continuous *AE* activity (HILDCAA's): Interplanetary Alfvén waves trains. *Planet. Space Sci.*, 35, 405 pp., 1987.

Tsurutani, B.T., T. Gould, B.E. Goldstein, W.D. Gonzalez, and M. Sugiura, Interplanetary Alfvén waves and auroral (substorm) activity: IMP-8. *J. Geophys. Res.*, 95, 2241, 1990.

Tsurutani, B.T., C.M. Ho, E.J. Smith, M. Neugebauer, B.E. Goldstein, J.S. Mok, J.K. Arballo, A. Balogh, D.J. Southwood, and W.C. Feldman, The relationship between interplanetary discontinuities and Alfvén waves: Ulysses observations. *Geophys. Res. Lett.*, 21, 21, pp. 2267-2270, 1994.

Tsurutani, B.T., W.D. Gonzalez, F. Guarnieri, Y. Kamide, X. Zhou, and J.K. Arballo, Are high-intensity long-duration continuous *AE* activity (HILDCAA) events substorm expansion events? *J. Atm. Solar-Terr. Phys.*, 66, 2, 167 pp., 2004.

K. Aarsnes, M.I. Sandanger, and F. Søraas, Department of Physics and Technology, University of Bergen, Allégaten 55, N-5007 Bergen, Norway. (e-mail: marit.sandanger@ift.uib.no; finn.soraas@ift.uib.no; kjell.aarsnes@ift.uib.no)

K. Oksavik, Department of Physics, University of Oslo, Postboks 1048 Blindern, N-0316 Oslo, Norway. (e-mail: kjellmar.oksavik@fys.uio.no)

D.S. Evans, and M.S. Greer, NOAA Space Environment Center, 325 BroadWay, Boulder, CO 80305, USA. (e-mail: David.S.Evans@noaa.gov; Sue.Greer@noaa.gov)

What Defines the Polar Cap and Auroral Oval Diameters?

Igor I. Alexeev

Skobeltsyn Institute of Nuclear Physics, Lomonosov Moscow State University, Moscow, Russia

A dependence of the polar cap magnetic flux on the solar wind dynamic pressure is studied. The model calculations of the relation of the polar cap to the polar oval magnetic fluxes at the ionospheric level are presented. For quiet conditions a comparison of the theoretical results with data have shown a good agreement. The model calculations give us a possibility to find not only the average polar cap magnetic flux but also the extreme values of the polar cap and auroral oval magnetic fluxes. These values can be reached in the course of the severe magnetic storm. The scaling law for the polar cap diameter changing for different subsolar distances is demonstrated.

INTRODUCTION

The polar cap magnetic flux or, in other words, magnetotail lobe flux is one of the key parameters which control the magnetospheric dynamics. As pointed out by *McPherron*, 1970, 1991, an increase of the magnetic flux in the magnetotail is connected with the substorm growth phase. After it, the magnetosphere goes to a metastable state, and an impulsive sporadic release of the excess energy become possible.

Determination of morphology of an open-closed field line boundary is one of the main problems of magnetospheric physics today [*Raeder et al.*, 1998]. It becomes rather essential since the global images in far UV obtained onboard the Polar, IMAGE and TIMED satellites make it feasible to receive an instant picture of the intensity of the upper atmospheric emissions. This intensity to a good accuracy can be thought to be proportional to the total energy of precipitating particles. Moreover, observations in several spectral ranges enable to separate the proton and electron precipitation regions [*Mende et al.*, 2003].

The particle flux measurements by the DMSP satellites during several decades make it feasible to obtain a statistical pattern of the fluxes in the polar regions. These fluxes are associated directly with the polar cap structure. Thus, the open field line region is identified as a region free of the precipitating energetic particle fluxes. In the polar cap energetic particles are absent, and the polar rain formed by the soft particle precipitations appear.

The magnetic field morphology in the polar region defines the zone of zero geomagnetic cut-off which is filled with solar cosmic ray particles during periods of increasing flux events associated with the solar flares. Detection of the equatorial boundary of a zone filled with the 1 MeV solar protons also marks the polar cap diameter. However, these measurements are feasible only during periods of the flux in the interplanetary space exceeding significantly a background level.

Detection of the atmospheric 6300 $\dot{A}$ line luminousity by onground photometers enables a definition of the polar cap boundary as the polar border of luminousity with intensity higher than 110 R [*Blanchard et al.*, 1997]. Data obtained by the CANOPUS photometers [*Blanchard et al.*, 1997] were compared with the region of open field lines determined using the MHD simulation results [*Rae et al.*, 2003]. In this paper all magnetic field lines have been separated into two types: closed lines haven two points of intersection with the Earth's surface in the both hemispheres, and open ones stretched into the interplanetary space. So, in this case the polar cap boundary is the boundary between the two-type magnetic field lines.

In spite of seeming simplicity of the above definition it cannot be thought undoubted. Firstly, it is not clear, to what type one should assign field lines going to large distances from the region under consideration? Secondly,

The Inner Magnetosphere: Physics and Modeling
Geophysical Monograph Series 155

10.1029/155GM27

the theta aurora observed for the northern IMF, the polar cap arcs, and other aurora emissions observed towards the pole from the auroral oval [*Østgaard*, 2003] indicate that the polar cap can be considered free of aurora only approximately. No one of the above mentioned "markers" of the polar cap can be thought undoubted (see *Mende et al.*, 2003).

Following [*Rae et al.*, 2003], in the present paper use is made of the definition of the polar cap as a region of open field lines stretching to the interplanetary space through the magnetopause (in the open magnetospheric model), or through the perpendicular section of the distant night-side tail (in the closed magnetospheric model). This definition has been used by *Coroniti and Kennel*, 2003. However, unlike [*Coroniti and Kennel*, 2003], we take into account variation of the magnetic flux in the magnetotail due to non-zero B_z component of the magnetospheric field normal to the tail current sheet plane.

Following [Schultz, 1997], the polar cap size is determined using model magnetic flux bookkeeping. *Schultz*, 1997 analysed the influence of the ring current on the polar cap diameter using a simple model including the geomagnetic dipole and uniform southward magnetic field. Hereafter, the paraboloid model [*Alexeev et al.*, 1996, 2003] is used. It enables obtaining an instantaneous configuration of the magnetosphere at various parameters of the solar wind and different phases of geomagnetic activity. After performing rather simple scale transformaions using magnetic flux bookkeeping, the relation between solar wind dynamical pressure and the size of the open field line region is obtained. Moreover, assuming *Bz*-component at the equatorial magnetosphere to be positive, the maximal sizes of the equatorward boundary of the auroral oval are obtained. These sizes can be attained during extremal magnetic storms.

CALCULATION OF MAGNETIC FLUXES IN THE CLOSED MAGNETOSPHERE

First of all the closed model of the magnetosphere is considered neglecting reconnection of the magnetospheric magnetic field and the IMF ($B_n = 0$ at the magnetopause). Let us show, that if the geomagnetic dipole is assumed to be screened by the solar wind plasma, the magnetic flux through the equatorial plane region located between the magnetopause and the Earth's surface remains almost constant independently of the magnetopause form and size.

Let us start with consideration of a flat magnetopause located at a distance R_1 from the dipole center. It is assumed for simplicity that the geomagnetic dipole is formed by the currents flowing over the surface of a sphere with the radius R_E (R_E is the Earth's radius equal to 6378 km). Inside the sphere of R_E the magnetic field is southward. It is uniform equaling $2B_0 = 60286$ nT.

Figure 1 shows the cross-section of this magnetospheric model. We assume that magnetic field upstream the magnetopause (at $x > R_1$) is zero. At $x < R_1$ it is a sum of the geomagnetic dipole field and the image dipole field. The image dipole is located upstream at the point $x = 2R_1$ and has magnetic moment equal to the geomagnetic dipole moment $M_E = B_0 R_E^3 = 30143\ \text{nT}\, R_E^3$. In this case the field at the subsolar point is $B_s = 2B_d(R_1) = 2M_E/R_1^3$. The field of currents on the magnetopause screening the dipole field (the Chapman-Ferraro currents) at the Earth's center is $B_1 = B_0 R_E^3 / 8R_1^3$. All magnetic field lines intersect the sphere surface twice in the southern and northern hemispheres. Also all field lines intersect equatorial plane. It occurs once outside the sphere R_E and at the other time inside the sphere R_E. The magnetic flux through the equatorial plane to the right of the magnetopause, Φ_e, is equal to an opposite-sign magnetic flux within the sphere R_E induced by the uniform field

$$-2B_0 + B_1 = B_0(-2 + R_E^3/8R_1^3).$$

Thus, to an accuracy up to terms $B_1/B_0 \sim 0.6 \cdot 10^{-4}$ for $R_1 \sim 10R_E$, the equatorial flux in the magnetosphere Φ_e is equal to Φ_d, where $\Phi_d = 2B_0 \pi R_E^2 = 7704.5$ MWb is the geomagnetic dipole magnetic flux through one of the hemispheres.

The same expression for the magnetic flux Φ_e can be obtained by direct integration of the B_z component of the

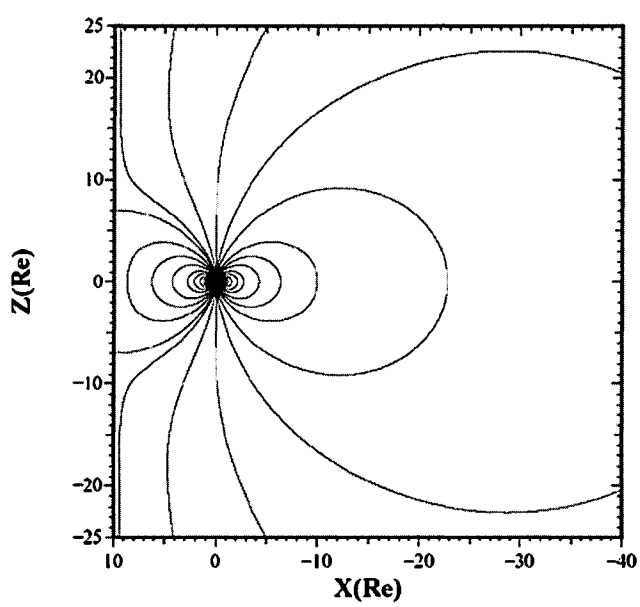

Figure 1. Meridional plane magnetospheric cross section. Magnetic field lines are shown.

magnetospheric magnetic field over the equatorial magnetospheric cross section:

$$\Phi_e = \int_{-\infty}^{R_1}\int_{-\infty}^{\infty} B_z dy dx = \int_{-\frac{\pi}{2}}^{\frac{\pi}{2}} Rd\phi \int_{R_E}^{\frac{R_1}{\cos\phi}} dRB_z + \int_{\frac{\pi}{2}}^{\frac{3\pi}{2}} Rd\phi \int_{R_E}^{\infty} dRB_z = \Phi_d\left(1 - \frac{R_E^3}{16R_1^3}\right), \quad (1)$$

where B_z is defined by the expression:

$$B_z = M_E\left(\frac{1}{R^3} + \frac{1}{R_2^3}\right). \quad (2)$$

$R = \sqrt{x^2 + y^2}$ and $R_2 = \sqrt{(x - 2R_1)^2 + y^2}$ are the distances to the geomagnetic dipole and to the image dipole in the equatorial plane. Cartesian coordinates are related with the spherical ones relations $x = R\cos\phi$ and $y = R\sin\phi$.

In the similar manner, using the fact that the magnetic fluxes through magnetospheric equatorial cross section and those within the sphere of R_E, are equal one can obtain an expression of the equatorial magnetic flux Φ_e for an arbitrary closed magnetospheric model. This magnetic flux is controled by the magnetopause current magnetic field strength at the Earth's center, B_1:

$$\Phi_e = \Phi_d\left(1 - \frac{B_1}{2B_0}\right) \approx \Phi_d = 7704.5 \text{ MWb}. \quad (3)$$

For a spherical magnetopause the field of Chapman-Ferraro currents at the Earth's center is $B_1 = 2B_0\frac{R_E^3}{R_1^3}$.

In the framework of the paraboloid model [*Alexeev*, 2003]:

$$B_1 = \frac{2}{3}B_0\frac{R_E^3}{R_1^3} \approx 20\frac{10.1R_E^3}{R_1^3} \text{ nT}. \quad (4)$$

Here $R_1 = 10.1R_E$ is the distance to the subsolar point calculated from the pressure balance:

$$B_s^2 = 2\mu_0 p, \text{ or } B_s = 40\sqrt{\frac{\pi p}{2}} \text{ nT, here } p \text{ in nPa}. \quad (5)$$

For the pressure $p = 2$ nPa the field is $B_s = 70.9$ nT and $R_1 = 10.1R_E$, since $B_s = kM_E/R_1^3$. In the paraboloid model the coefficient k of the field amplifying at the subsolar point is equal to 2.44. It has an intermediate value between $k = 3$ for a sphere and $k = 2$ for a plane magnetopause. It should be noted that the value very close to 2.44 has been obtained in the paper *Mead and Beard*, 1964.

MAGNETIC FIELD IN THE POLAR CAP

All magnetic field lines intersect the equatorial plane in the magnetospheric models which do not include magnetotail current sheet. In these models open field lines are absent. It is also true for the magnetospheric models in which the current sheet does not continue to the infinity but is bounded at some antisunward distance from the Earth. In these models the polar cap is also absent.

Let us bear in mind, following *Coroniti and Kennel*, 1972 that at large distances the magnetopause becomes tangential to the solar wind flux direction. The magnetic field in the tail lobes is determined by the balance between lobe magnetic field and thermal pressure of the magnetosheath plasma. Correspondingly, the current density in the tail current sheet tends to some constant value at $x \to -\infty$. The lobe magnetic field flux, Φ_{lobe}, tends also to the constant value, Φ_∞, at $x \to -\infty$. Mapping this flux to the ionospheric level, the polar cap magnetic flux, $\Phi_{pc} = \Phi_\infty$, is obtained (see Figure 2). In this case the Eq. (3) can be rewritten as

$$\Phi_d\left(1 - \frac{B_1}{2B_0}\right) = \Phi_e + \Phi_\infty = \Phi_{head} + \Phi_{PS} + \Phi_{lobe}, \quad (6)$$

here $\Phi_\infty = \Phi_{lobe}$, and the total equatorial magnetic flux, Φ_e, is divided on two parts: the closed field lines magnetic flux in the trapping particle region, Φ_{head}, and the closed field line

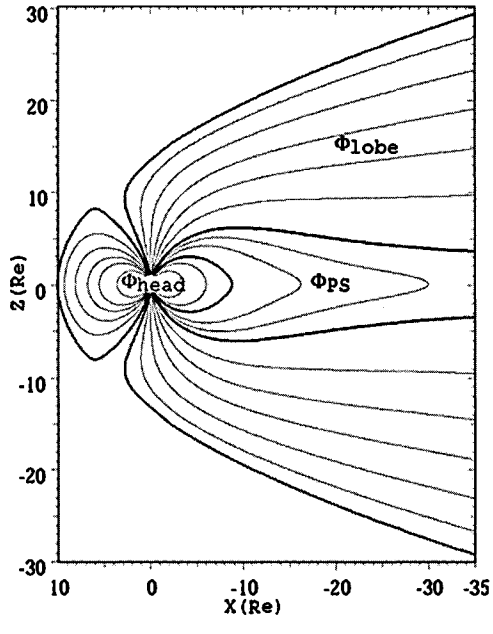

Figure 2. Closed paraboloid model. The noon-midnight cross section are shown. Φ_{head} marked the closed field lines in the trapping particles regions. Φ_{PS} noted the auroral oval field line region, and Φ_{lobe} marked the lobe field line bundle.

magnetic flux in the plasma sheet or auroral oval region, Φ_{PS} (see Figure 2).

Unlike to a popular opinion that the magnetotail appears due to reconnection of the IMF and the magnetospheric magnetic field, the above consideration shows that current in the magnetotail and the polar cap appear in the closed magnetospheric model [*Alexeev et al.*, 1998] as well. Here non-ideal flow past the magnetopause by the solar wind plasma should be taken into account. This non-ideality reveals itself in the fact that the plasma partially penetrates into the magnetosphere inspite that $B_n = 0$ everywhere on the magnetopause. This effect is stronger in the night equatorial magnetosphere, where $\nabla B \perp \mathbf{B}$ and the particle drift velocity is normal to the magnetopause. The solar wind particles penetrate the magnetospheric dawn flank then fly away to the dusk side and form the magnetotail plasma sheet. They also serve as the current carier in the tail current sheet which create a bundle of the lobe magnetic field lines.

Of course, this scheme ignores many important processes, but we consider it as a helpful idea. Let us examine quiet conditions when the energy flux into the magnetosphere is small and being balanced by a quiet level of energy losses. It is natural to assume here that the magnetic flux in the magnetotail lobes is equal to the magnetic flux through the magnetosphere equatorial plane beyond a circle of radius R_1. This flow is obtained in a model taking into account only dipole and its screening Chapman-Ferraro currents. The circle of radius R_1 is chosen because it approximately coincides with the outer boundary of closed drift orbit. It is a last orbit which do not cross the magnetopause neglecting the electric field of magnetospheric convection. Geomagnetic field lines intersecting the equatorial plane behind the circle of radius R_1 are already pushed into the night side by the plasma flow and they can form the magnetotail lobes without additional energy input.

Let us calculate this flux Φ_{et} at the geocentric distances $R_m > R > R_1$, where R_m is the distance to the magnetopause. We suggest that it is equal to a quiet flux in the polar cap. As before, integration of B_z over the equatorial plane yields:

$$\Phi_{et} = \int_{R_1}^{R_m(\phi)} \int_{0}^{2\pi} B_z \, R d\phi dR = \Phi_d \frac{R_E}{R_1}\left(1 - \frac{1}{3}\right) \qquad (7)$$

The Φ_{et} value corresponding to a quiet $R_1 = 10.1R_E$ is 508.55 MWb. This value is assumed to determine the size of the polar cap at the ground state of the magnetosphere.

An increase of the energy input into the magnetosphere due to reconnection of the magnetospheric field with the IMF leads to increase of the current in the magnetotail, field in the magnetotail lobes, and the polar cap magnetic flux. This increasing is restricted by two processes. Firstly, an excessive increase of current in the magnetotail can lead to a situation when a negative magnetic flux associated with the field of the magnetotail current system can exceed the positive flux Φ_{et} associated with the dipole and the Chapmen-Ferraro currents at $R_m > R > R_1$. In this case somewhere in the equatorial plane the sign of B_z is reversed with subsequent forming of a neutral line, the stability being broken with subsequent ejection of a plasmoid in the antisolar direction. Secondly, too close coming of the current sheet front edge to the Earth (in the trapped particle zone) leads to a disruption of the current sheet inner edge with subsequent closure of the current through the ionosphere.

The second process is not considered in the present paper. Let us calculate the upper boundary for the polar cap and polar oval diameters proceeding from the requirement for the magnetic flux crossed the equatorial plane to be positive. For this it should be known how the tail current system magnetic flux is distributed between the magnetosphere core (between the dayside magnetopause and the inner edge of the plasma sheet) and the plasma sheet (beyond the inner edge). In Figure 3 the tail current system field lines at the noon-midnight plane are shown. The magnetopause field line and the field line which bounded the current sheet field line bundle are noted by heavy solid curves. Inside of the region limited by the dotted curve in Figure 3 the tail current sheet is placed.

Calculations show that the flux through the core, Φ_{head}, is approximately a half of the total magnetic flux going to the infinity, Φ_∞. Saying more correctly, in a wide range of R_1 and R_2 (R_2 is a distance to the inner edge of the magnetotail current sheet) the ratio Φ_∞ to Φ_{head} changes slightly from

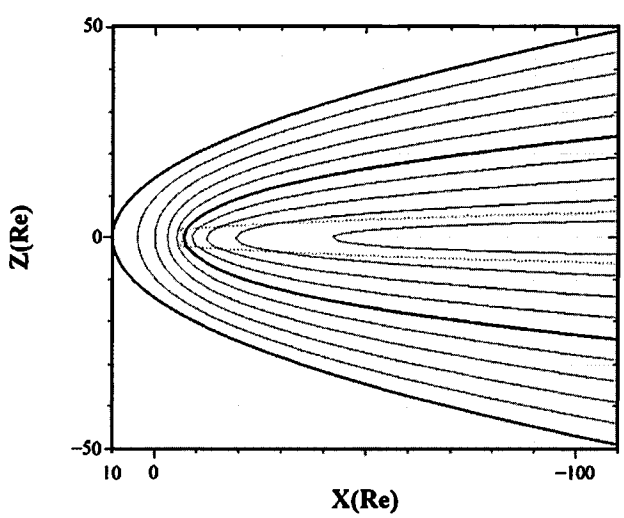

Figure 3. The tail current system magnetic field lines are shown. One can see that the total magnetic flux is distributed in equal parts on the core magnetosphere and on the plasma sheet. The tail current sheet is placed inside the dotted curve.

2.1 to 2.33. It is correct for R_1 and R_2 bigger than 4-5 R_E and lesser than 14 R_E. A value of the ratio Φ_∞ to Φ_{head}, used below is 2.29.

Thus, for a quiet magnetosphere the magnetic flux through the polar cap is

$$\Phi_{pc} = \Phi_d \frac{2R_E}{3R_1} = 508.55 \text{ MWb}. \quad (8)$$

Here the magnetic flux through the polar oval is 0.56 $\Phi_{pc} = 286.5$ MWb. In our consideration this flux is equal to the magnetic flux through the magnetotail current sheet. Correspondingly, the summary magnetic flux polewards from the oval equatorial boundary is 785 MWb. The both fluxes are inversely proportional to the magnetosphere characteristic scale R_1 or, finally, to the 6th-power root from the solar wind dynamical pressure (see Figure 4). During extremal increases of the solar wind plasma pressure up to 28 nPa, when the magnetopause intersects the geostationary orbit, these values increase by a factor of 1.55 up to 790 MWb for the polar cap flux and up to 1216 MWb for the summary auroral and polar cap flux.

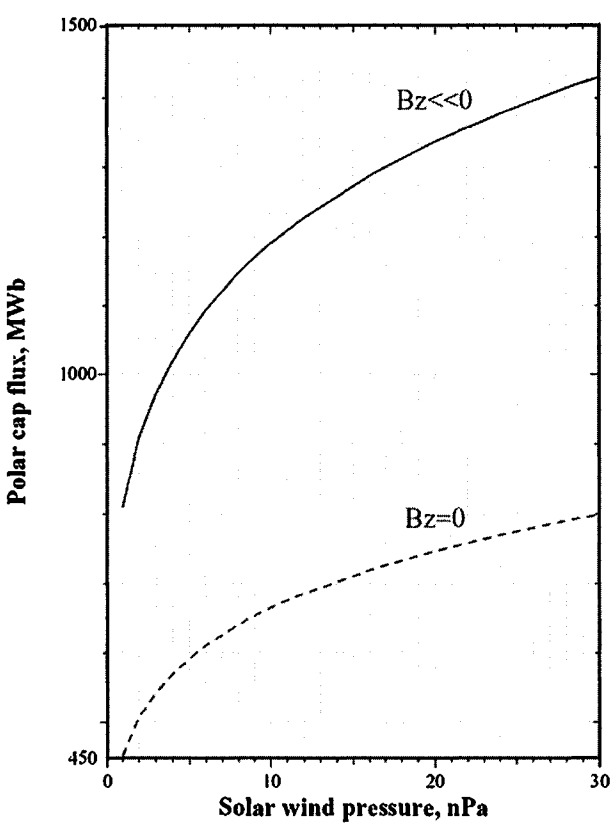

Figure 4. The dependence of the polar cap magnetic flux on solar wind dynamic pressure are shown. Dashed curve demonstrates the quiet time polar cap magnetic flux when IMF $B_Z \sim 0$. Solid curve presents the disturbed time polar cap magnetic flux when IMF $B_Z << 0$.

It is known that the magnetospheric field B_z-component decreases during the substorm growth phase. The magnetic field becomes more tail-like. Assuming $B_z \equiv 0$ in the magnetotail current sheet or, in other words, assuming the polar cap boundary and the equatorward oval boundary to coincide, one can obtain the upper limit for the tail current intensity at which neutral lines can not exist in the magnetosphere. Here the maximal value is $\Phi_{pc} = 908$ MWb. Increasing of the dynamical pressure up to 28 nPa can make this limit to be equal to 1411 MWb.

In Figure 4 the polar cap magnetic flux dependence on solar wind pressure are shown. The quiet time (IMF $B_z = 0$) polar cap magnetic flux dependence on solar wind pressure is given by dashed curve. The disturbed time (IMF $B_z << 0$) polar cap magnetic flux when B_z in the tail equal to zero is shown by solid curve.

Thus, even during huge disturbnces the polar cap boundary cannot move down below a circle of radius 25°. However, by moving the inner edge of the current sheet earthward the summary flux through the auroral oval and through the cap can increase to 2472 MWb (by a factor of 1.78). The maximal oval diameter is 69°. If the dayside boundary is assumed to move down to 70°, the midnight boundary of the auroral oval can move down to latitudes about 41°. During severe disturbances, auroras are observed in night hours at these latitudes. For polar auroras to move down to latitudes of 23° reported in the paper [*Tsurutani et al.*, 2003] either extremely high (never observed earlier) plasma pressure is necessary, or the observed auroras are induced by other (non-auroral) particles.

CONCLUSION

Appearance of the magnetotail is interpreted to be a result of penetration of magnetosheath ions in the magnetotail from its dawn equatorial flank. Lobe magnetic field flux is formed by the geomagnetic field lines pushed to the magnetotail due to the field deformation by the arriving solar wind flux. The current sheet inner edge is thought to be the line of constant field $B = const = B_s$ starting at the magnetospheric subsolar point. The magnetic flux in the magnetotail lobes is then inversely proportional to a distance to the subsolar point R_1 or to a 6-power root from the solar wind dynamical pressure ($p^{-1/6}$). The magnetic flux in the polar cap (or in the magnetotail lobes) 508.55 MWb corresponds to the quiet conditions ($p = 2$ nPa and $R_1 = 10.1\ R_E$). The polar cap angular dimension is here equal to 14.88° which is in a good accordance with observations (see, e.g., discussion in *Alexeev et al.*, 1996).

The analisis of a relation between the magnetic flux in the magnetotail lobes and the flux of field lines closed through the magnetotail current sheet made for the

magnetotail current system enables calculation of the total flux from the equatorward boundary of the polar oval to the pole. This flux also depends on R_1, equaling 785 MWb for the quiet solar wind. The oval diameter is 18.61°. If the dayside cusp latitude is assumed to be 78° under quiet conditions, the the nightside equatorial boundary is found at 65°. An increase of solar wind dynamical pressure and accumulation of energy in the magnetotail results in growing dimensions of the polar cap and oval. As the magnetospheric field B_z-component is required to be positive, maximal dimensions of the polar cap and oval are restricted by the maximal angular diameter of the oval being about 70°.

To connect unambiguously the magnetospheric structures with the phenomena at the ionospheric altitudes (boundaries of atmospheric luminousity, boundaries of precipitation of diffrent-energy particles, boundaries of penetration of the solar cosmic rays etc.), it is insufficient to understand quasi-stationary structure of the magnetospheric magnetic field. One should know much about convective electric field in the magnetosphere, field-alighned electric fields which are rather strong during disturbances at the auroral latitudes, particle interaction with the MHD waves, etc. Quasi-stationary large-scale structure of the magnetic field is a rather significant organizing factor determining morphology of many magnetospheric processes.

Acknowledgments. This research was supported by Russian Foundation for Basic Research Grants 01-05-65003 and 04-05-64396, INTAS Grant No. 03-51-3922 and by Grant Minnayki NSH - 2046.2003.2.

REFERENCES

Alexeev I.I., E.S. Belenkaya, V.V. Kalegaev, Y.I. Feldstein, and A. Grafe, Magnetic storms and magnetotail currents, *J. Geophys. Res.*, 101, 7737-7747, 1996.

Alexeev, I.I., E.S. Belenkaya, D.G. Sibeck, Open field line in closed magnetospheric model, *Geomagnetizm i Aeronomia*, 38, N1, 9-18, 1998. (in Russian).

Alexeev, I.I., Energy flux in the Earth's magnetosphere: storm - substorm relationship, *Space Sci. Rev.*, 107, 141-148, 2003.

Alexeev I.I., E.S. Belenkaya, S. Yu. Bobrovnikov, and V.V. Kalegaev, Modelling of the electromagnetic field in the interplanetary space and in the Earth's magnetosphere, *Space Sci. Rev.*, 107, 7-26, 2003.

Blanchard, G.T., L.R. Lyons, and J.C. Samson, Accurancy of using the 6300A auroral emission to identify the magnetic separatrix on the nightside of the Earth, *J. Geophys. Res.*, 102, 9697, 1997.

Coroniti, F.V. and C.F. Kennel, Changes in magnetospheric configuration in the substorm growth phase, *J. Geophys. Res.*, 77, 3361, 1972.

McPherron, R.L., Growth phase of magnetospheric substorm, *J. Geophys. Res.*, 75, 5592, 1970.

McPherron, R.L., Physical processes producing magnetospheric substorms and magnetic storms, *Geomagnetism*, 4, 593, 1991.

Mead, G. D. and D. E. Beard, J. Geophys. Res., 69, 1169, 1964.

Mende, S.B., H.U. Frey, M. Lampton, J.-C. Gerard, B. Hubert, S. Fuselier, J. Spann, R Gladstone, and J.L. Burch, Global observations of proton and electron auroras in a substorm, *Geophys. Res. Lett.*, 26, 1139-1142, 2001.

Mende, S.B., H.U. Frey, B.J. Morsony, and T.J. Immel, Statistical behavior of proton and electron auroras during substorm, *J. Geophys. Res.*, 108(A9) 1339, doi:1029/2002JA009751, 2003.

Østgaard N., D.L. Detrick, T.J. Rosenberg, R.R. Vondrak, H.U. Frey, S.B. Mende, S.E. Haland,, and J. Stadsnes, High-latitude dayside energetic precipitation and IMF B_Z rotations, *J. Geophys. Res.*, 108(A4) 8013, doi:1029/2002JA009350, 2003.

Rae, I.J., K. Kabin, R. Rankin, F.R. Fenrich, W. Liu, J.A. Wanliss, A.J. Ridley, T.I. Gombosi, and D.L. De Zeeuw, Comparison of photometer and global MHD determination of the open-closed field boundary, *J. Geophys. Res.*, 109, A01204, doi: 1029/2003JA 009968, 2004.

Raeder, J., J. Berchem, and M. Ashour-Abdalla, The Geospace Environment Modeling Grand Challenge: Results from a global geospace circulation model, *J. Geophys. Res.*, 103, 14,787, 1998.

Schultz, M., Direct influence of ring current on auroral oval diameter, *J. Geophys. Res.*, 102, 14,149-14,154, 1997.

Tsurutani, B.T., W.D. Gonzalez, G.S. Lakhina, and S. Alex, The extreme magnetic storm of 1-2 September 1859, *J. Geophys. Res.*, 108(A7) 1268, doi:1029/2002JA009504, 2003.

Igor I. Alexeev, Skobeltsyn Institute of Nuclear Physics, Lomonosov Moscow State University, Leninskie Gory, Moscow 119992, Russia. (e-mail: alexeev@dec1.sinp.msu.ru)

Modeling Inner Magnetospheric Electric Fields: Latest Self-Consistent Results

Stanislav Sazykin[1], Robert W. Spiro[1], Richard A. Wolf[1], Frank R. Toffoletto[1], Nikolai Tsyganenko[2], J. Goldstein[3], and Marc R. Hairston[4]

This paper presents some of the latest results of self-consistent numerical modeling of large-scale inner-magnetospheric electric fields obtained with the Rice Convection Model (RCM). The RCM treats plasma drifts, electric fields, and currents in the inner magnetosphere self-consistently in the quasi-static (slow-flow) approximation under the assumption of isotropic pitch-angle distribution. Event simulations of the magnetic storm of March 31, 2001 are used with two newly available RCM input models: an empirical model of the storm-time magnetospheric magnetic field, and an empirical model of the plasma sheet. Results show that the effect of severe distortion of the magnetic field during very large magnetic storms improves the ability of the RCM to predict the location of Sub-Auroral Polarization Stream (SAPS) events, although there is not perfect agreement with observations. Weakening of shielding by region-2 Birkeland currents during times of severe magnetic field inflation also improves comparison of the RCM-computed plasmapause location with data. Results of simulations with plasma boundary sources varying in response to measured solar wind inputs show that the plasma sheet may become interchange unstable under certain geomagnetic conditions.

1. INTRODUCTION

The large-scale physics of the inner magnetosphere can be investigated theoretically by solving time-dependent equations of particles drifting in an electric field self-consistently calculated from the current-continuity equation and a time-dependent assumed magnetic field [e.g., *Wolf*, 1983], an approach known as "convection modeling" [e.g., *Harel et al.*, 1981a,b].

The Rice Convection Model (RCM), a numerical code based on the quasi-static (slow-flow) approach [*Wolf*, 1983] and the theoretical tool of choice for this work, has been used extensively to explain or illuminate many observed large-scale dynamical phenomena in the inner magnetosphere (e.g., shielding by region-2 Birkeland currents of the low-latitude region from the main effects of magnetospheric convection, the formation and decay of the storm-time ring current, the shape of the plasmapause, generation of subauroral ion drift or polarization jet electric fields), and to study the possibility of interchange instability in the inner plasma sheet [e.g., *Toffoletto et al.*, 2003; *Sazykin et al.*, 2002].

Based on more than 30 years of extensive modeling and comparisons with observations, our understanding of the electrodynamics of this part of the magnetosphere is better than ever, though it is not without gaps. In this paper, we highlight several unresolved issues related to large-scale storm-time

[1] Physics and Astronomy Department, Rice University, Houston, Texas
[2] Universities Space Research Association and NASA Goddard Space Flight Center, Greenbelt, Maryland
[3] Space Science and Engineering Division, Southwest Research Institute, San Antonio, Texas
[4] Center for Space Sciences, University of Texas Dallas, Texas

The Inner Magnetosphere: Physics and Modeling
Geophysical Monograph Series 155

10.1029/155GM28

magnetospheric and ionospheric electric fields, and we present some of our latest results bearing on these issues. The results presented below are from RCM numerical simulations of the magnetic storm that took place on March 31, 2001.

Among the unresolved issues in the physics of the inner magnetosphere and magnetosphere-ionosphere coupling are the rapid westward flows that are observed equatorward of the diffuse aurora, typically in the dusk-midnight sector. Using instruments carried by early Russian spacecraft, *Galperin et al.* [1974] first discovered strong (>50 mV/m), narrow (~1° latitude) poleward ionospheric electric fields in this region and called them "polarization jets". They were independently reported in the U.S.A. [e.g., *Smiddy et al.*, 1977; *Maynard*, 1978; *Spiro et al.*, 1978] and termed SAID (Sub-Auroral Ion Drift) events by *Spiro et al.* [1979]. Recently, the term SAPS (Sub-Auroral Polarization Stream) was introduced to describe somewhat wider regions of less intense westward flow that occur in the same general region, primarily in major storms [*Foster and Burke*, 2002].

Southwood and Wolf [1978] proposed a mechanism for generation of enhanced subauroral electric fields that involves closure of dusk-side region-2 Birkeland currents across a region of low conductivity. Event simulations with the RCM [*Harel et al.*, 1981a,b] showed sub-auroral electric field structures consistent with *in-situ* electric field measurements and in agreement with the *Southwood and Wolf* [1978] explanation.

Despite this early (and subsequent) success in predicting observed SAPS, many event simulations have shown that the RCM has a tendency to predict SAPS that are weaker than those observed, with latitudinal locations that tend to be poleward of the observed SAPS. In this paper, we examine two of the three factors that we identify as being responsible for this discrepancy: the magnetic field model used with the RCM, and temporal variability in plasma sheet density and temperature during storms. The third relevant factor relates to details of the auroral contribution to the conductivity tensor at the equatorward edge of the diffuse aurora, which we will not address here. The same RCM simulations are also used to compare RCM-computed plasmapause shapes and locations with those derived from the Extreme Ultraviolet (EUV) imager on board the IMAGE spacecraft as an indication of how accurate the overall RCM-computed subauroral convection electric field is. Finally, initial results regarding electric field structures due to the interchange instability in the plasma sheet are presented and discussed.

2. MODEL AND EVENT DESCRIPTIONS

2.1. Rice Convection Model

As the RCM physics and numerical methods have been described by, among others, *Harel et al.* [1981a], *Wolf* [1983], *Sazykin et al.* [2002], and *Toffoletto et al.* [2003], our description here will be the minimum necessary for understanding of the results below.

In the slow-flow, closed-field-line region of Earth's magnetosphere, each chemical species s ($s = \{1,2,3\}$ for e^-, H^+, O^+) of charge q_s is assumed to be isotropic in pitch angle. At the model boundary, each species is assumed to have a $\kappa = 6$ distribution function. The distribution function is divided into K_s "channels" in terms of invariant energy λ, which is related to kinetic energy W through the flux-tube volume $V = \int ds/B$ as $\lambda_{k,s} = W_{k,s} \cdot V^{2/3}$ and remains invariant along drift trajectories. The particle content $\eta_{k,s}$ in channel s, expressed in terms of number density $n_{k,s}$ as $\eta_{k,s} = n_{k,s} \cdot V$, is another invariant except for source and loss terms. In the absense of plasma production, the evolution of $\eta_{k,s}$ is governed by an advection equation:

$$\left[\frac{\partial}{\partial t} + \frac{\mathbf{B} \times \nabla \left(\Phi + (\lambda_{k,s}/q_s) V^{-2/3}\right)}{B^2} \cdot \nabla\right] \eta_{k,s} = -L_{k,s} \quad (1)$$

where $L_{k,s}$ represents plasma loss mechanisms. The present runs include ion loss by charge-exchange and electron loss by precipitation. The electrostatic potential Φ satisfies the current conservation equation

$$\nabla \cdot \left(-\hat{\Sigma} \cdot \nabla \left(\Phi - \Phi_c\right)\right) = \frac{\mathbf{B}}{B} \cdot \nabla V \times \nabla P \quad (2)$$

where Φ_c transforms to a frame rotating with the Earth, and the field-aligned current on the right-hand side is expressed in terms of gradients of total particle pressure P and flux tube volume V. $\hat{\Sigma}$, the conductance tensor, includes contributions from both solar EUV (based on the IRI-90 empirical model) and from self-consistently estimated auroral electron precipitation at 30% of the strong pitch-angle scattering limit. There are no field-aligned potential drops.

The RCM solves $\Sigma_s K_s$ equations (1) and equation (2) iteratively, stepping in time. The main inputs to the model are the electric potential on the poleward boundary ("polar cap" potential) for (2) and the number density and temperature of particles at the poleward boundary for (1), which is assumed to be the only source of particles.

2.2. Magnetic Field Model

Equations (1) and (2) include the magnetic field, a quantity that is not calculated in the model but is instead a time-dependent input to it. Previously, for event studies we have used the theoretical magnetic field model of *Hilmer and Voigt* [1995] (HV). However, HV does not adequately represent inflation of the innermost magnetosphere during large disturbances, possibly contributing to the discrepancy

between the observed and RCM-predicted location and strength of subauroral electric field structures. Here, we present first results from using the new storm-time magnetic field model of *Tsyganenko et al.* [2003] (T03S); this magnetic field model is based on data from 37 large magnetic storms and was constructed to account for large distortions of the inner ($L < 10$) magnetosphere during storms.

2.3. Plasma Sheet Boundary Conditions

Since we neglect source terms such as ion outflow from the ionosphere in (2), the only source of particles into the modeling region (and therefore the storm-time ring current) is represented by the high-L boundary condition on η. Due to the scarcity of *in-situ* central plasma sheet data, the RCM has typically been used with constant boundary conditions. However, it is known that plasma sheet properties are directly correlated with solar wind properties. Therefore, for results presented here we have used the empirical plasma sheet model of *Tsyganenko and Mukai* [2003] to specify the number density and temperature of particle species at $(-13R_E,0,0)$ (GSM coordinates) as a function of solar wind density, velocity, and interplanetary magnetic field (IMF) B_z component. These values are assumed to be constant in local time along the boundary.

2.4. Magnetic Storm of March 31, 2001

A coronal mass ejection and related interplanetary shocks produced a large magnetic storm that started early on March 31, 2001. Figure 1 shows the solar wind dynamic pressure and the GSM z-component of the IMF measured by SWEPAM and MAG instruments on board the ACE spacecraft (time-shifted to the sub-solar magnetopause location), together with the SYM-H index taken to represent Dst. Extreme solar wind conditions, including high dynamic pressure and large negative IMF B_z, occurred intermittently and produced extreme magnetospheric conditions, e.g., cross-polar cap potential drop in excess of 200 kV, strong ring current, dayside magnetopause earthward of geosynchronous orbit, and plasmapause locations inside 2 R_E at some local times.

During most of the day on March 30, the magnetic field below 66° latitude is quasi-dipolar. The degree of magnetic field distortion during the main phase of the storm can be seen in the equatorial mapping of lines of constant magnetic latitude and longitude. Figure 2 shows this mapping at ~08:30 UT, which is the time SYM-H reached its minimum value. The 56° magnetic latitude line that maps to $L = 3.2$ in a dipole field maps to 7 R_E at midnight in the disturbed field. The dominance of the tail current contribution to the *Dst* [*Skoug et al.*, 2003] is consistent with the field representation by T03S.

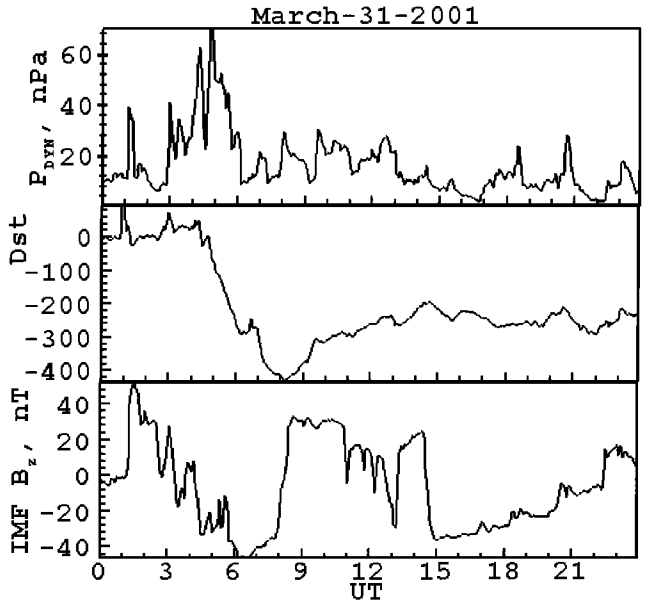

Figure 1. 5-min averaged solar wind dynamic pressure P_{dyn}, *Dst* (SYM-H) index, and the IMF B_z component for March 31, 2001. P_{dyn} and IMF B_z are from ACE time-shifted measurements.

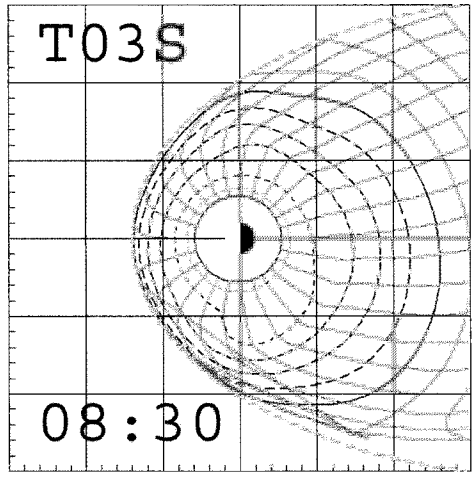

Figure 2. Mapping of lines of constant magnetic latitudes (innermost at 50°, step is 2°) and longitudes (step is 15°) to the equatorial plane using T03S magnetic field model, for ~08:30 UT on March 31, 2001 (time of Dst minimum).

The polar cap potential drop used as an input to the RCM was initially calculated from 5-minute averages of ACE solar wind and IMF data using the empirical relations of *Boyle et al.* [1997]. Since the polar cap potential apparently saturated at around 200 kV based on DMSP ion drift data [*Hairston et al.*, 2003], we have modified the expressions of

Boyle et al. so that if the potential drop exceeds 150 kV, the potential is reduced linearly to saturate at 200 kV.

Electric field measurements derived from DMSP drift meter and Millstone Hill incoherent-scatter radar data showed large subauroral electric field structures, which we identify as SAPS events. Simultaneous observations of total electron content (TEC) structures coincident with the plasmaspheric tails observed with the extreme ultraviolet (EUV) imager on board the IMAGE spacecraft, and subauroral electric field structures, have been reported by *Foster et al.* [2002].

3. RESULTS

We present results from three RCM simulations of this event. In the first two, we kept the plasma boundary condition constant throughout the event and varied the magnetic field model, using first the HV magnetic field model and then the T03S magnetic field model. Since T03S was found to improve our predicted electric fields (see below), a third simulation was done with T03S and with a time-varying plasma sheet boundary condition based on the empirical expressions of *Tsyganenko and Mukai* [2003].

3.1. Subauroral Electric Fields

Figure 3 compares the RCM-computed westward ion drift velocity (corresponding to poleward-directed electric field component perpendicular to **B**) in the ionospheric frame, obtained with HV and T03S magnetic fields. Superimposed is DMSP data along the spacecraft trajectory.

A SAPS, apparent as a secondary (equatorward) peak in the electric field, was seen by the DMSP ion drift meter and was also predicted by the RCM in both cases. While the location of the SAPS is in much better agreement with data in the T03S case, the magnitude of the peak is higher. A similar conclusion can be drawn from Figure 4, which is for roughly the same MLT in the subsequent pass, but in the southern hemisphere. A large uncertainty not addressed in these calculations (but the subject of ongoing research) is the dependence on details of the sub-auroral conductance distribution. Inaccuracies in our conductance model may well be responsible for the quantitative inaccuracy in our predictions of peak velocity in the SAPS.

3.2. Plasmapause

With launch of the IMAGE spacecraft and the subsequent availability of EUV He^+ 30.4 nm emission-based images of the plasmasphere, a new diagnostic tool has become available for indirect determination of the partially-shielded convection electric field in the innermost part of the magnetosphere. In the RCM, the location of the plasmapause is calculated by solving equation (2) for an electron energy "channel" with $\lambda = 0$ (cold) particles, which **E**×**B** drift in a time-dependent electric field. We compare this computed boundary shape with the plasmapause shape derived from EUV images based on gradients of the emission intensity as first reported by *Foster et al.* [2002] and subsequently verified by *Goldstein et al.* [2003].

Skoug et al. [2003] reported EUV plasmapause images for this storm. According to their analysis, the initial pre-storm

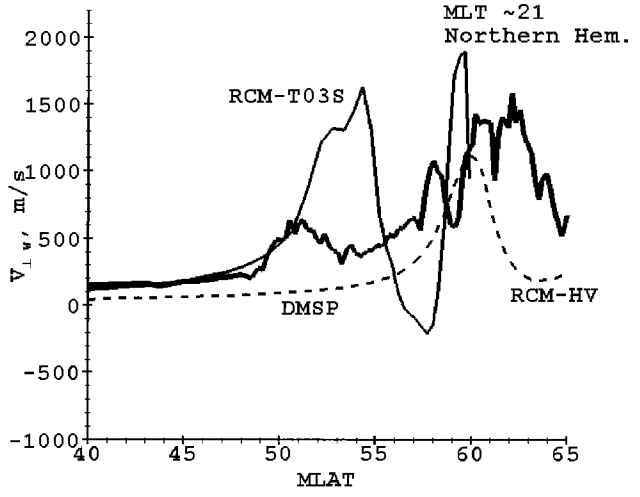

Figure 3. Westward ion drift (poleward electric field) component measured by the DMSP F15 ion drift meter along its trajectory for the pass that started at 15:06 UT, northern hemisphere (thick); RCM-computed ion drift component along the same trajectory (~21 MLT) obtained with T03S (solid thin) and HV (dashed) magnetic field.

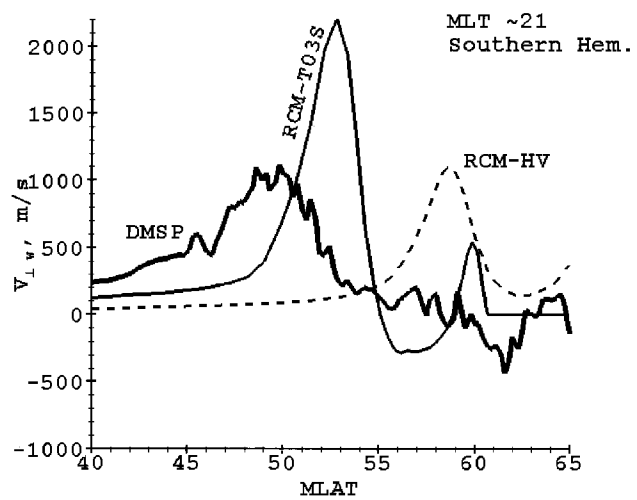

Figure 4. Same as Figure 3 but for the subsequent southern hemisphere pass.

[redacted]

shape of the plasmasphere was approximately circular, with the size of $L \sim 4$, and an indication of the a plasmaspheric tail at dusk. Our calculations at 00 UT on 3/31/2001 are in good agreement with the these observations. During the main phase of the storm, EUV images indicated a very strong plasmasphere contraction, to within $L \sim 2$ [*Skoug et al*, 2003]. Unfortunately, the quality of images during this period (03-07 UT) precluded derivation of the plasmapause location.

However, IMAGE-derived plasmapause locations were once again obtained for a period starting at ~15:30 UT. In Plate 1, we compare the IMAGE-derived shapes with those computed by the RCM using the HV and T03S magnetic field models. We should note that the algorithm for deriving EUV plasmapause locations is somewhat subjective, with the error estimated to be 0.1 to 0.4 R_E [*Goldstein et al.*, 2003]. Both RCM calculations and the data show a large plasmaspheric tail (plume) extending from the post-dusk plasmapause to the dayside magnetopause. While the dayside plasmapause location is more sensitive to the assumed distribution of the potential on the high-latitude boundary of the modeling region, the nightside plasmapause shape is mostly affected by the prompt-penetration electric field. In our experience, when compared to EUV data, the RCM tends to predict a larger plasmasphere on the nightside, especially near dusk. The discrepancy is larger for the HV case; with the T03S calculation giving better agreement with data.

The size of the plasmasphere is controlled by the strength of the convection and the effectiveness of region-2 Birkeland currents in shielding the subauroral latitudes from the convection electric field. Since for this storm, the plasmasphere was observed within $L \approx 2$, inflation of the magnetic field does not seem important. The shielding is weaker in the T03S case, allowing stronger electric fields on the nightside and thus making the plasmasphere smaller. Analysis of figures such as Plate 1 throughout the storm (not shown) leads us to conclude that the second discrepancy regarding larger bulge on the duskside is a persistent feature. Thus the RCM predictions for both the SAPS and the dusk-midnight plasmapause lie at higher L than the observations indicate.

3.3. Interchange Instability in the Plasma Sheet

Extreme variations of the solar wind and IMF parameters during this magnetic storm led us to investigate the susceptibility of the plasma sheet to the interchange instability. *Skoug et al.* [2003] reported geosynchronous *in-situ* particle observations of the plasma sheet being very close to the Earth and with number densities increasing more than a factor of 10 during the storm. The possibility of the inner edge of the plasma sheet and ring current becoming interchange-unstable has been demonstrated in an event simulation by *Sazykin et al.* [2002] (see also references therein). Solar wind control of the conditions for the interchange instability was discussed by *Golovchanskaya et al.* [2002].

When we allowed the RCM plasma sheet boundary conditions to vary in response to changing solar wind conditions, we found three intervals of interchange instability of the magnetosphere lasting from 30 min to 2 hours. An example of the resulting highly-structured electrostatic potential and field-aligned current patterns is shown in Plate 2. The primary physical effect of the interchange instability is to transport low-content flux tube "bubbles" earthward through the plasma sheet by forming elongated "fingers". An interesting consequence of this situation is its possible relevance to the formation of auroral arcs [*Golovchanskaya and Maltsev*, 2003].

4. SUMMARY

RCM simulations of the major magnetic storm of March 31, 2001 were used to compare RCM-computed electric fields with *in-situ* and remote sensing measurements.

The degree of inflation of the magnetic field controls the strength of the overall subauroral electric field, which can be seen in its influence on the shape and location of the plasmapause. Use of the T03S magnetic field model results in the RCM-computed nightside plasmapause being in a better agreement with IMAGE EUV data.

The inflation of the magnetic field also strongly affects the strength and the latitudinal location of the SAPS electric fields structures. Using T03S, which is arguably a better storm-time magnetic field model, results in the RCM predicting SAPS that are stronger and located more equatorward. This partially resolves the previous discrepancy between RCM-predicted and observed SAPS electric fields, although full agreement is still not achieved.

When the plasma sheet boundary condition is allowed to vary during the storm, model results indicate that the plasma sheet may become interchange unstable under certain solar wind conditions, although the details depend on several assumptions made in the calculations.

Acknowledgments. Work at Rice University was supported by the Upper Atmospheric Research division of the NSF under grant ATM-20101349 and by the NASA Sun-Earth Connection Theory Program under grant NAG5-11881. N.T. acknowledges support by grants from NASA's LWS (NAG5-12185) and NSF GEM (ATM-0296212) programs. The DMSP data were provided by support from NASA grant NAG5-9297. Work at Southwest Research Institute was supported by NASA SEC Guest Investigator grant NAG5-12787. We thank the ACE SWEPAM and MAG instrument teams and the ACE Science Center for providing the ACE data. SYM-H indices were obtained from Kyoto World Data Center for Geomagnetism, Japan.

REFERENCES

Boyle, C.B., P.H. Reiff, and M.R. Hairston, Empirical polar cap potentials, *J. Geophys. Res.*, 102, 111, 1997.

Foster, J.C., and W.J. Burke, ASPS: A new characterization for subauroral electric fields, *EOS*, 83, 393, 2002.

Foster, J.C., P.J. Erickson, A.J. Coster, J. Goldstein, and F.J. Rich, Ionospheric signatures of plasmaspheric tails, *Geophys. Res. Lett.*, 29, 1623, doi:10.1029/2002GL015067, 2002.

Galperin, Y.I., Y.N. Ponomarev, and A.G. Zosimova, Plasma convection in polar ionosphere, *Ann. Geophys.*, 30, 1-7, 1974.

Goldstein, J., M. Spasojevic, P.H. Reiff, B.R. Sandel, W.T. Forrester, D.L. Gallagher, and B.W. Reinisch, Identifying the plasmapause in IMAGE EUV data using IMAGE RPI in situ steep density gradients, *J. Geophys. Res.*, 108, 1147, doi:10.1029/2002JA009475, 2003.

Golovchanskaya, I.V., and Y.P. Maltsev, Interchange instability in the presence of the field-aligned current: Application to the auroral arc formation, *J. Geophys. Res.*, 108, 1106, doi:10.1029/2002JA009505, 2003.

Golovchanskaya, I.V., Y.P. Maltsev, and A.A. Ostapenko, High-latitude irregularities of the magnetospheric electric field and their relation to solar wind and geomagnetic conditions, *J. Geophys. Res.*, 107, 1001, doi:10.1029/2001JA900097, 2002.

Hairston, M.R., T.W. Hill, and R.A. Heelis, Observed saturation of the ionospheric potential during 31 March 2001 storm, *Geophys. Res. Lett.*, 30, 1325, doi:10.1029/2002GL015894, 2003.

Harel, M., R.A. Wolf, P.H. Reiff, R.W. Spiro, W.J. Burke, F.J. Rich, and M. Smiddy, Quantitative simulation of a magnetospheric substorm 1, Model logic and overview, *J. Geophys. Res.*, 86, 2217, 1981a.

Harel, M., R.A. Wolf, R.W. Spiro, P.H. Reiff, C.-K. Chen, W.J. Burke, F.J. Rich, and M. Smiddy, Quantitative simulation of a magnetospheric substorm 2, Comparison with observations, *J. Geophys. Res.*, 86, 2242, 1981b.

Hilmer, R.V., and G.-H. Voigt, A magnetospheric magnetic field model with flexible current systems driven by independent physical parameters, *J. Geophys. Res.*, 100, 5613-5628, 1995.

Maynard, N.C., On large poleward-directed electric fields at subauroral latitudes, *Geophys. Res. Lett.*, 5, 617, 1978.

Sazykin, S., R.A. Wolf, R.W. Spiro, T.I. Gombosi, D.L. De Zeeuw, and M.F. Thomsen, Interchange instability in the inner magnetosphere associated with geosynchronous particle flux decreases, *Geophys. Res. Lett.*, 29, 1448, doi:10.1029/2001GL014416, 2002.

Skoug, R.M., M.F. Thomsen, M.G. Henderson, H.O. Funsten, G.D. Reeves, C.J. Pollock, J.-M. Jahn, D.J. McComas, D.G. Mitchell, P.C. Brandt, B.R. Sandel, C.R. Clauer, and H.J. Singer, Tail-dominated storm main phase: 31 March 2001, *J. Geophys. Res.*, 108, 1259, doi:10.1029/2002JA009705, 2003.

Smiddy, M., M.C. Kelley, W. Burke, F. Rich, R. Sagalyn, B. shuman, R. Hays, and S. Lai, Intense poleward-directed electric fields near the ionospheric projection of the plasmapause., *Geophys. Res. Lett.*, 4, 543, 1977.

Southwood, D.J., and R.A. Wolf, An assessment of the role of precipitation in magnetospheric convection, *J. Geophys. Res.*, 83, 5227, 1978.

Spiro, R.W., R.A. Heelis, and W. B. Hanson, Ion convection and the formation of the mid latitude F-region ionospheric trough, *J. Geophys. Res.*, 84, 4255, 1978.

Spiro, R.W., R.A. Heelis, and W.B. Hanson, Rapid sub-auroral ion drifts observed by Atmospheric Explorer C, *Geophys. Res. Lett.*, 6, 657, 1979.

Toffoletto, F., S. Sazykin, R. Spiro, and R. Wolf, Inner magnetospheric modeling with the Rice Convection Model, *Space Science Rev.*, 107, 175-196, 2003.

Tsyganenko, N.A., and T. Mukai, Tail plasma sheet models derived from Geotail particle data, *J. Geophys. Res.*, 108, 1136, doi:10.1029/2002JA009707, 2003.

Tsyganenko, N.A., H.J. Singer, and J.C. Kasper, Storm-time distortion of the inner magnetosphere: How severe can it get? *J. Geophys. Res.*, 108, 1209, doi:10.1029/2002JA009808, 2003.

Wolf, R.A., The quasi-static (slow-flow) region of the magnetosphere, in *Solar-Terrestrial Physics,* edited by R.L. Carovillano and J.M. Forbes, 303, D. Reidel, Hingham, MA, 1983.

J. Goldstein, Space Science & Engineering Div., Southwest Research Institute, 6220 Culebra Rd., San Antonio, TX 78238.

M.R. Hairston, W.B. Hanson Center for Space Sciences, University of Texas Dallas, P.O. Box 830688 F022, Richardson, TX 75083.

S. Sazykin, R.W. Spiro, F.R. Toffoletto, R.A. Wolf, Physics and Astronomy Department, Rice University, MS-108, 6100 South Main St., Houston, TX 77005.

N.A. Tsyganenko, USRA/NASA Goddard Space Flight Center, Code 695, Greenbelt, MD 20771.

Comparison of MHD Simulations of Isolated and Storm Time Substorms

M. Wiltberger[1], S.R. Elkington[2], T. Guild[3], D.N. Baker[2], and J.G. Lyon[4]

The Lyon-Fedder-Mobarry global magnetohydrodynamic simulation has been used to model the magnetosphere during a variety of solar wind conditions. Early work with the simulation was concentrated on modeling isolated substorms and the global characteristics of magnetic storms. In this paper we will compare the results from simulations of isolated substorms to those occurring during magnetic storms. The substorm which occurred on August 27, 2001 was a fairly typical isolated substorm which had extensive set of satellite and ground based observations. The LFM simulation of the interval agrees with some of these observations. The simulation results also show that thin current sheets develop during the growth phase of substorms and are disrupted, in part, by flows originating the in mid-tail region prior to ionospheric signatures of substorm onset. Furthermore, detailed analysis of the energy partitioning in the magnetotail shows the transfer of energy from the lobes into the plasma sheet occurs a few minutes before substorm onset. The magnetic storm which began on March 31, 2001 was one of the largest magnetic storms during this solar cycle. In this storm-time interval a very large substorm occurred with an onset at 0630 UT. Results from this simulation agree with some observations made by the constellation of spacecraft present during this substorm. Comparison between the simulation results for these two events indicates that storm-time and isolated substorms share the same essential features, development of intense thin current sheets during growth phase, disruption of this current sheet linked to activity in the mid-tail region, and rapid recovery phases.

1. INTRODUCTION

Study of substorms has been a focus of magnetospheric physics since their discovery by *Akasofu* [1964]. Initial work in understanding these events placed the onset, driven by magnetic reconnection, in the near Earth region [*Hones*, 1979]. Later observations indicated that reconnection was not occurring in the near Earth region and that substorm onset may not be directly caused by reconnection [*Lui et al.*, 1992; *Lopez et al.*, 1993]. *Baker et al.* [1996] presents an excellent summary of the revision made to Near Earth Neutral Line (NENL) model and to account for the new observational evidence. While some controversy still remains the basic features of substorm, e.g. growth phase, explosive release, onset in the near Earth region, magnetic reconnection in the mid-tail region, etc., have obtained wide spread acceptance.

[1]High Altitude Observatory, National Center for Atmospheric Research, Boulder, CO.
[2]Laboratory for Atmospheric and Space Physics, University of Colorado at Boulder, Boulder, CO.
[3]Center for Space Physics, Boston University, Boston, Massachusetts.
[4]Department of Physics and Astronomy, Dartmouth College, Hanover, New Hampshire.

The Inner Magnetosphere: Physics and Modeling
Geophysical Monograph Series 155

10.1029/155GM29

One of the issues which allows for the controversy to continue is the lack of simultaneous observations throughout the magnetosphere during the onset of the substorm. A possible solution to this problem is to examine events within a global simulation. *Lyon et al.* [1998] showed that it was possible to use a global magnetohydrodynamic simulation to reproduce the growth, multiple onset, and recovery of an substorm which occurred on March 9, 1995. *Raeder and McPherron* [1998] used their MHD simulation to study the formation of the substorm current wedge and the dipolarization of the magnetic field at substorm onset. Coupling between the mid-tail region and the near Earth region via flow channels was seen in the December 10, 1996 substorm simulation conducted by *Wiltberger et al.* [2000]. While none these simulations includes an accurate model for reconnection physics, they are capable of reproducing the basic features of a magnetospheric substorm and providing a global picture into the physics of the magnetosphere.

The loading-unloading nature of the substorms has been determined to be a fundamental part of the phenomenon [*Vassiliadis et al.*, 1995]. An interesting question raised by *Baumjohann et al.* [1995] was to determine the difference in this process of substorms which occurred during storm times and those that occurred outside of a magnetic storm. They concluded that only substorms which occurred during the main phase of the storm, as opposed to substorms occurring later in the storm interval, show the same characteristics as isolated substorms and the NENL model.

In this paper we present the results from two LFM simulations of magnetospheric substorms. The next section of the paper provides a brief summary of the LFM magnetospheric model and the parameters that were used for each of the simulations. In the third section we present the results from the 0630 UT substorm on March 31, 2001 during a very strong storm interval. Section 4 presents the results from an isolated substorm which occurred shortly after 0400 UT on August 27, 2001. A comparison of the two substorm simulations is included in section 5. We end the paper with some brief conclusions about the simulation of storm time and isolated substorms with the LFM.

2. CODE DESCRIPTION

The LFM consists of two linked simulations [*Fedder et al.*, 1995a; *Fedder and Lyon*, 1995; *Mobarry et al.*, 1996] for modeling the interaction of the solar wind, the magnetosphere, and the ionosphere. The ideal magnetohydrodynamic MHD equations [*Chen*, 1984], numerically solved by the partial donor method [*Hain*, 1977, 1987], are used to model solar wind and magnetospheric plasmas. The ionosphere is simulated by solving a height integrated current continuity equation that has been coupled via empirical relationships to the magnetospheric simulation.

The MHD equations are solved in a region containing the solar wind and the magnetosphere. For the results discussed in this paper this region is essentially a cylinder 100 R_E in radius and 380 R_E long. The X axis extends from the sunward boundary at $X = 30\ R_E$ to the anti-sunward boundary $X = -350\ R_E$ The computational grid for the LFM has been adapted to place optimal resolution regions known *a priori* to be important, e.g. the magnetopause, magnetotail, etc. In the high resolution substorms studies the cells in the magnetopause region are approximately $0.25\ R_E$ long and cells in the solar wind are typically between $1.0\ R_E$ and $1.5\ R_E$. In the lower resolution storm studies these cells are between 2 and 3 times larger.

Although we are solving the ideal MHD equations, which are nondissipative, the effects of finite cell size produce a numerical proxy for resistivity and viscosity. The merging of magnetic fields occurs when oppositely directed magnetic fields are convected into a computation cell and the numerical averaging within the cell results in annihilation of the magnetic flux which is not possible within the context of ideal MHD. The resulting numerical resistivity is important only in regions where this "forced reconnection" situation scenario is possible. The work of *Fedder and Lyon* [1987] and *Fedder et al.* [1995a] showed that the subsequent rate of reconnection is largely controlled by the physical boundary conditions rather than the numerical method. The cross polar cap potential, which is an indirect measure of the global reconnection rate, shows little variation with increased resolution. This leads us to conclude that the grid resolution is not controlling the rate of reconnection.

An ionospheric simulation supplies the inner boundary condition for the MHD solution in the magnetosphere. The solution in the ionosphere is done by integrating the continuity equation for current over the height of the ionosphere to obtain a two dimensional potential equation for magnetosphere - ionosphere coupling,

$$\nabla_\perp \cdot \vec{J}_\perp = \nabla_\perp \cdot \Sigma \cdot \nabla_\perp \Phi = \vec{J} \cdot \vec{b}. \quad (1)$$

Here $\vec{J}_\perp$ is the height integrated current perpendicular to the magnetic field, Φ is the ionospheric potential, Σ is the height integrated anisotropic conductivity tensor. We have used the $\vec{J}_\perp = \Sigma \cdot \vec{E}$ form of Ohm's law to obtain the relationship between the field aligned currents (FAC) and the ionospheric potential in equation 1. The numerical solution for the ionospheric parameters strongly depends on the height-integrated conductivity tensor. This tensor includes empirical models for the effects of solar UV ionization and electron precipitation. The detailed empirical model for calculating the anisotropic conductivity tensor in the LFM is presented by *Fedder et al.* [1995b].

The inner boundary of the MHD domain is a sphere between 2 and 3 R_E in radius. The location is chosen as balance between the rapid increase in the Alfvén velocity as the altitude decreases, which leads to very short time steps, and the likelihood of activity extending to low latitudes in the ionosphere. The field-aligned currents are determined at the inner magnetospheric boundary and are then mapped instantaneously along dipole field lines to the ionosphere. The ionospheric solution for $\vec{E}$ is then mapped back to this boundary and used to define the boundary condition for the plasma velocity. Since the small cells in the high resolution substorm studies already require small time steps, and the substorm onset isn't likely to occur at low latitudes, we use a 3 R_E inner boundary. In contrast, the lower resolution storm studies need to extend the ionospheric boundary to lower latitudes due to expansion of the auroral oval outside its typical domain.

3. MARCH 31st 2001 STORM

Several solar flares and coronal mass ejections (CME) occurred on the Sun during late March 2001. A very powerful eruption on March 29 led to a 'halo' CME which eventual had a significant impact on the Earth's magnetosphere [*Baker et al.*, 2002a]. The solar wind observations made by the ACE satellite from its L1 monitoring position are shown in Figure 1. A density enhancement late on March 30th preceded the arrival of an interplanetary shock at ~0030 UT during which time the solar wind velocity increased to approximately 600 [km/s]. This velocity increase was followed by another increase at 0200 UT to greater than 700 [km/s]. The second velocity increase was also accompanied by a high solar wind number density and resulted in a significant solar wind ram pressure. The magnetic field structure after the passage of the interplanetary shock is quite complicated as indicated by the large rapid changes in IMF orientation. Immediately after the shock passage B_Z was northward with a strength of nearly 40 [nT]. B_Z undergoes several oscillations between ±40 [nT] in the period between the shock arrival and 0530 UT. After this time the IMF B_Z remains strongly southward, ~–50 [nT], for several hours. Since we used initial ACE data to drive this simulation the V_Y and V_Z components were set to zero. In addition, the simulation used the blue line in Figure 1 as the B_X in order to satisfy the numerical constraints, see *Wiltberger et al.* [2000] for a detailed explanation, on the front boundary.

As expected these solar wind conditions led to a very large geomagnetic storm. The D_{st} index, seen in Figure 2, reached a minimum value near –360 [nT] around 09 UT on March 31st. Global MHD simulations of the magnetosphere with isotropic pressures and temperatures do not contain sufficient physics to produce and maintain the strong ring current implied by the D_{st} index, but *Chen et al.* [1995] suggest using

$$D_{st}^{mhd} = B_z^e(t) - B_z^e(t=0), \tag{2}$$

where B_z^e is the equatorial magnetic field, as a proxy for the D_{st} index in the MHD simulation results. The cyan line in Figure 2 shows the results of this calculation taken from X = –5 R_E. The simulation captures the compression feature shortly after midnight on the 31st, but never produces the large

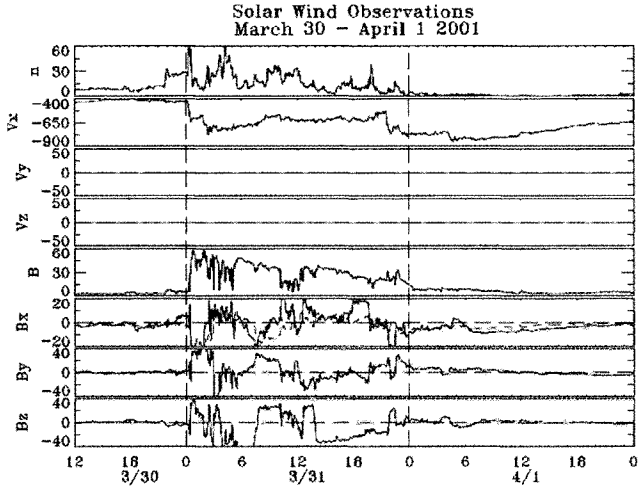

Figure 1. The solar wind data from ACE which was used to drive the LFM simulation for this interval. The dashed (gray) line in the B_X panel indicates the modified value of this parameter as described in Section 2.

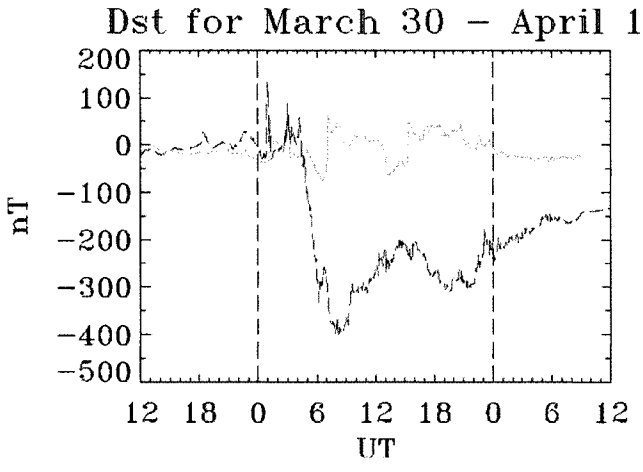

Figure 2. This figure shows a comparison between the WDC provisional *Dst* (black) and the simulation index (gray) as defined as the difference between the equatorial B_Z at time t and a reference time.

response seen in the index. The MHD simulation shows an initial decrease in the near Earth magnetic field which is caused by pressure driven currents within the inner magnetosphere which can be described by MHD. However, these currents recover much more rapidly than the real ring current, so the exponential decay features are not seen in the simulation results.

There were also a large number of substorms during this interval. Figure 3 compares the WDC provisional AL/AU index with the results from the LFM simulation. This interval includes four large substorms (AL < -1000 [nT]), one very large substorm (AL < -2500 [nT]), and several moderate substorms. The simulation results, shown by the cyan line in Figure 3, were calculated by finding the maximum ionospheric current in a sector surrounding midnight as the source term in a simple application of Ampere's Law. The simulation shows substorms occurring throughout the vast majority of the storm, but the magnitude of the AL index is not in very good agreement with the observations. Initially the substorms are equal or slightly larger than the observations, but by the 0630 UT substorm the response is significantly smaller in the LFM. It is worth noting that the simulated index continues to show substorm responses out until 1900 UT substorm, but clearly misses the 0500 UT substorm on April 1. We believe that the decreasing intensity of the substorm strength is a reflection of the depletion of plasma within the magnetotail which occurs in the simulation during prolonged periods of strong driving because the lack of plasma limits the ability of the simulation to produced the stretched magnetic field configuration required for large substorms.

The bottom panel of Figure 3 shows a blowup of the AU and AL indices for the first twelve hours of March 31. Of particular interest is the substorm whose onset is clearly seen at 0630 UT in the AL index. *Baker et al.* [2002a] used a vast array of magnetospheric spacecraft, including CLUSTER and POLAR, to provide both a 'telescopic' and 'microscopic' view of the processes occurring in this storm time substorm. The simulated AL index shows an excellent agreement with the onset time of this substorm. Unfortunately, this agreement is not indicative of the simulation capturing onset time within minutes. The usual practice in using the LFM is to determine a correction factor between simulation time and UT by assuming ballistic propagation of the solar wind from the ACE observation point to the Earth, but during intervals like this one, long duration with significant variation in solar wind speed, this method results in an average correction factor with a great deal of uncertainty. In order to facilitate comparison with satellite observations and the ion injection study by *Elkington et al.* [*this issue*] the correction factor has been adjusted to make the simulated substorm onset time agree with the observations. This adjustment results in an approximately 20 minute change from the average which is not unreasonable given the high variability of the solar wind speed during this period.

In Figure 4, simulation results are compared with the GOES 10 observations. As discussed by *Baker et al.* [2002a] GOES 10 was located at 22 LT and showed a dipolarization at 0630 UT. The B_X and B_Y features are consistent with the spacecraft begin inside the substorm current wedge at onset. The B_Z from the LFM simulation shows the dipolarization of the magnetic field at 0630 in good agreement with

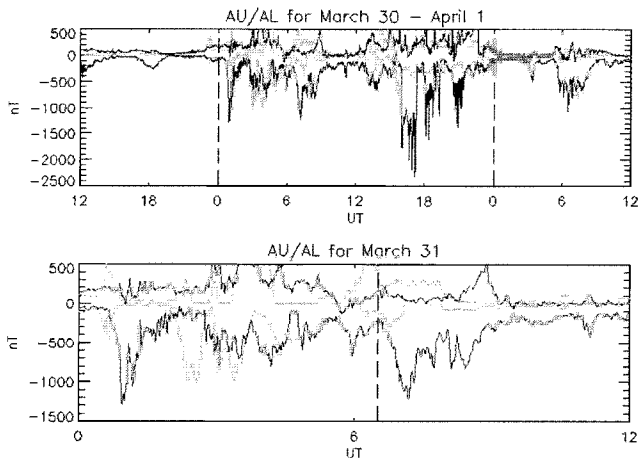

Figure 3. The top panel in this figure shows a comparison between the provisional WDC AU/AL data (black) and the simulation results (gray) for the entire magnetic storm interval. The bottom panel shows the same data for the first twelve hours of March 31st.

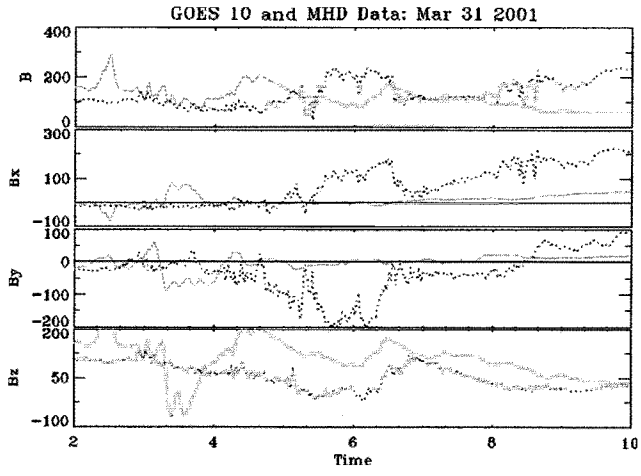

Figure 4. Simulation results (gray) are compared against GOES 10 observations (black). The simulation dipolarization characteristics compare well with GOES B_Z observations. The simulated B_X and B_Y components do not place with location within the SCW as seen in the observations.

the observations. The B_X and B_Y results are not in qualitative agreement with the observations and show that the location of the GOES 10 satellite was not within the simulated substorm current wedge. In addition, the simulated B_X does not show the recovery after the substorm that the observations indicate. This implies that the simulated plasma sheet was significantly depleted by the enhanced convection.

The strength of global modeling lies not within comparisons to individual satellite observations, but in visualizing vast portions of the magnetosphere at the same time. The left column in Plate 1 shows the evolution of the current sheet during the 0630 substorm. The cut of J_Y in the XZ plane five minutes prior to substorm onset in the top row shows the presence of an intense region of cross tail current embedded inside the plasma sheet. The middle row depicts the structure of current sheet in the XY plane at substorm onset. This figure shows a clear disruption of the current sheet concentrated in the premidnight sector consistent with the conclusions drawn by *Baker et al.* [2002a]. The high intensity wings located at $Y \sim \pm 10$ R_E are actually the magnetosheath which has been pushed very far Earthward by the combination of strong ram pressure and southward IMF. The state of the current sheet five minutes after substorm onset is shown in the bottom row of Plate 1. The disruption of current within the plasma sheet has expanded past midnight and well into the dawn sector, disrupting most of the intense current sheet that existed prior to substorm onset.

In summary, the LFM clearly produces substorms during this geomagnetic storm which was driven by very geoeffective solar wind conditions. The detailed analysis of this event is complicated by extreme solar conditions and the overlapping phenomena. The 0630 UT substorm is clearly seen in the simulated AL index and GOES 10 data. The global picture illustrated by the current sheet shows a substorm whose onset was located Earthward of -10 R_E and well into the premidnight sector.

4. AUGUST 27, 2001 SUBSTORM

An isolated magnetospheric substorm occurred early on August 27, 2001 and was monitored by a constellation of satellites. *Baker et al.* [2002b] used these numerous observations to determine that magnetic reconnection began in the mid-tail region, before the signatures of current disruption or auroral onset were observed, leading them to conclude that magnetic reconnection was the causative driver for this substorm. WIND observations of the solar wind were used to drive a high resolution simulation of the magnetosphere for this interval. These conditions include a fairly typical solar wind density (~5 [#/cc]) and velocity (~400 [km/s]), with a several hour period of southward IMF (~5 [nT]) which preceded the onset of the substorm.

The onset of the substorm was seen in CANOPUS magnetometer observations, which have been used to construct a set of CU and CL indices in the same fashion as the AU and AL indices. The ionospheric currents within the LFM were used to drive a Biot-Savart based calculation described in *Wiltberger et al.* [2003] to determine magnetic perturbations for the individual stations within the CANOPUS magnetometer chain. A comparison of CU/CL indices and those determined from the simulation are shown in Figure 5. The observations clearly indicate substorm onset at 0408 UT, while the simulation places the onset of the substorm eight minutes later at 0416 UT. Unlike the March 31st event we did not adjust the ballistic correction factor to make the simulated onset times align with the observations. In the simulation the expansion phase of the substorm does not produce as large a magnetic perturbation as observations would indicate, but *Shepherd and Shubitidze* [2003] have shown that local ground conductivities not included in the LFM model can affect the determination of the perturbation magnetic field. The simulated substorm undergoes a prolonged recovery phase which is shorter than the real substorm recovery phase.

A comparison between the CLUSTER 2 magnetic field measurements and the LFM results is shown in Figure 6. The spacecraft was located at (–19, –2, –1) in GSM coordinates. The high B_X values in comparison with B_Y and B_Z show that the spacecraft was located in the outer parts of a thick plasma sheet. At 0401 UT the magnetic field strength in each of the three components dipped briefly, which is interpreted by *Baker et al.* [2002b] as an encounter with the reconnection line which formed Earthward of the spacecraft and moved

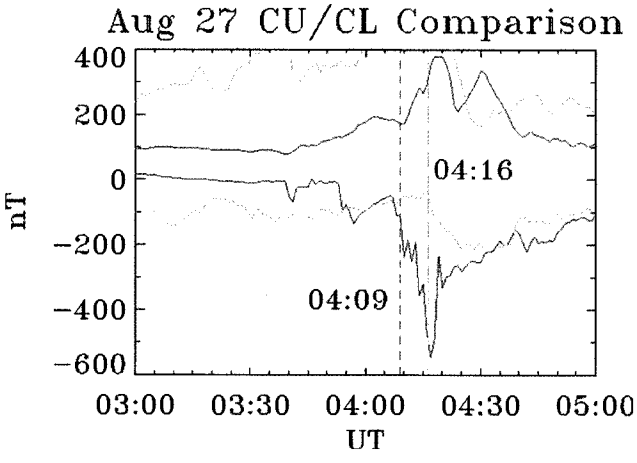

Figure 5. Simulated CU/CL results (gray) are compared with observations from CANOPUS stations (black). The simulation onset time of 0416 UT is marked with the long dashed line while the observed onset time at 0408 is shown with short dashed line.

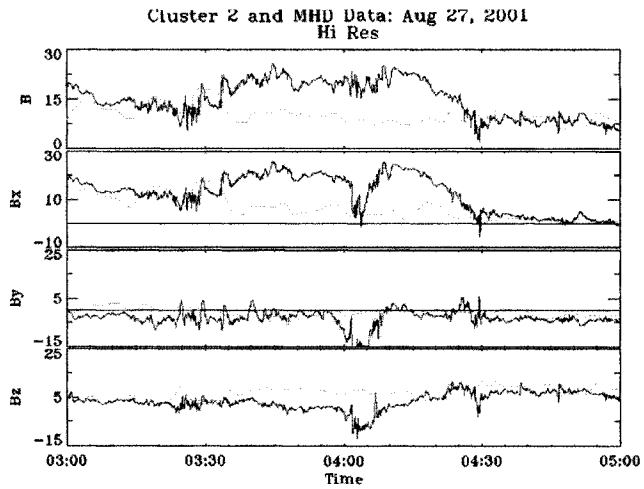

Figure 6. Simulation results (gray) are compared with Cluster 2 magnetic field observations (black). The simulation does not reproduce the encounter with the reconnection site seen in the cluster observations.

tailward as the expansion phase progressed. The LFM fields do not show any encounter with the reconnection site in the simulation. Examination of the global structure of the simulated magnetosphere places the CLUSTER 2 location approximately 5 R_E Earthward of the last closed field line in that sector. An attempt to displace the satellite's position further tailward in the simulation did produce an encounter with a tailward moving plasmoid, which means that sector in which reconnection began in simulation was not the same. Unfortunately, attempts to reproduce the magnetic structure seen by the CLUSTER 2 spacecraft by moving the location of the spacecraft within the simulation where unsuccessful.

The right hand column of Plate 1 illustrates the evolution of the current sheet in the simulation during this substorm. In the top row we see the current structure in the XZ plane five minutes prior to onset indicated by the simulated CL index. The strongest portion current sheet extends from $X = -10$ R_E to $X = -15$ R_E is embedded inside a weaker and broader current profile. At substorm onset (middle row), a disruption of the current sheet is occurring along the X axis near -11 R_E in a very limited local time sector. The arrows shown on top of the current show the structure of the plasma flow within the magnetotail. A burst of flow from the midtail region (25 R_E) propogates into the inner magnetotail leading to the disruption of the cross tail current in the midnight sector. The bottom panel of Plate 1 shows the status of current sheet five minutes later. The current intensities within the entire magnetotail have been reduced in strength with structure remaining roughly the same as the simulated CL onset time. The propagation of multiple flow bursts from the mid-tail into the near-Earth region caused the disruption the current sheet. This disruption leads to the CL index onset and can be interpreted as the reconnection region being the causative agent for the onset of the substorm in the simulation results.

The high resolution simulation combined with the isolated nature of this event allows us to examine the energy partitioning in the magnetotail during the evolution of the substorm. The first step in this process is illustrated in Plate 2. The background of the plate shows V_X in the XZ plane at 0337 UT during the growth phase of the substorm. The blue translucent surface defines the lobes of the magnetotail by selecting regions which have $P > 0.01$ nPa and $\rho > 0.2$#/cc. Automatic determination of the plasma sheet is conducted by searching in the magnetotail for regions with $\beta < 0.5$ and $T > 1$ keV. The plasma sheet is shown by the red translucent surface in Plate 2. Given these definitions, it is possible to step through the time history of the simulation and extract the plasma parameters inside both of these domains. Once this data has been extracted it is used to compute the total magnetic, kinetic, thermal energy within each domain. Figure 7 shows the partitioning of energy during the evolution of the substorm. The blue line indicates the lobe magnetic field energy while the green line is the sum of the kinetic and thermal energies in the plasma sheet. Both regions show an increase in energy starting around 0245 UT which continues until approximately 0315 UT, at which time both regions show a decrease in energy. We do not interpret this reduction in energy as a substorm onset because there is not clear transfer of energy from the lobe into the plasma sheet. At 0409 UT the lobe magnetic energy begins to show a significant reduction while the plasma sheet shows an increase indicating the transfer of energy stored in the magnetotail into the plasma sheet and the beginning of the substorm process in the magnetotail. This transfer of energy precedes the simulated CL onset by 7 minutes, another sign that within the simulation, reconnection in the mid-tail region precedes the disruption of current in the near-Earth region and the auroral onset of the substorm.

In summary, the LFM simulation of the August 27, 2001 interval produced a substorm which had characteristics similar to the actual event. The auroral onset as indicated by the CL index was several minutes later than the actual event and was also smaller in magnitude. The simulation did not reproduce the encounter with the reconnection that was observed by the CLUSTER 2 spacecraft. Both the structure of the current sheet and partitioning of energy within the magnetotail indicate that reconnection in the mid-tail preceded the disruption of current in the near-Earth region, and was probably the causative agent for the onset of the substorm.

5. DISCUSSION AND CONCLUSIONS

The previous sections have shown that the LFM can be used to simulate both isolated substorms and storm time

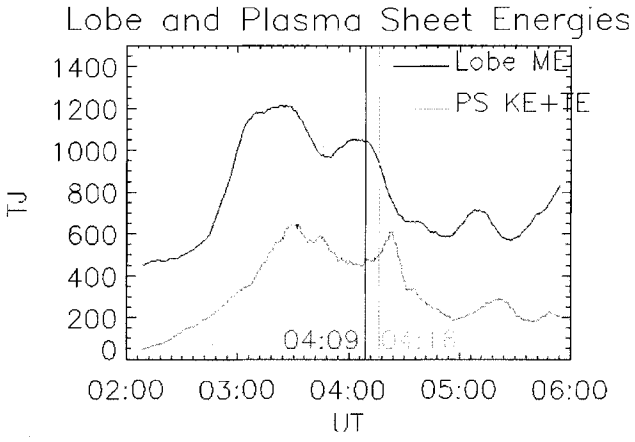

Figure 7. The partitioning of energy between the magnetic energy in the lobe (black) and the thermal and kinetic energy in the plasma sheet (gray) is plotted for the interval around substorm onset. The result show a clear transfer of energy from the lobe into the plasma sheet approximately 8 minutes prior to onset time determined from the simulated CL index.

substorms. The simulation results show several similarities between these two classes of events, along with some minor differences. We believe that the characteristic features of substorms within the simulation, e.g. current sheet thinning, disruption preceded by mid-tail activity, and formation of the substorm current wedge, are essentially the same between storm-time and isolated substorms. Improvements to the LFM model will be required to increase quantitative agreement with observations and to deal with some of the problems shown the simulation results for of both classes of substorms.

Plate 1 can be used to compare and contrast the structure of the current sheet during these two events. In the top row, five minutes before the respective onsets, we can clearly see that both simulations have developed intense thin current sheets which are embedded inside larger current sheets. The current sheet for the March 31, 2001 event is both significantly stronger and more Earthward than the current sheet in the August 27, 2001 event. This difference is due largely to the March 31st event occurring within the very strong driving of the magnetic cloud passage. The onset sector in the March event was located very far into the premidnight sector while the disruption of current in the August 27th event was in the midnight sector. The local time propagation of the disruption sector was also more clear in the March 31, 2001 substorm. The linkage to the magnetotail was more evident in the August 27, 2001, in part, because the state of the magnetotail prior to the onset was quieter, allowing for easier detection of the coupling process. Both simulations show the formation of an intense current sheet which is disrupted by the onset of the substorm via strong flows from the midtail region into the inner magnetosphere.

An important issue to consider in the comparison between the simulations of isolated substorms and storm-time substorms is the inability of the LFM to accurately model the development and persistence of the ring current. The role of the ring current in the substorm process is not completely understood. It is suspected that the development of the ring current will push the onset location earthward and encourage stronger growth phase. Simulation results from the December 10, 1996 substorm presented in *Wiltberger et al.* [2000] showed that while the ring current strength was not well represented the location and timing of the substorm was well captured. However, analysis of the role of the ring current in the simulation will be dramatically improved by the implementation of new model which embedded the Rice Convection Model inside the LFM [*Toffoletto et al.*, 2004]. The RCM will provide a multi-fluid representation of the inner magnetosphere and allows to investigate role of a strong ring current in the substorm process.

The ionospheric currents are used to construct auroral electrojet indices for determining both the onset time of the substorms and characteristics of their evolution. In both classes of events the simulation indices show the features of a growth phase, sudden onset, expansion phase, and recovery. The onset times can be within a few minutes of the actual onset time with the difference being due to a combination of timing errors and the nature of reconnection within the simulation. The peak intensity of the electrojet index is often underestimated for both classes of substorms. This is due in part to the simple method of calculating the simulated AL which depends upon only the maximum of the ionospheric current and not the entire ionospheric current distribution. The August 27th event along with other isolated substorm simulations [*Lyon et al.*, 1998; *Wiltberger et al.*, 2000], clearly show that the recovery phase can be much shorter than the actual event. In addition, the intensity of substorms in the later phases of the magnetospheric storm are significantly less intense than the actual events.

We believe that improving the agreement with the auroral indices requires better modeling in the magnetosphere, which is in turn driving the ionosphere. The weak late storm-time substorms in the LFM are due in part to the large reduction of plasma within the magnetotail during prolonged periods of strong convection. This strong convection leads to a loss of plasma to the magnetopause. Some of this lost plasma is replaced by ionospheric outflow. This outflow may also play a role in extending the length of the recovery phase in the isolated substorm simulations. The current magnetosphere - ionosphere coupling within the LFM is limited to electrodynamic phenomena. In order to test these hypothesis we will need to include mass flow in the model.

A first step in including ionospheric outflow into the LFM is to improve the quality of the ionospheric model used with in the simulation. The Thermosphere Ionosphere Nested Grid (TING) [*Wang et al.*, 1999] model is a variant of the Theremosphere Ionosphere Global Circulation Model [*Roble and Ridley*, 1994] developed at NCAR, which provides a three dimensional model of the thermosphere ionosphere system. We have begun the process of using this model to replace the ionospheric portion of the LFM simulation [*Wiltberger et al.*, 2004]. This new ionospheric module can provide information about the mass, momentum, and energy of plasma at the ionospheric foot point which can be input into an empirical acceleration model and used as an mass input in the magnetosphere. Advanced multifliud (electon and multiple ion species) numerics will be required to incorporate this plasma into the bulk of the magnetospheric simulation.

In conclusion, we have used the Lyon-Fedder-Mobbary global magnetohydrodynamic model of the magnetosphere - ionosphere system to simulate and contrast a storm-time substorm with an isolated substorm. The results show that substorms which occur inside of a magnetic storm show the same fundamental characteristics as isolated substorms. Comparison with actual substorm events is essential in determining weaknesses in the model and testing possible solutions to these problems.

Acknowledgments. We thank NCSA for the computational resources used to complete the simulation. The CANOPUS instrument array constructed, maintained and operated by the Canadian Space Agency, provided the data used in this study. We thank the ACE, WIND, CLUSTER, and GOES instrument teams for the data used within this paper. The National Center for Atmospheric Research (NCAR) is sponsored by the NSF. This work has been support in part by NASA grants ATM-0120950, NSF grants NAG5-126652, and NCAR.

REFERENCES

Akasofu, S., The development of the auroral substorm, *Planet. Space. Sci*, 12, 273, 1964.

Baker, D.N., T. Pulkkinen, V. Angelopoulos, W. Baumjohann, and R.L. McPherron, Neutral line model of substorms: Past results and present view, *J. Geophys. Res.*, 101, 12,975-13,010, 1996.

Baker, D.N., R.E. Ergun, J.L. Burch, J.M. Jahn, P.W. Daly, R. Friedel, G.D. Reeves, T.A. Fritz, and D.G. Mitchell, A telescopic and microscopic view of the magnetospheric substrom on 31 march 2001, *Geophys. Res. Lett.*, 29, doi:10.1029/2001GL014,491, 2002a.

Baker, D.N., W.K. Peterson, S. Eriksson, X. Li, J.B. Blake, J.L. Burch, P.W. Daly, M.W. Dunlop, A. Korth, E. Donovan, R. Friedel, T.A. Fritz, H.U. Frey, S.B. Mende, J. Roeder, and H.J. Singer, Timing of magnetic reconnection initiation during a global magnetospheric substorm onset, *Geophys. Res. Lett.*, 29, doi:10.1029/2002GL015,539, 2002b.

Baumjohann, W., Y. Kamide, and R. Makamura, Storms, substorms, and the near-Earth tail, *J. Geomagn. Geoelectr*, 1995.

Chen, F.F., *Introduction to Plasma Physics and Controlled Fusion*, 2nd ed., Plenum, New York, 1984.

Chen, J., J.A. Fedder, J.G. Lyon, and S.P. Slinker, Simulation of geomagnetic storms during the passage of magnetic clouds, *Geophys. Res. Lett.*, 22, 1749, 1995.

Fedder, J.A. and J.G. Lyon, The solar wind-magnetosphere-ionosphere current-voltage relationship, *Geophys. Res. Lett.*, 8, 880, 1987.

Fedder, J.A. and J.G. Lyon, The Earth's magnetosphere is 165 R_E long: Self-consistent currents, convection, magnetospheric structure, and processes for northward interplanetary magnetic field, *J. Geophys. Res.*, 100, 3623, 1995.

Fedder, J.A., J.G. Lyon, S.P. Slinker, and C.M. Mobarry, Topological structure of the magnetotail as function of interplanetary magnetic field and with magnetic shear., *J. Geophys. Res.*, 100, 3613, 1995a.

Fedder, J.A., S.P. Slinker, J.G. Lyon, and R.D. Elphinstone, Global numerical simulation of the growth phase and the expansion onset for the substorm observed by Viking, *J. Geophys. Res.*, 100, 19,083, 1995b.

Hain, K., Behavior of ionized plasma in the high latitude topside ionosphere, *NRL Memo. Rep.*, 3713, 1, 1977.

Hain, K., The partial donor method, *J. Comput. Phys*, 73, 131, 1987.

Hones, E.W., Transient phenomena in the mgnetotail and their relation to substorms, *Space Sci. Rev.*, 23, 393, 1979.

Lopez, R.E., H.E.J. Koskinen, T.I. Pulkkinen, T. Bsinger, T.A. Potemra, and R.W. McEntire, Simultaneous observation of the poleward expansion of substorm electrojet activity and the tailward expansion of current sheet disruption in the near-earth magnetotail, *J. Geophys. Res.*, 98, 9285-9295, 1993.

Lui, A.T.Y., R.E. Lopez, B.J. Anderson, K. Takahashi, L.J. Zanetti, R.W. McEntire, T.A. Potemra, D.M. Klumpar, E.M. Greene, and R. Strangeway, Current disruptions in the near-Earth neutral sheet region, *J. Geophys. Res.*, 97, 1461, 1992.

Lyon, J., R.E. Lopez, C. Goodrich, M. Wiltberger, and K. Papadopoulos, Simulation of the March 9m 1995 substorm: Auroral brightening and the onset of lobe reconnection, *Geophys. Res. Lett.*, 25, 3039-3042, 1998.

Mobarry, C., J.A. Fedder, and J.G. Lyon, Equatorial plasma convection from global simulations of the Earth's magnetosphere, *J. Geophys. Res.*, 101, 7859, 1996.

Raeder, J. and R.L. McPherron, Global mhd simulations of the substorm current wedge and depolarization, in *Proceedings of the Fourth International Conference on Substorms*, edited by S. Kokubun and Y. Kamide, pp. 343+, Kluwer Academic Publishers, 1998.

Roble, R.G. and E.C. Ridley, A thermosphere - ionosphere - mesosphere - electrodynamics general circulation model (TIME-GCM): Equinox solar minimum simulations (30-500km), *Geophys. Res. Lett.*, 21, 417-420, 1994.

Shepherd, S. and F. Shubitidze, Method of auxiliary sources for calculating the magnetic and electic fields induced in a layered earth, *J. Atm. Solar Terr. Phys.*, 65, 1151-1160, 2003.

Toffoletto, F.R., S. Sazykin, R.W. Spiro, R.A. Wolf, and J.G. Lyon, RCM meets LFM: Initial results from one-way coupling, *J. Atms. Solar Terr. Phys.*, p. in press, 2004.

Vassiliadis, D.V., A.J. Klimas, D.N. Baker, and D.A. Roberts, A description of the solar wind magnetosphere coupling based on nonlinear filters, *J. Geophys. Res.*, 100, 3495-3512, 1995.

Wang, W., T.L. Killeen, A.G. Burns, and R.G. Roble, A high-resolution, three dimensional, time dependent, nested grid model of the coupled thermosphere-ionosphere, *J. Atm. Solar Terr. Phys.*, 61, 385-397, 1999.

Wiltberger, M., T.I. Pulkkinen, J.G. Lyon, and C.C. Goodrich, MHD simulation of the december 10, 1996 substorm, *J. Geophys. Res.*, 106, 27,649-27,663, 2000.

Wiltberger, M., J.G. Lyon, and C.C. Goodrich, Results from the Lyon-Fedder-Mobarry global magnetosphereic model for the electrojet challenge, *J. Atm. Solar Terr. Phys.*, 65, 1213-1222, 2003.

Wiltberger, M., W. Wang, A. Burns, S. Solomon, J.G. Lyon, and C.C. Goodrich, Intial results from the coupled magnetosphere ionosphere thermosphere model: Magnetospheric and ionospheric responses, *J. Atm. Solar Terr. Phys.*, p. submitted, 2004.

M. Wiltberger, NCAR/HAO 3450 Mitchel Lane, Boulder, CO 80301. (wiltbemj@ucar.edu)

J.G. Lyon, Dartmouth College, Department of Physics and Astronomy, 6127 Wilder Laboratory, Hanover, NH 03755. (lyon@tinman.dartmouth.edu)

S.R. Elkington and D.N. Baker, University of Colorado at Boulder, Laboratory for Atmospheric and Space Physics, 1234 Innovation Drive, Boulder, CO 80301. (scot.elkington@lasp.colorado.edu, daniel.baker@lasp.colorado.edu)

T. Guild Boston University, Center for Space Physics, 725 Commonwealth Ave., Boston, MA 02215. (tguild@bu.edu)

Empirical Model of the Inner Magnetosphere H^+ Pitch Angle Distributions

Jacopo De Benedetti, Anna Milillo, Stefano Orsini, Alessandro Mura, and Elisabetta De Angelis

Istituto di Fisica dello Spazio Interplanetario, Rome, Italy

Ioannis A. Daglis

National Observatory of Athens, Penteli, Greece

An empirical model is presented in order to describe the pitch angle distributions of H^+ particles in inner magnetosphere. The data analysis is based on three-year observations made by the AMPTE/CCE/CHEM instrument in the energy range 1-300 keV and in the *L*-shell range 3-9, using the average proton fluxes with AE < 100 nT. The model consists of a multi-parametric functional form, that depends on pitch angle, energy, *L*-shell and a few independent factors. The factors are determined for every magnetic local time. This is the first model, able to accurately reproduce the average proton pitch angle distributions in the whole inner magnetosphere, revealing interesting statistical features. Many of these features have been already evidenced by previous studies and can be explained by processes theoretically interpreted. Furthermore, the model outlines some new features never analyzed before.

1. INTRODUCTION

Generally, the inner magnetospheric particle circulation is studied for reconstructing the longitudinal drift paths, driven by electric and magnetic fields, originating the ring current. Usually, both simulations and data analyses focus on studies related to the equatorial plane, where the ring current intensifies. Generally, the ion drift motions have been widely investigated, but important peculiar aspects related to the pitch angle distributions (PAD) still need to be clarified, like: i) MF drift shell splitting [e.g.: *Roederer*, 1967], ii) EF drift shell splitting [*Korth et al.*, 1983], iii) magnetopause shadowing [e.g.: *West et al.*, 1973].

Ejiri [1978] stated that lower pitch angle particles penetrate deeper in the magnetosphere. The PAD with minimum value at 90°, called butterfly distributions, observed during storm injection at low energies (<30 keV) and at geosynchronous orbit may be a signature of the ExB filter mechanism [*Candidi et al.* 1984; *Orsini and Candidi*, 1986] as well as of field-aligned acceleration processes [*Mauk*, 1986]. *Takahashi and Iyemori* [1990] traced the charged particles motion in a distorted dipolar magnetic field, finding different trajectories for particles at different initial pitch angle and energy, so that with decreasing pitch angle these drift more and more dawnward. In fact, at low pitch angles the westward oriented magnetic field gradient drift is less effective, whereas the ExB drift, eastward oriented, keeps constant. The ring current model developed by *Fok et al.* [1995] uses the AMPTE/CCE/CHEM proton data as initial condition and defines the initial PAD by fitting the data with a two-parameter function. The authors found that the pitch angle anisotropy is higher in the inner regions than in the outer regions; furthermore, the anisotropy increases during both recovery phases and quiet times [see also *Lui and Hamilton*, 1992]. Generally, fresh particles, convected from the plasma sheet, have more isotropic PAD. On the contrary, long time resident particles exhibit anisotropic PAD essentially for

The Inner Magnetosphere: Physics and Modeling
Geophysical Monograph Series 155

10.1029/155GM30

two reasons: i) they have different trajectories in the inner magnetosphere according to their pitch angle, originating both butterfly or pancake PAD; ii) they are affected by charge-exchange loss processes (acting on low energy ions that reach low altitudes at high latitudes, where the geocoronal density is higher) or by pitch angle scattering and wave-particle interactions (acting on high-energy particles, [*Fok et al.*, 1996], mainly at higher latitudes), thus generating pancake PAD. *Sibeck et al.* [1987a] presented a statistical study of tens-keV PAD for ions; *Sibeck et al.* [1987b] and *Chen et al.* [1998] analyzed specific PAD observed during disturbed periods.

A more complete analysis of PAD could be useful for the knowledge of the inner magnetospheric circulation. In fact, *Takahashi et al.* [1997], noticing that the drift shell splitting of the injected particles (caused by day-night magnetosphere asymmetry) could be back-traced, suggested to use the dispersive injection observations near noon outside the geosyncronous orbit as a tool for remote sensing the timing and extension of the boundaries of substorm injections. Recently, *Anderson and Takahashi* [2000] stated that in the day side a reverse pitch angle dispersion is registered during moderate Kp at higher distances. They explained this dispersion with the deformation of the day side magnetosphere that reduces the gradient and curvature drifts especially at higher pitch angles; so that the simulations of this effects during injection events could allow testing magnetic field models. Furthermore, an accurate analysis of the evolving PAD could be a tool for the interpretation and deconvolution of the ENA images taken by IMAGE; actually, such images are a combination of ENA generated along line of sights by ions at different pitch angles.

In this paper, we present an empirical model based on a statistical analysis of the H^+ PAD in the inner magnetosphere. This model is the most global model describing the PAD and involves the widest range of energies. It is obtained by using a data set derived from AMPTE/CCE/CHEM data, first presented by *Orsini et al.* [1994], taken between 1985 and 1987, as described in Section 2. The model describes the H^+ PAD via a functional form which best-fits the experimental data. The best-fit method, described in Section 3, is similar to that presented by *Milillo et al.* [2001] for analyzing the 90° proton fluxes. In Section 4, the main characteristics of the PAD globally observed in the inner magnetosphere are described.

2. DATA SET

The ion energy spectra collected between January 1985 and June 1987 by the CHEM (Charge-Energy-Mass) spectrometer [*Gloeckler et al.*, 1985] on board AMPTE/CCE satellite provided a full coverage of the equatorial inner magnetosphere. We use a data set [*Orsini et al.*, 1994] obtained by averaging the proton fluxes (F) as a function of energy (E), L-shell, MLT and pitch angle (α) according to three different AE activity levels. For the development of the presented model the 90° pitch-angle normalized fluxes, in the L-shell range 3-9, in the energy range 1-300 keV are analyzed. In Table 1, the independent quantities as well as their relative ranges are listed.

Aiming to address those geomagnetic activity conditions that were most frequently observed during the AMPTE/CCE/CHEM operative time (that is, around solar minimum), we have selected CHEM measurements at AE < 100 nT. As stated in *Milillo et al.* [2001], the data selection according to low AE index implies that storm time global physical processes, like large scale plasma convection and ring current development, are present in the data base. On the other hand, transient and localized substorm events (characterized by AE > 100 nT) have been excluded from the data-set, since they could potentially mask the global scale effects we want to analyze. It is worthwhile to stress that the obtained data-set is not simply an average of the magnetospheric proton distributions, neither a reproduction of any actual magnetospheric configuration corresponding to a precise storm phase. By excluding the periods with AE > 100 nT, this data-set reproduces an average of the most probable status of the magnetosphere during solar minimum.

In Plate 1 the color-coded proton fluxes vs L-shell, log(energy), and pitch angle for eight MLTs (0000, 0300, 0600, 0900, 1200, 1500, 1800, 2100) are shown as examples of the used data set. Preliminarily, the presence of bad data or background noise has been checked.

- *Milillo et al.* [2001] identified two signals in the low energy low L-shell ranges, respectively described by a Lorentzian function (*Lor*) and by a Gaussian function (*G1*), probably due to background noise caused by energetic electrons impacting the sensor, and/or due to sporadic events not excluded with the selection related to the AE index. Hence, we have excluded the data where $F/(Lor + G1) < 1.5$.
- We have excluded distributions where fluxes exhibit values below $F = 2000$ (cm^2 s sr keV)$^{-1}$, considering this as a typical statistical error of the data set.
- We have excluded the PAD strongly asymmetric, assumed to be affected by background noise or instrument malfunctions.

Table 1. Model Variables and Ranges of Validity.

normalized flux	f	
magnetic local time	h	00-23
L-shell	l	3-9
energy	$e = \log(E\ [\text{eV}])$	3.18-5.5
pitch angle	α [rad]	0-π

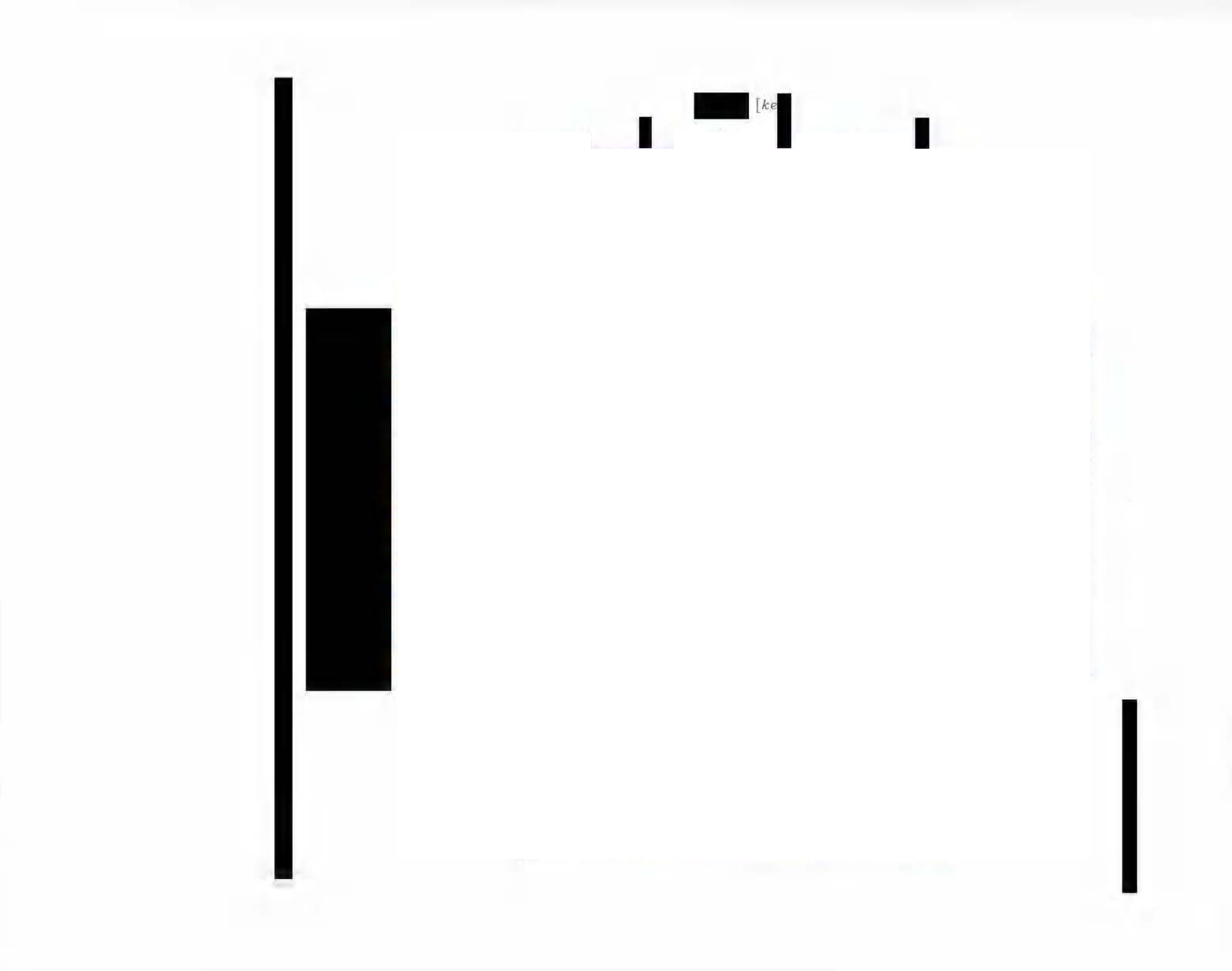

- Since the data set seems generally not well defined at low energy for *L*-shells lower than the position of the *Lor* function, we have excluded these data, keeping the high energy signal.
- Finally, we have excluded few scattered points not consistent with the global trend of the data.

3. DETERMINATION OF THE FUNCTIONAL FORM

In order to best-fit the experimental data with a functional form, we have applied a method as adopted by *Milillo et al.* [2001], by using a least square minimization procedure. The coefficient of linear correlation r^2 is obtained by maximizing the following expression:

$$r^2 = 1 - \left(\sum_{i=1}^{m} w_i (\hat{z}_i - z_i)^2 \Big/ \sum_{j=1}^{m} w_j (z_j - \bar{z})^2 \right) \quad (1)$$

where m is the number of points, z_j is the data value, $\hat{z}_j$ is the estimated value, $\bar{z}$ is the mean of the data value and w_j is the weight. The factors characterizing the best-fit functional form are obtained by minimizing the square of residuals. The errors are computed as standard errors.

According to a step by step procedure, we have first examined the PAD at energies e_i, *L*-shells l_i, and MLTs h_i, by a 2-dimensional best fit. For the used data we have adopted the weight $w_j = 1$. A two factor functional form of pitch angle α has been derived. At this point, these factors assume discrete values for each e_i, l_i, h_i (section 3.1).

Aiming to find an analytical dependence of these factors on both e and l, we have first studied the factor profiles versus e (section 3.2). The adopted weight used in this case is the inverse of the square of the relative standard error of each factor: $w_j = \left(\frac{p_j}{\Delta p_j} \right)^2$

Then, we have fitted the 3-D distributions by including the new functional form of α and e. The new factors have been analyzed in a similar way as a function of l, hence obtaining a functional form of α, e and l able to describe the PAD for every h_i (section 3.3).

In a future study we will include the analysis of the derived factors as a function of h, hence obtaining a single function describing the PAD in the inner magnetosphere.

3.1. The Pitch Angle Distributions

After a global inspection of the PAD present in the data base, we have realized that together with the pancake, the butterfly and the isotropic distributions, intermediate PAD are also observed (see Figure 1).

These distributions are best fitted by the following two-coefficients functional form:

$$f(\alpha) = A \cdot \cos\left(\alpha - \frac{\pi}{2}\right) + B \cdot \cos\left(2 \cdot \left(\alpha - \frac{\pi}{2}\right)\right) - A - B + 1 \quad (2)$$

The last terms are added in order to verify the condition: $f(\pi/2) = 1$.

Figure 1 shows a comparison between data points and best-fit function. Generally, the first coefficient A relates with low pitch angle profiles, while B better describes higher pitch angles. In particular:

- the pancake PAD is obtained by A and $B > 0$ (Fig. 1a);
- the butterfly PAD is obtained by A and $B < 0$ (Fig. 1b);
- the isotropic PAD is obtained by A and $B \sim 0$;
- intermediate PAD, like pancake around 90° and butterfly around 0° correspond to $A < 0$ and $B > 0$ (Figure 1c); while butterfly around 90° and pancake around 0° correspond to $A > 0$ and $B < 0$ (Figure 1d).

3.2. The Energy Dependence

In order to derive the A and B dependence vs energy, we have analyzed the normalized fluxes at 10° pitch angle f_{10}. In Figure 2, some examples of the trend of f_{10} vs energy are shown. It can be noticed that where f_{10} is greater than 1 the PAD are roughly butterfly, where it is close to 1 the PAD are isotropic and where it is less than 1 the corresponding PAD are pancake.

The energy trend of the normalized 10° pitch angle fluxes can be described trough an exponential function:

$$E_x = E_C \cdot \exp\left(-(e - 3.18) \cdot E_R\right) \quad (3)$$

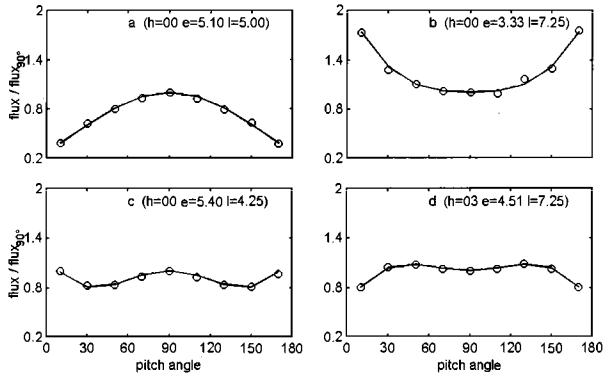

Figure 1. Samples of normalized PAD: data (circles) and model (lines). a) pancake ($A > 0, B > 0$); b) butterfly ($A < 0, B < 0$); c) and d) intermediate distributions described with $A < 0$, $B > 0$ and $A > 0$, $B < 0$, respectively.

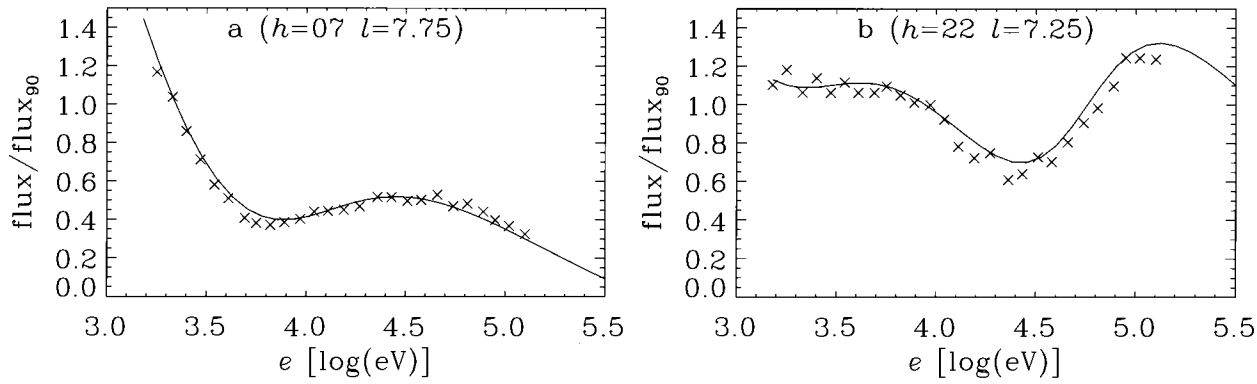

Figure 2. Samples of plots of normalized field-aligned flux vs energy: 10° pitch angle data (points) and 0° pitch angle model (lines). a) a single step function is recognizable; b) two steps functions are identifiable in the outer dusk sector.

and a step function (Logistic Dose Response):

$$S_f = d - \frac{A_S}{1 + \left(\frac{P_S}{e}\right)^{I_S}} \tag{4}$$

where E_C, E_R, d, A_S, P_S and I_S are parameters (≥ 0) to be determined by the best fit technique.

Neglecting the difference between the flux at $\alpha = 0°$ and at $\alpha = 10°$, we have compared these fluxes to the function (2) at $\alpha = 0°$:

$$f(\alpha = 0) = Z = -A - 2B + 1 = E_x - S_f \tag{5}$$

Since in the previous analysis we found that the PAD are mainly described by the A coefficient, while the modulation of the pancake at intermediate energy is better described by the B coefficient, we have assumed:

$$\begin{cases} B = \dfrac{S_f}{2} \\ A = 1 - E_x \end{cases} \tag{6}$$

By expanding function (2) by equations (6), we have obtained:

$$f(\alpha) = [1 - E_x] \cdot \cos\left(\alpha - \frac{\pi}{2}\right) + \frac{1}{2} S_f \times \cos\left(2 \cdot \left(\alpha - \frac{\pi}{2}\right)\right) + E_x - \frac{1}{2} S_f \tag{7}$$

Now, the normalized fluxes are described for every l_i and h_i as a function of α and e by means of 6 parameters.

In the analysis of each l_i and h_i we have noticed that, while in the inner regions the step function disappears, in the dusk region at l_i between 6 and 9 two step functions can be recognized (for instance see Figure 2b). Hence, in this region equation (5) becomes:

$$Z = -A - 2B + 1 = E_x - S_{f1} - S_{f2} \tag{5b}$$

and equation (7) depends on 9 parameters:

$$f(\alpha) = [1 - E_x] \cdot \cos\left(\alpha - \frac{\pi}{2}\right) + \frac{1}{2}[S_{f1} + S_{f2}] \times \cos\left(2 \cdot \left(\alpha - \frac{\pi}{2}\right)\right) + E_x - \frac{1}{2}[S_{f1} + S_{f2}] \tag{7b}$$

In Plate 2, the obtained functions at different h_i for $6 < l < 7$ and $l > 7.5$ are shown together with the absolute differential fluxes obtained by applying the present results to the empirical model of *Milillo et al.* [2001].

3.3. The L_shell Dependence

The analysis of the new set of 6 parameters (9 in the outer dusk region) vs l by using the best fit procedure, has produced a new functional form of 13 (19) parameters. The functional form in l of each of the 6 (9) parameters is shown in Table 2. The numerical values of the parameters, not shown here, have been computed for every h_i. Generally, r^2 is greater than 0.75.

Table 2. Functional Dependence on l of the Model Parameters.

A	E_C	$E_{Ca} \cdot \exp(-(l-3)) + E_{Cb} + E_{Cc} \cdot l$
A	E_R	$E_{Ra} + E_{Rb} \cdot l$
B	d	$d_a + d_b \cdot l$
B	A_S	$d - [A_{Sa} \cdot \exp(-(l-3)) + A_{Sb} + A_{Sc} \cdot l]$
B	P_S	$P_{Sa} + P_{Sb} \cdot l$
B	I_S	I_{Sa}

4. DISCUSSION AND CONCLUSIONS

In this section, the main global features of the PAD as evidenced by the model are outlined, by dividing the magnetospheric regions in: inner regions, and outer regions (night, day, dawn and dusk sides, respectively).

4.1. PAD in the Inner Regions (3.0 < l < 5.5)

In these regions generally the magnetic field is roughly dipolar, the electric potential lines are closed and the particle trajectories during quiet periods are mainly closed at all energies. Being the particles basically "old", the loss processes have deformed the isotropic PAD of the fresh particles. It follows that the PAD in these regions are generally pancake (as already described by *Sibeck et al.* [1987a]), independently on MLT.

In these regions the data set includes only fluxes in the high energy range (see Section 2), that is, the diffused population described by the G3 function in *Milillo et al.* [2001]. We find that these PAD are mainly described by parameter A, and that the pancake distributions are more pronounced at higher energies (given by the trend of the E_x function) and higher distances (in fact, generally E_C decreases with l up to $l = 5$, where it reaches its minimum). This reflects the action of the pitch angle dependent diffusion law: according to the theory [*Ejiri*, 1978], low pitch angle particles diffuse deeper and deeper with decreasing energy.

Where the low energy range data are available, we can see that the PAD gradually pass from pancake at high energies to almost butterfly at low energies. At lower energy, these distributions are related to the convected population (functions CO + G2 in *Milillo et al.* [2001]).

4.2. PAD in the Outer Regions (5.5 < l < 9.0)

Due to magnetic field asymmetries and open electric equipotential lines, the effects of MF drift shell splitting, EF drift shell splitting and magnetopause shadowing become more important in these regions. For this reason PAD MLT asymmetries are evident and can be noticed in Plate 2. In the following, the main asymmetries are described and explained in terms of particle trajectories.

4.2.1. Day-night asymmetry. i) At $E > 10$ keV the night side fluxes, generally, exhibit more isotropic distributions with respect to the day side where the PAD are usually pancake (compare in Plate 2 the high energy distributions at MLT 0000 and 1200). This could be the effect of the night side penetration of fresh particles that in the day side have longer residence times. ii) At $E < 10$ keV, while in the night side the PAD are butterfly, around noon the distributions are pancake (compare in Plate 2 the low energy distributions at MLT 0000 and 1200). The observed butterfly PAD could be explained through particle precipitation directly from the polar regions: generally, ions of solar wind or ionospheric origin ExB drift across the tail lobes in the anti-sunward direction, and evetnually they reach the plasma sheet, at a distance which depends on the ion initial energy. The particles at very low energy precipitate directly in the inner equatorial regions through the mentioned mechanism [*Candidi et al.* 1984; *Orsini and Candidi*, 1986] or through field aligned acceleration [*Mauk*, 1986]. This flux adds to the convected isotropic flux resulting in the observed butterfly distributions.

In the model, E_C - d (approximately Z at low energies) describes these asymmetries at low energies, being higher in the night side than in the day side (see Figure 3a).

4.2.2. Dawn-dusk asymmetry. iii) Usually, the PAD at E > 10 keV are pancake at dawn, and almost isotropic at dusk (compare in Plate 2 the high energy distributions at MLT 0600 and 1800). Particles at these energies drift westward at all pitch angles, hence the PAD of the convected particles are isotropic in the dusk sector, and they progressively become pancake while the particles drift through the day side toward dawn [*Takahashi and Iyemori*, 1990; *Sibeck et al.*, 1987a]. iv) On the contrary, at lower energies the PAD are butterfly at dawn and remain almost isotropic or slightly pancake at dusk (compare in Plate 2 the low energy distributions at MLT 0600 and 1800). This anisotropy could be explained as the

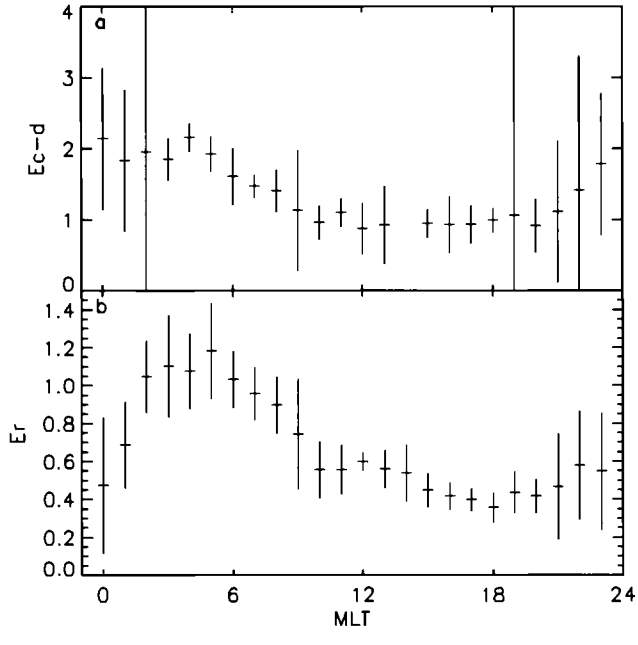

Figure 3. Quantity E_C - d (a) and parameter E_R (b) averaged between l 5.5 and 9.0 plotted versus MLT.

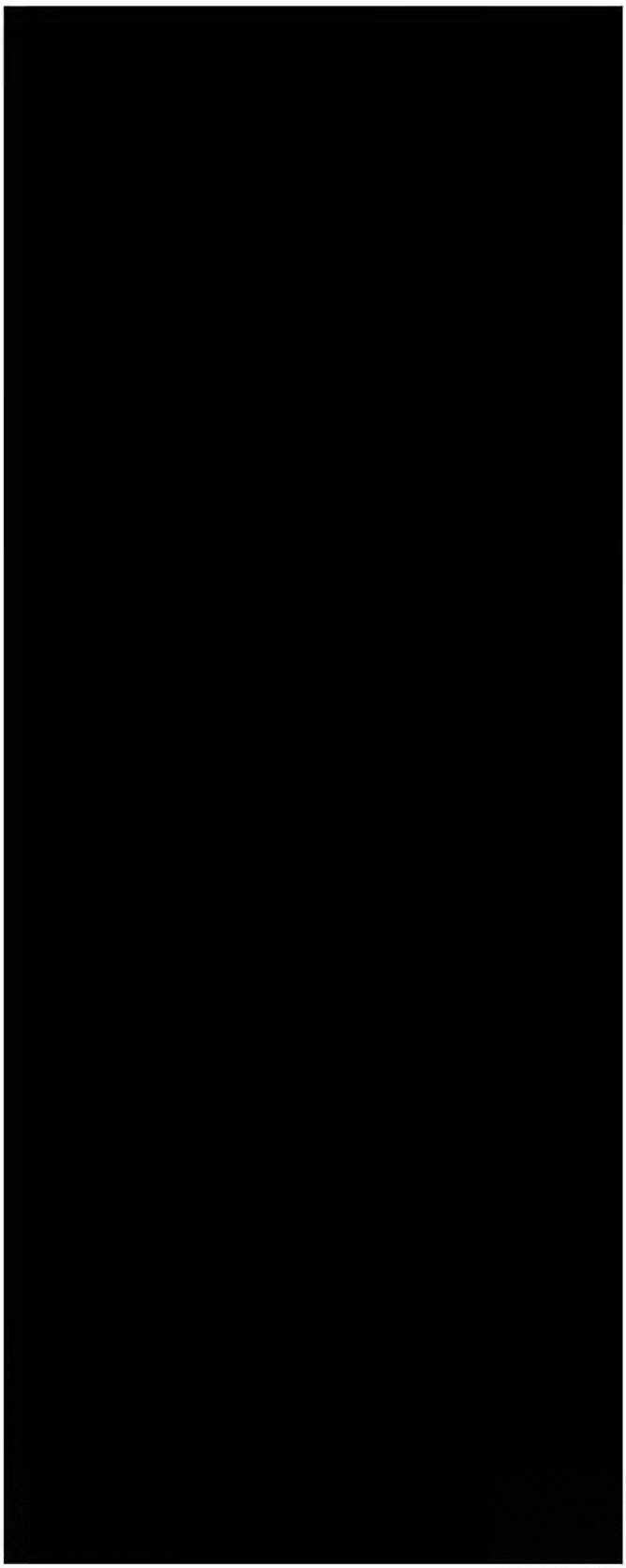

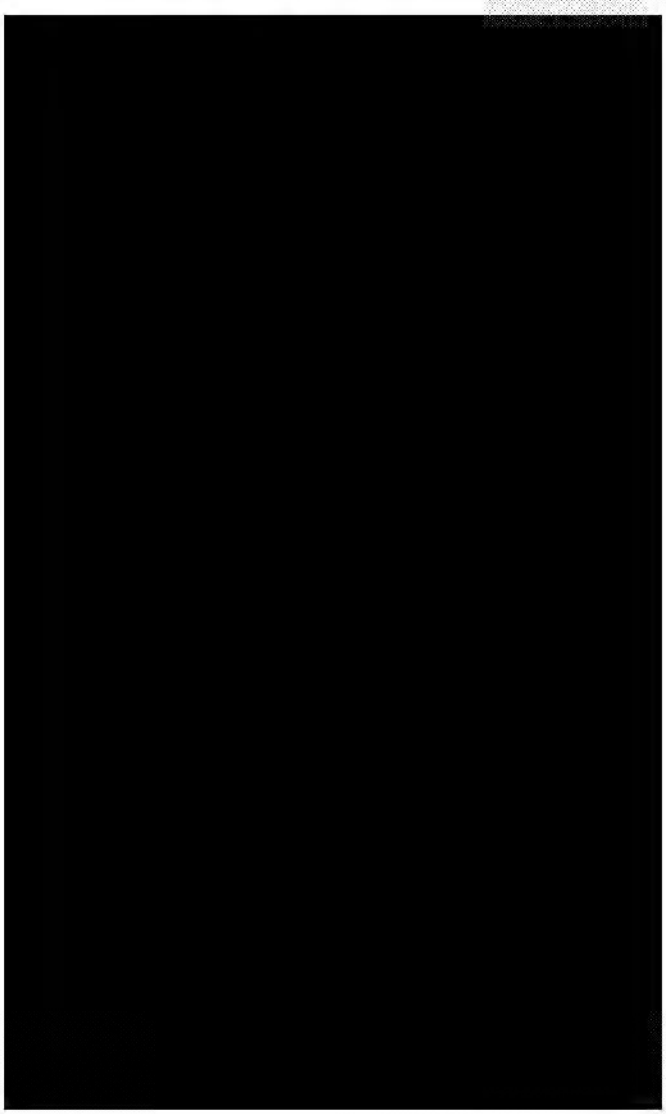

of the bulk of the storm time ring current (1 to 300 keV/*e*) with AMPTE/CCE, *Geophys. Res. Lett.,* 12, 325-328, 1985.

Korth, A., G. Kremser, A. Roux, S. Perraut, J.-A. Sauvaud, J.-M. Bosqued, A. Pedersen, and B. Aparicio, Drift boundaries and ULF wave generation near noon at geostationary orbit, *Geophys. Res. Lett.*, 10, N. 8, 639-642, 1983.

Lui, A.T.Y., and D.C. Hamilton, Radial profiles of quiet time magnetospheric parameters, *J. Geophys. Res.*, 97,19325-19332, 1992.

Mauk, B.H., Quantitative modelling of the 'convection surge' mechanism of ion acceleration, *J. Geophys. Res.,* 91, 13423-13431, 1986.

Milillo A., S. Orsini, I.A. Daglis, Empirical model of proton fluxes in the equatorial inner magnetosphere. 1. Development, *J. Geoph. Res.*, 106, 25713-25730, 2001.

Orsini, S., and M. Candidi, Ionospheric ion streams at altitudes below 14 R_E, *Geophysical Monograph 38, Ion Acceleration in the Magnetosphere and Ionosphere*, Ed. T. Chang,164, 1986.

Orsini, S., I.A. Daglis, and M. Candidi, K.C. Hsieh, S. Livi, and B. Wilken, Model calculation of energetic neutral atoms precipitation at low altitudes, *J. Geophys. Res.*, 99, 13489-13498, 1994.

Roederer, J.G., On the adiabatic motion of energetic particles in a model magnetosphere, *J. Geophys. Res.*, 72, 981-992, 1967.

Sibeck, D.G., R.W. McEntire, A.T.Y. Lui, and M. Krimigis, A statistical study of ion pitch angle distributions, in Magnetotail Physics, ed. by A.T.Y. Lui, 225-230, Johns Hopkins Press, Baltimore, Md., 1987a.

Sibeck, D.G., R.W. McEntire, A.T.Y. Lui, R.E. Lopez, and M. Krimigis, Magnetic field drift shell splitting: cause of during storms and substorms, *J. Geophys. Res.*, 92, 13485-13497, 1987b.

Takahashi, K., B.J. Anderson, S-I Ohtani, G.D. Reeves, S. Takahashi, T.S. Sarris and K. Mursula, Drift shell splitting of energetic ions injected at pseudo-substorm onsets, *J. Geophys. Res.*, 102, 22117-22130, 1997.

Takahashi, S., and T. Iyemori, Simulation of charged particle motions in realistic model magnetospheres and the effect of corotating electric field, *Ann. Geophys.*, 8, 503-510, 1990.

West, H.I., Jr., R.M. Buck, and J.R. Walton, Electron pitch angle distributions throughout the magnetosphere as observed on OGO 5, *J. Geophys. Res.*, 78, 1064-1081, 1973.

Jacopo de Benedetti, Anna Milillo, Stefano Orsini, Alessandro Mura, and Elisabetta De Angelis, Istituto di Fisica dello Spazio Interplanetario, ARTOV via del Fosso del Cavaliere 100, 00133 Rome, Italy.

Ioannis Daglis National Observatory of Athens, Institute for Space Applications and Remote Sensing, Metaxa and Vas. Pavlou of Athens, P. Pentesi, Athens, 15236, Greece.

Global Magnetospheric Dynamics During Magnetic Storms of Different Intensities

V.V. Kalegaev

Skobeltsyn Institute of Nuclear Physics, Moscow State University, Moscow 119899 Russia

N.Yu. Ganushkina

Geophysical Research, Finnish Meteorological Institute, Helsinki, Finland

Magnetospheric dynamics were investigated during the moderate magnetic storm on June 25-26, 1998 and the severe magnetic storm on October 21-23, 1999. Two models: event-oriented model, and theoretical paraboloid model were used to estimate the relative contributions from the ring, magnetotail and magnetopause currents to the *Dst*-index. The calculations were based on the "official" procedure of *Dst* calculations. The quiet time level and quiet time contributions from different current systems were subtracted from the horizontal component of magnetospheric magnetic field calculated for each modeled storm event and for each model separately. We used the magnetic field increase of 30% in order to take into account the effect of induced Earth currents. It was established that the ring current contribution to the *Dst* is comparable with the tail currents' for the moderate storm, but it dominates during the severe magnetic storm. The magnetic flux through the tail lobes is determined by the level of the substorm activity and the magnetospheric size. It is shown that it approaches maximum values ("saturates") during moderately disturbed conditions, and does not demonstrate the significant growth for more strong magnetic storms.

1. INTRODUCTION

Dynamics of storm-time magnetospheric current systems is still one of the open questions of magnetospheric physics. In spite of the many investigations carried out in recent years, an understanding of all the magnetospheric processes, which take place during magnetic storms, has not been achieved. Too many questions remain unanswered, such as that of magnetospheric currents' relative contributions to *Dst* during a magnetic storm. The tail current role in the magnetic storm development is of special interest [*Campbell*, 1973; *Alexeev et al.*, 1996].

The Inner Magnetosphere: Physics and Modeling
Geophysical Monograph Series 155

10.1029/155GM31

An analysis carried out on the base of satellite measurements [*Greenspan and Hamilton*, 2000; *Ohtani et al.*, 2001; *Skoug et al.*, 2003] shows that tail current can be responsible for a significant part of *Dst* variation. Unfortunately, the experimental investigations of this problem do not allow to quantitatively estimate the relative contribution of the magnetospheric magnetic field sources to *Dst*.

Nowadays, research of storm-time current systems based on experimental data analysis is often supplemented by global magnetospheric modeling. Several studies estimated the contributions of *Dst* sources based on model calculations [*Maltsev et al.*, 1996; *Alexeev et al.*, 1996; *Dremuchina et al.*, 1999; *Turner et al.*, 2000; *Alexeev et al.*, 2001; *Kalegaev et al.*, 2001; *Ganushkina et al.*, 2002; 2003]. However, different researchers mean different things by *Dst* contributions originated from magnetospheric sources. As a result, the authors of different investigations represent physically

different quantities by the term "tail current contribution to *Dst*". Adequately representing the *Dst* profile, these investigations often give different estimations for contributions of the magnetic field sources to *Dst* even for the same event. The differences between results obtained with different models can be very large (for the magnetic storm on 9-12 January, 1997, the tail current contribution, *DT*, is about 25% of *Dst* for T96 model [*Turner et al.*, 2000], while *DT* ~ *Dst* for paraboloid model [*Alexeev et al.*, 2001]). It was shown in *Alexeev et al.*, [2001] that they are most likely due to different approaches used in *Dst*-sources calculations. Up to date, the derivation procedure of the contribution to *Dst* from the magnetospheric magnetic field sources has not been described in details. On the other hand, there is no reason to suggest that we obtain the same maximum tail current/ring current relative contribution for different storms. There exists evidence that tail current role changes depending on the magnetic storm intensity [*Turner et al.*, 2001; *Ganushkina et al.*, 2003].

In this study, we investigate the magnetospheric current systems dynamics during two storm events, a moderate storm on June 25-26, 1998 when *Dst* reached –120 nT and an intense storm on October 21-23, 1999 with *Dst* dropped to –250 nT. On the base of the official method of *Dst* derivation from measurements, we describe in details the correct procedure for *Dst* and *Dst* sources calculations by any model of magnetospheric magnetic field. Following this procedure, we calculate the tail current/ring current relative contributions to *Dst* for storms of different intensities by the paraboloid model of the magnetosphere. The event-oriented model by *Ganushkina et al.*, [2003] is used to verify the obtained results. Based on calculations in the framework of the paraboloid model, we explain saturation of the magnetic flux through the tail lobes, when the tail current contribution to *Dst* approaches maximum values for moderately disturbed conditions and does not increase with further disturbance development. The ring current becomes the dominant *Dst* source during strongly disturbed conditions.

2. METHOD OF *Dst* DERIVATION FROM THE MODELING

One of the key goals of our investigation is to provide a method for correct calculation of the *Dst* sources using the magnetospheric models, consistent with the official procedure of *Dst* derivation. In this study we propose that magnetopause currents (CF), ring current (RC), and the tail current (TC) are the main contributors to *Dst*:

$$Dst = DR + DT + DCF, \qquad (1)$$

where *DR*, *DT*, and *DCF* are RC, TC, and CF contributions to *Dst*, respectively.

The partial ring current (PRC) is an important asymmetrical magnetic field source, which can contribute to *Dst*. Although the PRC-related magnetic field perturbations in the inner magnetosphere may be significantly large, especially during the magnetic storm's main phase, its contribution to *Dst* is relatively small [*Tsyganenko et al.*, 2003]. Moreover, the PRC location has not been sufficiently studied, and it is difficult to separate the PRC from the other magnetic field sources. In our calculations we propose that PRC contribution to *Dst* is a part of *DR*, as was used in [*Ganushkina et al.*, 2003; *Tsyganenko et al.*, 2003].

It was established that magnetospheric magnetic field variations produce terrestrial induced currents, preventing the external magnetic field penetration inside the Earth. Just as in the [*Greenspan and Hamilton*, 1999] study we use the value of 30% for the magnetic field increase due to induced currents, which, on average, is in good accordance with the investigations of [*Hakkinen et al.*, 2002]. The Earth's currents induced by different magnetospheric magnetic field sources are proposed to be included to the corresponding terms on the right side of (1).

Based on the official procedure of *Dst* derivation from the measurements [*Sugiura and Kamei*, 1991], we propose a method of *Dst* calculation in terms of magnetospheric models. It consists of three steps:

1. Calculation of the magnetic field horizontal component variation ($\delta H_i(t)$) (originated from the external (magnetospheric) and corresponding induced currents) at each location reporting to *Dst* observatories;
2. Calculating of the quiet magnetic field variation during the quietest day of the month ($\delta H_i^q(t)$), and subtracting them from $\delta H_i(t)$ for each observatory;
3. Determination of the *Dst*, averaging the normalized to the equator differences between storm-time and quiet-time magnetic field variations at the reporting stations for each hour:

$$Dst(t) = \frac{1}{4}\sum_{i=1}^{4}(\delta H_i(t) - \delta H_i^q(t)) \,/\, \cos(\theta_i), \qquad (2)$$

where θ_i are latitudes of observatories.

The proposed procedure also may be generalized to unambiguously describe *Dst* sources when the magnetic field model enables calculation of the magnetic field of different magnetospheric current systems. It allows us to compare the contributions of different sources to *Dst* obtained in terms of different models.

The *Dst* index presented by (2) may be rewritten as

$$Dst(t) = \frac{1}{4}\sum_{i=1}^{4}\frac{\delta H_i(t)}{cos(\theta_i)} - \frac{1}{4}\sum_{i=1}^{4}\frac{\delta H_i^q(t)}{cos(\theta_i)} = \delta H(t) - \delta H^q(t), \quad (3)$$

where the $\delta H(t)$ and $\delta H^q(t)$ are averaged over the equator storm-time and quiet-time variations of the magnetospheric magnetic field. The quiet-time level is a feature of the model, e.g. it is about zero for the paraboloid model. That is why the simple magnetic field calculation at the Earth's center used in [*Alexeev et al.*, 1996] gives a good agreement with *Dst*. However, the magnetic field sources have nonzero quiet day variations.

Representing storm-time and quiet-time variations as a sum of the contributions produced by all the magnetospheric current systems, one can obtain

$$Dst = \delta H_R - \delta H_R^q + \delta H_T - \delta H_T^q + \delta H_{CF} - \delta H_{CF}^q \quad (4)$$

Using (1) one can suggest that $DT = \delta H^T - \delta H_T^q$. We will determine the other *Dst* sources (*DR* and *DCF*) as result of subtraction of the corresponding quiet-time variation from storm-time one.

3. DESCRIPTION OF STORM EVENTS

Figure 1 shows the solar wind conditions and interplanetary magnetic field (IMF), as well as the geomagnetic indices during magnetic storms on June 25-26, 1998 and on October 21-23, 1999.

On June 25, 1998 the IMF B_z shows a sudden jump to more than +15 nT from the level of –13 nT at 2300 UT (Figure 1a). The solar wind dynamic pressure had several peaks around 8-10 nPa. The *AL* index reached a peak value of –1000 nT around 0255 UT on June 26. The *Dst* index started to decrease at the beginning of June 26 and reached –120 nT around 0500 UT.

During the intense storm on October 21-23, 1999 IMF B_z turned from + 20 nT to –20 nT at about 2350 UT on October 21 and dropped down to –30 nT around 0600 UT on October 22 (Figure 1b). Solar wind dynamic pressure showed two main peaks, a 15 nPa peak around 2400 UT on October 21 and a 35 nPa peak around 0700 UT on October 22. There were several peaks in the *AL* index reaching –1000 nT-1500 nT. The *Dst* index dropped to –230 nT at 0600-0700 UT on October 22.

4. STORM-TIME MAGNETIC FIELD MODELS

Based only on the measurements, we can not explicitly distinguish the contributions from different magnetospheric current systems, which are contained in the ground magnetic

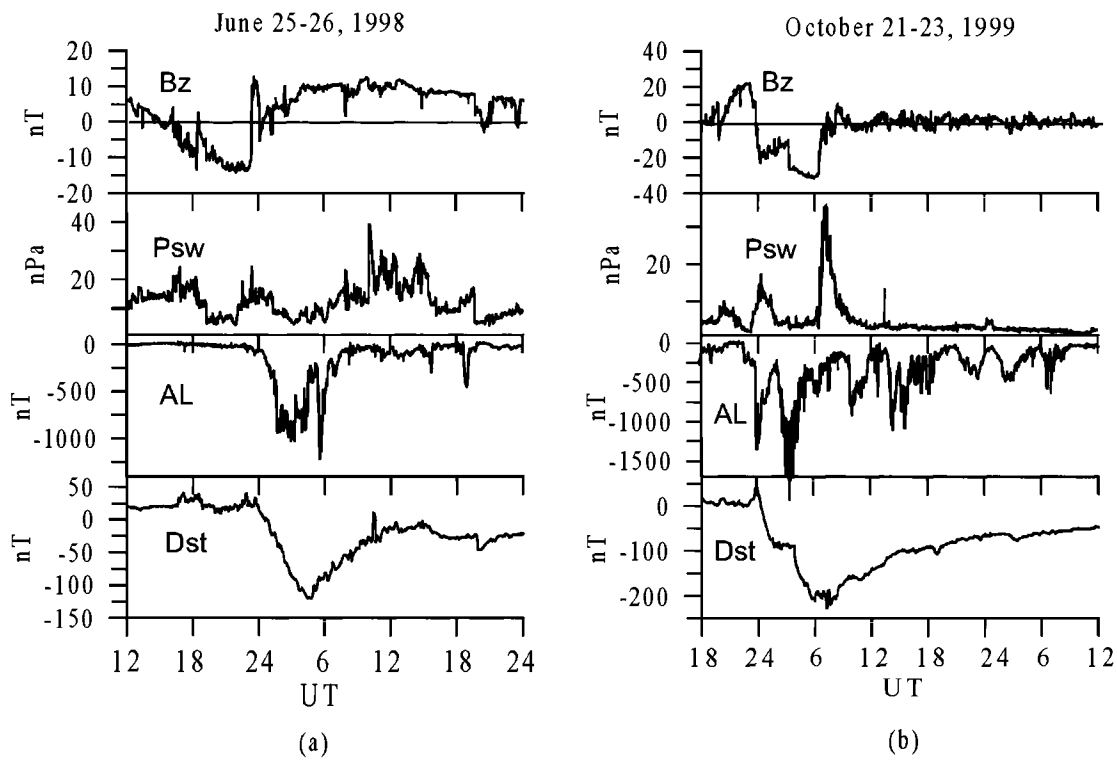

Figure 1. The IMF B_z, solar wind dynamical pressure, *AL* and *Dst* indices during June 25-26, 1998 moderate (a) and October 21-23, 1999 intense (b) storm events.

field. However, we can estimate them using the modern magnetospheric models, which can provide a separate calculation of the magnetospheric magnetic field sources. There are: the last Tsyganenko model, T01 [*Tsyganenko*, 2002a,b], the paraboloid model, A2000 [*Alexeev et al.*, 1996; *Alexeev et al.*, 2001], and the event-oriented model, G2003 [*Ganushkina et al.*, 2002, 2003].

In this study we use the paraboloid magnetospheric model A2000, which allows to investigate the storm-time dynamics of different current systems, as well as of their parameters. The paraboloid model of the Earth's magnetosphere [*Alexeev*, 1978; *Alexeev et al.*, 1996; *Alexeev et al.*, 2001] is based on an analytical solution of the Laplace equations for each large-scale current system in the magnetosphere with a fixed shape (paraboloid of revolution). The paraboloid model takes parameters of magnetospheric current systems (intensities and locations) as input. There are: the geomagnetic dipole tilt angle ψ, the magnetopause stand-off distance R_1, the distance to the inner edge of the tail current sheet R_2, the magnetic flux through the tail lobes Φ_∞, the ring current magnetic field at the Earth's center b_r, and the maximum intensity of the field-aligned current $I_\parallel$. These input parameters depend on the solar wind, IMF, and geomagnetic indices and can be determined from empirical data using submodels.

Several types of studies require an accurate representation of the magnetospheric configuration during a specific event. For such cases, event-oriented modeling is of key importance [*Ganushkina et al.*, 2002, 2003]. We use calculations in terms of this model to verify the results obtained by global magnetospheric model A2000. Event-oriented models contain free parameters whose values are evaluated from observations for each time period separately. Free parameters in the G2003 model are the radial distance of the westward ring current (R_{0west}) and partial ring current (R_{0part}) and the maximum current densities for westward (J_{0west}) and partial (J_{0part}) ring currents, the amplification factor for the tail current (*ATS*), and the additional thin current sheet intensity (A_{ntc}). By varying the free parameters we found the set of parameters that gives the best fit between the model and the in-situ magnetic field observations. The magnetic field measurements along the Goes 8,9, Polar, and Geotail orbits were used to compute the G2003 model parameters for the magnetic storms under consideration. The details of the fitting procedure can be found in (*Ganushkina et al.*, 2002).

5. MODEL *Dst* INDEX AND ITS SOURCES

The quiet days for the two storm events were June 17, 1998 and October 20, 1999 for the June 25-26, 1998 and October 21-23, 1999 storms. The average quiet time *Dst* were −0.58 nT and 2.74 nT, respectively.

Figure 2 shows the quiet time variations of the magnetic field calculated at the Earth's surface from the magnetopause current (dashed line, marked by "mp"), ring current (thick line, marked by "rc") and tail current (thin line, marked by "tc") together with the total modeled variation $\delta H^q(t)$ (line of circles) for June 17, 1998 (left) and October 20, 1999 (right) using (a) the A2000 paraboloid model, and (b) the G2003 event-oriented model. The ground induced currents effect (30% of the variation) was taken into account in all calculations.

We can see that the amplitudes of the calculated variations $\delta H^q(t)$ are about 8-10 nT for both models (see the bottom panels). The average values are about −5 nT for both events in terms of A2000 and about 0 nT and 2.5 nT in terms of G2003. Thus, the magnetic field variation calculated at the Earth's surface by these models during quiet conditions are negligible in comparison with storm-time variation which can be taken as *Dst* (see [*Alexeev et al.*, 1996]). However, the contributions from the individual current systems to *Dst* are, of course, not zero, as we can see from the top panels.

Figure 3 shows the model contributions and total *Dst* during June 25-26, 1998 and October 21-23, 1999 storm events calculated by A2000 model. We can see the contributions from the magnetopause current (dashed line, marked by "DSF"), ring current (thick line, marked by "*DR*") and tail current (thin line, marked by "*DT*") (top panel) together with the observed *Dst* (thick line) and the modelled *Dst* (thin line) (bottom panel) for June 17, 1998 (a) and October 20, 1999 (b). The ground induced currents effect (30% of the variation) was taken into account in the calculations. The quiet-time contributions from the different current systems are subtracted from the model magnetic field variations.

Figure 4 shows the model contributions and total *Dst* during June 25-26, 1998 (a) and October 21-23, 1999 (b) storm events calculated by G2003 model in the same format as in Figure 3. In general, both models provide *Dst*, which is in good agreement with the observed *Dst* index.

During the moderate storm on June 25-26, 1998, the A2000 and G2003 models show that the tail current begins to develop before the ring current. Its contribution to the *Dst* index almost follows the drop of the total *Dst*. During the storm main phase, the tail current gives a slightly larger contribution to *Dst* than the ring current. During the recovery phase, the ring current remains more enhanced than the tail current, although the G2003 model provides even more tail current contribution than the A2000 model.

The situation is quite different for the intense storm on October 21-23, 1999. The tail current develops first, when *Dst* begins to decrease in a manner similar to the tail current behavior during the moderate storm. During the storm maximum, the ring current is the dominant contributor to the *Dst* index.

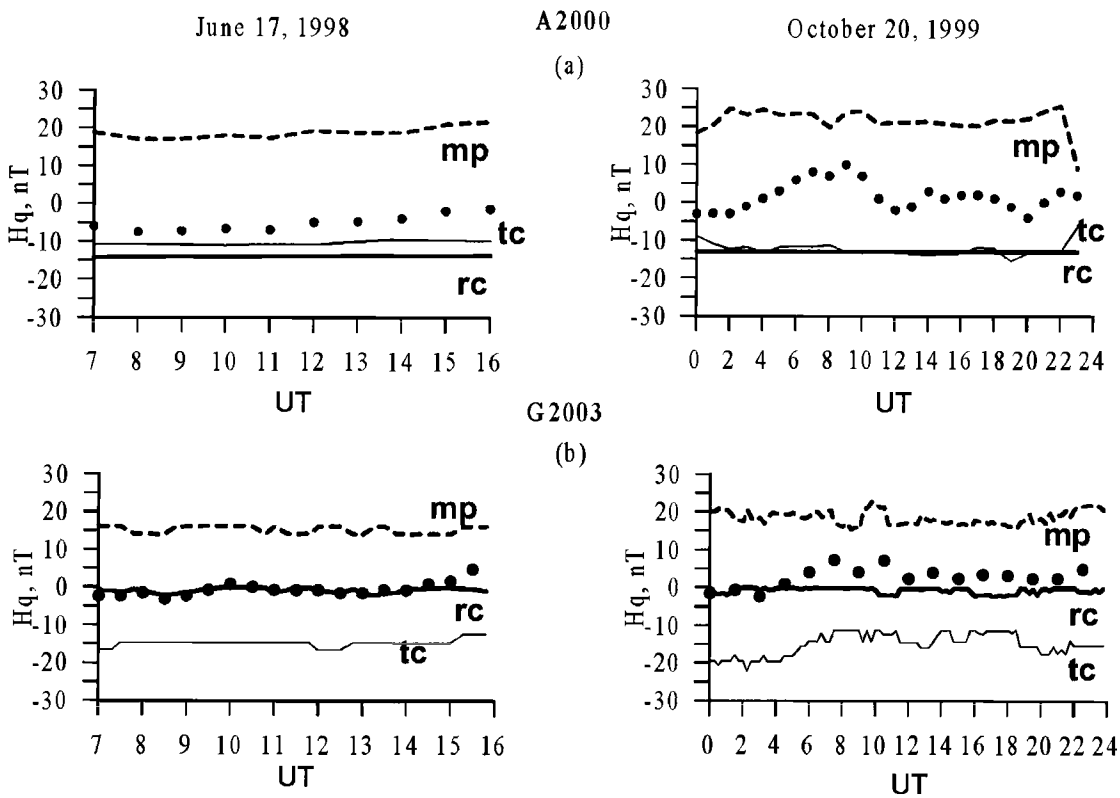

Figure 2. Quiet time variations of the magnetic fields from the magnetopause current (dashed line, marked by **mp**), ring current (thick line, marked by **rc**) and tail current (thin line, marked by **tc**) together with the total modeled variation $\delta H^q(t)$ (line of circles) for June 17, 1998 (left) and October 20, 1999 (right) using (a) the A2000 paraboloid model, and (b) the G2003 event-oriented model.

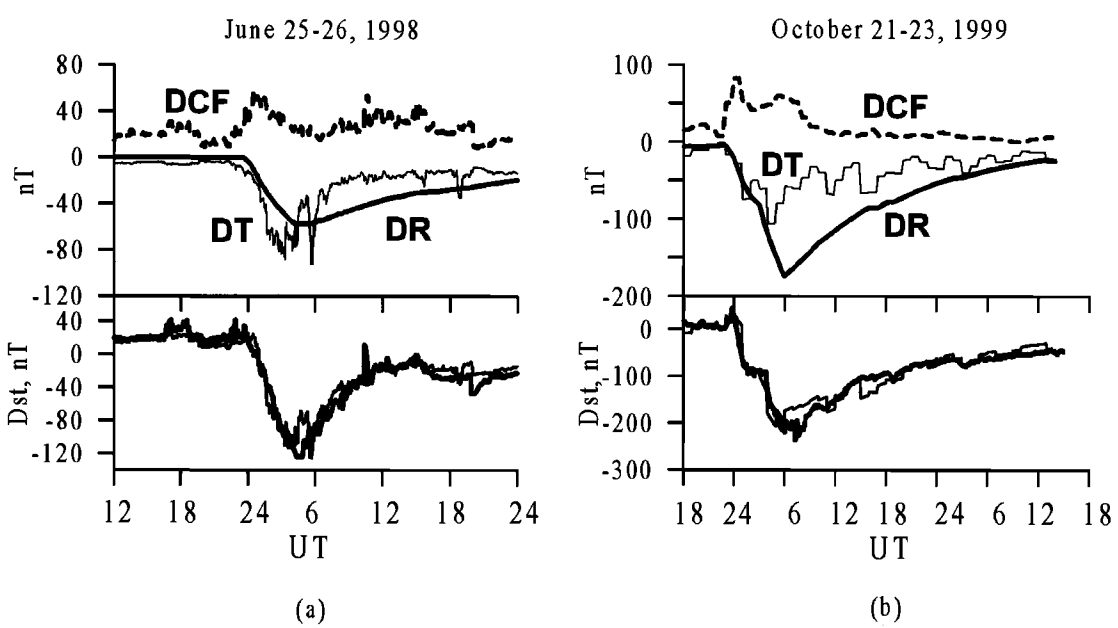

Figure 3. *Dst* sources (top panel), together with the observed *Dst* (thick line) and the modelled *Dst* (thin line) (bottom panel) for June 25-26, 1998 (a) and October 21-23, 1999 (b) magnetic storms calculated by A2000 model.

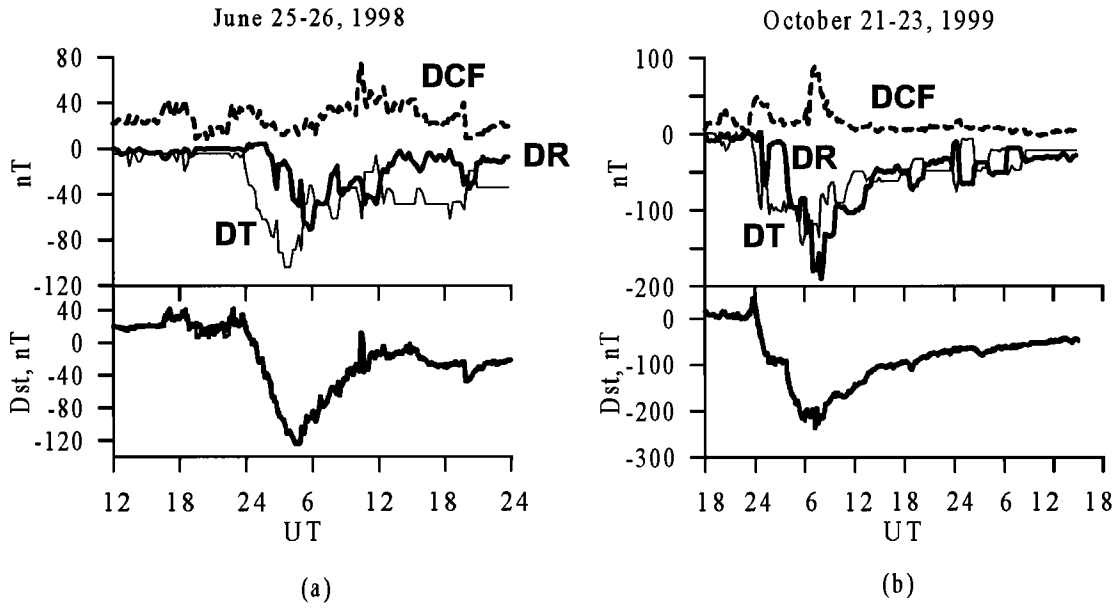

Figure 4. The same as in the Figure 3 calculated by G2003 model.

6. DISCUSSION

The event-oriented G2003 model, which is based on empirical data, gives excellent results in reproducing *Dst*, and confirms the results obtained by the global model A2000.

We can see that the tail current plays a significant role in the magnetic storm development. Computations of the tail current's contribution to *Dst* using the A2000 and G2003 models, show that during a storm, maximum *DT* can approach values comparable with the ring current contribution to *Dst*. Detailed investigation of tail and ring current dynamics shows that the tail current's (as well as other magnetospheric currents') contribution to *Dst* varies during a magnetic storm. Both models demonstrate similar behavior of the *Dst* sources: the tail current begins to develop earlier than the ring current and starts to decay while the ring current continues to develop. The magnetotail global changes during the magnetic storm are controlled mostly by the solar wind and the IMF, but are accompanied by sharp variations associated with substorm-related processes. The G2003 model reproduces the tail current development, which correlates well with the substorm-associated *AL/AE* index. Clear correlation of the tail current contribution to *Dst* with the substorm activity is also apparent in the results obtained from the A2000 model. The tail current development in that model is controlled by the magnetic flux through the tail lobes (which is the same as polar cap magnetic flux):

$$\Phi_{\infty} = \Phi_0 - \frac{AL}{7}\frac{\pi R_1^2}{2}\sqrt{\frac{2R_2}{R_1}+1} \qquad (5)$$

The geocentric distance R_1 to the subsolar point is a function of the solar wind dynamic pressure and IMF B_z component [*Shue et al.*, 1998]. The distance to the inner edge of the tail current sheet R_2 is obtained by mapping the equatorward boundary of the auroral oval at midnight, as given by [*Starkov*, 1993], to the equatorial plane. $\Phi_0 = 400MWb$ is the magnetic flux through the tail lobes during quiet conditions. The A2000 model parameterization is described in details by *Alexeev et al.* [2001].

The calculations show that the relationship between tail and ring currents depends on the magnetic storm intensity. Both models give tail current contribution to *Dst* comparable with the ring current contribution during a moderate storm, but ring current becomes the dominant contributor to *Dst* during an intense storm (see also [*Ganushkina et al.*, 2003]). Apparently, the magnetic flux through the tail lobes "saturates" during extremely disturbed conditions, while the ring current continues to develop. In particular, we can see that *AL/AE* index approaches similar values during both the moderate and the intense storms under consideration (see Fig. 1). The polar cap area also does not demonstrate a

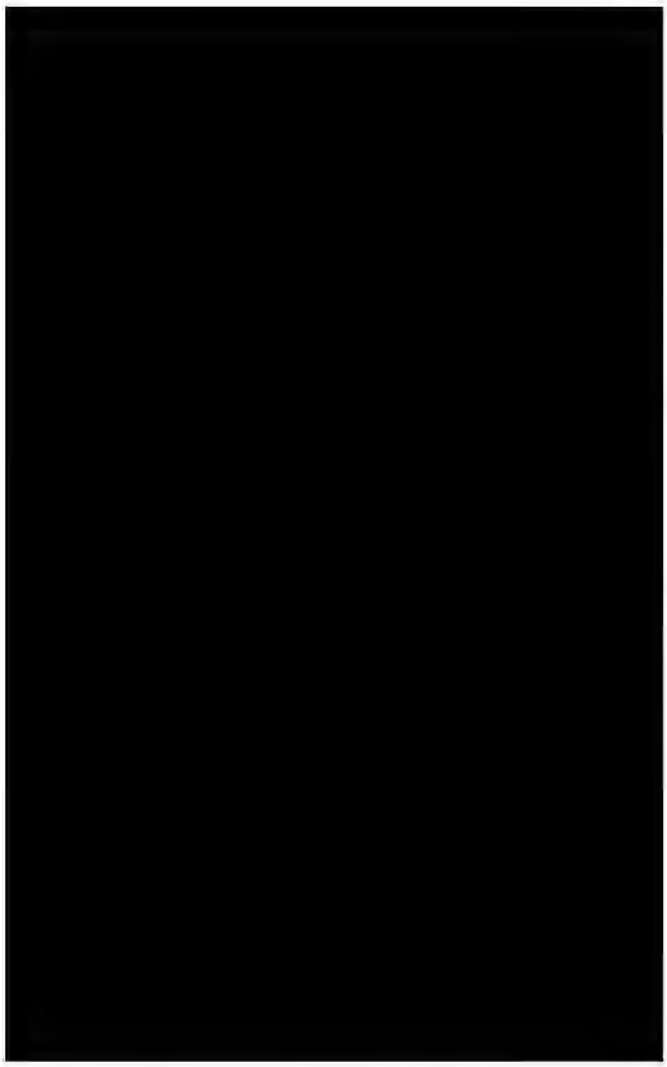

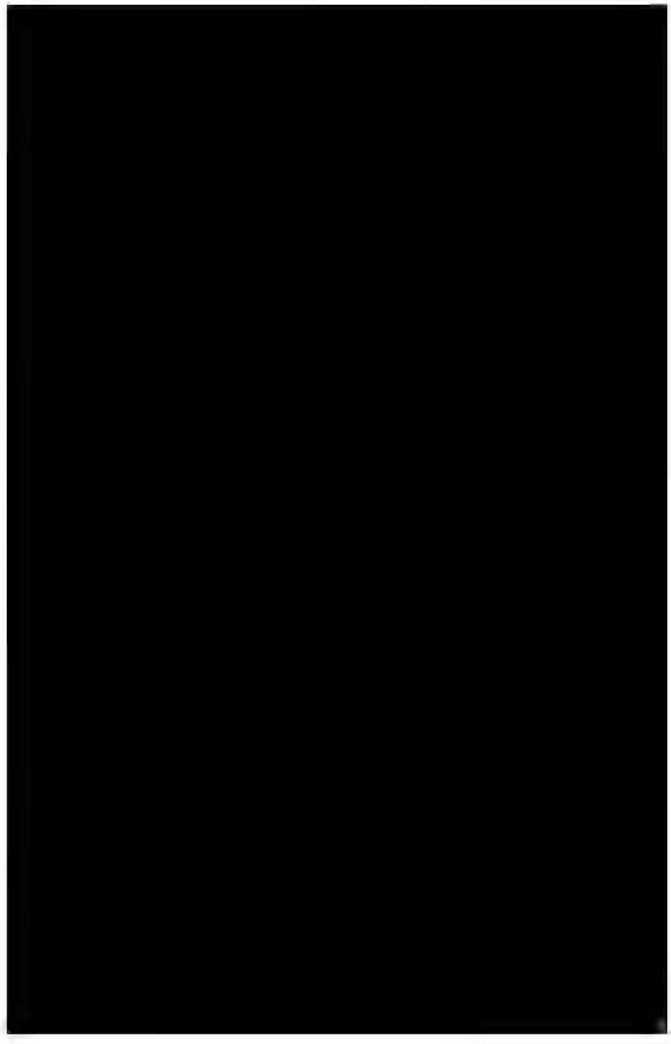

Acknowledgments. We would like to thank K. Ogilvie and R. Lepping for the WIND data, T. Nagai for the GEOTAIL magnetic field data, C.T. Russell for the POLAR magnetic field data, H.J. Singer for the Goes 8, 9, 10 magnetic field data, World Data Center C2 for Geomagnetism, Kyoto, for the provisional *AE*, *AL* and *Dst* indices data. The data were obtained from the Coordinated Data Analysis Web (CDAWeb). The work of N. Ganushkina was supported by the Academy of Finland. The work of V. Kalegaev was supported by Russian Foundation for Basic Research (Grants No 01-07-90117 and 04-05-64396).

REFERENCES

Alekseyev, I.I., Regular magnetic field in the Earth's magnetosphere, *Geomagnetism and Aeronomy*, 18, 447-452, 1978.

Alexeev, I.I., E.S., Belenkaya, V.V., Kalegaev, Y.I., Feldstein, and A., Grafe, Magnetic storms and magnetotail currents, *J. Geophys. Res.*, 101, 7737-7747, 1996.

Alexeev I.I., V.V, Kalegaev, E.S. Belenkaya, S.Yu. Bobrovnikov, Ya.I. Feldstein, and L.I.Gromova. The Model Description of Magnetospheric Magnetic Field in the Course of Magnetic Storm on January 9-12, 1997, Journal of Geophysical Research, *J. Geophys. Res.*, 106, 725,683-25,694, 2001.

Campbell, W.P., The field levels near midnight at low and equatorial geomagnetic stations, *J. Atmos. and Terr. Phys.*, 35, 1127, 1973.

Dremukhina, L.A., Y.I. Feldstein, I.I. Alexeev, V.V. Kalegaev, and M. Greenspan, Structure of the magnetospheric magnetic field during magnetic storms, *J. Geophys. Res.*, 104, 28,351, 1999.

Ganushkina, N. Yu., T.I. Pulkkinen, M.V. Kubyshkina, H.J. Singer, and C.T. Russell, Modelling the ring current magnetic field during storms, *J. Geophys. Res.*, 107, 10.1029/2001JA900101, 2002.

Ganushkina, N. Yu., T.I. Pulkkinen, M.V. Kubyshkina, H.J. Singer, and C.T. Russell, Long-term evolution of magnetospheric current systems during storms, accepted for publications for *Annales Geophysicae*, 2003.

Greenspan, M.E., and D.C. Hamilton, A test of the Dessler-Parker-Sckopke relation during magnetic storms, *J.Geophys. Res.*, 105, 5419-5430, 2000.

Häkkinen, L., T.I. Pulkkinen, H. Nevanlinna, R.J. Pirjola, and E.I. Tanskanen Effect of induced currents on Dst and on magnetic variations at midlatitude stations, *J. Geophys. Res.*, 107, 10.1029/2001JA900130, 2002.

Kalegaev V.V., I.I.Alexeev, and Ya.I.Feldstein, The Geotail and Ring Current Dynamics Under Disturbed Conditions, *Journal of Atm and Sol-Terr Phys, V. 63/5*, 473-479, 2001.

Maltsev Y.P., A.A. Arykov, E.G. Belova, B.B. Gvozdevsky and V.V. Safargaleev, Magnetic flux redistribution in the storm time magnetosphere, *J. Geophys. Res.*, 101, 7697, 1996.

Ohtani, S., M. Nose, G. Rostoker, H. Singer, A.T.Y. Lui, and M. Nakamure, Storm-substorm relationship: Contribution of the tail current to *Dst*, *J.Geophys. Res.*, 106, 21199-21209, 2001.

Shue, J.-H., J.K. Chao, H.C. Fu, C.T. Russell, P. Song, K.K. Khurana, and H. J. Singer, A new functional form to study the solar wind control of the magnetopause size and shape, *J. Geophys. Res.*, 102, 9497–9512, 1997.

Skoug, R.M., M.F. Thomsen, M.G. Henderson, H.O. Funsten, G.D. Reeves, C.J. Pollock, J.-M. Jahn, D.J. McComas, D.G. Mitchell, P.C. Brandt, B.R. Sandel, C.R. Clauer, and H.J. Singer, Tail-dominated storm main phase: 31 March 2001, *J. Geophys. Res.*, 108, 10.1029/2002JA009705, 2003.

Starkov, G.V., Planetary morphology of the aurora, In *Magnetosphere-Ionosphere Physics*, S.-Petersburg: Nauka, 85-90, 1993.

Sugiura, M., and T. Kamei, Equatorial *Dst* index 1957-1986,in *IAGA Bull. 40*, Edited by A. Berthelier, and M. Menvielle, Int Serv. of Geomagn. Indices Publ. Off., Saint Maur, France, 1991.

Tsyganenko, N.A., A model of the near magnetosphere with a dawn-dusk asymmetry: 1. Mathematical structure, *J. Geophys. Res.*, 107, 1179, 10.1029/2001JA0002192001, 2002a.

Tsyganenko, N.A., A model of the near magnetosphere with a dawn-dusk asymmetry: 2. Parameterization and fitting to observations, *J. Geophys. Res.*, 107, 1176, 10.1029/2001JA900120, 2002b.

Turner, N.E., D.N. Baker, T.I. Pulkkinen, and R.L. McPherron, Evaluation of the tail current contribution to *Dst*, *J. Geophys. Res.*, 105, No. A3, 5431–5440, 2000.

Turner, N.E., D.N. Baker, T.I. Pulkkinen, J.L. Roeder, J.F. Fennel, and V.K. Jordanova, Energy content in the storm-time ring current, *J. Geophys. Res.*, 106, No. A9, 19,149–19,156, 2001.

V.V. Kalegaev, Skobeltsyn Institute of Nuclear Physics, Moscow State University, Moscow 119899 Russia. (e-mail:klg@decl.sinp.msu.ru)

N. Yu. Ganushkina, Geophysical Research, Finnish Meteorological Institute, Helsinki, Finland.5.

A Back-Tracing Code to Study the Magnetosphere Transmission Function for Primary Cosmic Rays

Pavol Bobik[1], Matteo Boschini[2,3], Davide Grandi[3], Massimo Gervasi[3,4], Elisabetta Micelotta[3], and Pier-Giorgio Rancoita[3]

We have developed a code to reconstruct the Cosmic Rays trajectory in the Earth magnetosphere. This code solves the Lorentz equation and propagates a particle backward in time. The total magnetic field is evaluated by using the International Geomagnetic Reference Field (IGRF) 2000-2005 and the external magnetic field Tsyganenko-96. This code has been used both for a simulation of randomly generated inputs and for the analysis of the AMS-01 experiment data taken during the STS-91 Space Shuttle mission in June 1998. By a full spectrum simulation we have separated the primary Cosmic Ray component from the secondary one present at the altitude of AMS orbit (400 km). We have built the transmission function in the magnetosphere for 1998 for several regions with different geomagnetic latitude. The same simulation has also been performed for the magnetic conditions of the year 2005, the expected starting time of the long-duration AMS-02 data taking. Then we have estimated the variation of the transmission function with time and obtained the primary Cosmic Ray flux at the altitude of 400 km starting from the flux at 1 AU as predicted by the CREME96 model.

1. INTRODUCTION

The transmission function TF($\Re$) of the magnetosphere describes the probability that a particle with rigidity $\Re$, coming from outside, reaches a point inside the magnetosphere. The results depend on the particles incoming direction, position and time, besides the rigidity. Models of magnetosphere currently available [*Tsyganenko and Stern*, 1996] allow to obtain accurate particle tracing inside the magnetosphere, and therefore to get a precise evaluation of the transmission function. The probability approach of the transmission function is suitable particularly to smooth out the effect of discreteness during the computation. This approach can be applied both to discrete rigidity steps of a single place [*Bobik et al.*, 2001a] and to discrete geographical positions on the Earth surface [*Bobik et al.*, 2003]. In the present paper we use the transmission function (TF hereafter) to describe the probability for a range of rigidities from $\Re - \Delta\Re$ to $\Re + \Delta\Re$. In particular we consider the AMS experiment energy bins [*Alcaraz et al.*, 2000a] for the geographic regions covered by AMS orbit.

To evaluate the TF we use the calculation of trajectories in the geomagnetic field for a set of points at the AMS orbit excluding the South-Atlantic anomaly region. Following the Liouville theorem, if the cosmic ray flux is isotropic outside the magnetosphere, the flux in a random point inside the magnetosphere is the same in all the directions allowed for primaries, while it is zero in the forbidden directions [*Vallarta*, 1961]. Back-tracing calculation of the TF is based on the assumption that, at 1AU, cosmic rays are isotropically distributed in space. Besides this approach applies only to primary particles, i.e. particles coming from outside the magnetosphere. Around the cut-off rigidity we find the transition region of the TF: primary particles with rigidity

[1]Institute of Experimental Physics, Kosice, Slovak Republic
[2]CILEA, Segrate MI, Italy
[3]INFN sezione di Milano, Milano, Italy
[4]Universitá di Milano-Bicocca, Milano, Italy

The Inner Magnetosphere: Physics and Modeling
Geophysical Monograph Series 155

10.1029/155GM32

lower than cut-off can not reach the respective point of observation, while trajectories of very high energy particles are unaffected. Besides, trajectories forbidden to primaries could be populated by secondary particles, i.e. particles produced or scattered inside the magnetosphere, in particular in the highest shells of the atmosphere.

Back-tracing method [*Smart et al.*, 2000, *Bobik et al.*, 2001b] is based on the inversion of charge sign (Zq) and velocity vector (v) in the equation of motion for a particle with relativistic mass m in a magnetic field B:

$$m \cdot dv/dt = Zq\ [v \times B] \qquad (1)$$

In our simulation we have used as external geomagnetic field the *Tsyganenko96* model [*Tsyganenko and Stern*, 1996] (http://www-istp.gsfc.nasa.gov/Modeling/T96.html) and as internal geomagnetic field the IGRF model (DGRF 2000-2005) [*Barton*, 1997] (for a full description see web page: http://www.ngdc.noaa.gov/IAGA/wg8/table1.txt).

2. THE TRANSMISSION FUNCTION

2.1. Calculation

We evaluate the TF by back-tracing simulated particles. Starting positions of back-tracing cover a complete sphere at an altitude of 400 km (following the AMS orbit). This grid of points has been built in order to have the same elementary shooting surface. For every position in the grid, starting directions are uniformly distributed in a 2π outgoing hemisphere.

In this way we have built the transmission functions for the different regions of the AMS orbit. Thus we have obtained a set of 10 transmission functions. In table 1 these geomagnetic regions are defined, using the Corrected Geomagnetic (CGM) latitude. In order to compare results with the AMS-01 experimental data we have reproduced the experimental conditions:

Table 1: AMS-01 Geomagnetic Regions, Divided by Absolute Value of Geomagnetic (CGM) Latitude Θ_M (rad).

AMS-01 Regions	
Region Number	Geomagnetic Latitude
Region 1	$\Theta_M < 0.2$
Region 2	$0.2 \le \Theta_M < 0.3$
Region 3	$0.3 \le \Theta_M < 0.4$
Region 4	$0.4 \le \Theta_M < 0.5$
Region 5	$0.5 \le \Theta_M < 0.6$
Region 6	$0.6 \le \Theta_M < 0.7$
Region 7	$0.7 \le \Theta_M < 0.8$
Region 8	$0.8 \le \Theta_M < 0.9$
Region 9	$0.9 \le \Theta_M < 1.0$
Region 10	$1.0 \le \Theta_M$

1) Geographical polar regions have been excluded, i.e., $-51.6° \le$ latitude $\le +51.6°$;
2) The South-Atlantic anomaly region has been excluded;
3) The particles incoming directions are restricted to a cone of 32° from the detector axis, which is pointing at the geocentric zenith;
4) Energy bins have been defined equal to the bins used in AMS-01 data analysis.

For each point of the grid and for every rigidity $\Re$ we evaluated the ratio of the number of allowed trajectories over the number of all the directions. A trajectory is allowed when it crosses the boundary of the magnetopause or of a sphere with a radius of 25 Re (in the night-side tail). Besides we consider a trajectory as forbidden (for primaries) when it intersects the upper atmosphere (at 40 km altitude) or if it is confined inside the magnetosphere for more than 10 seconds. This ratio is the probability for particles with rigidity $\Re$ to reach this point starting from outside the magnetosphere. This ratio is then averaged over every point for each AMS region and for each rigidity bin and becomes the transmission function for a particle with rigidity $\Re$ inside the actual AMS region. Such a wide region for the average is able to smooth out the complex structure of penumbra changing from position to position and with rigidity [*Bobik et al.*, 2001a].

2.2. Results

In Figure 1 the TF evaluated for some of the geomagnetic regions of AMS orbit is shown. Calculation has been performed taking into account the geomagnetic conditions present during the AMS-01 observations (June 2-12, 1998): solar activity

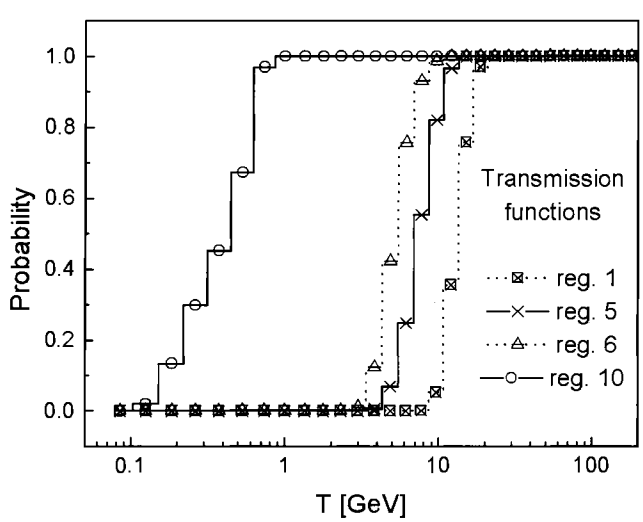

Figure 1. Transmission Function for AMS-01 regions 1,5,6, and 10, evaluated for June 1998 (see the text for details).

parameters have been averaged over the 10 days of the AMS-01 flight, while the chosen simulation time is June 8 (1998) at 10:00 am (UT). Geomagnetic regions are numbered according to table 1. As expected high values of the TF extend at lower energy by increasing the geomagnetic latitude. In fact close to the polar regions charged particles can easily reach a low orbit.

We can also evaluate the TF at the starting time of AMS-02 long duration flight on ISS, October 2005, as previously scheduled. In fact the models of the magnetosphere (IGRF/DGRF and Tsyganenko96) can be extrapolated for the next years. We used solar activity parameters (B_Y, B_Z, Dst and P_{dyn}) as measured in the same conditions during the solar cycle 21. Same conditions mean: negative solar field polarity (A < 0), declining phase, and sunspot number $5 < N_{SS} < 45$. These conditions happen between June 1984 and June 1986. Therefore the values of the solar activity parameters have been averaged over this time interval. In Figs. 2-3 we compare the results for the region 10 and region 1 for the time periods of June 1998 (AMS-01) and October 2005 (AMS-02). The observed variation of the TF is mainly due to the interaction of the Earth magnetic field with the Interplanetary Magnetic Field, at the magnetopause. As expected, the major change occurs for region 10, where low rigidity particles are involved. Minor changes are due to the long term variation of the Internal Geomagnetic Field.

3. PRIMARY PARTICLES' SPECTRA

3.1. Primaries in AMS-01 Region

The AMS-01 experiment has measured the spectrum of protons in the 10 geomagnetic regions, obtaining the spectrum of cosmic protons in the energy range: 0.22-200 GeV

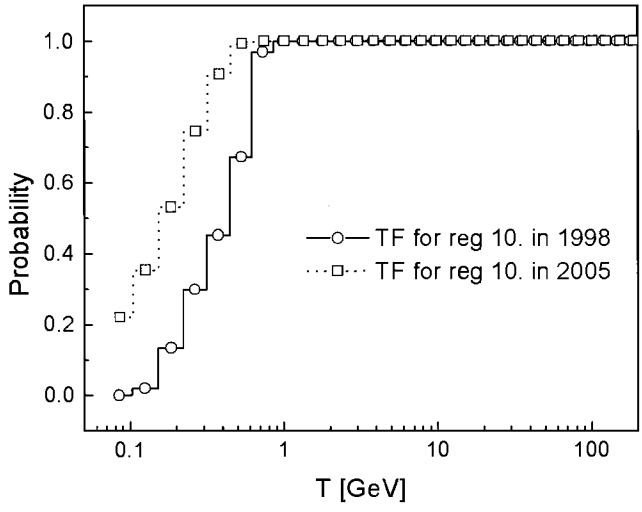

Figure 2. Transmission Function for AMS-01 region 10, evaluated for June 1998 and October 2005.

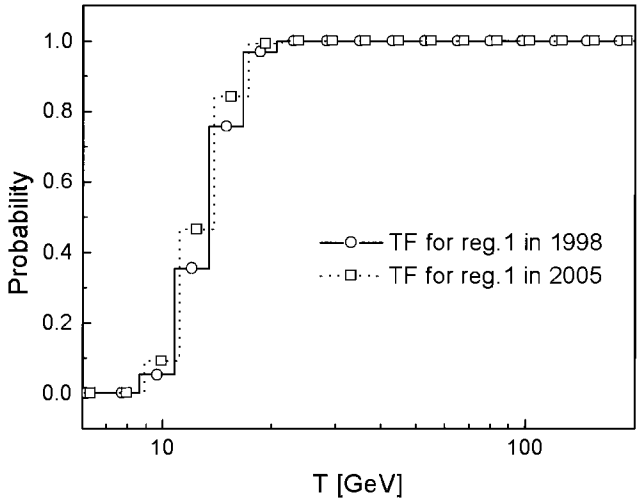

Figure 3. Transmission Function for AMS-01 region 1, evaluated for June 1998 and October 2005.

[*Alcaraz et al.*, 2000b]. We have evaluated the primary proton spectra at the Space Shuttle orbit (S_{SSO}) combining the measured AMS-01 cosmic proton spectrum (S_{1AU}) with the TF computed for the region i^{th}:

$$S_{SSO}(i) = S_{1AU} * TF(i) \quad (2)$$

Results are presented in Figure 4. A comparison of these primary spectra with the spectra measured at the Space Shuttle orbit [*Alcaraz et al.*, 2000a] is shown in Figure 5. Here a population of low rigidity secondary protons is present together with particles of primary origin.

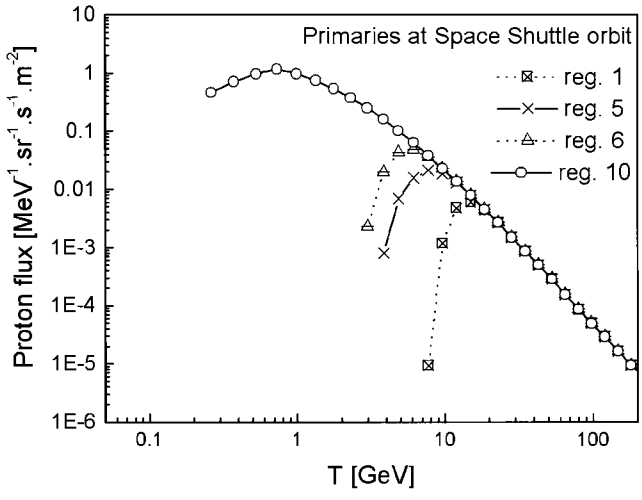

Figure 4. Primary proton spectra for AMS-01 regions 1,5,6, and 10, evaluated for June 1998.

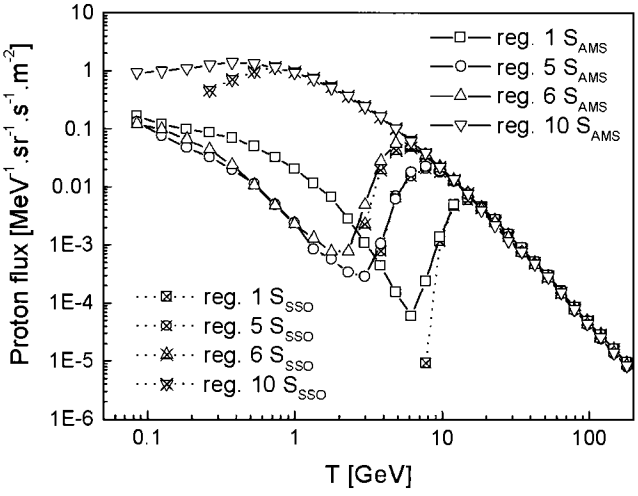

Figure 5. AMS-01 measured spectra (S_{AMS}) compared with the evaluated primary spectra (S_{SSO}), for the geomagnetic regions 1, 5, 6, and 10.

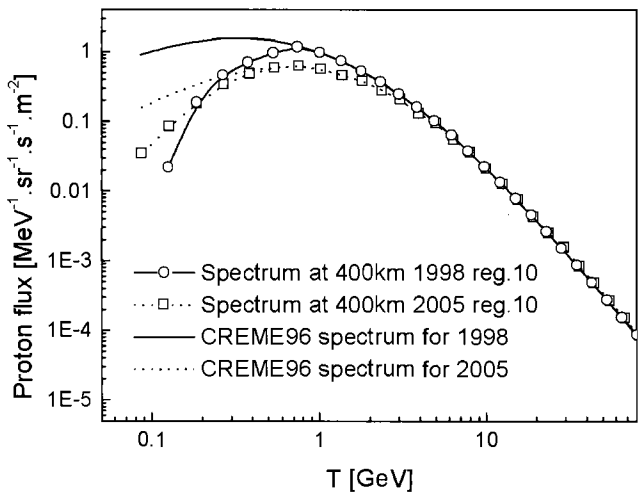

Figure 6. Primary proton spectra at AMS orbit (region 10) for June 1998 and October 2005.

By this comparison it is possible to separate the secondary component from the cosmic protons. The low rigidity cut-off of primaries is sharper than corresponding measured spectrum. This is an indication of the presence of secondary protons with energy above the dip.

3.2. AMS-02 Spectra in 2005

Estimations of the proton flux at 1AU for the next years can be obtained using the CREME96 model [*Tylka et al.*, 1997] (web page: http://crsp3.nrl.navy.mil/creme96).

However CREME96 is not taking into account some of the effects of CR propagation in the solar cavity. For this reason we have studied a normalization procedure able to reproduce available data within few percent [*Bobik et al.*, 2004]. The uncertainty for the predicted fluxes is larger at energy lower than few GeV because of the large solar modulation. For higher energy the accuracy of the predicted flux is not an issue.

Using the TF and CREME96 models, both evaluated for October 2005, and equation (2) we obtain expected AMS-02 primary spectrum for 2005 in the several geomagnetic regions, following the prescriptions listed in section 2. Actually the AMS-02 angular sensitivity is extended up to a cone of 45° from the detector axis, but we have evaluated the TF restricted to a cone of 32° from the geocentric zenith, in order to compare results with 1998 AMS-01 measurements.

A comparison of the primary proton spectra at the Space Shuttle (or ISS) orbit (~ 400 km altitude) for the region 10, evaluated for October 2005 and for June 1998 is shown in Figure 6. The predicted flux of primary protons during 2005 is significantly lower than during 1998 for an energy higher than 180 MeV, due to solar modulation variations.Conversely a higher magnetospheric transmission during October 2005 than in June 1998 in region 10, as shown in figure 2, produces a higher proton flux for the AMS-02 spectrum for particles with energy lower than 180 MeV. A comparison of the primary proton spectra at the Space Shuttle orbit for the region 1, evaluated for October 2005 and for June 1998 is shown in Fig. 7. In region 1, due to the higher energy of the involved particles, the flux variations are extremely reduced.

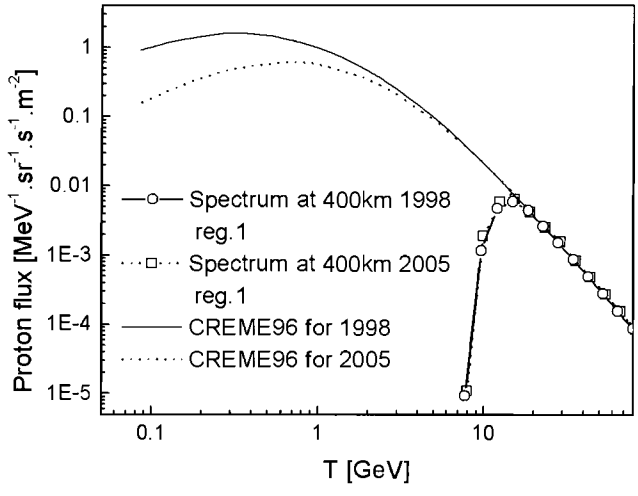

Figure 7. Primary proton spectra at AMS orbit (region 1) for June 1998 and October 2005.

CONCLUSIONS

The method of the magnetospheric transmission function in combination with measured (AMS-01) and simulated (CREME96) cosmic protons spectra has been successfully used to obtain the flux of primaries in several geomagnetic regions inside the magnetosphere. As AMS-01 has shown, measured spectra of protons at Space Shuttle orbit are contaminated by a population of secondaries. This method can be used to disentangle the contribution of primary protons to the measured spectra. Predictions for future experiments are also possible because both geomagnetic models and modulated proton model can be extrapolated.

Furthermore this method can be used to recover cosmic ray spectra outside the magnetosphere, starting from measured primary spectra in near Earth orbit, by inverting the relation (2). This method is restricted to energies higher than cut-off rigidity, in fact below the cut-off the TF is null and the procedure fails. An independent spectrum of primaries can be obtained from AMS-01 flux data through the separation by back-tracing of the measured particles (*Micelotta et al.*, private communication). Finally the same procedure can be applied to every measured spectrum of primary Cosmic Rays inside the magnetosphere. In fact the transmission function can be evaluated if the experimental conditions are known: time, position, and attitude of the experiment.

Acknowledgments. Slovak VEGA grant agency (grant 4064) is acknowledged. The authors thank the referees for the remarkable work done for the revision of the paper.

REFERENCES

Alcaraz J., *et al.* (The AMS collaboration), Protons in near Earth orbit, *Phys. Lett. B*, vol. 472, 215-226, 2000a.

Alcaraz J., *et al.* (The AMS collaboration), Cosmic Protons, *Phys. Lett. B*, vol. 490, 27-35, 2000b.

Barton C.E., International Geomagnetic Reference Field: The Seventh Generation, *J. Geomag. Geoelectr.*, vol. 49, 123-148, 1997.

Bobik P., K. Kudela, and I. Usoskin, Geomagnetic cutoff Penumbra structure: Approach by transmissivity function, *Proc. 27th ICRC.*, Hamburg, Germany, SH3.06, 4056-4059, 2001a.

Bobik P., M. Boschini, M. Gervasi, D. Grandi, K. Kudela, M. Potenza, and P.G. Rancoita, Study of Cosmic Ray access to a space detector by particle tracing in the Earth magnetosphere, *SIF Conference Proceedings*, vol. 73, 417-424, 2001b.

Bobik P., M. Boschini, M. Gervasi, D. Grandi, K. Kudela, E. Micelotta, and P.G. Rancoita, Cosmic ray spectrum at 1 AU: a transmission function approach to the magnetosphere, *Proceedings of ICSC 2003, ESA SP-533*, 633-636, 2003.

Bobik P., M. Boschini, M. Gervasi, D. Grandi, E. Micelotta, and P.G. Rancoita, A normalization procedure for Creme96 spectra, *Proceedings of 8th ICATPP 2003, World Scientific (Singapore)*, 49-54, 2004, Barone *et al.* Eds.

Smart D.F., M.A. Shea, and E.O. Flückiger, Magnetospheric Models and Trajectory Computations, *Space Sci. Rev.*, vol. 93 (1/2), 305-333, 2000.

Tsyganenko N.A., and D.P. Stern, Modeling the global magnetic field the large-scale Birkeland current systems, *J. Geophys. Res.*, vol. 101, 27187-27198, 1996.

Tylka A.J., J.H. Adams, P.R. Boberg, B. Brownstein, W.F. Dietrich, E.O. Flueckiger, E.L. Petersen, M.A. Shea, D.F. Smart, and E.C. Smith, "CREME96: A Revision of the Cosmic Ray Effects on Micro-Electronics Code", *IEEE Trans. Nuclear Sci.*, vol. 44, 2150-2160, 1997.

Vallarta M.S., Theory of the Geomagnetic Effects of Cosmic Radiation, *Handbuch der Physik*, vol. XLVI, 1961.

bobik@mib.infn.it
BOSCHINI@ICIL64.CILEA.IT
Davide.Grandi@mib.infn.it
emicelo@mib.infn.it
massimo.gervasi@mib.infn.it
piergiorgio.rancoita@mib.infn.it

Investigation of 3D Energetic Particle Transport Inside Quiet-Time Magnetosphere Using Particle Tracing in Global MHD Model

X. Shao[1,2], Shing F. Fung[1], L. C. Tan[3], K. Papadopoulos[4], M. Wiltberger[5], and M. C. Fok[6]

Due to the presence of a magnetic field minimum in the outer cusp region, energetic particles drifting toward dayside may experience large scale transport toward high latitude. Some particle maybe trapped at high latitude and then be scattered back. These particle orbits are termed as Shabansky orbits [*Shabansky*, 1971]. Particle trajectories inside the magnetosphere can be grouped into three classes: bouncing around the equator (trapped), going through Shabansky orbit or being elevated at dayside, and lost. Characterizing these three types of particle trajectory and their dependence on solar wind conditions can help understand the trapping and loss of energetic particles in the radiation belt. We developed 3D test-particle tracing codes to investigate particle transport in global MHD model magnetosphere. In the code, protons are traced with full-motion and electrons are traced with guiding-center approximation. In this paper, we lay out the framework of studying the trapping and lost regions systematically and effects of the enhancement of the solar wind velocity on these regions. We derived the so-called Shabansky Orbit Accessibility Map (SOAM) for both electrons and protons to visualize the three orbital characteristic regions as a function of the particle's initial position and pitch angle inside quiet-time magnetosphere.

1. INTRODUCTION

Because of its potentially hazardous space environment effects on space systems, the radiation belt (RB) has been a key subject of studies in space physics. Understanding the transport of energetic RB particles is important in characterizing the radiation belt. In situ measurements have revealed that the cusp is a region of weak or depressed magnetic field [e.g. *Fung et al.*, 1997]. The presence of a local magnetic field minimum in the outer cusp can lead to off-equator transports along the Shabansky orbit [*Shabansky* 1971]. Therefore, particle trajectories inside the magnetosphere can be grouped into three classes: (a) bouncing around the equator (fully-trapped); (b) going through Shabansky orbit or significantly gaining latitudes on the dayside (Shabansky-orbit); and (c) being lost.

Recent studies [*Sheldon et al.*, 1998; *Chen et al.*, 1998; *Trattner et al.*, 2001] led to a controversy regarding the role of the cusp in producing radiation belt particles. *Sheldon et al.* [1998] reported the trapping of the energetic electrons (30 keV to ~2 MeV) in the outer cusp region and suggested the possible diffusive filling of the electron radiation belts from the cusp. *Chen et al.* [1998] reported cusp energetic particle (CEP) (several hundred keV ions) events and suggested that the cusp region can be a major particle

[1] Space Physics Data Facility (SPDF), NASA Goddard Space Flight Center, Greenbelt, Maryland
[2] National Research Council Research Associate Program, Washington DC
[3] QSS Inc., Greenbelt, Maryland
[4] Department of Astronomy, University of Maryland, College Park, Maryland
[5] N CAR, Boulder, Colorado
[6] Laboratory for Extraterrestrial Physics (LEP), NASA Goddard Space Flight Center, Greenbelt

The Inner Magnetosphere: Physics and Modeling
Geophysical Monograph Series 155

10.1029/155GM33

acceleration region of the magnetosphere. But, the acceleration mechanism is not identified. *Trattner et al.* [2001] provided an alternative explanation that the cusp energetic particles (up to several hundred keV ions) might be accelerated at the quasi-parallel bow shock, then transported downstream and enter the cusp along newly reconnected field lines or some other entry mechanism. For ions with energy above 150 keV/e, the magnetosphere itself might circulate these particles to the cusp through Shabansky orbit. In order to understand the populating of the cusp with energetic particles, we need first to understand the circulation of energetic particles in the magnetosphere. We intended in this paper not to discuss about the cusp or shock region acceleration, but rather to characterize the three types of trajectory of magnetospheric particles and quantify the accessibility of Shabansky orbit.

At present, a number of particle-tracing based radiation belt models exist [*Li et al.*, 1993, *Elkington et al.*, 2002]. These test particle-based radiation belt models trace particles either in an empirical magnetospheric model or in a 2D cutplane from global MHD simulations. For relativistic electrons, off-equatorial transport was neglected. These models are not applicable to studying the accessibility of high latitude regions by magnetospheric particles. On the other hand, *Delcourt and Sauvaud* [1999] focused on the 3D transport of energetic protons in an empirical magnetic field model and demonstrated the populating of the cusp and boundary layers by energetic (hundreds of keV) equatorial particles (mainly protons). But it is not clear what the dependence on the initial launching location and pitch angle is for particles being able to access the dayside high latitude region. Therefore, we still do not have a clear picture about classifying the three types of particle trajectory.

Recently, we developed a 3D particle tracing code to trace energetic particles in Lyon-Fedder-Mobbary (LFM) global MHD model [*Fedder et al.*, 1995]. The global MHD model provides the particle tracing code with self-consistent electric and magnetic (EM) fields in the magnetosphere. In this paper, we show that by tracing a limited number of test particles from different locations and initial pitch angles, we can obtain the so-called Shabansky Orbit Accessibility Map (SOAM), with which we can study the grouping of the three types of particle trajectory. In this paper, we focused on the 3D transport of radiation belt particles inside the quiet-time magnetosphere formed with constant northward IMF.

In following sections, we first introduce our model of RB particle transport and validations of the codes. Then, using the model, three types of particle trajectory in the magnetosphere are identified for both energetic electrons and protons. SOAMs are constructed to understand the dependence of trapping, Shabansky-orbit and lost of the energetic particles on the initial launching location and pitch angle during different constant solar wind speeds.

2. SIMULATION MODELS

2.1. Overall Architecture of the Particle Transport Model

The newly developed radiation belt particle transport model utilizes the Lyon-Fedder-Mobbary (LFM) global MHD model [*Fedder et al.*, 1995] to provide EM fields in the magnetosphere and a 3D relativistic particle tracing code to study the spatial-temporal evolution of energetic RB electrons and protons in an evolving magnetosphere.

2.2. Global MHD Model

The electric and magnetic fields used to feed the 3D particle tracing code are taken from the LFM global MHD model [*Fedder et al.*, 1995; *Guzdar et al.*, 2001]. The core module of the LFM model is a three dimensional code that solves the ideal MHD equations in a conservative form. These equations are discretized and solved on a cylindrical staggered mesh, typically 60 R_E in radius and 330 R_E long, containing the solar wind and the magnetosphere. A spider web type computational grid places maximal resolution (0.2 to 0.4 R_E) on physically critical locations such as the bow-shock region and the inner magnetosphere. The code uses diffuse solar wind matching conditions along the outer edges of the computational domain. This permits time dependent solar wind parameters as input conditions. A simple supersonic outflow condition is used in the outer anti-solar boundary. The inner boundary is located on a geocentric sphere of radius 3 R_E, where the magnetospheric solution is matched to the solution of the ionospheric module. The ionospheric module represents the ionosphere and its coupling to the magnetosphere and solves a 2D height-integrated electrostatic potential equation.

2.3. 3-D Particle Tracing Models

Because the gyro-radius of energetic (a few hundred keV to MeV) electrons and protons in the Earth's magnetosphere differs by orders of magnitude, we developed different algorithms to trace motions of energetic electrons and protons. Namely, protons are traced with full motion and electrons are traced with guiding-center approximation.

2.3.1. Full momentum tracing for relativistic protons. *Delcourt and Sauvaud* [1999] show that for relativistic protons, full-momentum tracing is needed because in the compressed inner magnetotail and dayside cusp region,

the ratio between the gyro-radius of energetic (several hundred keV) protons and the gradient and curvature scale of the local magnetic field ($\varepsilon_r = \max(|\rho\nabla(\ln B)|, |\rho\hat{b} \bullet \nabla\hat{b}|)$) is large so that the magnetic moment (first adiabatic invariant) is not conserved. Typical criterion for the conservation of the first adiabatic invariant is $\varepsilon_r < 0.187$ [*Chirikov*, 1987]. For example, for a 500 keV proton with 90 degree pitch angle, the gyro-radius is about 0.32 R_E in a typical magnetic field of magnitude 50 nT at X ~ −7.5 R_E inside the magnetosphere. Local gradient scale and curvature scale can be <0.6 Re, resulting $\varepsilon_r > 0.53$ so that the magnetic moment is not conserved. Therefore, we trace the energetic proton by solving the full motion equations:

$$d(\gamma m_p \vec{V})/dt = q[\vec{E} + \vec{V} \times \vec{B}] \tag{1}$$

$$d(\gamma m_p c^2)/dt = q\vec{V} \bullet \vec{E} \tag{2}$$

where $\gamma = 1/\sqrt{1-(V/c)^2}$, $\vec{V}$ is the particle velocity.

The numerical scheme used to integrate the motion is similar to those used in particle codes [*Birdsall and Langdon*, 1991], namely a time-centered leap-frog scheme. Particle velocity ($\vec{V}^{n\pm1/2}$) is defined at half time step and particle position ($\vec{r}^{n\pm1}$) is defined at integer time step.

Let $\vec{u} = \gamma\vec{V}$ and consequently $(\gamma)^2 = 1 + (u/c)^2$, the motion equation can be written in the discretized form as

$$\vec{u}^{n+1/2} - \vec{u}^{n-1/2} = \frac{q\delta t}{m}[\vec{E}^n + \frac{1}{2\gamma^n}(\vec{u}^{n+1/2} + \vec{u}^{n-1/2}) \times \vec{B}^n] \tag{3}$$

Here, the velocity in the $\vec{V} \times \vec{B}$ term of equation (1) is treated with the Crank-Nicholson method. By rearranging Equation (3) and assuming $\vec{u}^{n-1/2}$, $\vec{E}^n$, $\vec{B}^n$, and $\gamma^{n-1/2}$ are known, we get equation (4) for $\vec{u}^{n+1/2}$:

$$\begin{aligned}&(\vec{u}^{n+1/2} + (q\delta t/m)(1/2\gamma^n)\vec{B}^n \times \vec{u}^{n+1/2}) \\ &= \vec{u}^{n-1/2} + (q\delta t/m)[\vec{E}^n + (1/2\gamma^n)\vec{u}^{n-1/2} \times \vec{B}^n]\end{aligned} \tag{4}$$

which can be easily solved with a linear equation solver. The particle position can be updated with $\vec{r}^{n+1} = \vec{r}^n + \vec{V}^{n+1/2}\delta t = \vec{r}^n + \vec{u}^{n+1/2}\delta t/\gamma^{n+1/2}$. The advancing time step is about 1/180 of proton gyration period.

2.3.2. Guiding-Center approximation for relativistic electrons. To trace energetic electrons using guiding-center approximation, we need to ensure that fields vary slowly in both space and time when compared to the particle's gyro-radius and gyro-period, or that the first adiabatic invariant is conserved. The MHD wave field varying time scale is on the order of second, which is much larger than the gyro-period of electrons, typically can be 0.001 second. The spatial criterion for the conservation of the first adiabatic invariant is given by $\varepsilon_r < 0.187$. As an example, the gyro-radius of MeV electron in 50 nT magnetic field is 0.015 R_E and the MHD simulation magnetic field variation scale is larger than 0.2 R_E (smallest grid resolution). This implies that in the absence of VLF higher frequency waves the first adiabatic invariant of relativistic electrons are mostly conserved in the inner magnetosphere.

The guiding-center motions of relativistic electrons are given by [*Northrop*, 1963]:

$$d(\gamma m_e \vec{V}_g)/dt = -e[\vec{E} + \vec{V}_g \times \vec{B}] - M\nabla B/\gamma \tag{5}$$

$$\frac{d(\gamma m_e c^2)}{dt} = -e\vec{V}_g \bullet \vec{E} + \frac{M}{\gamma}\frac{\partial B}{\partial t}, \tag{6}$$

where $M = P_\perp^2/(2m_e B)$ and $\gamma = 1/\sqrt{1-(V/c)^2}$. Here $\vec{V}_g$ is the electron guiding-center velocity, V is the magnitude of the electron velocity, and $P_\perp$ is the electron momentum perpendicular to the local magnetic field.

Equation (5) differs from the guiding-center motion equation presented in *Northrop* [1963] (Equation 1.12 in *Northrop* [1963]) with gamma factor being added to account for relativistic effects. As noted in *Northrop* [1963], Equation (5) is the most original guiding center motion equation. The guiding center velocity equations for parallel and perpendicular components, which consist of $\vec{E} \times \vec{B}$, gradient, curvature and parallel drift, can be derived from Equation (5) following procedures similar to those in *Northrop* [1963]. The advantage of using Equation (5) to describe the guiding center motion is that the parallel and perpendicular guiding center velocity is treated as an integrated entity and we don't need to project the velocity to the magnetic field back and forth during the calculation, which can otherwise be sources of numerical errors. Equation (6) has been averaged over electron gyro-period and is valid when $E_\perp/B << c$ (c is the speed of light), which is true for the electric field of MHD origin.

The numerical scheme used to integrate the guiding-center motion equation is again time-centered leap-frog scheme. The particle guiding-center velocity ($\vec{V}_g^{n\pm1/2}$) is defined at half time step and the particle position ($\vec{r}_g^{n\pm1}$) is defined at integer time step.

Similarly, let $\vec{u}_g = \gamma\vec{V}_g$, the guiding-center motion equation (6) can be discretized as

$$\begin{aligned}&\vec{u}_g^{n+1/2} - \vec{u}_g^{n-1/2} = -(\delta t/m_e)(M/\gamma^n)\nabla B^n \\ &-(e\delta t/m_e)[\vec{E}^n + (1/2\gamma^n)(\vec{u}_g^{n+1/2} + \vec{u}_g^{n-1/2}) \times \vec{B}^n]\end{aligned} \tag{7}$$

Here, the guiding velocity in the $\vec{V}_g \times \vec{B}$ term in Equation (6) is treated with Crank-Nicholson method. Rearranging Equation (11), we can get the equation about $\vec{u}_g^{n+1/2}$:

$$\vec{u}_g^{n+1/2} - (e\delta t / m_e)(1/2\gamma^n)\vec{B}^n \times \vec{u}_g^{n+1/2} = \vec{u}_g^{n-1/2} - (e\delta t / m_e)[\vec{E}^n + \frac{1}{2\gamma^n}\vec{u}_g^{n-1/2} \times \vec{B}^n] - (\delta t / m_e)(M/\gamma^n)\nabla B^n \quad (8)$$

which can be easily solved. Once $\vec{u}_g^{n+1/2}$ is solved, the particle guiding-center position can be updated with $\vec{r}_g^{n+1} = \vec{r}_g^n + \vec{V}_g^{n+1/2}\delta t = \vec{r}_g^n + \vec{u}_g^{n+1/2}\delta t / \gamma^{n+1/2}$. The advancing time step is adaptive and adjusted according to the parallel velocity along the magnetic field line.

2.3.3. Interpolation of MHD EM field and code validation. There can be two sources of error: the error originated form the numerical schemes used to integrate the particle motion equations and the error originated from further interpolation of the MHD field value to the particle location. Global MHD simulation outputs provide the EM field on the grid cells. We need to interpolate EM field to the particle location. For electric field, simple eight-point linear interpolation is used. For magnetic field, two kinds of interpolation have been tested: (a) interpolate and get the perturbed field at the particle location and then add the dipole field value back; (b) simple eight-point interpolation of the B field on the MHD grid.

Here, we present some results to benchmark the 3D particle-tracing codes. We traced particles with different initial energy, pitch angle and L, in a dipole field with no electric field. We tested the two interpolation schemes mentioned above. Scenario (a) essentially uses a smooth dipole field in our testing case and helps understand the error originated from the integration scheme. Scenario (b) is used to understand the error from the linear interpolation.

For relativistic protons, the particle motion is followed one complete circuit in local time with the full-motion tracing scheme. The error between initial and final energy is zero, as has been shown in *Birdsall and Langdon* [1991] that the tracing scheme conserves the particle energy. The relative errors between the initial and final values of the first, second adiabatic invariants are recorded. The first adiabatic invariant M is gyro-period-averaged to remove the first-order gyro-frequency variation in the instant value of M (due to the field inhomogeneity). The second adiabatic invariant is calculated with the integral $J = \oint p_{//} ds$ over full bounces during the tracing. For 90 degree pitch angle particle, we use the maximum off-equator deviation in Z as the error measure. Table 1 summarizes our results. In general, the numerical scheme of motion equation integration conserves M and J within 0.05% in scenario (a) and within 0.5% in scenario (b). Scenario (a) performs better than scenario (b).

Table 1. Relative errors with the tracing code for 20- and 500-keV **protons** with 45 and 90 degree pitch angle at L = 5 and 10 in a dipole field using interpolation scheme (a) interpolation of the perturbed field; (b) interpolation of magnetic field directly. M and J denote the first and second adiabatic invariant. Subscripts 0 and f denote the initial and final (after one orbit around the Earth) values. For 90 degree pitch angle particle, the error $|Z|_{max}$ is listed.

L	E_0 keV	Equ p. a.	$\left\|\frac{M_f - M_0}{M_0}\right\|$ in (a)	$\left\|\frac{M_f - M_0}{M_0}\right\|$ in (b)	$\left\|\frac{J_f - J_0}{J_0}\right\|$ or $\|Z\|_{max}$ in (a)	$\left\|\frac{J_f - J_0}{J_0}\right\|$ or $\|Z\|_{max}$ in (b)
5	20	90	4.4×10^{-5}	1.6×10^{-4}	10^{-9} Re	10^{-5} Re
5	20	45	2.3×10^{-6}	1.6×10^{-3}	$<10^{-6}$	4×10^{-4}
10	20	90	8.7×10^{-5}	3.9×10^{-4}	10^{-9} Re	10^{-6} Re
10	20	45	3.0×10^{-6}	4.5×10^{-3}	$<10^{-6}$	2×10^{-4}
5	500	90	1.6×10^{-6}	1.3×10^{-5}	10^{-9} Re	10^{-7} Re
5	500	45	3.4×10^{-4}	4.0×10^{-3}	6×10^{-6}	5×10^{-4}
10	500	90	$<10^{-6}$	8.8×10^{-4}	10^{-9} Re	10^{-6} Re
10	500	45	1.8×10^{-4}	1.2×10^{-3}	2×10^{-5}	3×10^{-4}

For relativistic electrons, the motion is similarly followed with the guiding-center tracing scheme (see section 2.3.2). The first adiabatic invariant is always conserved. The energy is also conserved throughout the tracing. Table 2 summarizes results. In general, the numerical scheme of integrating guiding-center motion equation conserves second adiabatic invariant J within 0.05% in scenario (a) and within 0.7% in scenario (b). Again, scenario (a) performs better than scenario (b). In actual simulations for both electrons and protons, we use the interpolation scheme (a) and only interpolate the perturbed magnetic field.

In the MHD simulation, the inner boundary is located on a geocentric sphere of radius 3 R_E. When particles go across

Table 2. Relative errors with the tracing code for 50- and 1000-keV **electrons** with 45 and 90 degree pitch angle at L = 5 and 10 in a dipole field using interpolation scheme (a) interpolation of the perturbed field; (b) interpolation of magnetic field directly. See Table 1 caption for further info.

L	E_0, keV	Equ. p. a.	$\left\|\frac{J_f - J_0}{J_0}\right\|$ or $\|Z\|_{max}$ in (a)	$\left\|\frac{J_f - J_0}{J_0}\right\|$ or $\|Z\|_{max}$ in (b)
5	50	90	6.3×10^{-8} Re	9.3×10^{-4} Re
5	50	45	$<10^{-6}$	2.8×10^{-3}
10	50	90	1.3×10^{-7} Re	6.6×10^{-5} Re
10	50	45	$<10^{-6}$	2.0×10^{-3}
5	1000	90	6.3×10^{-8} Re	1.2×10^{-4} Re
5	1000	45	$<10^{-6}$	6.3×10^{-3}
10	1000	90	1.3×10^{-8} Re	2.7×10^{-7} Re
10	1000	45	4.6×10^{-4}	6.0×10^{-4}

this boundary and enter the inner region, dipole field is switched on and the electric field is assumed to be zero. We also note that the co-rotation electric field is not included in the simulation since it has little effects on energetic particles for L > 6 regions. On the other hand, when particles are transported to the flank or magnetopause and meet the magnetic field line with invalid mirroring condition (i.e. open field lines), these particles will be transported away and hit the simulation outer boundary. When the particle exits the outer boundary, we mark the particle as being lost.

3. THREE TYPES OF PARTICLE TRAJECTORY IN THE MAGNETOSPHERE

The tracing codes were applied to identify the typical trajectories of energetic protons and electrons in a quiet-time Earth's magnetosphere. In this case, a steady state model magnetosphere is formed with a constant northward IMF = 5nT, solar wind velocity = 400 km/s, density = 5 /cc, and thermal speed = 40 km/s. The ionospheric conductivity = 5 mho. This idealized quiet-time magnetosphere has been studied by *Guzdar et al.* [2001]. Some features of the quiet-time magnetosphere are: the closed magnetotail length is around X = −38 R_E in the north-south plane; presence of cusp region reconnection consistent with *Kessel et al.* [1995]; four-cell ionospheric convection pattern consistent with *Kennel* [1985]; the ionospheric cross polar cap potential is around 8 kV; and the magnetospheric electric field is weak (<0.04 mV/m at geosynchronous orbit in the equatorial plane). The ionospheric four-cell potential pattern and the associated equipotentials in the equator simulated from the global MHD model [*Guzdar et al.*, 2001] are consistent with the empirical models based on observations [*Kennel*, 1995].

Plate 1 shows three types of trajectory, namely trapped, Shabansky-orbit, and lost, for energetic protons inside the steady state magnetosphere. The protons are launched at the night side along SM X axis. Plate 1A shows the trajectories of trapped protons. An 80 keV proton (white trace) launched from X = −6 R_E with 90 degree equatorial pitch angle drifts clockwise and remains in the equatorial plane (perturbations in Z within 0.002 R_E). The blue trace represents orbit of an 80 keV proton launched at x = −8 R_E with initial pitch angle 45 degree. It shows that the proton bounces around the equator while drifting clockwisely. Figure 1A shows conservation of the second adiabatic invariant vs. azimuthal angle along particle trajectory for protons in Plate 1A.

Plate 1B shows a 500 keV proton with 67.5 degree initial equatorial pitch angle executing the Shabansky orbit. Due to the existence of the cusp magnetic field minimum, the proton moves off toward high latitudes, instead of bouncing around the equator, and is trapped at high latitudes for a while. Then, the particle falls back to bouncing around the equator after

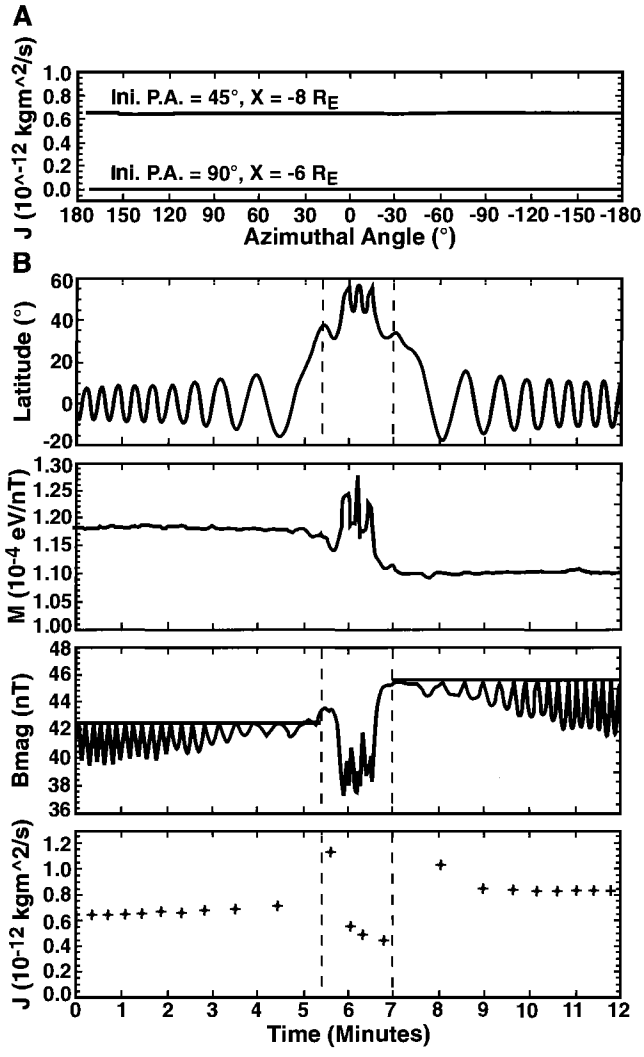

Figure 1. (A): The second adiabatic invariant vs. azimuthal angle for the trapped protons in Plate 1a. (B): Details for the particle experiencing Shabansky orbit in Plate 1b. In (B), top panel shows the evolution of the gyro-phase averaged latitude along the particle trajectory; second panel shows the gyro-phase averaged first adiabatic invariant along the particle trajectory; third panel shows the gyro-phase averaged magnetic field magnitude along the particle trajectory; bottom panel shows the second adiabatic invariant vs. time.

passing the dayside sector. To have a better understanding about the details of the proton executing Shabansky orbit, the evolutions of the first and second adiabatic invariants are shown in Figure 1B. The top panel in Figure 1B shows the evolution of the gyro-phase averaged latitude along the particle trajectory. The vertical dashed lines indicate when the particle goes through high-latitude region. The second panel in Figure 1B shows the evolution of the first adiabatic invariant M. The first adiabatic invariant is again gyro-phase averaged.

[redacted]

[redacted]

[redacted]

[redacted]

We can see that the first adiabatic invariant is not conserved at the high latitude region and when the proton falls off to bouncing around the equator at the dayside, the first adiabatic invariant changes from 11800 eV/nT to 11000 eV/nT. The third panel in Figure 1B shows the evolution of the gyrophase averaged magnetic field strength experienced by the proton and further illustrates the violation of the first adiabatic invariant in the high latitude region. The maximum magnetic field strength at the mirroring point (marked with horizontal lines) changes from 42.5 nT to 45.5 nT when the particle passes the high-latitude region. The bottom panel in Figure 1B shows the varying of the second adiabatic invariant (from 6.5×10^{-13} to 8.3×10^{-13} kgm^2/s) when the proton goes through the high latitude region. Note the second adiabatic invariant is calculated by integrating over full bounces which are identified with the particle parallel velocity changing from – to + (start), + to – and – to + (end) in the simulation. Since local field curvature in the cusp region is comparable to the proton gyro-radius, the first and second adiabatic invariants are not conserved [*Young et al.*, 2002]. The violation of the first and second adiabatic invariants as the energetic proton going through Shabansky orbit was previously shown by *Delcourt and Sauvaud* [1999]. Plate 1c shows a 500 keV proton trajectory experiencing loss.

Plate 2 shows three types of trajectory for RB electrons traced inside the same steady state magnetosphere. Plate 2A shows that the electrons are stably trapped around the equator and drift counter-clockwise around the Earth. Plate 2B shows the trajectory of 1MeV electron experiencing the Shabansky orbit. Plate 2C shows the trajectory of an electron being lost. Top panel of Figure 2 shows evolutions of the second adiabatic invariant for the trapped electrons in Plate 2A and the Shabansky-orbit electron in Plate 2B. For the trapped electrons, the second adiabatic invariant is conserved. For the Shabansky-orbit electron, the second adiabatic invariant changes to a lower value in the high latitude region and returns to initial value after falling back to bouncing around the equator at the dayside. In the guiding-center tracing, the first adiabatic invariant is conserved and the maximum magnetic field magnitude along the particle trajectory should be constant. This is illustrated in the second panel of Figure 2. To understand the origin of the Shabansky orbit, the magnetic field magnitude along two magnetic field lines threading through the electron trajectory are plotted in the bottom panel of Figure 2. The electron is originally trapped around the equator in the potential well formed on the field line (1). The appearance of two field-strength minimums along the field line (2) and the increased equatorial magnetic field magnitude (larger than the field-strength at the electron mirroring point) cause the violation of the second adiabatic invariant. The electron is transported to the high latitude and trapped in the upper part of the field line (2). But, after the electron exits being trapped at the high-latitude region,

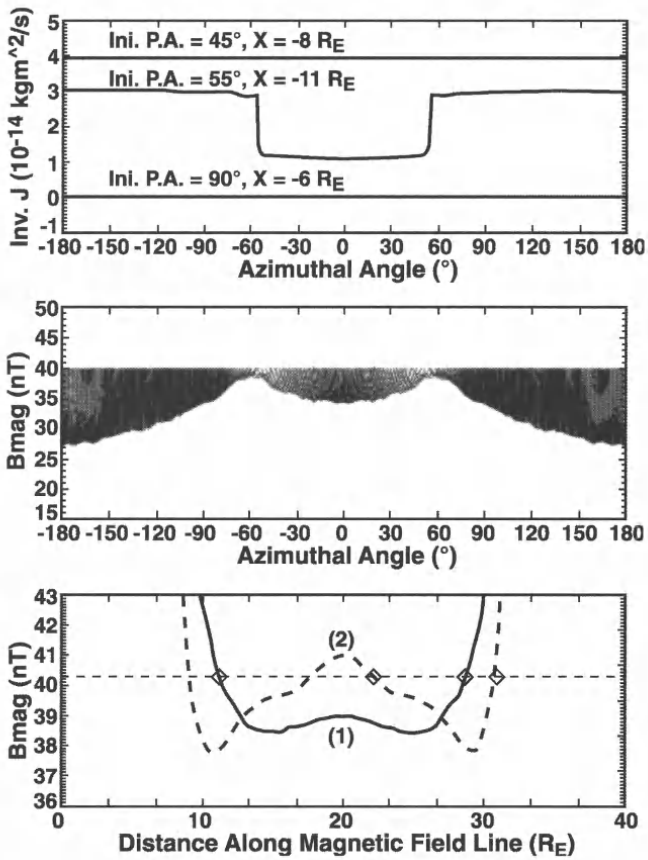

Figure 2. Top panel: the second adiabatic invariant vs. azimuthal angle for electrons in Plate 2a, b. Middle panel: The magnetic field magnitude along the trajectory of the electron experiencing Shabansky orbit (see Plate 2b). Bottom panel: showing changes in the magnetic field configuration when electron transits from being equatorially trapped to being trapped at high latitude. The magnetic field magnitude along two magnetic field lines threading through the electron trajectory are plotted. The horizontal dashed line at |B| = 40.3 nT indicates the mirroring point. Square diamonds mark mirroring points along each magnetic field line.

the second adiabatic invariant returns to its initial value. In this sense, it is conserved. These results are consistent with earlier picture depicted in *Shabansky* [1971].

4. SHABANSKY ORBIT ACCESSIBILITY MAP

By tracing particle trajectories, we can determine the fate of a particle (trapped, Shabansky-orbit, or lost) as function of initial position and equatorial pitch-angle of the particle. We introduce in this section the Shabansky Orbit Accessibility Map (SOAM) to determine the accessibility of the trapping, Shabansky-orbit and lost regions for particles originated from the tail. Plate 3A illustrates the configuration we used to derive the SOAM. In Plate 3A, pink dots along the X axis (from X = –6 to –14 Re) on the night side represent initial

positions of energetic particles being launched. The black lines on the dayside form two planar boundaries of a 3D sector (−45 degree < azimuthal angle < 45 degree), inside which we sum and average the latitude of the energetic protons. Here, 0 degree azimuth is along the sun-Earth line toward the sun. For electrons, the sector is smaller with −22.5 degree < azimuthal angle < 22.5 degree. Particles are initially launched every 0.1 R_E along the night X axis with pitch angle varying from 90 to 10 degree in 2.5 degree increment. Particles experiencing Shabansky orbit are transported either above or below the magnetic equator. When constructing the SOAM, we use the absolute value of the average latitude in the dayside sector.

We first construct the SOAM for a quiet-time magnetosphere with northward IMF as described in section 3. Top panel of Plate 3B shows the corresponding noon-midnight plane of the quiet-time model magnetosphere. We refer to this configuration as magnetosphere A. Plate 4A and 4B show SOAMs we derived for 500 keV protons and 1MeV electrons initially launched along the X axis (X = −6 to −14 Re) down the tail, respectively.

The SOAM shows the average dayside latitude vs. initial launching position and equatorial pitch angle of energetic particles. If the particle experiences bounce motion about the equator, then the average latitude = 0. The white region in the SOAM denotes the part of phase space from which particles will be lost. The colored region between the trapping and the lost region is the Shabansky-orbit region. From the SOAM, we can infer the average dayside latitude attained by a Shabansky-orbit particle. For example, a 500 keV proton launched at X = −10.1 R_E with 67.5 degree pitch angle have an average latitude of 50 degree on the dayside; a 1 MeV electron launched at X = −11.8 R_E with a pitch angle of 55 degree can have 55 degree in latitude.

We can see from Plate 4A and 4B that the overall structure of SOAMs for energetic electrons and protons are similar. Both maps show that particles with all pitch angles launched from X > −8 R_E along the tail X axis will be stably trapped around the equator. The Shabansky-orbit region has a concaved decaying slope. The general trend is that the electrons or protons launched further down the tail and with larger pitch angle are more susceptible to be transported to the Shabansky orbit on the dayside or to be lost. The initial launching position dependence of dividing the trapping, Shabansky-orbit, and lost regions can be explained by the fact that particles with same pitch angle launched further down the tail drift in larger geocentric radius and have easier access to the Shabansky -orbit or magnetopause regions. The pitch-angle dependence of dividing the three regions can be understood through the effect of drift-shell splitting according to *Roederer* [1970]. Due to the day-night asymmetry of the Earth's magnetic field, the particle drift orbits are pitch-angle dependent or disperse radially for different pitch-angles. In general, for particles launched from the same location down the tail, the larger the pitch angle the larger is the geocentric radius of the particle orbit intersected with the equator on the dayside. *Roederer* [1970] uses the first two adiabatic invariants of particles, namely the magnetic moment and the parallel motion integral, to explain the drift-shell splitting and didn't consider the effect of the Shabansky orbit. After taking the Shabansky orbit into account, there appears a transition region in SOAM. But the general trend in SOAM can still be explained by drift-shell splitting.

We can still see significant differences in fine structures between the SOAM of energetic electrons and that of protons in Plate 4A, B. The transition regions of trapping, Shabansky-orbit and lost for high energy protons in SOAM are more sporadic (or chaotic) and mixed than those of electrons. At high field line curvature regions, e.g. night side compressed inner tail and dayside high latitude cusp regions, the gyro-radius of the energetic protons is comparable to the field line curvature. In these regions, energetic protons suffer scatterings of the first and second adiabatic invariants [*Young et al.*, 2002]. These scatterings, coupled with effects of drift shell splitting, move particles chaotically to different orbits, which in turn is shown in the chaotic transition region in SOAM. Numerical discretization errors can also contribute to the complexity in the SOAM of energetic protons. On the other hand, the electron gyro-radius is much smaller than the field line curvature and transition region is smoother.

We also derived the SOAMs for protons and electrons in a more compressed magnetosphere to assess their dependences on the solar wind speed. The magnetosphere is driven with solar wind speed = 600 km/sec, IMF Bz = 5 nT and density = 5 /cc. This steady state magnetosphere is called magnetosphere B. Bottom panel of Plate 3B shows the corresponding noon-midnight plane configuration of the magnetosphere. The magnetotail in this case extends to X = −48 R_E and is more stretched. The current sheet is more compressed and moves closer to Earth. Plate 4C and 4D show the SOAMs for 500 keV protons and 1 MeV electrons, respectively. As we can see, there still exist three regions, namely trapping, Shabansky-orbit and lost regions. Higher solar wind velocity, however, causes the Shabansky-orbit region to move closer to Earth. In order to be stably trapped for all pitch angles, both electrons and protons need to be launched from X > −6.8 R_E along the tail X axis. In Plate 4C, there is a truncation region at initial launching X < −12 Re. In this region, the trapping and Shabansky-orbit regions are truncated and most protons will become lost. The appearance of the truncation region can be attributed to two factors. (1) In a more compressed tail, the cross tail drift velocity (in Y direction) of the proton is larger which moves the proton closer to the magnetopause on the flank and makes it easier to be lost. (2) in regions of high field line curvature, i.e. in a more compressed tail at midnight, the gyrophase-dependent scatterings of the first

3 [redacted]

[redacted]

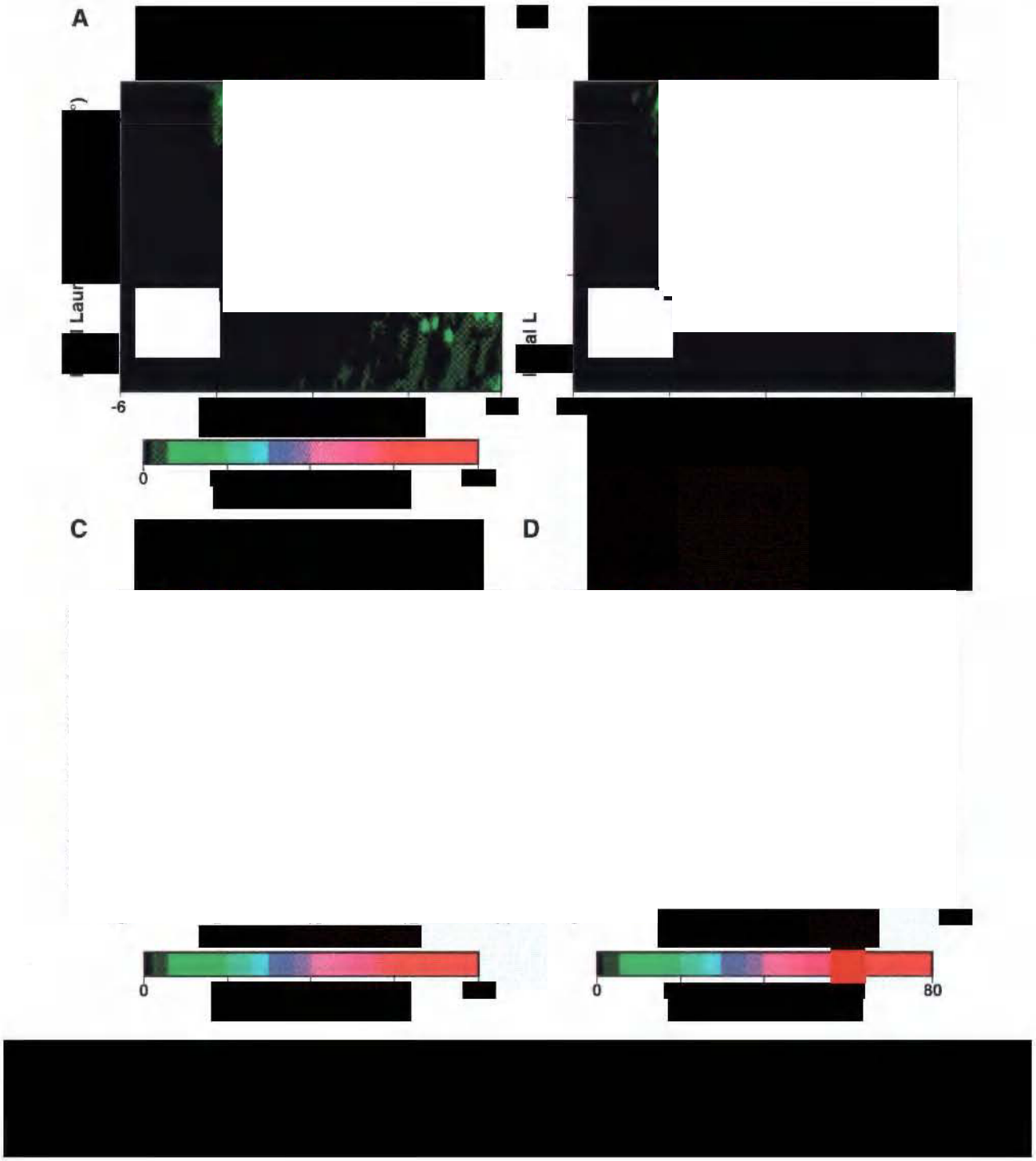
A
-6
0
C
D
0
0
80

and second invariants are prominent [*Young et al.*, 2002]. These scatterings can move particles chaotically to different orbits during their drifts to the noon regions and the truncation region ($X < -12\ R_E$) in Plate 4c looks mixed.

5. SUMMARY

We present a model to simulate the 3D trasport of magnetospheric energetic particles. The model combines a global MHD model and 3D particle tracing codes. Energetic protons are traced with full motion and electrons are traced with guiding-center approximation. Using the computational model, we identified three types of particle trajectory, namely trapped, Shabansky-orbit and lost, in a quiet-time magnetosphere. We also derived Shabansky Orbit Accessibility Map (SOAM) for both energetic electrons and protons inside a quiet-time magnetosphere with northward IMF to quantify the dependence of the three regions on the initial launching position and pitch angle. The general trend is that energetic electrons or protons launched further down the tail and with larger pitch angle are more susceptible to the Shabansky orbit on the dayside or to be lost. The transition from trapping to Shabansky-orbit and to the lost region for energetic protons is more sporadic and mixed than those for electrons. This is mainly due to the much larger gyro-radii of protons. We also derived the SOAMs in a more compressed quiet-time magnetosphere, in which the stretching of the tail causes the Shabansky-orbit region to move closer to Earth. Combining 3D particle tracing and global MHD simulation provides an integrated view of 3D energetic particle transport inside Earth's magnetosphere.

In the current computational model, atmospheric loss cone is not included. The SOAM will be affected in the bottom part below pitch angle = 10 degree if the loss-cone effects are included. Future work will be to study dependence of SOAMs on multi-parameters of the solar wind conditions and during magnetic storm and substorm events, and the populating the cusp by energetic particles.

Acknowledgements. X. Shao thanks National Research Council for supporting this work and P.N. Guzdar for discussions. We also thank J.G. Lyon and C.C. Goodrich for the global MHD model and discussions. Scientific computing were performed in NCSA and thunderhead cluster in NASA. This work is partially supported by NASA contract NAS 5-97059 and NASA RTOP 784-50-51-02.

REFERENCES

Birdsall, C.K. and A.B. Langdon, *Plasma Physics via Computer Simulation*, Institute of Physics Pub, 1991.

Chen, J.S., T.A. Fritz, R.B. Sheldon, H.E. Spence, W.N. Spjeldvik, J.F Fennell, S.Livi, C.T. Russell, J.S. Pickett, and D.A. Gurnett, Cusp energetic particle events: Implications for a major acceleration region of the magnetosphere, *J. Geophys. Res.*, 103, 69, 1998.

Chirikov, B.V., Particle dynamics in magnetic traps, in Kadomtsev, B.B. (Ed.), *Reviews of Plasma Physics, Vol.* 13, Consultants Bureau, New York, p. 1, 1987.

Delcourt, D.C., and J.A. Sauvaud, Populating of the cusp and boundary layers by energetic (hundreds of keV) equatorial particles, *J. Geophys. Res.*, 104, 22635, 1999.

Elkington, S.R., M.K. Hudson, M.J. Wiltberger, J.G. Lyon, MHD/particle simulations of radiation belt dynamics, *J. Atmos. Sol.-Terres. Phys.*, 64, 607, 2002.

Fedder, J.A., S.P. Slinker, J.G. Lyon, and R.D. Elphinstone, Global numerical simulation of the growth phase and the expansion onset for substorm observed by Viking, *J. Geophys. Res.*, 100, 19,083, 1995.

Fung, S.F., T.E., Eastman, S.A. Boardsen, and S.-H. Chen, High-altitude cusp positions sampled by the Hawkeye satellite, in *Proc. First Alfven Conference on Low-Latitude Magnetospheric Processes, Pergamon Press*, 22, 653-662, 1997.

Guzdar, P.N., X. Shao, C.C. Goodrich, K. Papadopoulos, M.J. Wiltberger, and J.G. Lyon, Three-dimensional MHD simulations of the steady state magnetosphere with northward interplanetary magnetic field, *J. Geophys. Res.*, 106, 275, Jan., 2001.

Kennel, C.F., *Convection and substorms, International Series on Astronomy and Astrophysics*, Oxford University Press, 1995.

Kessel, R.L., S.-H. Chen, J.L. Green, S.F. Fung, S.A. Boardsen, L.C. Tan, T.E. Eastman, J.D. Craven, and L.A. Frank, Evidence of high-latitude reconnection during northward IMF: Hawkeye observations, *Geophys. Res. Lett.*, 23, 583-586, 1996.

Li, X., I. Roth, M. Temerin, J.R. Wygant, M.K. Hudson, and J.B. Blake, Simulation of the prompt energization and transport of radiation belt particles during the March 24, 1991 SSC, *Geophys. Res. Lett.*, 20, 2423, 1993.

Northrop, T.G., *The adiabatic motion of charged particles*, Interscience Publishers, New York, 1963.

Roederer, J.G., Dynamics of Geomagnetically Trapped Radiation, *Physics & Chemistry in Space, Springer-Verlag*, New York, 1970.

Shabansky, V.P., Some Processes in the Magnetosphere, *Space Sci. Rev.*, 12, 299, 1971.

Sheldon, R.B., H.E. Spence, J.D. Sullivan, T.A. Fritz and Jiasheng Chen, The discovery of trapped energetic electrons in the outer cusp, *Geophys. Res. Lett.*, 25, 1825, 1998.

Trattner, K.J., S.A. Fuselier, W.K. Peterson, S.-W. Chang, R. Friedel, and M.R. Aelig, Origins of energetic ions in the cusp, J. *Geophys. Res.*, 106, 5967, 2001.

Young, S.L., R.E. Denton, B.J. Anderson, and M.K. Hudson, Emperical model for u scattering caused by field line curvature in a realistic magnetosphere, *J. Geophys. Res.*, 107, 1069, 2002.

Shing F. Fung, X. Shao, and L. C. Tan, NASA/GSFC, Code 632, Greenbelt, MD 20771, USA. (fung@mail630.gsfc.nasa.gov; shao@ mail630.gsfc.nasa.gov; ltan@mail630.gsfc.nasa.gov)

M. C. Fok, NASA/GSFC, Code 690, Greenbelt, MD, 20771, USA. (mei-ching.h.fok@nasa.gov)

K. Papadopoulos, Department of Astronomy, University of Maryland, Greenbelt, MD 20742, USA. (kp@spp.astro.umd.edu)

M. Wiltberger, NCAR, Boulder, CO 80301, USA. (wiltbemj@ucar.edu)